1-9051

Energy, Mines and Resources Canada
Énergie, Mines et Ressources Canada

CANMET
Canada Centre for Mineral and Energy Technology
Centre canadien de la technologie des minéraux et de l'énergie

PROGRESS IN SOLID ELECTROLYTES

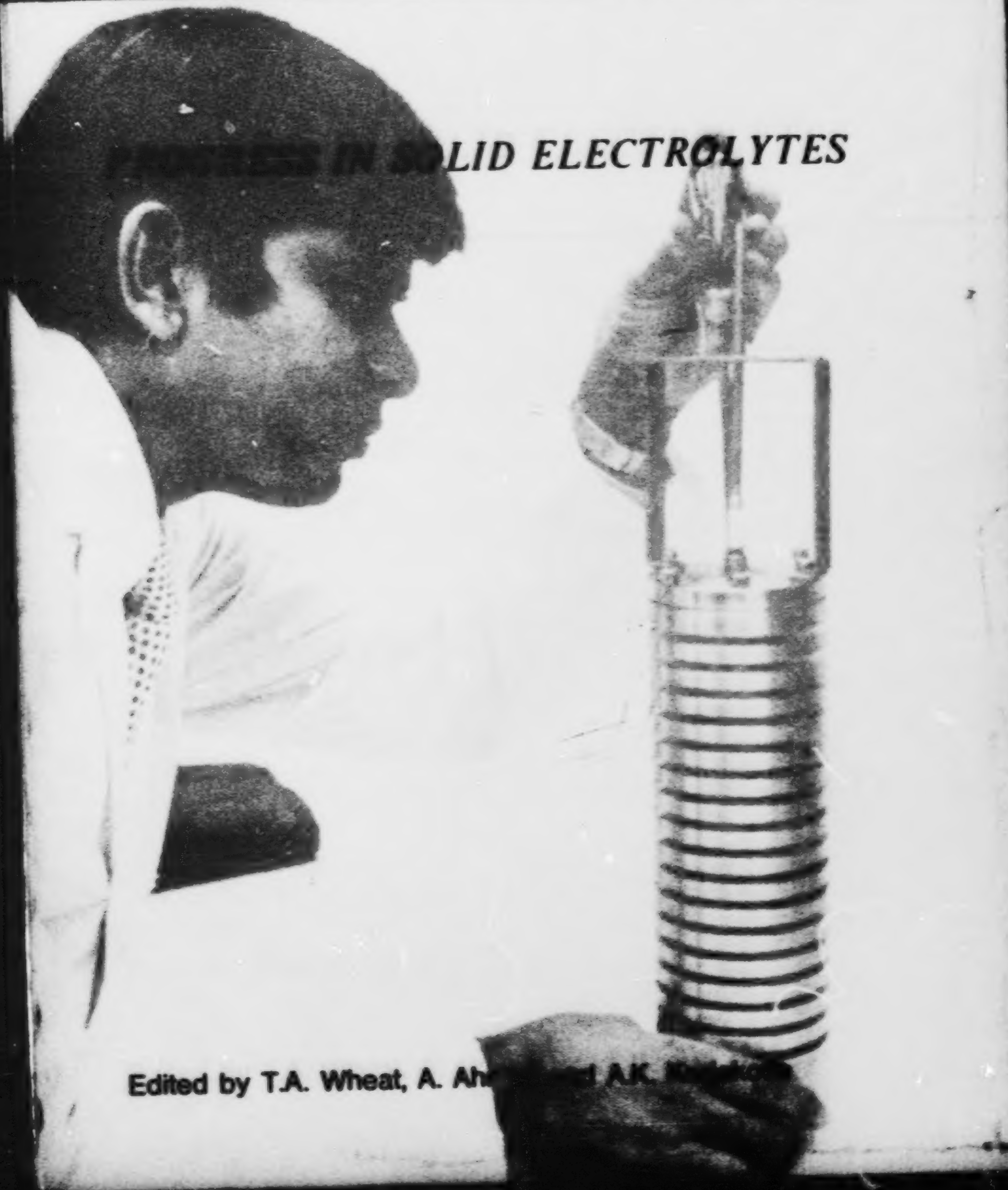

Edited by T.A. Wheat, A. Ahmad and A.K. Kuriakose

For additional copies write to:

The Editors,
Energy, Mines and Resources Canada
555 Booth Street
Ottawa, Canada
K1A 0G1

Cover Photo: Laboratory scale thermoelectric generator
(Courtesy Almax Industries Ltd., Lindsay, Ontario)

REQ. NO. 1-9051

PROGRESS IN SOLID ELECTROLYTES

CONTRACT REPORT NO. OSQ81-00102

Edited by T.A. Wheat, A. Ahmad and A.K. Kuriakose

CONTRACTOR: ASCOR

MICROMEDIA
DEC 22 1983

591 pp

ENERGY, MINES AND RESOURCES
OTTAWA, CANADA
ERP/MSL 83-94 (TR)

FOREWORD

Although the field of solid electrolytes has been the subject of fundamental research for many years, there has been an increasing interest in the development and commercial exploitation of a number of these materials in recent years. Latterly, this interest has been further stimulated by the growing appreciation of the need for more sophisticated energy and environmental management.

It is for these reasons that the CANMET laboratories together with many others around the world have been associated with the research and development of the various aspects of this rapidly growing group of materials. Although our own interests in the Department tend to be focussed on those applications related to the energy and minerals industries, it is characteristic of the broader scope of the field to note the references within this volume to the various electrical devices that are being examined as well as components directly related to the quality of life such as heart pacemaker batteries which have become commercially available.

Such advances are the result of many years' research in this and related fields and an important aspect of those efforts is the benefit derived from the transfer of ideas and information among the growing research community. It is the purpose of this volume to contribute to that exchange.

W.A. Gow,
Director

AVANT-PROPOS

Bien que depuis nombre d'années le domaine des électrolytes solides fasse l'objet de recherches fondamentales, on constate au cours des dernières années un intérêt de plus en plus marqué dans le développement et l'exploitation commerciale de ces matières. Dernièrement, une conscience croissante du besoin d'une gestion plus avancée de l'énergie et de l'environnement a stimulé cet intérêt encore plus.

Par conséquent, les laboratoires CANMET, ainsi que d'autres laboratoires partout dans le monde, se sont consacrés à la recherche et au développement des différents éléments de ce groupe de matières en pleine croissance. Bien que les propres interêts du ministère tendent à se concentrer sur les emplois éventuels relatifs aux industries de l'énergie et des minerais, il est caractéristique de la portée plus étendue de ce domaine de prendre note des références contenues dans ce livre au sujet des divers appareils électriques à l'étude ainsi qu'aux composants qui portent sur la qualité de la vie comme, par exemple, la disponibilité de piles pour "pace makers" pour patients cardiaques.

Un tel progrès est le résultat de nombreuses années de recherche dans ce domaine et dans des domaines connexes. Un élément très important de ces efforts est l'avantage fourni par les échanges d'idées et d'information dans la communauté de recherche qui ne cesse pas de croître. L'objectif de ce livre est de contribuer à cet échange d'information.

W.A. Gow
Directeur

PREFACE

This volume brings together comprehensive state-of-the-art papers on the recent developments in understanding and using solid electrolytes. Internationally recognized experts were invited by CANMET to contribute papers on selected topics in this rapidly expanding field. To expedite publication, this volume has been printed directly from the manuscripts as received from the authors and hence they are responsible for the opinions expressed.

In seeking contributions to this volume, an attempt was made to strike a balance between research- and development-oriented topics and hence the papers are loosely grouped under the general headings of behaviour (first cationic then anionic conductors) and applications. Collectively, they provide a current picture of the R&D in this field; in part, they reflect the significant developments that have occurred in recent years leading to commercial exploitation and, in part, they also indicate the challenges of the future.

The editors wish to thank the authors for their efforts and for the high quality and comprehensive nature of their papers. Particular thanks are due to members of ASCOR staff for their assistance in planning and expediting this publication. Lastly, thanks are also due to others who reviewed the initial scripts and offerred their comments prior the completion of the final 'camera ready' manuscripts.

May 1983

T.A. Wheat
A. Ahmed
A.K. Kuriakose

PRÉFACE

Ce livre réunit des mémoires complets portant sur la situation actuelle des derniers développements dans la compréhension et l'emploi des électrolytes solides. CANMET a invité des experts de renommée internationale à écrire des mémoires au sujet des certaines matières choisies de ce domaine en expansion rapide. Afin d'en accélerer la publication, on a fait imprimer les manuscrits dans leur état original. Par conséquent les opinions renfermées dans ce livre sont celles des auteurs telles qu'ils nous les ont presentées.

En cherchant des contributions à ce livre, nous avons essayé de maintenir un équilibre entre les matières de recherche et de développement. Donc, les mémoires sont rassemblés par groupes sous les rubriques générales de comportement (premièrement les conducteurs cationiques, puis les conducteurs anioniques) et d'usage. Ensemble, ils forment une représentation courante de la recherche et du développement dans ce domaine. En plus d'être le reflet des développements importants qui ont eu lieu au cours des années récentes et qui ont resulté en l'exploitation commerciale, ils indiquent également les défis que l'avenir va certainement nous lancer.

Les rédacteurs tiennent à remercier les auteurs de leur travail ainsi que de la haute qualité et l'essence compréhensive de leurs mémoires. On remercie tout particulièrement le personnel de l' ASCOR de leur aide dans la planification et la réalisation de cet ouvrage. En dernier lieu, nous désirons remercier tous ceux qui ont étudié les premières ébauches et qui nous ont offert leurs commentaires avant la préparation finale des "bleus".

T.A. Wheat
A. Ahmad
A.K. Kuriakose

Mai 1983

TABLE OF CONTENTS

FOREWORD i

AVANT-PROPOS ii

PREFACE iii

PRÉFACE iv

1. Nuclear Magnetic Resonance Studies in Solid Electrolytes
D. Brinkmann 1

2. Structure Studies, Potentials and Diffusion Paths of Fast Ionic Conductors
H. Schulz 27

3. Framework Structures for Na$^+$-Ion Electrolytes
J.B. Goodenough 53

4. Nasicon and Related Compounds: A Review
J.P. Boilot, G. Collin and Ph. Colomban 91

5. Sodium Ion Conductive Ceramics
K. Chu-Kun 123

6. Effect of Processing on Nasicon
A.K. Kuriakose, A. Ahmad and T.A. Wheat 141

7. The Deterioration of Sodium β/β''-Alumina Electrolytes in Sodium Environments
P.S. Nicholson 169

8. Particle Hydrates as Proton Conductors
P.J. Wiseman 197

9. Solid Silver and Copper (I) Ion Conductors and Their Applications
T. Takahashi 221

10. Silver Solid Electrolytes
B. Scrosati 257

11. Oxide Electrolytes with Fluorite Structure
E.C. Subbarao and H.S. Maiti 281

12. Electrical Properties of Ceramic Solid Solutions Based on Ceria
K. El Adham and A. Hammou 313

13. Anionic Conductivity in Oxides with the Fluorite and Related Structures
J.A. Kilner and J.D. Faktor 347

14. Determination of F^- Pathway by Neutron Diffraction Technique in Fluorite Type Fluorides: MF_{2+n}
J.M. Reau, S.F. Matar and J.L. Soubeyroux 391

15. Fluorite-Type Solid Electrolytes as Oxygen ion and mixed Conductors
B. Cales and A.M. Anthony 413

16. Kinetic Investigations with Solid Electrolytes
H. Rickert and G. Holzäpfel 441

17. Electrolytes for All-Solid-State Lithium Batteries and Hydrogen Fuel Cells
J. Jensen 473

18. The Lithium/Iodine Solid Electrolyte Pacemaker Battery
C.F. Holmes 489

19. The Development of Beta-Alumina Probes
A.D. Pelton, A. Dubreuil and M. Malenfant 503

20. Development of Sodium Solid Electrolyte Ceramics and Evaluation of Their Stability in Energy Conversion Devices
S.E. Prasad, R. Roy, K. El-Assal and M.K. Murthy 529

21. Static and Dynamic Properties of ZrO_2 Oxygen Sensor
C.T. Young 549

INDEX 581

NUCLEAR MAGNETIC RESONANCE STUDIES IN SOLID ELECTROLYTES

D. Brinkmann

Physics Institute, University of Zurich
Zurich, Switzerland

ABSTRACT

This paper is divided into two parts. In the first, we present those nuclear magnetic resonance (NMR) principles which are most frequently employed in studies of solid electrolytes. The following topics are discussed: the second moment and the chemical shift; the splitting of resonance lines due to quadrupole interactions; motional narrowing of NMR lines; the direct determination of the self-diffusion coefficient; relaxation times, particularly those arising from dipolar and quadrupolar coupling; correlation functions and their relation to diffusion models; effects due to parmagnetic impurities.

In the second part, some representative solid electrolytes such as Li_3N, Li_xAl_{1-x}, β-eucryptite, β-alumina, $RbAg_4I_5$, and PbF_2 are considered to demonstrate what kind of information on fast ion transport NMR may provide. The various kinds of information concern structural aspects such as site symmetries, site occupancies, presence of defects, changes of these paramaters at phase transitions and details of the dynamics. Here, NMR allows to determine activation energies, hopping times, self-diffusion coefficients, to discriminate between different types of motion and to detect dimensionally restricted motion or collective movements.

KEYWORDS: Self-diffusion and ionic conduction in nonmetals, nuclear magnetic resonance and relaxation.

RÉSUMÉ

Cette publication est divisée en deux parties. Dans la première partie nous passons en revue les méthodes de la résonance magnétique nucléaire (RMN) les plus couramment utilisées dans l'étude des electrolytes solides. Nous traitons les points suivants: second moment et le déplacement chimique; la décomposition des raies de résonance par les effets quadrupolaires; le rétrecissement par mouvement des lignes de résonance; une méthode directe de détermination du coefficient de self-diffusion; les temps de relaxation en particulier la relaxation due aux couplages dipolaires et quadrupolaires; les fonctions de corrélation et leurs relations avec les modèles de diffusion; les effets dûs aux impuretés paramagnetiques.

Au cours de la seconde partie nous passons en revue quelques électrolytes solides typiques tels que Li_3N, Li_xAl_{1-x}, l'eucryptite-β, l'alumine-β, $RbAg_4I_5$ et le PbF_2 afin de donner des détails sur le genre d'informations concernant le déplacement rapide des ions que peut nous livrer la RMN. Les renseignements ainsi obtenus concernent les aspects structurels tels que la symmetrie des sites cristallins, l'occupation ou la vacance de ces sites, la présence de défauts, les changements de tous ces paramètres lors de transition de phase ainsi que la dynamique de ces transitions. La RMN permet de déterminer l'énergie d'activation, les temps de sauts, le coefficient de self-diffusion. La RMN permet en outre de discerner entre les différents types de mouvement, de détecter des mouvements limités par la dimensionalité ou des mouvements collectifs.

INTRODUCTION

Nuclear magnetic resonance (NMR) is a spectroscopic method which can be used as a tool to probe the properties of condensed matter at the atomic level. NMR therefore has participated in the investigation of fast ion transport in solids right from the beginning of this new research field although extensive NMR studies are rather recent. In these activities NMR has proved to be a powerful technique not only complementing other methods but also providing information on the structure and dynamics of solid electrolytes which may not be available otherwise.

These applications of NMR in solid electrolyte studies have been well documented in several review articles. Reference (1) summarizes the activities before 1977. A thorough coverage of the years 1977, 1978, and early 1979 is given in Ref. (2) which also contains an extensive discussion of the motional correlation functions. The same period is also briefly reviewed in Ref. (3) together with a short summary of the standard NMR theory and the type of information it may yield in solid electrolytes and solid solution electrodes. In a similar way Ref. (4) deals with the next period till early 1981. Finally, there are articles of more general character (5,6) which emphasize the interpretative aspects of NMR.

With these reviews given the present paper is organized as follows. The first section discusses basic NMR principles and their relevance in solid electrolyte studies, it tries to convey the present state of the art of NMR work in this field. Special attention is paid to techniques or models which originated from the interest of NMR research in solid electrolytes. In the second section we review representative and illustrative NMR studies in solid electrolytes. Some examples are taken from the literature which appeared after 1980 thus bringing up to date at least partly the other reviews. However, we will also refer to significant older papers and to work not yet published.

Since several excellent text books on NMR exist of both comprehensive (7) and introductory (8,9) character, reference to them is only occasionally given as long as only basic principles are discussed.

PRINCIPLES OF NMR IN SOLID ELECTROLYTE STUDIES

Rigid lattice linewidth and splittings

We consider an ensemble of atomic nuclei with spin $\vec{I}$ and magnetic moment $\vec{\mu} = \gamma\hbar\vec{I}$ in a solid electrolyte single crystal. The gyromagnetic ratio γ is a characteristic constant of each magnetic isotope by which different nuclei are easily distinguished. To begin with, we assume $I = 1/2$ (i.e. nuclei such as H, F, Ag) and a rigid lattice, i.e. all atoms are stationary. If the spins are placed in a large static magnetic field H_o (which defines the z direction of a reference frame) and an oscillating field H_1 of angular frequency ω is applied in the x direction, resonance absorption is observed for $\omega = \omega_o = \gamma H_o$ where ω_o is the Larmor frequency. However, the NMR signal is not infinitely sharp because neighboring spins and unpaired electrons of paramagnetic impurities cause a local magnetic dipolar field which is added vectorially to $\vec{H}_o$. Since the local field depends on the arrangement of the neighboring spins, i.e. on the crystal structure, and on the orientation of the crystal in the external field H_o, there is a distribution of resonance frequencies and hence a finite linewidth $\Delta\omega$ (about 1-10 kHz).

The structural information contained in the linewidth may be obtained by determining the second moment, $\langle\Delta\omega^2\rangle$. It is defined as the mean square width of the resonance line measured from the center. $\langle\Delta\omega^2\rangle$ may be calculated for both single crystals and polycrystalline samples (7-9). If it happens that in a unit cell two spins, for instance the H nuclei in H_2O, are well separated from other pairs and other magnetic moments, the dipolar interaction within the pair will dominate all other interactions and cause a splitting of the resonance line. In the case of H_2O, the splitting of the H resonance in two lines is known as the Pake doublet whose frequency separation depends on the distance of the H nuclei and the orientation of the H-H bond with respect to H_o.

The linewidth $\Delta\omega$ can be measured either by a continuous wave (c.w.) experiment where essentially ω is swept through resonance or by a pulsed experiment in which an intense H_1 field, applied only for a short time, tilts the macroscopic nuclear magnetization by 90° into the xy plane. Due to the spread of Larmor frequencies the precessing individual spins get out of phase and hence the transverse magnetization decays to zero with a time constant T_2 called the transverse relaxation time. In a solid, T_2 is of the order 1-100 µs. The signal induced by the precessing magnetization is called free induction decay (FID) which is the Fourier transform of the c.w. signal. Therefore, $T_2 \sim 1/\Delta\omega$. For the rigid lattice one can show (7,8) that $\Delta\omega = A <\Delta\omega^2>^{1/2}$ where A is a constant of order unity depending on the particular line shape function.

If the external field H_o is not homogeneous an additional dephasing of the individual spins takes place which falsifies the T_2 measurement, i.e. the resonance line is broadened. However, the dephasing due to H_o inhomogeneities is reversible in contrast to the irreversible dephasing arising from spin-spin interactions. Therefore, a second H_1 pulse, applied at a time Δt after the first pulse and after the disappearance of the FID, can rotate all spins 180° about the H_1 axis thus reversing that part of the dephasing which is due to H_o inhomogeneities. At a time $2\Delta t$ the spins rephase to form the so-called echo-signal whose amplitude is proportional to exp $(-2\Delta t/T_2)$. This allows a measurement of the true T_2 provided the amplitude of the H_1 field is much larger than the inhomogeneity of H_o across the sample.

A special effect arises from the magnetic hyperfine interaction between the nuclear moments and the fields induced by electronic currents in the atom which are set up by the external field H_o. This coupling causes the chemical shift which is proportional to H_o and reflects the specific electronic structure of the molecular environment of a nucleus. Although this shift is usually buried in the linewidth it may be used to get information on chemical bonding.

The information provided by NMR is considerably enhanced if nuclei with $I>1/2$ are employed, for instance Li, Na, Cu, Al. These nuclei possess electric quadrupole moments which interact with inhomogeneous electric fields, i.e. electric field gradients (EFG), thus creating an additional spin energy. As a consequence, the NMR line is split into 2I components whose frequency separation depends on the magnitude of the EFG and its orientation with respect to H_o and on the magnitude of the quadrupole moments. The EFG at the nucleus of an atom arises from charges of unfilled electron shells of the atom itself (for instance from valence electrons), from a polarization of the atomic core by the valence electrons, and from all other charges outside the atom. The EFG which vanishes at sites of cubic symmetry is very sensitive to subtle changes in the neighboring charge distribution. Knowing the EFG thus provides information about local symmetry, nature of bonding, imperfections (such as defects, vacancies, stress), order-disorder phenomena (e.g. site occupancies), and especially changes of these properties at phase transitions. In its full entirety this information can only be obtained in single crystals; investigations of powder samples lack all knowledge about anisotropies.

Motional narrowing. Determination of diffusion constant

The discussion so far was concerned with static properties of the solid since we had assumed a rigid lattice. In a solid electrolyte, however, the diffusion of ions and defects and any other thermal motion such as molecular reorientations (e.g. of NH_4^+ groups) or phonons make the magnetic and electric fields which act on the spins time-dependent. Quite often it makes no difference whether the magnetic nuclei we consider belong to the stationary or mobile species, all what matters is the fluctuating local field; nevertheless we will encounter situations where one has to distinguish between mobile and non-mobile spins. The dynamics present in the crystal cause two profound effects, "motional narrowing" of the line-width and spin-lattice relaxation, the study of which allows NMR to elucidate details of the dynamical process. We start with a discussion of motional narrowing.

Let us assume that nuclei having $I = 1/2$ perform a long-range diffusion between different lattice sites which are distinguished by the instantaneous value of the local magnetic field. When the average time τ a nucleus spends at a site becomes comparable to the rigid lattice value of T_2 the nucleus "samples" many local fields resulting in a total decrease of the spread of the Larmor frequencies: the average $\Delta\omega$ is reduced and T_2 becomes larger. If τ is so small that $<\Delta\omega^2>^{1/2}\tau<<1$ where $<\Delta\omega^2>$ is again the rigid lattice second moment, one can show (7,8) that $1/T_2 \approx <\Delta\omega^2>\tau$. The minimum τ which can be measured by this method is determined by the homogeneity of the H_0 field. Unless high resolution techniques are used the minimum τ is about 10^{-7}s. Somewhat smaller values can be obtained if T_2 is deduced from the echo amplitude. Even shorter τ's are delivered from spin-lattice relaxation rates to be discussed later.

Quite often τ is described by an Arrhenius law, $\tau = \tau_0 \exp (E/kT)$, where E is the activation enthalpy of the hopping process and $1/\tau_0$ is the "attempt frequency" which is usually of the order of an optical phonon frequency ($10^{12} - 10^{13}$Hz). So, measuring the temperature dependence of T_2 yields E. Since the increase of T_2 usually takes place in a small temperature interval the E values obtained are less precise than those one can extract from spin-lattice relaxation measurements.

Related to the motional narrowing effect is the chemical exchange by which spins jump randomly back and forth between two sites with different local magnetic fields or EFG's. For instance, if the protons of different water molecules are exchanged at a rate which is much larger than the frequency separation of the two lines of the Pake doublet the spins "see" an averaged local field and the doublet signals coalesce into a single line. Similarly, if nuclei having a quadrupole moment jump between sites with different EFG's the quadrupole multiplet structure is changed.

If the mobile species in a solid electrolyte have magnetic nuclei the diffusion constant D of the solid can be measured directly by NMR employing the 90°-180° pulse sequence mentioned before to detect a spin-echo. Several procedures are known, one of the most satisfactory versions is the pulsed-gradient method (10). An external magnetic field gradient is applied in two pulses: one between the two H_1-pulses, the second between the 180°-pulse and the echo. The first gradient pulse produces an almost instantaneous phase shift of all precessing spins. If the spins would not diffuse, the 180° H_1-pulse and the second gradient pulse would exactly undo the effect of the first gradient pulse and the echo amplitude would be solely determined by T_2. Diffusion, however, causes the rephasing to be incomplete and the echo amplitude is attenuated allowing a determination of D. Only the changes of spins in space due to diffusion occuring between the two gradient pulses are important. Thus the pulsed-gradient experiment provides a precise definition of the time during which diffusion is being observed. By this method a value $D = 10^{-13} m^2/s$ for Ag in $RbAg_4I_5$ has been obtained (11).

Relaxation. BPP model

The richest source of information for NMR studies in solid electrolytes is the relaxation behavior of NMR signals, in particular the spin-lattice relaxation. Generally, relaxation describes the approach of the nuclear spins to thermal equilibrium. The transverse relaxation time T_2 introduced above is the time constant of the process which removes any transverse magnetization. It leads to an internal equilibrium of the spin-system described by a spin-temperature, i.e. a Boltzmann distribution among the Zeeman levels. In this process no energy is transfered between the spin system and the "lattice" by which we mean all degrees of freedom of a material except the spin system. The longitudinal or spin-lattice relaxation time T_1 is the time constant of the recovery of the longitudinal magnetization (parallel to H_0), for instance, after the perturbation by an 90°H_1 pulse. In this process energy is exchanged with the lattice and the spin system attains the lattice temperature. T_1 is conveniently measured by a 180° - 90° pulse sequence. The first pulse inverts the equilibrium magnetization and the second pulse measures the subsequent recovery which is quite often exponential. T_1 values may range from 30 μs for ^{127}I at the α-β phase transition in Ag I (12) to 10 s for ^6Li in Li_3N at 300 K (13). In a solid, T_1 is usually much longer than T_2.

A successful relaxation mechanism requires a time-dependent interaction acting on the spin system. There are two types of interactions which are significant in solid electrolytes: (i) magnetic spin-spin coupling either between like nuclear spins or between unlike spins (especially a nuclear spin and the electron spin of a paramagnetic impurity), and (ii) electric coupling between the quadrupole moment and an electric field gradient (EFG). The fluctuation of these couplings are brought about by the thermal motions present in the sample especially, of course, by the diffusion of either the nuclei under consideration or the other atoms. In the semiclassical theory of relaxation (7,8,14) the fluctuating part of the interaction Hamiltonian is treated as a perturbation of the static Zeeman Hamiltonian. The diagonal elements of the perturbation matrix cause a time-dependent modulation of the spin energy levels and therefore affect the z component of the local magnetic field thus yielding a contribution T_2' to the transverse relaxation time T_2. The off-diagonal matrix elements induce transitions between the levels and are responsible for the magnitude of T_1. However, they also affect the linewidth since they limit the lifetimes of the energy levels. The expression for T_2 is therefore $1/T_2 = 1/T_2' + 1/(2T_1)$. In conclusion, fluctuations at zero frequency are only effective for T_2 while fluctuations at the Larmor frequency influence both T_1 and T_2.

The fluctuating interaction can be described by a random function F(t) which depends upon time-dependent lattice variables. Then a correlation function of the form $G(t) = \langle F(t)F^*(0)\rangle$ is constructed which measures the persistence of the fluctuations and contains all the dynamical information one would like to obtain from the solid electrolyte. The relaxation rates $1/T_1$ and $1/T_2$ are proportional to various spectral densities $J(\omega)$ which are the Fourier transforms of different correlation functions. A simple form of $G(t)$ widely and very often successfully applied in NMR has been given in an early paper on relaxation by Bloembergen, Purcell, and Pound (15). This so-called BPP model assumes that $G(t) \sim \exp(-t/\tau_c)$, where τ_c is the correlation time of the fluctuations. For dipolar coupling between like spins the BPP theory yields

$$1/T_1 = C^2\{\tau_c/(1+\omega_0^2\tau_c^2)+4\tau_c/(1+4\omega_0^2\tau_c^2)\} \qquad (1)$$

$$1/T_2 = C^2\{\tfrac{3}{2}\tau_c+ \tfrac{5}{2}\tau_c/(1+\omega_0^2\tau_c^2)+\tau_c/(1+4\omega_0^2\tau_c^2)\} \qquad (2)$$

where C^2 being proportional to $\langle\Delta\omega^2\rangle$ is a measure for the strength of the interaction. Eqs. (1,2) are only valid for T_1, $T_2 \gg 2\pi/\omega_0$ (weak collision limit). In addition, Eq. (2) only holds for $\langle\Delta\omega^2\rangle^{1/2}\ \tau_c \ll 1$. For $\langle\Delta\omega^2\rangle^{1/2}\ \tau_c \gg 1$ we have $1/T_2 = \langle\Delta\omega^2\rangle^{1/2}$. If the relaxation is caused by diffusion, τ_c is usually identified with the mean residence time τ of an ion.

Fig. 1 shows the relaxation rates of Eq. (1) and (2) as a function of $\omega_0\tau_c$ which is proportional to $1/T$ if τ_c is thermally activated like $\tau_c = \tau_{co}\exp(E/kT)$. At high temperatures, i.e. for $\omega_0\tau_c \ll 1$, we have $1/T_1 = 1/T_2 = 5C^2\tau_c$ and the slope of both curves (in the log-log presentation) is E/k. At low temperatures, i.e. for $\omega_0\tau_c \gg 1$, $1/T_2$ approaches the rigid lattice value and $1/T_1$ becomes frequency dependent according to $1/T_1 = 2C^2/\omega_0^2\tau_c$ where the slope is now $-E/k$. $1/T_1$ has a maximum for $\omega_0\tau_c \approx 0.656$. To obtain reliable values for E and the prefactor τ_{co} one should fit Eq. (1) to the experimental data over the whole temperature range where data are available. Since $1/T_1$ peaks near $1/\tau_c \approx \omega_0 \approx 10^8\,s^{-1}$ the fit may yield correlation times in the range 10^{-6} to 10^{-10}s thus extending the range of values extracted from the motional narrowing method. Of course, the analysis of a certain relaxation process can only be meaningful if other relaxation mechanisms can be neglected. If different mechanisms are independent of each other the rate measured can in principle be decomposed according to $1/T_1 = (1/T_1)_a+(1/T_1)_b+\ldots$ where a, b,... denote different mechanisms.

For completeness, Fig. 1 also exhibits the temperature dependence of the relaxation rate $1/T_{1\rho}$ in the rotating frame. This frame of reference is defined by that component of the oscillating H_1 field which rotates around the H_0 direction in the same sense as the precession of the magnetization. $1/T_{1\rho}$ has a maximum near $\gamma H_1\tau_c \approx 1$. Since $\gamma H_1 \approx 10^5\,s^{-1}$ the range of τ_c values which may be probed by NMR is thus extended to larger values, i.e. to slow motions. Although this technique has been successfully applied in solids with low ionic conduction (17), it has not yet played a major role in solid electrolytes.

Diffusion models and dipolar correlation functions

To obtain from NMR relaxation information about microscopic details of the diffusion process involves two problems. First, one has to select an appropriate model to describe the diffusion process, second, the correlation function G(t) must be calculated. Since generally G(t) is a very complicated function involving correlations among both distinguishable particles and lattice sites (6) most studies are concerned with magnetic dipolar interaction. In this case one obtains two-particle correlation functions no matter whether the resonant nuclei are mobile or stationary. The literature on dipolar relaxation is enormous, we can only briefly summarize the main results. Ref. (2) gives a fairly detailed review of the literature up to early 1979.

The first improvement of the BPP model is due to Torrey (18) who introduced the random walk model which assumes independent movements of the spins in the lattice. This model was applied to polycrystalline samples yielding isotropic results. Further progress which is mainly due to the work of Barton and Sholl (19), Wolf (14), and Fedders and Sankey (20) was achieved by explicitly taking into account the discrete character of the crystal structure and the correlations between the motions of the spins. All authors essentially employed the so-called simple-hopping model of spin motion. In this model (21) it is assumed that the probability of a spin to hop from a site A to a neighboring vacant site B depends neither on the time nor the occupancy of sites other than A and B. The correlations are considered in different approximations. For instance, the monovacancy model of Wolf is exact if the concentration c of vacancies goes to zero, the multiple scattering approximation of Fedders and Sankey is exact for $c \to o$ and $c \to 1$.

For the calculation of the correlation functions the various authors have developed different techniques (19). The results usually exhibit mathematical complexity and cannot be presented in closed form. However, these three-dimensional (3D) models of hopping diffusion make similar predictions as the BPP model does. Especially the maximum value of $1/T_1$ and the value of $\omega\tau_c$ where it occurs differ by about a factor of 2 for the various models. The shape of the relaxation curve near the maximum and its width are influenced by details of the respective model. Therefore, in many cases the accuracy of the experimental data is not sufficient to unambiguously detect deviations from the simple BPP behavior or to distinguish among the more sophisticated models.

Almost always it has been assumed that the hopping particles do not interact with each other except that multiple occupancy of a single site is forbidden. Very recently, Fedders (23) has included short-ranged interaction in the calculation of the correlation function. He finds that at high frequencies T_1 is increased by a factor of 6 from its value for non-interacting particles.

Limiting behavior of T_1. Dimensionality effects

Theoretical results which do not depend on special approximations are important for analyzing experimental data, in particular when checking whether ionic motion is confined to one or two dimensions (1D or 2D). There exist exact results for the behavior of T_1 in the limiting situations $\omega\tau_c \ll 1$ and $\omega\tau_c \gg 1$, i.e. for the high- and the low-temperature side of the T_1 minimum. Richards (6) has presented such results for the hopping diffusion of non-interacting ions. For both magnetic and quadrupolar relaxation T_1 is proportional to $\omega^2\tau_c$ under the condition $\omega\tau_c \gg 1$ but independent of dimensionality. A dimensionality effect is expected in 1D and 2D systems at long times when the correlation functions decay more slowly since the particles have an increased probability to come back to an original position. Thus, for $\omega\tau_c \ll 1$ one finds $T_1 \sim (\omega/\tau_c)^{1/2}$ for 1D, $T_1 \sim [\tau_c \ln(1/\omega\tau_c)]^{-1}$ for 2D, and $T_1 \sim \tau_c^{-1}$ for 3D.

Recently, Sholl (22) has published a detailed analysis of the limiting behavior of the spectral densities $J(\omega)$ in liquids, cubic systems and 2D and 1D systems assuming magnetic dipole interaction between like spins. He obtains the same results as listed above and derives expressions for the proportionality factors which do not depend on ω. These coefficients are correct for any diffusive model whose long-range, long-time behavior may be described by the diffusion equation.

Quadrupole relaxation

So far we were mainly concerned with relaxation due to a modulation of the magnetic dipolar interaction. However, for spins with $I>1/2$ the time dependent fluctuations of the quadrupole interaction due to ionic motions are a powerful relaxation mechanism which usually dominates the magnetic relaxation. (Here we will neglect quadrupole relaxation due to lattice vibrations.) For a well resolved quadrupole spectrum of 2I lines (assuming half-integer spins) the relaxation is not describable by a single relaxation time (24). Generally, there are 2I time constants. Only when the spacing of the NMR lines becomes comparable to the dipolar linewidth a common temperature of the spin system is established and a single relaxation time will be observed. If furthermore a powder average is taken, one obtains (25) for $\omega\tau_c \ll 1$: $T_1/T_2 = (1/4)(I+1/2)^2$.

The correlation function G of the quadrupole interaction depends on whether the nuclei under consideration are stationary or mobile (6). An example of the first case is the relaxation arising from the diffusion of a charged point defect, for instance an impurity or interstitial ion or a vacancy. Then G depends on the site occupancy only because the mobile ions whose charge cause the field gradient fluctuations are indistinguishable particles. This problem is mathematically identical with the corresponding problem of dipolar relaxation due to diffusing ions (16). In the case of relaxation of mobile nuclei, the correlation functions involve correlations among both distinguishable particles and sites. Under certain assumptions (6) these functions can be reduced to either distinguishable particle or distinguishable site correlation functions.

Paramagnetic impurities

Doping of solid electrolytes with paramagnetic ions (e.g. Mn, Fe) can provide several types of information. First, the large effects of the paramagnetic ions on the NMR linewidth allows a "tagging" method (26) to determine which species is diffusing. Second, relaxation of mobile nuclei by stationary paramagnetic ions can be very effective because a mobile ion can easily diffuse into the vicinity of an impurity where it is relaxed. Since only single-particle motion is involved the method is well suited to probe hopping processes. Richards (27) has treated the relaxation by paramagnetic ions for a range of temperatures and for both nearest-neigbor and long-range dipolar interactions employing a discrete hopping model for the former and classical diffusion for the latter. As examples, he treated linewidth data in PbF_2: Mn and T_1 and T_2 data in Li_5AlO_4.

Richards (28) has further shown that relaxation due to paramagnetic ions in 1D systems is considerably different from that in 3D systems. In a perfect 1D system, within the framework of a random walk model, $1/T_1$ and

$1/T_2$ are proportional to c^2 (c = impurity concentration) at temperatures below the T_1 minimum. This contrasts with 3D systems where both rates show linear dependence upon c. In addition, in 1D the relaxation is highly non-exponential, i.e. not describable by a single T_1. In praxis, however, solid electrolytes such as eucryptite or hollandite are never ideal 1D systems. In such quasi-1D systems one has to allow for some small inter-channel hopping rate $W_\perp$ in addition to the rate $W_\parallel$ for hopping along the chains. For $(W_\perp/W_\parallel)>>c^2$, Richards (29) predicts $1/T_1 \sim c$. A detailed account of the calculation of approximate solutions for the continuum diffusion equation is presented in (30).

EXAMPLES OF NMR STUDIES IN SOLID ELECTROLYTES

The main objective of this section is to discuss representative NMR studies of solid electrolytes in order to illustrate what kind of information NMR yields by employing the principles we have presented in the first section. It is impossible to give a complete survey of the present literature. So we will only partly update the various review articles mentioned before. The examples are arranged according to substances.

Li_3N

The relative simple structure of this compound makes it very attractive for NMR studies. We will discuss recent NMR investigations (31) in which the resonances of both the stationary ^{14}N nuclei (with I = 1) and the mobile ^6Li (I = 1) and ^7Li (I = 3/2) were studied. To employ both Li isotopes deepens the insight and allows a double check of many results. All three resonances are split by quadrupole interaction. Based on a point-ion model, the electric field gradient (EFG) tensors at the two Li sites were calculated (32) and were found to be of the same order of magnitude as the experimental values thus supporting the conclusions of Schwarz and Schulz (33) that Li_3N is composed of Li^+ and N^{3-} ions. The different signs of the EFG's are in accord with conclusions drawn from the high-temperature behavior of the ^7Li quadrupole splitting. Lewis and Schwarzenbach (34) have calculated the EFG's from x-ray data and have refined the parameters of the multipole deformation functions against x-ray and NMR data simultaneously. For the EFG's of Li(1), Li(2), and N they have obtained the sign combination +, -, - in agreement with the point-ion model. However, N appears to be strongly polarized perpendicular to the hexagonal c axis whereas the NMR chemical shift of ^{14}N (32) suggests a deformation parallel to c.

The ion dynamics were studied in terms of two diffusion processes (31). The intralayer process which involves Li(2) ions of the Li_2N layers only was investigated via ^6Li and ^7Li relaxation. T_1 was calculated assuming an independent and isotopic diffusion of vacancies in these layers. The treatment is similar to the 3D example discussed in (16). From the fit to the experimental data the vacancy concentration was estimated in fair agreement with the value of ≈ 1 % deduced from X-ray data (35). The second diffusion process, although not independent from the first one, consists of the hopping of Li ions between sites (1) and (2) (interlayer diffusion). Thus the Li nuclei "see" a strongly fluctuating EGF (even changing its sign) which causes a temperature-dependent second-order quadrupolar shift of the central signal of the ^7Li spectrum. Similar to the treatment of the ^{23}Na shift in β-alumina (36,37,2) this shift is calculated assuming an exponential decay of the EFG correlation function. The correlation time τ_c is identified with the mean residence time of the hopping Li ions. The same model allows a calculation of the single ^6Li and the double ^7Li relaxation rate. The latter is in agreement with the experimental data and the general theory (24). All three sets of data yield essentially the same values for τ_c from which one obtains 0.62 eV for the barrier height of the vacancy migration (in agreement with the conductivity value) and 0.2 eV for the formation enthalpy of a vacancy. The consistency of the three sets of data proves the existence of the interlayer diffusion which is essential for the conductivity along the c-axis. This result is at odds with x-ray studies (35) which claim that only Li(2) ions are involved in this process.

Li_xAl_{1-x}

In this compound fast ionic motion is accomplished by vacancies (V_{Li}) on the Li sublattice which are permanently present and which co-exist with antisite Li defects (Li_{Al}) on the Al sublattice. We will discuss two recent NMR studies. In the first (38), measurements of ^7Li T_1 in powders for compositions with x = 0.49, 0.50, 0.51 are reported. The T_1 curves reveal a double minimum at low temperatures and a third minimum at high temperatures. The curves are deconvoluted by assuming three independent relaxation processes. The low-temperature data are analyzed on the basis of Torrey's theory for magnetic interaction (18) which takes place between diffusing Li ions. Activation energies and diffusion constants (through the Einstein relation $D = \langle r^2 \rangle / 6\tau$) are obtained.

The Li motions responsible for relaxation are explained in terms of the two-defect model. The authors suggest that a V_{Li} is trapped in the local field of Li_{Al}. One type of motion arises from V_{Li} which are loosely bound to Li_{Al}, this type is independent of composition below 50.7 atom % Li. The other type concerns the motion of free V_{Li} and increases below 50.7 % with increasing free V_{Li} concentration. The third type of relaxation is presumably due to appreciable Al motion.

The second study (39) reports T_1 measurements of ^7Li and ^{27}Al ($I = 5/2$) for compositions ranging from $x = 0.483$ to $x = 0.545$. In the ^7Li data a double minimum is not observed although otherwise the data are nearly identical to those of (38). Again, the ^7Li relaxation is analysed with Torrey's theory, however, an additional small quadrupolar contribution is taken into account. This contribution is provided by the fluctuating electric field gradients set up by the vacancy diffusion, they also cause the ^{27}Al relaxation. The analysis of the Li and Al relaxation data yields the temperature dependence of the correlation times of the field gradients (τ_V) and the dipolar fields (τ_{Li}). The ratio τ_V/τ_{Li} is related to the vacancy concentration. The NMR measurements indicate a stronger compositional dependence of the vacancy concentration than the density method. Further, the diffusion constant calculated from τ_{Li} depends more strongly on composition than the value obtained from electrochemical studies.

β-eucryptite (LiAlSiO₄)

The NMR interest in this structure stems from its pronounced one-dimensional (1D) character of ionic motion. Single crystal studies of ^7Li, ^6Li, and ^{27}Al NMR (40,41) could reveal details of this motion. For earlier NMR work with powder samples we refer to Ref. (2,6). Up to 480 K the ^7Li quadrupole spectra display the different EFG's of inequivalent sites. At higher temperatures the spectra change into a single quadrupole splitting (one central and two satellite lines) which is explained by an exchange of Li ions among all inequivalent sites thus averaging the EFG "seen" by the Li nuclei. Therefore two diffusion processes may be distinguished: diffusion along the main and secondary channels (1D intrachannel diffusion) and hopping between different channels (interchannel diffusion). The intrachannel diffusion exhibits some cooperative features. Evidence for a collective movement of ions along the chains is based on the observation of a small splitting of the central line persisting up to 550 K which can be calculated assuming magnetic dipolar interaction between (at least) three spin-3/2 nuclei within a chain. This phenomena is finally disturbed by interchannel hopping.

These diffusion processes show up also in the relaxation behavior of ^{7}Li. From a comparison of ^{7}Li and ^{6}Li data between 560 K and 710 K it was concluded that relaxation in this temperature region is caused by diffusion of Li ions towards paramagnetic impurities. The measurements were continued with single crystals doped with iron up to about 0.15 weight % Fe. At high temperatures one observes $1/T_1 \sim c$ (c = concentration) as Richards (29) predicts when some interchannel hopping is present. At room-temperature the experiments yield $1/T_1 \sim c^{1.5}$, while for a perfect 1D diffusion $1/T_1 \sim c^2$ is expected. This subject certainly requires further investigation.

β-alumina family

This is one of the solid electrolytes most intensively studied by NMR (2). Although it is a very attractive compound because of its 2D properties its rather complex structure does not allow a straightforward interpretation of the NMR data. A controversial point has been the asymmetrv of the $1/T_1$-vs-$1/T$ curve for ^{23}Na in Na-β-alumina, $Na_2O_3 \cdot 11\ Al_2O_3$ [for references, see (2)]. The slope on the low-temperature side of the rate maximum is smaller than that on the high temperature side. This is commonly explained by invoking a distribution of activation energies (42). Bjorkstam and Villa (36,37,2) have presented an alternative approach. Within the framework of the continuous diffusion model which is mostly applied to NMR studies in liquids, they have modeled the correlation function for uncorrelated diffusion appropriate to the 2D properties of β-alumina. On this basis, with a single activation energy, they could account for the angle, frequency, and temperature dependence of the ^{23}Na transition rates, the narrowing of the ^{23}Na satellite signals, and the temperature dependence of the ^{27}Al T_1's. The Bjorkstam-Villa model has been critioized by Walstedt et al. (43) on the grounds that it ignores the considerable disorder in the conduction planes due to deviations from stoichiometry. Further, it was questioned whether the motion is entirely two-dimensional. Walstedt et al. have obtained for ^{7}Li in mixed (Na,Li) β-alumina very nearly symmetrical $1/T_1$ curves for which the 2D diffusion model is not applicable. Instead, the result is taken as a confirmation of a co-ionic conductivity effect. On the other hand, the double-peak behavior of the ^{7}Li relaxation rate in Li β-alumina was taken as evidence for a dichotomy of ionic motion.

Bjorkstam and Villa were the first to demonstrate (36,37,2) that dynamical information is contained in the temperature dependence of the second-order quadrupolar shift (see also the example Li_3N) in essentially the same manner as in T_1 or T_2 data. Recently, similar studies in β"-alumina were reported (44). Configurational changes of the mobile ion sublattice in Na β-alumina and Na β"-alumina can be inferred directly from the appearance of an additional Na line in the spectrum when the temperature is lowered (45). The new line is assigned to Na ions in ordered microdomains. In Na β"-alumina the diffusional and short-range motions are hindered in the domains as suggested by changes in the relaxation rates. Villa and al. (46) have presented NMR and Raman evidence that a change occurs in the distribution of Li atoms in Li-containing β-aluminas.

Numerous proton NMR studies have been performed in β-aluminas. Sappoval and co-workers (47) have shown that from the temperature dependence of the proton second moment in NH_4β-alumina information can be obtained on the following subjects: (i) different types of motion (local, rotational, translational), (ii) geometry of the defect which is related to the non-stoichiometry (two pairs of NH_4^+ ions in displaced mid-oxygen positions), (iii) low dimensionality effects at heigher temperatures where the second moment is motionally narrowed. Ochadlick and Story (48) have noticed that the angular dependence of the proton second moment in NH_4β-alumina can be interpreted in terms of 2D diffusion.

$RbAg_4I_5$

This compound is of particular interest because it undergoes two successive phase transitions (T_{C1} = 208 K, T_{C2} = 122 K). The former at 208 K separates the two high-conducting α and β phases. An investigation of the relaxation rates of ^{87}Rb (I = 3/2) and ^{109}Ag (I = 1/2) offers the interesting opportunity to study the Ag diffusion as seen by the stationary Rb ions or as experienced by the mobile Ag ions themselves (49). In addition, a measurement of the central line of the ^{87}Rb quadrupole spectrum around T_{C1} proved that this transition is of first order thus supporting a neutron scattering study (50) and confirming earlier NMR work [see references in (49)] but in contrast to other reports in the literature [see (50) for references].

The ^{87}Rb relaxation arises from a quadrupole interaction due to diffusing Ag ions. Two time constants were observed similar to Li_3N and in accord with the general theory (24). Except for a critical behavior near T_{C1} the data could be fitted by two BPP type relaxation rates with a single activation energy of 0.13 eV for the thermally activated Ag jump frequency. The ^{109}Ag and ^{107}Ag resonances which are difficult to measure show a large isotropic chemical shift of 0.09 %. A small orientational dependence of this shift reflects some distortion of the Ag site from cubic symmetry. The ratio T_1/T_2 is quite large ranging from 10 to 100 depending on temperature. On these grounds it was concluded that the Ag relaxation arises from the variation of the anisotropic chemical shift experienced at different sites by the moving ions. The rates (Fig. 2) were interpreted as the sum of three contributions: (i) temperature-independent relaxation due to paramagnetic impurities, (ii) BPP type relaxation with activation energy 0.13 eV, (also found in diffusion and conductivity measurements), present in both the α and β phase, (iii) BPP type relaxation rate with activation energy 0.17 eV, present only in the β phase.

At the α-β phase transition the Rb relaxation exhibits critical behavior which is already present 25 K above T_{C1}. In contrast, the Ag relaxation rate shows no precursory effects of the phase transition but a steplike increase by a factor of 2 within a temperature range of 3 K. The results were tentatively interpreted by assuming a thermally activated (0.3 eV) "trial and error" hopping (51) of the Ag ions present in the α and β phase and unaffected by the phase transition. At T_{C1} the ratio of the characteristic times of this process becomes "critical" which leads to the formation of clusters with partially ordered Ag. The assumption of clusters seems to be in agreement with the observation of reflections, forbidden for cubic symmetry, in neutron scattering studies (50). At the α-β phase transition a steplike increase of the characteristic time for the configurational response occurs. The diffusion in the β-phase as seen with tracer and conductivity methods is dominated by the configurational response time with an activation energy of 0.17 eV. However, in the relaxation rate, both the "trial and error" hopping and the configurational response process show up giving the measured temperature dependence.

The diffusion constant D of ^{109}Ag has been measured in the two isostructural components $RbAg_4I_5$ and KAg_4I_5 (11) using the pulsed-gradient method (10). The T_{C1} values are slightly different in these compounds. Fig. 3 shows that the diffusion is thermally activated with energies that were also found in conductivity measurements (52). However, the relative changes of D at T_{c_1} are larger than the corresponding changes in the conductivity data. These differences are taken as evidence for a reduced correlation of the Ag motion in the high-temperature phase.

Fluoride conductors

Among the many fluoride conductors investigated by NMR, BaF_2 is a model substance for testing the applicability of the various theories (BPP, Torrey, Wolf's encounter model) concerning magnetic dipolar relaxation due to diffusing F^- ions ($I = 1/2$). For a review on this and other anionic conductors see Refs. (2,3,4).

In PbF_2: Mn the magnetic tagging method (26) has been applied to determine which species is diffusing. Doping of PbF_2 with small amounts ($\approx$ 0.01 - 0.1 molar %) of monovalent ions (e.g. NaF) drastically increases the mobility of the F ions (53) and results in anomalies in the temperature dependence of T_1 and $T_{1\rho}$: (i) The activation energies on both sides of the $T_{1\rho}$ minimum are different in contrast to the larger and nearly equal energies found in undoped samples; (ii) There is almost no frequency dependence on either side of the T_1 minimum. These anomalies are explained (53) by a very non-uniform mobility of the F ions around the impurity atoms. Richards (30) has pointed out that these effects, where the diffusion constant may be a function of the distance, can be handled in terms of his approximate solutions of the continuum diffusion equation (30).

CONCLUSION

The discussion of both the principles and the examples of NMR investigations in solid electrolytes has shown that the NMR technique is and certainly will remain a powerful tool for the study of static and dynamic properties of these compounds. However, to avoid misinterpretations of data especially in relaxation studies, a thorough understanding of the underlying NMR principles (e.g. knowledge about the nature of the interaction mechanism) is a prerequisite. Then, NMR can provide information concerning the following aspects. (i) Screening of new materials with high conductivity and identification of the mobile species. (ii) Site symmetry and location of ions which become mobile at higher temperatures; nature of the chemical bond; site occupancy, presence of defects (vacancies, impurity ions) and their geometry. (iii) Dynamics of the mobile ions, especially the determination of activation energies, hopping times (in the range 10^{-10} to 10^{-2}s), and self-diffusion coefficients (down to 10^{-13}m^2/s); discrimination between various types of motion, for instance long-range and local motion; anisotropy of diffusion (1D and 2D effects); collective motions. (iiii) The role of phase transitions.

REFERENCES

(1) M.S. Whittingham and B.G. Silbernagel, "NMR techniques for studying ionic diffusion" Solid Electrolytes Academic Press, New York 93-107, 1977.

(2) J.L. Bjorkstam and M. Villa, "NMR and EPR studies of superionic conductors" Magnetic Resonance Review 6: 1-57; 1980.

(3) C. Berthier, "NMR investigation of solid electrolytes and solid solution electrodes" Fast Ion Transport in Solids North Holland, 171-176; 1979.

(4) D. Brinkmann, "Applications of NMR in solid electrolyte studies" Solid State Ionics 5:53-58, 1981.

(5) J.B. Boyce and B.A. Huberman, "Superionic conductors: transitions, structures, dynamics" Physics Reports 51:189-265; 1979.

(6) P.M. Richards, "Magnetic resonance in superionic conductors" Topics in Current Physics Springer, Berlin 15:141-174; 1979.

(7) A. Abragam, "Principles of Nuclear Magnetism" Clarendon Press, Oxford; 1961.

(8) C.P. Slichter, "Principles of Magnetic Resonance" Springer, Berlin; 1978.

(9) A. Carrington and A.D. McLachlan, "Introduction to Magnetic Resonance" Harper and Row; 1969.

(10) E.O. Stejskal and J.E. Tanner, "Spin Diffusion Measurements: Spin Echos in the Presence of a Time-Dependent Field Gradient" J Chem Physics 42:288; 1965.

(11) H. Looser, M. Mali, J. Roos, D. Brinkmann, to be published.

(12) D. Brinkmann and W. Freudenreich, "Ion dynamics and transition to the superionic state in β-AgI" Solid State Comm. 25: 625-28; 1978.

(13) D. Brinkmann, M. Mali, J. Roos and R. Messer, "Inter-layer and intra-layer diffusion processes in Li_3N studied by ^{6}Li and ^{7}Li NMR" Solid State Ionics 5: 405-412; 1981.

(14) D. Wolf, "Spin temperature and nuclear spin relaxation in matter" Clarendon Press, Oxford, 1979.

(15) N. Bloembergen, E.M. Purcell, R.V. Pound, "Relaxation effects in NMR absorption" Phys Rev 73:679-705; 1948.

(16) M.H. Cohen and F. Reif, "Nuclear quadrupole effects in NMR" Solid State Physics 5:321-438; 1957.

(17) D.C. Ailion, "NMR techniques for Studying ionic diffusion in solids" Nuclear and Electron Resonance Spectroscopy Applied to Material Science, North Holland, 55-68; 1981.

(18) H.C. Torrey, "Nuclear spin relaxation by translational diffusion" Phys Rev 92:962-9; 1953.

"Nuclear spin relaxation by translational diffusion. II. Diffusion in a B.C.C. lattice" Phys Rev 96:690; 1954.

(19) See for example: W.A. Barton and C.A. Sholl, "Nuclear spin relaxation by translational diffusion in solids: V. Reciprocal-space formalism and meanfield theory" J Phys C 13:2579-94; 1980.

(20) For references see: O.F. Sankey and P.A. Fedders, "Correlation functions for simple hopping among the octahedral and tetrahedral sites in a body-centered-cubic lattice" Phys Rev B 22:5135-41; 1980.

(21) P.A. Fedders and O.F. Sankey, "The generalized atomic hopping problem-occupation correlation functions" Phys Rev B 15:3580-85; 1977.

(22) C.A. Sholl, "Nuclear spin relaxation by translational diffusion in liquids and solids: high and low-frequency limits" J Phys C 14:447-464; 1981.

(23) P.A. Fedders, "Effects of interactions between hopping particles and T_1 relaxation rates at low concentrations" Phys Rev B 25:78-82; 1982.

(24) E.R. Andrew and D.P. Tunstall, "Spin lattice relaxation in imperfect cubic crystals and in non-cubic crystals" Proc Phys Soc 78:1-11; 1961.

(25) P.A. Fedders, "Effects of large first-order static quadrupole splittings on $1/2 \to -1/2$ exponential spin-resonance decay rates" Phys Rev B 13:2768-72; 1976.

(26) R.D. Hogg, S.P. Vernon, and V. Jaccarino, "Magnetic "tagging" of superionic conductors" Phys Rev Lett 39:481-484; 1977.

(27) P.M. Richards, "Nuclear magnetic relaxation by

paramagnetic impurities in superionic conductors" Phys Rev B 18:6358-71; 1978.

(28) P.M. Richards, "Reduced nuclear magnetic relaxation by paramagnetic impurities in one dimension" Phys Rev B 20:2964-70; 1979.

(29) P.M. Richards, "Theory of NMR relaxation by paramagnetic impurities in a quasi-1D fast ion conductor" Solid State Ionics 5:429-432; 1981.

(30) P.M. Richards, "Variational calculation of NMR relaxation of diffusing ions by impurity centers" Phys Rev B 25:1514-20; 1982.

(31) For references see: D. Brinkmann, M. Mali, J. Roos, R. Messer, H. Birli, "Diffusion processes in the superionic conductor Li_3N - an NMR study" Phys Rev B 26:-, 1982.

(32) K. Differt and R. Messer, "NMR spectra of Li and N in single crystal of Li_3N: discussion of ionic nature" J Phys C 13:717-24; 1980.

(33) K.H. Schwarz and H. Schulz, "X-ray scattering for O^{2-} and N^{3-}" Acta Crystallogr A 34:994-9; 1978.

(34) J. Lewis and D.S. Schwarzenbach, "Electric field gradients and charge density in lithium nitride" Acta Crystallogr A 37:507-10; 1981.

(35) H. Schulz and K.H. Thiemann, "Defect structure of the ionic conductor lithium nitride (Li_3N)" Acta Crystallogr A 35:309-14; 1979.

(36) J.L. Bjorkstam and M. Villa, "Second-order quadrupolar and low-dimensionality effects upon NMR resonance spectra" Phys Rev B 22:5025-32; 1980.

(37) M. Villa and J.L. Bjorkstam, "^{23}Na and ^{27}Al in β-alumina solid electrolytes" Phys Rev 22:5033-41; 1980.

(38) T. Tokuhiro and S. Susman, "A NMR relaxation study of Li motion in superionic Li_xAl_{1-x} with x = 0.49, 0.50 and 0.51" Solid State Ionics 5:421-424; 1981.

(39) K. Kishio, J.R. Owers-Bradley, W.P. Halperin, and J.P. Brittain, "NMR study of pure and doped β-LiAl" Solid State Ionics 5:425-428; 1981.

(40) D. Brinkmann, M. Mali, J. Roos, E. Schweickert, "Dimensionality effects of Li diffusion in β-eucryptite studied by single crystal Li NMR" Solid State Ionics 5:433-436; 1981.

(41) E. Schweickert, M. Mali, J. Roos, D. Brinkmann, to be published.

(42) R.E. Walstedt, R. Dupree, J.P. Remeika, A. Rodriguez, "^{23}Na nuclear relaxation in Na β-alumina: barrier-height distributions and the diffusion process" Phys Rev B 15:3442-54; 1977.

(43) R.E. Walstedt, R.S. Berg, J.P. Remeika, R. Dupree, "Microscopic evidence for co-ionic conductivity in (Na,Li)β-alumina" Solid State Comm 37:209-211; 1981.

(44) J.L. Bjorkstam and M. Villa, "NMR techniques in the study of ionic diffusion in solids" Solid State Ionics 5:189-192; 1981.

(45) J.L. Bjorkstam, M. Villa, G.C. Farrington, "Temperature dependence of the Na$^+$ distribution in β-aluminas" Solid State Ionics 5:153-156; 1981.

(46) M. Villa, J.L. Bjorkstam, G. Mariotto, A. Fontana, E. Cazzaneli, "Lithium ion distribution and motion in β-alumina: an NMR and Raman investigation" J Chem Phys 76:2804-13; 1982.

(47) H. Arribart, H. Carlos, B. Sapoval, "Proton NMR in NH$_4^+$β-alumina: defect structure and low dimensionality effects" Solid State Ionics 5:253-256; 1981.

(48) A.R. Ochadlick, Jr and H.S. Story, "Paramagnetic impurities and proton motion in NH$_4^+$β and NH$_4^+$-H$_3$O$^+$β"-alumina" Solid State Ionics 5:257-260; 1981.

(49) H. Looser, D. Brinkmann, M. Mali, J. Roos, "The interdependence of mobile and stationary ions in RbAg$_4$I$_5$ - an NMR investigation" Solid State Ionics 5:485-488; 1981.

(50) S.M. Shapiro, D. Semmingsen, M. Salamon, "Neutron scattering study of the solid electrolyte RbAg$_4$I$_5$" Proc Int Conf on Lattice Dynamics Flammarion, Paris, 538-540; 1978.

(51) K. Funke, "Dynamic cage effect: comparison between α-RbAg$_4$I$_5$ and α-AgI" Fast Ion Transport in Solids, North Holland:609-612; 1979.

(52) R.A. Vargas, H.B. Salamon, C.P. Flynn, "Ionic conductivity and heat capacity of the solid electrolytes MAg$_4$I$_5$ near T_C" Phys Rev B 17:269-281, 1977.

(53) Hsu Hang, M. Engelsberg, I.J. Lowe, "Anomalous behavior of the F^{19} motional relaxation in PbF$_2$ doped with alkali halides" Solid State Ionics 5: 609-612; 1981.

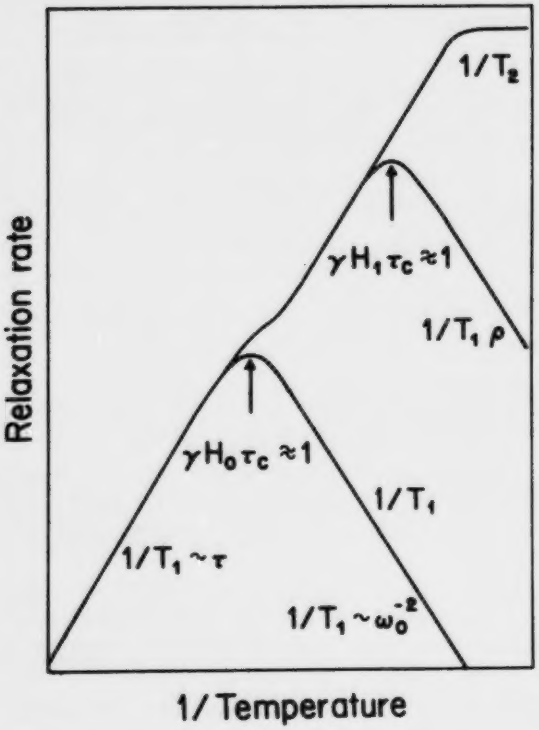
Relaxation rate
1/Temperature
1/T₂
γH₁τc ≈ 1
1/T₁ ρ
γH₀τc ≈ 1
1/T₁
1/T₁ ~ τ
1/T₁ ~ ω₀⁻²

Fig. 1 - General temperature dependence of the relaxation rates for the BPP model.

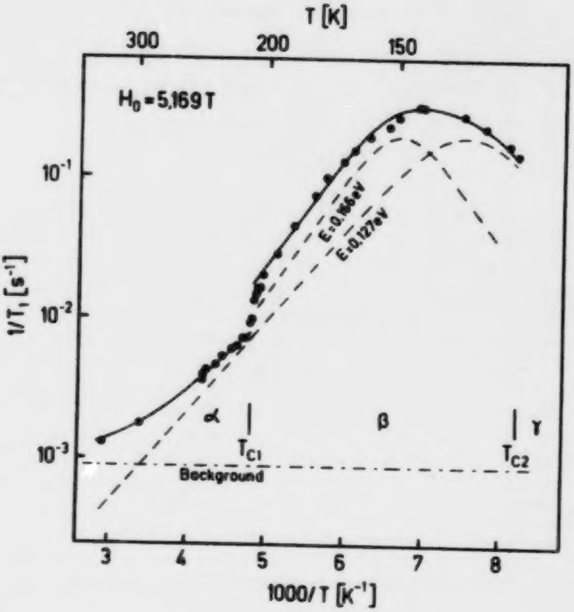

Fig. 2 - Temperature dependence of the ^{109}Ag relaxation rates in $RbAg_4I_5$ (from Ref. (49)). The dashed lines represent the contributions (i), (ii), and (iii) described in the text. Their sum is shown by the heavy line.

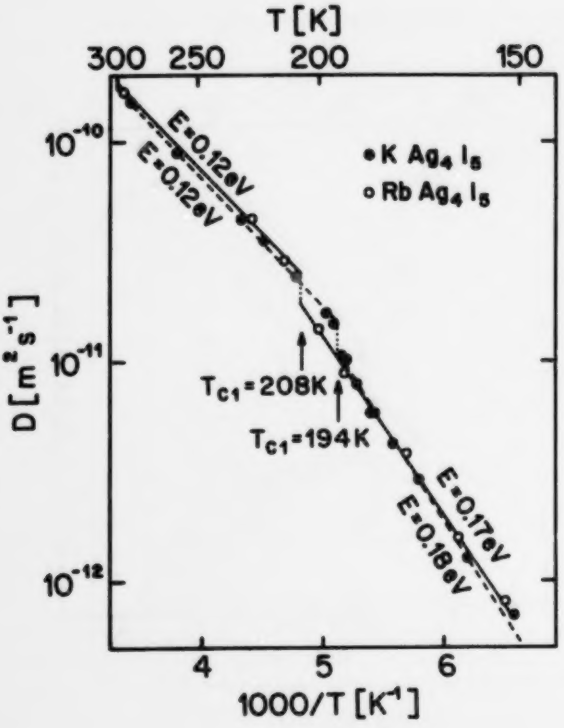

Fig. 3 - NMR determination of the ^{109}Ag self-diffusion coefficient in KAg_4I_5 and $RbAg_4I_5$ (from Ref. (11)). The activation energies were obtained from a linear fit to the data.

STRUCTURE STUDIES, POTENTIALS AND DIFFUSION PATHS OF FAST IONIC CONDUCTORS

Heinz Schulz

Max-Planck-Institut für Festkörperforschung
Heisenbergstr. 1, 7000 Stuttgart 80, F.R.G.

ABSTRACT

A picture of a fast ionic conductor on the atomic scale can be derived from crystal structure analyses based on elastic neutron or X-ray Bragg diffraction. They allow the calculation of an average nuclear or electron density and of anharmonic temperature factors. The temperature factor formalisms are based on a harmonic potential modified by anharmonic terms. The underlying so-called "effective one particle potentials" can be derived from the temperature factors by means of the probability density functions, which are the Fourier transforms of the temperature factors. These potentials can be combined to show the potential along the diffusion paths of the mobile ions.

Such structure investigations carried out as a function of temperature also allow to separate dynamical and static disorder.

The article describes the mathematical basis, the advantages and the shortcomings of this investigational method. The procedure is illustrated by some structural studies of fast ionic conductors.

KEYWORDS structure investigation, anharmonic thermal vibrations, probability density, diffusion path, effective one particle potential

RÉSUMÉ

Une image, à l'échelle atomique, d'un conducteur ionique rapide peut être obtenue par résolutions de structures cristallines au moyen de diffraction élastique de neutrons ou rayons X. Elles permettent le calcul d'une densité moyenne nucléaire ou électronique et des facteurs de température anharmoniques. Les formalismes des facteurs de température sont basés sur un potentiel harmonique, modifé par des termes anharmoniques. Les termes fondamentaux, nommés "potentiels effectifs d'une particule", peuvent être obtenus à partir des facteurs de température au moyen de fonctions probabilité de densité, qui sont les transformées de Fourier des facteurs de température. Ces potentiels peuvent être combinés pour mettre en évidence le potentiel le long des chemins de diffusion des ions mobiles.

De telles résolutions, effectuées en fonction de la température permettent aussi de séparer désordres dynamique et statique.

L'article décrit les bases mathematiques, l'avantage et les faiblesses de cette méthode d'étude, illustrée par quelques résolutions structurales de conducteurs ioniques rapides.

INTRODUCTION

The mobile ion species of a fast ionic conductor move rapidly through a framework which is formed by all other atoms of the crystal structure. The mobile ions carry out huge thermal vibrations and show a high degree of positional disorder. Sometimes it is nearly impossible to assign atomic sites to the mobile ions or to distinguish between regular and interstitial sites. Therefore, frequently the atomic arrangement of the mobile ions have been described as a molten substructure. This was shown for example already in 1936 by Strock in his structure determination of α-AgI (1). He assigned 42 atomic positions for only two Ag ions per elementary cell. He stressed in his paper that this is only a way to describe the liquidlike behaviour of the Ag substructure. In contrast to the Ag ions the I ions completely occupy the positions (000) and (1/2 1/2 1/2) in Strock's structure model.

These and similar results can be derived from elastic neutron or X-ray diffraction data. A so-called averaged nuclear or electron density can be calculated from the intensities of Bragg reflections. The densities of the mobile ions are often widely smeared out through the elementary cell. Sometimes these densities form connected bands building up one-, two- or three-dimensional patterns, which visualize the diffusion paths (e.g. β-alumina (2)).

Such smeared-out densities show clearly that the mobile ions occupy very flat potentials, flat at least in the direction of the diffusion path. Frequently, these potentials are strongly anharmonic. Such flat potentials cause the huge temperature factors often reported for the mobile ions in crystalline fast ionic conductors. "Standard structure investigations" usually fail to describe in a correct way these densities and temperature factors. Harmonic (parabolic) potentials are assumed for this type of investigation (Fig. 1). Such potentials are very unlikely to hold for the mobile ions (Fig. 2). As a consequence of this limitation, the observed densities are only partly described with one atomic site and therefore the observed density is distributed over several interatomic sites. However, these sites do not represent local potential minima.

The harmonic (parabolic) potential can be adapted to the "real" potential of the mobile ions by adding higher order terms (Fig. 1). The ions occupying such a potential carry out anharmonic thermal vibrations, which have to be described by anharmonic temperature factors in the course of a structure investigation. Some formalisms are available to calculate such anharmonic temperature factors by structure refinements. The corresponding potentials (correctly speaking: effective one particle potentials) can be calculated from the Fourier transform of the temperature factors, the so-called probability densities. Furthermore, the potential along the diffusion path can be calculated from a "joint probability density", which is quite independent of the used structure model.

This article focusses on the very recent development of this type of structure investigation. The second section deals with the mathematics, the third section describes case studies. It is not the aim of this article to give a survey of all known superionic crystal structures. Partly, they are described in this book. Furthermore, a survey of different types of ionic conductors and their crystal structures is given in the reference (3). Crystal chemical criteria for fast ionic conduction are reported in ref. (4). Diffuse scattering of fast ionic conductors is reviewed in ref. (5). A review on the study of anharmonic thermal vibrations in fast ionic conductors is given in ref.(6).

MATHEMATICAL TREATMENT

The lattice of a three-dimensional crystal may be described by the lattice vectors $\underset{\sim}{a}_1$, $\underset{\sim}{a}_2$, $\underset{\sim}{a}_3$, its reciprocal lattice by the vectors $\underset{\sim}{a}_1^*$, $\underset{\sim}{a}_2^*$, $\underset{\sim}{a}_3^*$. Each elementary cell contains N atomic positions, occupied by atoms with the scattering amplitude f_n.

The position of each atom can be described by the vector r_{mn}

$$\underset{\sim}{r}_{mn} = \underset{\sim}{r}_m + \underset{\sim}{r}_n(m) \tag{1}$$

where:

$$\underset{\sim}{r}_m = m_1\underset{\sim}{a}_1 + m_2\underset{\sim}{a}_2 + m_3\underset{\sim}{a}_3 \tag{2}$$

$\underset{\sim}{r}_m$ of eq. (2) is the lattice vector. $\underset{\sim}{r}_n(m)$ of eq. (1) is the position vector of the atom n in the elementary cell m. The sum of these two vectors describes the position of each atom in each elementary cell (eq. (1)). We assume now that the atoms deviate only by a small amount from an averaged position described by the vector $\bar{r}_n$ of eq. (3).

$$\underset{\sim}{\bar{r}}_n = \frac{1}{M}\sum_{m=1}^{M} \underset{\sim}{r}_n(m) \tag{3}$$

The position vector $\underset{\sim}{r}_n(m)$ can then be written as in eq. (4)

$$\underset{\sim}{r}_n(m) = \underset{\sim}{\bar{r}}_n + \underset{\sim}{u}_{mn} \qquad (4)$$

$\underset{\sim}{u}_{mn}$ describes the deviation of the atom n in the elementary cell m from its mean position.

The positions of the Bragg peaks are described by the reciprocal lattice vectors

$$\underset{\sim}{h} = h_1a_1 + h_2a_2 + h_3a_3 \qquad (5)$$

with h_1, h_2, h_3 integers

The wave scattered into a Bragg reflection can now be written as

$$F(\underset{\sim}{h}) = \sum_m^M \sum_n^N f_n \exp(2\P i\ \underset{\sim}{h}\underset{\sim}{r}_{mn}) \qquad (6)$$

Eq. (6) can be rewritten by means of eq. (1) and (4):

$$F(\underset{\sim}{h}) = \sum_n^N w_nf_n \exp(2\P i\ \underset{\sim}{h}\underset{\sim}{\bar{r}}_n)$$

$$\cdot \sum_m^M \exp(2\ i\P \underset{\sim}{h}\underset{\sim}{r}_m) \exp(2\P i\ \underset{\sim}{h}\ \underset{\sim}{u}_{mn}) \qquad (7)$$

The first part of the right side of eq. (7) represents an averaged distribution of the atoms. Therefore an occupation probability w_n is introduced in order to take into account that not all atomic positions may be occupied. The assignment of a displacement to an elementary cell shows up in the second part of eq. (7). Any correlation between displacements is taken into account by this expression. In the following it is assumed that such correlations are not present. Then eq. (7) can be reformulated by using the well known relation (8):

$$\overline{ab} = \bar{a} \cdot \bar{b}$$

$$\frac{\sum^M a_mb_m}{M} = \frac{\sum^M a_m}{M} \cdot \frac{\sum^M b_m}{M} \qquad (8)$$

Eq. (7) transforms into

$$F(\underset{\sim}{h}) = \sum_{n}^{N} w_n f_n \exp(2\pi i\, \underset{\sim}{h}\, \underset{\sim}{\bar{r}}_n) \cdot \frac{1}{M} \sum_{m}^{M} \exp(2\pi i\, \underset{\sim}{h}\, \underset{\sim}{u}_{mn})$$

$$\cdot \sum_{m'}^{M} \exp(2\pi i\, \underset{\sim}{h}\, \underset{\sim}{r}_{m'}) = \sum_{n} F_I \cdot \sum_{m} F_{II} \cdot \sum_{m'} F_{III} \qquad (9)$$

The third factor F_{III} of eq. (9) represents the Laue factor, which enhances the intensities at the Bragg reflections and which allows the rather simple and accurate measurements of the Bragg intensities compared to the background scattering. Using eq. (2) and (5) it can be written as:

$$F_{III}\ (\underset{\sim}{h}) = \sum_{m'_1}^{M_1} \sum_{m'_2}^{M_2} \sum_{m'_3}^{M_3} \exp(2\pi i\ h_1 m'_1 + h_2 m'_2 + h_3 m'_3)$$

$$= \exp(i\phi)\ G_1(h_1)\ G_2(h_2)\ G_3(h_3) \qquad (10)$$

where G_1-G_3 represent geometrical series. At a reciprocal lattice point, (10) reduces to

$$F_{III}(\underset{\sim}{h}) = \exp(i\phi)\ M_1 M_2 M_3 \qquad (11)$$

Eq. (11) shows the tremendous enhancement of $F(\underset{\sim}{h})$ at the position of a Bragg reflection. However, this advantage is offset by the fact that all correlations between the $\underset{\sim}{u}$ have been lost.

The second factor of eq. (9) plays the most important role in the structure investigations of fast ionic conductors.

$$F_{nII}(\underset{\sim}{h}) = \frac{1}{M} \sum_{m}^{M} \exp(2\pi i\ \underset{\sim}{h}\ \underset{\sim}{u}_{mn}) \qquad (12)$$

It is the Fourier transform of all displacements from the mean positions of the atomic position n. All the displacements $\underset{\sim}{u}_m$ of the atomic position n form a density, which may be described by a so-called probability density function $pdf_n\ (\underset{\sim}{u})$. Now the sum of eq. (12) can be replaced by the integral

$$F_{nII}(\underset{\sim}{h}) = \int pdf_n(\underset{\sim}{u}) \exp(2\pi i \, \underset{\sim}{h} \, \underset{\sim}{u}) dV$$
$$= T_n(\underset{\sim}{h}) \qquad (13)$$
$$\int pdf(\underset{\sim}{u}) dV = 1$$

Eq. (9) can now be written by using (11) and (13)

$$F(\underset{\sim}{h}) = (\sum_{n}^{N} w_n f_n T_n \exp 2\pi i \, \underset{\sim}{h} \, \underset{\sim}{r}_n) \, . \, \exp(i\phi).G_1.G_2.G_3 \qquad (14)$$

= structure factor . Laue lattice factor.

Eq. (13) and (14) show that the temperature factor of the structure factor equation is the Fourier transform of a probability density function. It does not tell anything on the nature of these displacements; static and dynamical displacements, correlated and uncorrelated displacements are altogether described by the temperature factor. In this sense the name "temperature factor" is misleading. The probability density function can be calculated from the temperature factor by Fourier transformation. In standard structure investigations the pdf is taken as a Gaussian function. Its Fourier transform is again a Gaussian function. These are the usual anisotropic temperature factors.

Up to now this is a pure mathematical treatment, no physics is involved. But it turns out that if a harmonic potential is assigned to an atomic position and the occupation of the energy levels is controlled by the Boltzmann factor

$$\exp(-V(\underset{\sim}{u})/kT) \qquad (15)$$

k : Boltzmann constant

T : Absolute temperature,

then $pdf(\underset{\sim}{u})$ is a Gaussian function. Therefore the usual anisotropic temperature factors can only describe thermal motion in a harmonic potential.

More general probability density functions, which can be Fourier-transformed, allow the calculation of more general temperature factors. Several series expansions are known, which have such properties, (6-10), but only the Gram-Charlier expansion allows the transformation from the reciprocal space (temperature factors) to the direct space (pdf) without approximations (6-8).

Furthermore it is not too hard to expand this series up to 6th order coefficients; these are necessary for the description of sixfold symmetry.

The probability density function and the temperature factor based on the Gram-Charlier expansion can be written as:

$$\begin{aligned} \mathrm{pdf}_n(\underset{\sim}{u}) &= (1+\tfrac{1}{3!}c_n^{pqr}H_{pqr}(\underset{\sim}{u}) \\ &\quad + \tfrac{1}{4!}\, d_n^{pqrs}H_{pqrs}(\underset{\sim}{u}) + \ldots)\mathrm{ph}_n(\underset{\sim}{u}) \end{aligned} \tag{16}$$

$$\begin{aligned} T_n(\underset{\sim}{h}) &= 1+\tfrac{1}{3!}(2\pi i)^3 c_n^{pqr}h_p h_q h_r \\ &\quad + \tfrac{1}{4!}(2\pi i)^4 d_n^{pqrs}h_p h_q h_r h_s + \ldots)\ \mathrm{Th}_n(\underset{\sim}{h}) \end{aligned} \tag{17}$$

$$\left.\begin{aligned} c^p H_p &= \sum_{p=1}^{3} c_p H_p \\ c^p h_p &= \sum_{p=1}^{3} c_p h_p \end{aligned}\right\} \quad \text{Einstein's summation convention}$$

$\mathrm{ph}(\underset{\sim}{u})$: harmonic probability density function (Gaussian function)

$\mathrm{Th}(\underset{\sim}{h})$: harmonic temperature factor (Gaussian function)

H : Hermite polynomials

The coefficients c^{pqr}, d^{pqrs},... represent tensors of rank 3, 4, ... and so on. The point symmetry of the atomic position under investigation causes restrictions between the coefficients. These restrictions are listed up to the fourth order in ref. (8). Equation (17) can be implemented in a least squares program. The refined coefficients c,d, ... can be used together with eq. (16) in order to calculate the pdf. The pdf(u) can be used to calculate a potential in the following way: The Boltzmann factor of eq. (15) relates the deviation $\underset{\sim}{u}$ to the potential $V(\underset{\sim}{u})$. Therefore it represents an unnormalized pdf.

$$T_n(\underset{\sim}{h}) \propto \int \exp(-V_n(\underset{\sim}{u})/kT)\exp 2\pi i(\underset{\sim}{h}\ \underset{\sim}{u})dV$$

The transformation results in

$$\begin{aligned} \exp(-V_n(\underset{\sim}{u})/kT) &= p_o \int T_n(\underset{\sim}{h})\exp(-2\pi i\ \underset{\sim}{u}\ \underset{\sim}{h})dV^{*} \\ &= p_o\ \mathrm{pdf}(\underset{\sim}{u}) \end{aligned}$$

P_o is a normalization factor. From $V_n(0) = 0$ follows $P_o = 1/\mathrm{pdf}(0)$.

Therefore

$$V_n(\underset{\sim}{u}) = kT \ln(\mathrm{pdf}(\underset{\sim}{u})/\mathrm{pdf}(0)) \qquad (18)$$

Eq. (18) relates a mathematical expression (pdf) with the effective one particle potential of an atomic position. However, physically meaningful results can only be obtained, if this potential is a modified harmonic (parabolic) potential, because the leading terms of eq. (16) and (17) are Gaussian functions (ph,Th), which are only modified by the sums in the brackets. Therefore it is important to prove this assumption. This can be done by structure investigations as a function of temperature. The temperature dependence of the mean square displacement $\overline{u^2}$ for an isotropic thermal motion in a harmonic potential can be written as shown in ref. (11):

$$\overline{u^2} = b \cdot T \qquad (19)$$

The constant b depends on the mass of the atom and the Debye temperature Θ. Eq. (19) holds for $T>\Theta$. $\overline{u^2}$ should show a linear temperature dependence in this temperature region (Fig. 3). For anisotropic temperature factors, $\overline{u^2}$ has to be replaced by a second rank tensor. As Fig. 3 shows, the refined $\overline{u^2} = 0$ for $T = 0$ or at least at very small positive $\overline{u^2}$ values. This holds also for crystalline phases which exist only in a limited temperature range.

As discussed above, ionic conductors are characterized by flat potentials for the mobile ions. Therefore a potential form as shown in Fig. 4a may be suitable (at least in a first approximation) for the treatment of the potential of the diffusing ions. As a consequence of this potential the atoms deviate from their mean position also at T = 0 K; they show a static displacement u_s (Fig. 4a). With increasing temperature a dynamical displacement u_d is added. The complete displacement measured by a temperature factor is now (12):

$$\overline{u^2} = u_s^2 + \overline{u_d^2} \qquad (20)$$

$\overline{u^2}$ as a function of temperature is shown in Fig. 4b. The extrapolation to T = 0 offers a simple possibility to determine u_s and to become aware of the fact that one deals with a pseudo temperature factor.

u_s^2 can be generated in different ways. For example it may be caused by a double well potential (Fig. 5). Such a situation is usually described by split atoms. These positions are no longer resolved, if the potential barrier is low compared with kT. In this case the central position of Fig. 4 is frequently used as an atomic position in structure investigations. A $\overline{u^2}$ vs T plot now looks as in Fig. 4b. It shows that an incorrect structure model has been applied. It has to be changed into a split atom model. The potentials of the split positions now have a harmonic character and the $\overline{u^2}$ vs T diagram has changed from Fig. 4b to Fig. 3b, proving that now the correct structure model has been applied.

It should be stressed here once more that a refinement of the atomic position of Fig. 5 with a central position instead of the split positions gives a reasonable result from a mathematical point of view, this means from a viewpoint of a probability density function. It fails when the pdf is transformed into a potential via the Boltzmann factor. This can be shown in the following way:

An isotropic temperature factor can be written in the form (11):

$$T(h) = \exp(-\frac{1}{2}\, h^2\overline{u^2}) \qquad (21)$$

The pdf of (21) is

$$\mathrm{pdf}\ (u) = (2\pi^2\ \overline{u^2})^{-2/3} \exp\ (-\ ur^2/2\pi\overline{u^2}) \qquad (22)$$

For a harmonic potential $\overline{u^2}$ can be replaced by eq. (19). Now putting eq. (22) into eq. (18) results in

$$V(u) = -kT\ .\ \overline{u^2}\ /(2aT)$$

$$= -k\ .\ \overline{u^2}/(2a) \qquad (23)$$

Eq. (23) is independent of temperature. Let us now assume that $\overline{u^2}$ of eq. (20) is dominated by the static displacement u_s^2 so that $\overline{u_d^2}$ can be neglected. In this case eq. (18) changes into

$$V(u) = kT\ \overline{u^2}/(2\pi\ \overline{u_s^2}) \qquad (24)$$

It follows that V(u) now shows a linear dependence on T becoming steeper and steeper with increasing temperature. If both terms of eq. (20) are not equal to zero, then the potential shows at least a pronounced temperature dependence. In this case the best approximation is the potential calculated from the data of the highest temperature investigated.

The mobile ions in fast ionic conductors move through the crystal by jumping from an atomic site to the next one. It follows that there should exist a probability density of these ions along the diffusion paths. It does not show up directly in the pdf of an isolated atomic site, but only in a so-called "joint pdf" (13). If N mobile ions occupy an elementary cell, then $\int \mathrm{pdf}\, dV = N$ holds independently of the way how many atomic positions are assigned to these ions. Bachmann (13) derived from this relation

$$\mathrm{pdf}(\underset{\sim}{r}) = \overset{I}{\Sigma} w_i\, \mathrm{pdf}_i\, (\underset{\sim}{r}) \qquad (25)$$

I : number of atomic sites assigned to the mobile ions

w_i: occupation probability of site i.

Eq. (25) can be used for all pdf's, this means also for those calculated only from harmonic temperature factors. This is a very important result. It allows the refinement of anharmonic thermal vibrations with harmonic (anisotropic) temperature factors and splitatoms. However, the final interpretation has to be carried out from a joint probability density map.

CASE STUDIES

In the following, structure investigations of fast ionic conductors are reviewed. They demonstrate the calculation of probability densities and potentials in the absence and presence of static disorder of the mobile ions.

Li_3N

Lithium nitride shows a high lithium ionic conductivity (14). Li_3N forms a hexagonal layer structure (15,16). Pure Li layers and Li_2N layers are arranged perpendicular to the c axis. The ionic conductivity takes place mainly in the Li_2N layers (Fig. 6). The temperature factors were refined with the Gram-Charlier expansion (eq. 17) with coefficients up to the 6th order (17). The temperature dependence of the second order coefficients is shown in Fig. 7. At a medium temperature they follow a straight line as required by eq. (19). At very low temperature the temperature factors become nearly constant due to zero point vibrations. At high temperatures the anharmonic contributions cause deviations from the straight line. The probability densities of all atoms were calculated with eq. 16. A pdf section through the Li_2N layer is displayed in Fig. 6. The Li(2) ion has pronounced threefold symmetry with large thermal vibrations towards the neighbouring Li(2) sites. The Li(2) potential along the line N-Li(2)-Li(2)-N of Fig. 8 has been calculated with eq. (18) and (25). The potentials show a cross-over at about 0.30 eV. This crossover is interpreted as the potential a Li(2) ion has to overcome during a jump from an occupied to an unoccupied site (17). 0.30eV of Fig. 8 compares well with the activation energy of Li_3N of about 0.25-0.28eV (18).

Ag_3SI

Three phases of silver sulfide iodide exist (19-22):

- One phase crystallizes in a bcc structure at T>515K. This α-Ag_3SI is isostructural with α-AgI. The (S,I) ions are statistically distributed over the corners and centers of the elementary cells. The three silver ions show a nearly continuous distribution as Fig. 15 shows (22,23).
- Another phase, the simple cubic β-phase (19-22) exists between 155K and 515K. It is characterized by an ordered distribution of the I and S atoms (Fig. 9). A statistical distribution of three Ag ions over 12 sites near the face centers was proposed from a crystal chemical point of view (24). The Ag ions occupy distorted S_2I_2 tetrahedra (Fig. 9). These positions allow to form longer Ag-I and shorter Ag-S bond distances.
- The third phase, the γ-phase, exists below 155K. Again the Ag ions are disordered (20-22). A β-phase single crystal transforms to a multidomain crystal at the (β,γ) phase transition (21,22).

The ionic conductivities decrease and the activation energies increase when going from $\alpha \rightarrow \gamma$(25).

β-Ag_3SI

The silver density in β-Ag_3SI is shown in Fig. 10. As expected from the discussion above, the Ag density is concentrated around the center of the face. However, the density does not show four maxima as suggested by Fig. 9, but only one at the face center. Therefore the structure investigation was started with the Ag sites at the face center (1/2 1/2 0). Due to the site symmetry only the coefficients u_{11} and u^2_{33} of the harmonic part of the temperature factor are independent variables. u^2_{11} and u^2_{33} describe the vibrations in and perpendicular to the $\{100\}$ faces, respectively. Their temperature dependence is shown in Fig. 11. Both coefficients follow a straight line as required by eq. (19). However, there exists an important difference between the two coefficients. The magnitude of $\overline{u^2_{33}}$ may be still considered as normal. Furthermore, u^2_{33} at 500K is about 3 times larger than the value extrapolated for T = 0K. u^2_{11} is unusually large. At 500K it corresponds to a "vibrational" amplitude of about 0.75Å. The extrapolation to T = 0K results in a huge static contribution to the temperature factor. $\overline{u^2_{11}}$ at 500K is only 30% larger than the extrapolated value at T = 0K! A site potential calculated with this u^2_{11} value must show a strong temperature dependence as required by eq. (24). This is demonstrated by the site potential along $\langle 100\rangle$ of Fig. 12a, which has been calculated with all refined coefficients up to 6th order (26). It follows that the Ag sites at (1/2 1/2 0) do not represent the Ag equilibrium positions.

In the next step the Ag positions were split as shown in Fig. 9. The site symmetry now allows the refinement of three independent second order coefficients. u^2_{33} is not affected by the split atom model, but $\overline{u^2_{11}}$ and u^2_{22} show now a pronounced temperature dependence (Fig. 11). The coefficients at T = 500K are now at least twice as large as the value extrapolated for T = 0K. It follows that the split atom model describes much better the Ag arrangement in ß-Ag_3SI than the model with the Ag sites at the face centers. However, the rather large static parts of $\overline{u^2_{11}}$ and $\overline{u^2_{22}}$ demonstrate that we deal again only with an approximation. The site potential calculated for the split atom model shows therefore also a temperature dependence (Fig. 12b), however, it is less pronounced than for the face center model in Fig. 12a and the high temperature potential can be used already as a good approximation of the "real" potential. Fig. 12b demonstrates further that the Ag ions occupy a double well potential, which has a very low potential barrier between the sites. The potential barrier is located at the face centers, the position which has been used as a Ag-"site" in the face center model. A similar potential barrier was found for direct jumps between nearest neighbours (see Fig. 9). These jumps form a ringlike path around the face center. It follows that the Ag ions can move with very low activation energy in an area around the center of the faces. This in complete agreement with measurements of far infrared reflectivity (27) and far infrared conductivity (28). Both papers give strong evidence for a preferred local motion in a double-well-like environment.

The analysis of the local Ag movement does not answer the question of how the Ag move through the crystal. The answer can be given by a further analysis of the Ag probability densities. For this discussion the {200} section of the ß-Ag_3SI structure is used (Fig. 13). The projection of this section is marked by the black line in Fig. 9. The section of Fig. 13 cuts a S ion and all Ag sites with <x = 1/2>. (< > points to all symmetrically equivalent positions). The corresponding Ag probability density is shown in Fig. 14. It has been calculated from the temperature factor coefficients of the Ag split atom model. At first, the pdf of each split position was calculated with eq.(16), then the joint pdf with eq. (25). Fig. 14 shows an increase of the probability density near the edges and a connection of these high local densities by a weak density near the corners, forming in this way a three-dimensional network of diffusion paths. This is the bent diffusion path No. 1 in Fig. 13. A similar, but straight diffusion path is marked as No. 2 in Fig. 13, but the Ag-S distance becomes too short compared to the usual Ag-S bond distance during the jumps along this path. Diffusion path No. 3 passes through the center of a I-I edge and again the Ag-I distance is unusually small at this point. From this point of view the most favourable path is No. 1 as found by the analysis of the joint pdf of Fig. 14.

α-Ag_3SI

The statistical distribution of the framework ions S and I in α-Ag_3SI causes a very high positional disorder of the Ag ions (Fig. 15). The density of Fig. 15 shows already clearly the three-dimensional net of the Ag diffusion paths. The weak Ag maxima in Fig. 15 at <1/2 1/2 0> and <1/4 1/2 0> were used for a structure refinement. The potential calculated from the refined temperature factor coefficients is shown in Fig. 16. It is remarkable that again the structure investigation results in a double well potential near the center of the face. This potential minimum is just the tetrahedral Ag position used in ß-Ag_3SI. It follows that the Ag ions prefer the tetrahedral sites in α-Ag_3SI, too. The number of these sites has been doubled at the phase transition due to the change from pc to bcc. This result allows the interpretation that at least small domains with an ordered S and I distribution exists. In addition a Ag interstitial site at <1/4 1/2 0> is generated at the phase transition (Fig. 16). This is probably the Ag position in tetrahedra, which are built of three or four I or S ions. Such tetrahedra have to exist due to the I,S disorder in the frame work.

REFERENCES

(1) L.W. Strock, "Kristallstruktur des Hochtemperatur-Jodsilbers α-AgJ", Z Phys Chem (B) 25:441-459; 1934. "Ergänzung und Berichtigung zu: Kristallstruktur des Hochtemperatur-Jodsilvers α-AgJ", Z Phys Chem (B) 31: 132-136; 1936.

(2) W.L. Roth, "Diffraction Studies of Superionic Conductors" in Solid Electrolytes (Academic Press, New York) 45-58; 1978.

(3) P. Hagenmuller and W. van Gool (Editors), Solid Electrolytes, (Academic Press, New York) 1978.

(4) H. Schulz, "Crystal Structure and Ionic Conductivity" Rev de Chem Min 17: 229-242, 1980.

(5) H. Schulz, "Diffuse X-ray Diffraction and its Applications to Materials Research" Current Topic in Mat Sc 8: (North Holland, Amsterdam) 275-379; 1982.

(6) H. Schulz, "Crystal Structures of Fast Ion Conductors" Annual Rev. Mat. Sc. (Ann. Rev. Inc., Palo Alto, USA) 12: 351-376; 1982.

(7) U.H. Zucker and H. Schulz, "Statistical Approaches for the Treatment of Anharmonic Motion in Crystals. I: A Comparison of the Most Frequently Used Formalisms of Anharmonic Thermal Vibrations", Acta Cryst A, 38: 563-568; 1982.

(8) International Tables for X-ray Crystallography Vol. IV (Birmingham, Kynoch Press) 1974.

(9) C.K. Johnson,"Addition of higher Cumulants to the Crystallographic Structure-Factor Equation: A generalized Treatment for Thermal-Motion Effects" Acta Crystallogr A 25: 187-194; 1969.

(10) F.Y. Edgeworth, The Law of Error, Proc Camb Philos Soc 20: 36-141; 1905.

(11) B.T.M. Willis and A.W. Pryor, "Thermal Vibrations in Crystallography" (Cambridge University Press, London) 1975.

(12) H. Schulz, "Influence of split atoms on anisotropic temperature factors", Z Kristallogr 136: 321-349; 1972.

(13) R. Bachmann, "Strukturuntersuchungen an schnellen Ionenleitern", Thesis, University of Karlsruhe (F.R.G.); 1982.

(14) U. v.Alpen, A. Rabenau und G.H. Talat, "Ionic Conductivity in Li_3N single crystals", *Appl Physics Lett* 30: 621-623; 1977.

(15) E. Zintl and G. Brauer, Konstitution des Lithiumnitrides, *Z Elektrochem* 41: 102-107, 1935.

(16) A. Rabenau and H. Schulz, "Re-Evaluation of the Lithium Nitride Structure", *J Less Common Mett* 50: 155-159; 1976.

(17) U.H. Zucker and H. Schulz, "Statistical Approaches for the Treatment of Anharmonic Motion in Crystals. II. Anharmonic Thermal Vibrations and Effective Atomic Potentials in the Fast Ionic Conductor Lithium Nitride (Li_3N)", *Acta Cryst A* 38: 568-576; 1982.

(18) M.F. Bell, A. Breitschwerdt and U. v. Alpen, "The Effect of Hydrogen on the Ionic Conductivity in Lithium Nitride," *Mat Res Bull* 16: 267-272; 1981.

(19) B. Reuter and K. Hardel, "Darstellung, Eigenschaften und Phasenverhältnisse von Ag_3SBr und Ag_3SJ", *Z anorg allg Chem* 340: 158-167; 1965.

(20) S. Hoshino, T. Sakuma and Y. Fujii, "A Structural Phase Transition in Superionic Conductor Ag_3SI", *J Phys Soc Jap* 47: 1252-1259; 1979.

(21) E. Perenthaler and H. Schulz, "Structures and Phase Transition of ß- and γ-Ag_3IS", *Acta Cryst* B37: 1017-1023; 1981.

(22) E. Perenthaler, H. Schulz, H.U. Beyeler "Structure Investigations, Atomic Potentials and Phase Transitions of the Fast Ionic Conductor Ag_3SI", *Solid State Ionics* 5: 493-496; 1981.

(23) E. Perenthaler and H. Schulz "Anharmonic Temperature Factors up to Sixth Order and Atomic Potentials in the Fast Ionic Conductor α-Ag_3SI, *Sclid State Ionics* 2: 43-46; 1981.

(24) B. Reuter and K. Hardel, "Die Kristallstrukturen von Ag_3SBr, ß- und α-Ag_3SJ" *Z anorg allgem Chem* 340: 168-180; 1965.

(25) G. Chiodelli, A. Magistris and A. Schiraldi, "Ag_3SBr and Ag_3SI: Ionic Conductivity of their Modifications in the T Range 93-573K", Z Physik Chem Neue Folge 118: 177-186; 1979.

(26) E. Perenthaler "Zusammenhang zwischen Ionenleitfähigkeit und Kristallstruktur am Beispiel von Silbersulfidiodid (Ag_3SI)", Thesis, Universitaet Karlsruhe; 1980.

(27) P. Bruesch, H.U. Beyeler and S. Straessler "Dynamics of Silver Ions in the Superionic Conductor Silver Sulfide Iodide (Ag_3SI)", Phys Rev B 25: 541-547; 1982.

(28) B. Gras and K. Funke "Non-Periodic Local Motion of Silver Ions in ß-Ag_3SI from Far-Infrared Conductivity Measurements", Solid State Ionics 2: 341-346; 1981.

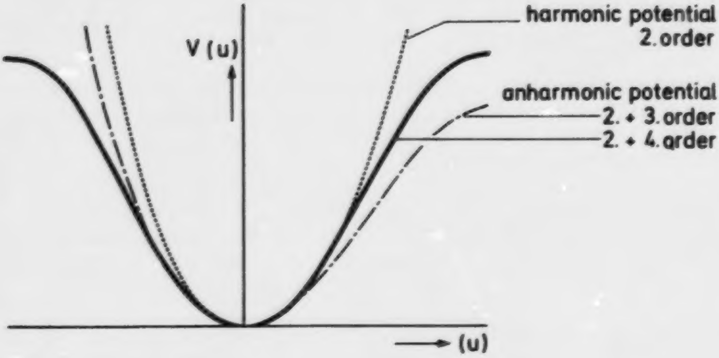

Fig. 1 Different potential forms.
Harmonic (parabolic, 2nd order) potential.
Pair potential (2. + 3. order coefficients).
Flat and symmetrical potential (2. + 4. order coefficients).

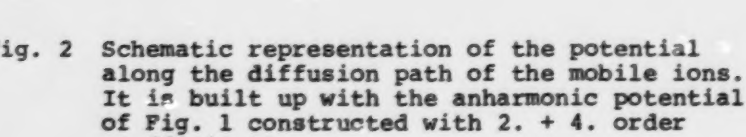

Fig. 2 Schematic representation of the potential along the diffusion path of the mobile ions. It is built up with the anharmonic potential of Fig. 1 constructed with 2. + 4. order coefficients.

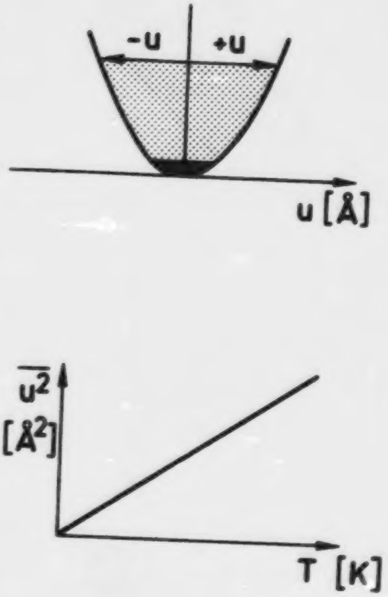

(a) thermal vibrational amplitudes at different temperatures. At low temperatures, energy levels mainly near to the bottom of the potential (black part) are occupied. With increasing temperature higher energy levels are also occupied. It follows that $\overline{u^2}$ increases.

(b) $\overline{u^2}$ as a function of temperature for a harmonic potential

Fig. 3 Thermal vibration in a harmonic potential.

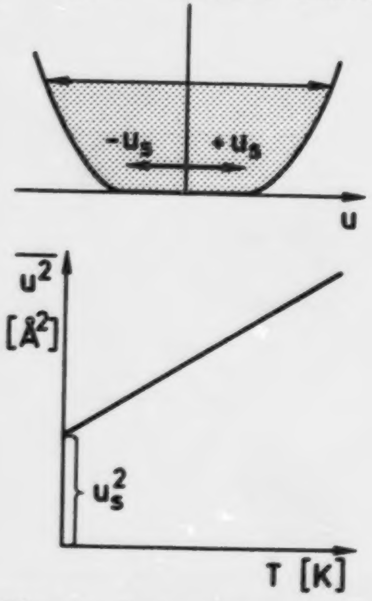

(a) potential form. ± u_s mark the flat part.

(b) mean square displacement $\overline{u^2}$ as a function of T of the potential shown in (a).

Fig. 4 Mean square displacements in a potential with a flat bottom.

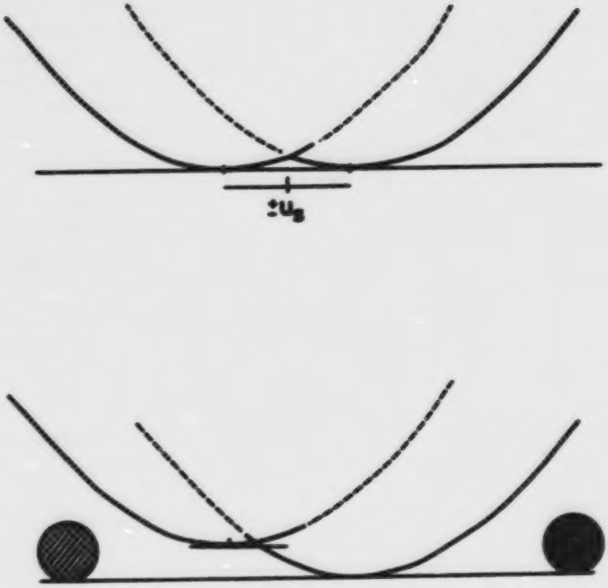

Fig. 5 Double well potential (solid line). Corresponding potentials of split positions (solid and dotted lines).

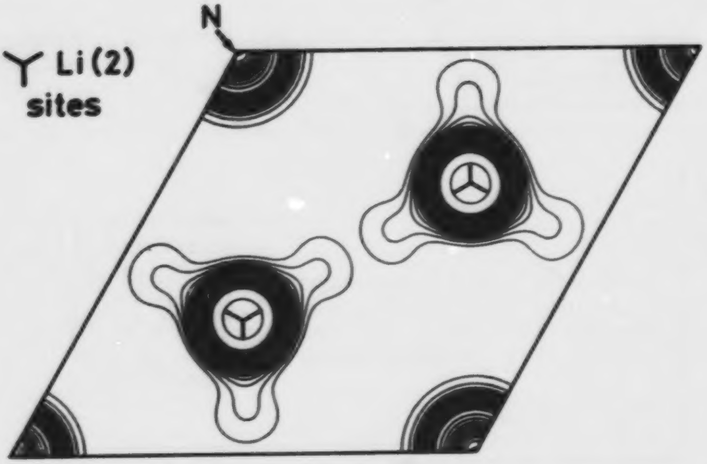

Fig. 6 Section through the probability density of Li_3N at $z = 0$ perpendicular to the c axis at 888K. N^{3-} and $Li(2)^+$ ions occupy the positions at (000) and (± 1/3, ± 2/3, 0) respectively. Lines 0.05, 0.1, 0.15, ..., 1.00, 1.50 Å^{-1}.

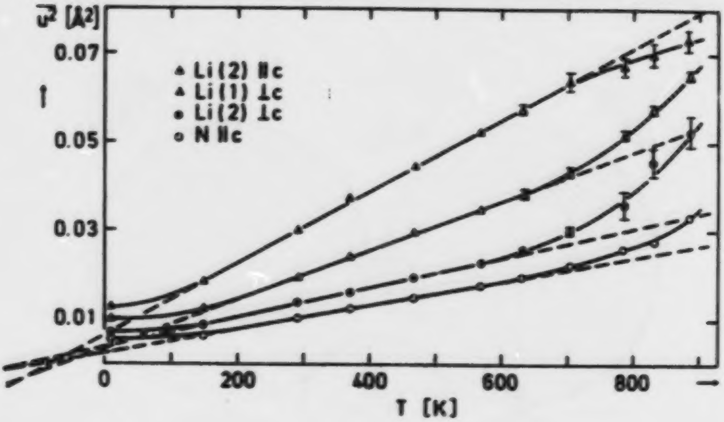

Fig. 7 Selected mean square displacements $\overline{u^2}$ in Li_3N as function of temperature.

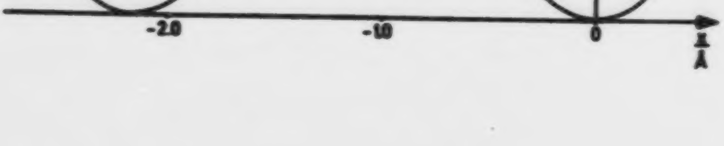

Fig. 8 Li(2) potential along the line N-Li(2)-Li(2)-N (compare with Fig. 6).

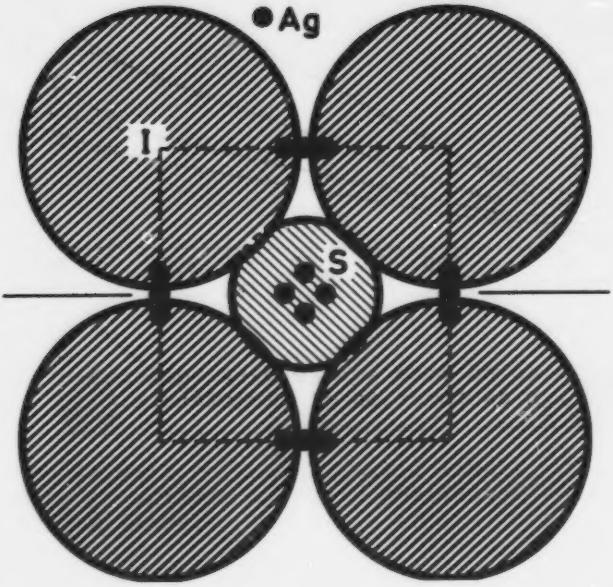

Fig. 9 Projection of the β-Ag_3SI structure along a <100> direction on a {100} face.

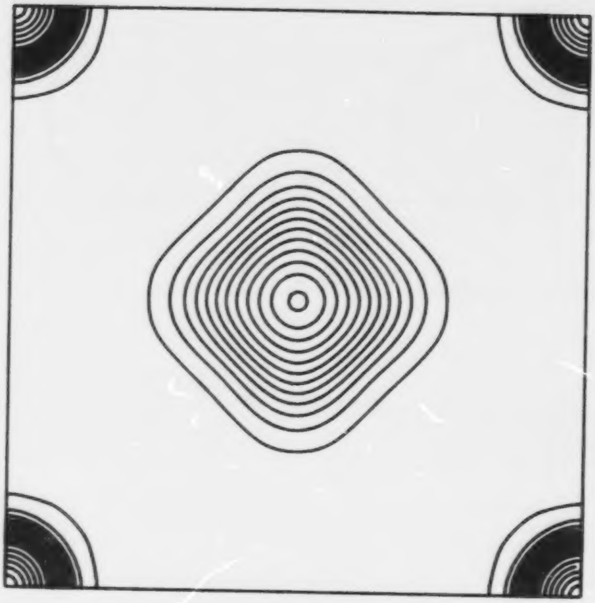

Fig. 10 β-Ag_3SI at room temperature. Electron density section at z = 0. I density at the corners. Ag density around the face center (contour intervals are $3e/Å^3$ up to $60e/Å^3$, then of $20e/Å^3$).
(from ref. 22).

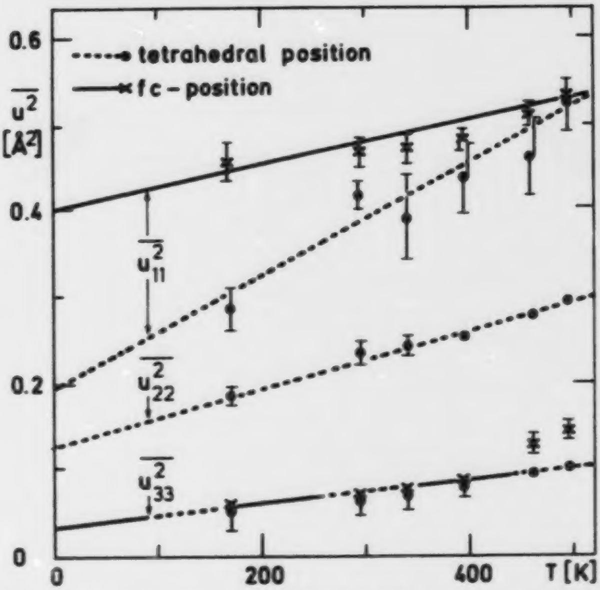

Fig. 11 Ag mean square displacements in β-Ag_3SI.

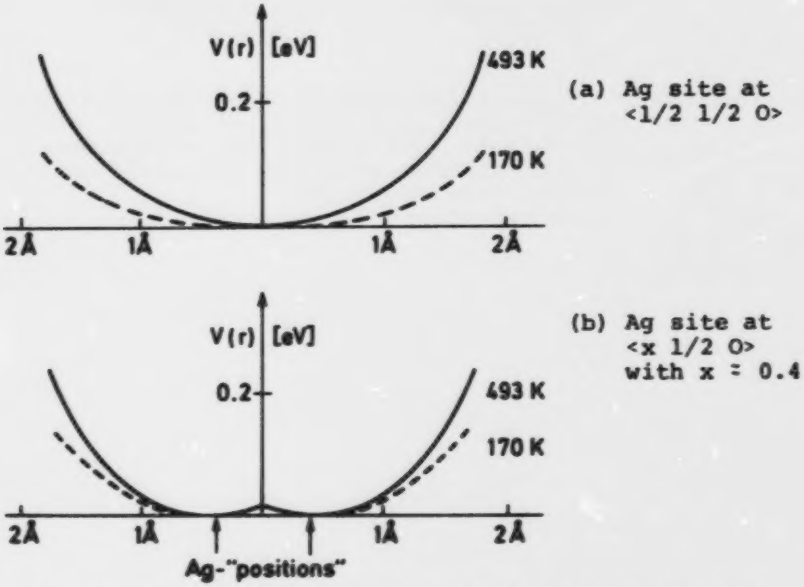

(a) Ag site at <1/2 1/2 0>

(b) Ag site at <x 1/2 0> with x ≈ 0.4

Fig. 12 Ag potentials in the {100} faces along the directions <x, 1/2, 0> for 170K and 493K.

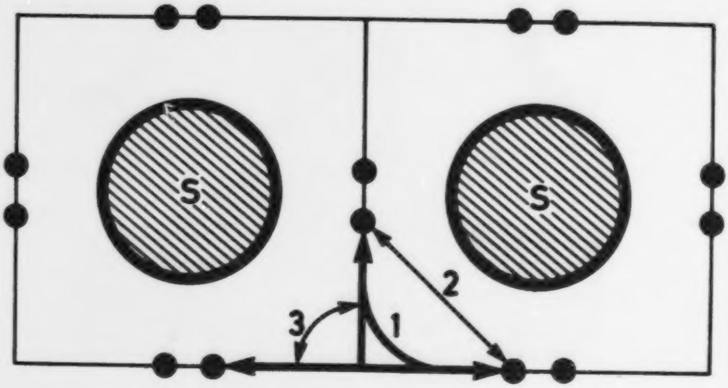

Fig. 13 {200} section of the β-Ag_3SI structure. The projection of this section on the (a_1a_2) plane is shown in Fig. 9 by the solid line.

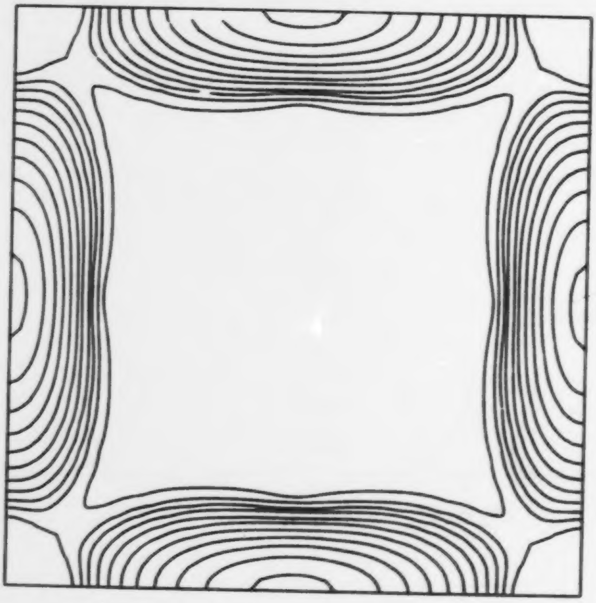

Fig. 14 Joint Ag probability density in the {200} section (compare Fig. 13).

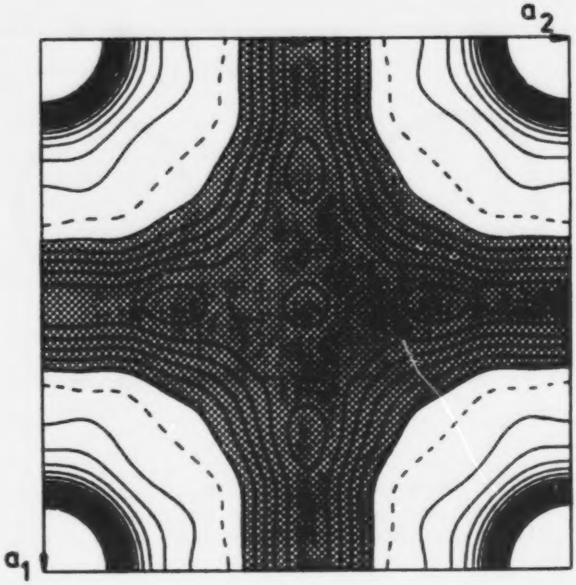

Fig. 15 α-Ag_3SI at 573K. Ag electron density in z=0 (lines spaced at 0.4e/Å^3 intervals). (from ref. 22).

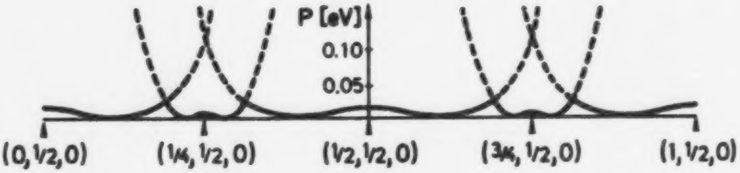

Fig. 16 Ag potential in α-Ag_3SI along the diffusion path parallel to <100>. (from ref. 22).

FRAMEWORK STRUCTURES FOR Na^+-ION ELECTROLYTES

John B. Goodenough

Inorganic Chemistry Laboratory, South Parks Road

Oxford, OX1 3QR, UK

ABSTRACT

An ideal solid Na^+-ion electrolyte has a transport number $t_{Na} \equiv \sigma_{Na}/\sigma = 1$ with, for power applications, a sodium-ion conductivity $\sigma_{Na} \geq 0.1 ohm^{-1} cm^{-1}$ at the operating temperature T_{op} and chemical stability in a specified cell environment. The problem of fabricating thin, dense, and homogeneous ceramic membranes is not addressed. The design criteria for fast Na^+-ion conduction are developed from straightforward theoretical considerations. They include (1) an adequate electrochemical "window", (2) restriction of the phenomenological activation energy to the motional enthalpy ($E_A \approx \Delta H_m$), (3) a geometric criterion for a small ΔH_m, and (4) optimization of occupation numbers where mobile ions move between energetically inequivalent sites. The advantage of stoichiometric vs. nonstoichiometric compounds is stressed. In stoichiometric compounds, a $\Delta H_m \approx kT$ allows multi-ion ring-diffusion excitations that may be of lower energy than excitation of single ions into interstitial sites. It is suggested that this phenomenon is operative in CuI, AgI, PbF_2 and Li_3N. Finally the following framework structures are discussed in terms of the criteria developed: (1) the Na-β aluminas, (2) $NaSbO_3 . 1/6\ NaF$, (3) defect pyrochlores, (4) carnegieite, (5) NASICON, and (6) $Na_5LnSi_4O_{12}$.

KEY WORDS: Sodium electrolyte, fast-ion (Superionic) conductors, diffusion, phase transitions, framework structures.

RÉSUMÉ

Un électrolyte solide pour le transport des ions Na^+ a idéaliment un numéro de transport $t_{Na} \equiv \sigma_{Na}/\sigma = 1$ avec - dans des application de puissance- un conductivité des ions de sodium $\sigma_{Na} \geq 0.1 ohm^{-1} cm^{-1}$ au température opératif T_{op} et pas de corrosion dans l'ambiance de l'application. On n'addresse pas le problème du fabrication des céramiques homogines et minces d'une grande compacité et avec une surface très extensive. Des specifications pour une mobilité élevée des ions Na^+ sont dévelopées avec des idées théoriques simples. Ils incluent (1) une "fenêtre" électrochimique adequate, (2) une énergie d'activation phénomenologique réservée à l'enthalpie de mouvement ($E_A = \Delta H_m$), (3) une spécification géometrique afin d'avoir une petite ΔH_m, et (4) l'optimisation des concentration des ions mobiles où ils traversent des sites inéquivalentes dans l'énergie. L'avantage d'un composé stoechiometrique contre nonstoechiometrique est signalée. Dans les composés stoechiometriques, une $\Delta H_m \approx kT$ permet des excitations d'un ensemble de plusieurs ions avec une énergie moins que celà d'une excitation d'un ion célibiataire à une site interstitielle. On peut penser que ce phénomène est opératif dans CuI, AgI, PbF_2 et Li_3N. Finalement, les structures suivantes d'escalate sont discutées du perspectif des spécifications dévelopées: (1) les aluminas Na-β, (2) $NaSbO_3.1/6\ NaF$, (3) des pyrochlores défectifs, (4) carnegieite, (5) NASICON, et (6) $Na_5LnSi_4O_{12}$.

INTRODUCTION

Definitions

1. Solid electrolytes. An ideal solid electrolyte is an electronic insulator and an excellent conductor of a single ionic species. It is chemically stable in the environment in which it operates, and it has a long life. These specifications allow definition of four "figures of merit" for any solid electrolyte.

(a) The magnitude of the conductivity σ_i of the desired mobile ion should be high enough to make tolerable the ohmic losses in the electrolyte in any specific application. For power applications at an operating temperature T_{op}, fast ionic conduction is required:

$$\sigma_i \geq 0.1 \text{ohm}^{-1}\text{cm}^{-1} \text{ at } T_{op} \tag{1}$$

(b) The transport number t_i should approach unity:

$$t_i \equiv \sigma_i/\sigma \approx 1 \tag{2}$$

where the total conductivity σ is the sum of the electronic conductivity σ_e and the conductivities of all the ionic species present:

$$\sigma = \sigma_e + \textstyle\sum_j \sigma_j \tag{3}$$

(c) The electrolyte must be chemically inert in the environment of an operating electrochemical cell. Specifically, this requirement means that the bottom of the electrolyte electron-conduction band must be energetically high enough that the electrolyte is not reduced at the anode, and the top of the electrolyte valance band must be energetically low enough that It is not oxidized by the cathode under working conditions. Ideally this condition is fulfilled by the "thermodynamic" window provided by the band edges. In practice, a larger "kinetic" window may be found acceptable.

(d) The material must be easily fabricated into thin, homogeneous membranes of required mechanical strength and near-theoretical density. Solid electrolytes are generally used as a low-loss separator of two liquid or gaseous reactants of an electrochemical cell. High power requires a large surface area and a thin membrane; the ohmic loss is proportional to the thickness of the separator. Chemical homogeneity and uniformly high density are prerequisites to long cycle life; "hot spots" that develop at chemical inhomogeneities or in regions of relatively high void density cause the cell to short out on successive cycling.

2. Ionic conductivity. In a crystal, the ionic conductivity is generally a tensor, $\underset{\approx}{\sigma}$, relating the applied electric field $\underset{\sim}{\varepsilon}$ to the current density $\underset{\sim}{j}$. In the absence of any mobile-ion gradients, Ohm's law gives

$$\underset{\sim}{j} = \underset{\approx}{\sigma} \cdot \underset{\sim}{\varepsilon} \qquad (4)$$

and a different scalar σ_{ij} describes the conductivity for each principal crystallographic direction. In amorphous or polycrystalline solids and in cubic crystals, as in liquids, the conductivity is isotropic and a single scalar σ_i is sufficient. In one-dimensional (1D) and two-dimensional (2D) crystals, on the other hand, it is essential to distinguish the conductivity in the unique direction, $\sigma_\parallel$, from that in the basal plane, $\sigma_\perp$. For example, $\sigma_\parallel \gg \sigma_\perp$ may be expected in 1D tunnel structures and a $\sigma_\perp \gg \sigma_\parallel$ in 2D layer structures. In the discussion to follow, an isotropic 3D conductivity σ_i will be discussed, but the adaptation required for a $\sigma_\parallel$ or a $\sigma_\perp$ will be indicated.

Ionic transport is a thermally activated diffusion process. Therefore, except in the temperature intervals where phase transitions occur, any scalar conductivity is described empirically - and phenomenologically - by an equation of the form

$$\sigma_i = (A/T)\ \exp(-E_A/kT) \qquad (5)$$

where the pre-exponential factor A and the effective activation energy E_A for a d.c. current are generally temperature-independent. Even in the case of protonic conduction in an aqueous acid, where proton tunneling across successive hydrogen bonds may introduce an important displacement current, a direct proton current requires a molecular rotation that introduces a finite activation energy E_A.

Fig. 1 illustrates the applicability of equation (5) for a few solid electrolytes having $\sigma \approx \sigma_i$, or a transport number $t_i \approx 1$. In the case of AgI, a first-order transition separates a normally conducting phase from a high-temperature phase exhibiting fast ionic conduction. In the cases of CuI and PbF_2, smooth transitions occur between these phases. A similar situation undoubtedly applies to $PbSnF_4$.

3. Motional enthalpy. Equation (5) may be derived phenomenologically from the general definition of the conductivity σ imparted by a density n of carriers of charge q having a mobility $\mu \equiv v/\varepsilon$, where v is the velocity of the charge carrier:

$$\sigma = nq\mu \qquad (6)$$

With the possible exception of protons within a hydrogen bond, ions are too heavy to tunnel from one crystallographic site to another, so they move diffusively. The Einstein expression for the drift mobility of a diffusing species is

$$\mu = qD/kT \tag{7}$$

where kT is the Boltzmann temperature factor and the diffusion coefficient

$$D = D_0 \exp(-\Delta G_m/kT) \tag{8}$$

contains the Gibb's free energy

$$\Delta G_m = \Delta H_m - T\Delta S_m \tag{9}$$

for the ion to jump from one atomic site to a near-neighbor vacant site so as to leave a final state that is energetically equivalent to the initial state. It follows from equations (6) to (9) that E_A in equation (5) contains the motional enthalpy ΔH_m in addition to any energy of excitation E_g that might be required to create mobile ions:

$$E_A = \Delta H_m + \dots. \tag{10}$$

The motional enthalpy

$$\Delta H_m = \varepsilon_b + \varepsilon_p \tag{11}$$

contains two terms, an energy barrier ε_b to hopping between sites when they are energetically equivalent and a local elastic-relaxation energy ε_p (polaron energy) that makes occupied and vacant sites energetically inequivalent. Since the jump time is long compared to the period of an optical-mode vibration, the mobile ion carries its local lattice relaxation with it. Therefore it is possible to speak about jumping between initial and final configurations that are energetically equivalent so long as the neighboring sites are energetically equivalent if both are empty or if both are occupied. This latter condition is fulfilled where the sites are crystallographically equivalent. In the discussion to follow, reference to energetically equivalent sites signifies that initial and final configurations associated with an ion jump are energetically equivalent.

4. Electronic mobility. Two types of electrons are distinguished: itinerant electrons, which tunnel between like atoms on energetically equivalent sites, and small polarons, which move diffusively like ions because the jump time between sites is longer than the lattice-relaxation time to trap them in

a local deformation. The mobilities of these two types of electrons must be distinguished:

$$\mu_e = \begin{cases} e\tau_s/m^* \text{ for itinerant electrons} \\ eD_e/kT \text{ for small polarons} \end{cases}$$

Itinerant electrons of effective mass m^* have a mean free time τ_s between scattering events. Small polarons typically have a room-temperature mobility $\mu_e < 0.1 cm^2/V\text{-sec}$; itinerant electrons have a $\mu_e > 0.1 cm^2/V\text{-sec}$. In general, itinerant-electron mobilities are many orders of magnitude greater than ionic mobilities, so a large electronic energy gap is needed to maintain a $t_i \approx 1$ at higher temperatures.

Material Design

The design of a solid electrolyte for a specific mobile ion begins with the choice of a host matrix. A Na^+-ion electrolyte, for example, would have the general formula $Na_xM_mX_n$, where M represents one or more cationic species and X one or more anionic species. In a Na^+-ion electrolyte, $(M_mX_n)^{x-}$ forms a host matrix within which the Na^+ ions are mobile. The ions represented by M and X must be chosen so as to provide not only an electronic insulator for the host matrix $(M_mX_n)^{x-}$, but also a thermodynamic window that ensures chemical instability in the presence of the cell reactants. In addition, the composition $(M_mX_n)^{x-}$ must be chosen so as to provide a structure that maximizes σ_{Na} of equation (5).

In order to obtain some insight into the structural criteria for fast Na^+-ion conduction, it is instructive to examine first a few model solid electrolytes and to compare their properties with simple theoretical considerations. The comparisons have led to two specific strategies for the design of Na^+-ion electrolytes: layered and framework hosts. The layered compounds have given inferior Na^+-ion conductivities, so only the framework hosts are reviewed here.

THEORY

General

An analytic expression for D_i can be obtained from the definition of the mobility:

$$\mu_i \equiv v_x/\varepsilon = qD_i/kT \tag{13}$$

where the velocity v_x in the direction of a field ε applied along the x-axis is the product of half the x-component of the jump vector ℓ between energetically equivalent sites and the difference in the transition probability for an ion to jump in a forward or a backward direction:

$$v_x = (\ell_x/2)fz(1-c)(\nu_+ - \nu_-) \tag{14}$$

where f is a "geometric correlation factor". The factor z(1-c) represents the fraction (1-c) of z nearest-neighbor sites that are empty, c being the concentration of energetically equivalent sites that are occupied. The jump frequencies

$$\nu_\pm = \nu_0 \exp[-(\Delta G_m \mp \tfrac{1}{2} q\varepsilon\ell_x)/kT] \tag{15}$$

contain, in addition to the attempt frequency ν_0, the contribution from the electric field to the free energy for an ion jump. In general, a $q\varepsilon\ell_x \ll 2kT$ reduces equation (13) to

$$\begin{aligned} \mu_i &= qD_i/kT = v_x/\varepsilon \\ &\approx (q/kT)(\ell_x^2/2)fz(1-c)\nu_0 \exp(-\Delta G_m/kT) \end{aligned} \tag{16}$$

For an isotropic system, $\ell_x^2/2$ may be replaced by $\ell^2/6$, and

$$D_i \approx \gamma(1-c)\ell^2\nu_0 \ \exp(-\Delta H_m/kT) \tag{17}$$

$$\gamma = (z/6)f \ \exp(\Delta S_m/k) \tag{18}$$

For 1D and 2D systems, the factor (z/6) in γ becomes, respectively, (z/2) and (z/4).

If N is the density of energetically equivalent sites available to the mobile ions, then $n_i = Nc$ and equations (6) and (16) give

$$\sigma_i = \gamma(Nq^2/kT)c(1-c)\ell^2\nu_0 \exp(-\Delta H_m/kT) \tag{19}$$

In this expression, an $N \sim \ell^{-3}$ makes $\sigma_i \sim \ell^{-i}$, so the ionic conductivity is inversely proportional to the jump distance ℓ. The attempt frequency $\nu_0 \approx 10^{-12} sec^{-1}$ is given by the optical-mode vibrational frequencies. The factor γ does not appear to be an important experimental variable. Therefore the designer of a new solid electrolyte must give primary concern to two parameters, the factor c(1-c) and the motional enthalpy ΔH_m.

Stoichiometry

At T=0K, stoichiometric compounds tend to have all their ions ordered into subarrays of crystallographically equivalent sites that are either full (c=1) or empty (c=0). This situation makes the product c(1-c) vanish, so σ_i vanishes also. The filled mobile-ion sites are the "normal" sites; the empty sites are "interstitial" sites. The energies of the normal and empty sites are separated by an energy gap

$$\Delta G_g = \Delta H_g - T\Delta S_g \tag{20}$$

where ΔS_g is the change in configurational and vibrational entropy due to excitation of an ion from a normal to an interstitial site. At finite temperatures, thermal excitations of ions across the energy gap ΔG_g is analogous to electron excitation across the energy gap of a semiconductor. Therefore, in the absence of electronic excitations,

$$N(1-c)=N_I c_I=\tfrac{1}{2}(NN_I)^{\frac{1}{2}}\exp(-\Delta G_g/2kT) \tag{21}$$

where the density of interstitial ions is $c_I N_I$. For a large ΔH_g, the product $c(1-c) = c$ remains small at any operational temperature T, and the effective activation energy of equation (5) becomes

$$E_A = \Delta H_m + \tfrac{1}{2}\Delta H_g \tag{22}$$

Most stoichiometric solids have a large ΔH_g, so ionic conductivity remains negligible at normal operating temperatures. However, stoichiometric fast-ion conductors such as CuI, AgI, PbF_2 and Li_3N clearly represent interesting exceptions that need to be examined.

From equation (20), we may infer that fast ionic conduction implies a small ΔH_g and a large ΔS_g so that ΔG_g vanishes above some transition temperature $T_t < T_m$, where T_m is the melting point. The transition may be first-order, as in AgI, or smooth as in PbF_2, see Fig. 1. At $T > T_t$, equation (22) reduces to

$$E_A = \Delta H_m \tag{23}$$

and fast ionic conduction occurs provided the motional enthalpy ΔH_m is small.

Since the transitions are order/disorder in nature, they may be characterized by an order parameter ξ that varies from $\xi=1$ at $T=0K$ to $\xi=0$ at $T=T_t$, see Fig. 2. A fundamental problem for fast ionic conduction in stoichiometric compounds is the identification of the lowest-energy excitation; these determine the definition of ξ and the energies that govern its temperature dependence.

Nonstoichiometry

The creation of mobile holes or electrons in a semiconductor is readily achieved by doping it p-type or n-type. In principle the situation is analogous in ionic conductors, see Fig. 3. However, the acceptor or donor states are much deeper in the ionic case. The reason for this difference resides in the itinerant versus localized character of the mobile species. In a broad-band semiconductor such as elemental silicon, doping with an acceptor atom like Al or a donor atom like P creates a hydrogen-like centre in which the itinerant hole or electron, trapped at low temperature by the effective lattice charge at the impurity, sees an electrostatic attractive force that is reduced by the inverse square of the dielectric constant. In this case, both the kinetic and potential energies experience screening by the lattice. With a localized mobile charge, only the potential energy is screened, so the electrostatic attractive force between the mobile vacancy or ion and the dopant that introduced it is only reduced by the inverse of the dielectric constant. Since the dielectric constant is generally greater than 10, the vacancies or ions are trapped by an energy $\Delta G_t \approx 0.5\text{-}1.0\,\mathrm{eV}$ that may be further enhanced by local lattice relaxations if the relative sizes of the dopant and host ions are different. Consequently, doping introduces a trapping enthalpy ΔH_t into E_A:

$$E_A = \Delta H_m + \lambda \Delta H_t, \quad \tfrac{1}{2} < \lambda < 1 \qquad (24)$$

Even if the dopant concentration is large enough to exceed the percolation limit for pathways having a continuous access to dopant near neighbors, a residual ΔH_t is present. Unless ΔH_t is very small, fast ionic conduction is only found at high temperatures; moreover, the electrostatic forces between the mobile species tend, at higher concentrations, to induce an ordering that makes energetically inequivalent the occupied and empty sites. Therefore any doping strategy must be considered carefully.

As an aside, it is worth noting that in mixed electronic/ionic conductors such as are used for electrode materials, the problem of a ΔH_t does not arise. The mobile ions or vacancies are charge-compensated in this case by itinerant electrons in a partially filled band, so they are not trapped at stationary charges.

Three Principles

From these simple theoretical considerations, three principles emerge to guide the designer of new solid electrolytes [1].

1. Site occupancy. At the operating temperature T_{op}, the structure must provide a set of energetically equivalent sites that are only partially occupied by the mobile ions:

$$c(1-c) \neq 0 \qquad (25)$$

Doping to produce a $c(1-c) \neq 0$ introduces an energetic inequivalence that must be minimized.

2. Bottleneck geometry. If the partially filled, energetically equivalent sites are interconnected by common site faces, then ΔH_m may be minimized by satisfying the simple geometric constraint

$$R_{face} > R_{excl} \qquad (26)$$

where R_{face} is the distance from the centre of the common intersite face to an ion defining its perimeter. If $R_{face} < R_{excl}$ holds, the mobile ion must push aside the perimeter ions in an intersite jump; the energy to do this enters ΔH_m. In a hard-sphere model, R_{excl} is the sum of the ionic radii of the mobile ion and a perimeter ion. If the perimeter and mobile ions are polarizable (or quadrupolarizable), the radius of the exclusion sphere may be softened, which reduces the effective R_{excl}. Therefore polarizable perimeter ions are generally advantageous to fast ionic conduction; and quadrupolarizable ions such as Ag^+ or Cu^+ are generally more mobile than alkali-metal ions of similar size.

3. Interpenetrating mobile-ion sites. If the occupied array of energetically equivalent sites are interconnected by sites of an interpenetrating set of equivalent sites accessible to the mobile ions, but of different energy, then only a small difference of the mobile-ion potential energies of the two sets of sites may be tolerated; and this condition is favored if the interconnecting sites are partially filled rather than empty:

$$\underline{c_i}(1-\underline{c_i}) \neq 0 \text{ and } \underline{c_n} = 1 \qquad (27)$$

As illustrated in Fig. 4, this principle follows from the fact that electrostatic repulsions between the ions in the filled and the partially filled sets of sites reduces the difference in the mobile-ion potential energies of the two sets of sites. However, the geometric criterion for the intersite interfaces must also be satisfied.

MODEL STOICHIOMETRIC ION CONDUCTORS

CuI

Low-temperature (T < 369°C) γ-CuI has the cubic zincblende structure of Fig. 5(a). High-temperature (T > 407°C) α-CuI has the same cubic-close-packed array of I^- ions, but with Cu^+ ions occupying octahedral and tetrahedral sites with a nearly statistical distribution [2]. The intervention of an intermediate β-CuI having hexagonal-close-packed I^- ions does not appear to be critical to the general argument of the γ-α transition. The γ phase is a normal ionic conductor with an $E_A \approx 1eV$; the α phase is a fast-ion conductor with an $E_A \approx 0.2eV$.

In the γ phase, Cu^+-ion ordering on the tetrahedral sites, Fig. 5(a), has made inequivalent the occupied and empty sites, Fig. 5(b). A high-pressure transformation of γ-CuI to the rocksalt structure shows that the potential energy of the octahedral sites lies an energy ΔG_g above the normal tetrahedral sites that is not too large. Thermal excitation of Cu^+ ions to octahedral sites reduces the splitting between the occupied and empty tetrahedral sites. Expansion of this energy reduction to terms linear in the number of thermally excited ions gives a

$$\Delta G_g = \Delta H_{g0} - c_0\varepsilon - T\Delta S_g \qquad (28)$$

where c_0 is the concentration of octahedral-site ions and ε is a finite energy. The term $c_0\varepsilon$ introduces a positive feedback that, at high temperatures ($T > T_t$), collapses the distinction between tetrahedral-site subarrays; the occupied and empty tetrahedral sites are then only distinguishable energetically by a lattice-relaxation energy ε_p. Moreover, the term $T\Delta S_g$ operates until ΔG_g vanishes, so at high temperatures $T > T_t$ ($T_t < T < T_m$) an α-CuI phase is stabilized in which the Cu^+ ions have nearly equal access to all tetrahedral and octahedral sites. The feedback term $c_0\varepsilon$ makes the transition sharp at T_t; it could even make it first-order.

Boyce et al [2] have used EXAFS to study as a function of temperature the Cu^+-ion density distribution throughout the interstitial space of the I^--ion array. They found that the tetrahedral-site/octahedral-site interface increased with temperature until $R_{face} \gtrsim R_{excl}$ at T_t. For $T > T_t$, an $E_A = \Delta H_m \approx 0.2eV$ is found.

A quantitative theory of the transition begins with the definition of the order parameter

$$\xi = (c_1 - c_2)/(c_1 + c_2) \qquad (29)$$

where c_1 and c_2 are the concentrations of Cu^+ ions on the two tetrahedral-site subarrays. However, any theory depends on a model of the elementary excitations that introduce disorder. Hayashi [3] has attained fair agreement between the observed and calculated T_t using a model of antiphase domains - "microcrystals" - bounded by {110} faces so as to preserve charge neutrality; he does not discuss how such antiphase domains might be created. The smallest domain could be a simple-cubic tetrahedral-site unit containing four sites 1 and four sites 2 that had been rotated 90° with respect to the host matrix. The motional activation energy required for such a rotation is ΔH_m, so the creation of antiphase domains is kinetically inhibited unless $R_{face} \gtrsim R_{excl}$ and $\Delta H_g < 10kT$.

AgI [4]

The low-temperature phase of AgI consists of a mixture of zincblende and sphalerite structures, but it is simpler for pedagogical purposes to consider the cubic zincblende phase. In this case, the ions appear to be excited into off-centre, pseudotetrahedral positions within the octahedral sites, Fig. 6(a), as the high-temperature phase has a body-centered I^- array with Ag^+ ions in the pseudotetrahedral sites, Fig. 6(b). The diffusionless transition of the I^- array is the classical Bainite transition; it is first-order. Although electrostatic interactions between Ag^+ ions prevent two ions from simultaneously occupying the same cube face of Fig. 6(b), only two out of three faces are occupied, which satisfies the condition $c(1-c) \neq 0$. In addition, the pseudotetrahedral sites share common faces for which the geometrical condition of equation (26) is easily satisfied. Since the compound is stoichiometric, there are no trap sites. Therefore at high temperatures ($T > T_t = 147°C$), the structure satisfies all the criteria for fast ionic conduction, and

$$E_A = \Delta H_m = 0.05 \text{ eV} \tag{30}$$

is the smallest known activation energy for a solid electrolyte.

The first-order β-α transition in AgI is quite analogous to the transition in CuI. The lower T_t in AgI indicates that ΔG_g is smaller, which is consistent with the low critical hydrostatic pressure ($P_c = 3$kbar) for transformation to the rocksalt structure. It is also consistent with the observation that substitution of Br^- for I^- to lower the lattice parameter [5], like the application of pressure [1], also lowers the transition temperature T_t, presumably by lowering ΔG_g.

PbF_2

Several simple difluorides crystallize with the fluorite structure of Fig. 7(a). Of these, PbF_2 shows the best F^--ion conductivity; it exhibits a smooth transition (T_t=438°C [7]) from normal to fast ionic conduction without any transformation of the face-centred-cubic subarray of Pb^{2+} ions. At T=0K, all the tetrahedral sites are occupied by F^- ions, and c=1. Attempts to account for the fast F^- -ion conductivity at higher temperatures in these fluorites have considered excitations to the empty octahedral sites; the results have not been satisfactory. It is necessary to find another type of excitation of lower energy that can introduce a $c(1-c)\neq 0$.

A clue comes from the structure of KY_3F_{10} and KBi_3F_{10} [8], which is illustrated in Fig. 7(b). As in PbF_2, the cations form a face-centered-cubic array. However, the anion/cation ratio is 2.5/1 rather than 2/1, so it is instructive to see how the extra F^- ions are accommodated within the structure. The edges of the fluorite cubic cell are doubled, and alternate quadrants contain, respectively, 8 F^- ions in tetrahedral sites and 12 F^- ions at common tetrahedral-site edges, but displaced toward the octahedral site. The fact that these two configurations coexist in this structure demonstrates that an elementary rotation by 45° of a simple cube of F^- ions in the fluorite structure would cost relatively little energy, provided the motional enthalpy ΔH_m is small; and a small ΔH_m is demonstrated by the fast ionic conduction at high temperature. Therefore the ΔG_g of interest is not between a tetrahedral and an octahedral single-ion site occupancy, but between simple-cubic configurations of F^- ions in tetrahedral sites and in common-edge (bottleneck) positions. Since there are twice as many bottleneck positions as tetrahedral sites, a finite ΔS_g makes

$$\Delta G_g = \Delta H_{g0} - c_e\varepsilon - T\Delta S_g \qquad (31)$$

decrease with increasing temperature through an order-disorder transition. The enthalpy ΔH_g also decreases with the concentration c_e of edge F^- ions, so there is a positive feedback that sharpens the transition.

High-temperature X-ray studies that take account of the anharmonic part of the mobile-ion potential have given direct evidence for a mobile-ion density that is distributed over the tetrahedral and edge positions, with little density in the octahedral sites [9]. Moreover, the availability of the edge positions can explain how LuF_3, which has tetrahedral and octahedral sites filled at low temperature, can be a fast F^- -ion conductor below the melting temperature without any transition of the Lu^{3+} ions from a face-centered-cubic subarray [10].

Li_3N

As illustrated in Fig. 8(a), Li_3N consists of -Li-N-Li-N- chains held together by Li^+ -ions in triangular sites of close-packed N^{3-} -ion layers. At low temperature all the triangular sites are filled (c=1). Nevertheless, at room temperature, it exhibits fast Li^+ -ion conduction in the Li_3N planes ($\sigma_\perp \approx 10^{-3}$ ohm^{-1}cm^{-1} $\gg \sigma_\parallel$) [11]. Moreover, X-ray studies [12] have demonstrated that there are few Li^+ -ion vacancies in the basal planes. The situation is analogous to PbF_2, only here the elementary excitation is a rotation of 6 Li^+ by 30° about a common N^{3-} ion to edge positions as illustrated in Fig. 8(b). This excitation requires a motional enthalpy 6 ΔH_m, and hence a small ΔH_m. Direct evidence in support of this model is again given by the X-ray mobile-ion density, which is distributed over both triangular and edge positions [12]. Since there are twice as many edge as triangular sites, the availability of edge positions makes $c(1-c)\neq 0$.

In this compound, Li^+-ion conduction along the c-axis apparently proceeds by correlated jumps of two Li^+ ions. A Li^+ ion of one layer displaces an interplanar Li^+ ion, which in turn moves into the other adjacent layer [13].

Summary

These examples of fast ionic conduction in stoichiometric solid electrolytes have illustrated the importance of a small ΔH_m and hence an $R_{face} > R_{excl}$. They have also made clear that microscopic models must consider multiple-ion, correlated excitations as well as single-ion excitations wherever ΔH_m is small. Moreover, a small ΔH_m may make "bottle-neck" positions accessible as site positions where $\Delta H_m \approx kT$. Therefore the design of a solid Na^+-ion electrolyte must begin with a strategy for making ΔH_m small, and hence for satisfying equation (26). This condition is not satisfied in the layer compounds, where Na^+ ions occupy trigonal-prismatic or octahedral sites sharing common faces or edges. The Na^+ ion is large enough to require framework structures.

FRAMEWORK STRUCTURES

Definition

Any compound $Na_x^+(M_mX_n)^{x-}$ that consists of a 3D host framework $(M_mX_n)^{x-}$ with an interconnected interstitial space is a framework structure. For example, the cubic tungsten bronzes Na_xWO_3 contain a cubic $(WO_3)^{x-}$ framework of corner-shared WO_6 octahedra forming the ReO_3 structure. As a solid electrolyte, this composition fails on two counts: (1) it is metallic and (2) the cube faces provide too small a bottleneck, $R_{face} < R_{excl}$. Although the former could be handled by making $Na_x(Ta_xW_{1-x})O_3$, the geometric constraint forces consideration of other framework structures where an $R_{face} > R_{excl}$ can be formed.

An oxide framework is preferred as its fabrication can be done in air and the $O^{2-}:2p^6$ valence band is stable enough to be chemically inert against most oxidizing agents. Sulfides may also be acceptable, but most work to date has been with oxides. In an oxide, an $R_{face} = 2.4Å$ is desired for Na^+-ion electrolytes as the Na^+ ion is neither polarizable nor quandrupolarizable, and the polarizability of an O^{2-} ion is modest.

Three classes of framework structures must be distinguished at the outset: (1) tunnel or 1D structures such as the hexagonal tungsten bronze structure of Fig. 9(a), (2) 2D structures such as the Na-β-alumina structure of Fig. 9(b), and (3) 3D structures in which the mobile ions can move rapidly in three dimensions. Although 1D structures may be satisfactory as films having their unique axis oriented parallel to the direction of Na^+-ion transport, they cannot be the optimal device. Any stacking faults or disorder would tend to block the tunnels, and the range of applications is limited. Consequently, primary attention has been paid to the 2D and 3D materials.

The Na-β Aluminas

The model 2D materials are the β and β" aluminas, see Fig. 9(b). A stoichiometric Na-β alumina, $Na_2O.11Al_2O_3$, contains $Al_{11}O_{16}$ spinel slabs perpendicular to the [111] axis; the slabs are connected by oxygen bridges within the intervening Na-O layers. Two crystallographically inequivalent Na^+-ion sites exist in the Na-O plane: a more-stable Beavers-Ross (BR) site and a less-stable anti-Beavers-Ross site (aBR). These sites are connected by a rectangular interface perpendicular to the Na-O plane, the mid-oxygen (mO) position, that has an $R_{face}(=2.71Å) > 2.4Å$. In Na-β" alumina, the spinel slabs are shifted with respect to each other so as to make the Na-O planes mirror planes and the BR and aBR sites crystallographically equivalent. There is also some puckering of the Na-O layers so that the mobile ions move in a thin, conducting slab rather than strictly within a plane. Stoichiometric compounds with the Na-β structure have, at T=0K, c=1 for the BR sites and c=0 for the aBR sites, which makes them relatively poor conductors. On the other hand, $c(1-c)\neq0$ in the Na-β" analogues, and these exhibit higher 2D Na^+-ion conduction [14].

In practice, Na-β alumina always contains excess Na_2O corresponding to the chemical formula $(1+x)Na_2O.11Al_2O_3$ with x=0.22. The extra O^{2-} ions randomly occupy the mO positions, where they are stabilized by Al^{3+}-ion displacements within the spinel slabs. The two extra Na^+ ions introduced with an interstitial O^{2-} ion occupy nearest-neighbour mO positions and displace the nearest-neighbour Na^+ ion on BR positions to mO positions. Thus the Na^+-ion potential energy tends to be smoothed in the neighbourhood of the interstitial Na_2O units, and a c(1−c)≠0 is also introduced. The result is an enhanced Na^+-ion mobility [15].

Substitution of Mg^{2+} or Li^+ ions for Al^{3+} ions in the spinel blocks may be charge-compensated by extra Na^+ ions in the Na-O planes without introduction of interstitial O^{2-} ions. This procedure tends to stabilize β" structures, but both "ion-rich" β and β" phases corresponding to $Na_{1.7}O$ conducting planes have been prepared and studied with a combination of X-ray diffraction and diffuse-X-ray scattering as a function of temperature [16]. Two-dimensional Na^+-ion correlations were observed in which microdomains of Na-vacancy ordering in aBR sites had a coherence length that decreased with increasing temperature and was reflected in the E_A obtained from conductivity measurements. In Na-β", a coherence length ξ=70Å and an E_A=0.35eV at $T < 300K$ evolved to a high-temperature state with a ξ=20Å and an E_A=0.10eV. In "ion-rich" Na-β, on the other hand, a $\xi > 150Å$ was found and also an R_{face}=2.31Å < R_{excl}, which significantly reduces the Na^+-ion conductivity. However, in the usual Na-β alumina, where R_{face}=2.48Å and ξ=40Å, fast ionic diffusion was found. These studies again emphasize the significance of the geometrical constraint of equation (26) and of the tendency for coulomb interactions between mobile ions to induce short-range order, particularly where a finite ΔH_m inhibits correlated multi-electron excitations.

The Na-β aluminas have been intensively worked on since 1967, when it was proposed that they be used in a Na-S battery [17]. Nevertheless, the development of a reliable ceramic separator having a long cycle life continues to plague commercialization of the cell. A 2D material has anisotropic thermal expansion, which is undesirable for repeated thermal cyling between room temperature and 350°C, the operating temperature of the cell. Sintering of the alumina without loss of Na_2O requires special ceramic techniques, uniformity of density and chemical homogenity is difficult to achieve, and the membranes are sensitive to water and CO_2, which can enter the conducting planes and cause degradation of the ceramic surface. There is therefore ample motivation to design alternate, 3D Na^+-ion electrolytes.

3D Frameworks

Although Li^+ and Cu^+ ions may be small enough to diffuse rapidly in close-packed arrays of large, polarizable anions, the Na^+ ion is not. Fast Na^+-ion diffusion requires an $R_{face} \geq$ 2.4Å, which can be accommodated by pentagonal or, preferably, hexagonal intersite faces as in Fig. 9(a) or by a rectangle formed from tetrahedral sites sharing a common corner as in Fig. 9(b). The problem is to find structures in which Na^+-ion sites are interconnected in 3D by such common interfaces.

1. $NaSbO_3.1/6$ NaF. The cubic high-pressure form of $KSbO_3$ has the body-centered $(Sb_{12}O_{36})^{12-}$ framework illustrated in Fig. 10(a) [18]. Pairs of edge-shared SbO_6 octahedra form Sb_2O_{10} groups that share corners. The framework contains empty tunnels that run parallel to the four {111} directions and intersect at the origin, taken as the centre of the cube face of Fig. 10(a), and body-centre positions. The intersection sites are large octahedra sharing faces with the tunnel segments between them; and the tunnel segments consist of three face-shared octahedra that have been significantly flattened along the tunnel axis. On proceeding along a tunnel axis from an origin to a body-centre position, successive interfaces are bounded by O_1, O_2, O_2 and O_1 anions as indicated in Fig. 10(b). The O_1-O_2 and O_2-O_2 sites 16f and 8c are bounded by puckered hexagonal rings, so that the shared O_1 or O_2 faces have an R_{face} that approaches R_{excl}. It suggested that the Na^+-ion analogue might meet the constraint of equation (26), and $NaSbO_3$ was prepared by ion exchange in molten $NaNO_3$ [19]. At room temperature, R_{face}=2.40Å$\approx R_{excl}$ for the O_2 faces and R_{face}=2.73Å for the O_1 faces. Moreover, the Na^+-ion conductivity was good, although not competitive with Na-β" alumina.

This structure contains three distinguishable sites that could be occupied by Na^+ ions: the intersection sites, the 16f sites and the 8c sites. Annealed samples have the primitive space group Pn3 with the mobile ions ordered into alternate tunnel segments having a single K^+ ion in 8c sites or two K^+ ions in the two 16f sites. This order suggests a lower potential energy at 8c positions, but coulomb repulsions stabilize 16f occupation in doubly occupied segments. Lack of occupancy of the intersection sites indicated that anions might be stabilized there, and $KSbO_3.1/6KF$ was prepared at atmospheric pressure [20]. Ion exchange in molten $NaNO_3$ gives the sodium analogue $NaSbO_3.1/6NaF$ in which the F^- ions occupy the intersection sites and the extra Na^+ ions are incorporated into the tunnel segments. The tetrahedra formed by the O_1 faces and the F^- ions are large enough to permit Na^+-ion hopping between tunnel segments, so introduction of F^- ions at the tunnel intersection sites 2a has little influence on the Na^+-ion mobility.

2. Defect pyrochlores. The cubic structure of the pyrochlores $A_2M_2X_6X'$ contains an (M_2X_6) framework of corner-shared octahedra and an interpenetrating A_2X' array of corner-shared $X'A_4$ tetrahedra, Fig. 11. The large A cations occupy a flattened X^--ion octahedral site having X' ions on opposite sides. With space group Fd3m and the origin chosen at an octahedral site, the A and X' atoms are located at positions 16d and 8b.

Fluorides and oxides having a large A^+ ion (K^+, Rb^+ or Cs^+) and a chemical formula $A^+(M_2X_6)^-$ may crystallize with a defect-pyrochlore structure in which the A^+ ions occupy 8b positions and the 16d positions are empty [21-23]. Moreover the 16d sites are flattened into a puckered hexagonal ring, so an $R_{face} > 2.4Å$ is found. This observation suggests that the potential-energy difference between 16d and 8b sites for A^+-ion occupancy is small and can be adjusted by altering the relative sizes of the framework and the A^+ ions. It was hoped that defect pyrochlores containing Na^+ ions could be prepared by ion exchange of K^+ ions, but preliminary attempts in this direction were plagued by the introduction of extra Na_2O with the Na^+ ions, the extra O^{2-} ions occupying the 8b positions [20].

3. The Carnegieite Structure. The cubic form of $Na^+(AlSiO_4)^-$, carnegieite, has an $(AlSiO_4)^-$ framework of corner-shared tetrahedra, Fig. 12. The Al^{3+} and Si^{4+} ions are ordered in a zincblende subarray with O^{2-} ions between each Al-Si pair. The interstitial space, occupied by Na^+ ions, is of equal volume, but displaced by half a lattice parameter. Each Na^+-ion site has four tetrahedrally oriented, like near-neighbor sites; the interfaces are hexagons formed from tetrahedral-site edges. Unfortunately, this cubic phase collapses at lower temperatures so as to have shorter Na-O bonds. However, the cubic framework can be supported by the introduction of additional atoms, but these tend to block the mobile-ion pathways. The compound $Na^+(AlSiO_4)^-.\frac{1}{4}Na_2O$, for example, is stable in the cubic form. It shows interesting, but not competitive, Na^+-ion transport despite interference from the extra O^{2-}ions [20].

4. NASICON. The compound $NaZr_2(PO_4)_3$ has the hexagonal framework illustrated in Fig. 13 [24]. Along the c-axis, face-shared octahedral or trigonal-prismatic sites are ordered as

$$-Zr_0-V_t-Zr_0-M_1-Zr_0-$$

where Zr_0 is an octahedral Zr^{4+} site, V_t is a vacant trigonal-prismatic site,and M_1 is an octahedral site available to Na^+ ions. These chains are interconnected by PO_4 tetrahedra that share all their corners with the Zr_0 sites; the Zr_0 octahdra share all their corners with PO_4 tetrahedra. For every M_1 site there are three M_2 sites. The M_2 sites, not shown in Fig. 13, form hexagonal-close-packed layers perpendicular to the c-axis; they occupy the same planes as the O^{2-} ions nearest neighbor to Na^+ ions in M_1 sites. The bottleneck between M_1 and M_2 sites consists of a puckered hexagonal ring bounded alternately by tetrahedral-site and octahedral-site edges. In $NaZr_2(PO_4)_3$, the M_1 sites are filled (c=1) and the M_2 sitec are empty (c=0), so the compound is a poor Na^+-ion conductor even though $R_{face}=2.5Å_3 > R_{excl}=2.4Å$ satisfies the geometrical constraint of equation (26).

The compound $Na_4Zr_2(SiO_4)_3$ has the same framework [25], and in this case both the M_1 and M_2 sites have c=1. This compound is an even poorer Na^+-ion conductor than $NaZr_2(PO_4)_3$. However, the solid solutions $Na_{1+x}Zr_2P_{3-x}Si_xO_{12}$ can be made, and compositions with $x=2$ have an $E_A \approx 0.24$eV with Na^+ -ion conductivities competitive with those of Na-β" alumina above 350°C [20]. Compositions with $x \approx 2$ have been called NASICON (sodium superionic conductor).

Many laboratories, in attempting to verify these results, have found excess free zirconia and chemical instability against molten sodium. These findings have led to the exploration of Zr-deficient compounds with the same structure, including the phosphates $Na_{1+4x}Zr_{2-x}(PO_4)_3$. Apparently Na^+ ions may substitute for Zr^{4+} ions in the Zr_0 sites, charge compensation occurring by additional Na^+ ions on the M_2 sites and, at least at low temperature, some occupancy of V_{trig} sites. If the compounds are prepared so as to avoid exsolution of zirconia, they are chemically stable [26,27]. Phase-diagram studies to aid such preparations have been initiated [28].

The versatility of the framework has also been explored [29]; a wide range of ions can be substituted for Na^+, Zr^{4+} and P^{5+}. The most extensive studies have been with compounds $Na_3M_2(PO_4)_3$, where M is a trivalent cation (Sc^{3+}, Fe^{3+}, Cr^{3+}). However, the best Na^+-ion conductivities occur with the NASICON compositions, which have the largest cell volume.

Problems with phase transitions occurring between room temperature and 300°C have been reported [30,31]. Two types of phase transitions have been identified [32]. Sodium-rich samples tend to incorporate Na^+ ions in the V_{trig} sites at low temperature, and a phase transition is associated with their transfer to M_1 and M_2 sites. At higher temperatures there is a change in the relative occupancies of M_1 and M_2 sites that is reflected in the c/a ratio [33]. Moreover, components with three Na^+ ions per formula unit, as occurs with NASICON itself, may exhibit a minor ionic distortion in which the M_2 sites become distinguishable: $3M_2 \rightarrow M_3 + 2M_4$ [34], which allows for ordering of the Na^+ ions into M_1+2M_4 sites. The degree of order and the sharpness of the order-disorder transition depend on the particular framework and the relative energies of the M_1 and M_2 sites in the hexagonal phase. Optimum Na^+-ion conductivity is found where the potential energies of these two sites are nearly equal and the cell volume is a maximum.

Although it is possible to visualize Na^+-ion conduction via Na^+-ion hopping between M_2 sites, the dominant Na^+-ion conduction path involves hopping between M_1 and M_2 sites [29]. However, in ceramic materials it is always important to consider the grain-boundary contribution to the net impedance. As in the Na-β aluminas, Na^+-ion conduction across the grain boundaries is fast. Nevertheless the grain-boundaries make an important contribution to any equivalent circuit and may dominate the conductivity at high temperatures [35].

Zirconium-deficient NASICON is now used commercially in primary cells, and it remains a strong contender with Na-β and β" alumina for use in any high temperature Na-S cell.

5. $Na_5LnSi_4O_{12}$. A report [36] that nearly half the Na^+ ions could not be located in a structure determination of $Na_5YSi_4O_{12}$ stimulated exploration in three laboratories on the potential of this structure for fast Na^+-ion conduction [37-39]. The structure consists of $Si_{12}O_{36}$ rings interlayered and stuffed with the 8/3 immobile Na^+ ions per formula unit - Na_1^+, Na_2^+ and Na_3^+ - so as to form columns parallel to the c-axis in hexagonal space group R3c. The columns are bridged by Ln^{3+} ions, and the remaining 7/3 mobile Na^+ ions per formula unit occupy interstitial space between the columns. The polycrystalline conductivity increases linearly with the radius of the Ln^{3+} ion, and Fig. 14 compares the Na^+ -ion conductivity of $Na_5GdSi_4O_{12}$ with that of other framework ceramics [37]. Single-crystal studies [38] reveal a $\sigma_{\parallel} \approx 30\sigma_{\perp}$. X-ray diffraction combined with diffuse-x-ray scattering has identified the conduction pathways parallel and perpendicular to the c-axis [40]. Three crystallographically distinguishable sites share common faces having $R_{face} > 2.4Å$ to form chains parallel to the c-axis; two are occupied by Na_5^+ and Na_1^+ ions, the third, V_{Na}, is vacant. The Na^+ ions are arranged in triples within the chains:

$$-V_{Na}-Na_6^+-Na_5^+-Na_6^+-V_{Na}-$$

so as to optimize the electrostatic repulsions in the chain. These sites may be considered energetically (quasi) equivalent with a $c(1-c) \neq 0$. A Na^+ ion can jump into a V_{Na} from one triple to induce a similar jump from the opposite end of the receiving triple. A mobile Na_4^+ ion bridges to Na_6^+ ions in the conducting channels via a common interface having an $R_{face} < R_{excl}$, which makes $\sigma_{\perp} < \sigma_{\parallel}$.

From Fig. 14, it is seen that at 350°C, the operating temperature of a Na-S cell, at least three material options are now available. However, the preparation of suitable ceramic membranes continues to be a challenging problem even though VARTA has developed an operational receipe for Zr-deficient NASICON. The fact that the NASICON framework, and perhaps others, may be cast as a glass offers scope for further development. In the case of $Na_5YSi_4O_{12}$, ceramic materials have been reported to be especially sensitive to small soda deficiencies [40].

REFERENCES

1. J.B. Goodenough, "Skeleton Structures", Solid Electrolytes, P. Hagenmuller and W. Van Gool, eds, Academic Press, NY: Chap. 23, 1978.

2. J.B. Boyce, T.M. Hayes and J.C. Mikkelsen, Jr. "Extended-x-ray absorption-fine-structure investigation of mobile-ion density in superionic AgI, CuI, CuBr, and CuCl" Phys Rev B23: 2876-2896; 1981.

3. H. Hayashi, "Theory of the superionic transition in CuI" J Phys Soc Japan 51:811-817; 1982.

4. M.B. Salamon, ed., Physics of superionic conductors, Springer-Verlag 1979.

5. K. Shahi and J.B. Wagner, Jr., "Phase transition and the Ag^+-ion diffusion in AgI: effect of homovalent Br^--ion substitution" Phys Rev B23:6417-6421; 1981.

6. A.J. Majumdar and R. Roy, "Experimental study of the polymorphism of AgI", J Phys Chem 63:1858-1860; 1959.
   P.C. Allen and D. Lazarus, "Effect of pressure on ionic conductivity in rubidium silver iodide and silver iodide" Phys Rev B17:1913-1927; 1978.

7. W. Schröter and J. Nölting, "Specific heats of crystals with the fluorite structure" J Phys (Paris) 41:C6 20-23; 1980.

8. J.L. Soubeyroux, J.M. Réau, S. Matar, G. Villeneuve and P. Hagenmuller, "Etude par diffraction, neutronique des solutions solides $K_{1-x}Bi_xF_{1+2x}$ et $Rb_{1-x}Bi_xF_{1+2x}$" Solid State Ionics 6:103-111; 1982.

9. H. Schulz, Proc. 2nd European Conference on Solid State Chemistry, Eindhoven University of Technology, 7-9 June 1982, in press.

10. L.E. Nagel and M. O'Keeffe, "Highly conducting fluorides related to fluorite and tysonite" Fast-ion Transport in Solids: Solid-state Batteries and Devices, W. Van Gool, ed.: 165-172; North-Holland/Elsevier 1973.
M. O'Keeffe and B.G. Hyde, "Relations between the structures of the rare-earth fluorides and high chalcocite (Cu_2S), Implications for solid-electrolyte behavior" J Solid State Chem 13:172-175; 1975.

11. U. von Alpen, A. Rabenau and G.M. Talat, "Ionic conductivity in Li_3N single crystals" Appl Phys Lett 30:621-623; 1977
A. Rabenau, "Lithium nitride, Li_3N, an unusual ionic conductor" Festkorperprobleme XVIII: Advances in Solid State Physics 18:77-108; Pergamon/Vieweg, Braunschweig 1978.

12. H. Schulz and K.H. Thiemann, "Defect structure of the ionic conductor lithium nitride (Li_3N)" Acta Crystall A35:309-314; 1979.

13. D. Brinkmann, M. Mali, and J. Roos, "Diffusion processes in the superionic conductor Li_3N: an NMR study" Phys Rev B26:4810-4824; 1982.

14. W.L. Roth, R.E. Benenson, V.K Tikku, J.L. Briant, and B. Dunn, "Li and Mg stabilized beta aluminas" Solid State Ionics 5:163-166; 1981.

15. W.L. Roth, F. Reidinger, and S. LaPlaca, "Studies of stabilization and transport mechanisms in beta and beta" alumina by neutron diffraction" Superionic Conductors, G.D. Mahan and W.L. Roth, eds: 223-241; Plenum 1973.

16. J.P. Boilot, G. Collin, Ph. Colomban, and R. Comes, "X-ray scattering study of the fast-ion conductor β"-alumina" Phys Rev B22:5912-5923; 1980.

17. N. Weber and J.T. Kummer, "Sodium-sulfur secondary battery" Proc 21st Ann Power Sources Conf 37-39; 1967.

18. P. Spiegelberg, "X-ray studies on potassium antimonates" Ark Kemi 14A:1-12; 1940.

19. H.Y-P. Hong, J.A. Kafalas, and J.B. Goodenough, "Crystal chemistry in the system M antimonate (M=lithium, sodium, potassium, rubidium, thallium, and silver) J Solid State Chem 9:345-351; 1974.

20. J.B. Goodenough, H.Y-P. Hong, and J.A. Kafalas, "Fast Na^+-ion transport in skeleton structures" Mater Res Bull 11:203-223; 1976.

21. D. Babel, G. Pausewang, and W. Viebahn, "Structure of some fluorides, oxides and oxyfluorides of the $RbNiCrF_6$ type" Z Naturforsch 22B:1219-1220; 1967.

22. J.L. Fourquet, C. Jacobini, and R. de Pape, "Les pyrochlores $A_IB_2X_6$: mise en evidence de l'occupation par le cation A_I de nouvelles positions cristallographiques dans le groupe d'espace Fd3m" Mater Res Bull 8:393-403; 1973.

23. C. Michel, D. Groult, and B. Raveau, "Sur des nouveaux pyrochlores $ASbWO_6$ (A=K, Rb, Cs, Tl)" Mater Res Bull 8:201-210; 1973.

24. L.O. Hagman and P. Kierkegaard, "The crystal structure of $NaMe_2{}^{IV}(PO_4)_3$" Acta Chem Scandinav 22:1822-1832; 1968.

25. R.G. Zizora, A.A. Voronkov, N.G. Shumyatskaya, V.V. Ilyukhin and N.V. Belov, "Crystal structure of $Na_4Zr_2(SiO_4)_3$" Sov Phys Dokl 17:618-620; 1973.

26. J.A. Kafalas and R. Cava, "Effect of pressure and composition on fast Na^+-ion transport in the system $Na_{1+x}Zr_2Si_xP_{3-x}O_{12}$" Proc Int Conf on Fast Ion Transport in Solids, May 21-25, 1979; Lake Geneva; P. Vashishta, J.N. Mundy and G.K. Shenoy, eds; 427-430; Elsevier 1979.

27. U. von Alpen, M.F. Bell and H.M. Hofer, "Compositional dependence of the electrochemical and structural parameters in the NASICON system" Solid State Ionics 3-4:215-218; 1981.

28. A. Clearfield, P. Jerus and R.N. Cotman, "Hydrothermal and solid-state synthesis of sodium zirconium silico phosphate" Solid State Ionics 5:301-304; 1981 and unpublished research.

29. D.P. Birkett, unpublished research.

30. U. von Alpen, M.F. Bell and W. Wickelhaus, "Phase transition in NASICON" Mater Res Bull 14:1317-1322; 1979.

31. J.P. Boilot, J.P. Salanié, G. Desplanches and D. Le Potier, "Phase tranformation in $Na_{1+x}Zr_2Si_xP_{3-x}O_{12}$" Mater Res Bull 14:1469-1477; 1979.

32. J.P. Boilot, G. Collin and R. Comes, "Phase transition in NASICON compounds $Na_3Sc_2P_2O_{12}$ and $Na_{1+x}Zr_2Si_xP_{3-x}O_{12}$" Solid State Ionics 5:307-310; 1981 and "Evidence of a relation between structural defects and phase transitions in NASICON type compounds" Solid State Comm to be published.

33. C. Delmas, R. Olazcuaga, G. LeFlem, P. Hagenmuller, F. Cherkaoui and R. Brochu, "Crystal chemistry of the $Na_{1+x}Zr_{2-x}L_x(PO_4)_3$ (L=Cr,In,Yb) solid solutions" Mater Res Bull 16:285-290; 1981.

34. H.Y-P. Hong, "Crystal structure and crystal chemistry in the system $Na_{1+x}Zr_2Si_xP_{3-x}O_{12}$" Mater Res Bull 11:173-182; 1976.

35. S. Fujitsu, M. Nagai, T. Kanazawa and I. Yasui, "Conduction paths in sintered ionic conductive material $Na_{1+x}Y_xZr_{2-x}(PO_4)_3$" Mater Res Bull 16:1299-1309; 1981.

36. B.A. Maksimov, Yu. A. Kharitonov and N.V. Belov, "Crystal structure of the Na-Y metasilicate $Na_5YSi_4O_{12}$" Sov Phys Dokl 18:763-765; 1974.

37. R.D. Shannon, H.Y. Chen and T. Berzins, "Ionic conductivity in $Na_5GdSi_4O_{12}$" Mater Res Bull 12:969-973; 1977.

38. H.V. Beyeler and T. Hibma, "The sodium conductivity paths in the superionic conductors $Na_5RESi_4O_{12}$" *Solid State Comm* 27:641-643; 1978.

39. H.Y-P. Hong, J.A. Kafalas and M. Bayard, "High Na^+-ion conductivity in $Na_5YSi_4O_{12}$" *Mater Res Bull* 13:757-762; 1978.

40. B.A. Maximov, I.V. Petrov, A. Rabenau and H. Schulz, "X-ray investigations and possible mechanism for the ionic conductivity in $Na_5YSi_4O_{12}$ and $Na_5ScSi_4O_{12}$" *Solid State Ionics* 5:311-314; 1982.

41. J.J. Bentzen and P.S. Nicholson, "Preparation and characterization of dense sodium superionic conducting $Na_5YSi_4O_{12}$ (NYS) *Mater. Res. Bull* 17:541-548; 1982.

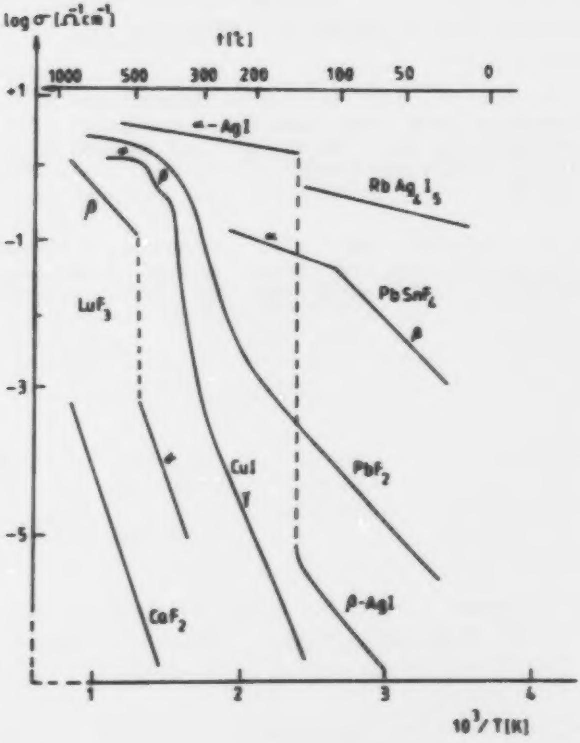

Fig. 1(a) Conductivity versus reciprocal temperature for various solid electrolytes.

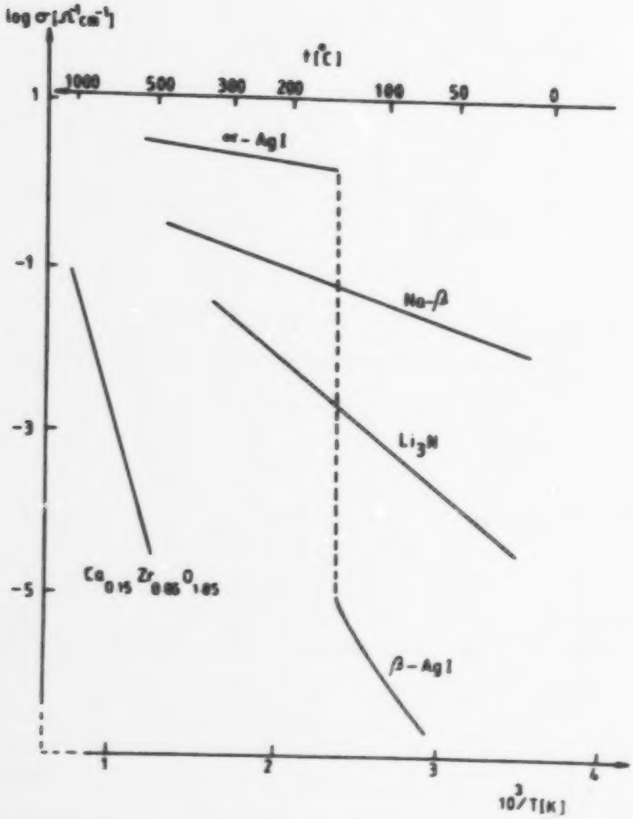

Fig. 1(b) Conductivity versus reciprocal temperature for various solid electrolytes.

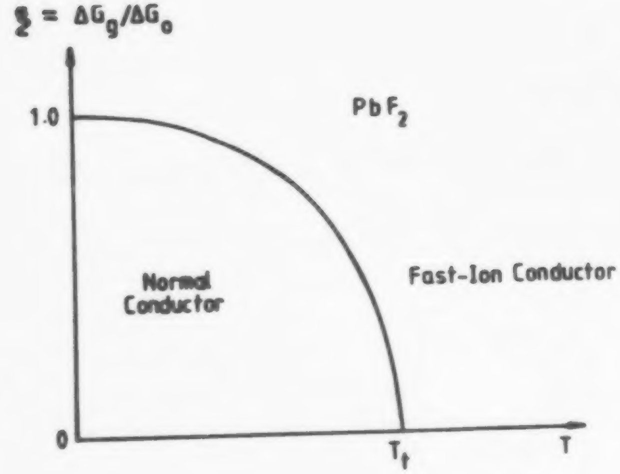
$\xi = \Delta G_g/\Delta G_o$
1.0
PbF$_2$
Normal Conductor
Fast-Ion Conductor
0
T_t
T

Fig. 2(a)

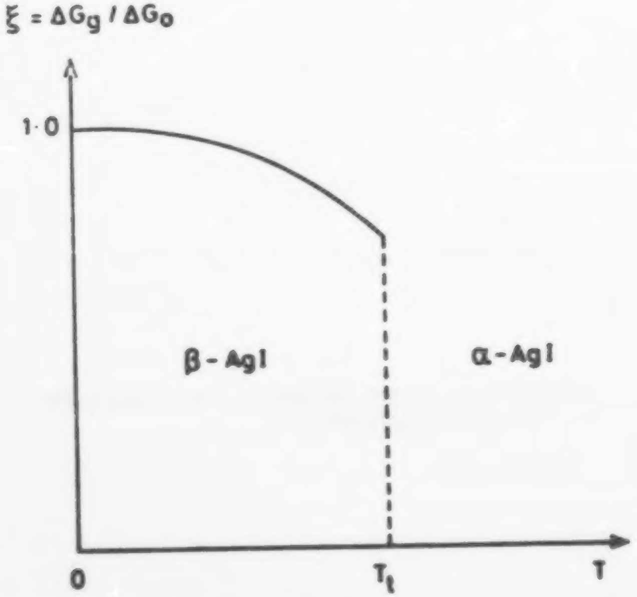
$\xi = \Delta G_g / \Delta G_o$
1·0
β - AgI
α - AgI
0
T_t
T

Fig. 2(b)

Fig. 2 Temperature variation of the order parameter ξ for (a) smooth and (b) first-order transitions.

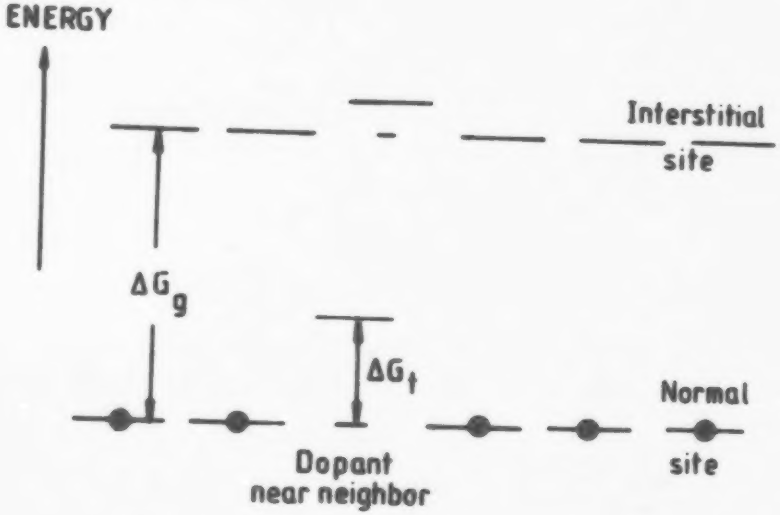
ENERGY
Interstitial site
ΔG_g
ΔG_t
Normal site
Dopant near neighbor

Fig. 3 Doping for ionic conductivity: occupied-site (–●–) and vacancy (——) energies.

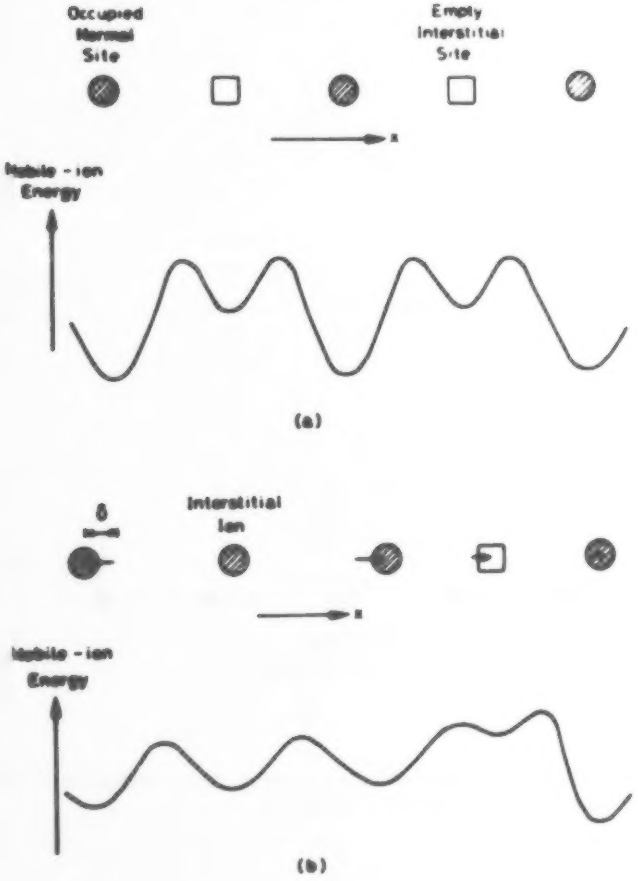
Occupied
Normal
Site
Empty
Interstitial
Site
x
Mobile - ion
Energy
(a)
δ
Interstitial
Ion
x
Mobile - ion
Energy
(b)

Fig. 4 Flattening of the mobile-ion potential by occupancy of immediate sites.

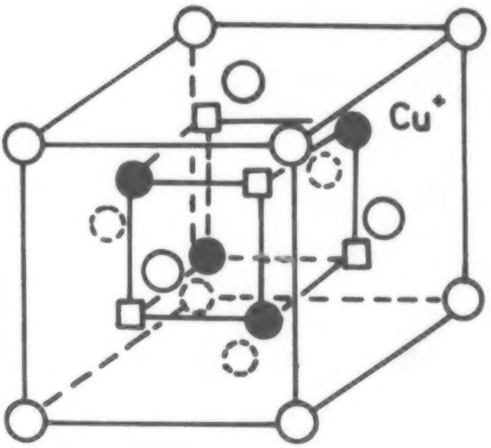

Fig. 5(a)

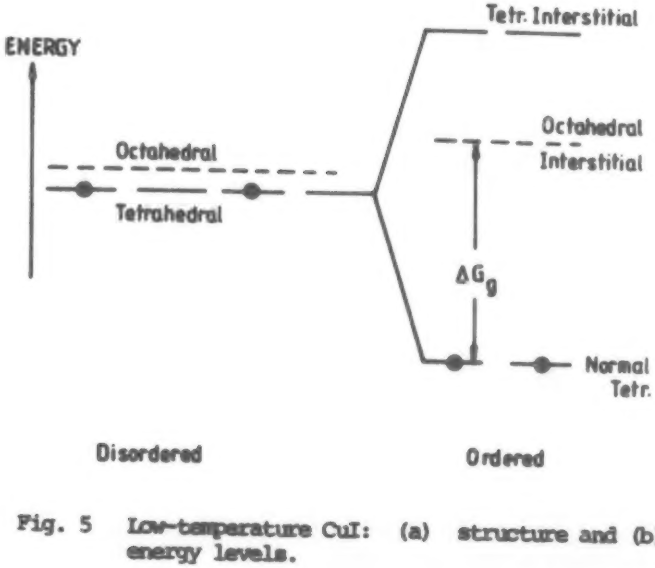
ENERGY
Octahedral
Tetrahedral
Tetr. Interstitial
Octahedral
Interstitial
ΔG_g
Normal
Tetr.
Disordered
Ordered

Fig. 5(b)

Fig. 5 Low-temperature CuI: (a) structure and (b) schematic energy levels.

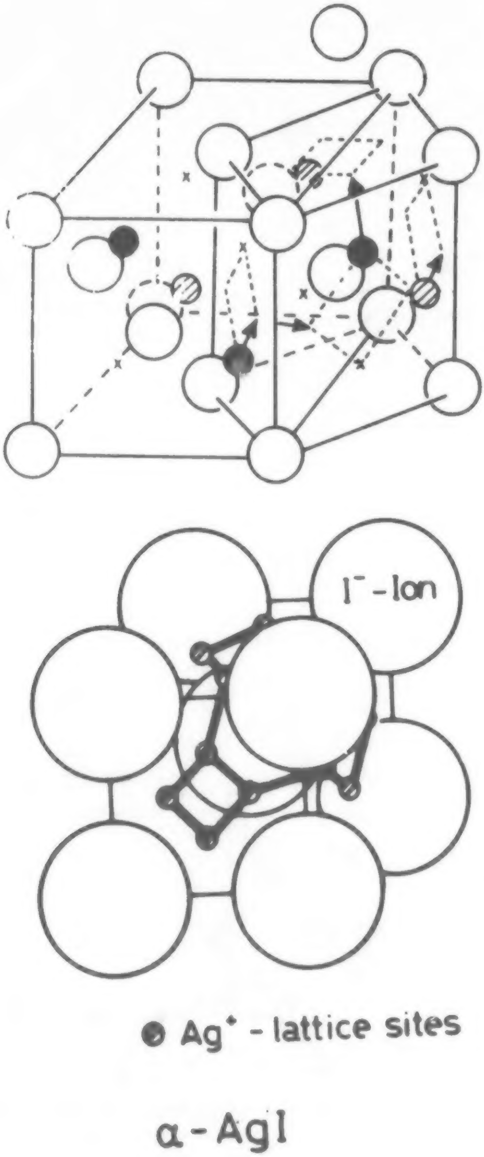
I⁻-Ion
● Ag⁺ - lattice sites
α-AgI

Fig. 6(a)

Fig. 6(b)

Fig. 6 Structures of (a) cubic β-AgI with elementary excitations and (b) α-AgI.

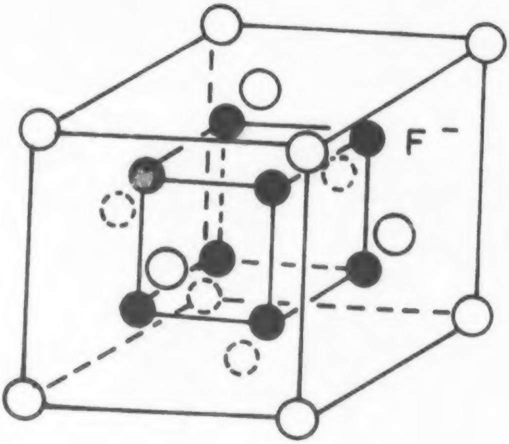

Fig. 7(a)

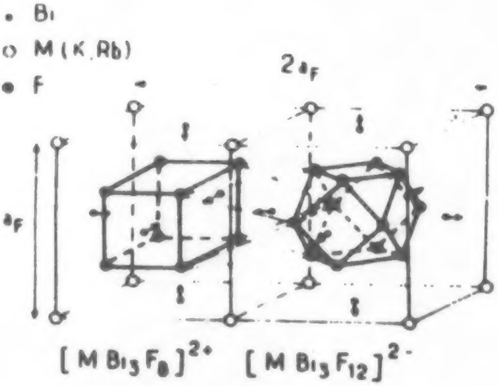
• Bi
○ M (K,Rb)
● F
2a$_F$
a$_F$
[M Bi$_3$ F$_8$]$^{2+}$
[M Bi$_3$ F$_{12}$]$^{2-}$

Fig. 7(b)

Fig. 7 Structures of (a) fluorite and (b) MY_3F_{10}, M=K, Rb, after [8].

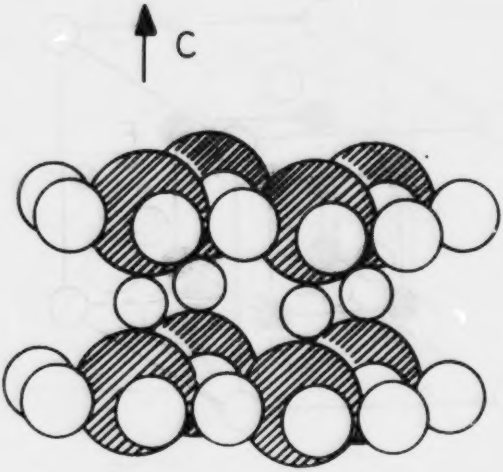

Fig. 8(a)

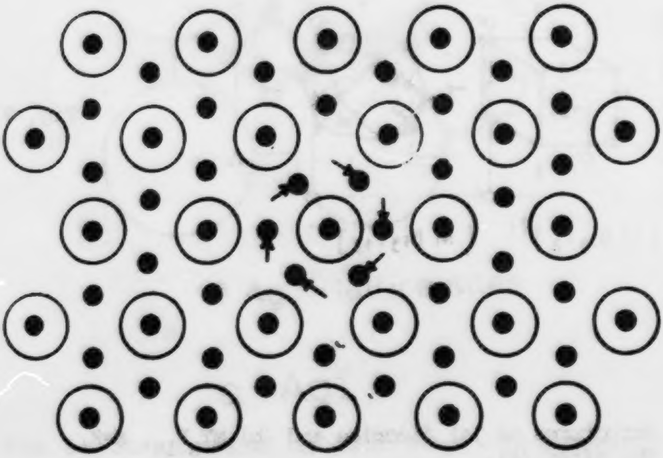

Fig. 8(b)

Fig. 8 Li_3N: (a) structure and (b) proposed basal-plane coöperative excitations.

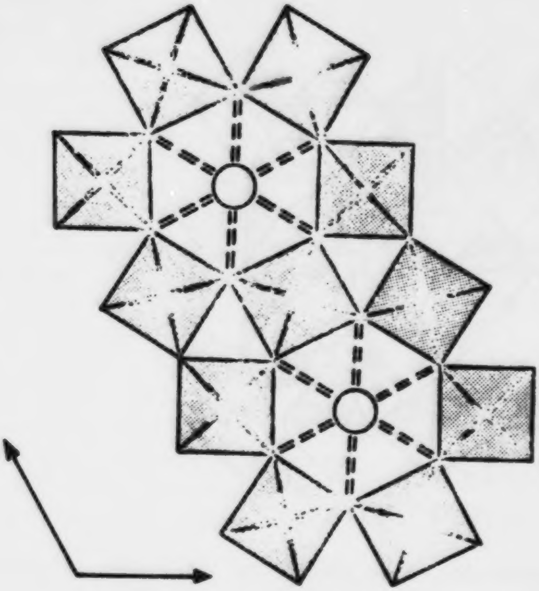

Fig. 9(a)

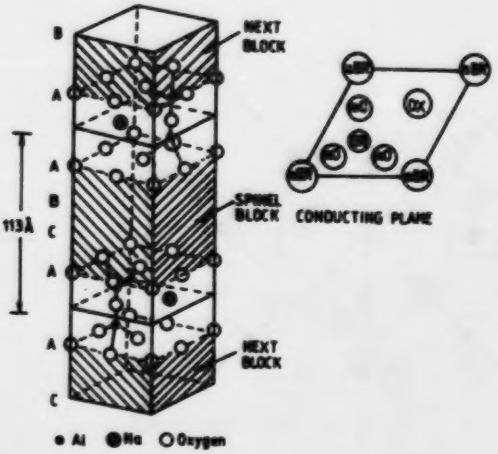
B
A
A
B
C
A
A
C
113Å
NEXT BLOCK
SPINEL BLOCK
NEXT BLOCK
CONDUCTING PLANE
● Al
● Na
○ Oxygen

Fig. 9(b)

Fig. 9 Frameworks of (a) hexagonal tungsten bronze and (b) Na-β alumina.

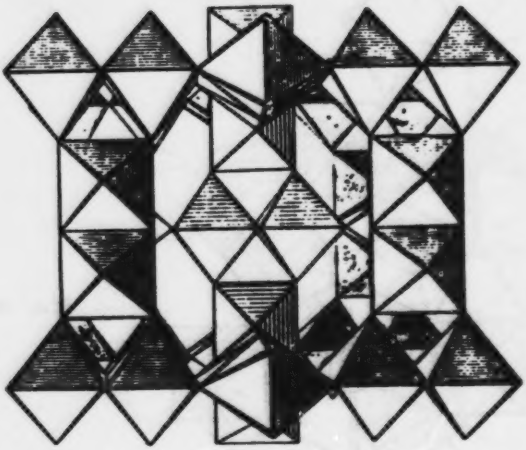

Fig. 10(a)

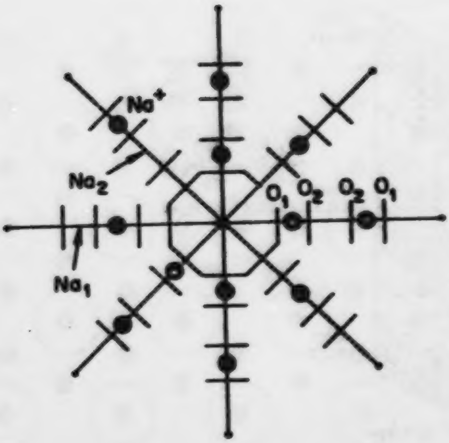
Na$^+$
Na$_2$
Na$_1$
O$_1$
O$_2$
O$_2$
O$_1$

Fig. 10(b)

Fig. 10 Cubic KSbO$_3$ structure: (a) framework and (b) schematization of eight <111> tunnel segments.

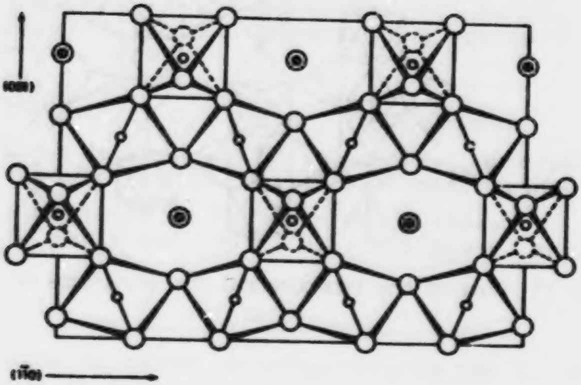

Fig. 11 The (110) projection of a cubic pyrochlore.

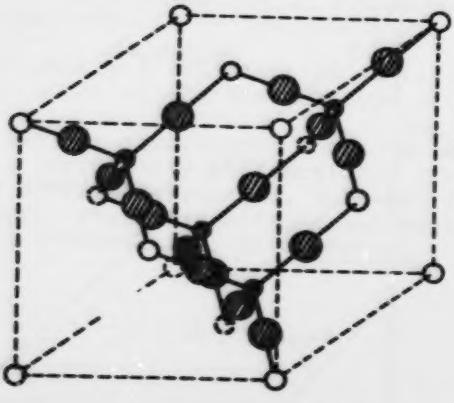

Fig. 12 The $(AlSiO_4)^-$ framework of cubic carnegieite.

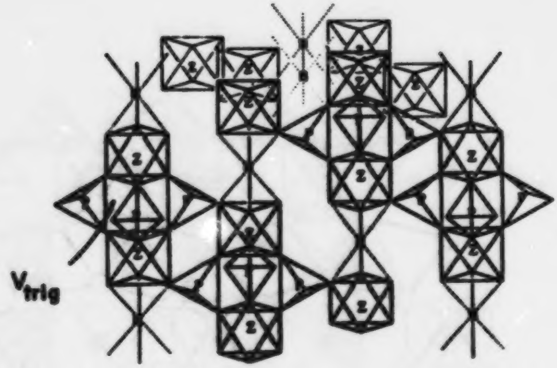

Fig. 13 View of the rhombohedral R$\bar{3}$c structure of $NaZr_2(PO_4)_3$.

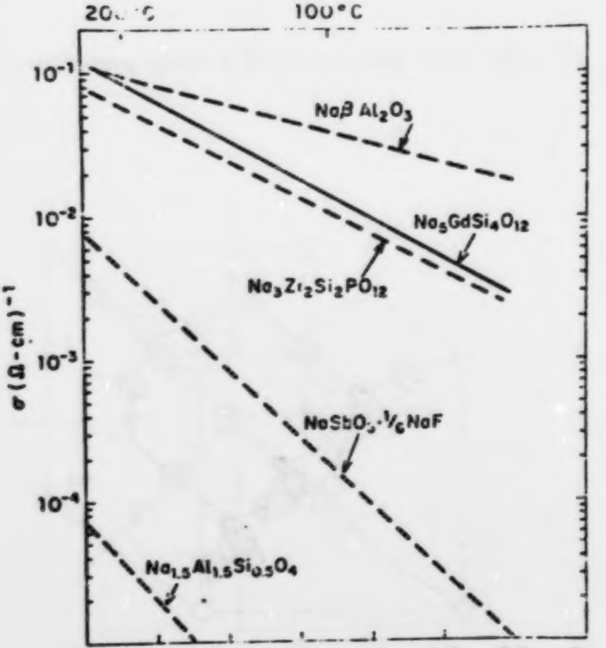

Fig. 14 Na^+-ion conductivity versus reciprocal temperature of some framework structures, after [37].

NASICON AND RELATED COMPOUNDS : A REVIEW

J.P. Boilot, G. Collin*, Ph. Colomban
Laboratoire de Physique de la Matière Condensée
Ecole Polytechnique, 91128 Palaiseau, France
*Laboratoire de Physique des Solides
Université de Paris-Sud, Bât 510, 91405 Orsay, France

ABSTRACT

An overview of recent developments in the field of sodium fast-ion conductors with the structure type of NASICON ($Na_3Zr_2Si_2PO_{12}$) or $Na_5YSi_4O_{12}$ is presented. The main features concerning these materials are:

- Existence, homogeneity range, stability and elaboration techniques : single crystals, ion exchange, ceramic process (comparison between ball milling and wet-chemical techniques : problem of the free zirconia), thick film, glass.

- NASICON ceramic electrolyte in sodium-sulfur battery : corrosion tests in molten sodium.

- Non-stoichiometry : substitution in tetrahedral or/and octahedral sites of the NASICON-type structure.

- Relation between microscopic characteristics : average structure (from X-ray diffraction), local structure (from X-ray diffuse scattering, infrared and Raman spectroscopy), phase transitions and macroscopic ones : electrical conductivity, dilatometry.

KEYWORDS : NASICON, preparation, electrical properties, non-stoichiometry, structural aspects, phase transitions.

RÉSUMÉ

Les récents développements dans le domaine des superconducteurs ioniques aux sodium, à structure type NASICON ($Na_3Zr_2Si_2PO_{12}$) ou type $Na_5YSi_4O_{12}$ sont présentés.

Les principaux aspects étudiés sont :

- Existence, domaine d'homogénéité, stabilité des phases et techniques d'élaboration : monocristaux, échange ionique, céramiques (comparaison entre synthèse à l'état solide et par voie chimique : problème de la zircone libre), couches épaisses, verres.

- Céramique type NASICON utilisée comme électrolyte solide dans l'accumulateur Na/S : tests de corrosion dans le sodium liquide.

- Non stoechiometrie par substitution dans les sites tétraedriques et/ou octaedriques de la structure NASICON.

- Relation entre caractéristiques microscopiques : structure moyenne (détermination par diffraction X), structure locale (détermination par diffusion X, spectrométrie infrarouge et diffusion Raman), transition de phase et caractéristiques macroscopiques : conductivité électrique et dilatométrie.

INTRODUCTION

Sodium-ion conductors in polycrystalline ceramic forms have potential use in several electrochemical devices including sodium-sulfur storage cells, sodium heat engines, sodium winning devices and low power devices (electrochemical sensors, electrochromic displays...). For each device several physical properties are required of the sodium-ion conductor : high ionic conductivity, very low electronic conductivity, good mechanical strength for sealing the electrolyte to cell components, low porosity, very low cost...

Sodium β''-alumina has been known as one of the solid electrolytes for secondary batteries, but sodium-ion mobility in this phase is two-dimensional. Blocking grain boundaries of impurity phases can reduce polycrystalline conductivity and result in current focusing and electrolyte degradation. H.Y-P HONG found a new system $Na_{1+x}Zr_2Si_xP_{3-x}O_{12}$ $(0<x<3)$ possessing a three-dimensional network of SiO_4 and PO_4 tetrahedra corner-shared with ZrO_6 octahedra. The network is built up of $Na_{1+x}Zr_2Si_xP_{3-x}O_{12}$ units and $(1+x)Na^+$ occupies the three-dimensional interstices.

These compounds sinter at substantially lower temperature than Na-β''-alumina and are of considerable interest for all applications. For example $Na_3Zr_2Si_2PO_{12}$ (x=2) shows Na^+ ionic conductivity comparable to that of sodium β''-alumina. This new solid electrolyte was named NASICON (sodium superionic conductor). Moreover, a ferroelectric behaviour has been observed in $Na_3Sc_2P_3O_{12}$.

In this paper, we present recent developments of fundamental and applied aspects of the NASICON system, $Na_{1+x}Zr_2Si_xP_{3-x}O_{12}$, and of other isostructural compounds $M^+M'^{III}(PO_4)_3$ (M=Na,Li,Aq M'= Sc,Fe,Cr) as well as other interesting framework solid electrolytes such as $Na_5YSi_4O_{12}$, $Na_5GdSi_4O_{12}$.

MATERIAL SYNTHESES

The discovery of fast-ion conduction in NASICON (11) and in other isostructural phases, especially those containing Li^+ instead of Na^+ (13), has been the cause of a new interest for the synthesis and the fabrication of these compounds and some others of a very similar type. Unfortunately, it has been shown that it is difficult to obtain NASICON as a pure phase and consequently different preparative processes have been tested. Moreover, all the physical properties and the homogeneity range of the phases are not well defined. The purpose of this section is to point out the results which have been obtained on phase diagrams and to compare the various methods of preparation of single crystals, powders, ceramics, thick films or glasses.

The end members of the solid solution $Na_{1+x}Zr_2Si_xP_{3-x}O_{12}$ have been known since 1930 for the silicate one (2) and since 1967 (4) for the phosphate one. The crystalline structure is representative of an extensive group of isomorphous phosphates (4,5) and silicates (6,7,12). The paper of HONG (10) showed the great extension of the stability domain of the NASICON phase in the quaternary diagram $Na_2O-ZrO_2-SiO_2-P_2O_5$. A greater extension of the phase has been observed in pure sodium (64,68) and lithium phosphate compounds (13).

In the same way, the fast-ion conduction in the $Na_5MSi_4O_{12}$ compound (M=Gd,Y,...) was known in 1977 (14, 18), but the structure was described earlier (12).

For all these compounds, three methods of preparation are usually used : (i) crystal synthesis (see Table I), (ii) ionic exchange (see Table II), (iii) powder preparations using a conventional solid-state reaction (see Table III) or a wet-chemical process (see Table IV).

Single Crystals

Hydrothermal syntheses for silicates and flux methods for phosphates are the main techniques which have been used in order to synthesize single crystals with a NASICON-type structure (Table I). Nevertheless, attempts to obtain $Na_3Zr_2Si_2PO_{12}$ single crystals have given no results so far, although the synthesis of $Na_{5.5}ZrSi_{0.5}P_{2.5}O_{12}$ composition (64,68) seems to show that it could be possible.

Powders

Numerous processes have been employed to obtain NASICON and other compositions with related structures (Table III).

On the one hand, conventional processing using ball-milling techniques, has led to products containing zirconia traces. The presence of these free-zirconia particles is due to the persistence of unreacted zirconia (17,30) and/or to a precipitation during the cooling stage of the sintering cycle (35,57). It can be noted that free ZrO_2 has a deleterious effect in Na/S cells, due to possible microcracks in the ceramic which decreases the lifetime of the cell.

On the other hand, according to VON ALPEN, $Na_4Zr Si_3O_{10}$ and $Na_{3.1}Zr_{1.55}Si_{2.3}P_{0.7}O_{11}$ compositions (51) have been prepared without free zirconia. Moreover, the preparation of NASICON (x=2) using a metal-organic sol-gel process (63,64) clearly shows the possibility of obtaining pure phases at low temperature (1100°C). But, free zirconia appears at higher temperature and for other compositions.

Wet-chemical processes using inorganic or metal-organic reagents have been tested (see Table IV) :

BOILOT et al (30) have used a gel obtained from an aqueous solution : the silicate sol is made by mixing $Na_2O.3SiO_2.3H_2O$ and $Na_2O.SiO_2.5H_2O$; the corresponding amounts of $NH_4H_2PO_4$ and $ZrO(NO_3)_2,2H_2O$ were dissolved in a minimal quantity of boiling water to give solutions and the simultaneous addition of the three solutions led to a solid gel. The gel was dried and the x=2 compound was formed at 1000°C.

QUON et al (35) mixed a $Zr(OH)_4$ slurry with a silica sol (which had been obtained from a mixture of tetraethyl orthosilicate, formic acid and ethanol) and aqueous solutions of $NH_4H_2PO_4$,Na_2CO_3, and formic acid. Then the mixture was dispersed in isopropanol to give a glass-like compound, dried at 110°C, calcined at 750°C and sintered.

GORDON et al (57) used a similar technique : ammonium zirconium carbonate solution, colloidal silica, sodium nitrate, $(NH_4)_2HPO_4$ and citric acid were mixed. The mixture was then heated at about 120°C; at that stage a glassy transparent material is formed. Calcinations at 400 and 900°C led to fine particles. Sintering was performed between 1175 and 1300°C.

$Na_5YSi_4O_{12}$ (59) and $Na_5GdSi_4O_{12}$ (38) are prepared thanks to a similar method ; appropriate amounts of aqueous solutions of sodium carbonate, sodium silicate and Gd acetate (or Y nitrate) were mixed to give a suspension of Gd(Y) hydroxide in a sodium silicate/carbonate solution. This suspension was sprayed into liquid nitrogen and the resulting powder was freeze-dried. All this was followed by calcination in air at 530°C.

PERTHUIS et al (63) used a method with metal alcoholates ; i.e., a mixing of N-zirconium propoxide (or N-titanium butoxide) and tetraethoxysilane was added to an aqueous solution containing either M^+ hydroxide (Na,K) or chloride (Na,K,Li) or nitrate (Ag) and $NH_4H_2PO_4$. Hydrolysis of the metal alkoxide gives a polymerized gel of hydroxide which retains M^+ cations. After drying and heating at 300°C the powder exhibits a large surface area (100 m^2/g) and an amorphous structure. Crystallization is achieved between 600 and 900°C according to the composition.

Ionic Exchange

Solid electrolytes are commonly ion exchangers. First HONG (10) has displayed the exchange properties of NASICON : Li^+, Ag^+, K^+ compounds have been prepared for some compositions (see Table II) by exchange of Na compounds in molten nitrates. However this exchange increases the local disorder. NASICON has also been synthesized by exchange of wadeite glass and thermal treatment (67). Contrarily to the NASICON structure, only Li^+ and Ag^+ can be substituted for Na^+ ions in the $Na_5Gd(Y)Si_4O_{12}$ framework (18).

The most particular feature is the ability to prepare NASICON compounds by exchange reaction of $Zr(HPO_4)_2,H_2O$ (ZrP) in Li^+, Na^+, Ag^+, K^+ aqueous solutions and followed by a thermal treatment between 700 and 1200°C (15,32,39,57). Hydrothermal exchange with Na_4SiO_4 is also possible (53). ZrP has a layered structure and the bringing together of the layers leads to the NASICON framework.

Ceramics, Thick Films and Glass

Superionic ceramics are useful for energy production, conversion or storage (24) and for low-power applications such as sensors, microbatteries, displays or capacitors ; the latter applications require a good adaptation of the preparation process to the microelectronic technology (44,69). Thus thick films (10-50 μm) of NASICON have been obtained by using silk-screen printing on sapphire substrate and convenient sintering (63). Glass technology is also well adapted for the design of microelectronic devices, but so far only very small samples have been obtained by quenching (67).

Ceramic is the more usual form of NASICON electrolytes. Electrical properties (bulk σ_b and grain boundary σ_{gb} conductivities) have been studied for the $x=2$ composition (17,20,43,56). Various activation energies (as a function of thermal cycles) for both bulk- and grain-boundary conductivities are reported and phase transitions occur at different temperatures for both curves.

Static corrosion tests in molten sodium have been made between 250 and 400°C ; at 400°C corrosion is moderate to severe whatever the ceramic process (57) ; however, high-density specimens prepared either by hot pressing or conventional sintering followed by Hot Isostatic Pressing (HIP) have exhibited the best resistance to static corrosion at moderate temperature (75-340 h at 250-375°C); specimens prepared from mechanically mixed powders have improved corrosion resistance in liquid Na when attrition milling (as compared to ball milling) is used. On the other hand, SCHMID et al (66) have observed the structural change of $Na_3Zr_2Si_2PO_{12}$ and $Na_{3.1}Zr_{1.55}Si_{2.3}P_{0.7}O_{11}$ compositions after immersion in liquid Na at 300°C, and showed that lattice parameters changes could be sufficient to explain the observed fractures in the ceramic. However, small NASICON tubes with composition x=2 to x=2.4 have been able to cycle over 20 times in Na/Na or Na/S cells operated at a current density of 200 to 800 mA/cm^2 (25,36,57). It should be noted that such a performance is not easily achieved.

$Na_5ErSi_4O_{12}$ and a Li derivative have been tested in secondary cells Na/TiS_2 or Li/TiS_2 (27) using laboratory experimental cells.

NON-STOICHIOMETRY IN NASICON TYPE COMPOUNDS

The conducting-ion concentration and electrical properties of NASICON type compounds can be modified by means of :

- the substitution by Si^{4+} ions for P^{5+} ions in the tetrahedral sites,
- the substitution by M^+, M^{2+}, M^{3+}, M^{5+} ions for Zr^{4+} in the octahedral sites.

These two non-stoichiometry mechanisms imply a change of the Li^+ or Na^+ concentration in order to obtain the electrical compensation.

Substitution in Tetrahedral Sites

- The system $Na_{1+x}Zr_2Si_xP_{3-x}O_{12}$ $0<x<3$ (Table I-IV):

This solid solution in the system $NaZr_2(PO_4)_3$-$Na_4Zr_2(SiO_4)_3$ has been studied by HONG (10) and it is the origin of the numerous studies which have been performed on NASICON type compounds. The structural investigation at room temperature has revealed the rhombohedral symmetry of these phases (space group $R\bar{3}C$) along with the possibility of a monoclinic distortion for the composition range $1.8<x<2.2$ (space group C2/c).

It can be noticed on Table V that both electrical conductivity at 300°C and activation energy of polycrystalline samples vary but slightly in the composition range x=1.8 to x=2.4. The x=1 compound and particularly the x=3 compound display higher resistivities.

x=2 is the material which is generally named NASICON for sodium superionic conductor. At 300°C, the transport properties of $Na_3Zr_2Si_2PO_{12}$ (x=2) are clearly equivalent to those of β"-alumina at temperatures

T>300°C, but inferior for T<300°C. A much improved pre-exponential factor is consistent with the three-dimensional character of the Na^+-ion transport in $Na_3Zr_2Si_2PO_{12}$.

- The system $Na_{1+x}Zr_{2-x/3}Si_xP_{3-x}O_{12-2x/3}$:

According to VON ALPEN et al (51), the system $Na_{1+x}Zr_2Si_xP_{3-x}O_{12}$ with $0.4<x<2.8$ cannot be prepared as pure monophases because free zirconia always occurs as an impurity. Consequently, these authors have studied a new solid solution which is defined by the end compounds $NaZr_2P_3O_{12}$ and $Na_4ZrSi_3O_{10}$. In the system $Na_{1+x}Zr_{2-x/3}Si_xP_{3-x}O_{12-2x/3}$, it has been found that in the composition range $0<x<1.6$ there exists a low-conducting phase with a rhombohedral symmetry which can be produced as a monophase. In the composition range $1.6<x<2.3$ a high-conducting phase is obtained with a monoclinic crystal symmetry, including the end phase $Na_4ZrSi_3O_{10}$. The compound $Na_{3.1}Zr_{1.55}Si_{2.3}P_{0.7}O_{11}$, which corresponds nearly to a composition x=2.3, has an ionic conductivity which exceeds that of NASICON by half a decade at RT ($2-3.10^{-3}\Omega^{-1}cm^{-1}$). But this composition belongs to the monoclinic range and probably, structural transitions (see below) make it unstable in contact with molten sodium at elevated temperatures (300°C) (51,65,66).

Another composition $Na_{2.94}Zr_{1.49}Si_{2.2}P_{0.8}O_{10.53}$ which corresponds nearly to x=2.2 is within the rhombohedral region and is characterized by a conductivity of $0.13\ \Omega^{-1}cm^{-1}$ at 300°C ($10^{-3}\Omega^{-1}cm^{-1}$ at RT). This material seems to be well suited for application as a separator in Na/S cells (65).

Substitution in Octahedral Sites

- The system $Na_{1+3y}(Zr_{2-y}Na_y)(PO_4)_3$ $0<y<1$:

The $Na_4(NaZr)(PO_4)_3$ composition (y=1) has been synthesized in a single-crystal state (64,68). The structural determination has shown that this formula can be deduced from $NaZr_2(PO_4)_3$ by substitution of Na atoms for zirconium atoms on octahedral sites and by filling the Na_1 and Na_2 sites with extra sodium ions necessary for the charge compensation. The symmetry of these crystals is rhombohedral (space group R32) (68).

Moreover other compositions have been studied : $Na_2Zr(PO_4)_2$, $Na_5Zr_4(PO_4)_7$, $Na_7Zr_5(PO_4)_9$ (10,11,64) which can be respectively written $Na_{2.5}(Na_{0.5}Zr_{1.5})(PO_4)_3$ y=0.5, $Na_{1.86}(Na_{.28}Zr_{1.72})(PO_4)_3$ y=0.28 and $Na_2(Na_{.33}Zr_{1.66})(PO_4)_3$ y=0.33 in order to respect the NASICON type structure.

The variation of the conductivity in this system is unknown, but this large variation in stoichiometry suggests that a large class of compounds can be stabilized with the NASICON-type structure. Consequently other high-conducting compounds may be found in future.

- Other systems where Zr^{4+} ions can be substituted by M^{5+} or M^{3+} ones in octahedral sites:

$(Li,Na)_{1-x}Zr_{2-x}(Ta,Nb)_x(PO_4)_3$ $0<x<1$ (13,48)

and $Na_{1+x}(Y,Cr,In,Yb)_xZr_{2-x}(PO_4)_3$ $0<x<2$ (37,45)

STRUCTURAL ASPECTS OF NASICON TYPE COMPOUNDS

The fundamental lattice of NASICON-type compounds is rhombohedral with sometimes a slight monoclinic deformation. It exhibits lattice constants (in trigonal notation) in the range 8.70-9.20 Å and 21.50-22.80 Å for a_{trig} and c_{trig}, respectively, and includes around hundred atoms per unit cell which makes it rather difficult to describe or to represent. However, a simplification can be introduced if one remarks that this complicated structure is derived from that of glaserite $K_3Na(SO_4)_2$. This latter corresponds to a small trigonal cell represented on Figure 1a in which one observes along c a succession of octahedra $Na-O_6$ on $z=1/2$ and of six-coordinated antiprisms K_1-O_6 (flattened octahedra) on $z=0$. Each one of these sites shares corner oxygen with the SO_4 tetrahedra distributed on $z \simeq 1/4$ and $\simeq 3/4$ and the remaining K_2^+ ions occupy the loose 9-coordinated sites on $z \simeq 1/8, 5/8$. It can be noted that this stacking is one of numerous frameworks of earth minerals (33,47).

The NASICON-type structure can be described as a rhombohedral superstructure of this glaserite cell with $a_{Nas}=a_{glas}\sqrt{3}$ and $c_{Nas}=3_{glas}$ associated with the usual rhombohedral origin shift. Under these conditions the fundamental type stacking is conserved with a succession of ZrO_6 octahedra and Na_1O_6 antiprisms, along the different 3-fold axis, sharing corner oxygen with the $(Si,P)O_4$ tetrahedra. The Na_2^+ ion occupies an irregular eight-coordinated site close to the K_2^+ site of glaserite (1,33).

The first crystal-structure determination of a NASICON-type material was performed in 1968 by HAGMAN and KIERKEGAARD who studied the $NaM'^{IV}_2(PO_4)_3$ compounds with M'^{IV}=Ge,Ti,Zr and found them to be isomorphous (5). In the same paper they examined the structure of a single crystal of $NaZr_2(PO_4)_3$ from data collected on Weissenberg photographs. They established that the space group was $R\bar{3}c$ and gave the lattice constants

a_{trig}=8.8043(2) Å and c_{trig}=22.7585(9) Å. The authors described the fundamental structure with the PO_4 tetrahedra and ZrO_6 octahedra linked by corners to a 3D-network with each oxygen atom belonging simultaneously to a PO_4 group and to a ZrO_6 group, and the Na^+ ions localized in the strongly distorded octahedra between the ZrO_6 along the c axis (Figure 1b).

HONG (10) examined, on powders, the homogeneity range $(1-x)NaZr_2(PO_4)_3-(x)Na_4Zr_2(SiO_4)_3$ and found a monoclinic deformation within the 1.8-2.2 region, space group C 2/c. He also reexamined the structure of $NaZr_2(PO_4)_3$ on a single crystal with intensity data collected on a 4-circle diffractometer. The lattice constants a_{trig}=8.815(1) Å and c_{trig}=22.746(7) Å are close to the previous ones and the atomic coordinates found by HONG are consistent (in the limit of standard deviation) with those of HAGMAN and KIERKEGAARD. But HONG with a higher number of independent reflections could also refine the anisotropic temperature factors and doing so he displayed the high anisotropy of the Na^+ ion with large thermal vibration terms in the trigonal plane (U_{11}, U_{22}, U_{12}), compared to the U_{33}term along the c axis.

In the same paper HONG deduced from the x=0 position an atomic arrangement for the monoclinic cell of the x=2 term $Na_3Zr_2Si_2PO_{12}$, assuming a partial occupation of the second Na position (Na_2 position in a rhombohedral cell shifted into Na_2-Na_3 in the monoclinic one). The author also examined the effect of ion exchange and showed that, even for x=2, with Li^+,K^+ and Ag^+ the materials remain rhombohedral $R\bar{3}c$, the only one exception is thus Na^+ which exhibits the monoclinic deformation.

The other extremity of the solid solution $Na_4Zr_2(SiO_4)_3$ was first studied by SIZOVA et al (7) who found the usual $R\bar{3}c$ rhombohedral space group for this composition and proposed a crystal structure, from a limited number of data, with the two Na^+ positions fully occupied, the other atoms keeping positions close to the x=0 prototype. They showed that the polyhedron around Na_2^+ ion is very loose with ten Na-O distances within the range 2.47-2.90 Å.

This structure was recently reexamined by TRAN QUI et al (52) also on a single crystal. They found a $R\bar{3}c$ group with the exception of some reflections incompatible with the c glide plane. They refined the crystal structure at RT, 300°C, and 620°C from intensity data collected on a 4-circle diffractometer. Their lattice constants at RT were a_{trig}=9.198 Å and c_{trig}=22.210 Å. Their atomic coordinates were not very different from the previous ones though much more precise. The authors also discussed the possible Na^+-ion pathway in the structure and showed that only little change occurs at high temperature.

The crystal structure determination for the intermediate NASICON composition revealed itself to be very complicated. Indeed, in addition to the high difficulty of crystal preparation, comes a further problem of non-stoichiometry due to an unavoidable substitution of some Na^+ ions on the Zr sites leading to the general formula $Na_{(1+x+y)}Zr_{(2-y/4)}Si_xP_{3-x}O_{12}$. In these materials, as it was recently shown by BOILOT et al (68), there are 4Na sites (space group R32) :

- The regular Na_1 and Na_2 sites previously encountered though the Na_2 one is shifted into 2 independent sites.
- Na_3 sites taking the place of Zr sites in order to present along the 3-fold axis the succession

  Na_1-Na_3-Na_3-Na_1-Zr-Zr-Na_1...
- A Na_4 interstitial site strongly off-centered in the 6-coordinated antiprism localized between two Zr sites. The occurence of such additional Na^+ sites and the associated Zr displacements lead to a great local disorder with tetrahedra distortions and give rise to structural phase transitions (see below). The Raman spectra of these compounds are close to the ones observed for glasses , Figure 2, (49,63,64).

The difficulties encountered for the study of intermediate compositions led people to examine a material in which the x=3 formula is spontaneously realized: $Na_3Sc_2(PO_4)_3$ which powders are monoclinic at RT and exhibit two structural phase transitions. But at the present time the papers, concerning the crystals, do not indicate clearly that they behave in the same way.

a) EFREMOV and KALININ (16) concluded to a monoclinic cell for their crystal a=16.10 Å, b=9.105 Å, c=8.528 Å γ=127°15 -non centrosymmetric space group Bb- and a composition $Na_{3.00(1)}Sc_2(PO_4)_3$ with two independent sodium positions per site.

b) HONG (31) adopted a monoclinic deformation for his crystal a=15.461 Å, b=9.016 Å, c=8.913 Å, γ=124°80 -centrosymmetric space group B2/b- and found a composition $Na_{2.33(1)}Sc_2(PO_4)_3$. He showed that his crystal represented the direct NASICON type whereas that of EFREMOV et al is the anti-NASICON type.

c) DELBECQ et al (34) published the powder lattice constants at RT a=15.407 Å, b=9.100 Å, c=8.525 Å, γ=123°60. More recently SUSMAN et al (62) gave for this

LT phase another set of lattice constants for the powder a=16.045 Å, b=9.066 Å, c=8.922 Å and γ=126°92.

d) BOILOT et al (50) published structural results showing that at RT single crystals of $Na_3Sc_2(PO_4)_3$ are not monoclinic but strictly rhombohedral $R\bar{3}c$. Recently they showed that the initially calculated composition $Na_{2.92(3)}Sc_2(PO_4)_3$ can be brought to $Na_{3.00(4)}Sc_2(PO_4)_3$ when anharmonic terms are introduced in the refinements (68). They also showed that the thermal vibrations are very different for the two Na^+-ion types : large in the trigonal plane for Na_1 and on the contrary large in the c direction for Na_2. The results concerning the lattice symmetry are in agreement with those of TRAN QUI et al (54) who also found a rhombohedral lattice at RT but with a rather different composition $Na_{2.52}Sc_2(PO_4)_3$.

On the contrary, for intermediate and high-temperature phases the whole set of available data agrees with a rhombohedral symmetry but again with rather dispersed compositions running from $Na_{2.64}$ per unit formula at 200°C, on single crystals by TRAN QUI et al (54), to $Na_{3.00}$ -but this composition was apparently imposed- on powders at 100 and 200°C by SUSMAN et al (62), going through $Na_{2.87(3)}$ at 100°C and $Na_{2.82(3)}$ at 200°C on single crystals by BOILOT et al (50). The latter authors showed first that upon heating a transfer from Na_1^+ site into Na_2^+ site occurs which was confirmed by other papers. Recently they showed that, as at RT, the introduction of 3rd and 4th rank tensors in the calculations led in each case to the $Na_{3.00(4)}$ composition (68).

PHASE TRANSITIONS IN NASICON TYPE COMPOUNDS

All NASICON-type compounds have this particular feature, they generally have structural transitions in the temperature range RT-200°C. The order of these transitions and consequently associated thermal effects are dependent on the nature of the isostructural compound. Moreover, variations of electrical conductivity and especially dilatometric anomalies which result from these transitions can induce some degradation on ceramic tubes.

- Two first-order transitions have been observed by DTA (50,61) , Figure 3a , X-ray diffraction (50,62) and dielectric measurements (23,34,46) in polycrystalline samples of $Na_3Sc_2(PO_4)_3$: NASICON(Sc). The first transition at about 65°C corresponds to the cross-over from the monoclinic symmetry (C2/c space group) to the rhombohedral one ($R\bar{3}c$ space group) and is accompanied by a fivefold increase in ionic conductivity but only a small decrease in activation energy (from 0.56 eV to

0.45 eV). The second one at 170°C does not change the rhombohedral symmetry but is associated with a high decrease in activation energy from 0.45 to 0.15 eV (61) (Figure 3b').

Polycrystalline samples of $Na_3Fe_2(PO_4)_3$: NASICON (Fe) or $Na_3Cr_2(PO_4)_3$: NASICON(Cr) exhibit a similar behavior (19,41).

- In the $Na_3Zr_2Si_2PO_{12}$ compound : NASICON(Zr) only one second-order structural transition has been observed in a polycrystalline sample in a large temperature range (100-200°C) (29,30,36). This also corresponds to the cross-over from monoclinic (C2/c) to rhombohedral symmetry ($R\bar{3}c$). The associated thermal effect is weak, perhaps because it is spread over a large temperature range and is only observed on the DSC curve (Figure 3a').

In the transitional range, the Arrhenius plot of the ionic conductivity ($\ln\sigma T$ vs $1/T$) (20,29,30,56) (Figure 3b') and the NMR study (26) (^{23}Na relaxation time vs temperature recording) show a gradual and reproducible change from an activation energy of 0.40 eV (low temperature $T<400$ K) to 0.23 eV (high temperature $T>460$ K). Moreover, a sharp increase of the thermal expansion is observed (25,30) which has a deleterious effect for solid-electrolyte application in view of sealing difficulties with glass or metal.

A recent study (68) of single crystals with the NASICON-type structure has clearly shown structural modifications according to the temperature and the influence of the nature of octahedral atoms, non-stoichiometry and structural defects on the order of these transitions and associated thermal effects :

i) A single crystal with a composition $Na_{5.3}Zr(Si_{0.3}P_{2.7})O_{12}$ shows two first-order transitions at respectively 86 and 129°C which have been observed on the DTA curve and from the evolution of the a and c parameters versus the temperature (Figure 4a).

- At room temperature the structural investigation by X-ray diffraction shows the well known sodium sites Na_1-Na_2 entirely filled, the partial occupation of interstitial site Na_4 and the off-centering of zirconium atoms from the theoretical octahedral position of 00z which leads to a three-dimensional trigonal superlattice (Figure 5a). In fact the hexagonal symmetry seems only apparent and results probably from a superposition of locally monoclinic domains.

- At 120°C a change in the zirconium off-centering is observed and another superstructure cell appears which results from a new long-range order of zirconium atoms (Figure 5b).

- At 200°C zirconium atoms are localized on the theoretical position 00z and as expected no superstructure is observed (Figure 5c). The Na_4 occupation factor is strongly decreased and this suggests a sodium-ion transfer to other interstitial sites of high energy.

ii) Single crystals from another preparation with a composition close to $Na_5Zr(PO_4)_3$ exhibit a different behaviour. Figure 4b shows the temperature dependence of the trigonal a and c parameters of these crystals. The continuous evolution demonstrates that the decrease of the correlations between structural defects (Na interstitial and off-centered zirconium) and its final disappearance, two effects which corresponded to well-separated phase transitions in the previous single crystal, merge into a smooth single transformation. Correlatively thermal effects are only observed on DSC curves and spread over a large temperature range. At room temperature, structural investigation shows that only a local superstructure is observed by X-ray scattering studies, resulting from a very small off-centering of zirconium atoms in the xy plane. Another fact is that a major part of interstitial sodium ions can be transferred, during the second transition, to Na_2 sites which are normal sites of the NASICON-type structure. This transfer to low-energy sites is in agreement with the small associated thermal effect.

The results obtained from those single-crystal studies on NASICON-type compounds have allowed others to comment on the results for different isostructural compounds:

For instance, in $Na_3Zr_2Si_2PO_{12}$, a monoclinic deformation has been observed at room temperature in polycrystalline samples (29,30,36). This can be due to long range correlations between off-centering $Zr-Na_4-Si$ defects or perhaps only between off-centering Zr which are probably enhanced in this high zirconium concentraration compound. For this composition, however, sodium on Na_4 or perhaps on Na_1 sites can be easily transferred to largely non-occupied Na_2 sites. Consequently, the zirconium centering does not require an important energy and can take place continuously over a large temperature range. This is in agreement with the small associated thermal effect reported for this compound.

In conclusion, it seems that NASICON-type compounds generally exhibit two-phase transitions in the temperature range RT-200°C :

The first can be directly related to the off-centering of octahedral atoms (zirconium) which sometimes involves a monoclinic deformation of the structure at RT. This transition which corresponds to a change of correlations between off-centered atoms is influenced by the nature of octahedral atoms, the occupation factor of Na sites and by the non-stoichiometry due to the substitution by Na^+ ions for octahedral atoms or by the substitution by Si^{4+} ions for P^{5+} ions ;

The second effect involves centering of octahedra atoms and Na^+ occupation transfer from Na_4 or Na_1 to Na_2 or interstitial positions. This corresponds to a decrease of octahedra atomic repulsions and to the formation of a superionic-conducting state characterized by a low-activation energy.

Finally, from vibrational spectroscopy studies (49, 64), the NASICON structure can be described as an isolated tetrahedra network (nesosilicates) which defines sodium and zirconium sites. The partial occupation of these sites leads to tetrahedra distortions and previously reported phase transitions are preceeded by a gradual apparition of a tetrahedra disorder from 200 K.

STRUCTURE OF $Na_5YSi_4O_{12}$ TYPE COMPOUNDS

$Na_5RESi_4O_{12}$(where RE is a rare-earth atom such as Sm,... Lu,Y,Sc) are other highly conductive compounds with a framework structure. The structure (9,14,21,22, 55) is characterized by $Si_{12}O_{36}$ rings parallel to the basal plane of the hexagonal cell (space group $R\bar{3}c$). These rings, separated by Na_1 tetrahedra and Na_3 octahedra are stacked to form large rigid columns parallel to the c axis (Figure 6a). The hexagonal unit cell contains 18 formula units and 48 of the 90 Na^+ ions are located within the rings and are assumed to be immobile. The conducting paths (parallel to the c axis) are wholly confined to the space between the rings and contain the sites Na_5 and Na_6.

Conductivity measurements performed by SHANNON et al (18) revealed linear dependence of the conductivity with the RE cation's radius. Compounds with smaller M^{3+} ions (Sc,Lu) exhibit lower conductivity than the corresponding ones with larger M^{3+} ions such as Y and Sm. The size of the channels is determined by the size of M^{3+} ions. Moreover, the single-crystal conductivity of $Na_5YSi_4O_{12}$ has been investigated by BEYELER et al (55) and RT conductivities are respectively 0.0032 $\Omega^{-1}cm^{-1}$ parallel to the c axis and 0.08 $\Omega^{-1}cm^{-1}$ perpendicular to the c axis. The higher conductivity parallel to c shows that the channel diameter is larger than the optimum size in $Na_5YSi_4O_{12}$. A recent diffuse scattering study (60) on $Na_5YSi_4O_{12}$ and $Na_5ScSi_4O_{12}$ has shown that main channels were connected by the highly mobile Na_4 ions which provide additional paths for ionic movement and explain the high conductivity perpendicular to the c axis (Figure 6b).

REFERENCES

(1) B. Gossner, "Über die Kristallstruktur von Glaserit und Kalium Sulfate" Neues Jahrb Mineral 57:89-116; 1928.

(2) J. Von d'Ans and J. Löffler, "Untersuchungen in System $Na_2O-SiO_2-ZrO_2$" Z Anorg u allg Chem Bd 191(22):1-35; 1930.

(3) N.L. Bowen, J.F. Schairer and H.W.V. Williems, "The ternary system : $Na_2SiO_3-Fe_2O_3-SiO_2$" Am Jour Sc Fifth Ser XX(120):404-455; 1930.

(4) M. Sljukisc, B. Matković, B. Prodić and S. Scarnicar, "Preparation and crystallographic data of phosphates with common formula $MM_2'(PO_4)_3$" Croatica Chemica Acta 39:145-148; 1967.

(5) L.O. Hagman and P. Kierkegaard, "The crystal structure of $NaMe_2^{IV}(PO_4)_3$" Acta Chem Scandinav 22:1822-1832; 1968.

(6) V.G. Chukhlantsev and K.V. Alyamovskaya, "Preparation of zirconosilicates and hafnosilicates from oxides under hydrothermal conditions" Russian J Inorg Chem 15:1489-1490; 1970.

(7) R.G. Zizova, A.A. Voronkov, N.G. Shumyatskaya, V.V. Ilyukhin and N.V. Belov, "Crystal structure of $Na_4Zr_2(SiO_4)_3$" Sov Phys Dokl 17:618-620; 1973.

(8) G. Baussy, R. Caruba, A. Baumer and G. Turco, "Minéralogie expérimentale dans le système ZrO_2-SiO_2-Na_2O-H_2O-correlations pétrogénétiques" Bull Soc Fr Minéral Cristallogr 97:433-444; 1974.

(9) B.A. Maksimov, Yu A. Kharitonov and N.V. Belov, "Crystal structure of the Na-Y metasilicate $Na_5Y Si_4O_{12}$" Sov Phys Dokl 18:763-765; 1974.

(10) H.Y.-P. Hong, "Crystal structure and crystal chemistry in the system $Na_{1+x}Zr_2Si_xP_{3-x}O_{12}$" Mat Res Bull 11:173-182; 1976.

(11) J.B. Goodenough, H.Y.-P. Hong and J.A. Kafalas, "Fast Na^+-ion transport in skeleton structure" Mat Res Bull 11:203-220; 1976.

(12) B.A. Maksimov, L.N. Dem'yanets, V.V. Ilyukhin, L.N. Kharitonov and N.V. Belov, "Crystal structures and comparative crystal chemistry of synthetic Sc and Y germanates (silicates)" Sov Phys Crystallogr 21:539-542; 1976.

(13) B.E. Taylor, A.D. English and T. Berzins, "New solid ionic conductors" Mat Res Bull 12:171-182; 1977.

(14) R.D. Shannon, H.Y. Chen and T. Berzins, "Ionic conductivity in $Na_5GdSi_4O_{12}$" Mat Res Bull 12:969-973; 1977.

(15) A. Clearfield, S.P. Pack and J.M. Troup, "On the mechanism of ion exchange in zirconium phosphate $LiZr_2(PO_4)_3$" J Inorg Nucl Chem 39:1437-1442; 1977.

(16) V.A. Efremov and V.B. Kalinin, "Determination of the crystal structure of $Na_3Sc_2(PO_4)_3$" Sov Phys Crystallogr 23:393-396; 1978.

(17) M.L. Bayard and G.C. Barna, "A complex impedance analysis of the ionic conductivity in $Na_{1+x}Zr_2Si_x P_{3-x}O_{12}$ ceramics" J Electroanal Chem 91:201-209; 1978.

(18) R.D. Shannon, B.E. Taylor, T.E. Gier, H.Y. Chen and T. Berzins, "Ionic conductivity in $Na_5YSi_4O_{12}$ silicates" Inorganic Chem 17:958-964; 1978.

(19) M. Pintard-Screpel, F. d'Yvoire and F. Remy, "Polymorphisme et conductivité ionique du phosphate $Na_3 Fe_2(PO_4)_3$" C R Academ Sci Paris 286:C381-383; 1978.

(20) A. Hooper, "Conductivity studies of dense polycrystalline $Na_3Zr_2Si_2PO_{12}$" Proc 2nd Int Meet Solid Electrolytes, September 20-22, 1978; St Andrews; 6.12:1-3; 1978.

(21) H.U. Beyeler and T. Hibma, "The sodium conductivity paths in the superionic conductors $Na_5RESi_4O_{12}$" Solid State Comm 27:641-643; 1978.

(22) H.Y.-P. Hong, J.A. Kafalas and M. Bayard, "High Na^+-ion conductivity in $Na_5YSi_4O_{12}$" Mat Res Bull 13:757-762; 1978.

(23) S.A. Okonenko, S. Yu Stefanovich, V.B. Kalinin and Yu N. Venevtsev, "New ferroelectric $Na_3Sc_2(PO_4)_3$" Sov Phys Solid State 20:1647-1648; 1978.

(24) P. Vashishta, J.N. Mundy and G.K. Shenoy, eds; Proc Int Conf on Fast Ion Transport in Solids, May 21-25, 1979; Lake Geneva; Elsevier 1979.

(25) G.R. Miller, B.J. McEntire, T.D. Hadnagy, J.R. Rasmussen, R.S. Gordon and A.V. Virkar, "Processing and properties of $Na\beta''$ alumina and NASICON electrolytes" in ref. 24, 83-86; 1979.

(26) C.E. Hayes and D.C. Ailion, "NMR observations of Na ionic diffusion in $Na\beta''$ alumina and NASICON" in ref.24, 297-300; 1979.

(27) T. Palanisamy, R.L. Kerr and J.T. Maloy, "Synthesis, characterization and utilisation of $M_5ErSi_4O_{12}$ as solid electrolyte in alkali metal/TiS_2 cells" in ref.24, 427-430; 1979.

(28) J.A. Kafalas and R. Cava, "Effect of pressure and composition on fast Na^+ ion transport in the system $Na_{1+x}Zr_2Si_xP_{3-x}O_{12}$", in ref.24, 419-422; 1979.

(29) U. Von Alpen, M.F. Bell and W. Wickelhaus, "Phase transition in NASICON" Mat Res Bull 14:1317-1322; 1979.

(30) J.P. Boilot, J.P. Salanié, G. Desplanches and D. Le Potier, "Phase transformation in $Na_{1+x}Si_xZr_2P_{3-x}O_{12}$" Mat Res Bull 14:1469-1477; 1979.

(31) H.Y.-P. Hong, "Crystal structure and ionic conductivity of a new superionic conductor $Na_3Sc_2P_3O_{12}$" in ref.24, 431-433; 1979.

(32) A. La Ginestra, C. Ferragina and P. Patrono, "Ag-zirconium phosphate system" Mat Res Bull 14:1099-1109; 1979.

(33) M. Vlasse, C. Parent, R. Salmon, G. Le Flem and P. Hagenmuller, "The structures of the $Na_3Ln(XO_4)_2$ phases (X=P,V,As)" J Solid State Chem 35:318-324; 1980.

(34) C.J. Delbecq, S.A. Marschall and S. Susman, "Evi-

dence of a structural phase change in the fast ionic conductor $Na_3Sc_2P_3O_{12}$" Solid State Ionics 1:145-149; 1980.

(35) D.H.H. Quon, T.A. Wheat and W. Nesbitt, "Synthesis, characterization and fabrication of $Na_{1+x}Zr_2Si_xP_{3-x}O_{12}$" Mat Res Bull 15:1533-1539; 1980.

(36) G. Desplanches, M. Rigal and A. Wicker, "Phase transformation in an $Na_3Zr_2Si_2PO_{12}$ ceramic" Bull Amer Ceram Soc 59:546-548; 1980.

(37) M. Nagai, S. Fujitsu and T. Kanazawa, "Ionic conductivity in the system $NaZr_2(PO_4)_3$-$Na_3Y(PO_4)_2$" J Am Ceram Soc 63:476-477; 1980.

(38) J.J. Bentzen and P.S. Nicholson, "The preparation and characterization of dense highly conductive $Na_5GdSi_4O_{12}$" Mat Res Bull 15:1737-1745; 1980.

(39) S. Yamaka, "Ionic conductivity in anhydrous crystalline zirconium phosphate" J Inorg Nucl Chem 42:717-720; 1980.

(40) T. Takahashi, K. Kuwabara and M. Shibata, "Solid state ionic conductivities of Na^+ ion conductors on Nasicon" Solid State Ionics 1:163-175; 1980.

(41) F. d'Yvoire, M. Pintard-Screpel and E. Bretey, "Les phosphates $Na_3M_2^{III}(PO_4)_3$ (Cr,Fe=M) et $Na_3Cr_3(PO_4)_4$: données cristallographiques et conductivité ionique" C R Acad Sci Paris 290:C185-188; 1980.

(42) A.K. Ivanov-Shits, "Electrical conductivity of single crystals of superionic conductor $Na_5YSi_4O_{12}$" Sov Phys Solid State 23:84-86; 1981.

(43) W. Bogusz, F. Krok and W. Jakubowski, "Bulk and grain boundary electrical conductivity of NASICON" Solid State Ionics 2:171-174; 1981.

(44) Ph. Schnell, G. Velasco and Ph. Colomban, "β-alumina like thin films" Solid State Ionics 5:291-294; 1981.

(45) C. Delmas, J.C. Viala, R. Olazcuaga, G. Le Flem and P. Hagenmuller, "Ionic conductivity in Nasicon type phases $Na_{1+x}Zr_{2-x}L_x(PO_4)_3$ (L=Cr,In,Yb)" Solid State Ionics 3/4:209-214; 1981.

(46) S. Yu Stefanovich and V.B. Kalinin, "Ionic conductivity of the ferroelectric $Na_3Sc_2(PO_4)_3$" Sov Phys Solid State 23:2043-2044; 1981.

(47) P.B. Moore, "Complex crystal structures related to glaserite, $K_3Na(SO_4)_2$: evidence for very dense packing among oxysalts" Bull Mineral 104:536-547; 1981.

(48) M. Nagai, S. Fujitsu, T. Kanazawa and H. Yanagida, "The dependence of structure and conductivity in three-dimensional phosphate ionic conductors" J Materials Sci 16:1633-1642; 1981.

(49) Ph. Colomban, M. Barj and G. Lucazeau, "Vibrational spectra of different phases belonging to the β/β'' alumina and to the NASICON family" Solid State Ionics 5:193-196; 1981.

(50) J.P. Boilot, G. Collin and R. Comes, "Phase transition in NASICON compounds $Na_3Sc_2P_3O_{12}$ and $Na_{1+x}Zr_2Si_xP_{3-x}O_{12}$" Solid State Ionics 5:307-310; 1981.

(51) U. Von Alpen, M.F. Bell and H.H. Höfer, "Compositional dependence of the electrochemical and structural parameters in the NASICON system" Solid State Ionics 3-4:215-218; 1981.

(52) D. Tran Qui, J.J. Capponi, J.C. Joubert and R.D. Shannon, "Crystal structure and ionic conductivity in $Na_4Zr_2Si_3O_{12}$" J Solid State Chem 39:219-229; 1981.

(53) A. Clearfield, P. Jerus and R.N. Cotman, "Hydrothermal and solid state synthesis of sodium zirconium silicophosphate" Solid State Ionics 5:301-304; 1981.

(54) D. Tran Qui, J.J. Capponi, M. Gondrand, M. Saïb, J.C. Joubert and R.D. Shannon, "Thermal expansion of the framework in Nasicon-type structure and its relation to Na^+ mobility" Solid State Ionics 3-4:219-222; 1981.

(55) H.U. Beyeler, R.D. Shannon and H.Y. Chen, "Ionic conductivity and structure of the conduction paths of $Na_5YSi_4O_{12}$" Solid State Ionics 3-4:223-226; 1981.

(56) W. Bogusz, "Influence of thermal cycling on properties of NASICON" Phys Stat Sol (a) 66:K109; 1981.

(57) R.S. Gordon, G.R. Miller, B.J. McEntire, E.D. Beck and J.R. Rasmussen, "Fabrication and characterization of Nasicon electrolytes" Solid State Ionics 3-4:243-248; 1981.

(58) F. Cervantes Lee, J. Marr, F.P. Glasser, "Compounds in the Na_2O-Y_2O_5-SiO_2 system" Ceramics International 7:43-47; 1981.

(59) J.J. Bentzen and P.S. Nicholson, "Preparation and

characterization of dense sodium superionic conducting $Na_5YSi_4O_{12}$" *Mat Res Bull* 17:541-548; 1982.

(60) B.A. Maximov, I.V. Petrov, A. Rabenau and H. Schulz, "X-ray investigations and possible mechanism for the ionic conductivity in $Na_5YSi_4O_{12}$ and $Na_5ScSi_4O_{12}$" *Solid State Ionics* 6:195-200; 1982.

(61) L. Boehm, C.J. Delbecq, E. Hutchinson and S. Susman, "Fast ion conduction and phase transitions in various preparations of $Na_3Sc_2P_3O_{12}$" *Solid State Ionics* 5:311-314; 1982.

(62) S. Susman, C.J. Delbecq and T.O. Brun, "Structure and conductivity of the Nasicon analog $Na_3Sc_2(PO_4)_3$" *Proc Electrochemical Soc, Spring Meet,* May 9-14, 1982; Montreal; Ext Abst:1172-1173; 1982.

(63) H. Perthuis, Ph. Colomban, J.P. Boilot and G. Velasco, "Chemical preparation of NASICON type compounds by sol-gel method for thick films elaboration" *Proc 5th CIMTEC, Int Conf on Modern Technology of Ceramics*, June 14-19, 1982; Lignano-Sabbiadoro; Elsevier; 1982.

(64) M. Barj, Ph. Colomban and G. Lucazeau, "Vibrational study of NASICON-like fast ionic conductors" *Proc 8th Int Conf Raman Spectr* September 6-11, 1982; Bordeaux, J. Lascombe and P.V. Huong eds, John Wiley and Sons, New York, 1982.

(65) U. Von Alpen and M.F. Bell, "Structural and electrochemical investigation of new compounds in the phase system $Na_2O-ZrO_2-SiO_2-P_2O_5$" *Proc Electrochemical Soc Spring Meet*, May 9-14, 1982; Montreal; Ext Abst 1170-1171; 1982.

(66) H. Schmid, L.C. de Jonghe and C. Cameron, "Chemical stability of NASICON" *Solid State Ionics* 6:57-63; 1982.

(67) M. Lejeune, Ph. Colomban and J.P. Boilot, "Fast potassium ion conduction in quenched KASICON glass" *J non Cryst Solids* to be published 1982.

(68) J.P. Boilot, G. Collin and R. Comes, "Evidence of a relation between structural defects and phase transitions in NASICON type compounds", *Solid State Comm* to be published.

(69) G. Velasco, J. Ph. Schnell, M. Nouailles and M. Croset, "Advanced microelectronics technology for solid state ionic devices" *Solid State Protonic Conductors I.* J. Jensen and M. Kleitz eds, Odense University Press; 1982.

TABLE I : SINGLE CRYSTAL SYNTHESIS

Compounds	Procedure	Experimental (ref)
$NaZr_2(PO_4)_3$	B_2O_3 flux	X-rays (Li,K,Rb,Cs and Hf,Ti, Ge isomorphs) (4,5,10)
$Na_5Zr(PO_4)_3$	Na_3PO_4 flux	X-rays, Raman (Si/P substitution) (49,50,64,68)
$Na_3Sc_2(PO_4)_3$	Na_3PO_4 flux $Na_4P_2O_7$ flux	X-rays, Raman, dielectric properties (16,23,31,34,50,54)
$Na_3Fe_2(PO_4)_3$	Na_3PO_4 flux	X-rays (Cr isomorph) (3,41)
$Na_{4,5}Yb_{1,5}(PO_4)_3$	Grain Growth in ceramic	X-rays (33)
$Na_3Er(VO_4)_2$	Na_3VO_4	X-rays (33)
$Na_4Zr_2(SiO_4)_3$	Melt growth NaF flux hydrothermal synthesis	Phase diagram, X-rays Raman (1,6,7,8,52,64)
$Na_5YSi_4O_{12}$	NaF flux hydrothermal synthesis	X-rays, conductivity (Sc isomorphs) (18,42,55,60)

TABLE II : IONIC EXCHANGE ELABORATION

Compounds	Starting compound	Experimental (ref)
$\left.\begin{matrix}Ag\\Li\\K\end{matrix}\right) Zr_2(PO_4)_3$	$NaZr_2(PO_4)_3$ $\alpha Zr(HPO_4)_2, H_2O$	X-rays, DTA, TG (10,15,32)
$\left.\begin{matrix}Na\\Li\\K\end{matrix}\right)_2 Zr(PO_4)_2$	α-and γ-$Zr(HPO_4)_2, H_2O$	X-rays, DTA, TG (39,53)
$\left.\begin{matrix}Li\\Ag\\K\end{matrix}\right)_3 Zr_2Si_2PO_{12}$	Na isomorph	X-rays, DTA (10)
$Na_{3,2}Zr_{1,2}Si_3P_{0,8}O_{12}$	Wadeite glass	X-rays, Raman (49,67)
$\left.\begin{matrix}Ag\\Li\end{matrix}\right)_5 GdSi_4O_{12}$	Na isomorph	X-rays, DTA (Y isomorph) (18)

TABLE III : POWDER PREPARATION (Classical process)

Compounds	Densification %	Conductivity† $(\Omega cm)^{-1}$ Activation energy (eV)	Experimental (ref)
NASICON* $0.4<x<3$	70-99	1 to 4×10^{-1} (300°C) 0.15 to 0.36	X-rays (11,29,35,36,66) Mg,Zn,Y,Ti,Sb,V,Nb,Ta doping(40). Grain boundary conductivity, Na cells(17,25,28,56)
$Na_{3.1}Zr_{1.55}Si_{2.3}P_{0.7}O_{11}$		2×10^{-1}(300°C) 0.26	Na tests(51,65,66)
$Na_4ZrSi_3O_{10}$		1.6×10^{-3}(300 °C) 0.44	Na tests(51,65,66)
$NaZr_2(PO_4)_3$	70-95	2.5×10^{-5}(200°C) 0.53 10^{-3}(200°C) 0.42	X-rays, IR, Raman(10,11,13,64). Hf,Ta,Nb substitution. Y,Ca,Nb substitution (37,48)
$LiZr_2(PO_4)_3$	85-95	1.5×10^{-3}(200 °C) 0.43	X-rays. Hf,Ta,Nb,Mg substitution (13,64)
$Na_3Sc_2(PO_4)_3$	70-93	1.7×10^{-1}(300°C) 0.19	X-rays, Raman (31,49)
$Na_3Fe_2(PO_4)_3$		10^{-2}(300 °C)	X-rays (Cr substitution) (3,19,41)
$Na_5GdSi_4O_{12}$	70-95	3×10^{-1}(300 °C) 0.28	X-rays, ATD, Fe,Sc,Y,In, Gd,Er,Lu,Sm substitution (14,18,38,58)
$Li_5GdSi_4O_{12}$		10^{-6} 0.47	X-rays, Na isomorph, Na/$TiS_2$and Li/TiS_2cells (27)

---

*NASICON : $Na_{1+x}Zr_2Si_xP_{3-x}O_{12}$

†Corresponding to the best composition

TABLE IV : POWDER PREPARATION (Wet-chemical process)

Compounds	Densification %	Conductivity† $(\Omega cm)^{-1}$ Activation energy (eV)	Experimental (ref) (Starting reagents, characterization)
NASICON* $1.6<x<2.4$		1.6×10^{-1} (300°C) 0.2	Zr nitrate, silica sol, X-rays, dilatation (30)
	95-98		$Zr(OH)_4$ slurry, silica sol, X-rays, DTA (35)
	90-98	$\sim10^{-1}$ (300°C)	Zr carbonate, silica sol, high isostatic pressure Na/Na cells (57)
NASICON* $0<x<3$ $NaZr_2(PO_4)_3$ to $Na_5Zr(PO_4)_3$			Si,Zr alkoxides, phosphate sol, X-rays, IR, Raman, Li,K,Ag isomorphs (63,64)
$Na_5GdSi_4O_{12}$	99-100	2.6×10^{-1} (300°C) 0.19	Silica sol, Gd acetate, (Y isomorph) (38,59) X-rays

---

†Corresponding to the best composition

*NASICON : $Na_{1+x}Zr_2Si_xP_{3-x}O_{12}$

TABLE V : CONDUCTIVITIES AT 300°C AND ACTIVATION ENERGIES (σT vs T^{-1}) OF DENSE CERAMIC SPECIMENS IN THE SYSTEM $Na_{1+x}Zr_2P_{3-x}Si_xO_{12}$ (Ref 11)

Composition (x)	Structure	$\sigma 300\ (\Omega.cm)^{-1}$	ε_a (eV)
0.4	R	5.3×10^{-4}	0.26
0.8	R	2.9×10^{-3}	0.31
1.2	R	2.6×10^{-2}	0.27
1.6	R	4.8×10^{-2}	0.32
1.8	M	1.25×10^{-1}	0.24
2.0	M	2×10^{-1}	0.29
2.2	M	1.7×10^{-1}	0.24
2.4	R	1.1×10^{-1}	0.26
2.6	R	3.6×10^{-2}	0.24
2.8	R	1.8×10^{-2}	0.24

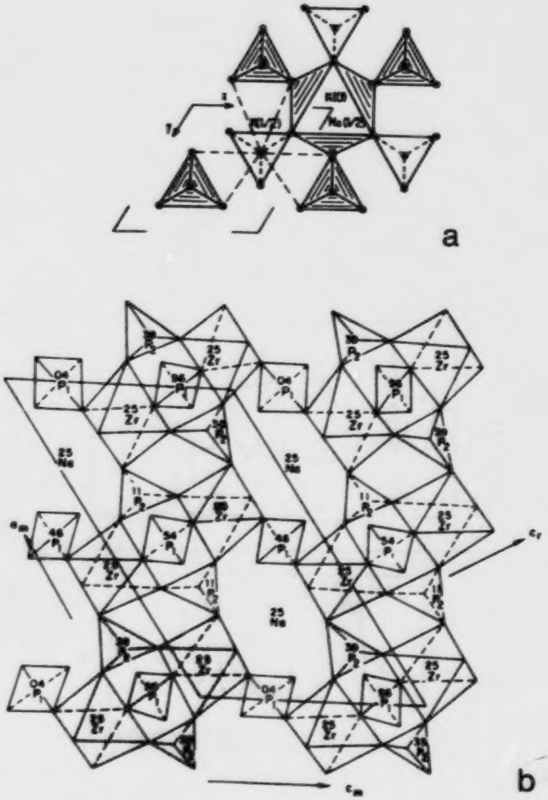

Figure 1: (a) The glaserite structure projected down the threefold axis (ref 33); (b) Projection of half the unit cell along the a_r-axis of rhombohedral $NaZr_2P_3O_{12}$ (ref 10).

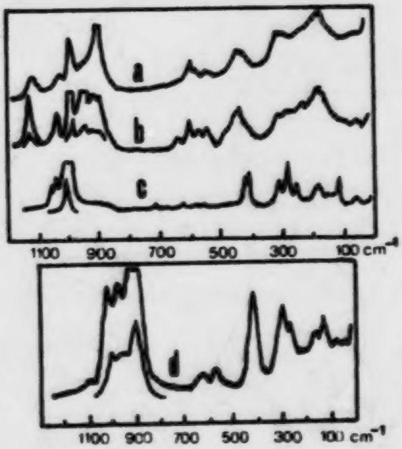

Figure 2: Raman spectra of NASICON-type compounds at RT; (a) $Na_{5.5}Zr(Si_{0.5}P_{2.5})O_{12}$ single crystals; (b) $Na_5Zr(PO_4)_3$ single crystals (ref 49,64); (c) $Na_2Zr(PO_4)_2$ powder (ball milling process) (ref 64); (d) $Na_3Zr_2Si_2PO_{12}$ powder (chemical process) (ref 63,64).

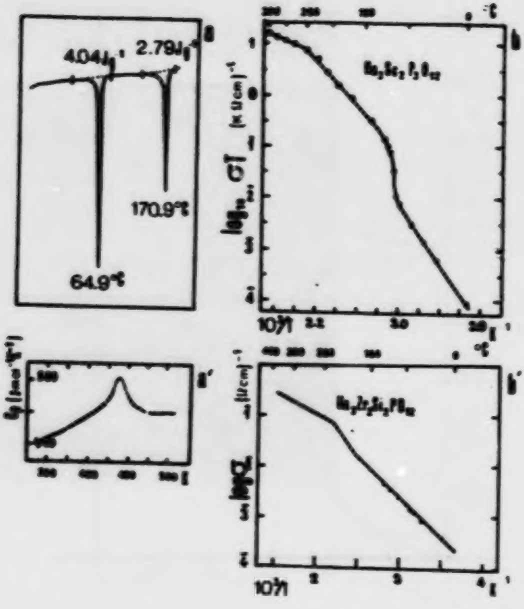

Figure 3: Phase transitions from polycrystalline samples.
NASICON(Sc): (a) DTA curve; (b) Temperature dependence of the conductivity (lnσT vs 1/T) (ref 61);
NASICON(Zr): (a') DSC curve; (b') ionic conductivity as a function of the inverse absolute temperature. (ref 29)

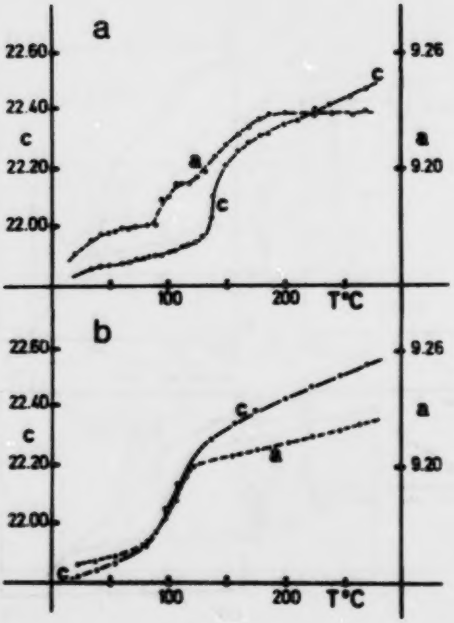

Figure 4: Evolution of a and c hexagonal parameters versus temperature (ref 68): (a) $Na_{5\cdot3}Zr(Si_{0\cdot3}P_{2\cdot7})O_{12}$ single crystals exhibit two structural transitions; (b) $Na_{5\cdot1}Zr(Si_{0\cdot1}P_{2\cdot9})O_{12}$. Transition is spread over the temperature range 80-130°C.

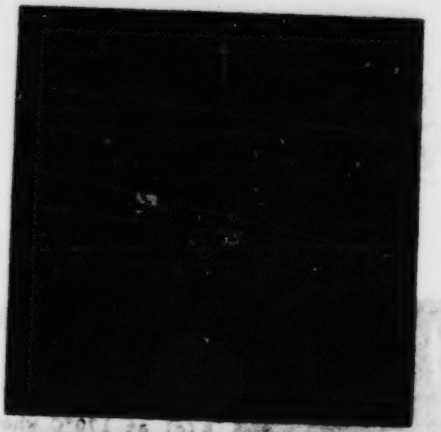

(a) at room temperature with superstructure reflections of type I.

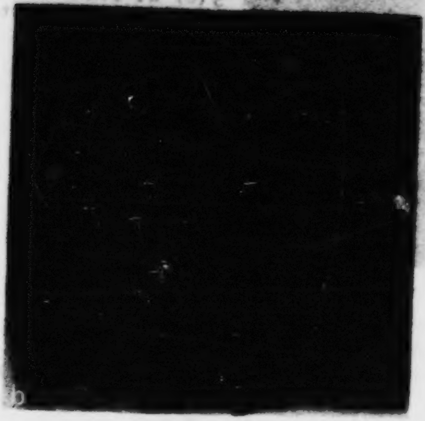

(b) at 120°C showing the type II superstructure reflections.

Figure 5: Precession photographs of the h01 layer (hexagonal indexation) of $Na_{5.3}Zr(Si_{0.3}P_{2.7})O_{12}$ (λ=Cu Kα) at three different temperatures.

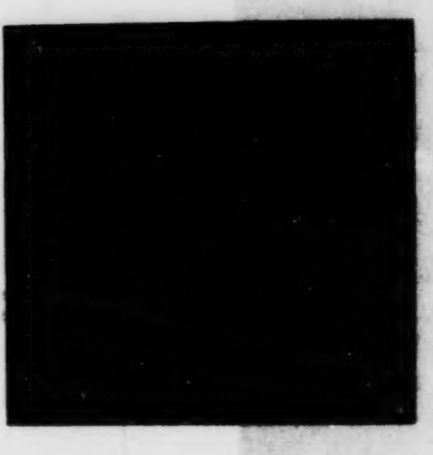

5 (c) at 170°C when the substructure reflections remain.

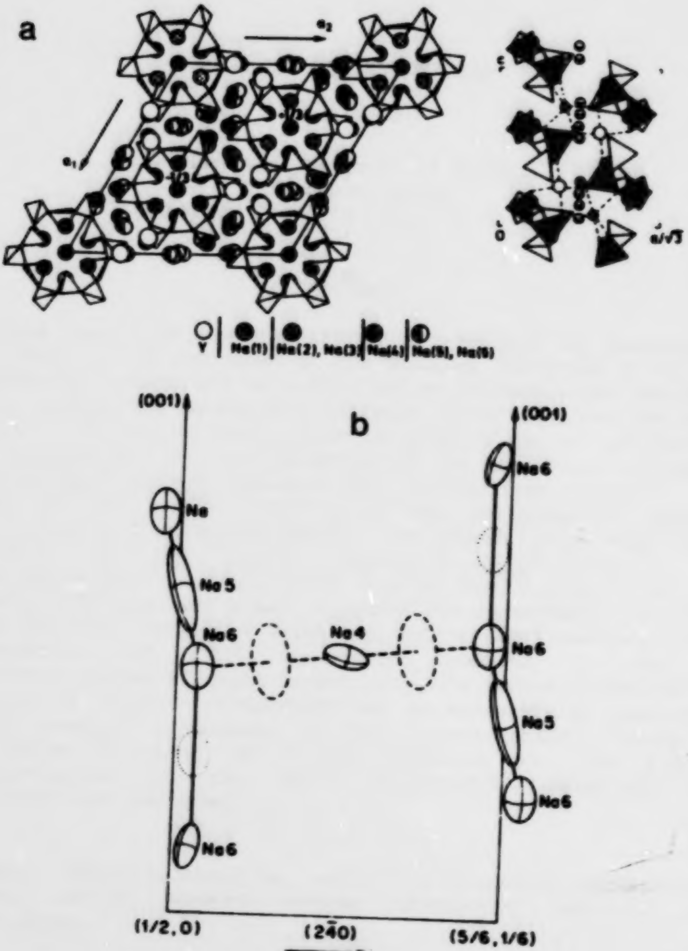
a
a2
a1
-1/2
c
0
a/√3
Y
Na(1)
Na(2), Na(3)
Na(4)
Na(5), Na(6)
b
(001)
(001)
Na
Na 5
Na 6
Na 4
Na 6
Na 6
Na 5
Na 6
Na 6
(1/2,0)
(2$\bar{4}$0)
(5/6,1/6)

Figure 6: (a) Crystal structure of $Na_5RESi_4O_{12}$. The $Si_{12}O_{36}$ rings are stacked along the three-fold axis of the rhombohedral R3c space group. The RE^{3+} ions link these rings. Only Na ions at Na_4, Na_5 and Na_6 are mobile (ref 60). (b) Conductivity paths and the thermal ellipsoids of relevant sodium ions. The dashed circles indicate the barriers for the conduction perpendicular to c, the dotted ellipses symbolize the large voids in the conduction path parallel to c (ref 55).

SODIUM ION CONDUCTIVE CERAMICS

Kuo Chu-Kun

Shanghai Institute of Cermics
Academia Sinica
Shanghai, People's Republic of China

ABSTRACT

This paper reviews the status of research on Na-conducting solid electrolytes performed at the Shanghai Institute of Ceramics. The essential points can be summarized as follows: (a) Fabrication studies include the development of beta-, beta"-aluminas and Nasicon materials. A detailed description is given of the gel processing of beta"-alumina and data are presented on the liquid-drying technique used to prepare Nasicon ceramics with limited free zirconia. (b) A search for new solid electrolytes was performed by ionically substituting in the Nasicon family. The lowest resistivity obtained at 300°C in the system $Na_3Zr_{2-x}Yb_xSi_{2-x}P_{1+x}O_{12}$ is 7.19 ohm.cm for $x=0.8$. (c) Application studies involving Na/S batteries, sodium purification and a sodium sensor are described. (d) An EPMA method has been developed which can follow simultaneously the ion concentration and metal deposition processes in the solid electrolyte during electron injection. The sodium accumulation at the point of electron bombardment can be successfully simulated by an ion-transport process. The relationships between the distribution patterns of sodium deposits and the transport characteristics of the solid electrolyte materials under bombardment are discussed.

KEYWORDS: solid electrolyte, sodium ion conductor, sodium sulphur battery, sodium sensor, sodium deposition, electron probe microanalysis.

RÉSUMÉ

L'auteur rend compte de l'état des recherches effectuées à l'institut des céramiques de Shanghai sur les électrolytes solides utilisant des conducteurs ioniques rapides au Na^+. Les études de fabrication portent sur des alumines bêta et bêta", de même que sur des matériaux de la famille des nasicons. L'auteur décrit en détails le monde de préparation d'une alumine bêta" par la méthode du gel. Les chercheurs ont mis au point une technique de séchage en phase liquide qui permet d'élaborer des céramiques de nasicons de manière à en limiter la teneur en zirconia libre. De nouveaux électrolytes solides s'obtiennent par substitution ionique dans la famille des nasicons. La plus basse résistivité obtenue à 300°C dans le système $Na_3Zr_{2-x}Yb_xSi_{2-x}P_{1+x}O_{12}$ est de 7.19 ohms.cm pour une valeur de $x=0,8$. L'auteur décrit également des etudes d'application dans lesquelles il est question de piles au Na/S, de purification du sodium et de détecteurs au sodium. Les chercheurs ont mis au point une méthode de micro-analyse par sonde électronique capable de suivre simultanément la concentration ionique et le dépôt de métaux dans l'électrolyte solide au cours de l'injection d'électrons. On peut réussir à simuler l'accumulation de sodium au point de bombardement électronique au moyen d'un processus de transport ionique. L'auteur examine finalement les relations entre les courbes de distribution des dépôts de sodium et les propriétés des matériaux de l'électrolyte solide du point vue du transport.

INTRODUCTION

There has been a rapid development in the study of solid electrolytes because of their potential use in energy conversion and production systems as well as in ionics, since beta-alumina was first reported as a fast-ion conductor in 1967 (1,2). Up to the present, many new solid electrolytes exhibiting fast ionic conduction have ben discovered and a number of devices such as high energy-density batteries, solid-state cells, analysis sensors, and various other ionic devices have been developed therefrom. Moreover, the solid-electrolyte cell may also serve as a useful tool for electrochemical and thermodynamic investigations.

The Shanghai Institute of Ceramics has been involved in the study of sodium-ion conductors since the early seventies. This paper gives a brief account of the research conducted in the field of materials fabrication and their applications.

MATERIAL FABRICATION

Fabrication studies have been carried out on beta-, beta"-aluimina and Nasicon ceramics. The properties of these ionically conductive ceramics are presented in Table 1.

Beta alumina material is fabricated by the usual process. Sintering is done in a protective atmosphere to control the vaporization of Na_2O during sintering. In most cases, beta alumina has been used in Na/S battery performance test and preparation of various electrochemical devices.

Due to the high sintering temperature, which makes the ceramic processing hard to control, and the relatively low conductivity of beta-alumina, we began to fabricate beta"- alumina ceramics (3). A gel method was developed by which homogeneous beta"-alumina precursor powders with the appropriate dopants, lithia and/or magnesia, could be prepared. The gel was formed by dripping or spraying ammonium hydroxide into a solution composed of the nitrates of sodium, aluminum and lithium and/or magnesium. It was shown that the gel formation was closely related to the pH value of the solution. A stable gel could be obtained only when the pH value was adjusted to about 5.

Dehydration proceeded under vacuum at 60-70°C for some tens of hours. The dried gel contained about 10 wt% Na_2O. X-ray diffraction analysis indicated that the decomposition products of the gel, between 500-900°C, were amorphous and starting from 1000°C, a mixture of beta- and beta"-alumina was formed.

Ceramics sintered at 1600°C for 5 minutes reached 98.5% theoretical density. The microstructure was duplex in nature. X-ray powder patterns revealed that in addition to the beta- and beta"-aluminas there also occurred a small amount of $NaAlO_2$ and α-Al_2O_3 in sintered specimens. Annealing is therefore necessary in order to obtain single-phase beta" and consequently lower the electical resistivity, Fig. 1. The microstructure of the ceramic after annealing is shown in Fig. 2.

Nasicon ceramics were prepared by a solid-state reaction method (4). As seen in Table 1, the Nasicon ceramics so prepared always have a small amount of free zirconia as a second phase. We have tried a liquid drying method by atomizing a citrate solution of the appropriate composition into 95% or absolute alcohol to precipitate the citrate salt mixture. In the liquid drying process, no loss of phosphorus was found. The loss of zirconium and silicon was also negligible on adjusting the pH value of the solution to 7, and the loss of sodium was compensated by adding excess sodium to the solution. The precursor powder thus prepared after drying in vacuum was fired at 900-950°C under flowing oxygen and found to be completely converted to the Nasicon phase. The synthesis temperature is thus about 200°C lower than that required for conventional solid-state reaction. The Nasicon material could be sintered to 95% theoretical density with practically no free zirconia and a relatively fine grain size.

Research work on Nasicon was also directed to examining the effect of chemical composition on the resistance to attack by molten sodium. The experimental results confirmed that a decrease of the zirconia content would be helpful in increasing the stability of Nasicon in liquid sodium.

SEARCHING FOR NEW SODIUM ION CONDUCTORS

More recently, several compounds or solid solutions with framework structures, such as Nasicon (5,6) and sodium gadolinium silicate (7), were prepared with high ionic conductivities comparable to those of the beta- and beta"-aluminas. The three-dimensional conduction behaviour of these crystals, which may result in a more even distribution of current density during charge-discharge cycles of batteries based on these materials, has received considerable attention from both theoretical and practical sides. Our primary interest is to synthesize new ionic conductors in the Nasicon family. Two approaches of aliovalent substitution have been carried out on the end members of the Nasicon solid solution series. They are: (a) replacing a part of Zr^{4+} ions in the $NaZr_2P_3O_{12}$ by Y^{3+}, Yb^{3+}, In^{3+} or Zn^{2+} ions, which may produce excess interstitial sodium ions in the host lattice and thus stimulate a cooperative motion between the sodium ions in the normal and interstitial sites (8); and (b) replacing a part of Zr^{4+} ions in $Na_4Zr_2Si_3O_{12}$ by Ta^{5+}, which may produce vacancies in the lattice, necessary for ion transportation.

The solubility limits determined in the systems $Na_{1+x}Zr_{2-x}Y_xP_3O_{12}$, $Na_{1+x}Zr_{2-x}Yb_xP_3O_{12}$ and $Na_{1+x}Zr_{2-x}In_xP_3O_{12}$ are at x=0.8, 0.9 and 1.8 respectively. No additional peaks other than those of $R\bar{3}C$ solid solution phase have been detected in the X-ray diffraction patterns. The plots of the lattice parameters and the resistivity versus the composition of the solid solution are illustrated in Fig. 3 and 4.

According to Pauling's ionic radii values, all the radius ratios:

$$r_{Y^{3+}}/r_{O^{2-}} = 0.657,\ r_{Yb^{3+}}/r_{O^{2-}} = 0.614 \text{ and } r_{In^{3}}/r_{O^{2-}} = 0.579,$$

are within the octahedral coordination limits. It would be expected that the substitution in the host $R\bar{3}C$ lattice would take place in the ZrO_6 octahedra and miscibility region would become wider when the difference in sizes between the Zr^{4+} and the substituting cations becomes smaller.

It can be seen from Fig. 3 that the lattice parameters a_o and c_o in the Y- and the Yb-substituted and a_o in the In-substituted solid solutions increase with increasing x; whereas c_o in the system containing indium decreases. The expansion of the crystalline lattice of the solid solutions can be reasonably explained in the light of displacing Zr^{4+} ions with ions of larger size. The shortening of the c axis in the In-containing phase, on the other hand, seems likely to be associated with the particular electronic configuration of the indium ion which has a silver core pattern and will be considerably more polarizing.

The lowest resistivities determined at 350°C in the three systems are 151, 101 and 135 ohm.cm for x=0.8, 0.9 and 1.2 respectively. The activation energies are 0.37, 0.35 and 0.27 eV.

No $R\bar{3}C$ solid solution was detected in either Zn- or Ta- substituted systems.

Compared with the usual Nasicon solid solution series, the systems of yttrium and ytterbium substitution show somewhat lower ionic resistivity with similar solid solution contents. The essential difference is that the solubility limits for the latter two systems are lower. So further investigation was conducted in the system $Na_3Zr_{2-x}Yb_xSi_{2-x}P_{1+x}O_{12}$, where a double replacement of $(Zr^{4+} + Si^{4+})$ by $(Yb^{3+} + P^{5+})$ appears in the Nasicon phase. The lowest resistivity at 300°C is 7.19 ohm.cm for $x=0.8$. The activation energy for bulk conductivity in the high-temperature region is 0.22 eV and that for the grain boundary component is 0.7 eV.

APPLICATIONS

Beta (Na/S) Battery

The principles of the Na/S battery are well known from numerous publications (1, 9, 10). The overall chemical reaction in the cell can be summarized as $2Na + xS = Na_2S_x$ or $2Na + Na_2S_x = 2Na_2S_{x/2}$. Due to the low specific gravity of sodium, sulphur and sodium polysulphides, the energy density of the Na/S cell is high: the theoretically calculated energy density is 790 $Wh.kg^{-1}$. A number of Na/S cells have been designed and constructed in this Institute. Their characteristics and performance data are given in Table 2.

Typical charge-discharge curves of the Na/S cell are illustrated in Fig. 5. The discharge curves can be divided into three sections, namely, the initial section, the steady section and the decrease section. It is well known that there is a wide miscibility gap existing in the liquid phase of the Na-S system which is intrinsically responsible for the extended steady voltage region during the discharge period. The concentration polarization effect at the cathodic melt may possibly account for the decrease section that usually comes before the solubility limit of the sodium rich side ($Na_2S_{5.2}$ at 350°C) is reached.

On the charge curve, there occurs a region where the cell voltage rises very rapidly. This may be taken as the end point of charging. As it is known, the rapid increase in charging voltage arises essentially from the formation of the sulphur-rich phase in the miscibility gap. If a large part of the solid electrolyte membrane in the Na/S cell is covered by a layer of this insulting sulphur-rich liquid, the internal resistance of the cell will greatly increase. In addition, when the nonconductive layer spreads over a large area on the surface of the solid electrolyte, a concentration of the ionic current must occur at the domains where sodium polysulphide rich liquid is still in contact with the electrolyte. This may frequently lead to a breakdown of the solid electrolyte. As a consequence, excessive charging in the two-phase region of the Na-S system should be avoided (11). Otherwise, some additives or a sulphur compartment which is favorable to the charge transfer process should be used (12).

A six-tube cell with the tubes connected in parallel was designed. We then connected 80 of these multi-tube cells, in both series and parallel, to form a 6 kW battery assembly. The ability of the battery to power a small electric vehicle was successfully demonstrated. It has run intermittently for 38 charge-discharge cycles.

Purification of Sodium

Due to the highly selective nature of beta-alumina to only sodium ions, pure sodium may be prepared by the electrolysis of either bulk sodium or a sodium-containing salt through a beta-alumina membrane. Good results have been obtained: the total impurity content can be kept to a very low level, less than 0.02%, especially for the non-metallic elements (C, P, N, Cl, O etc.).

The method has an additional advantage of having a high current efficiency.

Sodium Sensor

Based on the measurement of emf's of the solid electrolyte cell $Na/Beta\text{-}Al_2O_3/Na_xHg_{1-x}$, $x=0.00001-0.005$, an analytical probe was made to measure the sodium concentration in dilute sodium amalgams (13). Very pure sodium, obtained in-situ by electrolysis, was used as the reference electrode in the beta- alumina tube. Moreover, there is almost no self discharge in storage because of the low electron transference number of the beta alumina which was determined to be 10^{-7} to 10^{-6} at 100° to 300°C (14). So the emf of the cell is very stable. It has remained unchanged over a period of two years.

EPMA STUDY OF THE SODIUM DEPOSITION PROCESS

The electrolytic degradation of the solid electrolyte during the operation of Na/S cells or other electrochemical devices has received considerable attention in the last ten years. Several models of electrochemical and mechanical degradation of beta- or beta"-alumina materials have been proposed (15-19). It has been shown that sodium deposition is largely responsible for the degradation process: it is always initiated at the electrode where electron injection is possible, and the degradation usually occurs at places where the transport of sodium atoms formed is hindered (15, 16, 20-22).

Electron probe microanalysis (EPMA) was performed on beta-, beta"-aluminas and Nasicon materials. The EPMA technique makes it possible to inject electrons and to count the accumulated sodium atoms simultaneously; it is also valuable in investigating sodium deposition in microscopic regions (23).

A typical curve presenting the increase of NaKα counts with electron bombardment time is shown in Fig. 6. We have successfully approximated the accumulation of sodium counts on the basis of ion transportation with a diminished carrier concentration. The following equation can be fitted to the experimental data:

$$Q = a(1-\exp(-bt)) + Q_0\exp(-bt)$$

$$a = n_0/K_2$$

$$b = K_1 K_2 ZeuE$$

where Q is the NaKα X-ray counts, n_0 the initial concentration of the current carrier (here, the mobile sodium ions), Ze the carrier's charge, u the mobility of the carrier, E the electric field strength, t the time, and K_1 and K_2 are constants. The calculated curve is shown in Fig. 6 by a dashed line together with the fitted parameters. It was found that the sodium accumulation curve became smoother when large crystals were bombarded under similar experimental conditions whereas the curve increased quickly as the polycrystals became smaller in size. This may be related to the high resistance to ion transportation at grain boundaries at low temperatures.

It was found that as the sodium content increases, the counts of aluminum and oxygen go down slightly.

Various patterns of the distribution of sodium deposition are shown in Fig. 7. The sodium deposition for the three-dimensional conductor (Nasicon) and for the isotropic plane of beta-alumina single crystal was found to be non-directional. However, if the injected electron is parallel or tilted to the ion-conductive plane of beta"-alumina, deposition will preferably occur along the c-axis. This fact should further confirm the ion concentration and metal deposition at the bombarded point.

Electron bombardment of the beta"-alumina polycrystals with a scanning beam revealed that the sodium deposition was usually initiated at cleavages or edges of the crystals. This means that, where sites for ion transference and sodium accumulation are available, deposition will occur preferentially.

SUMMARY

In this Institute, major effort has been devoted to Na fast-ion conduction with particular attention to materials fabrication and Na/S battery testing. The investigation of beta-, beta"-alumina and Nasicon has focussed on the processing and improvement of properties. Single- and multi-tube cells have been designed and tested for their performance and lifetime.

Some attention has also been given to other applications for sodium-ion conductors such as sodium purification and sodium analysis.

Some fundamental studies are being carried out on the crystalchemical and electrochemical behaviour and on the ion-transport processes in various compounds in a search for new ionic conductors in order to understand the ionic conduction and degradation processes.

Table 1 - Properties of Ionic Conductive Ceramics

Material	Composition (wt%)	Density (g.cm^{-3})	Resistivity at 350°C (ohm.cm)	Grain size (μm)
Beta	Na_2O 7.5–8	3.20	7–10	10
	MgO 2–2.5			
	Al_2O_3 Bal.			
Beta"-SR	Na_2O 8.99	3.19	6–6.5	20–30 on the average
	Li_2O 0.8			
	Al_2O_3 Bal.			
Beta"-GEL	Na_2O 9.1–9.4	3.20	5	Duplex 3–5 (matrix) 10–30 (5–10%) 100 (few%)
	Li_2O 0.7–0.8			
	Al_2O_3 Bal.			
Nasicon	Na_2O 17.52	3.20	3	10
	ZrO_2 46.45			
	SiO_2 22.65			
	P_2O_5 13.38			

*Beta = Beta-alumina; Beta" = Beta"-alumina;
SR = By solid-state reaction method;
GEL = By gel method.

Table 2 - Performance Characteristics of Na/S Cells

	Single Tube Cell	6 Tube Cell
Dimension	Dia. 3 by 25 cm	6 by 6 by 30 cm
Specific Energy	130 Wh.kg^{-1}	160 Wh.kg^{-1}
	230 Wh.1^{-1}	250 Wh.1^{-1}
Operation Power	1.5 V, 12 A	1.5 V, 50 A
Capacity	30 Ah	130 Ah

REFERENCES

1. Yung-Fang Yu Yao and J.T. Kummer. "Ion exchange properties of and rates of ionic diffusion in beta-alumina"; J Inorg Nuclear Chem 29:2453-2475; 1967.

2. J.T. Kummer and N. Weber. "A sodium-sulphur secondary battery"; Soc Automotive Engrs Trans 76:1003-1007; 1968.

3. Wen Ting-lian and Chen Meng-da. "Effects of sintering and annealing on the sodium ion conductivity and the microstructure of beta"-alumina"; J Chinese Silicate Soc 9:258-264; 1981.

4. Lin Zu-xiang and Yu Hui-jun. "The fabrication and properties of $Na_3Zr_2Si_2PO_{12}$ solid electrolyte"; J Chinese Silicate Soc 9:439-443; 1981.

5. H.Y-P. Hong. "Crystal structures and crystal chemistry in the system $Na_{1+x}Zr_2Si_xP_{3-x}O_{12}$"; Mater Res Bull 11:173-182; 1976.

6. J.B. Goodenough, H.Y-P. Hong and J.A. Kafalas. "Fast Na^+-ion transport in skeleton structures"; Mater Res Bull 11:203-220; 1976.

7. R.D. Shannon, H.-Y. Chen and T. Berzins. "Ionic conductivity in $Na_5GdSi_4O_{12}$"; Mater Res Bull 12:969-973; 1977.

8. Tian Shun-bao and Lin Zu-xiang. "The relation between phase composition and electrical conductivity in $Na_{1+x}Zr_{2-x}M_x(PO_4)_3$ system"; J Chinese Silicate Soc 9:433-438; 1981.

9. N.K. Gupta and R.P. Tischer. "Thermodynamic and physical properties of molten sodium polysulphides from open-circuit voltage"; J Electrochem Soc 119:1033-1039; 1972.

10. J. Fally, C. Lasne, Y. Lazennec and P. Margotin. "Some aspects of sodium-sulphur cell operation"; J Electrochem Soc 120:1292-1295; 1973.

11. Kuo Chu-Kun, Li Shan-tin and Yen Yi-ming. "Recent studies on sodium deposition in beta and beta"-alumina solid electrolytes"; Proc 15th Chinese Conf Chem Phys Power Sources 136-139; 1981.

12. W. Fischer. "State of development and prospects of sodium/sulphur batteries"; Solid State Ionics 3/4:413-424; 1981.

13. Sun Cheng-wen and Cao Jia-di. "Determination of the sodium content in dilute sodium amagams using Na/Na-beta-alumina probe"; Anal Chem (Chinese) 8:411-415; 1980.

14. Sun Cheng-wen and Guo Zhu-kun (Kuo Chu-Kun). "Electronic conductivity in MgO doped sodium beta alumina"; J Chinese Silicate Soc 9:444-449; 1981.

15. R.D. Armstrong, T. Dickinson and J. Turner. "Breakdown of beta-alumina ceramic electrolyte"; Electrochim Acta 19:187-192; 1974.

16. G.J. Tennenhouse, R.C. Ku, R.H. Richman and T.J. Whalen. "Deterioration in ceramic electrolytes for sodium-sulphur batteries"; Amer Ceram Soc Bull 54:523-527; 1975.

17. R.H. Richman and G.J. Tennenhouse. "A model for degradation of ceramic electrolytes in Na-S batteries"; J Amer Ceram Soc 58:63-67; 1975.

18. D.K. Shetty, A.V. Virkar and R.S. Gordon. "Electrolytic degradation of lithia-stabilized polycrystalline beta"-alumina"; Fracture Mechanics of Ceramics 4; ed. by R.C. Bradt, D.P.H. Hasselman and F.F. Lange, Plenum Publishing Corp; 651-665; 1978.

19. L.A. Feldman and L.C. De Jonghe. "Initiation of model 1 degradation in sodium-beta alumina electrolytes"; J Mater Sci 17:517-524; 1982.

20. Li Xiang-ting and Guo Zhu-kun (Kuo Chu-Kun). "Observation of the electrolytic deposition of sodium in beta-alumina ceramics"; J Chinese Silicate Soc 7:271-274; 1979.

21. J.C. De Jonghe, L. Feldman and P. Millett. "Some geometrical aspects of breakdown of sodium beta-alumina"; Mater Res Bull 14:589-595; 1979.

22. Kuo Chu-Kun and Li Shan-tin. "Electro-mechanical degredation of polycrystalline beta-alumina"; Ceram International 7:98-101; 1981.

23. Li Xiang-ting and Guo Zhu-kun (Kuo Chu-Kun). "EPMA study on sodium deposition in beta-alumina"; J Chinese Silicate Soc 9:276-278; 1981.

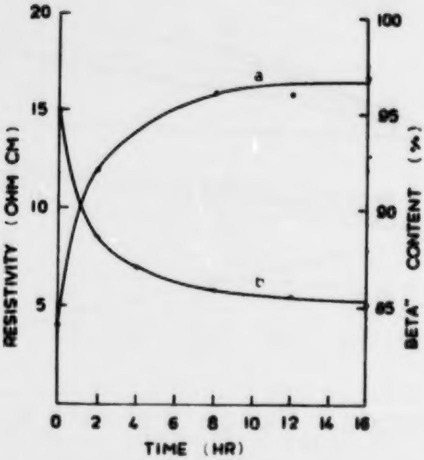

Fig. 1 - Effect of annealing time on (a) beta"-alumina content and (b) resistivity.

Fig. 2 - Microstructure of beta"-alumina ceramic after annealing.

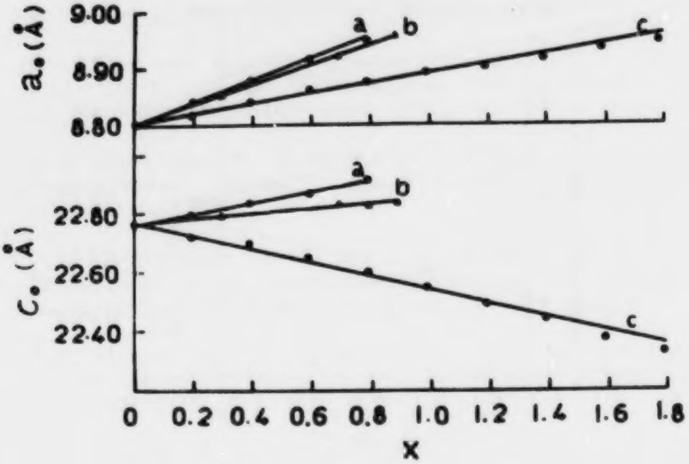

Fig. 3 - Variation of the lattice parameters of $Na_{1+x}Zr_{2-x}M_xP_3O_{12}$ solid solutions with x: (a) M = Y; (b) M = Yb; (c) M = In.

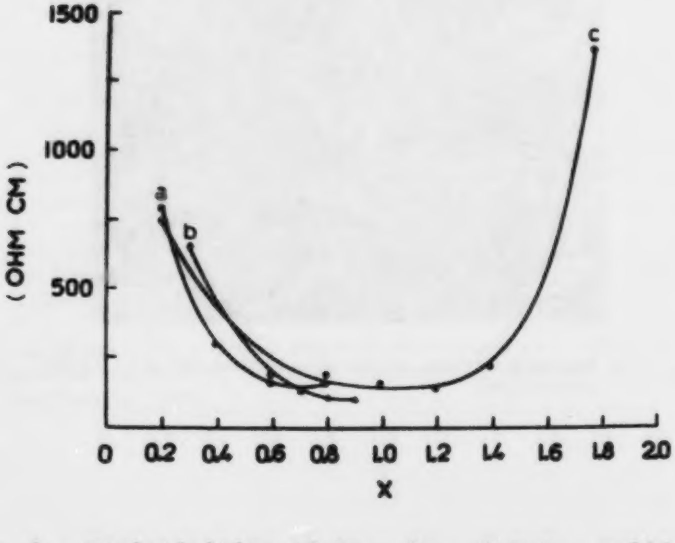

Fig. 4 - Resistivities of $Na_{1+x}Zr_{2-x}M_xP_3O_{12}$ solid solutions: (a) M = Y; (b) M = Yb; (c) M = In.

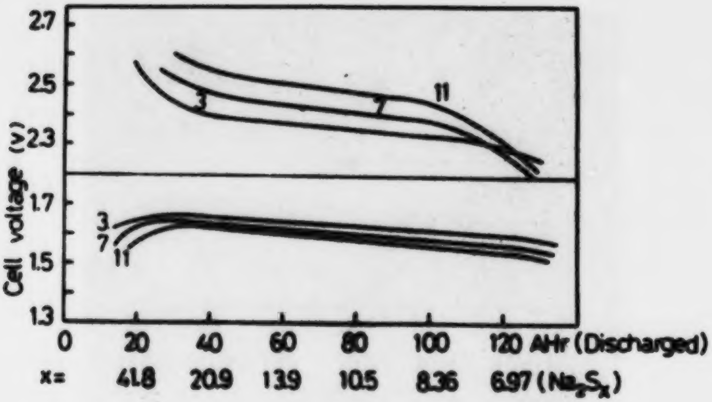

Fig. 5 - Discharge and charge curves of 6-tube cell. The numbers on the curves refer to the number of charge-discharge cycles. Discharge at 50 A (top) and charge at 30 A (bottom).

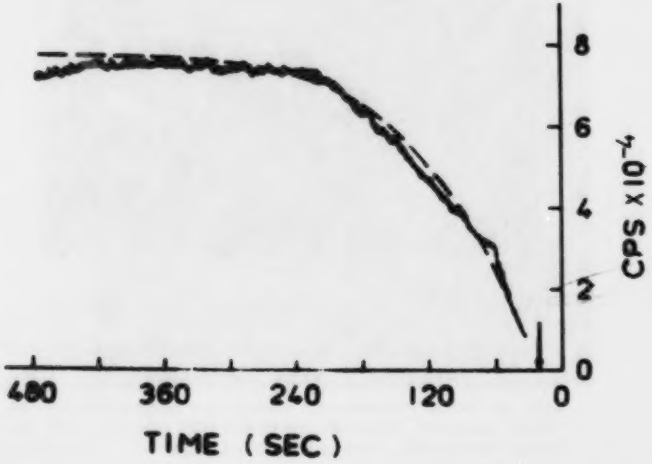

Fig. 6 - Sodium accumulation curve of beta"-alumina crystal during electron bombardment. The arrow indicates the start of bombardment. Fitted parameters of the calculated curve: a = 78100, b = 0.01193, Q_o = 7727.

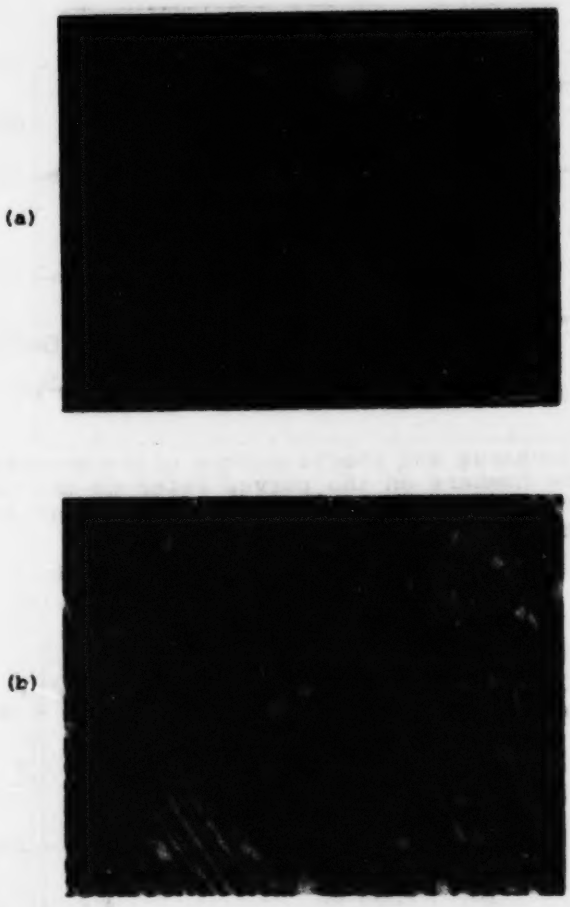

Fig. 7 - EPMA sodium deposition: (a) on beta-alumina, electron bombardment at fixed point on (00.1) plane of beta-alumina crystal lattice, NaK_α X-ray image; (b) on beta-alumina crystal lamellae, scanning bombardment, secondary-electron image; (c) on beta"-alumina, electron bombardment at fixed point, secondary-electron image; (d) on beta"-alumina, scanning bombardment, secondary-electron image.

(c)

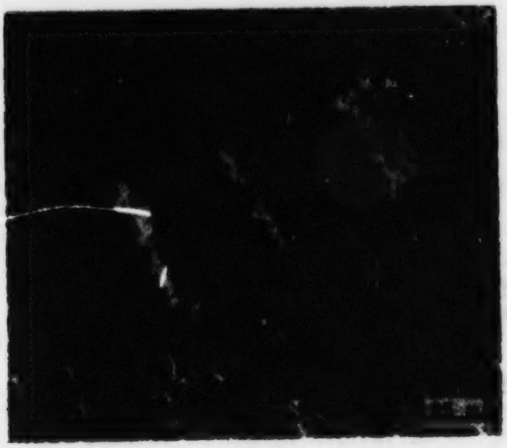

(d)

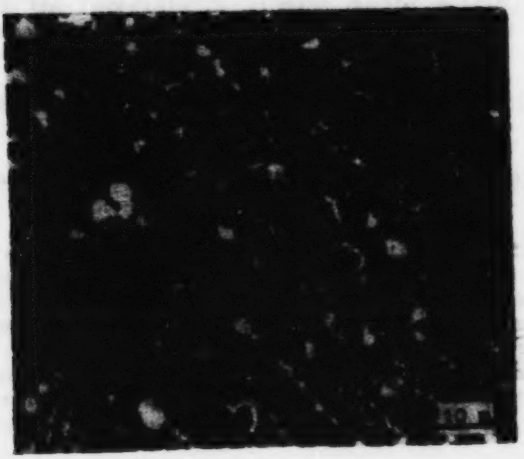

INFLUENCE OF PROCESSING ON NASICON

A.K. Kuriakose, A. Ahmad and T.A. Wheat

Mineral Sciences Laboratories, CANMET
Energy, Mines and Resources Canada
Ottawa, Canada

ABSTRACT

The effect of various processing parameters on the behaviour of sintered Hong and von Alpen Nasicons is reported for both ball-milled and gel-processed materials.

Evidence is presented that considerable amounts of phosphorus can be lost from the system during sintering. In the Hong materials, this loss results in the precipitation of zirconia from solution, particularly when the material is sintered at temperatures over 1200°C.

All Nasicons react with water to some degree and this reactivity is enhanced at high x values (increased SiO_2 content). Contamination of the materials by alumina during milling increases the rate of reactivity of the sintered material to water by approximately four decades.

A glass phase exists in all compositions irrespective of the powder synthesis method or sintering process. The glass is essentially a sodium silicophosphate containing some dissolved zirconia; it has a high ionic conductivity and is readily degraded by water.

The measured bulk ionic conductivity and the activation energy values were found to be dependent on the composition and processing parameters. In particular, extended sintering affects the Hong and the von Alpen series of compositions differently; the former suffer a decrease in conductivity whereas the latter exhibit an increase in conductivity with sintering time. These effects are related to the compositional and resulting microstructural changes that occur on extended sintering.

KEYWORDS: Nasicon, processing, microstructure, glass, reactivity

RÉSUMÉ

L'action de divers paramètres de traitement sur le comportement des céramiques Nasicon type Hong et von Alpen concrétionnées est presentée et à l'égard des matières soumises à la synthèse à l'état solide et à l'égard de celles traitées à l'état colloide.

On présente des preuves du fait que des quantités importantes de phosphore peuvent s'échapper du système pendant la phase de concrétionnement. Dans le cas des matières Hong, cette perte résulte en la précipitation de zircone de solution, tout particulièrement lorsque la matière est concrétionnée à des températures dépassant 1200°C.

Toutes les céramiques type Nasicon réagissent à l'eau, à un certain degré et cette réactivité est augmentée à des indices x plus élevés. (augmentation de la teneur en SiO_2) La contamination des matières par l'alumine pendant la synthèse augmente le taux de réactivité à l'eau de la matière concretionnée par environ quatre décades.

Il existe une phase de verre dans toute composition indépendamment de la méthode de synthèse à poudre ou du procédé de concretionnement. Le verre est essentiellement un phosphate de silicium de sodium qui contient de la zircone dissoute; il possède une haute conductivité ionique et il est vite dégradé par l'eau.

La conductivité en volume mesurée et les indices d'énergie d'activation se sont montrés dépendants de la composition et des paramètres de traitement. En particulier, un concrétionnement prolongé affecte de façons différentes les compositions Hong et von Alpen. Celles-là subissent une réduction de conductivité tandis que celles-ci indiquent une augmentation de conductivité par rapport à la période de concrétionnement. Ces effets sont reliés aux modifications de composition et aux changements microstructuraux subséquents qui ont lieu pendant des périodes de concrétionnement prolongées.

INTRODUCTION

Since the first report of hign ionic conductivity in the Nasicons by Hong (1) in 1976, there has been considerable interest in exploiting the materials because of their ease of synthesis and isotropic conductivity compared with the sodium beta"-aluminas. That interest has also led to an examination of a number of ionically substituted derivatives (2-6).

There are two aspects of the basic Hong compositions that have been closely examined by various groups: the frequent occurrence of second-phase monoclinic zirconia in sintered material (7-11) and, more recently, the durability of various types of Nasicons (12-14). The occurrence of zirconia was initially thought to be due to the poor reactivity of the raw materials used for the synthesis and hence several groups examined the use of highly reactive zirconia or its precursor (7,9,15). On the other hand, researchers at the Max Planck Institute simply used a zirconia-deficient variation of the original Hong compositions to produce, insofar as determinable by XRD analysis, a series of single-phase compositions (10).

More recently, the durability of the Hong and von Alpen series of materials has been examined by several authors (12,13) and specific materials have been reported to fail in the presence of sodium at the elevated temperatures required for the operation of a Na-S battery, and this has led to the suggestion that these materials may not be durable. Yet, reports from Germany indicate that some of the von Alpen materials have sufficient durability for use in Na-S cells (10).

For these reasons, the Hong and von Alpen Nasicons have been produced by the authors, using both conventional and gel- processing techniques so that the effect of various processing parameters on the properties of these materials could be examined.

EXPERIMENTAL

Powder Syntheses

Essentially, two series of materials have been examined based on the general Nasicon compositions first reported by Hong (1) $\{Na_{1+x}Zr_2Si_xP_{3-x}O_{12}\}$ and later modified by von Alpen et al. (10) $\{Na_{1+x}Zr_{2-x/3}Si_xP_{3-x}O_{12-2x/3}\}$, both in the range of 1.5 x 2.2. Each series of material was produced by two different processes: one based on the originally reported ball-milling (BM) process and a second based on a gel-processing (G) technique reported by Quon et al. (15).

In the case of the G materials, the effect of alumina contamination in the product was investigated by using high density alumina or zirconia milling media separately for the dispersion of the powder in isopropyl alcohol prior to the final vacuum drying stage. For the milling in the BM process, only zirconia milling media were used. The one exception to the reported von Alpen BM process (10) used in the present work was the substitution of a commercially available reactive high-purity zirconia (Harshaw Electronic Grade, 99.99+%, mean size less than 1 micrometer) for the zirconium acetonylacetate used in the original work.

Calcination and Sintering

All powders were calcined in air using platinum ware for times varying from 1 to 4 h within the temperature range from 750 to 1150°C as required to maximize the subsequent sintered density. The calcined powders were uniaxially pressed into cylindrical specimens 1.27 cm in diameter by 0.3-0.6 cm in thickness using a pressure of 140 MPa. In some cases, especially when the calcination temperatures were high, a double pressing technique was required to develop dense, strong, green samples. In such cases, the powder was first pressed at 210 MPa, ground into a fine powder and then repressed at 140 MPa. The purpose of the initially high pressure was to simply densify the powder, but as previous experience with similar powders had shown that internal microcracks are formed in compacts pressed above ~200 MPa, a final forming pressure of 140 MPa was selected. A PVA binder also was employed in some cases for the same purpose. In these cases the PVA was burned off before sintering.

Sintering of the G samples was carried out at temperatures optimized to give maximum density. The BM materials were sintered at temperatures close to those reported by the original workers. The samples were sintered either in air or wrapped in platinum foil and buried in powder of the same composition for periods ranging from 15 min to 16 h. In all cases, rapid heating and cooling of about 10 min to and from the sintering temperatures were employed.

Characterization

The various sintered materials were examined using standard X-ray diffraction (XRD) techniques, reflected light microscopy of polished sections, scanning electron microscopy (SEM), in either the secondary-electron or back-scattered mode, of either fractured or polished surfaces, and microprobe analyses of polished surfaces. The latter were obtained using a Cameca Camebax-Micro system operated at 15 kV with a beam current of 10^{-9} A allowing elemental concentrations to be determined from approximately a 1 μm diameter elemental volume. Short line traces were obtained sequentially for the elements: Na, Al, Si, P, and Zr. Initially, the general composition was checked using a Si(Li) energy dispersive spectrometer capable of detecting elements present in excess of 0.5 wt%. The raw data were corrected using the National Bureau of Standards program CORREX, for which data the errors are ±0.2%.

The reactivity with water was determined by suspending the samples in a fixed amount of constantly stirred distilled water maintained at a constant temperature (±0.1°C) and measuring the pH of the extract with time.

Ionic conductivity was measured by an ac complex impedence technique. The sample dimensions were so chosen that the sample impedence was much larger than that of the sample holder from room temperature to 300°C. The faces of the sample discs were dry polished using 400-mesh SiC paper prior to the application of either Pt paste or dc sputtered Pt electrodes. The measurement system consisted mainly of a Solartron 1174 frequency response analyser and a Solartron electrochemical interface controlled by a Hewlett-Packard 9845B computer. Impedence measurements were carried out between room temperature and 300°C at approximately 25°C intervals in the frequency range from 10 Hz to 300 kHz. During measurement, the sample cell was flushed with dry argon to avoid problems due to possible moisture adsorption. Details of the experimental set-up and cell design are given elsewhere (16).

RESULTS AND DISCUSSION

Sintering Behaviour

The effect of temperature on the densification, and the kinetics of sintering, of Nasicons have been described elsewhere (17). The full densification of most of the compositions takes place within a narrow temperature range of 25 to 50°C and also within a short sintering time of about 15 min as illustrated in Fig. 1 & 2. The narrow densification temperature range and the fast sintering kinetics suggest a liquid phase sintering mechanism for Nasicons, although this finding is not in agreement with that of McEntire et al. (18).

There is also a difference between the Hong and the von Alpen materials in their sintering behaviour. The ideal sintering temperature decreases with an increase in the x value in the case of the Hong materials, but increases for the von Alpen samples. The reason for this behaviour may be due to differences in the liquidus curves of the two solid-solution series, data on which are not available.

X-ray Analysis

All the Hong samples showed the presence of small amounts of monoclinic zirconia in addition to Nasicon when they were sintered above 1200°C, as observed by others (7-11). However, the x = 2.1 and 2.2 gel-processed samples could be sintered at 1125°C and these samples did not show free zirconia.

The von Alpen samples showed only the Nasicon phase irrespective of processing technique or sintering temperature. Typical X-ray diffraction patterns of the two types of materials are given in Fig. 3.

Microstructural Features

Optical Microscopy

Because of the fine-grained microstructure of these materials, only limited information could be obtained by optical microscopy. It showed that most samples had relatively low porosity and that some Hong samples contained a low concentration (up to ~5 vol%) of free zirconia. However, these features could be more easily observed using the SEM.

Scanning Electron Microscopy

In Fig. 4 are presented two SEM micrographs of Hong and von Alpen Nasicons prepared by the G process and sintered above 1200°C. The Hong material contains a fine dispersion of free zirconia, but the von Alpen product does not contain any free zirconia as originally reported (10). However, the Hong Nasicon shows the presence of a third phase and the von Alpen sample a second phase although XRD indicated only two phases and one phase respectively. All the Nasicon materials irrespective of their method of preparation (G or BM) showed this behaviour. Some of the von Alpen materials with high x value (2.1 and 2.2) had a considerable amount of the second phase, yet this was not detected in the XRD pattern. Also, this second phase was found by EDAX spot analysis to contain less zirconia than the Nasicon phase, Fig. 5. Because of these considerations, this additional phase is assumed to be principally a glass.

Contamination by alumina considerably increases the amount of the glass phase that can be as observed microstructurally. This effect is dramatically illustrated in Fig. 6 which shows the development of a considerable amount of sodium aluminum silicophosphate glass at the interface between Nasicon and alumina powder when sintered in contact. The Nasicon has lost a substantial part of its non-zirconia constituents to the glassy interface and has precipitated copious amounts of free zirconia in the process.

The effect of sintering time on the microstructure of Hong Nasicon at x = 1.5 is shown in the SEM micrographs in Fig. 7. Because of the vaporization loss of Na and P from the surface (left side of Fig. 7), large amounts of residual zirconia are precipitated at the surface. The size and amount of the zirconia crystals exsolved increase with an increase in the sintering time. The amount of the dark grey glassy phase also increases with an increase in the sintering time. It is also observed that, as a result of the precipitation and growth of the zirconia crystals and their consequent expansion on cooling, the body of the Nasicon disc cracks profusely after the 16 h sintering, Fig. 8. No such zirconia precipitation and cracking occur in the von Alpen samples, Fig. 9. The amount of glass phase is small at low x values, but it generally increases with an increase in the x value in both Hong and von Alpen products.

Quantitative Microanalysis

A number of compositions in both series of materials have been examined. Table I presents the analyses of the G processed Hong materials prepared from powder dispersed using alumina grinding media. The alumina contamination is seen to be preferentially concentrated in the glass phase. However, a similar phase (free from alumina) was also present, to a lesser extent, in the zirconia-milled compositions, indicating that its formation is an intrinsic characteristic of the materials.

A comparison of the theoretical and measured concentrations of the elements in the Nasicon phase in the G-processed Hong samples, Table I, indicates that the quantity of phosphorus is significantly reduced except at $x = 2.0$. The reduction in phosphorus content may result from the volatilization of a major portion occurring probably simultaneously with the precipitation of the zirconia from the crystal lattice. The final Nasicon phase produced can then be deficient in both zirconia and phosphorus and the remaining material will appear to contain a higher concentration of soda and silica than the original, as is actually found in most cases. It is not clear why there was little phosphorus loss from the $x = 2.0$ composition.

Because of the generally fine-grained microstructure of all materials examined, it was frequently impossible to obtain reliable microanalyses of the glass itself without any influence from the surrounding Nasicon. However, on occasions relatively large regions of this phase were observed in the SEM, Fig. 10, and semi-quantitative analysis indicated the material was a sodium silicophosphate with a low concentration of zirconia. Subsequent microprobe analysis of this phase in a von Alpen sample, with $x = 1.8$ and which had been maintained at 1275°C and quenched, showed the composition of the phase in that case to be approximately $Na_3Zr_{0.7}Si_2PO_{9.4}$.

Reaction with Water

Although it has been reported that Nasicons are stable to water (19) it was observed earlier that certain Nasicon samples ($x > 2.2$) crumble into a powder when exposed to high humidity (20,21). Hence the stability to water of both Hong and von Alpen series of materials, processed by both G and BM methods, was determined between 23 and 35°C.

It was observed that the pH of the water increased on contact with Nasicons and the rate of change of pH with time served as a simple indicator of the sensitivity of Nasicons to water. The results of this study show that all Nasicons react with water to varying degrees; at high values of x the rate of reaction is also high (see Fig. 11). Also the BM materials were found to react up to 500 times faster than their G processed counterparts (14).

The reaction rates (rate of change of $[OH^-]$) are generally linear but deviations from linearity occur, especially when $x > 2.1$. It is assumed that the linear reaction between Nasicons and water is the hydrolysis, and the nonconformity to linear kinetics at high x values is caused by side reactions such as the interaction between the alkali produced by the hydrolysis and the Nasicon, which can take place at high pH values (22).

For comparison, a sample of the alumina-free glass found in von Alpen $x = 1.8$ was synthesised using the G process and fabricated into discs by pressing and sintering at 975°C. This material was found to react with water 100,000 times faster than some of the Nasicons (14).

It was also observed that the samples containing alumina as an impurity reacted about 6000 times faster than that which were free from this impurity, Fig. 12. As was shown earlier, there was an increase in the glass content of the specimen when alumina impurity was present and most of the alumina in the system was present in the glass. This indicates that there may be a connection between the amount of glass present in the Nasicon and its increased reactivity with water.

Electrical Characterization

Typical impedance and admittance diagrams are shown in Fig. 13. The use of either platinum paste (Engelhard) or sputtered platinum electrodes did not significantly affect the observed impedance plots. An equivalent circuit (23,24) which approximates the low temperature impedance behaviour of these polycrystalline samples is shown as an inset in Fig. 13(a) where R_b represents the bulk resistance of the crystallites, R_{gb} and C_{gb} represent the resistance and capacitance effects at the grain boundaries and C_{dl} represents the double layer capacitance at the electrode-electrolyte interface. The geometric capacitance in the frequency range 10 Hz to 300 kHz would be negligible and is not shown in the proposed equivalent circuit. Impedance and admittance plots similar to those in Fig. 13 were obtained for the other compositions also.

The bulk ionic conductivity was derived from the high frequency intercept with the real axis of the impedance diagram. In order to check that the high frequency resistive component relates to the bulk transport of ions rather than interfacial effects, the ac signal amplitude was varied over a factor of 10 and found to have no effect on the observed resistance values.

The high frequency semicircle represents the parallel combination of the intergranular resistance R_{gb} and capacitance C_{gb} whereas at low frequency the electrode contribution C_{dl} to the ac response is characterized by a quickly rising $|Z"|$ with decreasing frequency. This straight line portion of the impedance plot presumably deviates from the vertical due to the surface roughness effects as indicated by Armstrong et al. (25). The semicircle describing the grain boundary impedance becomes smaller with increasing temperature and has a negligible contribution to the total impedance above 100°C in most cases.

From a plot of log (σT) against 1/T, Fig. 14 (where σ is calculated from the high frequency intercept in the impedance diagram) the activation energy for sodium ion conduction has been estimated. No hysteresis was detected in the temperature dependence of conductivity during heating and cooling cycles. The slight bend in the activation energy plots below 200°C has been shown by others to be due to the monoclinic-rhombohedral transformation (26). The data are summarized in Table II.

Analysis of the conductivity data and activation energy plots reveals that these materials are sensitive to composition and processing parameters. The highest bulk ionic conductivity at 300°C was obtained for a Hong composition (H1, $x = 1.5$) sintered at 1300°C for 1 h. An increase in the sintering time (16 h) leads to a considerable decrease in the conductivity of this material. This could be due to the increased concentration of precipitated zirconia in the microstructure and the associated development of an extensive microcrack network, Fig. 8.

This behaviour is in contrast to that of the von Alpen series of materials for which extended sintering results in an increase in conductivity. In these cases, no zirconia is precipitated and no microcracks are formed, Fig. 9. The only change is a slight increase in the crystal size of the Nasicon. This contradictory behaviour between the two series of materials was observed for both BM- and G-processed materials and was most pronounced for samples sintered under conditions that promoted the loss of phosphorus (samples sintered in open containers).

This difference in behaviour between the Hong and von Alpen materials can be qualitatively understood to result from the compositional changes that occur during the firing cycle. Microprobe data have established that considerable amounts of phosphorus are lost from the samples during sintering, and XRD, SEM and microprobe data suggest that a sodium silicophosphate-based glass is also formed in the microstructure of both series of materials. This results in the crystalline Nasicon phase itself in both the Hong and von Alpen series of materials becoming deficient in Na, Si and P during firing and that deficiency is enhanced with extended sintering times, i.e., the effect is qualitatively equivalent to adding zirconia to the Nasicon.

In the case of the Hong materials this results in the precipitation of free zirconia as the solubility limit is exceeded. Because the loss of volatile components occurs most readily from the surface of the sample, a higher amount of zirconia precipitation occurs at the surface. This surface layer may contribute to a reduction in the total conductivity of the Hong material with sintering time; alternatively the decrease of bulk conductivity in this case may be attributable to the formation of the extensive microcrack network.

No such precipitation occurs in the von Alpen materials as they have a lower zirconia content (presumably the solubility limit is not exceeded) and hence no microcracks develop. However, the crystal size increases and the composition of the Nasicon is progressively changed towards that of the higher conducting Hong material. Therefore, the conductivity increases with increasing sintering time, i.e., the composition and conductivity of extensively sintered von Alpen compositions tend towards those of Hong.

Comparison of the conductivity of BM- and G-processed materials showed that the latter have a slightly higher conductivity. This difference could be attributed to the greater degree of compositional inhomogeneity that is to be expected in the BM materials.

Conductivity data for the synthesized glass composition (determined in an $x = 1.8$ von Alpen material) are also shown in Table II. It can be seen that the conductivity is essentially independent of sintering time but, because of a lowered liquidus point, the sintering temperature employed in this case was lower than that used for the host Hong or von Alpen material. At high temperature (300°C) the conductivity of this phase approaches that of Nasicons. Unfortunately, the very high reactivity of this material appears to render it unattractive for most solid electrolyte applications.

SUMMARY

A loss of phosphorus from Nasicons during sintering at about 1225°C has been shown. In the case of Hong material, this loss promotes the precipitation of free zirconia in the matrix whereas the von Alpen materials remain zirconia-free even on extended sintering up to 16 h. As the sintering period in air is increased, the Hong materials form an increasing concentration of free zirconia, part of which is formed preferentially on the surface of the material. The increased internal zirconia concentration is also associated with the development of internal microcracks in the material, which results in a gradual reduction in measured conductivity. This behaviour is in contrast to that of the von Alpen series of materials which do not form free zirconia and do not develop internal microcracks and show an increase in the bulk conductivity with increased sintering time.

Examination of the effect of temperature on sintered density suggests both series of materials sinter by a liquid phase mechanism.

Extended sintering time in air also promotes the formation of a third phase in Hong and a second phase in the von Alpen materials. Microanalysis suggests that these phases consist of a sodium silicophosphate containing a low concentration of zirconia. This additional phase is found in all sintered Nasicons irrespective of composition or method of synthesis but the amount varies depending on composition; at low x values, the amount is low. The material exists principally as a glass. The occurrence of this phase, together with the loss of phosphorus that occurs on sintering, results in the composition of the Nasicon in the von Alpen materials effectively becoming richer in zirconia and tending towards that of the equivalent highly conductive Hong composition. Consequently, the conductivity of the von Alpen compositions improves with sintering time.

All materials react with water to some degree - the rate of reaction increasing with x in both series of materials. However, the degradation rate of sintered material is significantly increased when $x > 2.0$. The rate of reaction is increased approximately 500 times when the material is synthesized by the BM process and alumina contamination of a Hong composition results in a five decade increase in reactivity. The glass phase degrades most rapidly of all.

ACKNOWLEDGEMENTS

The authors are indebted to R.H. Packwood and V.E. Moore of the Physical Metallurgy Research Laboratory for the microprobe analysis, to D.R. Owens, Mineralogy Section, for SEM analysis, to A.J. Hanson and G.A. MacDonald, Ceramic Section, and T. Sanders and J. DiRocco, University of Waterloo, for their technical assistance.

REFERENCES

1. H.Y-P. Hong "Crystal structures and crystal chemistry in the system $Na_{1+x}Zr_2Si_xP_{3-x}O_{12}$"; Mat Res Bull 11:173-182; 1976.

2. C. Delmas, R. Olazcuaga, G. Le Flem, P. Hagenmuller, F. Cherkaoui and R. Brochu "Crystal chemistry of the $Na_{1+x}Zr_{2-x}L_x(PO_4)_3$ (L = Cr, In, Yb) solid solutions"; Mat Res Bull 16:285-290; 1981.

3. C. Delmas, J.C. Viala, R. Olazcuaga, G. Le Flem, P. Hagenmuller, F. Cherkaoui and R. Brochu "Ionic conductivity in Nasicon type phases $Na_{1+x}Zr_{2-x}L_x(PO_4)_3$ (L = Cr, In, Yb)"; Solid State Ionics 3/4:209-214; 1981.

4. R.J. Cava, E.M. Vogel and D.W. Johnson Jr. "Effect of homovalent framework cation substitutions on the sodium ion conductivity in $Na_3Zr_2Si_2PO_{12}$"; J Amer Cer Soc 65: C157-159; 1982.

5. B.E. Taylor, A.D. English and T. Berzins "New solid ionic conductors"; Mat Res Bull 12: 171-182; 1977.

6. M. Nagai, S. Fijitsu, T. Kanazava and H. Yanagida "The dependence of structure and conductivity in three dimensional phosphate ionic conductors"; J Mat Sci 16: 1633-1642; 1981.

7. M.L. Bayard and G.G. Barna "A complex impedance analysis of the ionic conductivity in $Na_{1+x}Zr_2Si_xP_{3-x}O_{12}$ ceramics"; J Electroanal Chem 91: 201-209; 1978.

8. J.P. boilot, J.P. Salanie, G. Desplanches and D. Le Potier "Phase transformation in $Na_{1+x}Zr_2Si_xP_{3-x}O_{12}$ compounds"; Mat Res Bull 14: 1469-1477; 1979.

9. R.S. Gordon, G.R. Miller, B.J. McEntire, E.D. Beck and J.R. Rasmussen "Fabrication and characterization of Nasicon electrolytes"; Solid State Ionics 3/4: 243-248; 1981.

10. U. von Alpen, M.F. Bell and H.H. Hoffer "Compositional dependence of the electrochemical and structural parameters in the Nasicon system $Na_{1+x}Zr_2Si_xP_{3-x}O_{12}$"; Solid State Ionics 3/4: 215-218; 1981.

11. T.A. Wheat and J.M. Starchuk "Examination of compositional variations in Na-zirpsio ceramics"; J Can Cer Soc 50: 7-16; 1981.

12. H. Schmid, L.C. De Jonghe and C. Cameron "Chemical stability of Nasicon"; Solid State Ionics 6: 57-63; 1982.

13. G.J. Tennenhouse and G.M. Crosbie "The reaction of sodium with ionic conductors containing P-O bonds at elevated temperatures"; paper presented at the annual meeting of the American Ceramic Society; Cincinatti, 1982.

14. A.K. Kuriakose, T.A. Wheat, A. Ahmad and J. DiRocco "The stability of Na-zirpsios in water"; submitted for publication in J Can Cer Soc (1983).

15. D.H.H. Quon, T.A. Wheat and W. Nesbitt "Synthesis, characterization and fabrication of $Na_{1+x}Zr_2Si_xP_{3-x}O_{12}$"; Mat Res Bull 15: 1533-1539; 1980.

16. A. Ahmad, T.A. Wheat, A.K. Kuriakose and B. Kindl "Sodium beta"-aluminas by aqueous spray drying"; submitted for publication in J Can Cer Soc (1983).

17. A.K. Kuriakose, T.A. Wheat, and A. Ahmad "Synthesis, sintering and microstructure of Nasicons"; paper presented at the annual meeting of the American Ceramic Society; 1983 and submitted for publication in Amer Cer Soc Bull (1983).

18. B.J. McEntire, G.R. Miller and R.S. Gordon "Sintering of polycrystalline ionic conductors: β"-alumina and Nasicon", in Mat Sci Res 13: Sintering Processes, ed. G. Kuczynski, Plenum, 517-524; 1980.

19. J.J. Auburn and D.W. Johnson Jr. "Conductivity of Nasicon ceramic membranes in aqueous solutions"; Solid State Ionics 5: 315-316; 1981.

20. D.E. Amm, S.L. Segel and M. Sayer "Nuclear magnetic resonance of sodium conducting ceramics"; paper presented to the annual convention of the Canadian Ceramic Society; Calgary, 1982.

21. T.A. Wheat, A.K. Kuriakose and R.H. Packwood "The sodium zirpsios: their development and behaviour"; paper presented to the annual convention of the Canadian Ceramic Society; Calgary, 1982.

22. M.F. Bell, Queen's University, Private Communication; 1982.

23. U. von Alpen, M.F. Bell, R. Brautigan and H. Laig-Horstebrock "Sodium ion conductors - Nasicon and β"-alumina" in Fast Ion Transport in Solids; P. Vashishta and J.N. Mundy (eds.) Elsevier, New York, 1979; 443-446.

24. W. Bogusz, W. Jakubowski and F. Krok "On the complex admittance plots of β"-alumina and Nasicon ceramic samples"; Solid State Ionics 7: 287-289; 1982.

25. R.D. Armstrong and R.A. Burnham "The effect of roughness on the impedance of the interface between a solid electrolyte and a blocking electrode"; J Electroanal Chem 72: 257-266; 1976.

26. U. von Alpen, M.F. Bell and W. Wichelhaus "Phase transition in Nasicon ($Na_3Zr_2Si_2PO_{12}$)"; Mat Res Bull 14: 1317-1322; 1979.

Table 1 - Elemental concentrations as a function of composition in sintered compacts prepared from powder dispersed using Al_2O_3 grinding media.

Composition x	Elemental concentration, wt%*					
	Na	Zr	P	Si	Al	
2.2	15.120	26.244	3.375	9.599	7.147	g
	12.048	38.270	2.357	9.123	0.863	n
	13.76	34.13	4.63	11.56	-	t
2.1	15.255	27.997	3.679	9.690	5.666	g
	14.421	34.112	3.324	9.140	1.729	n
	13.38	34.26	5.23	11.08	-	t
2.0	16.495	30.026	5.614	8.693	6.016	g
	16.692	32.597	5.848	9.684	0.183	n
	13.00	34.39	5.84	10.59	-	t
1.9	11.267	32.649	4.586	7.935	7.868	g
	15.993	35.396	5.593	9.382	0.208	n
	12.61	34.52	6.45	10.10	-	t
1.8	12.779	33.288	3.332	8.721	8.056	g
	13.590	40.482	4.202	8.656	0.445	n
	12.23	34.65	7.06	9.60	-	t

*Balance oxygen.

g - glass phase; n - Nasicon phase and t - theoretical concentrations

Table II - Ionic conductivity and activation energy data for various Nasicon samples

Sample I.D	X	Sintering Condition	Density g/mL	$\sigma_b\ \Omega^{-1}\ cm^{-1}$		Activation Energy (eV)	
				At 25°C x 10^4	At 300°C x 10^2	Below 200°C	Above 200°C
H1 (Gel) *	1.5	1300°C, 1 h	3.20	8.24	17.0	0.35	0.25
H2 (Gel) *	1.5	1300°C, 16 h	3.13	1.08	2.26	0.38	0.11
VA1 (Gel) *	1.5	1150°C, 1 h	3.13	1.45	5.20	0.42	0.2
VA2 (Gel) *	1.5	1150°C, 16 h	3.04	1.70	6.60	0.49	0.18
VA3 (Gel) *	2.0	1175°C, 1 h	3.04	1.56	5.50	0.44	0.21
VA4 (Gel) *	2.0	1175°C, 16 h	3.05	2.10	6.80	0.43	0.22
VA5 (BMSD)**	1.5	1150°C, 1 h	3.06	0.57	2.23	0.44	0.22
VA6 (BMSD)**	1.5	1150°C, 16 h	3.05	0.94	5.45	0.43	0.22
NG1 ***	2.0	975°C, 1 h	2.79	0.09	1.00	0.47	0.32
NG2 ***	2.0	975°C, 16 h	2.84	0.11	1.20	0.52	0.26

H = Hong's Composition; VA = von Alpen's Composition; * (Gel) = Gel processed;
** (BMSD) = Ball milled Spray dried; *** NG = Nasicon glass

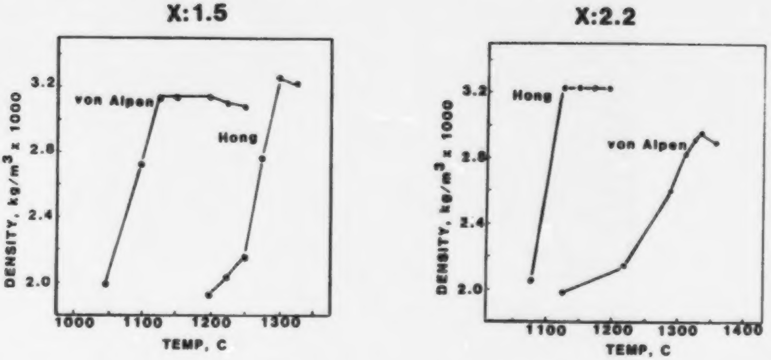

Fig. 1 - Plot of sintered density vs. temperature for Hong and von Alpen Nasicons. Sample thickness: 3 mm; Sintering time: 15 min

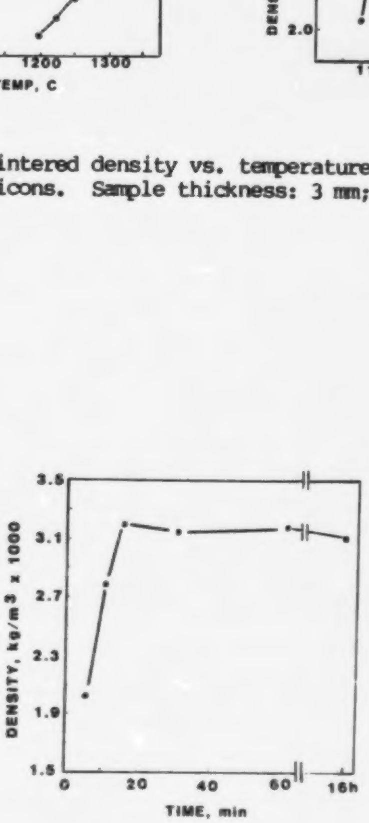

Fig. 2 - Plot of sintered density vs. sintering time for a von Alpen Nasicon of x = 1.8. Sample thickness: 3 mm; Temp: 1175°C.

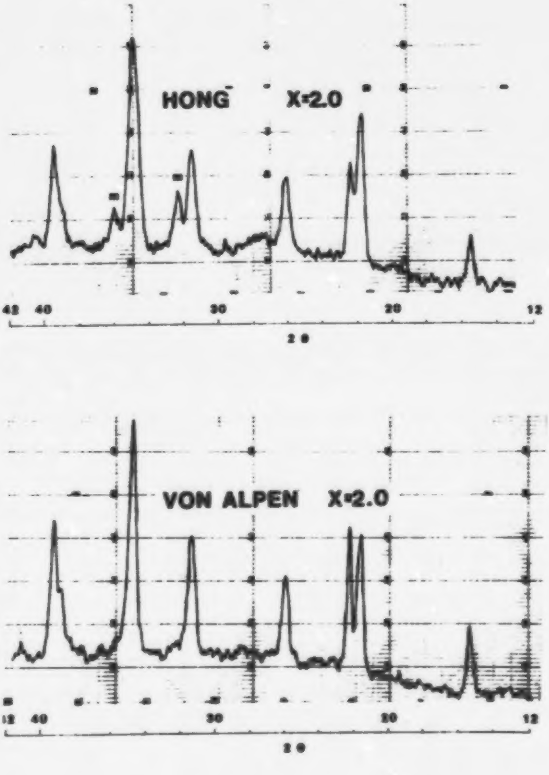

Fig. 3 - Partial XRD patterns of sintered Hong and von Alpen Nasicons at x = 2.0. Sintering temp: Hong, 1225°C; von Alpen, 1175°C; Sintering time: 15 min; Radiation: Co Kα. The mark 'm' indicates monoclinic zirconia.

Fig. 4 - SEM of polished sections of Hong (top) and von Alpen Nasicons. White phase: zirconia; light grey phase: Nasicon; dark grey phase: glass.

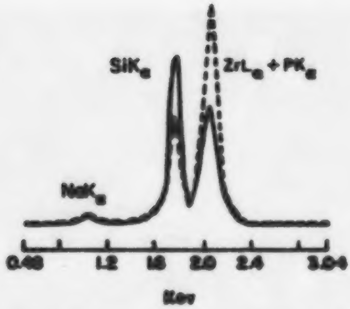

Fig. 5 - Energy dispersive X-ray peaks for Na-K$_\alpha$, Si-K$_\alpha$ and Zr-L$_\alpha$ + P-K$_\alpha$. The broken line and the solid line represent, respectively, the spectra of the light grey and dark grey phases in Fig. 4 (bottom).

Fig. 6 - SEM of a polished section of the interface between Hong Nasicon and alumina when sintered in contact. The dark phase at the top is the site of the alumina; the bottom portion is the Nasicon substrate and the grey interface a sodium aluminosilicophosphate with some dissolved zirconia from which alpha alumina has precipitated.

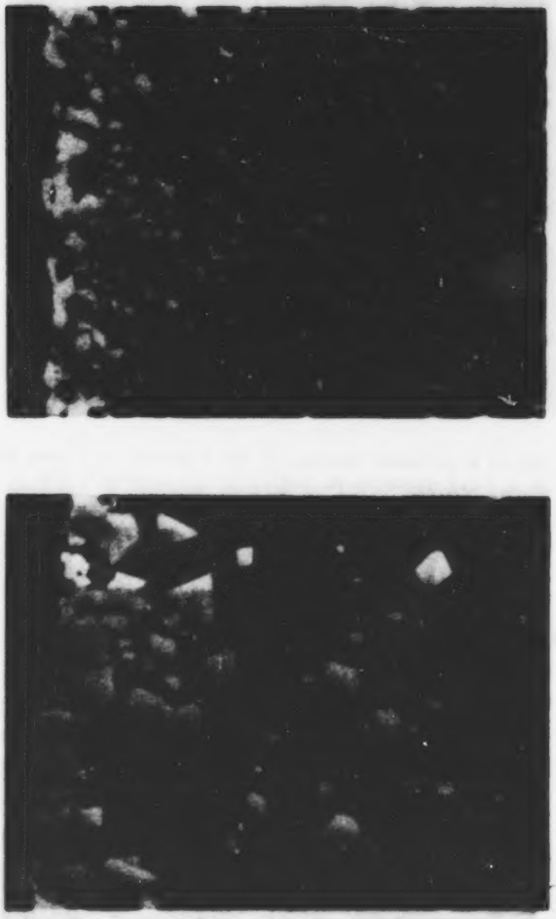

Fig. 7 – SEM of polished sections of a Hong Nasicon of $x = 1.5$ sintered at 1300°C for 1 h (top) and 16 h.

Fig. 8 - SEM of a polished section of the interior of a Hong Nasicon of x = 1.5 sintered at 1300°C for 16 h showing the extensive microcrack network.

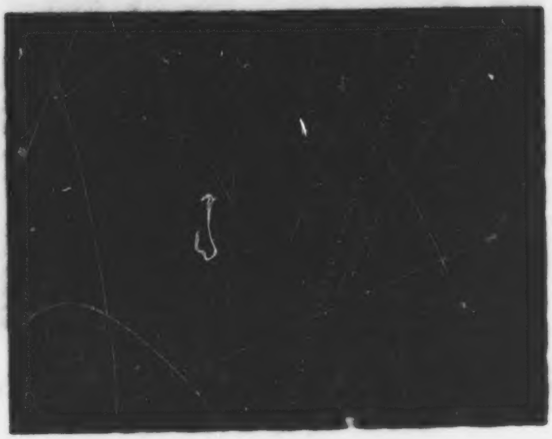

Fig. 9 - SEM of polished section of a von Alpen Nasicon of x = 1.5 sintered for 16 h at 1175°C.

Fig. 10 - SEM of polished section of a Hong Nasicon sample of x = 1.8, showing a relatively large inclusion of the glassy phase.

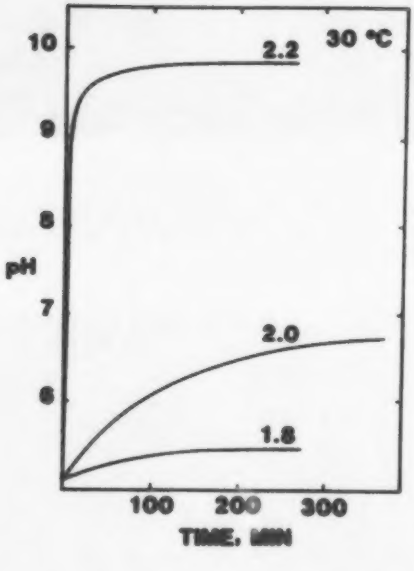

Fig. 11 - Plot of pH vs. time for Hong samples, showing the increased reactivity at a high x value.

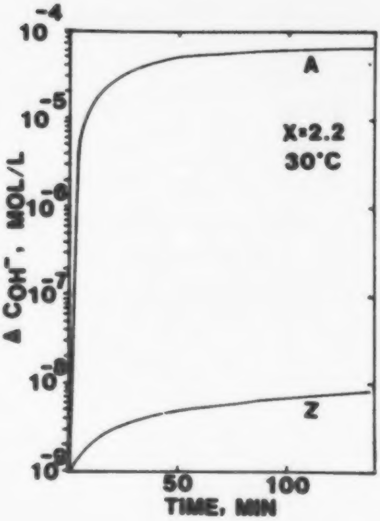

Fig. 12 - Plot of [OH⁻] vs. time for Nasicon samples with and without alumina as impurity: Curve A - alumina milled; Curve Z - zirconia milled.

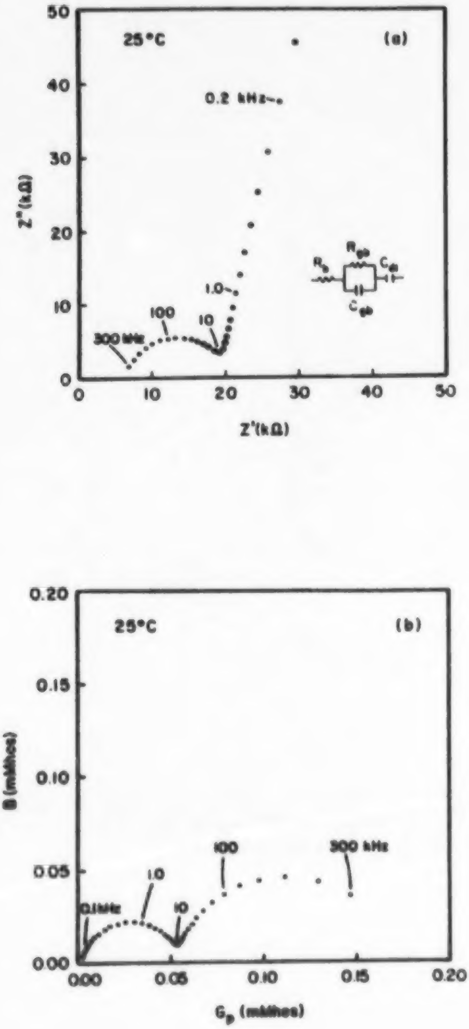

Fig. 13 - Typical complex plots of (a) impedance and (b) admittance for Nasicon: Sample, von Alpen ($x = 1.5$); Electrodes, Platinum.

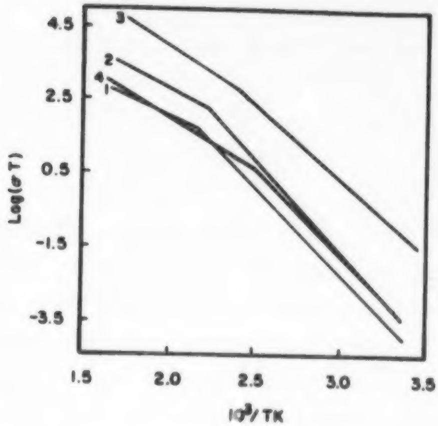

Fig. 14 - Temperature dependence of the bulk ionic conductivity of Nasicons of x = 1.5. Samples 1 and 2, von Alpen, sintered 1 h and 16 h respectively; samples 3 and 4, Hong, sintered 1 h and 16 h respectively.

THE DETERIORATION OF SODIUM β/β''-ALUMINA ELECTROLYTES IN SODIUM ENVIRONMENTS

Patrick S. Nicholson

Department of Metallurgy & Materials Science
McMaster University
Hamilton, Ontario, Canada

ABSTRACT

The mechanisms proposed to explain the deterioration of Na-β/β''-Al_2O_3 electrolytes in Na environments are reviewed. A phenomenological model is presented which describes the process in terms of its physical characteristics. It is suggested that supersaturation of the sodium-ion conduction planes occurs above a critical current density and this leads to local oxygen-ion oxidation, sodium metal precipitation and lattice collapse. The feasibility of the model is demonstrated.

KEYWORDS: deterioration β/β''-Al_2O_3; sodium cells; sodium ion conductors; supersaturation degradation.

RÉSUMÉ

Le rapport étudie les mécanimes présentés pour expliquer la détérioration des électrolytes Na-β/β"-Al_2O_3 dans les milieux riches en Na. Il présente un modèle phénoménologique qui décrit le processus en fonction des caractéristiques physiques. L'auteur suggère qu'une fois dépassé une densité critique de courant, il y a sursaturation des plans de conduction de l'ion sodium entraînant l'oxydation locale des ions-oxygène, la précipitation du sodium métal et l'effrondrement du réseau. Il montre la faisabilité du modèle.

INTRODUCTION

Electrolyte degradation is an important problem in the use of $\beta\text{-}Al_2O_3$ in Na-S batteries and much effort has been expended to understand and combat the processes involved.

The following facts about degradation of β-alumina electrolytes in Na environments are generally agreed upon.

(a) it always initiates at the liquid-sodium/electrolyte interface.

(b) it progresses into the ceramic at a constant rate for a given current density.

(c) the degradation rate increases with temperature.

(d) a critical current density exists below which the electrolyte does not degrade.

(e) it accompanies the charging cycle of the Na-S battery and not the discharging cycle.

(f) discolouring (blackening) is always observed to accompany deterioration.

(g) the deterioration rate is increased in the presence of K^+, Ca^{2+} and H_3O^+ impurities.

(h) the grain size of the polycrystal has little or no influence on the degradation kinetics. This is of interest as it suggests that the natural flaw size (usually taken as the grain size, an assumption reasonable in the β-alumina case in view of the easy cleavage of the β and β" crystals) plays no role in the degradation process.

(i) the degradation kinetics are independent of the fracture strength of the pristine ceramic. This observation is probably linked to (h).

(j) surface polish reduces degradation.

REVIEW OF THEORIES OF DEGRADATION

The simple concept that the rate of discharge of Na^+ into current-focusing-flaws in the Na/electrolyte interface is faster than the liquid can exit from these flaws to the bulk sodium, led to the development of the Poiseuille pressure model for electrolyte degradation.

For a round pipe of radius r in which a liquid is flowing with a velocity v, the viscous resistance at a point on the radius, y, is the product of the surface area and the viscosity (η) times the velocity gradient, i.e.,

$$2 \pi y \eta \frac{dv}{dy}$$

This results in a pressure drop $\pi y^2 \frac{dP}{dx}$,

$$\text{so} \qquad - 2 \pi y \frac{dv}{dy} = \pi y^2 \frac{dP}{dx}$$

$$\text{or} \qquad v = \frac{-y^2}{4\eta} \frac{dP}{dx} + C_1$$

At the cylinder wall, $y = r$ and $v = 0$,

$$\text{so} \qquad C_1 = \frac{r^2}{4\eta} \frac{dP}{dx}$$

$$\text{or} \qquad V_y = \left(\frac{r^2-y^2}{4\eta}\right) \frac{dP}{dx}$$

If within this pipe at radius y, a cylinder of wall thickness dy is considered, then the quantity of liquid flowing through this wall is:

$$dQ = \text{area x velocity}$$

$$= [\pi(y + dy^2) - \pi y^2] \left(\frac{r^2-y^2}{4\eta}\right) \frac{dP}{dx}$$

Integrating between y = r and y = 0 gives:

$$Q = \frac{\pi r^4}{8\eta} \frac{dP}{dx}$$

If the liquid flowing has a molar volume, Vm, then:

$$Q = Vm \frac{dN}{dt}$$

where $\frac{dN}{dt}$ is the rate of passage of one molecular weight

$$\text{so} \qquad Vm \frac{dN}{dt} = \frac{\pi r^4}{8\eta} \frac{dP}{dx}$$

For a crack of length a and diameter 2b which is focusing Na^+ at its tip, then;

$$\frac{dN}{dt} = \frac{i}{F} \text{ / unit area}$$

where i is the current density. The area of such a crack at x is $2\pi b\ (a-x) + 1/2(4\pi b^2)$ where x is the distance from surface into the crack. As b << a, then the crack area = $2\pi b(a-x)$. The quantity of Na/sec = $\frac{dN}{dt}$ = $2\pi b(a-x)\ \frac{i}{F}$ moles/sec,

$$\text{so} \quad \frac{dP}{dx} = \frac{8\eta\ Vm}{\pi b^4}\ 2\pi b(a-x)\ \frac{i}{F} = \frac{16\ Vm\ \eta(a-x)\ i}{Fb^3}$$

To obtain the pressure developed, this term must be integrated from x = 0 to x = a. This results in

$$P = \frac{8\ Vm\ \eta\ i\ a^2}{Fb^3}\ .$$

Calculating P for Na at 300°C, using the following parameters;

$$Vm = 23.7\ cm^3/mole$$

$$\eta = 0.32 \times 10^{-2}\ poise$$

$$i = 0.5\ A/cm^2$$

for a 5μm crack of width 10 Å, gives;

$$P = 84\ MPa\ .$$

If this is assumed to concentrate at the crack tip, then K_1 = 0.33 MPa √m. This value is significantly below K_{Ic} (= 3-4 MPa √m).

Other problems which arise from assuming that P is the source of crack growth and thus degradation of the electrolyte are:

(a) P should decrease with T via the viscosity term. Degradation increases with increasing temperature.

(b) for a given current density, P should increase as crack length-squared, increasing K_1 and so accelerating the damage. It is known that, at constant current density, the deterioration progresses through the ceramic at a constant rate.

(c) applied compressive stress to the degrading material should decrease the deterioration rate, in fact, it increases it.

Shetty, Gordon and Virkar (1) used fracture mechanics to examine the damage potential of developing internal pressure in a circular crack of length 2ℓ in an infinite plate.

They demonstrated that;

$$i_{crit} = \frac{4b^3(1-\nu^2)\gamma_{eff}^2 F}{12\eta E\pi^2 V_m \ell}$$

where ℓ is the semi-minor axis of the elliptical section of the crack, ν the Poisson Ratio for the material, γ_{eff} the effective fracture surface energy, F the Faraday and E the Young's Modulus of the material. Using $\gamma_{eff} = 20\ J/m^2$, $\ell = 25\mu m$ and known values of E and ν of $\beta''-Al_2O_3$ and η and Vm of liquid Na, gives an $i_{crit} = 1500\ A/cm^2$!

In fact, all attempts to backcalculate to the critical current density ($2-3\ A/cm^2$) via the Poiseuille pressure model result in grossly exaggerated i_{crit} values.

In 1980, Virkar et al. (2) suggested that such high current densities could occur around the periphery of areas of electrolyte not wetted by the sodium metal.

They used analogous electrical parameters for stress and deflection, i.e., current and voltage respectively. One problem with this model is that whereas stress cannot be transmitted across the surfaces of a crack, if the crack is full of discharged sodium liquid, the current can be transmitted across it. However, a non-wetted surface region will be non-conducting and the current will focus along its periphery. To simulate conditions of non-wetting, Virkar et al. painted one edge of electrolyte samples with silver paint leaving a paint-free central strip. Na was titrated to this surface and the fracture strength of the samples subsequently determined. It was demonstrated that non-wetting could result in very high local current densities.

Certainly this model points up problems with wetting of the electrolyte by the liquid sodium. The drawbacks of the Poiseuille pressure source of deterioration were still extant and in 1981 Virkar (3) modified the model further. As the crack tip is the point of closest approach of the catholyte to the anode, it has been assumed in most models that the current concentrates at crack tips. Virkar relaxed this restriction and allowed the crack to be fed Na from its sides as well.

The P(ℓ) equation he obtained is:

$$P(\ell) = \left(\frac{7.353\text{x}10^{7}}{\ell^{1/4}}\right) i^{1/4} \quad \text{dynes/cm}^{2}$$

$$\text{i.e.} \quad P(\ell) \propto 1/\ell^{1/4}$$

for a constant current density. Consequently the increasing pressure expected as the crack lengthens is outweighed by relief of this pressure. This observation increases the problems with the Poiseuille pressure model of degradation and these are further compounded if one calculates the critical current density via the Griffith criterion, i.e.,

$$P_{cr} = \sqrt{\frac{E\,\gamma_{eff}}{0.366(1-\nu\ )\ell}} = \frac{2.455\text{x}10^{8}}{\ell^{1/2}} \quad \text{dynes/cm}$$

Hence extension initiates when

$$\frac{2.455\text{x}10^{8}}{\ell^{1/2}} = \left(\frac{7.353\text{x}10^{7}}{\ell^{1/4}}\right) i^{1/4}$$

$$\text{i.e.} \quad i_{crit} = \frac{124.39}{\ell}$$

which overestimates values of critical current density (for 100 μm crack i_{crit} = 12,400 A/cm^2!). Clearly the two major problems with the Poiseuille pressure models are the small values of pressure produced for practical values of current density and the temperature dependence of the degradation process being the opposite of that observed.

Surface flaws do play a significant role in the degradation process. Armstrong et al. (4) cycled Na/Na, β-Al_2O_3 cells using electrolyte pellets with varying grades of surface polish. They noted that the electrolyte with the highest polish (1μ diamond) gave the best lifetime. It is most likely then that surface flaws do focus the passing current. If 500 mA/cm^2 is the current density and the average grain size of the ceramic is 20μm with an aspect ratio of 10:1 and we assume that one-third of the neighbouring grains feed this flaw (this number is microstructurally controlled by the two dimensional nature of the conduction process and is discussed in more detail later), the surface area of unit depth of flaw is $40\mu m^2$ and if it focuses the current passage within a one-grain-volume of electrolyte around it, then it gathers the current from $(800\mu m^3 + 2\pi(400)\mu m^3) \times \frac{1}{3}$ or $1100\mu m^3$. At 500 mA/cm^2, the current focusing on such a flaw is ~ 10^{-5} amps. Now this current will discharge $10^{-5}/96{,}500 \times 23.7 \times 10^{-12}$ μm^3/sec of Na (or $2370\mu m^3$/sec.). The flaw volume will be < 20 μm^3 so its ability to accommodate this large volume of sodium is questionable. Whereas the Poiseuille pressure models increase the flaw volume by assuming the discharge to occur into the original flaw, an alternative model suggested by the results of de Jonghe envisages the discharge to occur ahead and around the original flaw subsequently linking up with it.

The apparent independence of degradation on the ceramic grain size can be explained by the supersaturation model to be presented. The Poiseuille pressure model would predict increasing damage with grain size as the natural flaws would be larger and the stresses at their tips therefore proportionally increased.

A model developed by Tennenhouse et al. (5) attempted to explain the degradation by capillarity, stress and current-activated dissolution of the ceramic at the crack tip. Al was undetected in the liquid sodium following degradation however, negating such a mechanism.

In 1979 Virkar et al. (6) examined the ceramic blackening phenomenon. Of interest in this work was the utilization of temperatures below the melting point of sodium. It was found that deterioration (via blackening) was much more rapid in this case. The solid sodium in the flaws renders it impossible for the Na^+ travelling under the influence of the impressed current to discharge and their reduction and precipitation within the ceramic microstructure is inevitable.

The same year de Jonghe et al. (7) passed a given current density through a dogbone-shaped electrolyte sample. The cathode turned black and sodium metal was detected inside the grains and along the grain boundaries. Blackening was not observed in the narrow section of the sample even at 10 A/cm^2. Clearly more concentrated current focussing must occur. On the basis of the cathode-localised blackening, de Jonghe et al. concluded that electron injection was needed to produce discoloration. This is not so however; many workers have reported blackening of β-Al_2O_3 in liquid Na with no current passage. The rate of blackening was observed to be constant for any given current density and surface cracking was observed. As previously observed, non-wetting problems and associated high current densities and local heating could induce such cracking and this could constitute the initial phase of the degradation.

The idea of two modes of degradation was suggested by de Jonghe et al. in 1981 (8). Having examined a number of tubes from General Electric cells, the cracking mode was identified as being separate from the blackening phenomenon. The Ford workers had noted that the blackening occurs with no current passage when the electrolyte is exposed to liquid sodium. Following 10 days immersion at 300^{o}C in liquid Na, a darkened layer of 0.5 mm thickness was developed. Transmission electron microscopy of this layer failed to identify the defects causing the darkening and it was concluded that the source must be point defects rather than second-phase precipitates. Rassmussen et al. (9) recently reported that, on careful polishing, the blackening is in fact a deep violet colour indicating the existence of colour centres. De Jonghe et al. suggested the coloration is associated with loss of oxygen. They also noted some electronic conductivity developed. Extended times of service were observed to result in sodium colloids and microcracks in the discolored layer and in some cases, Mode I cracks were observed therein. Microcracks and pitting were also observed by Powers et al. (10) in regions of heavy blackening. Two points of interest here are:

(a) β/β''-Al_2O_3 electrolytes are known to age with service time, i.e., their resistivity increases (10); and

(b) Bovin (12) demonstrated by high resolution electron microscopy that conduction planes in β''-Al_2O_3 can be made to vanish by electron beam heating. Na metal "sweats" out of the foils.

Further to the experiment on colour centres in degraded β-Al_2O_3, Gourier and Wicker (13) examined blackened electrolytes by ESR. This technique allows detection of unpaired electrons in the structure. It is also sensitive to the mobility of electrons. The degraded ceramics gave a wide intense signal superimposed on the 6-line spectrum of Mn^{II}. The appearance of Mn^{II} aside, the observed signal belongs to a paramagnetic centre (c-centre). The g factor (1.94) and line shape suggest an unpaired electron bonded at a lattice site in the aluminate structure. A second similar centre was also detected (a D-centre). This centre had the following characteristics:

(a) g-factor close to that for a free spin

(b) a line shape indicating the rapid motion of an unpaired electron

(c) temperature independent paramagnetism between 140 and 300°K.

These observations led them to assign this centre to colloidal Na of 1 µm size. De Jonghe detected such colloids in sections with advanced blackening. The D-centre concentration was observed to increase with time of contact with liquid sodium.

With a view to combatting deterioration, Kuribayashi and Nicholson (14) examined the progress of deterioration of samples electrolysed under both compressive and tensile applied stress. Four-point-bend notched bars were mounted in a furnace at 300°C and Na^+ was titrated to the notch tip from molten $NaNO_2/NaNO_3$ eutectic liquid in contact with the unnotched side of the bar. Electrical contact was made with the notch via silver paint. The bars were loaded in three ways, with the notch tip under tension, under bending compression and under uniaxial compression. The current density and the test temperature were varied. Following a given titration time, damage to the bars was assessed by measuring their apparent fracture toughness in an Instron machine at room temperature.

Two β"-aluminas were examined, one with a higher strength and finer grain size than the other. The ability to resist degradation appears independent of either, when no external stress is applied. This observation suggests that artificial surface flaws introduced by mechanical damage or possibly localised heating, are responsible rather than the natural grain-sized flaws which exist in brittle materials.

As expected, all samples electrolysed under tensile applied stress suffered enhanced degradation but the stronger finer-grained material survived to higher current densities. This differentiation between the stronger and the weaker materials suggests an enhancement mechanism based on the grain size of the material.

Unexpectedly, applied compressive stresses (in bend or uniaxially) enhanced the degradation of all samples. Such stresses should oppose the Poiseuille pressure and retard degradation by that mechanism. The observed enhancement indicates another deterioration mechanism is operational. Further to these experiments, both materials were loaded at current densities and tensile stresses known incapable of producing failure in 24 hours at 280°C and the time-to-failure at constant current density and tensile stress was determined as a function of temperature (T). With increasing T, the liquid Na viscosity will diminish and, for a fixed inflow of Na^+ (determined by the current density), the Poiseuille pressure should decrease. The lifetime (t_f) of the samples should therefore increase. In fact, the reverse was observed indicating increased deterioration with temperature. A plot of ln $1/t_f$ vs. 1/T gave a process activation energy of 6.6 ± 0.5 k cals/mole, a value close to that for Na^+ diffusion (5.5 k cals/mole). This suggests that the diffusion of Na^+ is rate-controlling the degradation process and that other reactions involved in the degradation (ripening of Na precipitates, microcracking etc.) involve less energy. The accelerated degradation under stresses of both sign and the differential between the higher and lower strength materials can be explained in terms of the sodium precipitation. Both stresses will reduce the material back-stress opposing precipitation but on planes and boundaries of different orientation, i.e., applied compressive stresses will lower the resistance to precipitation on planes and boundaries parallel to the applied stress axis; applied tensile stresses will lower the backstress on planes perpendicular to the applied stress axis. De Jonghe observed sodium precipitates on the planes and boundaries of degraded electrolytes in the vicinity of the sodium electrode. The backstress opposing such precipitation will be a function of the pristine strength of the electrolyte and will be inversely proportional to its grain size, so producing the observed material differentiation.

This summary of the physical observations associated with the degradation process, led the present author to suggest that the following reaction is occuring (11)

$$\begin{aligned} &\mathrm{Na(melt)} + 0(5)^{2-} + \mathrm{Na}^{+}\mathrm{(electrolyte)} \\ &\quad \rightarrow \mathrm{Na(melt)} + \mathrm{Na(electrolyte)} + V_{\mathrm{Na}} \\ &\quad + (0)_{\mathrm{Na}} + (e)^{\bullet}_{o} \end{aligned} \qquad (1)$$

where $0(5)^{2-}$ is an oxygen ion in the 0(5) position on the conduction plane, Na(electrolyte) is atomic (later colloidal) sodium in the electrolyte interior, $(O)_{Na}$ is atomic oxygen dissolved in sodium liquid or colloids and $(e)^{\bullet}_{O}$ is an electron trapped on an O(5) site (a colour centre). This reaction explains the purple colour via the unpaired electron on an aluminate site, the colloidal sodium suggested by ESR and detected by electron microscopy, the lattice collapse (via O(5) removal) as observed by electron microscopy and the onset of electronic conductivity.

The reaction will apply both to electrolyte darkening on immersion in liquid sodium and to the more severe deterioration experienced when a current is passed. In the former case, the liquid sodium robs O(5) from the electrolyte starting at the surface, giving a darkened layer whose thickness increases with time. The Na(electrolyte) in this case will be uniformly distributed in the darkened region. When Na^+ is titrated across the electrolyte in an applied field, the system is "forced" and the focussing effect of the surface flaws will lead to a less uniform distribution and increased levels of Na(electrolyte). Stresses local to the focussing flaws will be much higher and the electrolyte will sustain more damage. This explains why the degradation in the Na/S cell during charging is much more severe than in liquid sodium. The same reaction will apply in both cases but the level of Na(electrolyte) (and the concomitant elimination of O(5)) will be much less in the liquid sodium immersion case.

The restriction of feeder grains to one-third of those adjacent to a flaw is based on percolation experiments conducted on mixed $\beta/\beta''-Al_2O_3$ ceramics (15), single- and poly-crystal data and the micro-structural morphology local to the flaw. A percolation model of the conductivity of $\beta/\beta''-Al_2O_3$ as a function of $f(\beta)$ gives a close fit to the experimental data except the experimental results are uniformly shifted to f(β) values lower by one third (in the model it is assumed that β-Al_2O_3 is non-conducting and β"-Al_2O_3 is conducting). This suggests that the non-conducting volume fraction of the microstructure has been consistently underestimated by one third. On this basis, it is assumed that on average, one third of the microstructure is blocking with respect to sodium ion transport. This number is much less than the decreased conductivity of polycrystalline β/β"-aluminas vis à vis their single crystals, i.e., single crystals are 10X more conductive suggesting 90% of the microstructure is blocking. Considering a point intersection with the flaw surface (flaw assumed of zero width), a sphere of line intersections is possible with this point but only half of this sphere resides in the potential-drop direction imposed on the system. Those intercepts in the negative V direction cannot discharge Na^+ at the point of flaw contact. Clearly ~ 50% of the grains peripheral to the flaw cannot discharge Na^+ into it. This figure will be > 50% in fact, for those grains with conduction planes parallel to the flaw cannot discharge Na^+ either. Also even those grains in ideal orientation to feed the flaws may not be themselves fed by neighboring grains, i.e. their Na channels may be blocked at their entrance. The three figures considered, i.e., 0.66, 0.1 and < 0.5 suggest that ~ 33% of the grains intersecting the flaw feed Na^+ to the flaw.

MODEL FOR DEGRADATION IN AN APPLIED FIELD

With respect to electrolyte deterioration in an applied field it is suggested that Na^+ ions saturate the available sites in the β/β"-Al_2O_3 grains feeding current-focusing flaws and, under the influence of the impressed current flow, oxidise the O(5) ions to produce colour centres, Na atoms (which move to local grain boundaries and pores) and vacant sodium sites. These latter permit continued diffusion of Na^+. The occurrence of these reactions must result in local structural collapse.

The feasibility of the supersaturation of Na^+ sites in grains peripheral to an Na-liquid-filled flaw remains to be demonstrated. This will now be attempted. The basic premise will be that, if Na^+ ions arrive at conduction-plane sites faster than they can be diffused on and discharged, supersaturation will occur and reaction 1 will be favoured.

Evidently $Na(\ell)$-surface flaws are important. Although it has been shown that degradation is not a function of grain size, let us assume that the flaw size and the average grain size are equally 20 μm. It is reasonable to assume that the flaw will influence the Na^+ diffusion within those grains that intercept it. In this case, the Na^+ ions see single-crystal discharge paths to the $Na(\ell)$ in the flaw. Hence, it is assumed that the flaw influence is felt for a distance of one grain size from the flaw-tip. Assume the flaw is unit depth and it is fed by 0.33 of the grain area on its periphery. The flaw focuses the current approaching it and let us assume that it focuses a volume of the shape shown in Figure 1. The flaw focuses the current by reason of its closer proximity to the anode. As the current approaches the cathode, the focusing power of the flaw will diminish, giving the triangular prism shape of influenced-volume for the body of the flaw. The flaw tip is the most powerful focusing location and its influence is shown as a hemi-cylinder. The surface area of the influenced volume is equal to $[(4 \times 20 \times 10) + 2 \times 1 \times \sqrt{800} + 20\pi] = 900\ \mu m^2$. If a current density of 0.5 A/cm^2 is travelling through the electrolyte, then the current focusing on the flaw is

$$0.5 \times \frac{900}{10^8}\ \text{A} \qquad (= 45\text{x}10^{-7}\ \text{A})$$

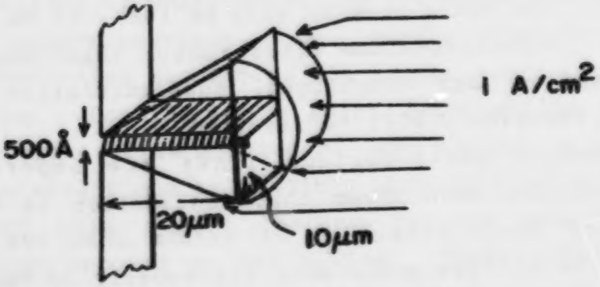

Surface area of flaw-influence = 900 μm^2

Figure 1 - Model for Flaw-Focusing Volume

In terms of moles of Na discharged into the crack this is;

$$\frac{45\text{x}10^{-7}}{96{,}500} = 5\text{x}10^{-11}\ \text{moles/sec}$$

Now one mole of Na = $6\text{x}10^{23}$ atoms, so $5\text{x}10^{-11}$ moles = $30\text{x}10^{12}$ atoms/sec are discharged.

The Na^+ ions feed down the β-Al_2O_3 conduction planes and these are 11.2 Å apart in the β-Al_2O_3 structure. The number of conduction planes feeding the flaw surface is

$$\left(\frac{2\text{x}20\text{x}0.05\text{x}0.33}{11.2\text{x}10^{-4}}\right) + \left(\frac{2\text{x}20\text{x}0.33}{11.2\text{x}10^{-4}}\right) + \left(\frac{0.33\text{x}0.05\pi}{11.2\text{x}10^{-4}}\right) = 1.23\text{x}10^{4}$$

[the first term is associated with the sides of the flaw (500 Å apart); the second term is the area of top and bottom of the flaw and the third the area of flaw tip. The number of planes into flaw tip is determined by the flaw-tip area (assumed 0.05 µmØ)]. The total area of these planes in the 20 µm-grains of unit depth will be

$$20 \times 1.23 \times 10^{4}\ \mu\text{m}^{2}$$

The basal plane area of the unit cell is ~ 30 $Å^{2}$ and this area contains two possible Na^{+} sites, i.e., a BR and an MO(β-Al_2O_3). The total number of available sites for Na^{+} is thus;

$$\frac{25\text{x}10^{4}}{30\text{x}10^{-4}\text{x}10^{-4}} \times 2 = 1.6 \times 10^{12}$$

In stoichiometric β-Al_2O_3, half these sites contain Na^{+} so only half of them are empty. As we are trying to determine whether we get all-sites-full and excess Na^{+} left we must consider those Na^{+} already present on sites. Hence, the number of empty sites = $\underline{0.8} \times 10^{12}$. If we look at the number of available sites and the atoms of sodium discharging, for the series of current densities, the following table can be constructed;

iA/cm^2	i_{focus}	moles Na	# atoms of Na*	# of Empty Sites β-Al_2O_3	 β"-Al_2O_3‡
0.5	4.5×10^{-6}	0.466×10^{-11}	2.76×10^{12}	0.8×10^{12}	1.6×10^{12}
1.0	9×10^{-6}	0.93×10^{-11}	5.58×10^{12}	0.8×10^{12}	1.6×10^{12}
1.5	13.5×10^{-6}	1.39×10^{-11}	8.34×10^{12}	0.8×10^{12}	1.6×10^{12}
2.0	18×10^{-6}	1.86×10^{-11}	11.2×10^{12}	0.8×10^{12}	1.6×10^{12}
2.5	22.5×10^{-6}	2.3×10^{-11}	14.0×10^{12}	0.8×10^{12}	1.6×10^{12}

(*assuming $N = 6\times10^{23}$ atoms/gram atom)
($\ddagger$ β"-Alumina: 3 sites are now available/unit cell (2BR + 1MO) but 2 of these are occupied (stoichiometric β"-Al_2O_3; the higher conductivity is associated with the lack of the ABR bottleneck in the β"-Al_2O_3; see diffusivity later), so sites/30 Å = 3, hence total number of available sites is

$$\frac{2}{3} \times \frac{20\times10^{4}}{30\times10^{-4}\times10^{-4}} \times 3 = 1.6 \times 10^{12}$$

Clearly the possibility exists that the sites could become saturated. Now it is necessary to consider the diffusivity of the Na^+ in both structures as a function of temperature. Let us assume that, having arrived at the periphery of the flaw-influenced-volume, the Na^+ can diffuse through single grains to discharge into the liquid Na (assumed inside the flaw). The diffusivities of interest are therefore the single crystal values and these are summarized in the following table;

Phase	T	D
Na-β	300	2.39×10^{-4} cm^2/sec
Na-β	400	2.39×10^{-4} cm^2/sec
Na-β''	300	9.56×10^{-4} cm^2/sec
Na-β''	400	14.3×10^{-4} cm^2/sec

Using the Einstein relationship;

$$x = 2\sqrt{Dt}$$

for t = 1 sec and D values from the table, then the distance a Na^+ will travel/sec (x) can be estimated for β- and β''-Al_2O_3, i.e.,

Phase	T	x
Na-β	300°C	308 µm
Na-β	400°C	308 µm
Na-β''	300°C	612 µm
Na-β''	400°C	747 µm

So Na^+ in Na-β-Al_2O_3 is travelling 308 µm/sec at 300°C. Now the number of sites in 308 µm is $308/5\times10^{-4}$ = 6.0×10^5 assuming the intersite distance is ~ 5Å. So the time of residence/site is

$$\frac{1}{6.0\times10^5} = 0.16 \times 10^{-5} \text{ secs}$$

Considering the 20 µm to be travelled from the periphery of the flaw-influenced volume to the flaw itself, the number of sites to be traversed is $0.2\times10^4 \times20 = 4\times10^4$; so the time to travel this distance is $4\times10^4\times0.16\times10^{-5} = 0.06$ secs. Now as current densities are increased, the number of Na^+ arriving at the periphery increases and the question arises, do more arrive/sec than can be transferred/sec, i.e., by the time the Na^+ ions have moved one site immediately ahead of the Na^+ just arriving, have too many arrived for the sites just vacated to accommodate them? The number of planes feeding into the flaw is 1.23×10^4. Taking the first sites of these planes (assumed 1 μm width), the number of sites on planes at the exit lines into the flaw are $0.2\times10^4\times1.23\times10^4$, i.e., 2.4×10^7. These empty in 0.16×10^{-5} secs. In this time the following number of Na^+ arrive;

i (A/cm^2)		# Na^+
0.5	$(2.76\times10^{12}\times0.16\times10^{-5})$ =	0.44×10^7
1.0		0.90×10^7
1.5		1.34×10^7
2.0		1.8×10^7
2.5		2.24×10^7

comparing these values with the # of sites available for these ions, the sites in β-Al_2O_3 approach saturation at 2.5 A/cm^2 at both 300°C and 400°C.

The same calculations for β''-Al_2O_3 give the following results.

$i(A/cm^2)$	# Na^+ (400°C)	# Na^+ (300°C)
0.5	0.19×10^7	0.22×10^7
1.0	0.39×10^7	0.44×10^7
1.5	0.58×10^7	0.67×10^7
2.0	0.78×10^7	0.9×10^7
2.5	1.0×10^7	1.12×10^7

The sites do not become saturated.

DISCUSSION

Although these results show that the sites do not become saturated for β''-Al_2O_3, two important factors have been overlooked, i.e.

(a) the influence of the $f(\beta)$ and

(b) the influence of impurities.

Grains of β-Al_2O_3 peripheral to the flaw will become overloaded and reaction 1 could occur therein giving structural collapse. Also possible is the diversion of the unaccepted Na^+ from the β-Al_2O_3 grains to the β''-Al_2O_3 grains around the flaw periphery. This in turn may lead to the overloading of the β''-Al_2O_3 channels.

The model does explain the rate-controlling role of the diffusion of Na^+ and the constant progress of deterioration with time. The increased degradation with temperature is probably associated with the temperature coefficient of reaction 1.

The role of impurities, especially K^+, H_3O^+, Ca^{2+} and Si^{4+} in the degradation process has been suspected for some time. K^+ and H_3O^+ with their known ease of exchange for Na^+ in β-alumina and their larger size vis à vis Na^+ will cause mechanical damage. In fact, it has been clearly demonstrated that Na-β-Al_2O_3 and Na-β"-Al_2O_3 polycrystals when ion-exchanged in KNO_3 or H_2SO_4 suffer considerable damage and powder fragments result.

Recently Rasmussen et al. (9) assessed the various parameters reported to influence degradation and investigated the influence of the sodium purity. Two grades of Na were used;

(a) "impure" 480 ppm Ca/30 ppm K,

(b) "pure" < 10 ppm Ca/313 ppm K.

They found that the purity strongly influenced the performance of the electrolyte; the purer material giving twice the life of the impure. Differences of average grain size made little or no difference. The role of Ca^{2+} in the degradation is not clear but it appears much more detrimental than K^+. It has approximately the same ionic radius as Na^+ (~ 1.0 A), but its divalency will render it harder to move on the conduction plane ($D_{Ca^{2+}} < D_{Na^+}$). It will also preclude Na^+ from another site on the plane for electrical neutrality reasons and, being a centre of positive charge, it will repel Na^+ attempting to diffuse to discharge. Si^{4+} is especially deleterious to β"-Al_2O_3 (13). If the smaller, more electro-negative Si^{4+} ion enters the conduction plane, it could have a more pronounced effect than Ca^{2+}. The smaller ions (eg. Li^+, $r = 0.74$ A) are known to move more slowly than Na^+ in the β-alumina structures. It is hypothesised that Li^+ resides further into the interstice between the O^{2-} ions of the spinel block than Na^+, making it more difficult to move. This would apply even more so to

Si^{4+} (r = 0.40 Å). It would also preclude 4 sites to Na^+ and would repel any mobile Na^+. The tetrahedral coordination of Si^{4+} with oxygen is possible in ß"-Al_2O_3 wherein latent oxygen tetrahedra exist due to the offset of the oxygen planes above and below the conduction planes. The O(5) would make the oxygen tetrahedral interstice too large for Si^{4+} and its formation could locally distort the conduction plane and decrease the mobility of Na^+. Oxygen tetrahedra could not form between the two mirror oxygens of ß-Al_2O_3 so Si^{4+} is unlikely to reside on the conduction plane of ß-Al_2O_3.

Powers et al. (10), observing a small decrease in resistance on the initiation of new electrolyte put this down to H_3O^+ from the atmosphere. It is known that, unless extreme precautions are taken, ß- and ß"-Al_2O_3 form NaOH and Na_2CO_3 on the surface. Further to this, Heavens (16) detected a distortional layer 5 µm deep on the surface of ß-Al_2O_3. This surface layer had a 1% expansion of the c-axis and it was due to H_3O^+ exchange with the atmosphere. Polishing removed the layer and it reformed after air-exposure for several weeks. Field-assisted ion-exchange of H_3O^+ from dilute HCl demonstrated the same layer development with a progressive change in lattice parameter.

SUMMARY

A model is presented for the degradation of ß/ß"Al_2O_3 electrolytes in Na environments. The recognised physical characteristics of the material during degradation are incorporated. The model predicts that sodium ion diffusion is rate-controlling the degradation process and that critical current density of ~ 3A/cm^2 will lead to accelerated degradation.

It is suggested that more Na^+ ions are focussed into grains peripheral to flaws than can be transmitted by those grains. This results in localised oxidation of oxygen ions to give sodium atoms, electrons trapped at oxygen sites (colour centres), the eventual collapse of the conduction planes by removal of the O(5) ions spaced between the structural spinel blocks and the onset of electronic conduction. It is further suggested that the sodium atoms coalesce in metal or oxide colloids and the dense microstructure is microcracked as a result. These microcracks facilitate further sodium precipitation and eventually join up with the sodium in the main flaw giving a sodium "dendrite" progressing through the electrolyte section. The feasibility of this "supersaturation" concept is demonstrated for $\beta/\beta''-Al_2O_3$ at 300°C.

REFERENCES

1. D.K. Shetty, R.S. Gordon and A.V. Virkar, "Fracture Mechanics of Ceramics", Vol. 4, pg. 651, ed. Bradt, Hasselman and Lange.
2. A.V. Virkar, L. Viswanathan and D.R. Biswas, J Matls Sci 15: 302; (1980).
3. A.V. Virkar, J Matls Sci 16:1142; (1981).
4. R.D. Armstrong, T. Diahuison and J. Turner, Electrochim Acta 19: 189; (1974).
5. G.J. Tennerhouse, R.C. Ku, R.H. Richman and T.J. Whalen, Bul Am Ceram Soc 54 (5): 523; (1975).
6. A.V. Virkar and L. Viswanathan, J Am Ceram Soc 62 (9-10): 528; (1979).
7. L.C. de Jonghe, L. Feldman and Millett, Matls Res Bul 14: 589; (1979).
8. L.C. de Jonghe, L. Feldman and A. Beuchele, J Matls Sci 16: 780; (1981).
9. J.R. Rasmussen, G.R. Miller and R.S. Gordon, Abstract #720, Ann. Conv. Electrochem. Soc., Montreal (May, 1982).
10. R.W. Powers, M.W. Brecker and P.S. Park (ibid.), Abstract #725.
11. P.S. Nicholson, J Matls Sci (in press).
12. J.O. Bovin, Nature 273: 136; (1978).
13. D. Gourier and A. Wicker, Abstract #722, Ann Conv of Electrochem Soc , Montreal (May 1982).
14. K. Kuribayashi and P.S. Nicholson, submitted to J Matls Sci
15. D. Smith, M. Bell, M. Sayer and P.S. Nicholson, Proc. of IEA Conference, Pasadena, California, June 1982, Annex V.
16. S.N. Heavens, J Matls Sci 17: 965; (1982).

PARTICLE HYDRATES AS PROTON CONDUCTORS

P.J. Wiseman

Inorganic Chemistry Laboratory, South Parks Road,
Oxford OX1 3QR, U.K.

ABSTRACT

The development of solid materials that possess high protonic conductivity has received practical stimulus from possible applications in low-temperature fuel-cells, storage batteries and electrochromic devices. Recent work has shown that small, hydrated oxide particles are a large class of proton-conducting materials that range from electrical insulators to metallic conductors. This article outlines the nature of these particle hydrates and considers possible areas of practical application.

KEYWORDS: proton conduction, solid electrolyte, fuel-cell, hydrous oxide, particle hydrate.

RÉSUMÉ

Les possibilités d'application aux piles à combustible à basse température, aux accumulateurs et aux dispostifs électrochromiques ont stimulé la mise au point de substances à l'état solide ayant une haute conductivité protonique. Des travaux récents montrent que les petites particules d'oxydes hydratés forment une grande classe de substances conductrices de protons, dont la gamme s'étend des isolants électriques aux conducteurs métalliques. Le présent article expose les propriétés fondamentales de ces particules d'hydrates et en explore les domaines éventuels d'application pratique.

INTRODUCTION

Work in the area of fast-ion conduction in solids is usually considered to have commenced with the discovery in 1967 of the high Na^+-ion conductivity in sodium β-alumina, $(Na_2O)_{1+x}\cdot 11Al_2O_3$ (1). This electrically insulating material has an ionic conductivity of 1.4×10^{-2} $ohm^{-1}cm^{-1}$ at 300 K with an activation energy of 16 kJ mol^{-1}; the room temperature (300 K) diffusion coefficient is $4 \times 10^{-7} cm^2 s^{-1}$. Similarly the discovery of fast-proton conduction in solids has been variously cited as 1972 with the du Pont patents on the NAFION perfluorocarbon sulphonic acid polymer (σ(300 K) = $5 \times 10^{-2} ohm^{-1} cm^{-1}$) (2), 1973 with the reported conductivity of σ(298 K) = $3 \times 10^{-4} ohm^{-1}cm^{-1}$ for H_3OClO_4 (3) and 1976 with the patent on phosphomolybdic and phosphotungstic acids, $H_3PM_{12}O_{40}\cdot 29H_2O$ (4). The latter compound (M=Mo) has a room temperature conductivity of 1.8×10^{-1} $ohm^{-1}cm^{-1}$ (80% relative humidity) with an activation energy of 16 kJ mol^{-1} (5).

Such claims do little justice to the enormous amount of earlier work in classical ion-exchange chemistry. Indeed, the first transport measurements on β-alumina exploited the ion-exchange properties of the material (1). It may be argued that ion-exchange materials normally involve water-logged structures and that the conductivity of Na-β alumina is superior to that of anhydrous exchangers. Nevertheless, all the best proton conductors contain water molecules as an essential constituent. Familiar fast-proton conductors, such as $H_3PMo_{12}O_{40}\cdot nH_2O$, sulphonic acid resins, $Zr(HPO_4)_2\cdot H_2O$, $HUO_2PO_4\cdot 4H_2O$, $ThO_2\cdot nH_2O$ and $Sb_2O_5\cdot nH_2O$ were cited in tabulations of inorganic ion-exchangers in the 1950's and early 1960's (6). Of course kinetic measurements gave mixed-ion effective diffusion parameters (e.g. H^+/Na^+) but even if proton diffusion were the slow step (which is unlikely) an effective diffusion coefficient of $10^{-7} cm^2 s^{-1}$ for H^+/Na^+ exchange in $ThO_2\cdot nH_2O$ is indicative of fast-proton transport (7). Indeed a $Zr(HPO_4)_2\cdot nH_2O$/teflon composite electrolyte with a conductivity of $1.7 \times 10^{-4} ohm^{-1}cm^1$ was used at an early stage in a room temperature fuel-cell (8). Similarly an effective diffusion coefficient of $3 \times 10^{-8} cm^2 s^{-1}$ for Cs^+/K^+ exchange on $Zr(HPO_4)_2\cdot H_2O$ has been measured (7). It is unfortunate that the separation between ion-exchange and solid state chemistry is still so large that much relevant work in the former area is overlooked by solid state chemists and vice versa. One theme of this review is that the field of ion-exchange chemistry contains many electronically insulating compounds with high protonic conductivity (protonic electrolytes). A theoretical analysis of ion-exchange rates indicates that ion-exchange is a necessary, but not sufficient criterion for fast-ion conduction; only the fastest exchangers will have conductivities of practical interest (9-13). In this review article the features of ion-exchange compounds that are conducive to fast-proton transport are described.

Practical stimulus to this area has arisen from the possibility of utilising a solid proton conductor as a fuel-cell electrolyte. The thermodynamics of the fuel-cell reaction $H_2 + \frac{1}{2}O_2 = H_2O$ are optimised by a low-temperature operation; this is a consequence of the negative entropy change (an electrolysis cell has the reverse characteristics). This is advantageous for solid proton conductors which are, at present, characterised by destructive loss of water at high temperature. Unfortunately the kinetics of cheap oxygen electrodes are too slow at room temperature. As described later in this review the nature of the current range of proton conductors poses a major limitation to this application. However, low-temperature applications, such as electrochromic devices (where high protonic conductivity is required of the electrolyte and cathode components) or perm-selective membranes, are more plausible possibilities.

PARTICLE HYDRATES

This review is concerned with the group of proton conductors that the author has termed particle hydrates (14) and which includes many of the best protonic electrolytes. Reference to the application of the model to mixed protonic-electronic conducting materials is made in passing since a detailed exposition is to appear elsewhere. Applications of the latter materials are to be found as traditional and advanced battery cathodes and as electrochromic cathodes. It will also be apparent that certain aspects of particle hydrates are of a fundamental nature. In the context of this review such diversions are not made and emphasis is placed on providing background ideas that facilitate a search for new, low temperature, fast protonic electrolytes.

Typical particle hydrates are hydrous oxides, oxide-hydroxides or hydroxides, such as $ThO_2 \cdot nH_2O$ and $In(OH)_3 \cdot nH_2O$ (15), where protonic conductivity is observed for poorly crystalline material (where n is large) but not for the crystalline phase (where n is very small). A general structural description of these materials is made below which then allows a discussion of a wider range of protonic electrolytes.

Theoretical studies of solids, normally the domain of the physicist, have concentrated on the concept of an infinite lattice because the regular periodicity was the essential simplifying feature. Unfortunately the assumptions of the model are often forgotten with the result that the properties of solids are assumed to be independent of particle size. While this may be approximately true for 'bulk' properties (e.g. lattice constants, specific heats, heats of solution, e.t.c.) those properties associated with the surface regions of the solid may alter quite drastically. Of particular importance is the fact that practical applications of solids often use particle sizes of much smaller dimensions than those studied in 'pure' research. The simplest conceptual picture of a solid that obviates these difficulties is to consider each particle of the solid as a unique giant molecule. The change in properties with particle size then becomes predictable rather than unexpected.

As an illustration of some important concepts we consider a very simple molecular process: the hydration of the Cl_2O_7 molecule shown in Fig.1. Cleavage of the molecule requires the addition of a water molecule; clearly this does not alter the overall electronic charge of the system. In the first step we recognise that the compounds are electronically and coordinatively satisfactory. The formation of a three-coordinate fragment is most unlikely if donor molecules (here H_2O) are present, either in a liquid phase or even at low concentrations in a gaseous phase. Also, the electronegativity of Cl(VII) ensures substantial protonic dissociation in the second step; for complete dissociation this produces $H_3O^+ClO_4^-$ for $Cl_2O_7 \cdot 3H_2O$ and $H_5O_2^+ClO_4^-$ for $Cl_2O_7 \cdot 5H_2O$ (16,17) (they would be predicted to be strong acids by Pauling's rules). Solid perchloric acid was an early fast-proton conductor (3). The ClO_4^- ions are arranged in a regular manner (i.e. a crystalline material) and the high conductivity stems from the large concentration of hydrated protons. This is coupled (since the dissociation will not be 100% and there will be free H_2O molecules and ClO_3OH groups) with rapid proton mobility by a cooperative Grotthus mechanism. The proton mobility in $HClO_4 \cdot 2H_2O$ should be even greater but this material is liquid at room temperature. Further addition of water molecules disorganises the regularity of the solid (dissolution); the proton conductivity should be further enhanced by the increased proton mobility but the ClO_4^- ions, while remaining intact, no longer constitute a solid. Solid perchloric acid (and its hydrate) may be considered to contain this acidic aqueous solution in a more concentrated and constrained form. H_3O^+-ions in $HClO_4 \cdot H_2O$ may be replaced by Na^+-ions to form $NaClO_4$ which also contains tetrahedral ClO_4^- units. This can be viewed as an ion-exchange process. This simple example provides a good basis for examining the properties of small oxide particles created by the fracture of much larger, three-dimensional oxide macromolecules.

Several possibilities arise when an oxide crystal is fragmented. The lattice energy may be so altered that a new structure occurs at small particle sizes. This is a little studied area. In the case of agglomerated, water-stabilised oxide fragments direct lattice imaging by electron microscopy has shown that small ZrO_2 and ThO_2 particles with the fluorite structure persist to particle diameters of ~25Å (18-20). A similar conclusion is reached (21) from X-ray radial distribution analysis of colloidal suspensions of ThO_2 particles (~40Å diameter). However, further fragmentation of ThO_2 particles gives face-shared Th_4 tetrahedral chains, e.g. the $[Th_6O(OH)_6(H_2O)_n]^{16+}$ unit shown in Fig.2 (21). They are related to (because the fluorite structure contains Th_4 tetrahedra), but are not fragments of, the macroscopic ThO_2 structure (which involves edge and vertex-linked Th_4 units). On the other hand, fragments of cubic zirconia do persist in solution (Fig.3, (22)). A notable feature of the latter cluster is that the eight-fold coordination of the Zr atom is preserved (albeit distorted). This may be compared with the fracture and dissolution of Cl_2O_7. $[Zr_4(OH)_8(H_2O)_{16}]^{8+}$ is also found in zirconyl salts e.g. $ZrOCl_2$ is $[Zr_4(OH)_8(H_2O)_{16}]Cl_8 \cdot 2H_2O$ (23,24). We note, in both Th and Zr cases, that basic dissociation has occurred (Zr(IV) has a smaller charge and larger size that Cl(VII)). Similarly hydrolysis of $Al_2(SO_4)_3$ gives $[Al_2(OH)_2(H_2O)_8]^{4+}(SO_4)_2 \cdot 2H_2O$ with cis-bridging of two octahedra (25).

If, as may often be the case, the basic parent structure is retained on fragmentation there remains the boundary problem - the surface must be terminated in as energetically favourable manner as possible. How this is achieved will depend on the environmental conditions at the time of fracture. A satisfactory possibility, e.g. for ThO_2, is that the eight-fold oxygen coordination of the bulk Th atoms is maintained at the surface; it is clearly energetically favourable for the ion of lower charge to terminate the surface. Table 1 shows that for small particle sizes this necessitates a stoichiometry in excess of 1:2 (an example of a compositional dependence on the particle size). Excess oxygen can be incorporated (as in the Cl_2O_7 fragmentation) by using freely available H_2O

molecules (either if prepared in solution or adsorbed from the atmosphere). Otherwise alternative donor species will be used for this purpose (of course an optimum coordination may not necessarily be reached). Thermodynamically the process is described by the variation in the surface tension intensive variable.

The solvating molecules will be firmly bound (chemisorbed) to the surface and be held quite tenaciously. For example, exposure to oxygen of silica glass that has been fragmented in ultra-high vacuo results in an initial heat of adsorption of 300 kJ mol^{-1}. Removal of the chemisorbed molecules may require temperatures from 300°C to over 1000°C resulting in immediate, or kinetically delayed exothermic sintering of highly reactive, surface unsaturated oxide particles; this is an irreversible process.

The solid consists of large agglomerates of these small hydrated oxide particles (typically 1000-10,000Å). Additional (physisorbed) water molecules act as the binding agent with a concentration dependent on the relative humidity and the inter-particle ionic concentration. This loosely bound water is responsible for the swelling properties of the solid and the large water contents observed (e.g. $ThO_2 \cdot 4.24H_2O$); it is lost reversibly at low temperatures.

As in the $Cl_2O_7 \cdot nH_2O$ case a proton dissociation equilibrium must exist between the H_2O groups on the particle surface and the immobilised H_2O molecules in the inter-particle region (this process is analogous to the partial dissociation of a weak acid in aqueous solution). Acidic dissociation will be promoted by small metal atoms of high positive charge (i.e. large Z/r ratio) and basic dissociation by large metal atoms of low charge. The dissociation will give rise to a charged oxide particle - negatively charged for acidic dissociation (c.f. $H_3O^+ClO_4^-$) and positively charged for basic dissociation (c.f. $[Zr_4(OH)_8(H_2O)_{16}]^{8+}(OH^-)_8$). Both types will give rise to protonic conductivity dependening on the concentration and mobility of hydrated protons (or hydroxyl groups) in the liquidlike inter-particle region.

So far the small hydrated oxide particles have been considered to arise from mechanical fragmentation (or vacuum sputtering) and subsequent exposure to a humid atmosphere. However, most materials have not been prepared in this manner (although sputtered WO_3, of small particle size, is observed to sorb water and possess proton conduction properties of importance in eletrochromic cathodes (26)). A fundamental property of small particles is electrolyte sorption (or invasion) into the agglomerated bulk. As the particle size becomes smaller so the charges of the oxide particles increases and the repulsion promotes the formation of a colloidal suspension. Addition of small quantities of electrolyte stabilises agglomerate formation and, thermodynamically, residual electrolyte in such a material prepared by precipitation techniques can never be completely removed by washing. Ultimately colloid formation or dissolution will occur. Monitoring the conductivity of the washings is not necessarily informative. First, the equilibrated external solution is not necessarily identical to the equilibrated internal solution (the chemical potentials of a particular ion must be equal inside and outside the solid). Secondly, the colloidal suspension itself involves substantial acidic or basic dissociation and will have a high conductivity. Electrolyte sorption of H^+ or OH^- containing electrolytes represents an additional contribution to the protonic conductivity. It can be minimised but never fully eliminated by washing. Ideally more work should be done on mechanically, or thermally, fragmented particles exposed to controlled environments, rather than on materials grown from small coordination polyhedra in solution. Of course, deliberate soaking of electrolyte onto a porous substrate represents an easy means of increasing the protonic conductivity of an inherently poor conductor (c.f. supported liquid electrolytes). Even the proton conductivity of a NAFION membrane may be increased by immersion in very strong acid.

Dissociated H_3O^+ or OH^- ions may be cation or anion exchanged by equilibration with an external electrolyte solution (which can also invade the solid). For amphoteric particles, where dissociation is incomplete, cation exchange is enhanced by a high external pH and anion exchange is favoured by a low pH (14). Where the exchange capacity (for anions and cations) is zero the particles must have net zero charge and the pH of the added solution is unaltered by addition of the solid. This is because alteration of the H^+-ion concentration in the external solution necessitates a charge compensating change in the external A^+ or X^- concentrations of the exchanging eletrolyte; this is zero if no exchange has taken place (unless partial dissolution of the solid occurs). The pH where no ion-exchange occurs is called the point of zero charge (p.z.c.) or isoelectric point (27). This is a useful parameter for estimating the likely dissociation direction in the absence of an exchange medium. If the p.z.c. is very high the particles are probably positively charged and there will be a substantial OH^- concentration in the liquid-like region (e.g. hydrous ZnO p.z.c. ~ 10). If it is very low then H_3O^+ dissociation probably occurs (e.g. hydrous Sb_2O_5 ~ 0.5). An intermediate value indicates that the particle charge may be switched by small changes in the pH of the exchange solution; in the absence of this exterior medium the internal dissociation is difficult to assess. There is an urgent need for a technique that can distinguish, unambiguously and quantitatively, the location of protons (surface-OH, OH^-, H_2O, H_3O^+ etc.) in this type of material. On the particle hydrate model the maximum exchange capacity (i.e. at low and high pH) should be compatible with the limiting charges of the particles when they are fully protonated and deprotonated. Also, facile swelling should produce the normal exchange order $Cs^+ > Rb^+ > K^+ > Na^+ > Li^+$.

The liquid-like region must be regarded as an essential part of the solid - it can only be altered by a change in external conditions. It is responsible for the high proton conductivity often exhibited by these materials. The liquid content facilitates densification and particle hydrates are often compressed to transparent pellets by the simple expedient of cold pressing. A schematic picture of the model (assuming acidic dissociation) is shown in Fig.4. A further aspect of the model is that if the particle contains a suitable transition metal in a mixed oxidation state then the individual particles will electronically conduct as may the solid as a whole. The latter bulk property requires sufficient particle connection through the solid to permit long-range electron transport. This can usually be achieved by partially sintering the material at a moderate temperature (200-300°C).

It is apparent that the protonic conductivity, the ion-exchange properties and even the composition of the material will be particle-size dependent. As the particles become larger the effects beome smaller but do not disappear completely (Table 1). They are types of thermodynamic size effects.

There is a reasonable body of evidence to support these ideas of a direct and circumstantial nature (including the known properties of colloidal suspensions). Important results are:

(i) the identification of parent structures and particle and agglomerate sizes by electron microscopy (electron diffraction and dark-field photography (28); direct lattice imaging (18,20)).

(ii) the correlation of (i) with the structure and sizes of colloidal suspensions by X-ray radial distribution analysis. For example, X-ray studies show colloidal particles of fluorite ThO_2 of $\sim$40Å diameter some of which are joined together in no specific orientation. This picture also emerges from electron microscope work on agglomerated material.

(iii) the characterisation of loosely and firmly bound water by thermogravimetric methods. Also, the use of high-temperature X-ray (29) and electron microscope (20) methods to relate the loss of chemisorbed water to particle sintering. Typically $ThO_2 \cdot 3.26H_2O$ shows no particle sintering below 400°C even though 86% of the water has been lost reversibly (28).

(iv) the increase of proton conductivity with decrease in particle size as measured by A.C. (14,15), D.C. (30) and pulsed n.m.r. methods (31).

(v) the variation of ion-exchange capacities with pH and particle size and its correlation with particle charges (6,14).

(vi) the measurement of p.z.c.'s (27) and their rationalisation in terms of atom electronegativities. It is to be hoped that as more powerful techniques emerge it will prove possible to examine the nature of this type of material in more detail.

While the model was developed to explain the unusual properties of poorly crystalline materials many aspects are relevant to crystalline proton conductors. A crystalline material such as $H_3PMo_{12}O_{40} \cdot 29H_2O$ (Fig.5) has a clear structural relation to the particle hydrates. We may consider it as a hydrated fragment of the hypothetical mixed-oxide $P_2W_{24}O_{77}$ of different structure. It may be regarded as a particle hydrate where structural re-organisation has occurred to tie up the boundary bonding requirements in a neat and energetically efficient manner (c.f. the case of shear structures versus random defects). Indeed the unit is so stable that it is used uniquely in the structure and can, therefore, pack in a periodic manner (c.f. the poorly crystalline particle hydrates where the wide variation in particle sizes prevents long-range order). Proton dissociation is extensive and the free water content is high and humidity dependent (32). Related globular ions are $[Al_{13}O_4(OH)_{25}(H_2O)_{11}]^{6+}$ in $[Al_{13}O_4(OH)_{25}(H_2O)_{11}](SO_4)_3 \cdot 16H_2O$ (33) and $Nb_6O_{19}{}^{8-}$ in $Na_7(H_3O)Nb_6O_{19} \cdot 14H_2O$ (34). The aluminium polymeric cation is a fragment of the defect-spinel, γ-Al_2O_3.

Transport properties of the OH^- and H^+-exchanged analogues of these compounds have not been measured.

$HUO_2PO_4\cdot 4H_2O$ is a particle hydrate of hypothetical $U_2P_2O_{11}$ ($W_2P_2O_{11}$ does exist). In this case it is infinite $UO_2PO_4^-$ layers that are particularly stable and a crystalline compound results containing acidic dissociation. There is conflicting evidence for water and electrolyte sorption properties of this material (35); the latter possibly contributes to the reported high conductivity (36). We can similarly draw structural analogues to the strings and layers of NAFION and clay particles (37). An interesting feature of crystalline proton conductors is that smaller particles (e.g. fractured layers or strings) have a contribution to the proton conductivity from intra- and inter-particle regions.

The particle hydrate classification can be usefully employed for proton conductors that have concurrent sorption/swelling properties. When the solid has continuous three-dimensional linkage then the swelling properties are much reduced, the materials are difficult to densify and the ion-exchange order is anomalous; they are better classified as framework hydrates e.g. the pyrochlore structure of crystalline antimonic acid, $(H_3O^+)_2Sb_2O_6\cdot H_2O$ (14) and hydrous β"-alumina, $0.84MgO\cdot 5Al_2O_3\cdot 3.8H_2O$ (38). Although $Sb_2O_5\cdot nH_2O$ can be prepared by a variety of methods, producing different parent structures and degrees of crystallinity, (15,39-43) the highest conductivity occurs for the phase of lowest crystallinity where inter-particle transport may be dominant.

The particle hydrate terminology is a useful means of describing and relating such materials and, in particular, of emphasising particle size variations of solid state properties. It is to be hoped that as size effects become more widely recognised this label will become redundant.

CHARACTERISTICS OF GOOD PROTONIC ELECTROLYTES

Table 2 contains a list of some good protonic electrolytes which, together with the principles outlined above, enable useful guidelines to be deduced for the purposeful synthesis, or search, for new proton conductors. We may list the following key features which are discussed below.

(i) The material should be a rapid ion-exchanger with a high exchange capacity in the absence of external pH adjustment.

(ii) It should exchange predominantly cations or anions when the external pH is adjusted.

(iii) The point of zero charge should be either large or small.

(iv) It should have a high water content.

(v) The metal atom should preferably be either a small, highly charged ion, or a large, low-charged ion.

(vi) If it is a poorly crystalline material it should have as small a particle size as possible.

These guidelines can be rationalised as follows.

Fast-ion exchange implies a reasonable protonic diffusion coefficient; a high exchange capacity (in the absence of pH adjustment) suggests the possibility of substantial protonic dissociation (but see comments in (14)); together they indicate good proton conductivity.Crystalline antimonic acid and hydrogen uranium phosphate are rapid cation exchangers with large exchange capacities of 5.08 and 2.60 meq g^{-1} respectively; $ThO_2 \cdot nH_2O$ has an anion exchange capacity of 0.2 meq g^{-1} (pH 7.5); pyrophyllite, $Al_2Si_4(OH)_2O_{10}$, has a cation exchange capacity of 0.04 meq g^{-1}.

If the exchange capacity is little affected by a large pH change then either surface deprotonation is easy and surface protonation is hard ($H_3O^+ \cdot nH_2O$ formation and cation exchange) or vice versa (OH^- formation and anion exchange). If the change is very marked (e.g. cation to anion exchange) the material is amphoteric and the liquid-like region is only weakly basic or acidic. For acidic, cation exchangers the p.z.c. should be small; for basic, anion exchangers it should be large; for amphoteric cation/anion exchangers it should be intermediate. Thus NAFION, $H_3PMo_{12}O_{40} \cdot nH_2O$, $Sb_2O_5 \cdot nH_2O$ and $HUO_2PO_4 \cdot nH_2O$ are cation exchangers only, whereas $ThO_2 \cdot nH_2O$ and $In(OH)_3 \cdot nH_2O$ are amphoteric. $WO_3 \cdot nH_2O$, $ThO_2 \cdot nH_2O$ and $ZnO \cdot nH_2O$ have p.z.c.'s of ~ 0.5, 8.2 and 10.3 respectively. The charge:radius ratio of the metal atom is a useful, if crude, measure of the likely direction of the surface equilibria.

A high water content should increase the proton mobility and generally increase the conductivity e.g. σ (293 K) for $ThO_2 \cdot nH_2O = 2.5 \times 10^{-4}$, 4.0×10^{-5} and 5.0×10^{-6} $ohm^{-1}cm^{-1}$ for $n = 4.2$, 3.4 and 2.9 respectively (15). It also leads to readily fabricated pellets. At fixed humidity the water content should increase with a decrease in particle size (more is required to stabilise the surface and the inter-particle ion concentration will be larger; solvation exploits the free energy of ion solvation and dilution). Similarly the $H_3O^+ \cdot nH_2O$ or OH^- concentrations will increase with a decrease in particle size; this correlates with the general trend of an increase ion-exchange capacity with a decrease in particle size for hydrous oxides. The p.z.c. should tend towards a more acidic (low) or basic (high) value as the particle size decreases. As a result the proton conductivity is expected to increase as the particles become smaller.

APPLICATIONS

It is clear from the above discussion that the role of water in these materials is critical to their transport characteristics. Without humidity control pellet cracking can occur above 50°C and, even, at near 100% humidity, extended operation above 100°C will be unlikely at atmospheric pressure; this is a major limitation to a fuel-cell application. Dehydration rapidly reduces the measured conductivity and, for poorly crystalline materials at higher temperatures, irreversible sintering may occur. Despite these comments measurements above 100°C are scarce and further studies are needed before firm conclusions can be drawn. A second problem in a fuel-cell configuration is that although interfacing with a porous electrode material should be good, it will not be as effective as with a liquid electrolyte. The latter are plagued by corrosion problems at the electrolyte/electrode interface which will be reduced, but not eliminated by the use of acidic or basic solid proton conductors. Nevertheless, NAFION membranes have been used in fuel-cells althoughthe acidity of the material necessitates Pt electrodes.Its high conductivity (due to ready dissociation of surface sulphonic acid groups into the water-logged region) coupled with the excellent mechanical properties of a polymer sheet makes this compound a difficult material to improve upon. A significant advance has been the use of polymer/particle hydrate composites e.g. porous polyethylene/$Zr(HPO_4)_2 \cdot nH_2O$ (44) and polyvinylidene fluoride (or polysulphone)/antimonic acid (45). However, there is a clear unfilled gap for a higher temperature proton conductor.

It follows, therefore, that the use of particle hydrates in fuel-cells requires the development of a cheap, low-temperature oxygen electrode. Of course, in this event a simple liquid electrolyte may be superior.

More promising are applications in low-temperature devices as described previously. As well as their relevance to proton conductivity in solids some of these materials are good model systems for the study of size effects in solids. Such studies will enable a further link to be forged between solid state and molecular chemistry.

REFERENCES

(1) Y.F. Yu Yao and J.T. Kummer, "Ion exchange properties of and rates of ionic diffusion in beta-alumina" J Inorg Nucl Chem 29: 2453-2475; 1967.

(2) W.G.F. Grot, G.E. Munn and P.N. Wolnsley, "Perfluorinated ion-exchange membranes", presented at 141st National meeting, the Electrochemical Society, Houston, Texas, May 7-11, 1972.

(3) A. Poitier and D. Rousselet, "Conductivite electrique et diffusion du proton dans le perchlorate d'oxonium" J Chim Physique 70: 873-878; 1973.

(4) O. Nakamura, T. Kodama, O. Isao and Y. Miyake, Japanese Patent 76/106,683, 1976.

(5) O. Nakamura, T. Kodama, I. Ogino and Y. Miyake, "High-conductivity solid proton conductors: dodecamolybdophosphoric acid and dodecatungstophosphoric acid crystals" Chem Lett 1: 17-18; 1979.

(6) C.B. Amphlett, "Inorganic ion exchangers", Elsevier Publishing Company, 1964.

(7) G.H. Nancollas and R. Paterson, "The kinetics of ion exchange on zirconium phosphate and hydrated thoria" J Inorg Nucl Chem 22: 259-268; 1961.

(8) R.P. Hamlen, "Ionic conductivity of zirconium phosphate" J Electrochem Soc 109: 746-749; 1962.

(9) G.E. Boyd, A.W. Adamson and L.S. Myers, "The exchange adsorption of ions from aqueous solutions by organic zeolites. II. Kinetics" J Amer Chem Soc 69: 2836-2848; 1947.

(10) D. Reichenberg, "Properties of ion-exchange resins in relation to their structure III, Kinetics of exchange" J Amer Chem Soc 75: 589-597; 1953.

(11) W.A. England, K. Mizushima, P.J. Wiseman and J.B. Goodenough, "New fast ion conductors", Proceedings of the European Communities Meeting on advanced batteries, 195-205, 1979.

(12) W.A. England, J.B. Goodenough and P.J. Wiseman, "Ion exchange reactions of mixed oxides", paper submitted to J Solid State Chem.

(13) W.A. England, J.E. Birkett, J.B. Goodenough and P.J. Wiseman, "Ion exchange reaction in oxides with the Rb_xMnO_2 structure", paper submitted to J Solid State Chem.

(14) W.A. England, M.G. Cross, A. Hamnett, P.J. Wiseman and J.B. Goodenough, "Fast proton conduction in inorganic ion-exchange compounds" Solid State Ionics 1: 231-249; 1980.

(15) D.J. Dzimitrowicz, J.B. Goodenough and P.J. Wiseman, "A.C. Proton conduction in hydrous oxides" Mater Res Bull 17: 971-979; 1982.

(16) M.R. Truter, "A detailed refinement of the crystal structure of hydroxonium perchlorate" Acta Cryst 14: 318-319; 1961.

(17) I. Olovsson, "Hydrogen-bond studies. XXIX. Crystal structure of perchloric acid dihydrate, $H_5O_2{}^+ClO_4{}^-$" J Chem Phys 49: 1063-1067; 1968.

(18) J.R. Fryer, J.L. Hutchison and R. Paterson, "An electron microscope study of the hydrolysis products of zirconyl chloride" J Colloid Interface Science 31: 238-248; 1970.

(19) J.R. Fryer, J.L. Hutchison and R. Paterson, "Electron microscope observations of the initial stages in the hydrolytic polymerisation of zirconyl chloride" Nature 226: 149-151; 1970.

(20) D. Cherns, D.J. Dzimitrowicz and P.J. Wiseman, unpublished work.

(21) M. Magini, A. Cabrini, G. Scibona, G. Johansson and M. Sandstrom, "On the structure of highly hydrolysed thorium salt solutions" Acta Chem Scand A30: 437-447; 1976.

(22) G.M. Muha and P.A. Vaughan, "Structure of the complex ion in aqueous solutions of zirconyl and hafnyl oxyhalides" J Chem Phys 33: 194-199; 1960.

(23) A. Clearfield, "Structural aspects of zirconium chemistry" Rev Pure Appl Chem 14: 91-108; 1964.

(24) A. Clearfield and P.A. Vaughan, "The crystal structure of zirconyl chloride octahydrate and zirconyl bromide octahydrate" Acta Cryst 9: 555-558; 1966.

(25) G. Johansson, "The crystal structure of $[Al_2(OH)_2(H_2O)_8](SO_4)_2 \cdot 2H_2O$ and $[Al_2(OH)_2(H_2O)_8](SeO_4)_2 \cdot 2H_2O$" Acta Chem Scand 16: 403-420; 1962.

(26) R.J. Hurditch, "Electrochromism in hydrated tungsten-oxide films" Electronics Letters 11: 142-144; 1975.

(27) G.A. Parks, "The isoelectric points of solid oxides, solid hydroxides and aqueous hydroxo complex systems" Chem Rev 65: 177-198 (1965)

(28) A.M. Barrett, "Structure and transport properties of some non-crystalline solids", Part II thesis, Oxford University, 1982.

(29) J.H. Smart, "Structural stability of some solid ionic conductors", Part II thesis, Oxford Univerisity, 1981.

(30) D.J. Dzimitrowicz and P.J. Wiseman, "A four-point D.C. method for solid proton conductors", in preparation.

(31) L.D. Kingston, "Structural and transport properties of some non-crystalline solids", Part II thesis, Oxford University, 1981.

(32) O. Nakamura, I. Ogino and T. Kodama, "The water content and humidity ranges of dodecamolybdophosphoric acid and dodecatungstophosphoric acid crystals", Mater Res Bull 15: 1049-1054; 1980.

(33) G. Johansson, "On the crystal structure of the basic aluminium sulphate $13Al_2O_3 \cdot 6SO_3 \cdot xH_2O$", Arkiv Kemi 20: 321-342; 1963.

(34) A. Goiffon, E. Philippot and M. Mauria, "Structure cristalline du niobate 7/6 de sodium $(Na_7)(H_3O)Nb_6O_{19} \cdot 14H_2O$" Rev Chim Mineral 17: 466-470; 1980.

(35) J.S. Lundsgaard, Energy research laboratory, Odense University, private communication.

(36) M.G. Shilton and A.T. Howe, "Rapid H^+-conductivity in hydrogen uranyl phosphate - a solid H^+ electrolyte", Mater Res Bull 12; 701-706; 1977.

(37) S.H. Sheffield and A.T. Howe, "High proton conductivity in pressed pellets of H-montmorillonite, H-Al-montmorillonite and H-Al-Fe-montmorillonite clays", Mater Res Bull 14: 929-935; 1979.

(38) G.C. Farrington and J.L. Briant, "Hydronium beta alumina: a fast proton conductore", Mater Res Bull 13: 763-773; 1978.

(39) W.A. England, M.G. Cross, A. Hamnett, P.J. Wiseman and J.B. Goodenough, "New fast proton conductors", paper presented at Faraday Division Electrochemistry Group Meeting, Oxford, March 28-30, 1979.

(40) W.A. England and R.C.T. Slade, "N.M.R. study of proton transport in crystalline antimonic acid", Solid State Commun. 33: 997-999; 1980.

(41) Y. Piffard, M. Dion and M. Tournoux, "Ion exchange properties of the two phases potassium antimony oxides $K_2Sb_4O_{11}$ and $K_3Sb_5O_{14}$. The protonic conductor $(H_3O)_2Sb_4O_{11}$", C R Seances Acad Sci, Ser C 290: 437-440; 1980.

(42) H. Watelet, J-P. Picard, G. Baud, J-P.Besse and R. Chevalier, "Un nouveau conducteur protonique $[H(H_2O)_n]_{12}Sb_{12}O_{36}$ (n > 1)", Mater Res Bull 16: 1131-1138; 1981.

(43) U. Chowdhry, J.R. Barkley, A.D. English and A.W. Sleight, "New inorganic proton conductors", Mater Res Bull 17: 917-933; 1982.

(44) C.R. Gardner, R. Paterson and D.L. Short, "A study of the self-diffusion coefficients of chloride ion in membranes and particles of hydrous zirconia as a function of variable chloride ion capacity", J Inorg Nucl Chem 34: 2057-2066; 1972.

(45) H. Vandenborre, R. Leysen and L. Baetsle, "Alkaline inorganic-membrane-electrolye (IME) water electrolysis", Int J Hydrogen Energy 5: 165-171; 1980.

(46) M. Lal and A.T. Howe, "High proton conductivity in pressed pellets of zinc-chromium hydroxide" J Chem Soc Chem Commun 15: 737-738; 1980.

(47) Y. Wing, M. Lal and A.T. Howe, "Proton conducting membranes composed of hydronium alunite", Mater Res Bull 15: 1649-1654; 1980.

(48) G. Alberti, M. Casciola, U. Constantino, G. Levi and G. Ricciardi, "On the mechanism of diffusion and ionic transport in crystalline insoluble acid salts of tetravalent metals - I", J Inorg Nucl Chem 40: 533-537; 1978.

(49) W.A. England, "Ionic mobility in inorganic solids", D. Phil Thesis, Oxford University, 1980.

Table 1

particle diameter	n in MO_n
25Å	2.6
100Å	2.15
1000Å	2.015
5000Å	2.003
1µm	2.0015
0.1mm	2.000015

Table 2

Compound	σ(300 K)/ ohm^{-1}/cm^{-1}	E_a(300 K)/ $kJ\ mol^{-1}$
1M HCl	5×10^{-1}	11
$H_3PMo_{12}O_{40}\cdot 29H_2O$	1.7×10^{-1}	15.5
NAFION	5×10^{-2}	
$Sb_2O_5\cdot 5.43H_2O$	7.5×10^{-3}	16.4
$HUO_2PO_4\cdot 4H_2O$	4×10^{-3}	
$In(OH)_3\cdot 1.42H_2O$	3.5×10^{-3}	24.1
$Zn_2Cr(OH)_7\cdot nH_2O$ (46)	6×10^{-4}	
$SnO_2\cdot 2H_2O$	4.1×10^{-4}	19.3
$ThO_2\cdot 4.6H_2O$	4×10^{-4}	20.3
H_3OClO_4	3×10^{-4}	
$H_2Al_3(SO_4)_2(OH)_7$ (47)	3×10^{-4}	
$(H_3O)_2Sb_4O_{11}(H_2O)_{1.1}$	2×10^{-4}	40.5
$HNbO_3\cdot nH_2O$	1.5×10^{-4}	20.9
$Ga_2O_3\cdot 4.15H_2O$	1.3×10^{-4}	33.2
$Zr(HPO_4)_2\cdot H_2O$ (48,49)	$\sim 10^{-4}$	
Montmorillonite	$\sim 10^{-4}$	
$ThO_2\cdot 2.9H_2O$	4×10^{-5}	
$ZrO_2\cdot 1.75H_2O$	2×10^{-5}	33.8
$Cr(OH)_3\cdot 2.7H_2O$	$\sim 10^{-5}$	16.4
$H_3Al(PO_4)_2\cdot H_2O$ (49)	$\sim 10^{-5}$	
$Al(OH)_3\cdot H_2O$	$\sim 6 \times 10^{-8}$	36.3
H_2O	4×10^{-8}	
ice (263 K)	10^{-8}	

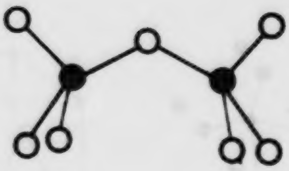

$$Cl_2O_7 + H_2O = ClO_4^- + H_2OClO_3^+ = 2\ HOClO_3$$

$$2HClO_4 + 2H_2O = 2H_3O^+ + 2ClO_4^-$$

Fig. 1 - Hydration of Cl_2O_7. Filled circles, Cl; unfilled circles, O.

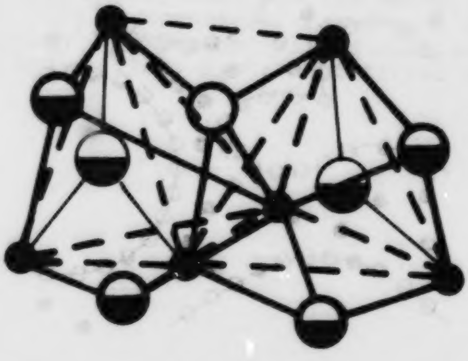

Fig. 2 - Th_6O_7 framework in $[Th_6O(OH)_6(H_2O)_n]^{16+}$. Small filled circles, Th; half-filled circles, OH; open circle, O.

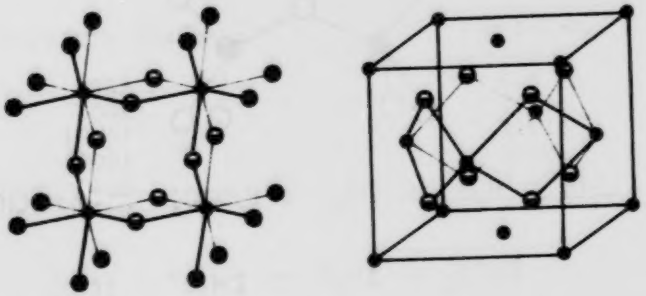

Fig. 3 - $[Zr_4(OH)_8(H_2O)_{16}]^{8+}$ and its relation to the fluorite structure. Small filled circles, Zr; half-filled circles, OH; large filled circles, H_2O

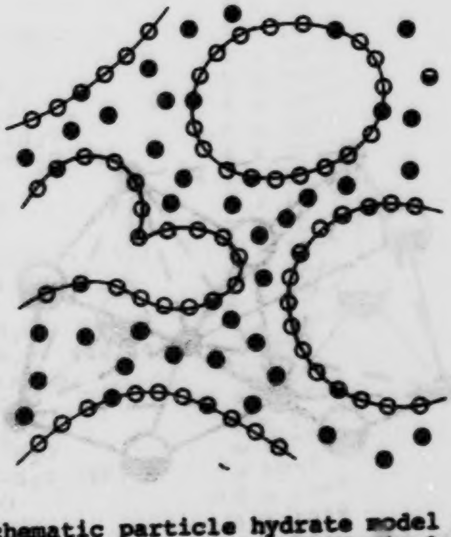

Fig. 4 - Schematic particle hydrate model assuming acidic dissociation. Open circles, O; half-filled circles, OH; filled circles, H_2O; hatched circles, H_3O^+.

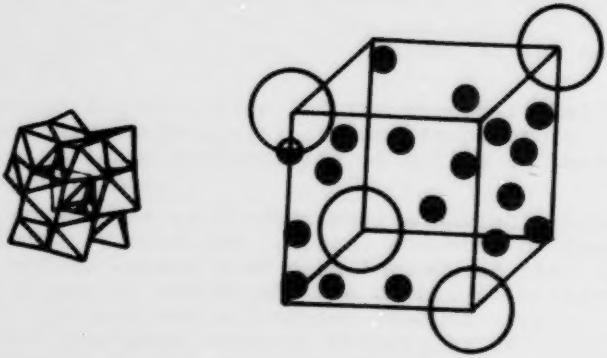

Fig. 5 - $PMo_{12}O_{40}^{3-}$ polyanion and the $H_3PMo_{12}O_{40}\cdot 29H_2O$ structure (schematic). Large open circles, $PMo_{12}O_{40}^{3-}$ polyanion; filled circles, H_2O; hatched circles, H_3O^+; half-filled circle, OH.

Fig. 4 - [illegible]

SOLID SILVER AND COPPER(I) ION CONDUCTORS AND THEIR APPLICATIONS

Takehiko Takahashi

Emeritus Professor of Nagoya University
Nagoya, Japan

ABSTRACT

High ionic conductivity in solid electrolytes at room temperature has been found mainly in silver-ion conductors based on silver iodide and copper(I)-ion conductors which have copper(I) halides as the main constituents.

Altough silver iodide and the copper(I) halides have low ionic conductivity at room temperature, they exhibit high ionic conductivity as solids at relatively high temperatures.

In an attempt to develop solids having a high ionic conductivity at room temperature, a number of foreign cations and/or anions have been introduced into the lattice of silver iodide and the copper(I) halides. As a result, the highest silver-ion conductivity of 0.27 $S.cm^{-1}$ has been found in $RbAg_4I_5$ at 24°C which is synthesized by introducing rubidium ions into the lattice of silver iodide. By incorporating rubidium ions into the lattice of copper(I) chloroiodide, the highest copper(I)-ion conductivity attained at 25°C was 0.34 $S.cm^{-1}$.

In this paper, a review is given of various solid silver- and copper(I)-ion conductors having high conductivity at room temperature. Proposed conduction mechanisms are discussed and some of the applications for these materials are outlined.

KEWORDS: solid silver-ion conductor, solid copper(I)-ion conductor, heat of transport, mixed conductor, potential memory element, capacitor.

RÉSUMÉ

Parmi les semiconducteurs, c'est surtout dans les conducteurs ioniques en argent à base d'iodure d'argent et les conducteurs en cuivre(l) constitués principalement d'halogénures de cuivre que l'on a obtenu jusqu'ici de bonnes conductivités ioniques à la température de la pièce.

L'iodure d'argent et les halogénures de cuivre(l) présentent une faible conductivité ionique à la température de la pièce, mais ils donnent des solides très conducteurs à des températures assez élevées.

Afin d'obtenir des solides ayant une forte conductivité ionique à la température de la pièce, les chercheurs ont tenté d'introduire des cations ou des anions étrangers dans le réseau de l'iodure d'argent ou des halogénures de cuivre(l). La meilleure conductivité ionique de l'argent, 0.27 $S.cm^{-1}$ a été obtenue à 24°C dans le $RbAg_4I_5$, que l'on synthétise en introduisant les ions de rubidium dans le réseau de l'iodure d'argent. En incorporant les ions de rubidium dans le réseau du chloroiodure de cuivre(l), les chercheurs ont obtenu la plus haute conductivité ionique du cuivre(l), 0.34 $S.cm^{-1}$ à 25°C.

L'auteur examine tour à tour divers conducteurs ioniques à base d'argent et de cuivre(l) solides qui ont une bonne conductivité à la température de la pièce; il explique le mécanisme de leur conduction ionique et traite de leurs applications possibles.

INTRODUCTION

Despite the sweeping trend towards solid-state components in the field of electrical engineering, the use of solid-state electrolytes at room temperature has been very limited until recently because materials having a sufficient room-temperature conductivity were discovered only about 20 years ago.

In the early 1960's, Ag_3SI was found to exhibit a relatively high silver-ion conductivity at room temperature. Using this material, a galvanic cell was constructed having a current density of 1-2 mA/cm^2 with no appreciable polarization at room temperature (1). This success was to shed new light on the application of solid electrolytes at room temperature.

Since Ag_3SI was found, a number of solid silver- and copper(I)-ion conductors exhibiting high room-temperature conductivities have been discovered. These conductors are mainly stoichiometric materials having a disordered cationic sub-lattice.

They have been tested for practical applications such as solid electrolytes for solid-state batteries, capacitors, coulometers and other devices.

SOLID SILVER ION CONDUCTORS

General Aspects

In 1914, Tubandt and Lorenz found that the conductivity of solid silver iodide near its melting point was higher than that of the molten material (2). At temperatures lower than 147°C, solid silver iodide is a mixture of the β- and γ-phases. The former has a hexagonal close-packed iodide sub-lattice exhibiting the wurtzite structure whereas the latter is a face-centered cubic structure of the zincblende type. The room-temperature conductivity of silver iodide is $\sim 10^{-6}$ $S.cm^{-1}$; the charge carrier is the silver ion arising from Frenkel disorder of the silver sub-lattice.

Above 147°C, the crystal structure of silver iodide transforms to the high-temperature α-phase which has a body-centred cubic structure of iodide ions. Two silver iodide entities are contained in a unit cell: the two silver ions have been considered to be distributed over the 42 available sites. In this picture of the α-AgI structure, which was developed from the observed intensities of the diffraction lines in the Debye X-ray pattern, the silver ions are considered to be almost free to move three dimensionally suggesting they are in a "quasi-molten" or "liquid-like" state. This is also suggested by the anomolously low entropy of fusion for silver iodide (11.3 J/degree.mol) which is in contrast to the values for the alkali halides that are close to a mean value of 24 J/degree.mol. The value of the entropy of transition of silver iodide from the low- to the high-temperature form at 147°C of 14.5 J/degree.mol (3-5) further suggests that the silver ions exist in a liquid-like state in α-AgI, i.e., the silver ion sub-lattice may be considered to melt at 147°C whereas the remaining iodide sub-lattice collapses at 552°C, the melting point of silver iodide.

In such a structure, the silver ions can be considered to diffuse randomly in the crystal suggesting that a jump-diffusion model for the migration of silver ions can be applied, if the correlation factor can be neglected. In this model, the diffusion process for the transport of ions can be regarded as jumps between lattice sites or interstitial sites for which the diffusion coefficient D_i of the ions i is represented by

$$D_i = L^2/6(\tau_R + \tau_J) \qquad (1)$$

where τ_R is the mean residence time, τ_J the average jump time and L the average jump distance of i. Values for L, τ_{R_0} and τ_J of the silver ions in α-AgI were found to be 5 Å, 7.5 psec and 16.5 psec, respectively, by microwave, far-infrared and quasielastic neutron scattering studies (6,7). Adopting these data, D_i is calculated by equation (1) to be $1.8.10^{-5}$ $cm^2.sec^{-1}$. The ionic conductivity σ_i is given by the relation

$$\sigma_i = C_i D_i Z_i^2 F^2/RT \qquad (2)$$

where C_i is the concentration of mobile ions and Z_i their valency. From equation (2), σ_i is calculated to be 1 $S.cm^{-1}$ at 250°C assuming all the silver ions are mobile. The measured conductivity of silver iodide at 250°C is 1.7 $S.cm^{-1}$.

Though some modifications to the simple model above may be necessary, fairly good agreement is obtained between the magnitude of the measured ionic conductivity and the value predicted by this model. This may suggest that all the silver ions in α-AgI are almost free to move and that most of the jump attempts are successful. However, the difference between the calculated and measured conductivities suggests that the silver ions do not move isotropically in α-AgI and that the correlation factor can not be neglected.

According to EXAFS measurements (8), τ_R has been found to be larger than τ_J contrary to the results from the quasielastic neutron scattering study; also, a shorter jump distance (L) has been estimated (close to the nearest neighbour 12(d) sites), i.e., 1.79 Å (9).

Accordingly, there is some difficulty in applying the simple jump-diffusion model to α-AgI.

Neutron diffraction analysis has indicated that the silver ions are found preferentially in oblong ellipsoidal regions or spaces centred at the tetrahedral 12(d) sites and that there is a large anharmonic contribution to the thermal vibrations in the direction of the octahedral 6(b) sites, suggesting that the <100> directions should be regarded as channel-like diffusion paths for the silver ions (6). As the 12(d) sites are the furthest away from the iodide ions, they have the minimum potential energy. The vibration of the silver ions is coupled with that of the iodide ion sub-lattice and the silver ions can move in the direction of the (b) sites, i.e., in the <100> direction, with a fairly short relaxation time. However, other work has shown that the silver ions do not move in <100> but in <110> directions which are also the directions connecting the nearest neighbour 12(d) sites (9). In any case, the silver ions are considered to be at the centre of the iodide-ion polyhedra which share faces successively with each other to form the silver-ion conducting passageways.

In contrast, the low-temperature modification, β-AgI, which has a hexagonal structure, has each silver ion co-ordinated by an iodide tetrahedron, resulting in a low silver-ion conductivity (10). In β-AgI, however, a passageway for the interstitial silver ions can be considered to form geometrically by sharing faces successively between iodide tetrahedra and octahedra. These interstitial silver ions, however, will not contribute to the conductivity as only 1% of the total silver ions present occupy the centre of the above octahedra even at 140°C.

Another low-temperature polymorph, γ-AgI, is formed at room temperature by the addition of an aqueous $AgNO_3$ solution which is in excess of the stoichiometric proportion to precipitate silver iodide. This polymorph is known to have a disordered structure at room temperature (11) and though it has a conductivity of $\sim 10^{-3}$ $S.cm^{-1}$ at room temperature, it is readily affected by heat.

Accordingly, to develop a silver-ion conductor based on silver iodide that has a high conductivity at room temperature, the iodide polyhedra in β-AgI need to share faces with at least neighbouring polyhedra to result in a network of conducting paths as in α-AgI. Hence, foreign anions or cations have been incorporated in the silver iodide lattice to increase the degree of face sharing by the iodide-ion polyhedra. This reduces the number of iodide ions compared with the number of silver ions in β-AgI or it co-ordinates a greater number of iodide ions to the incorporating foreign cation than to the silver ion.

Partial Substitution of the Iodide Ions in Silver Iodide with Foreign Anions

The first success in developing a solid with high ionic conductivity at room temperature was achieved by introducing the sulphide ion into the lattice of silver iodide (12). If an equi-molar mixture of silver iodide and silver sulphide is reacted together at ∿550°C, the compound Ag_3SI is obtained which has a high silver-ion conductivity of 10^{-2} $S.cm^{-1}$ at 25°C. This material transforms from the β- to the α-phase at 225°C. The low-temperature β-form, has a simple cubic structure (with a lattice constant of 4.897 Å) in which the sulphide ion is at the centre of the cube and the silver ion is distributed among four positions 0.5 Å apart from the centre of each face of the cube in the <100> direction (13). There is one Ag_3SI in a unit cell and the three silver ions are distributed statistically over 12 available interstitial sites in the (100) plane of the cube to give β-Ag_3SI a high silver ion conductivity like α-AgI.

Significant electronic conductivity is developed in Ag_3SI with deviations from stoichiometry. To retain a low electronic conductivity, the Ag_3SI must be synthesized by heating the silver iodide and silver sulphide reagents under a high vapour pressure of sulphur. For example, when the reagents are heated for 17 hours at 550°C under a sulphur pressure of one atmosphere, an electronic conductivity as low as 10^{-8} $S.cm^{-1}$ is obtained at room temperature (1). Thus Ag_3SI is a good silver-ion conductor at room temperature except for its disadvantage of being decomposed by iodine with a resulting decrease in its conductivity (14).

Stimulated by this success, oxyacid ions have been introduced into the silver-iodide lattice in an attempt to obtain solids with a high silver-ion conductivity at room temperature. Up to the present, BO_2^- (15,16), PO_3^- (17), VO_3^-(18), NbO_3^-(18), SeO_4^{2-}(19,20), TeO_4^{2-}(20), CrO_4^{2-}(21-23), WO_4^{2-}(16,21-25), MoO_4^{2-}(16,21-23,26-31), $Mo_2O_7^{2-}$(26,31), $Cr_2O_7^{2-}$(20,31-33), SO_4^{2-}(34), PO_4^{3-}(35-37), AsO_4^{3-}(31,38), VO_4^{3-} (38), and $P_2O_7^{4-}$ (20,35-37,39) were found to be effective in giving high ionic conductivity to silver iodide at room temperature. When cooled rapidly from their melts, most of these systems have a tendency to form glasses which tend to crystallize when annealed for a long time, thereby decreasing their conductivities somewhat in many cases. For example, in the AgI-Ag_2MoO_4 system, the conductivity and activation energy for conduction decrease when the system is crystallized as shown in Fig. 1. The figure also shows that the conductivity increases as the concentration of silver iodide increases; at the same time, the glass transition temperature, Tg, decreases. In most cases, crystallization begins in the range from 60-70°C, however, the AgI-Ag_2WO_4 system is exceptionally stable up to the melting point, ∿300°C.

Figure 2 shows the silver-ion conductivity of the AgI-Ag_2WO_4 system in its crystalline form obtained by Takahashi et al. (24). The materials were obtained by heating a mixture of silver iodide and silver tungstate at 400°C under vacuum for ∿18 hr followed by slow cooling to room temperature. The highest room-temperature conductivity is found for material containing 20 mole% silver tungstate which corresponds to $Ag_6I_4WO_4$. The highest conductivity for the crystalline form is $4.7.10^{-2}$ $S.cm^{-1}$ and its activation energy for conduction is 15 kJ/mole. The conductivity is somewhat lower than that for the glassy form, but the difference is not as large as in the molybdate system shown in Fig. 1. This is also the case in the pyrophosphate system in which the highest room-temperature conductivity of 9.10^{-2} $S.cm^{-1}$ is obtained for $Ag_{19}I_{15}P_2O_7$ that has an activiation energy for conduction of 13 kJ/mole (35).

In the tungstate system, the compound which has the highest silver-ion conductivity is considered to be $Ag_{26}I_{18}W_4O_{16}$ not $Ag_6I_4WO_4$ (40-42). This discrepancy has not been resolved. Geller et al., have determined the crystal structure of $Ag_{26}I_{18}W_4O_{16}$ and shown that there are two entities in a monoclinic unit cell that contains 88 iodide tetrahedra and two octahedra sharing faces to provide a three-dimensional network for the movement of the silver ions. Two tetratungstate ions in a unit cell are surrounded by 120 polyhedra formed by iodide and oxide ions, eight of which are octahedra fully occupied by silver ions, and the remaining 112 polyhedra are tetrahedra or five-cornered polyhedra. Of these polyhedra, 56 share faces with the iodide polyhedra to form the silver-ion conducting passageways. The total number of mobile silver ions is 23.2, i.e., 44.5% of the silver ions in a unit cell.

Glassy silver-ion conductors have also been found in the systems AgX(X=I,Br)-$AgPS_3$ (17), AgI-Ag_2S-As_2S_3 (43) and Ag_2S-GeS_2 (44). The highest conductivities of $2.5.10^{-2}$ $S.cm^{-1}$, 3.10^{-2} $S.cm^{-1}$ and $1.35.10^{-3}$ $S.cm^{-1}$ have been found at 25°C for the compositions 0.65AgI-0.35$AgPS_3$, 0.65AgI-0.35$AgAsS_2$ and 0.55Ag_2S-0.45GeS_2, respectively.

Partial Substitution of the Silver Ions in Silver Iodide with Foreign Cations

The alkali metal ions such as Rb^+, K^+, NH_4^+ (45-49), the organic substituted ammonium ions (50-55), the sulphonium and selenonium ion (56,57) and the carbonium ions (58) have effectively been introduced into the lattice of silver iodide to give solids with a high silver-ion conductivity at room temperature.

Of these conductors, $RbAg_4I_5$ is known to exhibit an ionic conductivity of $2.7.10^{-1}$ S.cm^{-1} at 24°C. This material has a simple cubic structure in which the iodide ions are arranged as tetrahedra and interconnected by the sharing of faces so that there are continuous channels of connected iodide tetrahedra extending throughout the crystal. The silver ions are located in the centres of these tetrahedra and easily diffuse through the tetrahedra faces to adjoining tetrahedral sites. The ratio of tetrahedra to silver ions is 3.5 which means that there are 2.5 empty sites adjacent to each occupied site thereby permitting fast ion diffusion (59). Figure 3 shows the variation of conductivity with reciprocal temperature for some the alkali-ion-doped silver iodides.

Ammonium ions in which the hydrogen is replaced by various organic radicals have also been effectively introduced into the lattice of silver iodide to obtain solids with a high room-temperature conductivity. For example, double salts of substituted ammonium iodide QI and silver iodide are prepared by the reaction $QI + nAgI \longrightarrow QAg_nI_{n+1}$ in an inert atmosphere at temperatures between 125° and 165°C. Also the organic substituted ammonium iodides: tetraalkylammonium iodide, saturated and unsaturated azacyclic substituted ammonium iodide, and polyquaternaryammonium or polyamine iodide have been effectively reacted with silver iodide. From a study of the variation of room-temperature electrical conductivity with composition for tetraalkylammonium silver iodide reported by Owens (50), it was found that the highest conductivity occurs at ~87 mole% AgI suggesting that the empirical formula for this material is close to QAg_7I_8. The charge carriers are silver ions and the electronic conductivity is only $\sim 10^{-10}$ S.cm^{-1} at room temperature.

The structural investigation of the Me_4NI-AgI system has been carried out by Geller and Lind (60), who found the composition of tetramethylammonium silver iodide to be $[(CH_3)_4N]_2Ag_{13}I_{15}$. In this compound, the hexagonal unit cell contains three entities and there are eight crystallographically nonequivalent sets of sites for the silver ions, that is, six 18 fold sets, one 6 fold set, and one 9 fold set. Thus 39 silver ions are distributed, though nonrandomly, over 123 available sites. The iodide ions are at the corners of face sharing tetrahedra. These tetrahedra are connected to create two kinds of channels. One of them ends at the crystal surfaces and may serve for the diffusion of the silver ions through the crystal.

The pyrrolidinium, piperidinium, and quinuclidinium groups and the pyridinium and quinolinium groups of the substituted ammonium iodide have also been found by Owens et al. (51) to give conductive solid electrolytes when combined with silver iodide. In the former groups, the highest silver ion conductivity has been found for the 1,1-dimethylpyrrolidinium iodide-silver iodide system ($C_7H_{16}NI{\cdot}8AgI$) with $6.3{\cdot}10^{-2}$ $S.cm^{-1}$ at 22°C. In the latter groups, the pyridinium iodide-silver iodide adduct ($C_5H_6NI{\cdot}8AgI$) has been found to show the highest silver ion conductivity of $4{\cdot}10^{-2}$ $S.cm^{-1}$ at 22°C. The structure of the C_5H_6NI-AgI electrolyte has been determined by Geller (61) and Geller and Owens (62) who found the stoichiometric composition of $(C_5H_5NH)Ag_5I_6$. In this compound, the iodide ions are arranged to show two sets of tetrahedra, 24(m) and 6(f) and one set of octahedra, 4(c) in a unit cell. These polyhedra are interconnected by sharing faces which form channels. In the hexagonal unit cell, there are two $(C_5H_5NH)Ag_5I_6$ groups and the ten silver ions are distributed over 34 available sites. The site occupancy of the silver ions is 4% of the 24(m) sites, 91% of the 6(b) sites and 89% of the 4(c) sites at 23°C. The ratio of the polyhedra to the silver ions is 3.4 which means that there are 2.4 empty sites available for the silver ions and the silver ions can diffuse three dimensionally through the tunnels.

In general, the structural investigations have shown that the cation-substituted silver iodides contain face-sharing polyhedra formed by the iodide ions and the silver ions diffuse through the resulting pathways (63). Figure 4 shows the temperature dependence of conductivity for five of the QI-AgI electrolyte systems. Further, divalent- and trivalent-substituted ammonium iodides have been found by Berardelli et al. (52) to combine with silver iodide giving high silver-ion conductivity at room temperature. Coetzer and Thackeray (53,55) have found that some quaternary polyamine iodide-AgI electrolytes have conductivities varying from $2.3{\cdot}10^{-1}$ to $10.9{\cdot}10^{-1}$ $S.cm^{-1}$ at 20°C. These are the hexamethyl alkylenediamine diiodide-AgI and the heptamethyl hydrodiethylene triamine triiodide-AgI systems. The highest conductivities are obtained at silver iodide concentrations from 86-94 mole%. According to the structural analysis, the iodide ions form a framework of face-sharing polyhedra (generally tetrahedra) which provide continuous channels for the movement of the silver ions which reside within the iodide polyhedra but are distributed non-randomly throughout the crystals at room temperature. The positively charged ammonium ions stabilize the iodide-ion lattice or combine with the iodide ions forming additional polyhedra.

Highly conductive silver-ion electrolytes have been found by Takahashi et al. (56) and Linford et al. (57) in the RSI-AgI systems in which high conductivity is developed inthe alkyl and alkylene substituted sulphonium iodides. For example, in the $C_5H_{11}SI$-AgI, Me_3SI-AgI and Me_2EtSI-AgI systems, the highest conductivities, obtained at 84 mole%, were 4.10^{-2}, 6.10^{-2} and 2.10^{-2} $S.cm^{-1}$, respectively, at 25°C. Linford et al. have found high conductivity in the bis-sulphonium iodide-AgI and the trimethyl selenonium iodide-AgI systems represented by the general formulas $(CH_3)_2S^+(CH_2)_nS^+(CH_3)_2$ $2I^-\cdot xAgI$, where n is 3,4 or 5 and $(CH_2)S^+(CH_2)_nS^+(CH_2)_m$ $2I^-\cdot xAgI$ where m is 4 or 5 and n is 2 or 3 or $(CH_3)_3SeI\cdot xAgI$. The highest conductivities have been found for $Ag_{13}(CH_3)_2S(CH_2)_3S(CH_3)_2I_{15}$ to be 10^{-2} $S.cm^{-1}$ and for $(CH_3)_3SeI$-85 mole% AgI to be 4.10^{-3} $S.cm^{-1}$ at room temperature.

Christie et al. (58) have found a high silver-ion conductivity of 6.10^{-3} $S.cm^{-1}$ at 22°C in the tropyllium iodide (C_7H_7I)-AgI system for 80-85 mole% AgI.

Partial Substitution of the Silver and Iodide Ions in Silver Iodide with Foreign Cations and Anions

Highly conductive silver-ion electrolytes have been obtained by introducing the mercuric ion and the chalcogenide ions such as sulphide, selenide and telluride ions into the lattice of silver iodide (64-68). These electrolytes are compounds having a body-centred cubic structure. However, only in the case of the sulphide-ion containing materials is the α-AgI structure to be found in which 2.25 silver ions are distributed statistically over 42 available sites. The other compounds have a diffraction symmetry of m3m and the number of available sites for silver ions in a unit cell is not 42 but 30, i.e., the 6(b) and 24(h) sites. The mercuric ions do not contribute to the conductance. In Fig. 5 the plots of silver-ion conductivities are shown against the reciprocal of the absolute temperature.

Mellors et al. (69,70) have found that the introduction of the potassium or rubidium ion and the cyanide ions is effective in giving high silver-ion conductivity. For example, a conductivity of $1.4.10^{-1}$ $S.cm^{-1}$ is obtained for the composition 4AgI.KCN with an activation energy for conduction of 8.1 kJ/mole.

Heats of Transport of Silver Ions

In general, the thermoelectric power θ of high conductivity solid electrolytes is given by

$$e\theta = -q^*/T + S - k\ln C_+$$

where q^* is the heat of transport, C_+ the concentration of the vacant sites of the mobile ions. S is the sum of the entropy in the electrode and the temperature gradient of the standard chemical potential of the mobile ions. In most cases, as $S-k\ln C_+$ and q^* are considered to be independent of temperature, $e\theta$ is represented as a straight line against $1/T$ giving q^* from its slope.

The highly conductive silver-ion electrolytes may be classified by comparing the heats of transport for the silver ions with the activation energy for their conduction, Table 1 (71-79). The heats of transport for silver ions in α-AgI and in the inorganic anion- and cation-substituted silver iodides have almost the same values as the activation energies for silver-ion conduction. Whereas, in the alkyl ammonium iodide-silver iodide systems, the heats of transport for silver ions are smaller than the activation energies. From these results, one may conclude that the silver ions in alkylammonium substituted silver iodide are not all mobile (e.g., for substantial polaron coupling) but need some extra energy as is also required in conventional ionic solids. Of these conductors, the pyridinium salt ($(C_5H_6N)Ag_5I_6$) shows an exceptional relationship between the thermoelectric power and the reciprocal of the absolute temperature which indicates that C_+ may be dependent on temperature. From an analysis of the crystal structure of $(C_5H_6N)Ag_5I_6$ (62), C_+ can be evaluated at each temperature. In this case, a plot of $e\theta + k\ln C_+$ against $1/T$ has been shown to be a straight line from the slope of which q^* has been found to be 0.17 eV which is in good agreement with the activation energy for conduction, 0.16 eV (50°-100°C).

Applications of Silver Ion Conductors

Solid silver-ion conductors have been tested as electrolytes for solid batteries, energy storage devices, electrochromic displays and other electrochemical devices. However, as silver is rather expensive, only a few devices have been developed commercially. For example, a proportional timer, a memory element with read-out and an electrical integrator with long-term stability characteristics have been developed and are commercially available. One of the practical configurations of a memory element named Memoride is shown in Fig. 6 (80). One electrode is silver and the counter or signal input electrode and the reference or voltage detection electrode are of a silver ion-electron mixed conductor. The amount of electricity input to the device is memorized as a change in activity of the silver in the silver input electrode and can be determined by measuring the voltage between this electrode and the detection electrode. The mixed conductor electrode must have high ionic and electronic conductivities at room temperature.

The high temperature α-phases of the silver chalcogenides have high ionic and electronic conductivities. At room temperature, however, they exist as the β-phases which have very low ionic conductivities (81).

In order to obtain a solid with a high ionic and electronic conductivity at room temperature, the orthophosphate or pyrophosphate ion has been successfully introduced into the lattice of silver chalcogenides. In Table 2, typical examples are listed showing their ionic conductivities at 25°C. The electronic conductivity is about two orders of magnitude higher than the ionic conductivity. The first one in the Table has an α-silver selenide like structure (82) and the second and third solid solutions have α-silver sulphide like structures (83). Of these solid solutions, $(Ag_2Se)_{0.925}\cdot(Ag_3PO_4)_{0.075}$ exhibits the largest silver activity change for a deviation r from the composition equilibrated with silver (82). In Fig. 7, a coulometric titration curve for $(Ag_2Se)_{0.925}(Ag_3PO_4)_{0.075}$ at 95°C is illustrated where E is the potential difference between the platinum electrode and one of the silver electrodes in the cell

$$Ag|RbAg_4I_5|(Ag_2Se)_{0.925}\underset{\overset{\uparrow}{Pt}}{}(Ag_3PO_4)_{0.075}|RbAg_4I_5|Ag$$

Reproducible results have been obtained up to a potential of 160 mV for both the addition and removal of silver. Similar curves are obtained in the range from room temperature to 100°C. In the commercially available device, the $AgI-Ag_2WO_4$ system is used as the electrolyte. A high reproducible voltage change is obtained between the reference electrode and the signal input electrode in the charging and discharging process from 0 to 120 mV. Thus the quantity of electricity input or output can be memorized in the form of voltage. For example, a device having a rated capacity of 50 μAh can be charged with 40 mA in a few seconds and can act as a timer for many hours. This element can be operated over the temperature range from -20° to +60°C for up to 10^6 charge-discharge cycles and the readout deviates from the correct number of input coulombs by 5.5% at the most. These elements have been developed by S. Electric Co., Japan (80) and are also recommended for use as an integrating or memory device which can detect temperature, noise, light and other physical quantities. Other applications such as a variable resistor with memory, and a solid-state display system have been proposed (80).

SOLID COPPER(I) ION CONDUCTORS

Partial Substitution of the Copper Ions in Copper(I) Halide with Foreign Cations

Because of the similarities in the properties of the silver ion and the copper(I) ion, attempts have been made to synthesize solid copper(I) ion conductors, having a high room-temperature ionic conductivity, by incorporating foreign ions into the lattice of copper(I) halides.

High conductivity copper(I) ion conductors, stable at room temperature, were synthesized by introducing organic substituted ammonium halides into the lattice of copper(I) halides and first reported by Takahashi et al. (84), Takahashi and Yamamoto (85) and Lazzari et al. (86). Figure 8 shows the copper(I) ion conductivies of the bicyclic ammonium halides-copper(I) halides system.

High copper(I) ion conductivity has also been obtained in the tricyclic ammonium halides-copper(I) halides system where the highest room temperature conductivity appears in the bromide system. These conductors are not solid solutions but compounds and they are prepared by heating the corresponding mixtures at 100°-150°C. In addition to solid state reaction, they can also be synthesized by co-precipitation from aqueous solutions. The transport number of the copper(I) ion in these conductors has been found to be almost unity. The reason why these substituted ammonium halides give rise to high copper(I) ion conductivity at room temperature has not yet been clearly understood. However, in the bromide system, it has been recognized that the size of the substituted ammonium ions has to be about 4.7 Å to obtain high conductivity at room temperature. The ion size here means the length of the minor axis of the ellipse.

The heat of transport for the copper(I) ions in these organic substituted ammonium bromide-copper(I) halide systems has always been found to be smaller than their activation energy for conduction (87). This suggests that the migration mechanism of the copper(I) ions in these conductors may be considered to be similar to that of the silver ions in most of the organic ion substituted silver ion conductors.

Further, copper(I) ion conductors having a high conductivity at room temperature have been found by Sammells et al. (88), Takahashi et al. (89) and Shemilt et al. (90) using organic substituted ammonium halides such as the quinuclidine, quinuclidone, pyridine, piperidine and morpholine derivatives that may be considered to be flexible structures. In contrast, no materials with a high conductivity at room temperature have been obtained by introducing, for example, N-methyl pyrrolidinium ions which have a planar structure or tetramethyl ammonium ions which have a rigid tetrahedral structure. This result differs from that obtained with the silver ion conductors.

Chan et al. (91) have analysed the crystal structure of $(C_5H_5NH)_2Cu_5Br_7$, which has a conductivity of $1.7.10^{-2}$ $S.cm^{-1}$ at 19°C. The orthorhombic unit cell contains four entities and the 20 Cu^+ ions are distributed non-uniformly over 52 tetrahedral sites. The bromide tetrahedra share faces in such a manner that undulating channels are formed in the <100> and <010> directions, and right- and left-handed helical channels are formed in the c-direction. The channels are interconnected thereby forming a three-dimensionally conducting solid electrolyte. A detailed examination of the conduction pathways and Cu^+ ion site occupancies leads to the prediction that the conductivity in the b-direction should be somewhat higher than that in the a-direction, and that the conductivity in the c-direction will be substantially lower than in the a-direction. The lattice parameters are $a=13.09\pm0.03$ Å, $b=14.04\pm0.03$ Å and $c=11.78\pm0.02$ Å.

Further high conductivity copper(I) ion conductors have been found in the $CuI-C_5H_{10}SCH_3I$ and $CuI-C_4H_8OSCH_3I$ systems by Takahashi et al. (92) and Dahm et al. (93). The highest conductivity at 25°C of $1.4.10^{-3}$ $S.cm^{-1}$ has been found in the $CuI-C_5H_{10}SCH_3I$ system having 83.4 mole% CuI.

When inorganic cations are introduced into the lattice of copper(I) halides, the rubidium chloride-copper(I) chloride system (87,94) has been found to show high room temperature conductivity. The charge carriers were proved to be copper(I) ions and the highest conductivity was found in the compound $Rb_3Cu_7Cl_{10}$. Matsui and Wagner (94,95) showed, however, that the compound with the highest copper(I) conductivity is not $Rb_3Cu_7Cl_{10}$ but $RbCu_3Cl_4$ which has a conductivity of $2.25.10^{-3}$ $S.cm^{-1}$ at 25°C.

An interesting group of copper(I) ion conductors, found by von Alpen et al. (96), is represented by CuTeX (X=Cl,Br,I). In Fig. 9 their conductivities are shown against the reciprocal of the absolute temperature. These compounds crystallize with tetragonal symmetry. In CuTeX, the infinite fourfold tellurium helices are arranged parallel to the c-axis and X_4-tetrahedra are linked into unlimited chains along the c-axis by sharing sides. Within the chains, this mode of X_4-tetrahedra offers three symmetrically independent positions for tetrahedrally coordinated atomic sites which are found to be statistically occupied by the copper(I) ions. The electronic conductivity at room temperature is $\sim10^{-8}$ $S.cm^{-1}$.

Partial Substitution of the Copper(I) and Halide Ions with Foreign Cations and Anions

The most successful results have been obtained in the copper(I) iodide-rubidium chloride system. The highest conductivity has been found for $Rb_4Cu_{16}I_7Cl_{13}$ and first reported by Takahashi et al. (97). In Fig. 10 its conductivity is shown as a function of the reciprocal of absolute temperature. The unit cell of this compound has a cubic symmetry with a lattice parameter of 10.0±0.01 Å. The copper(I) ionic conductivity of $3.4.10^{-1}$ $S.cm^{-1}$ of this compound at 25 °C is the highest ionic conductivity ever found at room temperature in the solid state. Geller et al. (98) have maintained their opinion that the high conductivity material in this system must be $RbCu_4Cl_3I_2$ which is considered to be isostructural with $RbAg_4I_5$ and has also been studied by Vershinin et al. (99,100). Geller et al, observed a solid solution range in the cubic phase having the composition $RbCu_4Cl_{3+x}I_{2-x}$ $(0\leq x\leq 0.40)$ (101,102). They found $RbCu_4Cl_3I_2$ to be thermodynamically stable in the narrow temperature range $200^{\circ}\pm15^{\circ}C$ and the solid solution $RbCu_4Cl_{3+x}I_{2-x}$ $(0.02\leq x\leq 0.40)$ to be stable from at least 78k to the preparaton temperature which depends on x. The highest conductivity of $RbCu_4Cl_3I_2$ measured by Kleitz et al. (103) was $4.75.10^{-1}$ $S.cm^{-1}$ at room temperature but the conductivity is unstable and tended towards lower values, whereas the conductivity of $Rb_4Cu_{16}Cl_{13}I_7$ ($x=0.25$ in $RbCu_4Cl_{3+x}I_{2-x}$) at room temperature was $3.6.10^{-1}$ $S.cm^{-1}$ and stable with the activation energy for conduction of 0.045 eV. Tokumoto et al. (104) have pointed out that the x value is not in the range $0\leq x\leq 0.40$ but only $0.125\leq x\leq 0.25$ before other compounds segregate. Takahashi et al. (105) have determined the phase diagram of the CuCl-CuI-RbCl system and found that $Rb_4Cu_{16}Cl_{13}I_7$ has a narrow solid solution range of $Rb_4Cu_{16}Cl_{13-x}I_{7+x}$ $(-0.2\leq x\leq 0.5)$ with a lattice constant ranging from 10.008 to 10.022 Å and conductivities varying from $3.7-2.8.10^{-1}$ $S.cm^{-1}$ at 25 °C. Chaney et al. (106) measured the electronic conductivity of $Cu_{16}Rb_4I_{7+x}Cl_{20-(7+x)}$ $(0\leq x\leq 1)$ to be 5.10^{-16} $S.cm^{-1}$ at room temperature. Actually, the open circuit voltage of the cell $Cu.Rb_4Cu_{16}I_7Cl_{13}|Rb_4Cu_{16}I_7Cl_{13}|Cu_{1.75}Se$ was found to be stable by Takahashi et al. (107) while the open circuit voltage of the cell with $RbCu_4I_2C_{13}$ as the electrolyte is unstable as shown in Fig. 11. This indicates the $RbCu_4I_2Cl_3$ is unstable at room temperature. Turkovic et al. (108) have found that exposure of $RbCu_4Cl_3I_2$ to the atmosphere causes the formation of $RbCuO_2$, $RbClO_4$, CuI and CuCl.

Geller et al. (98) and Turkovič et al. (108) have determined the crystal structure of $RbCu_4Cl_3I_2$ at 25 °C and found the lattice constants to be a=10.032±0.003 Å in the former study and 10.008 Å in the latter study.

In this material, there are three sets of tetrahedral sites for copper(I) ions with a total of 56 sites. All the tetrahedra have both Cl$^-$ and I$^-$ ions at apices but the co-ordination polyhedra for the Rb$^+$ ions contain only Cl$^-$ ions. The occupancies of the two sets of 24-fold sites are almost equal but that of 8-fold sites is still very low and thus the overall distribution is non-uniform. Tokumoto et al. (104) have found that $Rb_4Cu_{16}I_7Cl_{13}$ is most readily obtained as a single phase in agreement with the work of Takahashi et al. (97). However, the X-ray diffraction patterns showed that the compounds $RbCu_4I_{2-x}Cl_{3+x}$ $(0.125 \leq x \leq 0.25)$ have a cubic symmetry with a systematic extinction for the (h00) lines ($h \neq 4n$ where n is an integer) showing that the crystal structure belongs to the space group of the enantiomorphic pair $P4_332$ and $P4_132$ which can be realized with the formula $RbCu_4I_2Cl_3$ as indicated by Geller et al. (98) and Turkovič et al. (108). This result conflicts with the composition for the single phase compound. Tokumoto et al. (104) have suggested that one of the ways to resolve the conflict is to consider that the compound is stabilized by a partial random substitution of anions.

Geller et al. (109) have found that $NH_4Cu_4Cl_3(I_{2-x}Cl_x)$ is isostructural with $RbAg_4I_5$ in the range $0.09 \leq x \leq 0.13$ and for the composition of $x = 0.33$ has a room temperature conductivity of $2.1.10^{-1}$ S.cm^{-1} when freshly prepared. These electrolytes are not stable thermodynamically except at temperatures between 130°C and their melting points of ∿170°C. Geller et al. (110) have found a conductivity of $7.6.10^{-1}$ S.cm^{-1} in $CsCu_4Cl_3I_2$ at 158°C.

Applications of Copper(I) Conductors

These materials will be exploited in the same manner as the silver ion conductors. For example, the following galvanic cells have been proposed:

$Cu|7CuBr.C_6H_{12}N_4CH_3Br|Se(S,Te)$ (111)
$Cu|47CuBr.3C_6H_{12}N_22CH_3Br|Cu_{1.8}S$ (85,111) or TiS_2 (112)
$Cu|Rb_4Cu_{16}I_7Cl_{13}|Cu_{1.75}Se$ (107)

The open circuit voltages of these cells are 0.373, 0.470 and 0.268V, respectively. Figure 12 shows the discharge curves of the last cell with constant loads. In most cases, the anodic polarization is predominant.

Some copper(I) ion conductors have been tested as electrolytes in capacitors and other devices. For example, Sekido and Ninomiya (113) proposed a solid state double layer device using $7CuBr.C_6H_{12}N_4CH_3Br$ and $Rb_2Cu_8I_3C_{17}$ as electrolytes. The configuration of the proposed capacitor is represented as $C|Rb_2Cu_8I_3Cl_7|Cu.$-Cu_2S. When a voltage lower than the decomposition voltage is applied between the C anode and Cu electrode, the anions are in excess in the vicinity of the anode. This makes the positive charge accumulate at the anode in order to compensate the excess negative charge thereby forming a double layer at the C anode and forming a capacitor. In this device, Cu_2S is used for the reference and voltage detection electrode. A similar device, developed using a silver-ion conductor, has been studied by Sekido and Ninomiya (113).

SUMMARY

Solids exhibiting high ionic conductivity at room temperature have been limited to silver and copper(I) ions conductors. In these conductors, the fast migration of the ions requires interconnected channels in which the ions partially occupy lattice sites having essentially equal site occupation energies, and the activation energies for ion jumps from one site to another are small. The activation energy for ionic diffusion, which corresponds roughly to the barrier height between adjacent sites for uncorrelated ionic motion, must be a function of size or polarizability of the ion and cross section of the path. In the case of silver and copper(I) conductors, these factors must be in conformity with a low diffusion barrier height to some extent. The future effort in developing new high conductivity solid silver and copper(I) ion conductors must concentrate on finding the critical match between these two factors. The discovery of new solid silver and copper(I) ion conductors exhibiting much higher conductivity at room temperature must lead to more widespread practical applications. It is expected that this will be achieved to some extent in the near future.

REFERENCES

(1) T.Takahashi and O.Yamamoto, "The $Ag|Ag_3SI|I_2$ solid electrolyte cell" Electrochim Acta 11:779-787; 1966. "Polarization of the solid electrolyte cell $Ag|Ag_3SI|I_2$" ibid 11:911-917; 1966.

(2) K.Funke, "AgI-type solid electrolytes" Progress Solid State Chem 11:345-402: 1976.

(3) M.O'Keeffe, "Cooperative aspects of ionic motion" in "Fast Ion Transport in Solids" Ed W.van Gool,p. 233-247; 1973,North-Holland Publ Co, Amsterdam.

(4) M.O'Keeffe and B.G.Hyde, "The solid electrolyte transition and melting in solids" Phil Mag 33:219-224; 1976.

(5) W.Van Gool, "Introduction to the theory of solid electrolytes" in "*Solid Electrolytes*" Ed P.Hagenmuller and W.van Gool, p.9-26; 1973,Academic Press, New York.

(6) K.Funke, "AgI-type solid electrolytes:Properties at frequencies between 10^9 and 10^{13} Hz" in "*Superionic Conductors*" Ed G.D.Mahan and W.L.Roth, p.183-199; 1976, Plenum Publ Corp, New York.

(7) G.Ecbold,K.Funke,J.Kalus and R.E.Lechner, "Cation motion in α-silver iodide" *Phys Letter* 55A:125-126; 1975.

(8) J.B.Boyce and T.M.Hayes, "Structure and its influence on superionic conduction:EXAFS studies" in "*Physcs of Superionic Conductors*"Ed M.B.Salamon,p. 5-44; 1979,Springer-Verlag, Berlin Heidelberg.

(9) S.Hoshino,T.Sakuma and Y.Fujii, "Distribution and anharmonic thermal vibration in α-AgI" *Solid State Commun* 22:763-765; 1977.

(10) D.O.Raleigh, "Structural principles for silver halide superionic conductors" *J Electrochem Soc* 124: 1157-1160: 1977.

(11) T.Takahashi,K.Kuwabara and O.Yamamoto, "The electrical conductivity and crystal structure of silver iodide" *ibid* 116:357-360; 1969.

(12) T.Takahashi, "Solid silver ion conductors" *J Appl Electrochem* 3:79-90; 1973.

(13) S.Hoshino,T.Sakuma and Y.Fujii, "A structural phase transition in super ionic conductor Ag_3SI" *J Phys Soc Japan* 47:1252-1259; 1979.

(14) B.B.Owens,G.R.Argue,I.L.Groce and L.D.Hermo, "Stability of the solid state cell $Ag|Ag_3SI|I_2$" *J Electrochem Soc* 116:302-313; 1969.

(15) A.Magistris,G.Chiodelli and S.Schiraldi, "Formation of high conductivity glasses in the system $AgI-Ag_2O-B_2O_3$" *Electrochim Acta* 24:203-203; 1979.

(16) A.Schiraldi and E.Pezzati, "Fast ionic diffusion in AgI-Agoxysalt glasses" *Solid State Ionics* 5: 675-678; 1981.

(17) J.P.Malugani,G.Robert and R.Mercier, "Etude comparative des verres $AgPS_3$-AgX et $AgPO_3$-AgX avec X=I,Br" *Mat Res Bull* 15:715-720; 1980.

(18) B.B.Scholtens,A.Brouwer and G.H.Broers, "$AgVO_3 \cdot 4AgI$ and $AgNbO_3 \cdot 4AgI$:Two new solid silver electrolytes at room temperature" J Appl Electrochem 8:165-168; 1978.

(19) D.Kunze, "Silver ion conducting electrolyte with glass-like structure" in "Fast Ion Transport in Solids" Ed W.van Gool,p.405-411; 1973, North-Holland Publ Co, Amsterdam.

(20) A.Schiraldi,G.Chiodelli and A.Magistris, "AgI-Agoxysalt electrolytes for solid state cells" J Appl Electrochem 6:251-255; 1976.

(21) G.Chiodelli,A.Magistris and A.Schiraldi, "Some solid electrolyte cells" Electrochim Acta 19:655-656; 1974.

(22) A.Magistris,A.Schiraldi and G.Chiodelli, "Complex admittance of AgI-Agoxysalt high conductivity solids" ibid 22:689-692;1977.

(23) A.Magistris,G.Chiodelli and G.V.Campari, "Stable and metastable phases in the system $AgI-Ag_2XO_4$(X=Cr,Mo,W)" Z.Naturforsch 31A:974-977; 1976.

(24)T.Takahashi,S.Ikeda and O.Yamamoto, "Solid state ionics:A new high ionic conductivity solid electrolyte $Ag_6I_4WO_4$ and use of this compound in a solid-electrolyte cell" J Electrochem Soc 120:647-651; 1973.

(25) R.D.Armstrong,T.Dickinson and K.Taylor, "Intergranular impedance of silver tungstate-iodide electrolyte" J Electroanal Chem Interfacial Electrochem 78:45-54, 1977.

(26) F.Bonino,M.Lazzari,A.Lonardi,B.Rivolta and B.Scrosati "Physicochemical investigation of the silver iodide-silver polymolybdate systems in the solid state" J Solid State Chem 20:315-321; 1977.

(27) T.Minami,H.Nambu and M.Tanaka, "Formation of glasses with high ionic conductivity in the system $AgI-Ag_2O-MoO_3$" J Amer Ceram Soc 60:283-284; 1977. "Comparison of ionic conductivity between glassy and crystalline solid electrolyte in the system $AgI-Ag_2O-MoO_3$" ibid 60:467-469; 1977.

(28) T.Minami and M.Tanaka, "Ionic conductivity of superionic conducting glasses in the pseudobinary system $AgI-Ag_2MoO_4$" J Solid State Chem 32:51-55; 1981. "Structure and ionic transport of superionic conducting glasses in the system $AgI-Ag_2O-MoO_3$" J Non-Crys Solid 38/39:289-294;1980.

(29) T.Minami,T.Katsuda and M.Tanaka, "Infrared spectra and structure and superionic conducting glasses in the system AgI-Ag_2O-MoO_3" J Non-Crys Solid 29:389-395; 1978.

(30) J.Kuwano and M.Kato, "High ionic-conductivity glass:Glass formation and ionic conduction in the AgI-Ag_2MoO_4 system" Denki Kagaku 46:353-358;1978.

(31) M.Lazzari,B.Scrosati and C.A.Vincent, "An investigation of some modified AgI solid electrolytes containing AsO_4^{3-}, $Cr_2O_7^{2-}$ and $Mo_2O_7^{2-}$ anions" Electrochim Acta 22:51-58; 1977. "Solid electrolytes with a glass-like structure" J Amer Ceram Soc 61:451-455; 1978.

(32) B.Scrosati, A.Ricci and M.Lazzari,"Electrochemical properties of a new solid electrolyte in the system silver iodide-silver dichromate" J Appl Electrochem 6:237-242: 1976.

(33) J.Kuwano and M.Kato, "High ionic-conductivity glass:Silver iodide-silver dichromate system" Denki Kagaku 43:734-739; 1975.

(34) T.Takahashi,E.Nomura and O.Yamamoto, "Solid state ionics.High ionic conductivity solid in the silver halide-silver sulfate system" J Appl Electrochem 2:51-57; 1972.

(35) T.Takahashi,S Ikeda and O.Yamamoto, "Solid-state-ionics-Solid with high conductivity in the systems silver iodide-silver oxyacid salts" J Electrochem Soc 119:477-482; 1972.

(36) T.Minami,Y.Takuma and M.Tanaka, "Superionic conducting glasses:Glass formation and conductivity in the AgI-Ag_2O-P_2O_5 system" J Electrochem Soc 124:1659-1662; 1977.

(37) T.Minami and M.Tanaka, "Formation region and high conductivity glasses in the system AgX-Ag_2O-P_2O_5" Rev Chim Minér 16:283-292; 1979.

(38) B.Scrosati,F.Papales,G.Pistoia and M.Lazzari, "Two new silver electrolytes of possible use in solid-state batteries"J Electrochem Soc 122:339-343;1975.

(39) J.Kuwano,T.Isoda and M.Kato, "High ionic-conductivity glass:Glass formation and ionic conduction in AgX(X=Cl,Br,I)-$Ag_4P_2O_7$ system" Denki Kagaku 45:104-110; 1977.

(40) L.Y.Y.Chan and S.Geller, "Crystal structure and conductivity of 26-silver 18-iodide tetratungstate $Ag_{26}I_{18}W_4O_{16}$" J Solid State Chem 21:331-347: 1977.

(41) A.Turkovič, "Conductivity tensor for the solid electrolyte $Ag_{26}I_{18}W_4O_{16}$" Fizika 12:366-370;1980.

(42) G.F.Ruse and S.Geller, "Growth of single crystals of the solid electrolyte $Ag_{26}I_{18}W_4O_{16}$" Rev Chim Minér 17:254-262; 1980.

(43) G.Robert,J.P.Malugani and A.Saida, "Fast ionic silver and lithium conduction in glasses" Solid State Ionics 3/4:311-315; 1981.

(44) J.L.Souquet and E.Robinel, "Glass formation and ionic conduction in the M_2S-GeS_2(M=Li,Na,Ag) systems" ibid 3/4:317-321; 1981.

(45) J.N.Bradley and P.D.Green, "Potassium iodide + silver iodide phase diagram;High ionic conductivity KAg_4I_5" Trans Faraday Soc 62:2069-2075; 1966. "Solid with high ionic conductivity in group I halide systems" ibid 63:424-430; 1967.

(46) B.B.Owens and A.G.Argue, "High conductivity solid electrolyte MAg_4I_5" Science 157:308-310; 1967. "High conductivity solid electrolyte system RbI-AgI" J Electrochem Soc 117:898-900; 1970.

(47) L.P.Topol and B.B.Owens, "Thermodynamic studies in the high-conducting solid systems RbI-AgI, KI-AgI, and NH_4I-AgI" J Phys Chem 72:2106-2111; 1968.

(48) D.O.Raleigh, "Ionic conductivity of single-crystal and polycrystalline $RbAg_4I_5$" J Appl Phys 41: 1876-1877; 1970.

(49) J.S.Kasper, "Inorganic silver ion conductors" in "Solid Electrolytes" Ed P.Hagenmuller and W.van Gool, p.217-235; 1978,Academic Press, New York.

(50) B.B.Owens, "A new class of high-conductivity solid electrolytes:Tetraalkylammonium iodide-silver iodide double salts" J Electrochem Soc 117: 1536-1539; 1970. "Solid electrolyte batteries" in "Advanced Electrochemistry and Electrochemical Engineering Ed P.Delahay and C.W.Tobias, 8:1-62; 1971, John Wiley and Sons, New York.

(51) B.B. Owens,J.H.Christie and G.T.Tiedeman, "High-conductivity solid electrolytes:C_aH_bNI-AgI double salts" J Electrochem Soc 118:1144-1147, 1971.

(52) M.L.Berardelli,C.Biondi,M.DeRossi,G.Fonseca and M. Giomini, "Polymethonium-silver iodide compounds as high-conductivity solid electrolytes" ibid 119: 114-118; 1972.

(53) J.Coetzer and M.M.Thackeray, "Solid electrolytes: Methyl substituted diamine diiodide-silver iodide double salts" Electrochim Acta 21:37-38; 1976.

(54) K.Shahi and S.Chandra, "Electrical conductivity of solid electrolytes $Ag_{13}(Q_4N)_2I_{15}$ ($Q=CH_3$ and C_2H_5)" J Phys C:Solid State phys 8:2255-2261; 1975.

(55) M.M.Thackeray and J.Coetzer, "The electrical conductivity and crystal structures of polyamine iodide/silver iodide solid electrolytes" in "Fast Ion Transport in Solids" Ed P.Vashishta,J.M.Mundy and G.K.Shenoy, p.577-580; 1979, Elsevier North Holland, New York. "The electrical conductivity of polyamine iodide/silver iodide solid electrolytes" Electrochim Acta 24:495-502; 1979. "The crystal structure of the solid electrolyte $Ag_{44}I_{53}(C_{11}H_{30}N_3)_3$" Acta Cryst B34:71-75; 1978.

(56) T.Takahashi,N.Wakabayashi,T.Miyazaki and O.Yamamoto, "Silver-ion solid electrolytes with high conductivity:Silver iodide-sulfonium iodide double salts" Nippon Kagaku Kaishi 266-270; 1975.

(57) R.G.Linford,J.M.Pollock and C.F.Randell, "Solid state batteries containing silver sulphonium iodide electrolyte" Nature 256(5516):398-399; 1975. "New silver iodide-bis-sulphonium diiodide solid electrolytes for solid state battery systems" in "Power Sources" Ed D.H.Collins 6:511-526; 1977,Academic Press, London.

(58) J.H.Christie,B.B.Owens and G.T.Tiedeman, "High-conductivity solid electrolytes. Tropyllium iodide-silver iodide system" Inorg Chem 14:1423; 1967.

(59) S.Geller, "Crystal structure of solid electrolyte, $RbAg_4I_5$" Science 157:310-312; 1967.

(60) S.Geller and M.D.Lind, "Crystal structure of the solid electrolyte $[(CH_3)_4]_2Ag_{13}I_{15}$" J Chem Phys 52:5854-5861; 1970.

(61) S.Geller, "Crystal structure of the solid electrolyte $(C_5H_5NH)Ag_5I_6$ at -30°C" Science 176:1016-1019; 1972.

(62) S.Geller and B.B.Owens, "Silver ion site-distribution, structure and conductivity of the solid electrolyte pyridinium hexaiodopentaargentate,$(C_6H_5NH)Ag_5I_6$,between -30 and 125°C" J Phys Chem Solids 33: 1241-1250; 1972.

(63) S.Geller, "Crystal structure and conductivity in AgI-based solid electrolytes" in "Fast Ion Transport in Solids" Ed W.van Gool,p.607-615; 1973, North-Holland Publ Co, Amsterdam.

(64) T.Takahashi and O.Yamamoto, "The electrical conductivity of solid electrolytes(V) The electrical conductivity of the system Ag_2S-Ag_2HgI_4." Denki Kagaku 33:733-737; 1965.

(65) T.Takahashi,O.Yamamoto,K.Tsukada and A.Baba,"Electrical conductivity of solid electrolytes(VI) The electrical conductivity of the Ag_2S-HgI_2 system" ibid 35:32-36; 1967.

(66) T.Takahashi,O.Yamamoto and K.Kuwabara, "The electrical conductivity of solid electrolytes(VII) The Ag_2Se-HgI_2 system" ibid 35:264-268; 1967.

(67) O.Yamamoto and T.Takahashi, "The electrical conductivity of solid electrolytes(VIII) The electrical conductivity of the AgI-Ag_2S-HgI_2 system" ibid 35: 651-656; 1967.

(68) T.Takahashi,K.Kuwabara and O.Yamamoto, "The electrical conductivity of solid electrolytes(IX) The Ag_2Te-AgI-HgI_2 system" ibid 35:682-687; 1967. "The electrical conductivity of solid electrolytes(X) The Ag_2Se-AgI-HgI_2 system" ibid 36:530-534; 1968. "Solid-state-ionics:Studies on the solid electrolytes in the system Ag_2X-AgI-HgI_2" J Electrochem Soc 120:1607-1612; 1973.

(69) G.W.Mellors and D.V.Louzos, "Ionic conductance in solids I. Compounds formed between silver iodide and the cyanides of metals of group IA" J Electrochem Soc 118:846-850; 1971.

(70) G.W.Mellors,D.V.Louzos and J.A.van Lier, "Ionic conductance in solids II. The phase diagram of the KCN-AgI system and some observations on the stability of cyanide-iodide compounds" ibid 118:850-853; 1971.

(71) T.Takahashi,O.Yamamoto and E.Nomura, "Thermoelectric power of the silver iodide-alkali iodide solid electrolyte system" Denki Kagaku 38:360-364; 1970.

(72) K.Shahi and S.Chandra, "EMF measurements on the thermocell $Ag(T_1)|AgI|Ag(T_2)$" Z Naturforsch 30a: 1055-1059; 1975. "Electrical conductivity and thermoelectric power of $Ag_6I_4WO_4$ solid electrolyte" phys stat sol(a) 28:653-661; 1975.

(73) A.Schiraldi and E.Pezzati, "Thermoelectric power of the system $AgI-Ag_2XO_4$(X=Mo,W)" Z Naturforsch 31a:1077-1080; 1976.

(74) K.Shahi, "Transport studies on superionic conductors" phys stat sol(a)41:11-44; 1977.

(75) A.Schiraldi,G.Chiodelli and A.Magistris, "Thermoelectric power of AgI-Agoxysalt ionic solids" J Power Sources 2:257-264, 1977/78.

(76) J.A.Cowen,C.L.Foiles and D.L.Edmunds, "Thermopower measurements in $RbAg_4I_5$ films" in "Fast Ion Transport in Solids" Ed P.Vashishta,J.N.Mundy and G.K. Shenoy, p.593-595; 1979, North-Holland,New York.

(77) L.B.Coleman, "Thermoelectric power studies of phase transitions in fast ion conductors" ibid p.601-603; 1979.

(78) S.M.Girvin, "Thermoelectric power of superionic conductors" J Solid State Chem 25:65-75; 1978.

(79) M.N.Avasthi,M.Saleem amd M.T.El-Gemal, "Phase transition and heat of transport studies of the $Ag_{19}I_{15}P_2O_7$ superionic conductor" Solid State Ionics 6:43-45; 1982.

(80) H.Ikeda and K.Tada, "Sanyo's couliodes and memoriodes" in "Applications of Solid Electrolytes" Ed T.Takahashi and A.Kozawa, p.40-45;1980,JEC Press, Cleveland.

(81) T.Takahashi and O.Yamamoto, "Solid-state-ionics: Coulometric titration and measurements of the ionic conductivity of beta Ag_2S and beta Ag_2Te and use of these compounds in an electrochemical analog memory element" J Electrochem Soc 118:1051-1057; 1971.

(82) T.Takahashi and O.Yamamoto, "Solid-state-ionics-Mixed ionic and electronic conduction in $Ag_2Se-Ag_3PO_4$ solid solutions" ibid 119:1735-1740; 1972.

(83) T.Takahashi,E.Nomura and O.Yamamoto, "Coulometric titration of stabilized α-Ag_2S like phase at room

temperature" Denki Kagaku 41:127-131; 1973. "Solid state ionics-The ionic conductivity of the Ag_2S-$Ag_{1.70}Te$-AgX system(AgX;$Ag_4P_2O_7$,Ag_3PO_4 and $AgPO_3$)" J Appl Electrochem 3:23-29; 1973.

(84) T.Takahashi,O.Yamamoto and S.Ikeda, "Solid-state-ionics-High conductivity solid copper ion conductors:N-alkyl(or hydro)-hexamethylenetetramine halide-copper(I) halide double salts" J Electrochem Soc 120:1431-1434; 1973.

(85) T.Takahashi and O.Yamamoto, "Solid-state-ionics-High conductivity solid copper ion conductors:N,N'-dialkyl(or dihydro)-triethylenediamine dihalide-copper(I) halide double salts" ibid 122:83-86;1975.

(86) M.Lazzari,R.C.Pace and B.Scrosati, "Electrochemical properties of the N-N'-dimethyltriethylene-diamine dibromide-cuprous bromide solid electrolyte" Electrochim Acta 20:331-334: 1975.

(87) T.Takahashi, "Silver and copper ion conductors in the solid state" Pure & Appl Chem 50:1091-1098; 1978.

(88) A.F.Sammels,J.Z.Gougotas and B.B.Owens, "High conductivity solid electrolytes, double salts of substituted organic ammonium halides and cuprous halides" J Electrochem Soc 122:1291-1296; 1975.

(89) T.Takahashi,N.Wakabayashi and O.Yamamoto, "Solid-state-ionics-High conductivity solid copper ion conductors:Organic ammonium halide-copper(I) halide double salts' ibid 123:129-132; 1976.

(90) J.M.Shemilt,B.C.H.Steele and J.E.Weston, "Investigation of the electrode/electrolyte interface for the Cu^+ ion solid electrolyte N,N'-dimethyl-triethylene diamine-copper(I) bromide" Solid State Ionics 2:1-11; 1981.

(91) L.Y.Y.Chan,S.Geller and P.M.Skarstad, "The crystal structure of the Cu^+ ion conductor,$(C_5H_5NH)_2Cu_5Br_7$" J Solid State Chem 25:85-99; 1978.

(92) T.Takahashi,N.Wakabayashi and O.Yamamoto, "High-conductivity solid copper ion conductors:the sulphonium halide-copper(I) halide systems" J Appl Electrochem 7:253-256; 1977.

(93) R.H.Dahm,S.Hackwood,R.G.Linford and J.M.Pollock, "Copper-ion solid-state battery systems involving sulphonium iodide electrolytes" Nature 272:522-524; 1978.

(94) T.Matsui and J.B.Wagner,Jr., "Investigations on a high conductivity solid electrolyte system,RbCl+CuCl" J Electrochem Soc 124:941-944; 1977.

(95) T.Matsui and J.B.Wagner,Jr., "Inorganic copper ion conductors" in "Solid Electrolytes" Ed P.Hagenmuller and W.van Gool, p.237-252; 1978.

(96) U.v.Alpen,J.Fenner,J.D.Marcoll and A.Rabenau, "Structural aspects and high Cu^+-ionic conductivity in compound of CuTeX(X=Cl.Br,I)" Electrochim Acta 22:801-803; 1977.

(97) T.Takahashi,O.Yamamoto,S.Yamada and S.Hayashi, "Solid-state ionics:High copper ion conductivity of the system CuCl-CuI-RbCl" J Electrochem Soc 126:1654-1658; 1979.

(98) S.Geller,J.R.Akridge and S.A.Wilber, "Crystal structure and conductivity of the solid electrolyte α-$RbCu_4Cl_3I_2$" Phys Rev B19:5396-5402; 1979.

(99) N.N.Vershinin,E.P.Dermanchuk,N.G.Bukum and E.A.Ukshe, "Impedance of cells with a solid electrolyte $Cu_4RbCl_3I_2$" Elektrokhimiya 17:383-387;1981.

(100) N.N.Vershinin,Yu.I.Malov and E.A.Ukshe, "Study of $Cu|Cu_4RbCl_3I_2$ interface by the potentiostatic pulse method" ibid 18:255-260; 1982.

(101) K.Nag and S.Geller, "The solid electrolyte system $RbCu_4Cl_3(I_{2-x}Cl_x)$ $0 \leq x \leq 0.4$ I. Stability" J Electrochem Soc 128:2670-2675; 1981.

(102) S.Geller,K.Nag and A.K.Ray, "The solid electrolyte system $RbCu_4Cl_3(I_{2-x}Cl_x)$, $0 \leq x \leq 0.4$ II. Electrical conductivity" ibid 128:2675-2678; 1981.

(103) M.Kleitz,J.R.Akridge and J.H.Kennedy, "Conductivity of $RbCu_4Cl_{3+x}I_{2-x}$ and copper electrode reaction computerized complex analysis" Solid State Ionics 2:67-72; 1981.

(104) M.Tokumoto,N.Ohnishi,Y.Okada and T.Ishiguro, "Preparation and characterization of the solid electrolyte system $RbCu_4I_{2-x}Cl_{3+x}$ $(-0.25 \leq x \leq 0.75)$" ibid 3/4:289-293; 1981.

(105) T.Takahashi,R.Kanno,Y.Takeda and O.Yamamoto, "Solid state ionics-The CuCl-CuI-RbCl system" ibid 3/4:283-287; 1981.

(106) C.Chaney,D.F.Shriver and D.H.Whitmore, "Polarization study on the solid electrolyte $Cu_{16}Rb_4I_{7+x}Cl_{20-(7+x)}$ $(0<x<1)$" ibid 5:505-508; 1981.

(107) T.Takahashi, K.Kuwabara, M.Miura and M.Nakanishi, "Solid electrolyte cell using the electrolyte of the CuCl-CuI-RbCl system" J Appl Electrochem 12: 213-218; 1982.

(108) A.Turković, B.Grẑeta-Plenković and B.Etlinger, "Powder data for the solid electrolyte α-$RbCu_4Cl_3I_2$" J Appl Cryst 15:103-104; 1982.

(109) S.Geller, J.R.Akridge and S.A.Wilber, "$NH_4Cu_4Cl_3(I_{1.9}Cl_{0.1})$, a new highly conducting solid electrolyte" J Electrochem Soc 127:251-254; 1980.

(110) S.Geller, A.K.Ray, H.Z.Fardi and K.Nag "New solid electrolyte: Cesium copper chloride iodide ($CsCu_4Cl_3I_2$)" Phys Rev B: Condens Matter 25:2968-2970; 1982.

(111) T.Takahashi and O.Yamamoto, "Solid-state ionics-Solid electrolyte cell with copper ion conductors" J Appl Electrochem 7:37-43; 1977.

(112) M.Lazzari, G.Razzini and B.Scrosati, "Investigation on various cathodic materials in copper solid-state power sources" J Power Sources 1:57-63; 1976/77.

(113) S.Sekido and Y.Ninomiya, "Solid state electric-double-layer elements using Cu^+ ion conductive solid electrolyte" Solid State Ionics 3/4:153-156; 1981.

Table 1 The heat of transport and the activation energy for conduction of the silver ions in various silver ion conductors.

Electrolyte		Heat of Transport (eV)	Activation Energy for Conduction (eV)
α-AgI		0.052	0.051
$RbAg_4I_5$		0.086	0.092
$Ag_6WO_4I_4$		0.14	0.16
$Ag_2Hg_{0.25}S_{0.5}I_{1.5}$		0.15	0.14
aAgI·bQI			
Q	a/b		
Tetramethylammonium	6.5	0.115	0.17
Pyridinium	3.6	0.091	0.178
1,3-dimethylpyridinium	6.7	0.130	0.126
1,2,6-trimethylpyridinium	6.7	0.146	0.148
1,2,4,6-tetramethylpyridinium	6.7	0.145	0.235
1-methylpyrrolidinium 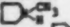	8	0.077	0.123
1-methylthioniacyclopentane	5.25	0.146	0.193
N-methylhexamethylenetetramine	5	0.114	0.142

Table 2 Ionic conductivity of mixed conductors at 25 °C.

$(Ag_2Se)_{0.925}(Ag_3PO_4)_{0.075}$	0.13 $S\cdot cm^{-1}$
$(Ag_2S)_{0.69}(Ag_{1.7}Te)_{0.205}(Ag_4P_2O_7)_{0.025}$	0.16 $S\cdot cm^{-1}$
$(Ag_2S)_{0.50}(Ag_{1.7}Te)_{0.45}(Ag_3PO_4)_{0.05}$	0.25 $S\cdot cm^{-1}$

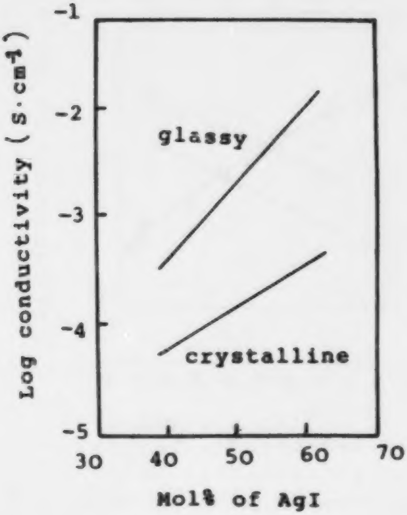

Fig. 1 - Composition dependence of the conductivity of the AgI-Ag_2MoO_4 system at room temperature. (Ref. 27)

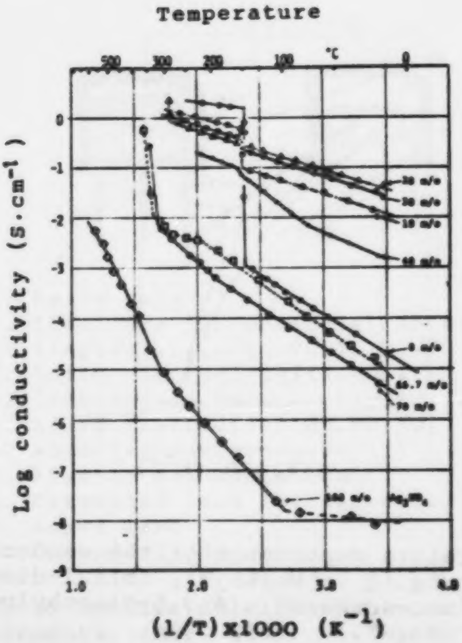

Fig. 2 - Electrical conductivity of the system AgI-Ag_2WO_4. (Ref. 24)

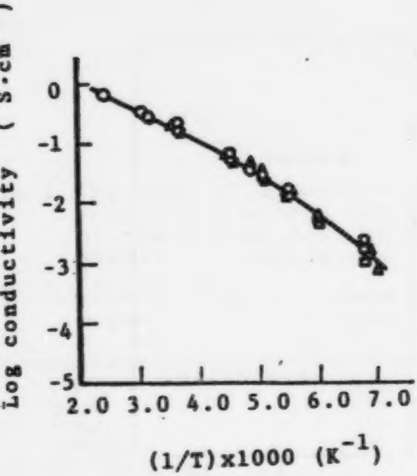

Fig. 3 - Electrical conductivity of MAg_4I_5. ○ $RbAg_4I_5$ △ KAg_4I_5; □ $(K_3Rb)_{0.25}Ag_4I_5$. (Ref. 12)

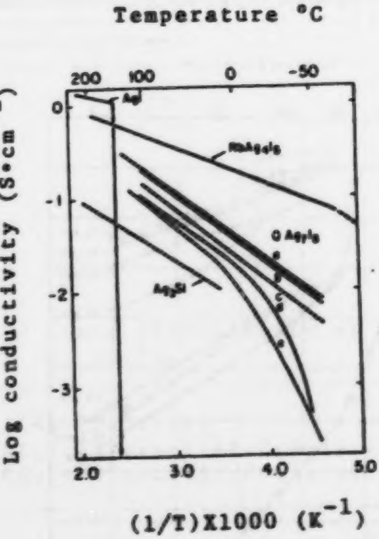

Fig. 4 - Temperature dependence of the conductivities of QAg_7I_8.{Q (a)$Me_2Et_2N^+$, (b)1,1-dimethylpyrrolidinium, (c)Me_4N^+, (d)3,5-dimethylpyridinium, and (e)Et_4N^+.}. (Ref. 50)

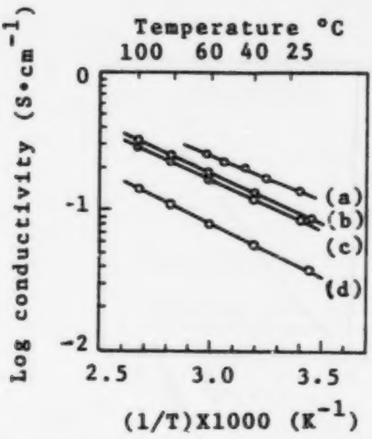

(a)$Ag_{2.0}Hg_{0.25}S_{0.5}I_{1.5}$
(b)$Ag_{1.85}Hg_{0.40}Te_{0.65}I_{1.35}$
(c)$Ag_{1.80}Hg_{0.45}Se_{0.70}I_{1.30}$
(d)$Ag_{2.0}Hg_{0.5}Se_{1.0}I_{1.0}$

Fig. 5 - Conductivities of the system AgI-Ag_2Chal.-HgI_2. (Ref. 68)

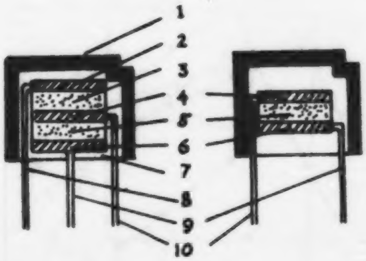

1. Resin case
2. Electrode for potential detection [$(Ag_2Se)_{0.925}(Ag_3PO_4)_{0.075}$]
3. Solid electrolyte[$Ag_6WO_4I_4$]
4. Cathode[$(Ag_2Se)_{0.925}(Ag_3PO_4)_{0.075}$]
5. Solid electrolyte[$Ag_6WO_4I_4$]
6. Anode[Ag powder+$Ag_6WO_4I_4$]
7. Plastic encapsulation
8. Potential lead for detection
9. Anode lead
10. Cathode lead

Fig. 6 - Cross section of electrochemical functional elements. (Ref. 80)

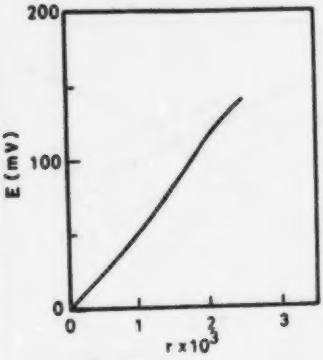

Fig. 7 - Coulometric titration curve for $(Ag_2Se)_{0.925}$ $(Ag_3PO_4)_{0.075}$. (Ref. 82)

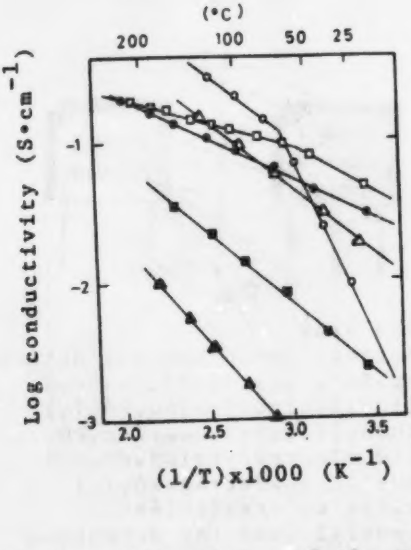

Fig. 8 - Temperature dependence of the electrical conductivity of $17CuCl \cdot 3C_6H_{12}N_2 2HCl$ (○), $4CuCl \cdot C_6H_{12}N_2 2CH_3Cl$ (△), $7CuBr \cdot C_6H_{12}N_2 2HBr$ (□), $47CuBr \cdot 3C_6H_{12}N_2 2CH_3Br$ (●), $17CuBr \cdot 3C_6H_{12}N_2 2C_2H_5Br$ (▲), and $17CuI \cdot 3C_6H_{12}N_2 2CH_3I$ (■). (Ref. 85)

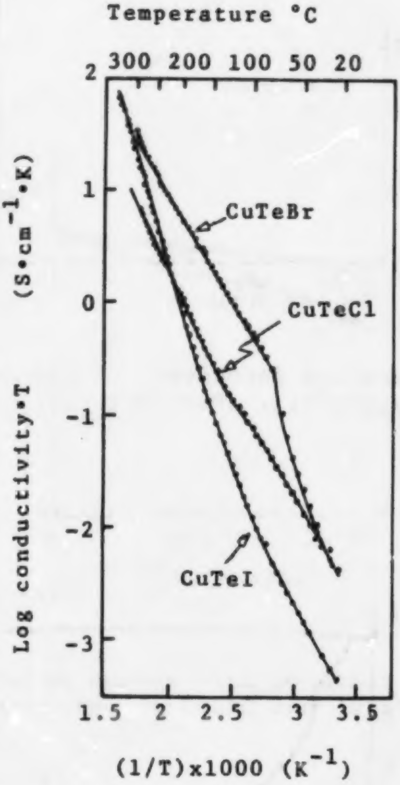

Fig. 9 - Log (σT) versus 1/T for CuTeX(X=Cl,Br,I). (Ref. 96)

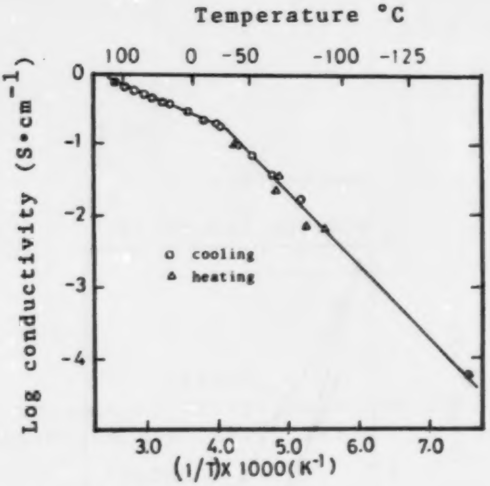

Fig. 10 - Temperature dependence of the conductivity of $Rb_4Cu_{16}I_7Cl_{13}$. (Ref. 97)

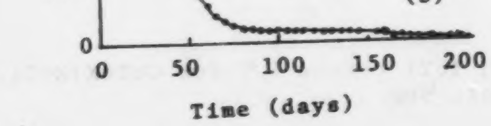

Fig. 11 - Open circuit voltages of the cells Cu,X|X| $Cu_{1.75}Se$ where X is the electrolyte. In (a) X=$Rb_4Cu_{16}I_7Cl_{13}$ and in (b) X=$RbCu_4I_2Cl_3$. (Ref. 107)

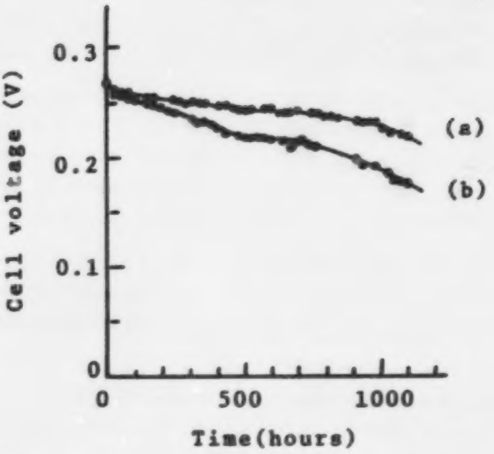

Fig. 12 - Discharge curves with constant loads at room temperature. (a)100kΩ and (b)50kΩ. (Ref. 107)

SILVER SOLID ELECTROLYTES

Bruno Scrosati

Istituto di Chimica Fisica,University of Rome,Italy.

ABSTRACT

After a brief description of the characteristics and of the transport mechanism of low-conducting silver halides,the properties of silver solid electrolytes of the AgI-substituted type are examined in detail.

In particular,the formation of these electrolytes, characterized by a disordered structure with a number of defects largely exceeding that of the mobile silver ions,is rationalized on the basis of the theory of Phillips on the ionicity of binary compounds.

Some attention is then dedicated to vitreous silver solid electrolytes,with a brief discussion on their transport and themodynamic properties.

Finally,the application of silver solid electrolytes is critically examined,especially taking into account the electrode-electrolyte interfacial phenomena. Some of the solid-state devices which have reached a development stage of technological interest are mentioned.

KEYWORDS:silver ionic conductors,silver solid electrolytes,vitreous solid electrolytes,silver solid-state devices.

RÉSUMÉ

On décrit brièvement les caractéristiques et les mécanismes de transport des halogénures d'argent de faible conductivité,puis on examine en détail les électrolytes solides à l'argent dont le réseau cristallin est du type AgI.

En se basant sur la théorie de Phillips sur l'ionisation des composés binaires,on explique en particulier la formation de ces électrolytes caractérisés par une structure désordonnée comportant des défauts beaucoup plus nombreux que celle des électrolytes contenant des ions argent mobiles.

On traite ensuite des électrolytes vitreux à l'argent en décrivant rapidement leurs caractéristiques de transport et leurs caractéristiques thermodynamiques.

On termine par un examen critique de l'application des électrolytes solides à l'argent en tenant spécialement compte des phénomènes qui interviennent à l'interface électrode-électrolyte. On mentionne en outre des exemples d'application dont la réalisation est assez avancée pour présenter un intérêt technique.

SILVER IONIC CONDUCTORS

Solid compounds characterized by ionic transport in their lattice have been known since the beginning of this century. Classical examples are the silver halides which have a conductivity caused by silver ion movements throughout a partially defective lattice where the number of defects is much lower than the number of the mobile ions.

These defects arise as a consequence of the thermal motion of the atoms in the lattice at any temperature higher than absolute zero,and consist of point defects,i.e. of vacant lattice sites and of atoms pushed from their original position to interstitial positions, and of impurity atoms either in the lattice or in interstitial positions(1).

Such point defects may be basically organized as Schottky pairs (consisting of cation and anion vacancies) or as Frenkel pairs (consisting of cation interstitials and cation vacancies).

The silver halides mainly exhibit Frenkel type defects and the silver-ion transport depends essentially on the degree of intrinsic disorder (due to thermal vibrations of the lattice) as well as on the extrinsic disorder(induced by impurities dissolved in the lattice either accidentally or intentionally). In fact,these factors determine the number and the energy of the point defects,be they interstitials or vacancies.

The defects act as intermediates in a multistep process or as an initial and a final position in an elementary motion step,which is associated with a jump of an ion from a lattice position to a neighbouring vacant site(1).

This hopping model for ionic conductivity in silver halides and,more generally,in compounds characterized by point defects in their lattice is well known and the reader is referred to various text books and specific reviews in the field for extended theoretical treatments(2). Here we may only recall that,on the basis of the hopping model,it is possible to derive the following expression for the ionic conductivity σ of a solid ionic conductor:

$$\sigma = (A/T) \exp -\{(E_D+E^{*}/kT)\} \qquad |1|$$

where A is a constant typical of the given conductor, E_D is the energy of formation of a defect pair, E^* is the activation energy for the hopping process and kT is the thermal energy of the lattice.

Since E_D is generally negligible compared with E^* the expression is more commonly reported in its approximated logarithmic form:

$$\ln \sigma = \ln(A/T) - (E^*/kT) \qquad |2|$$

This equation reveals that the ionic conductivity in solids increases with temperature and that a plot of log σ versus 1/T, allows the calculation of the activation energy E^* .

The silver halides, and more generally the point-defect solid conductors, necessarily exhibit a very low conductivity at room temperature, because of the very low equilibrium concentration of the defects.

In Figure 1, where some typical examples of such conductors are considered, it is shown that the effective conductivity remains below approximately 10^{-3} Sm^{-1} at room temperature, a value definitely too low for practical interest.

Also illustrated in the same Figure is the behaviour of silver iodide, AgI, which at 149 °C undergoes a phase change accompanied with a sudden jump in conductivity. Indeed, the low-temperature β-phase of AgI has a hexagonal packed structure with point defects, while the high-temperature α-phase has a disordered open structure with a large number of sites available for the mobile silver ions. In the α-form the defect concentration is so high that it is possible to consider that all the lattice cations are able to contribute to the conduction process. This means that the energy barrier between each empty site is very small, to the point that the silver ions become spread around the entire cation sub-lattice as soon as the thermal energy of the lattice, kT, is comparable or higher than the activation energy for motion(1).

Effectively the conductivity of the α-form is four orders of magnitude higher than that of the β-form of silver iodide. Because of this, α-AgI could be of interest for practical applications. However, the phase change and the variation in conductivity which accompanies it,are totally reversible,thus limiting the high conductivity to the range of stability of the α-form in the high-temperature region.

Therefore,the conductivity of the silver halides and generally that of the alkali halides and similar point defect compounds,remains very modest at room temperature and this has confined for long time these solid ionic conductors to the role of academic curiosities.

The situation changed dramatically about 15 years ago with the discovery of new solid compounds having at room temperature a conductivity of the same order as that shown by α-AgI. The major characteristic of these compounds is the fact that,like α-AgI, they have a defective structure with a number of defects largely exceeding that of the mobile ions.

The most classical example is silver rubidium iodide,$RbAg_4I_5$,where the 16 silver ions of the unit cell are statistically distributed over 56 tetrahedral sites (3-6). Such a condition is provided by a system of multiple face-sharing iodide ion polyhedra,some of which are occupied by the silver ions. The interconnected polyhedra provide a network of passageways through which silver ions may migrate with a very low energy of activation.

This characteristic of fast-ion transport has led to references to $RbAg_4I_5$ and similar compounds as *superionic conductors* or even as *superionics*. This terminology is in my opinion inappropriate since it may imply a non-existing connection with electronic superconductors. It appears more correct to classify the highly conducting compounds as *solid electrolytes*,since they, having a high ionic conductivity accompanied by an almost negligible electronic transport,show properties similar to those offered by the common liquid electrolytes and in fact find analogous type of application.

SILVER SOLID ELECTROLYTES

Following the dicovery of the MAg_4I_5 compounds (where $M = Rb, K$ or NH_4), a large number of silver solid electrolytes have been characterized in the last decade. Some of the more common examples are listed in Table 1.

The common feature of these compounds is an extended disordered structure with interlinked polyhedra (preferably tetrahedra) of the fixed ions, which create pathways (formed by a series of tetrahedral sites) through which the silver ions may easily migrate.

This structural characteristic, as well as the various theoretical models which have been proposed to account for such a fast-ion transport, have been discussed in a series of excellent review papers(6-11), to which the reader is referred for detailed information.

These highly conductive materials are all based on silver iodide, to which either large foreign cations (generally, K^+, Rb^+, NH_4^+ and a variety of organic substituted ammonium ions) or anions (mainly oxoanions) have been added in relatively small proportions.

Typically these silver solid electrolytes, often called of the AgI-substituted type, are prepared by melting a stoichiometric mixture of AgI and the parent iodide or the silver oxosalt and then cooling the resulting mixture at room temperature. In the case of cation-substituted AgI electrolytes, generally of crystalline type, the preparation is completed by an annealing around 150 °C. In the case of anion-substituted AgI electrolytes, generally metastable phases or glasses, the preparation requires a very fast quenching of the melted mixture.

It therefore appears that the basic condition for high conductivity is realized by a simple anion or cation substitution in silver iodide. Such a process leads to the formation of a double salt with a disordered structure and a fast silver ion-transport. However, it is surprising that this conditions is only obtained in the case of silver iodide. Indeed, over 50 silver solid electrolytes based on AgI are known(12,13),whereas not a single compound with high ionic conductivity has been obtained by similar cationic or anionic substitution of AgBr or of AgCl.

This peculiarity has been in part explained by Phillips on the basis of his theory of ionicity(14,15) for binary compounds of the A^NB^{8-N} type(e.g. AgX or CuX,with X = I,Br,Cl).Phillips proposed that for the polarizable bonds,characteristic of the 'soft' structures of these compounds,there is a balance between covalent and ionic forces which in turn determines phase transitions between competing structures. The phase transition merely facilitates the formation of ternary structures while their stabilization is basically governed by the propriety of the A-B bond. The closer the ionicity f_i of a given A^NB^{8-N} compound is to a critical value of 0.785,the lower will be the free energy difference,ΔG_T, between the two possible configurations which the compound may assume,i.e.,the four-fold and the six-fold coordination(see Table 2).

When a foreign ion is added to a compound characterized by an ionicity close to 0.785 and the mixture is brought to a temperature near or above the phase transition(where presumably the A ions are separated from the B partners),a double salt is formed with a 'scaffolded' structure which results as a compromise between the two possible basic configurations.These structures may be regarded as formed by a skeletal framework of minority ion complexes decorated by loosely bound,quasi-interstitial,majority cations,thus accounting for the fast ionic transport.

This theory is supported by a series of experimental results.First there is the fact that silver iodide, having an ionicity very close to the critical value (e.g. f_iAgI=0.770),is the compound which can give rise to ternary compounds with high conductivity,after addition of foreign cations or anions.

Furthermore,while AgI is normally tetrahedrally coordinated(f_i< 0.785),AgBr and AgCl are octahedrally coordinated(f_i> 0.785). This leads to negative ΔG_T values and therefore excludes the possibility of inducing more stable disordered structures,even with the addition of large substituting ions,as is also experienced.

Finally,considering the difference in ionicity values of the copper halides with respect to that of the silver halides(see Table 2),it is reasonable to expect that much larger substituting ions would be required to induce comparable disordered structures.This is indeed the case,as experimentally verified:highly conductive copper solid electrolytes have been obtained from all the three copper halides by cationic substitution with very large alkylammonium salts(16-19).

VITREOUS SILVER SOLID ELECTROLYTES

The theory of Phillips,however,is unable to account for the formation of an important class of silver solid electrolytes having a glass-like structure. These electrolytes are still of the AgI-substituted type as they are obtained by a fast quench of a molten mixture of silver iodide and a silver oxosalt.

A large number of these ionic conducting glasses have been discovered and characterized(20-26). The physico-chemical properties of a typical example,i.e., that formed by the combination of 4AgI with Ag_3AsO_4,are reported in Figure 2 (23). It may be noticed that the X-ray spectrum is totally peak-free,which shows the vitreous character of the electrolyte,and that the compound decomposes before melting which shows the metastable character of the electrolyte.

It is not easy to suggest a model capable of justifying the high ionic conductivity observed in these vitreous silver electrolytes.It is,however,reasonable to suppose that also in these compounds there may be structural channels for the migration of the ions. Such an arrangement could develop in the fused mixture of the silver iodide and the silver oxosalt, with the formation of microdomains of organized structures of the iodide sublattice. Such a structure would then be frozen during the fast-quenching process involved in the preparation.Indeed,it is reasonable to assume that the high viscosity of the melts may prevent the rearrangement of the ions in a macroscopic crystalline structure,thus leading to the vitreous character of the electrolytes.

It is also important to consider that while the oxoanions favour the formation of the iodide sublattice necessary to assure the high mobility of the silver ions (this again in agreement with the theory of Phillips), they also may originate low-energy sites which may trap a part of the silver ions,thus subtracting them from the conduction process. This explains the fact that anion-substituted AgI electrolytes generally have a lower conductivity than cation-substituted ones (see Table 1).

As shown in Figure 2,as the temperature increases, the glassy electrolyte undergoes a devitrification process followed by a decomposition into low-conductive crystalline phases.As already remarked,the compound is then thermodynamically unstable.However,the kinetics of the devitrification process are generally very slow,becoming appreciable only at high temperatures. The stability at room temperature remains generally high enough to ensure for the majority of these glassy electrolytes the possibility of practical applications.Indeed,these electrolytes possess a series of specific advantages,with respect to crystalline cation-substituted AgI compounds, which mainly are the stability in moisture and in uncomplexed iodine and the plasticity.These features make them almost unique for important specific applications (26).

APPLICATION OF SILVER SOLID ELECTROLYTES

In the evaluation of the possible application of the silver solid electrolytes,and of solid electrolytes in general,one has first to take into account the electrode-electrolyte interface problems.

Phenomena such as differences in the expansion and contraction coefficients between electrode and electrolyte materials may lead to progressive contact loss with consequent increase in the interfacial resistance. This situation becomes even more critical when the solid-state cell is submitted to reversing-polarity cycles. In such a case,as schematically illustrated in Figure 3,contact heterogeneities result during charging in dendritic-type deposits which,upon cycling,lead to a progressive increase of the internal resistance and ultimately to the fracture of the entire cell.

These interfacial effects are generally so severe as to practically exclude the concrete possibility of developing solid-state rechargeable devices. Even in primary applications,the interfacial phenomena play a key role in the electrode polarizaion behaviour.

A common expedient to alleviate these effects consists in mixing the electrodic active material with the electrolyte and then pressing this mixture into a single pellet which acts as a composite electrode. In such a way a large surface area is obtained,with consequent reduction of the current density and thus of the electrode polarization.

Indeed,such an electrode configuration has been used in the realization of one of the first solid-state batteries of practical importance. This cell had the basic structure:

$$Ag \ / \ RbAg_4I_5 \ / \ RbI_3 \qquad |3|$$

and it was realized by subsequently compressing a pellet of silver mixed with the electrolyte, the electrolyte($RbAg_4I_5$) and a pellet of rubidium triiodide, again mixed with the electrolyte.

For this battery,as generally for each solid-state systems,it is necessary to use as anode a material of the same nature as the mobile ion in the electrolyte,to assure the electric transport through the cell (e.g., in the case of cells using silver solid electrolytes, the anode must be based on silver).

The choice of the cathode is in principle less restricted,even if limited by thermodynamic factors.In fact,the difference in potential between the chosen cathodic material and the silver anode,must not exceed the decomposition potential of the electrolyte.

In the case of AgI-substituted silver solid electrolytes,the decomposition potential is on average around 0.69 V at room temperature. The most suitable electrodic couple for these electrolytes would then be the silver-iodine one,which is characterized by the reaction:

$$Ag + \tfrac{1}{2}I_2 \rightarrow AgI \qquad |4|$$

to which is associated a thermodynamic potential of 0.689 V at 25 °C.

However, cation-substituted electrolytes, such as $RbAg_4I_5$, are unstable in the presence of iodine, so that cathodes with reduced iodine activity must be used, as for instance the rubidium triiodide of cell |3|.

Other alternative iodine-based electrodes for the realization of silver solid-state batteries, are the iodine charge transfer complexes. A typical example is the iodine-phenothiazine (I_2-Ph) complex. These materials behave as excellent iodine electrodes, both in terms of stability and performance(28,29). In fact, solid-state batteries of the type:

$$Ag\ /\ Ag_7I_4AsO_4\ /\ I_2\text{-}Ph \qquad |5|$$

have been successfully realized(30).

Both batteries of type |3| and |5| show very promising performance, as indicated by the typical discharge and polarization curves of Figures 4 and 5, respectively. However, the high cost of the materials and the relatively low value of the specific energy, seem to severely limit the range of technological applications of these batteries.

On the other hand, the interest in silver solid-state power sources could be sensibly stimulated if a fully rechargeable system would be realized. Detailed kinetic studies of silver(31,32) and iodine-based(28, 29,33) electrodes in silver solid electrolytes have been carried out to evaluate this possibility. The results typically indicate that both electrodes are basically reversible but their practical rechargeability is limited by the already mentioned interfacial polarization phenomena(see Fig.3).

These problems might be overcome by the use of layer-type compounds(e.g., the transition metal dichalcogenides, such as TiS_2) successfully employed as reversible intercalation electrodes in liquid electrolyte batteries(34). The electrode process, which implies the insertion of the electroactive species between the Van der Waals layers of the dichalcogenide, seems of particular interest when utilized in solid-state cells. In fact, the insertion process should result in an expansion of the depth of the interface with consequent reduction of nucleation and other polarization effects commonly experienced with metal surfaces.

Indeed,kinetic studies carried out on various insertion compounds indicate that these intercalation electrodes are much more cyclable than pure metals in solid-state cells,as shown by the comparison between the two related polarization curves,reported in Figure 6 (35). However,the cycling operation of these electrodes may be limited to shallow regimes because of diffusion problems of the electroactive species. Under such conditions, a large number of cycles have been effectively obtained with a Ag_xNbS_2 electrode in contact with the $Ag_7I_4AsO_4$ silver vitreous solid electrolyte(35).

Another approach for the improvement of the cyclability of a solid-state cell,is related to the use of electrodes having an extended range of stoichiometry. Typical examples are the silver dichalcogenides,such as $Ag_{2-x}Se$ or $Ag_{2-x}Te$,which may assume a variable silver composition. It follows that the voltage of a cell of the type:

$$Ag\ /\ Ag_6I_4WO_4\ /\ Ag_{2-x}Se \qquad |6|$$

depends on the level(x) of silver concentration in the $Ag_{2-x}Se$ compound(36).Since the silver dichalcogenide is a mixed ionic(via silver ions) and electronic(via electrons) conductor,it is possible to cycle the cell by moving silver in and out of the selenide. The voltage of the cell (0 - 120 mV at 25 °C) and the cycling regimes(about 50 $\mu A\ cm^{-2}$) are possibly too low to make it of interest as a practical secondary battery.

On the other hand,the fact that the cell,after having been charged to a certain degree,maintains the acquired voltage for a long time,makes the cell very suitable as a solid-state memory element. Indeed the device is now produced commercially for this purpose(37) , with the three-electrode configuration schematically indicated in Figure 7(38).

The change in silver composition in the $Ag_{2-x}Se$ mixed conductor,induced by a current pulse,results in an output voltage 'memorized' between the silver reference and the selenide. The cell can be cycled to the desired voltage level in few seconds,assuming thus the characteristic of a low-speed,long-storage component, of great utility in integrated circuits. In conclusion, the device represents a very valid example of the role that electrochemical solid-state cells may assume in the present technology.

REFERENCES

(1) See for instance:
S.Pizzini ang G.Bianchi,La Chimica e l'Industria, 54:224;1972 and related references.

(2) See for instance:
F.A. Kroger"The Chemistry of Imperfect Crystals" North Holland,Amsterdam;1964;
C.Kittel,"Introduction to Solid State Physics" Wiley,New York;1966;
A.Lidiard,"Handbuch der Physik",Flugge Ed.Bond XX, Springler Verlag,Berlin;1957;
N.N.Greenwood,"Ionic Crystals,Lattice Defects and Nonstoichiometry",Butterworths,London;1970;
H.M.Rosenberg,"The Solid State",Clarendon,Oxford, 1975.

(3) B.B.Owens and G.R.Argue,Science,157:308;1967.

(4) S.Geller,Science,157:310;1967.

(5) S.Geller,"Fast Ion Transport in Solids",W.van Gool Ed.,North Holland,Amsterdam;1973.

(6) H.Wiedersich and S.Geller,"The Chemistry of Extended Defects in Non-Metallic Solids",North Holland, Amsterdam:629;1970.

(7) R.D.Armstrong,R.S.Bulmier and T.Dickinson, J Solid State Chem 8:219;1973.

(8) D.O.Raleigh,J Electrochem Soc 124:1157;1977.

(9) M.D.Ingram and C.A.Vincent,Annual Reports of the Chemical Society:23;1977.

(10)S.Geller"Physics of Superionic Conductors",Springer-Verlag,Berlin,Heidelberg,New York;1979.

(11)J.B.Bates and G.C.Farrington,"Fast Ionic Transport in Solids",North Holland,Amsterdam;1981.

(12)T.Takahashi,J Appl Electrochem 3:79;1973.

(13)P.McGeehin and A.Hooper,J Materials Sci 12:1;1977.

(14)J.C.Phillips,Rev Mod Phys 42:317;1970.

(15)J.C.Phillips,J Electrochem Soc 123:934;1976.

(16)T.Takahashi,O.Yamamoto and S.Ikeda,J Electrochem Soc 120:1431;1973.

(17)T.Takahashi and O.Yamamoto,J Electrochem Soc 122: 83 ;1975.

(18)A.F.Sammels,J.Z.Gougoutas and B.B.Owens,J Electrochem Soc 122:1291;1975.

(19)M.Lazzari and B.Scrosati,J Power Sources,1:333; 1976/77.

(20)B.Scrosati,A.Ricci and M.Lazzari,J Appl Electrochem 6:237;1976.

(21)F.Bonino,M.Lazzari,A.Lonardi,B.Rivolta and B.Scrosati,J Solid State Chem 20:315;1977.

(22)M.Lazzari,B.Scrosati and C.A.Vincent,Electrochim Acta 22:51;1977.

(23)M.Lazzari,B.Scrosati and C.A.Vincent,J Am Ceram Soc 61:451;1978.

(24)M.Lazzari,C.A.Vincent and B.Scrosati,"Fast Ion Transport in Solids",Vashista,Mundy,Shenoy Eds., North Holland,Amsterdam:713;1979.

(25)A.Magistris,A.Schiraldi and G.Chiodelli,Electrochim Acta 22:689;1978.

(26)T.Minami,Y.Takuma and M.Tanaka,J Electrochem Soc 124:1659;1977.

(27)B.B.Owens,"Advances in Electrochemistry and Electrochemical Engineering",P.Delahay and C.W.Tobias Eds, Vol.8,Wiley-Interscience,New York;1971.

(28)B.Scrosati,M.Torroni and A.D.Butherus,"Power Sources 4",D.H.Collins Ed.,Academic Press.,London:453; 1973.

(29)M.Pampallona,A.Ricci,B.Scrosati and C.A.Vincent, J Appl Electrochem 6:269;1976.

(30)B.Scrosati,F.Papaleo,G.Pistoia and M.Lazzari, J Electrochem Soc 122:339;1975.

(31)R.D.Armstrong,T.Dickinson,H.P.Thirsk and R.Whitfield,J Electroanal Chem 29:301;1971.

(32)B.Scrosati and A.D.Butherus,J Electrochem Soc 119:128;1972.

(33)B.Scrosati,J Electrochem Soc 120:78;1973.

(34)M.S.Whittingham,Prog Solid State Chem 12:41;1978.

(35)M.Patriatca,A.Voso,B.Scrosati,F.Bonino and M.Lazzari,Solid State Ionics 6:15;1982.

(36)T.Takahashi and O.Yamamoto,J Electrochem Soc 118:1051;1971.

(37)Sanyo Technical Review 4:3;1972.

(38)Chemistry International 4:5;1981.

TABLE 1 - Some typical examples of silver solid electrolytes.(12).

electrolyte	conductivity at 25°C (Sm^{-1})
$RbAg_4I_5$	27
KAg_4I_5	21
$NH_4Ag_4I_5$	19
$QAg_6I_7(C_nH_mNI.6AgI)$	
Q=tetramethylammonium	4
Q=diethyldimethylammonium	6
Q=tetraethylammonium	1
KAg_4I_4CN	14
$RbAg_4I_4CN$	18
$Ag_7I_4PO_4$	2
$Ag_{19}I_{15}P_2O_7$	9
$Ag_6I_4WO_4$	5
$Ag_7I_4AsO_4$	0.4

TABLE 2 - Ionicity and free energy difference of phase transition of some A^NB^{8-N} compounds (15).

A^NB^{8-N} compound	$0.79-f_i$	ΔG_T (kcal/mol)
AgCl	-0.07	
AgBr	-0.06	
AgI	0.02	0.5
CuCl	0.05	4.5
CuBr	0.05	4.5
CuI	0.10	8.5

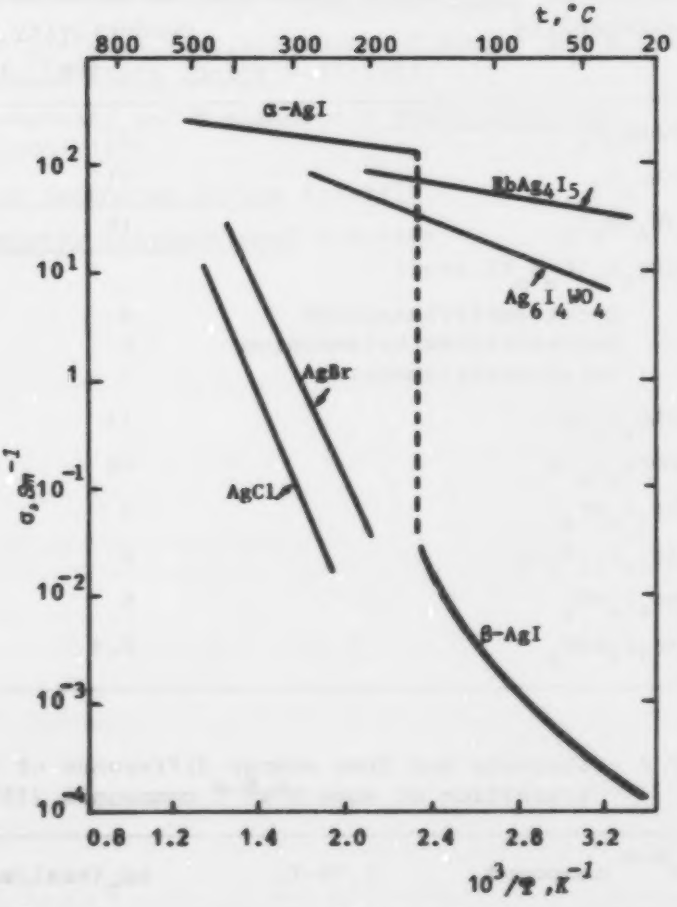

Fig. 1 Conductivity of some silver-ion conductors.

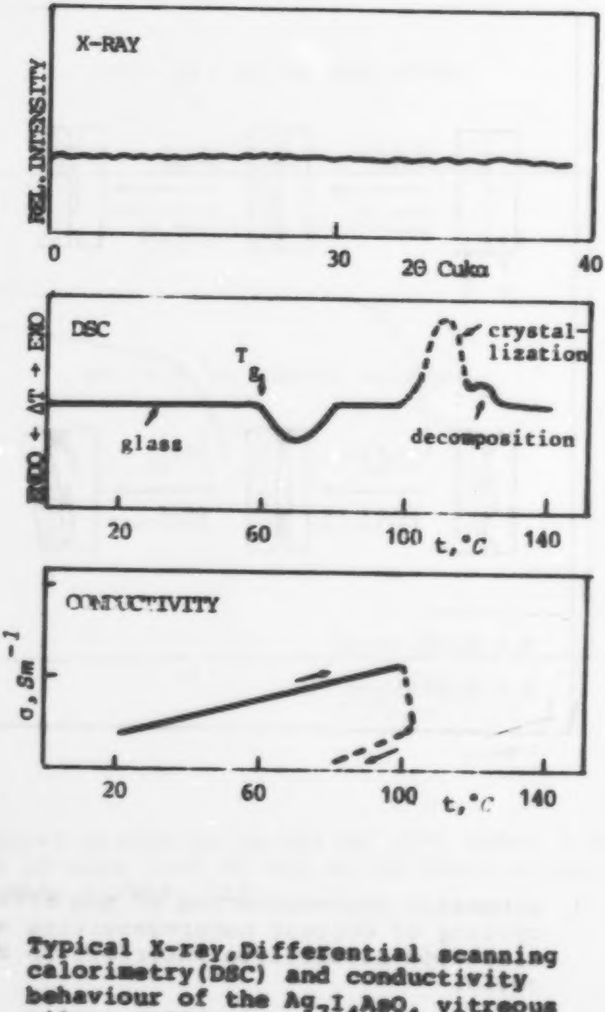

Fig. 2 Typical X-ray, Differential scanning calorimetry (DSC) and conductivity behaviour of the $Ag_7I_4AsO_4$ vitreous silver solid electrolyte.

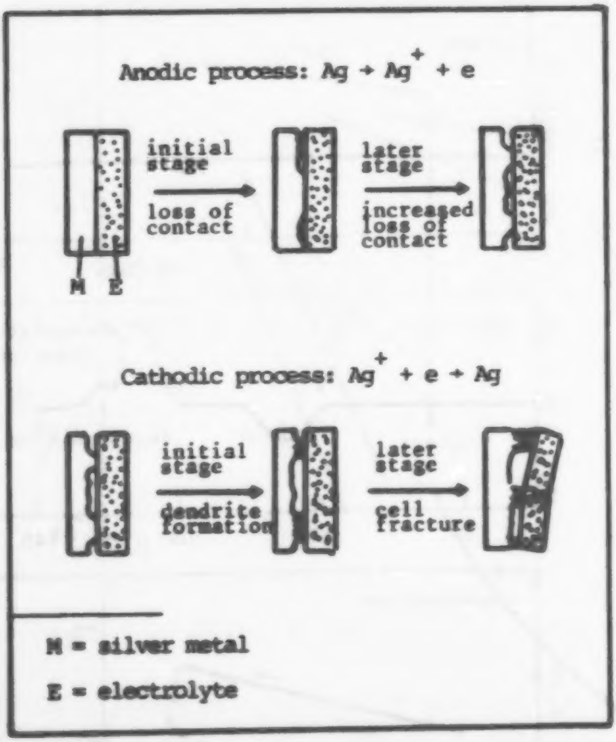
Anodic process: $Ag \rightarrow Ag^+ + e$
initial stage
loss of contact
later stage
increased loss of contact
M
E
Cathodic process: $Ag^+ + e \rightarrow Ag$
initial stage
dendrite formation
later stage
cell fracture
M = silver metal
E = electrolyte

Fig. 3 Schematic representation of the effect upon cycling of contact heterogeneities at the electrode-electrolyte interface in solid-state cells.

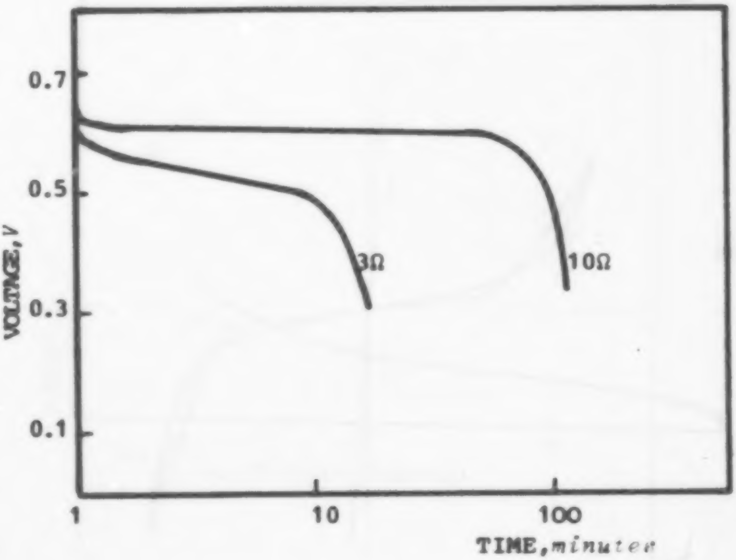

Fig. 4 Typical discharge curves at 25°C under 3 ohms and 10 ohms load of the solid-state battery $Ag/RbAg_4I_5/RbI_3$ (27).

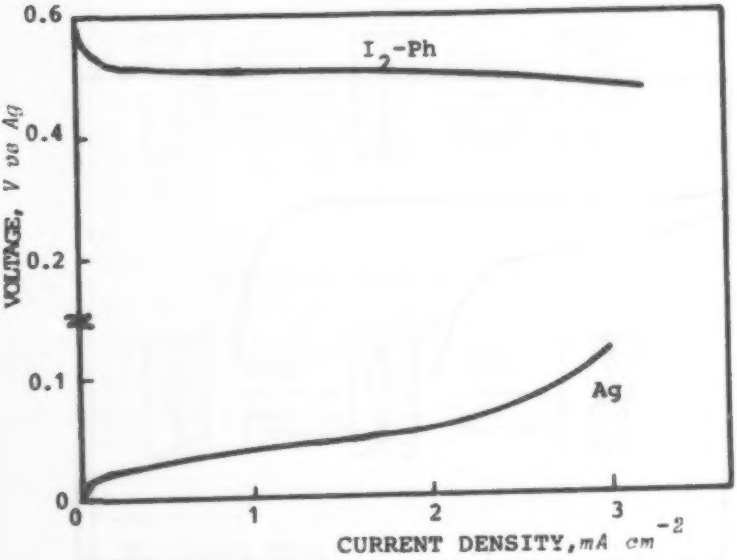

Fig. 5 Typical polarizations of the silver anode(Ag) and the iodine-phenothiazine(I_2-Ph) cathode in the solid-state cell Ag/$Ag_7I_4AsO_4$/I_2-Ph (30).

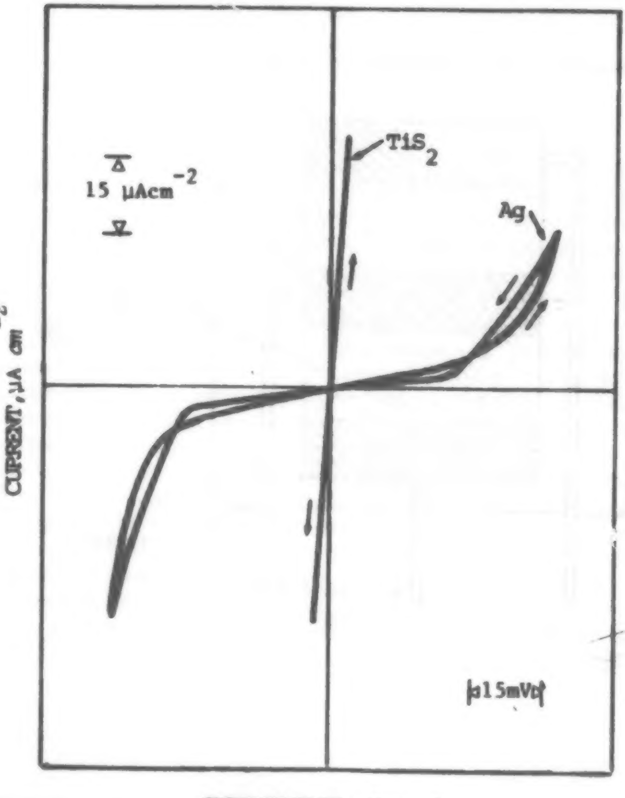

Fig. 6 Typical cathodic and anodic polarization cycles for Ag metal and the TiS_2 intercalation compound, in composite pressed cells using the $Ag_7I_4AsO_4$ vitreous solid electrolyte.

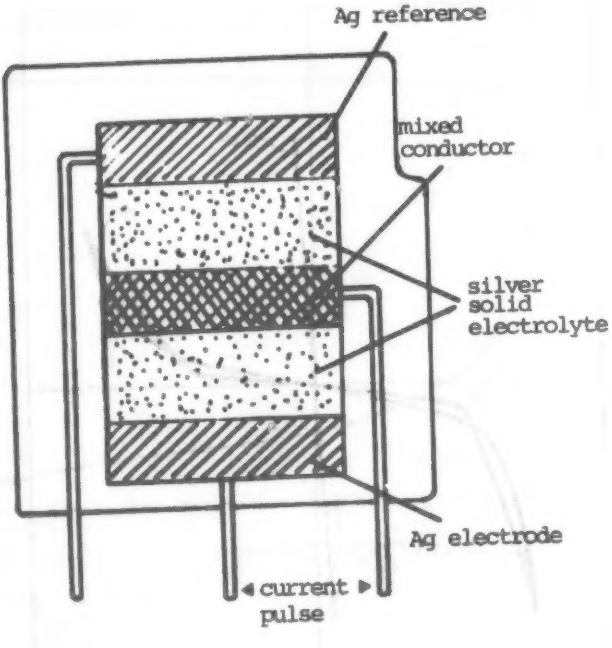
Ag reference
mixed conductor
silver solid electrolyte
Ag electrode
current pulse

Fig. 7 Schematic diagram of the solid-state, three-electrode, storage cell 'memoriode', based on a variable composition mixed conductor (37,38).

OXIDE ELECTROLYTES WITH FLUORITE STRUCTURE

E.C. Subbarao and H.S. Maiti

Tata Research Development &Design Centre,
Pune, INDIA

Indian Institute of Technology,
Kharagpur, INDIA

ABSTRACT

Oxide electrolytes based on zirconia, thoria, ceria and bismuth oxide crystallise with either perfect or distorted fluorite structure. They are characterized by their high oxygen ion conductivity which is due to highly mobile oxygen vacancies whose concentration is fixed by the aliovalent impurities. The ionic transference number and consequently the usefulness of the solid electrolytes is limited to specific ranges of temperature and oxygen partial pressure. Variations of conductivity and transference number of important oxygen ion conductors with experimental parameters are considered and their suitability for specific applications is discussed. Important technological applications of these electrolytes include oxygen pump, high temperature fuel cells for energy conversion, high temperature electrolysis of steam to generate hydrogen and also as a catalyzer for various chemical reactions. Working principle, design, construction and performance of these devices are discussed in detail with emphasis on more recent developments. Electrode materials and the importance of electrode-electrolyte interface reaction are also considered.

KEY WORDS:- Oxide electrolytes, fluorite, oxygen sensor, fuel cell, electrolyser.

RÉSUMÉ

Les oxydes électrolytes à base d'oxydes de zirconium, de thorium, de cérium et de bismuth cristallisent avec la structure partaite ou déformée de la fluorine. Ce qui les caractérise, c'est leur forte conductivité pour l'ion exygène causée par la grande mobilité des trous d'oxygène, dont la concentration est déterminée par les impuretés de valence différente. Le nombre de transport ionique, et par conséquent l'utilité des électrolytes solides, est limité à des plages spécifiques de température et de pression partielle de l'oxygéne. On considére la variation de la conductivité et du nombre de transport des conducteurs importants d'ion d'oxygène en fonction des paramètres expérimentaux et l'on traite de leur applicabilité à des cas spécifiques. Parmi les applications technologiques importantes de ces électrolytes, citons: les détecteurs d'oxygène pour systèmes gazeux et liquides, les pompes électrochimiques à oxygène, les piles à combustible à haute température pour conversion d'énergie, l'utilisation pour électrolyse à haute température de la vapeur pour produire de l'hydrogène et l'emploi comme catalyseur de diverses réactions chimiques. On traite du principe de fonctionnement, de la conception, de la construction et du rendement des produits en question en mettant l'accent sur les développements des plus récents. On considère aussi la matière des électrodes et l'importance de la réaction à l'interface électrode-électrolyte.

INTRODUCTION

Oxide electrolytes constitute the most important class of anion conducting solid electrolytes mainly due to their wide range of commercial as well as research applications. They are characterised by exceptionally high oxygen ion conductivity which is, however, few orders of magnitude lower than the conductivity of most of the cationic conductors, and therefore are useful only at elevated temperatures (400-1600°C). Development of these electrolytes has been actively pursued during the last two decades by multi-disciplinary groups.

It is interesting to note that the most useful oxide electrolytes crystallise either in the perfect or slightly distorted fluorite structure. These are normally solid solutions in which the major components are ZrO_2, HfO_2, ThO_2, CeO_2 or Bi_2O_3 doped with aliovalent oxides like CaO, MgO, Y_2O_3, Sc_2O_3 or rare earth oxides in the composition range 0-20 m/o. Amongst these, either CaO or Y_2O_3 doped ZrO_2 were the first to be developed and even now, these are the electrolytes used in most of the applications. Addition of the impurity oxides not only results in an enhanced oxygen ion conduction by increasing the oxygen vacancy concentration but is required in some cases (e.g. ZrO_2, HfO_2 and Bi_2O_3) to stabilise the host oxide by forming a cubic fluorite phase which is otherwise not present in the pure oxide (e.g. ZrO_2, HfO_2) or not obtained at room temperature (e.g. Bi_2O_3).

These electrolytes, in combination with suitable electrodes, are conveniently used in high temperature electrochemical cells for technological applications such as high temperature fuel cells, high temperature electrolysis of water to generate hydrogen and oxygen sensors for furnace flue gas, automobile exhaust and molten steel, and for the measurement of thermodynamic and kinetic parameters of various alloys and oxides.

Different aspects of these electrolytes were earlier reviewed (1-4). The aim of this article is to discuss certain specific aspects of these electrolytes with emphasis on the technological applications with energy implications.

CRYSTAL STRUCTURE AND PHASE STABILITY

In the atomic arrangement of the fluorite (CaF_2) structure, each cation is surrounded by eight oxygen ions and each oxygen ion is tetrahedrally coordinated by 4 cations. While pure ThO_2 and CeO_2 crystallise in the fluorite structure, pure ZrO_2 is obtained in monoclinic form at room temperature. However, the cubic fluorite phase in ZrO_2 is obtained by forming solid solutions with various oxides of di - or tri-valent cations. Since high oxygen ion conduction is closely related to the structural features of the fluorite phase, a knowledge of phase stability in different solid electrolyte systems is of fundamental importance.

The oxides most commonly used to stabilise the cubic fluorite phase in ZrO_2 are CaO, MgO, Y_2O_3 , Sc_2O_3 and a number of rare earth sesqui-oxides. Phase diagrams of the zirconia binary systems containing these oxides have been studied extensively; however, controversies exist especially about the compositional limits as well as the low temperature stability of the cubic fluorite phase. The eutectoid decomposition of the fluorite phase at around 1220°C and an order - disorder transition around 1000°C have been reported in CaO doped ZrO_2 (5-9). The most recent phase equilibrium diagram of the system in the region ZrO_2- $CaZrO_3$, determined by Stubican and Ray (10), is shown at 2000°C and the room temperature equilibrium phases are monoclinic ZrO_2 solid solution and an ordered phase, $CaZr_4O_9$, produced as a result of long range defect ordering. It may, however, be noted that the low temperature ordered phase is obtained only when the samples quenched from high temperature ($>$ 1700°C) are annealed at 1000°C for very long time (usually for several weeks). Under normal cooling conditions, the cubic phase is retained at room temperature.

The cubic phase in ZrO_2-MgO system is usually obtained above 1400°C, below which it undergoes eutectoid decomposition.

The fluorite phase field in the ZrO_2- Y_2O_3 system is much wider than in any other system. Stubican et al (11) placed the cubic phase field limits as 9 to 55 m/o Y_2O_3 at 2000°C, while Srivastava et al (12) set the limits at 7 and 50 m/o Y_2O_3. It was shown by Ioffe et al (13) that the cubic phase might be obtained with only 4.5 m/o Y_2O_3 if the samples are prepared by special chemical methods. The cubic phase is stable down to room temperature by normal cooling but decomposes to monoclinic solid solution and a compound, $Zr_4Y_3O_{12}$, when the quenched samples are annealed for long enough time. The phase equilibrium diagram of the system is shown in Fig. 2.

Cubic fluorite phase is also obtained in ternary systems containing ZrO_2. Phase diagrams of some of the systems e.g. ZrO_2-Y_2O_3-MgO, ZrO_2- CaO-MgO have been discussed by Stubican and Hellmann (14).

Phase diagrams for the ThO_2 and CeO_2 base electrolytes have not been studied in detail, though the solubility limit of different oxides in these systems have been determined (15-21).

Pure bismuth sesqui-oxide has two thermodynamically stable polymorphs (22, 33) : a monoclinic α- form stable below 730°C and a f.c.c. δ - form stable above this temperature. The form may be regarded as a defect fluorite type including a large number of vacant oxygen sites with a formula $Bi_4O_6\square_2$ where $\square$ represents oxygen ion vacancy. The oxide also has two metastable polymorphs termed as β and γ phases crystallising in the tetragonal and b.c.c. structures respectively.

While the α phase is a poor p-type conductor, the δ phase has an extremely high oxygen ion conductivity (24,25). The high temperature phase can be stabilized at lower temperatures by a number of oxide additions such as Y_2O_3, V_2O_5, Ta_2O_5 and WO_3(26). The rhombohedral phase formed by the addition of oxides of large cations like Ca, Ba and La is also reported to have high oxygen ion conductivity.

DEFECT STRUCTURE AND ELECTRICAL CONDUCTIVITY

Defect Equilibria

Some of the basic criteria which must be satisfied by an oxide electrolyte suitable for **technological applications are:** (i) it must have a high electrical conductivity (σ), (ii) transference number for oxygen ion should be very close to unity ($t_{O^{2-}} >$ 0.99), (iii) it can be formed into dense shapes without having any permeability to molecular oxygen. Electrical properties of the oxides are closely related to the nature and concentration of the predominent defect present in them(4,27,28). Most common structural disorder in fluorite type oxides are oxygen vacancies together with interstitial oxygen ions. At high oxygen partial pressures of the gas phase, one expects oxygen interstitials to predominate in the oxide while at lower oxygen partial pressures vacancies become important. Most of the fluorite type oxides contain these lattice defects in their fully ionised state under all conditions of temperature and oxygen partial pressures. In pure CeO_2, Tuller and Nowick (29) have, however, suggested singly ionised vacancies to be dominant at relatively low oxygen partial pressures. Non-stoichiometry in the oxides results when the charge compensation takes place by creation of excess electronic defects like quasi-free electrons (e) or electron holes (h). Such defect equilibria may be represented by following equations using Kröger- Vink notation

$0 \rightleftharpoons \tfrac{1}{2}O_2\ (g) + V_O^{\bullet\bullet} + 2e'$ (for vacancy) (1)

$\tfrac{1}{2}O_2\ (g) \rightleftharpoons O_i'' + 2h^{\bullet}$ (for interstitial) (2)

Defect situation of these types lead to the predominance of electronic charge carriers whose concentration is proportional to either $P_{O_2}^{-1/6}$ or $P_{O_2}^{+1/6}$ depending on whether they are n-type or p- type respectively.

With an addition of even a trace amount of aliovalent oxide to the fluorite electrolytes the concentration of oxygen vacancies far exceeds that of the interstitials and also that of the electronic charge carriers. Taking CaO-doped ZrO_2 as an example, the defect reaction may be written as

$$CaO \longrightarrow Ca_{Zr}'' + V_O^{\cdot\cdot} + O_O \qquad (3)$$

in which case the neutrality condition is

$$\left[Ca_{Zr}''\right] = \left[V_O^{\cdot\cdot}\right] \qquad (4)$$

This leads to an enhanced oxygen ion conduction whose magnitude remains independent of oxygen partial pressure. However, at relatively high temperatures and under extreme conditions of oxygen partial pressure intrinsic defect reactions (eqns. 1 & 2) take over. Consequently, oxygen partial pressure dependent electronic conductivity appears. Mixed conduction is observed in the transition region where the concentration of both ionic and electronic charge carriers are comparable. It should, however, be noted that the mobility of electronic charge carriers is about 100-1000 times higher than that of the ions and therefore even a small concentration of the former contributes significantly to the total conductivity.

Electrical Conductivity and Electrolytic Domain

The variation of isothermal electrical conductivity with oxygen partial pressure for some fluorite type oxide electrolytes is plotted in Fig.3. Ionic conduction region in each case is depicted by the horizontal portion of the plots. The behaviour of ZrO_2 and CeO_2 base electrolytes are similar except that CeO_2, being more easily reducible has its n-type conduction region extending upto a much higher oxygen partial pressure than that of ZrO_2. Both of them do not show any p-type conductivity below one atmosphere oxygen pressure. On the other hand, ThO_2 electrolytes are mixed conductors with significant p-type conduction down to a oxygen partial pressure of about 10^{-6} atm. and become n-type at much lower oxygen partial pressure compared to any other electrolyte.

The oxygen partial pressure limits of ionic conduction region in most cases are strongly temperature dependent. According to Patterson (30, 31) both the high and low oxygen partial pressure limits are linearly related to the inverse of absolute temperature and therefore on a P_{O_2} - 1/T plane two intersecting straight lines are obtained corresponding to the lower and upper limits. The lines corresponding to t_{ion}=0.99 represent the boundaries for the "electrolytic domain" for a specific oxide (Fig.4).

In most applications, even a trace amount of electronic conductivity in the electrolyte strongly deteriorates the performance of the devices. Accordingly accurate determination of the electronic contribution is extremely important for these electrolytes, for which Wagner's polarisation measurement (32) using blocking electrodes, Kleitz et. al's measurement of the oxygen semi-permeability through the electrolyte under different experimental conditions (33),Ramanarayanan's (34) new technique of directly determining the low oxygen partial pressure limit may be employed.

Compositional Effect

As expected from eqn. 4, the ionic conductivity of an oxide electrolyte is proportional to the concentration of dopant oxide. However, in practice, the linearity is observed only at very low concentration while at higher dopant levels it deviates from linearity and often goes through a peak followed by a gradual decrease. Formation of defect complexes through coulombic interaction between the impurity cations and the oxygen vacancies is believed to be responsible for the observed non-linear variation of electrical conductivity at lower defect concentrations. Lowering of conductivity at higher concentrations has been attributed to the formation of "defect clusters" or "zones" involving long range defect interactions. The ordered phase appears only when the quenched specimens are aged at temperatures around 1000°C for long time. This is accompanied by a significant increase in resistivity of stabilized zirconia electrolytes and is the cause of great concern particularly during their use in high temperature fuel cells. Formation of the ordered phases in aged specimens has been confirmed using electron diffraction techniques (7,8).

TECHNOLOGICAL APPLICATIONS

As mentioned earlier, oxide electrolytes have many important applications both in the research laboratories and in commercial devices. Due to their high temperature stability and selectivity for oxygen ions, they can, in principle, be used in any high temperature process involving measurement or control of oxygen activity and also in high temperature electrochemical energy conversion involving oxygen as the active species. In the following sections the working principle and construction of some of the technologically important devices using oxide electrolytes are discussed.

Oxygen Sensors

One of the most convenient ways to measure oxygen content in a solid, liquid or gaseous system is to form an electrochemical cell of the type

$$P_{O_2}\,(\mathrm{Me})/\text{Oxide electrolyte}/(\mathrm{Me})P_{O_2}\ (\mathrm{ref})$$

(unknown) (known reference)

in which Me represents a metal electrode. The open circuit emf of the cell is given by

$$E = \frac{RT}{4F}\ \ln\left[P_{O_2}(\mathrm{ref})/P_{O_2}\right] \qquad (5)$$

for an electrolyte having predominantly ionic conduction($t_{ion} \cong 1$) Other notations in the equation have their usual meaning. One of the faces of the electrolyte is kept in contact with the unknown system maintaining thermodynamic equilibrium while a known oxygen partial pressure on the other side is used as the reference. The magnitude of the measured emf at a suitable temperature provides a direct indication of the unknown oxygen content. The principle has been successfully used in various types of oxygen sensors suitable for specific applications. Advantages of these electrochemical sensors are :(i) quick and continuous measurement, useful for automatic feedback control system; (ii) good accuracy and (iii) no requirement of any elaborate experimental arrangement. The fact that the devices must be operated at elevated temperatures becomes an added advantage for some applications while this creates difficulty in others.

Either calcia or yttria stabilised zirconia is usually used as the electrolyte in most of the commercial sensors. Partial substitution of the stabiliser by MgO has been tried to improve thermal shock resistance and to reduce the cost. Partially stabilised zirconia is unsuitable for applications requiring continuous measurement, due to pronounced aging. Thoria base electrolytes have been occasionally used particularly for the measurement of very low levels of oxygen in molten steel or molten sodium. Higher conductivities of ceria and bismuth oxide electrolytes have not been commercially exploited mainly because of their high cost and limited electrolytic domain. Air is the most common reference system used in these sensors. Neverthless metal-metal oxide coexistence electrodes are quite common for certain applications.

Eventhough the working principle and fabrication of these sensors are relatively simple their performance, particularly the reproducibility and reliability, strongly depend on a number of factors which not only include material parameters of the electrolyte and the electrode but also the design aspects of the actual sensors and the specific purpose for which they are used. Importance of some of these parameters has been recently discussed by Steele et al (35). Lower conductivity of the electrolyte results in high cell impedance and attainment of thermodynamic equilibrium becomes difficult. Cell impedance of less than I kilo-ohm is preferred for most applications.

One of the ways of lowering cell impedance is to use thinner electrolytes which also helps in lowering the operating temperature. Self supported electrolytes of 0.4 - 0.5 mm thickness can be produced by hot pressing technique. Preparation of thinner film ($<1 \mu m$) oxygen sensors using R.F. sputtering technique has been suggested (36-38). The complete sensor is fabricated by successive deposition of electrode and electrolyte on a metallic substrate. Either platinum saturated with oxygen or porous nickel incorporating enough oxygen to convert a part of the metal to its oxide may be used as the reference electrode while sputtered platinum film on the top of the electrolyte is used as the measuring electrode. Operating temperature of as low as 400°C has been suggested, using calcia stabilized zirconia as the electrolyte.

Existence of even a small amount of electronic conductivity in the electrolyte causes considerable error in the developed emf not only because the eqn. (5) becomes invalid but also due to oxygen semipermeability through the electrolyte (39). The latter becomes more significant if the oxygen partial pressure gradient across the electrolyte is high. This problem may be eliminated by the use of a stabilized zirconia point electrode (39,40) or by a suitable choice of reference electrode, usually a metal-metal oxide system.

All commercial electrolytes are used in polycrystalline form. Their microstructure plays a significant role in sensor performance. To avoid molecular diffusion of oxygen through the electrolyte, its porosity should be as low as possible (about 1% for liquid metal baths and much less for gas phase monitors). Commercial zirconia electrolytes usually contain small amount of Al_2O_3 and SiO_2 as impurities which are believed to be concentrated at the grain boundaries either as a glassy phase or ternary crystalline compounds. Presence of these and other precipitated phases adversely affects the electrical conductivity of the electrolyte and the response time of the sensor. Measurement accuracy and response time also depend on electrode kinetics which is in turn determined by the electrode morphology (method of preparation) and its catalytic activity. This is particularly true for gas phase monitors operating at lower temperatures (500-600°C) and used to monitor oxygen content of gas mixture containing reactive gases like CO, H_2, CH_4 etc.

Aside from oxygen sensors based on open circuit emf measurement, diffusion limited current measurement through a constriction in the electrolyte tube has also been suggested as an efficient oxygen sensor (41).

Car Exhaust Sensors

The use of three way catalytic system down the exhaust pipe of car engines has become a standard practice to satisfy the stringent requirements of emission control in several parts of the world. However, for most efficient functioning of the catalyst and also for fuel economy, the air-to-fuel ratio (A/F) of the engine must be controlled within a narrow range preferably by an automatic feedback control system. A solid electrolyte oxygen monitor with an electrical output varying with the oxygen partial pressure of the exhaust gas serves as an effective sensing device for this control system. The principal constitutents of the engine exhaust are unburnt hydrocarbon (HC), oxides of nitrogen (NO_x), H_2, CO_2, CO, O_2 etc. whose concentration varies with A/F ratio. The ratio of actual A/F ratio to the stoichiometric A/F ratio is called λ. In the fuel rich region ($\lambda < 1$) there are high concentrations of CO and HC whose values decrease with increasing value of A/F. Excess oxygen appears in the lean region ($\lambda > 1$) and the concentrations of CO_2 and NO_x become maximum in the lean region very close to the stoichiometric ratio ($\lambda = 1$). The concentration of H_2 is approximately 1/3 that of CO and the variation of H_2O follows that of CO_2. Such variations of the exhaust constituents lead to a significant change in oxygen partial pressure and sensor emf with A/F ratio with an abrupt change at the stoichiometric ratio($\lambda = 1$) (Fig. 5). Obviously the sensitivity of the sensor is maximum near the stoichiometric A/F ratio and nearly insensitive both in the rich and lean regions. The solid electrolyte sensors are thus useful to control the A/F ratio only within a narrow range around $\lambda = 1$ which has become the normal operational range for most of the sensors developed so far (45-50).

Yttria stabilized zirconia is invariably the electrolyte used for this purpose mainly due to its high conductivity. The cost may be reduced by substitution (upto 50%) of Y_2O_3 by MgO (51). The details of construction of these sensors are shown in Fig.6. They are usually constructed with a one end closed electrolyte tube or electrolyte disc sealed at the end of a ceramic tube (usually forsterte) (52). Platinum paste painted on either side of the electrolyte forms the porous electrode and also provides the catalytic surface for quick attainment of thermodynamic equilibrium between the reactive gaseous constituents. The conducting paint is extended upto the open ends of the tube and acts as the electrical leads. Outside surface of the open end of the tube is sealed to a metallic housing with either a metallic or graphite gasket. The sensor is inserted into the exhaust manifold normally through a spark plug shell. The outside surface of electrolyte tube is exposed to the exhaust gas while the inside of the tube is open to air (reference electrode). For protection against erosion by the exhaust gas, the electrode is normally covered by a porous ceramic (spinel) coating. The complete tube is protected with a metallic shroud . Since the emf change of the sensors within their working range of A/F rafio is very large,the effect of temperature is relatively insignificant. Sensors are therefore heated directly by the exhaust gas and no auxiliary heater becomes necessary.

The ideal sensor response depicted in Fig. 5 is obtained only in laboratory with synthetic gas mixtures. However, the sensors exposed to actual car exhaust often exhibit non-ideal behaviour mostly due to the non-equilibrium chemical and electrochemical reactions occuring at the platinum electrodes (42,44). The non-ideality of the response may be of several types: 1)abruptness of the voltage change may be absent; 2) voltage difference between the lean and the rich regions may be low; 3) voltage over the entire range may be low; 4) the step-like transition may shift away from the $\lambda = 1$ position;5) aging of the electrolyte causing increasing of response time (50,54). As expected, the non-ideal behaviour strongly depends on the electrode material and electrode structure. Use of the ceramic coating on the platinum electrode usually improves the equilibrium condition with a consequent increase in voltage step even though the position of the step is slightly shifted. Response time is the time required to change the sensor voltage from its lean (or rich) value to the set point which is usually the mean of the lean and the rich voltages. The response time of commercial sensors is generally about 200 ms at 350°C but reduces to few milliseconds at 700°C.

The main function of the three way catalysts are to oxidise unreacted CO to CO_2 and to reduce NO_x to N_2. Their effectiveness as well as fuel economy are best when the engine is operated slightly on the lean side, but, in this region, solid electrolyte sensors are inherently insensitive to change in A/F ratio and have a strong temperature dependence. Even then, attempts have been made to use lean A/F ratio sensors by precise measurement of emf changes and by overcoming the temperature effect by an additional electronic circuit which algebraically adds a voltage equivalent to temperature change to the measured sensor emf or by intentionally introduced electronic conductivity in the electrolyte by doping with Fe_2O_3 (43). The electronic conductivity having lower activation energy than for the ionic conduction, becomes significant only at low temperature ($< 300^{\circ}$C). The sensor output decreases due to internal short circuit and compensates for the normal increase due to reduced temperature. The success of such an internally compensated electrolyte is however yet to be proved on a commercial scale. On the other hand, Vitter and Henault (55) have used Pb-PbO co-existent electrode replacing air and found that the emf remained unaltered throughout the temperature range (400-1000°C).

Oxygen Monitors for Industrial Furnaces

Another important application of solid electrolyte oxygen sensors is the measurement of oxygen content of the flue gases of industrial furnaces for improving the combustion efficiency of boilers, glass tanks and metallurgical furnaces which use either liquid or gaseous fuels. For maximum combustion efficiency, it is sufficient to operate the furnaces with a slight excess ($\sim 0.5\%$) of oxygen compared to the stoichiometric A/F ratio. However in the absence of a monitoring device they are normally operated with 5-10% excess oxygen (equivalent to 25-50% excess air) to make sure that there is no unburnt fuel but this leads to significantly poor combustion efficiency. The performance of solid electrolyte sensors for a continuous and accurate monitoring of oxygen content is much better than that of others. For example, in boilers, the fuel saving ranges upto 30% compared to 3% with paramagnetic sensors (40). Referring to Fig.5 these sensors are required to be operated in the lean region very close to the stoichiometric ratio (λ=1.01-1.10). The working emf range is therefore quite low(50-100 mv depending on temperature) and does not vary significantly with changing values of λ but has a strong temperature dependence.

Two different designs are most common for these sensors: (1) In-situ sensors in which the sensor head usually consisting of a small length of one end closed zirconia tube which is sealed at the open end to a metallic tube is inserted through the furnace wall and exposed directly to the hot flue gas. (2) In another design the flue gas is pumped out of the furnace and allowed to flow through an electrolyte tube with both ends open, kept inside a small electrically heated furnace. In a slight modification of this design the electrolyte tube is replaced by a disc. Hot flue gas and preheated air are injected against the opposite faces of the disc to keep it hot. No extra furnace is used. For each of these designs platinum paint is used as the metal electrodes and air as the reference. Filters are necessary for dust control.

The flue gas temperature in industrial furnaces often varies over a wide range and creates several problems for the in-situ monitors:(1) it leads to fluctuations in the measured emf directly as well as indirectly through changes in the reaction constants of different gaseous constitutents.(2) Rapid temperature changes lead to temperature gradients across the electrolyte and consequent thermal emf. It may also develop cracks in the electrolyte due to thermal shock. To overcome these difficulties the sensor head is usually fitted with an auxiliary heater. The lattor design has the disadvantage that is may not indicate the exact furnace temperature condition. This is particularly true because the flue gas usually contains reactive gases like CH_4, CO, H_2etc. However the design is very suitable for portable type oxygen analysers which are used not only for combustion control but for many other applications like oxygen measurement in ambient air and also in high purity inert gases, measurement of theoretical amount of air for fuel gas etc. Such analyzers are being commercially produced by a number of companies in Japan and USA(56).

The flue gases usually contain significant amounts of H_2O together with various oxides of sulphur(SO_x). Both these vapours may condense together on the electrolyte and deteriorate its properties if the temperature is too low. For the sensors other than the in-situ type, the problem can be avoided with the help of "gas samplers",which eliminate these poisonous gases by condensation or by washing by water jet.

Such oxygen sensors are also useful to monitor the oxygen content inside the controlled atmosphere furnaces usually used for bright annealing or carburisation of steel, to avoid too reducing an atmosphere which causes decarburization or too oxidising an atmosphere which leads to oxidation of the surface. The temperature involved in this case is comparatively higher (800-1000°C)and the desired oxygen partial pressure is much lower ($\sim 10^{-20}$atm.). Under these conditions a small amount of electronic conductivity is usually introduced in the electrolyte.

The impurities in the electrolyte must be kept at a minimum. e.g. transition metals to limit the electronic conductivity and SiO_2 and MgO to limit the porosity due to evaporation of SiO and Mg. Since metallic platinum becomes brittle under reducing atmosphere, it is preferable to use either Ni-Cr or Au-Pd. To reduce the effect of electronic conductivity, reference electrode of lower oxygen partial pressure, usually metal-metal oxides like Ni-NiO, $Cu-Cu_2O$, Fe-FeO etc.may be used instead of air. These redox systems can be sealed inside a solid electrolyte tube and with that it is possible to fabricate the sensors in the miniaturised form. The accuracy of these units depends to a large extent on the kinetics of equilibrium of the redox system which are too slow below 800°C. However, Pd-PdO system has been found satisfactory down to 400°C (57,58).

Oxygen Probes for Liquid Metals

The most important metallurgical processes requiring accurate determination of oxygen content in liquid metals are steel making and copper refining. Solid electrolyte oxygen probes have been most successful for both the processes. Conventionally, the oxygen content of the molten steel bath is determined by vacuum fusion in the laboratory and takes a minimum of 8-10 minutes. On the other hand, solid electrolyte oxygen probes provide a much quicker (20-30 seconds) and convenient method for oxygen measurement. In steel melts oxygen is present both as dissolved gas in the metal and also as solid or gaseous oxides entrapped within the bath. It is the chemical activity of dissolved oxygen which actually controls the steel making process and is also the quantity measured by the electrochemical probe.

Liquid metal oxygen probes are invariably of in-situ type for which the metal bath itself forms the working electrode. Either stabilised zirconia or doped thoria and hafnia can be used as the electrolyte due to their better chemical stability at the high temperatures involved (> 1300°C for steel melt and > 1100°C for liquid copper). However, ZrO_2 being the cheapest is mostly used in commercial probes. At these high temperatures, conductivity of the electrolyte is not a limiting parameter. Typical conductivity of calcia stabilized zirconia at 1600°C is 0.5 ohm^{-1} cm^{-1}, Partially stabilised zirconia with somewhat lower conductivity is usually preferred due to its better thermal shock resistance. Electronic conductivity of the electrolytes, however, becomes significant at the steel melting temperatures and is the cause of great concern particularly for measurement of very low oxygen activities. In this respect thoria base electrolytes have an edge over the others.

Considerable controversy exists regarding the low oxygen partial pressure limit (which is set by the appearance of significant electronic conductivity)down to which a zirconia electrolyte can be successfully used. Results of conductivity and polarization measurements at lower temperatures (<1000ºC) when extropolated to 1600ºC give a value of oxygen partial pressure of 10^{-10} atm. as the boundary of the ionic domain corresponding to 0.1% electronic conduction and may be considered as the lower limit of oxygen measurement of steel melt, which has actually been varified experimentally(59,60),or to lower values,if shorter time of measurement is used(61,62). As expected, the limits can be reduced to 1 ppm by using yttria doped thoria electrolytes. The exact value of the lower limit also depends on the particular reference electrode used in the measurement. Metal-metal oxide co-existence electrode (Mo-MoO_2, Cr-Cr_2O_3,Nb-Nb_2O_5 and Ta-Ta_2O_5) are most common even though air has also been used occasionally. The appearance of electronic conductivity induces oxygen transport across the electrolyte even under open circuit condition and changes the oxygen activity at the measuring electrode. This is, however, not a serious problem in one reading probes since the measurement is completed within a very short time(20-30 sec) and one can measure the emf reasonably accurately. But the emf equation for an ideal electrolyte (t_{ion}=1)as given by eqn(5) is not valid under this condition. Schmalzreid(63)has suggested a modified emf equation.

The design and construction of these sensors have been discussed by several investigators(64-66). One reading disposable probes are usually made with a disc type electrolyte sealed at the end of a silica tube of approximately 5 mm diameter and 40-50 mm length(66,67). The tube is partly filled with a mixture of Cr-Cr_2O_3 in which the end of a platinum lead wire is inserted. The open end of the tube is fixed at the end of a ceramic block(Fig. 7a)which also holds a molybdenum rod acting as the second electrical lead and a Pt/Pt-Rh thermocouple inside a protective silica 'U' tube. All these probe elements are covered with a steel cap to protect them from mechanical damage. The detachable assembly is mounted to a lance for immersion into the molten steel bath. For continuous measurement, the silica tube is replaced by a larger one end closed electrolyte tube. The tube is usually preheated and immersed slowly into the liquid metal to prevent damage due to thermal shock. The probes may be permanently installed in the wall or bottom of the furnace. Flowing air or oxygen is usually preferred as the reference. A faster response time is claimed for a needle type probe(Fig.7b)in which a metallic conductor of

1.5-2.5 mm dia. is used as the core(68). It is coated with a thin layer of reference electrode which is in turn covered with a layer of electrolyte. This needle replaces the sealed silica tube in one reading probes.

Oxygen content of molten copper is an important parameter which determines its quality. Higher oxygen content introduces brittleness and consequently makes subsequent wire drawing difficult. Zirconia oxygen probes are extensively used for continuous monitoring of oxygen activity of molten copper during continuous casting of wire rods particularly in the copper refineries of Japan(69,70). These probes are constructed with one end closed stabilised zirconia tubes which are permanently fixed over the tandish keeping the closed end immersed in the flowing metal. Fe-FeO, preferably in the form of fine powders (-200 mesh)of metallic iron exposed to air is used as the reference electrode(71). Metallic powders slowly oxidise during use. The life of these probes is 100-150 hrs.

Continuous measurement even with tubular probes in any liquid system at high temperatures (>1000°C) is always difficult due to high rate of oxygen permeation, mechanical failure, chemical attack and deterioration of the reference electrode. The problems may be partly avoided by using a non-isothermal rod type, successfully used in the laboratory and pilot plant by Alcock et al(72,73). The tip of the rod is immersed into the liquid and the reference electrode is kept at a lower but known temperature attached part way along the rod. The cell voltage now includes a thermoelectric contribution.

High Temperature Fuel Cells and Steam Electrolyzers

Existence of high oxygen ionic conductivity in the oxides like stabilised ZrO_2 with extremely good thermal and chemical stability has also led to the development of High Temperature Fuel Cell (HTFC) for direct conversion of fuel energy to electricity (74-77). Unlike conventional low temperature fuel cells, it is an all-solid-state device avoiding the use of corrosive liquid electrolytes. Moreover its efficiency is much higher because of the higher temperature (800-1100°C) of operation which has also a favourable effect on the electrode kinetics giving rise to lower polarization losses with consequent higher current and power densities.

The HTFC is basically an electrochemical cell using an oxide electrolyte on one side of which a gaseous fuel is burnt and the oxygen required for combustion is supplied from the other side of the electrolyte. Necessary temperature is maintained by the heat of combustion. The cell may be represented as :

Fuel gas (anode) | Oxide electrolyte | air or oxygen (cathode)

The open circuit voltage(E_o)which arises due to a large difference (about 20 orders of magnitude) in oxygen activity between the cathode and the anode, is given by an expression similar to eqn.(5).

$$E_o = \frac{-\Delta G}{nF} = \frac{-RT}{nF} \ln \left[P_{O_2}(\text{cathode})/P_{O_2}(\text{anode}) \right] \qquad (6)$$

where ΔG is the free energy change for the combustion reaction and n is the number of electrons taking part in the reaction. H and CO are the commonly used fuels for experimental cells, however, fossil fuels like natural gas or gasified coal have also been used after necessary reforming. The theoretical voltage of a fuel cell using either H_2 or CO is around I volt.

For hydrogen, the combustion reaction which is represented by

$$2H_2 + O_2 \longrightarrow 2H_2O \qquad (7)$$

is equivalent to synthesis of steam and is exothermic in nature. In a fuel cell oxygen is transported through the electrolyte from the cathode to the anode when a load is connected to the external circuit(Fig.8a). The same device can also be used as a High Temperature Steam Electrolyzer (HTSE) in which the reverse reaction is performed by driving oxygen in the opposite direction through the application of an external voltage(Fig.8b). To compensate for the endothermic effect, heat has to be supplied from outside. The HTSE is once again a highly efficient device to generate hydrogen which is probably going to be the energy of the future. Thermodynamic analysis(78-80) has established that HTSE can operate with 50% higher energy efficiency than the low temperature alkaline water electrolyzers.

Intensive research activities on the development of HTFC have been in progress since the early 1960's in several laboratories particularly at Westinghouse Research and Development Centre,USA and Brown Boveri and Cie, West Germany. A short-lived programme was also taken up at AERE, U.K. Several battery modules have been successfully tested under laboratory conditions; however, there is still a long way to go before the technology becomes economically viable. Major difficulties lie in the development and selection of materials for high temperature application and in respect of their compatibility with the electrolyte. Design and fabrication of the cell are the other significant steps in the successful development of both HTFC and HTSE.

Electrolyte

Since both the devices are operated under closed circuit condition,resistance and polarization losses are important parameters to be controlled at a desired level. Therefore, highest conducting electrolyte is preferred. However, from the consideration of thermal stability, extent of electrolytic domain as well as electrical conductivity, stabilized zirconia has been found most satisfactory among the various oxygen ion conductors. Doped ceria and doped perovskite type oxides(e.g. $CaTi_{0.7}Al_{0.3}O_{2.85}$) have been suggested(81,82) but they are not likely to replace zirconia. ZrO_2

with either 15 m/o CaO or 8-10 m/o Y_2O_3(75,83) or 4 m/o each of Y_2O_3 and Yb_2O_3(84) are the common electrolytes used for this purpose. Assuming the electrolyte polarization as the only source of electrical loss and from the knowledge of resistivity of the electrolyte, one can calculate the maximum allowable electrolyte thickness for a specific power density to be attained. The results of such a calculation for a power density of 0.25 W/cm^2 are presented in Table I for two different operating temperatures. At 1000°C, a maximum thickness of 2 mm is permissible for the highest conducting electrolyte but only 0.2 mm thickness for the lowest conducting electrolyte. The thickness needs to be further reduced to obtain higher power densities.

Electrode Materials

Materials with high electronic conductivity as well as stability at the operating temperatures and oxygen partial pressures are used as electrodes. Metallic nickel and cobalt have been most satisfactory anode materials. For better thermal expansion matching,cermets of zirconia with either Ni or Co have also been used (75,85). Selection of cathode material is one of the most difficult tasks in fuel cell design. Due to the highly oxidising environment only noble metals like Pt or Ag or mixed oxides with high electronic conductivity act as suitable cathode materials and have been used in most investigations. SnO_2 doped(3 m/o)In_2O_3 has been favoured by Westinghouse(86)and AERE(75),Sr-doped $LaMnO_3$ by Brown Boveri(88),pervoskite type oxides like Bi-doped $LaNiO_3$(87) and pure Ca-doped $LaCoO_3$by the Japanese workers(89,90). Cathodes made of $LaNiO_3$ have been tested at 1000°C for more than three years without affecting their properties.

Design and fabrication

The most convenient way of constructing an HTFC is to use a tubular thin walled but impervious electrolyte which is coated on either side with porous electrode films. The fuel is usually burnt inside the tube and consequently the inner electrode acts as the anode while the outer electrode is exposed to the oxidant.

The electrolyte is used whether in the free standing tubular configuration with 0.4-0.5 mm thickness and about 25 mm diameter(76) or in the form of thin films(20-30μm) supported on a porous ceramic tube(91). The free standing electrolyte tubes are usually fabricated either by isostatic pressing(92)or by plasma spraying on a salt coated mandrel(75). Porous electrode films(20-100μm thickness) are usually prepared by plasma spraying.For ease of fabrication and efficient current collection, the length of each cell is limited to 10-12 mm. However, for convenience of gas flow and to obtain a battery module, a number of these cells are joined together end to end to form a longer tube. Series connection between the cell is obtained through overlapping of tube edges. This is usually achieved through a bell and spigot arrangement used by Westinghouse(93) or a cone and socket arrangement which has been favoured by Brown Boveri(76)(Fig.9). For gas tightness and electrical connection an interconnection material(ICM)is used between the segments. A suitable interconnection material should have low electronic resistivity preferably less than 20 ohm.cm(76),good chemical stability under both air and fuel atmosphere and at the high operating temperature, good sinterability and compatibility with the electrolyte as well as both electrodes. The materials commonly used are : $CoCr_2O_4$ with 2% Mn(94),$LaCrO_3$ doped with Sr and Ni(95),$LaMnO_3$doped with Sr(88),TiO_2 doped with Nb_2O_5, Ta_2O_5 or WO_3(75).$LacrO_3$ doped with Mg and Al has also been used recently by Westinghouse(96).

The thin film cells which hold much greater promise for future development are fabricated by successive deposition of electrode, electrolyte and interconnection material on a porous support tube usually made of stabilised zirconia with a wall thickness of 1-1.5 mm, outer diameter of 12 mm and about 200 mm long. The cross section of the cell is schematically shown (Fig.10). Total thickness of the cell is 100 μm with individual film thickness varying between 20-50 μm. Chemical or electrochemical vapour deposition technique is usually employed for preparation of the films(85).

Performance

Drawing current from a fuel cell causes considerable drop in the voltage compared to its open circuit value. Total electric power loss is a linear function of current density and is composed of several independent contributions like voltage drop due to the electrolyte, electrode and interconnection material resistances and polarization losses at electrolyte-electrode interfaces. Fig.11 shows a typical power loss curve together with the relative contributions from various sources. It also includes the variation of output power which obviously goes through a maximum at an intermediate current density.

Power density obtained in different experimental cells vary widely and is quite sensitive to the materials used, design criteria,fuels used and other operating conditions. Values of 0.07 to 0.5 w/cm^2 have been reported by various investigators;however, 0.3 w/cm^2 is a typical value obtained in most cases.

Two efficiency terms are common in HTFC terminology. The electrical efficiency of the cell(ηE) is the ratio of the output voltage(E)to the theoretical open circuit voltage (E_o) while the overall thermal efficiency (ηT) is the ratio of the electrical power (P) delivered by the cell to the thermal power (Δ H) supplied which is the enthalpy change of the combustion reaction.

$$\eta_E = E/E_o, \eta_T = P/\Delta H \qquad (8)$$

it may be shown that at maximum power, ηE is only 50% which is too low an efficiency for economic power generation. So HTFC's must be operated at current densities less than that corresponding to maximum power. In the AERE design(75)of an HTFC power plant,it has been assumed that an electrical efficiency at a power output of 0.45 w/cm^2 corresponding to a peak power of 0.53 w/cm^2. The calculated overall thermal efficiency then becomes 40% and 32% for 85% and 65% fuel utilization respectively, using H_2/CO fuel mixture obtained by reforming CH_4. On the other hand, workers at Westinghouse(97)expected to achieve an electrical efficiency as high as 80% and overall thermal efficiency of 60% with an optimally designed battery using gasified coal as the fuel. This, however, looks to be too optimistic. According to Brown Boveri calculations(76), HTFC plants of atleast 10 MW capacity will have the overall efficiency of 45-55%. Life tests at several laboratories have shown that the batteries can be safely operated for atleast five years without significant deterioration.

For electrolysis, an external voltage greater than E_o must be applied across the cell. The excess voltage is required to compensate for the overvoltage losses which increase with increasing current density. As mentioned earlier, steam electrolysis is an endothermic reaction and therefore heat has to be supplied from outside. Either the whole or part of this requirement may be met by the heat produced from the over voltage phenomenon.

The efficiency of the electrochemical process decreases with increasing overvoltage and is maximum when there is no overvoltage loss i.e. whole of the heat requirement is supplied thermally. It follows from these discussions that the overall efficiency of both HTFC and HTSE increases as the overvoltage is reduced. In the following section we shall discuss the parameters which govern this phenomenon.

Electrode polarization

It may be noted in Fig.11 that the major contributions to the overvoltage loss arise from the ohmic drop in the electrolyte (25% of total loss,and polarization at the electrodes(40% of total).In the thin film cells, the ohmic drop is negligible, consequently the second one is the only one to be controlled to minimise the total loss. Extensive research effort has gone into understanding the mechanism of electrochemical reactions which causes the polarization loss but with only limited success. Results obtained are very often ambiguious and contradictory to each other. A detailed discussion has been presented elsewhere (4,98).

The overall electrode reaction

$$\tfrac{1}{2}O_2 \text{ (gas) } + V_O^{\bullet\bullet} \text{(electrolyte) } + 2e'\text{(electrode)} = O_O\text{(electrolyte)} \qquad (8)$$

takes place through several intermediate steps and it is difficult to identify which ultimately determines the polarization. Some of the rate controlling steps are:(1) gaseous diffusion within the pores of the electrode(2) adsorption/desorption on the electrode surface(3) bulk, surface or interface diffusion of adsorbed oxygen (4) charge transfer etc. The importance of electrocatalysis in steam electrolyzers has been demonstrated (99-102) and accordingly it is expected that the adsorption reaction

$$\tfrac{1}{2}O_2(\text{gas}) \rightleftharpoons 2O_{(\text{ads.})} \qquad (9)$$

is the rate controlling step. The surface condition of the electrode is therefore of extreme importance.

Characteristics of different electrode materials have been studied by specific current (current per unit length of three phase contact) measurement across a single contact electrode - electrolyte interface. Among the metallic materials studied as air electrode, the highest current has been obtained with Rh and the lowest with Au. Among the oxides $La_{0.5}\,Sr_{0.5}\,FeO_3$ has given the highest current. The order of increasing currents is(99) $Au < In_2O_3 < NiO < La_{0.95}\,Mg_{0.05}\,Cr_{0.85}\,Al_{0.15}\,O_3 < Co_3\,O_4 < Pt < Cr_2O_3 < Pd < PrCo\,O_3 < La_{0.5}\,Sr_{0.5}\,FeO_3 < Rh$. Similar measurements with fuel electrode materials were carried out by Schouler and Isaacs(99) who have found that the current decreases in the order $La(Al,Mg)CrO_3 < Mo < Ni < Co < Fe$.

Miscellaneous

The high oxygen ion diffusion through stabilized zirconia can be used to construct an electrochemical oxygen pump. By applying a voltage, defined by eqn. 5 , to the platinum electrodes of a zirconia tube through which a gas to be purified passes, oxygen can be pumped out to the required level. It can be used to purify gases, for colometric titration, and in dies used for hot pressing of ferrites. Solid electrolytes can be used for p^H control also.

SUMMARY

Oxide solid electrolytes represent the most important class of ionic conductors, particularly at elevated temperatures. Chemical inertness, stability and ease of fabrication make these electrolytes attractive for practical devices, such as oxygen sensors for automotive and furnace control besides in deoxidation of liquid metals, high temperature fuel cells and steam electrolyzers. Specialised applications include electrochemical oxygen pumping and p^H measurement.

Table I : Resistivity and permissible electrolyte thickness in a fuel cell with power density 0.25 W/cm^2

Electrolyte	800°C		1000°C	
	ρ(Ohm cm)	Thickness (mm)	ρ(Ohm cm)	Thickness(mm)
ZrO_2- 15 CaO	250	0.04	50	0.2
ZrO_2- 10 Y_2O_3	45	0.22	10	1
ZrO_2- $4Y_2O_3$-$4Yb_2O_3$	20	0.5	5	2

REFERENCES

1. T.H.Etsell and S.N.Flengas,Chem.Rev.70:339;1970 .
2. W.L. Worrellin Topics in Applied Physics Vol.21(Solid Electrolytes)S.Geller ed.(Springer-Verlag),Berlin,1977)p.143.
3. R.M.Dell and A.Hooper in Solid Electrolytes,P.Hagenmuller and W.Van Gool eds.(Academic Press,New York,1978)P.291.
4. E.C.Subbarao and H.S.Maiti,Solid State Ionics(in press).
5. T.Y. Tien and E.C.Subbarao,J.Chem.Phys.39:1041;1963.
6. R.E.Carter and W.L.Roth in Electromotive Force Measurements in High Temperature Systems,C.B.Alcock ed.(Elsevier, Amsterdam 1968)p.125.
7. J.G.Allpress and H.J. Rossell,J.Solid State Chem.15:68;1975
8. B.Hudson and P.T.Moseley,ibid, 19:383;1963.
9. S.R.Ray and V.S.Stubican,Mat.Res,Bull, 12:549;1977 .
10. V.S.Stubican and S.P.Ray,J.Am.Ceram.Soc. 60:534;1977 .
11. V.S.Stubican,R.C.Hink and S.P.Ray,ibid, 61:17;1978 .
12. K.K. Srivastava, R.N.Patil,C.B.Choudhary,K.V.G.K.Gokhale and E.C.Subbarao,Trans.&J.Brit.Ceram.Soc. 73:85;1974 .
13. A.I.Ioffe,V.N.Strekaloyskii,D.S.Rutman and S.V.Karpachov,Dokl. Akad,Nauk SSSR, 207:646;1973 .
14. V.S.Stubican and J.R.Hellmann in ref.14 a, p.25 .

14a. A.H. Heuer and L.W.Hobbs eds.Advances in Ceramics,Vol.3 (The Am.Ceram.Soc.,Columbus,1981).

15. G. Brauer and H.Gradinger,Z.Anorg.Allgem.Chem.276:209;1954.
16. E.C.Subbarao,P.H.Sutter and J.Hrizo,J.Am.Ceram.Soc.48:443;1965.
17. A.M.Diness and R.Roy,J.Mater.Sci. 4:613;1969.
18. H.M.Mobius, H.Witzamann and W.Witte,Z.Chem. 4:152;1964 .
19. E.K.Keler,N.A.Godina and A.M.Kalinina,Zh.Neorg.Khim,1:2557;1955.
20. D.J.M.Bevan,W.W.Barker and R.L.Martin in Proc.4th Conf.on Rare Earth Research,Phoneix,Ariz.,L.Eyring,ed.(Gordon and Breach,New York,1965)p.441.
21. T.Kudo and H.Obayashi,J.Electrochem.Soc. 122:142;1975.
22. G.Gattow and D.Schutze,Z.Anorg.Allgem.Chem. 328:44;1964 .
23. G.Gattow and H.Schroder,ibid, 318:176;1962 .
24. M.G.Hapase and V.B.Tare, Indian J.Pure & Appl.Phys.5:401;1967.

25. C.N.R.Rao,G.V.Subbarao and S.Ramadas,J.Phys.Chem.73:672;1969.
26. T.Takahashi and H.Iwahara,Mat.Res.Bull. 13:1447;1978.
27. R.J.Brook in Electrical Conductivity in Ceramics and Glass N.M.Tallan ed.Part A(Marcel Dekker,New York,1974)p.179.
28. C.B.Choudhary,H.S.Maiti and E.C.Subbarao in ref.28a, p.1.
28a. E.C.Subbarao,ed.Solid Electrolytes and their Applications, Plenum,New York, 1980.
29. H.L.Tuller and A.S.Nowick,J.Electrochem.Soc.126:209;1979.
30. J.W.Patterson,ibid 118:1033;1971.
31. J.W.Patterson in Electrical Conductivity in Ceramics and Glass Part B,N.M.Tallan ed.(Marcel Dekker, New York 1974)p.453.
32. C.Wagner in Proc.Int.Comm.Electrochem.Thermodyn.and Kinetics-Lindau(Butterworths,London,1955)p.361.
33. M.Kleitz,E.Fernandez,J.Fouletier and P.Fabry in ref.14a,p.349.
34. T.A.Ramanarayanan,J.Electrochem,Soc.128:2487;1981.
35. B.C.H.Steele,J.Drennan,R.K.Slotwinski,N.Bonanos and E.P.Butler in ref. 14a, p.286.
36. M.Croset,J.P.Schnell and G.Velasco,J.Appl.Phys.48:775;1977
37. C.F.Baner,L.B.Welsh,K.J.Youtsey and F.R.Szofram,U.S.Pat.No. 4,040, 929 (1977).
39. J.Foultier ,P.Fabry and M.Kleitz,J.Electrochem.Soc.123:204; 1976.
40. J.Foultier and G.Vitter in ref. 40a, p. 108.
40a. T.Takahashi and A.Kozawa,eds.,Applications of Solid Electrolytes,(The Electrochemical Society of Japan,JEC Press,Tokyo, 1980).
41. Westinghouse Electric Corp.U.S.Pat.No.1,523,550(1978).
42. E.M.Logothetis in ref.14a,p.338.
43. D.S.Howarth and R.V.Wilhelm Jr.General Motors Report No.GMR-2572 (1978).
44. W.J.Fleming,J.Electrochem.Soc. 124:21;1977.
45. D.S.Eddy, U.S.Pat.No.3,616,274(1971).
46. W.J.Fleming,D.S.Howarth and D.S.Eddy,SAE Trans.82:1969;1973.
47. D.S.Eddy,IEEE Trans.Veh. Technol, 125:VT-123;1974.
48. H.Dueker,K.H.Friere and W.D.Haccker,Paper No.750 223,SAE Congress Detroit (1975) .
49. E.Harnan.H.Manager,andL.Steinke,Paper No.770401 ibid Detroit (1977).
50. C.T.yong and J.D.Bode,Paper No.790 143,ibid Detroit(1977).
51. R.V.Wilhelm Jr.and D.S.Eddy,Am.Cerm.Soc.Bull. 56:509;1977.
52. J.E.Dillon,U.S.Pat.No.4,040,930(1977).
53. R.E.Hetrick and E.M.Logothetis,Appl.Phys.Lett.34:117;1979.
54. H.U.Gruber and H.M.Wiedermann,Paper No. 800 017,SAE Congress Detroit (1980).
55. G.Vitter and M.Aenanet,French Pat.No.77,16404(1977).
56. T.Sugimoto in ref.40a; p.114.
57. C.H.Deportes,M.Henanlt,F.Tasset and G.Vitter,U.S.Pat.No. 4045,319 (1977).
58. B.C.H.Steele Brit Pat.No.42 546(1969).
59. W.A.Fischer and D.Janke,Arch.Eiserhuttenw 39:89;1968 and 40:707;1969.
60. K.Schwendtfeger,Trans.Met.Soc.AIME 239:1276;1967.
61. R.Fruehan,L.J.Nartonik and E.T.Turkdogan,ibid 245:150;1969.

62. K. Suzuki A.Ejima,M.Kato and K.Sanbongi,Trans ISIJ 17:477;1977.
63. H. Schmalzried, Z.Phs.Chem. 38:87;1963.
64. D.Janke in ref. 14a,p.149.
65. K.P.Jagannathan,S.K.Tiku,H.S.Ray,A.Ghosh and E.C.Subbarao in ref. 28a, p. 301.
66. W.Shuli,Solid State Ionics 3/4:581;1981.
67. G.R. Fitterer, J.Met. 19:92;1967.
68. D.Janke, Solid State Ionics, 3/4:559;1981.
69. K.Nakata, N.Sato and K.Takeda,ibid 3/4:563;1981.
70. N. Uhiyama, ibid 3/4:567;1981.
71. Z.Kozuka in ref. 40a, p. 139.
72. C.B.Alcock in High Temperature Chemistry of Inorganic and Ceramic Materials, F.P.Glasser and P.E.Potter,eds.(The Chemical Society, London, 1977) p.116.
73. T.H.Etsell and C.B.Alcock, Solid State Ionics,3/4:621;1981.
74. J.Weisbart and R.J.Rurka in Fuel Cells, G.J. Young ed. Vol.2 (Reinhold, New York, 1963) p.27.
75. T.L.Markin,R.J.Bones and R.M.Dell in Superionic Conductors G.D.Mahan and W.L.Roth eds(Plenum,New York 1976) p.15.
76. F.J.Rohr in Solid Electrolytes P.Hagenmuller and W.Van Gool eds. (Academic, New York, 1978) p.431.
77. Workshop on High Temperature Solid Electrolyte Fuel Cells, H.S.Isaacs,S.Srinivasan and I.L.Harry eds.Brookhaven National Laboratory, Upton, New York (1978), (BNL 50756).
78. H.S.Spacil and C.S.Tedmon Jr.,J.Electrochem Soc. 116:1618;1969.
79. H.S.Isaacs,J.A.Fillo,V.Darg,J.R.Powell,M.Steinberg,F.Salzaro and R.Benenati in Proc.Sump.Industrial Water Electrolysis vol. 78-4 S.O.Srinivasan,F.J.Salzano and A.R. Landgrebe eds.(The Electrochem. Soc. 1978) p. 249.
80. W.Doenitz, R.Schmidberger and E.Steinheil in ibid p. 266.
81. P.N.Ross Jr. and T.G.Benjamin,J.Power Sources, 1:311;1976/77.
82. T.Tarkahashi in Physics of Electrolytes Vol.2, J.Hladik ed. (Academic Press, New York, 1972)p.989.
83. D.H.Archer E.F.Sverdrup and R.L.Zahrardnik,Chem.Eng.Progr. Symp. Ser. 60:64;1964.
84. H.H.Eysel and F.J.Rohr, BBC Nachrichten 49:532;1967.
85. A.O.Isenberg in Proc.Symp.Electrode Materials and Processes for Energy Conversion and Storage Vol.77-6 J.E.D.McIntyre, S.Srinivasan and P.G.Will eds. (The Electrochem Soc. 1977)p.683.
86. E.F.Sverdrup,D.H.Archer and A.D.Glasser,Adv.Chem.Ser.90:301; 1969.
87. R.Steiner,F.J.Rohr and W.Fischer,Proc.4th Int.Symp.Fuel Cells, Antwerp 1972, p. 113.
88. F.J.Rohr, Proc. EUCHEM-Conf. Elman (1975).
89. Y.Ohno,S.Nagata and H.Sato,Solid State Ionics,3/4:439;1981.
90. S.Nagata,Y.Ochno and H.Sato in ref. 40a, p.193.
91. A.O.Isenberg,Solid State Ionics,3/4:431;1981.
92. R.Steiner,Energy Conversion, 12:31;1972.
93. D.H.Archer,L.Elikan and R.L.Zahradnik in Hydrogen Fuel Cell Technology,B.S.Barker ed.(Academic Press,New York,1965)p.51.
94. C.C.Sun, E.W.Hawk and E.F.Sverdrup,J.Electrochem.Soc.119: 1433;1972.
95. W.Baukal,W.Kuhn,H.Kleinschmager and F.J.Rhor,J.Power Sources,

1:203;1976.

96. R.J.Ruka in Proc.Symp. Industrial Water Electrolytes, S.Srinivasan, F.J. Salzano and A.R. Landgrebe (The Electrochemical Society 1978) p.56.
97. E.F. Sverdrup, C.J.Warde and A.D.Glasser, Westinghouse scientific paper 71-9E6-FCELA-P1 (1971).
98. H.S. Isaacs in ref. 14a, p.406.
99. E.J.L. Schouler and H.S. Isaccs, Solid State Ionics 5:555; 1981.
100. E.J.L. Schouler,M. Kleitz, E. Forrest, E. Fernandez and R. Fabry, ibid 5:559; 1981.
101. H.S. Isaacs and L.J. Olmer, J. Electrochem. Soc.129:436;1982.
102. L.J. Olmer and H.S.Isaccs, ibid 129:346;1982.
103. H.S.Maiti and E.C. Subbarao , J.Electrochem Soc. 123:1713; 1976.
104. J.E. Bauerle, J.Chem. Phys. 45:4162; 1966.
105. H.L. Tuller and A.S. Nowick, J.Electrochem Soc. 122:255;1976.
106. R.B. Blumenthal, F.S. Burgner and J.E. Garnier, ibid 120: 1230; 1973.

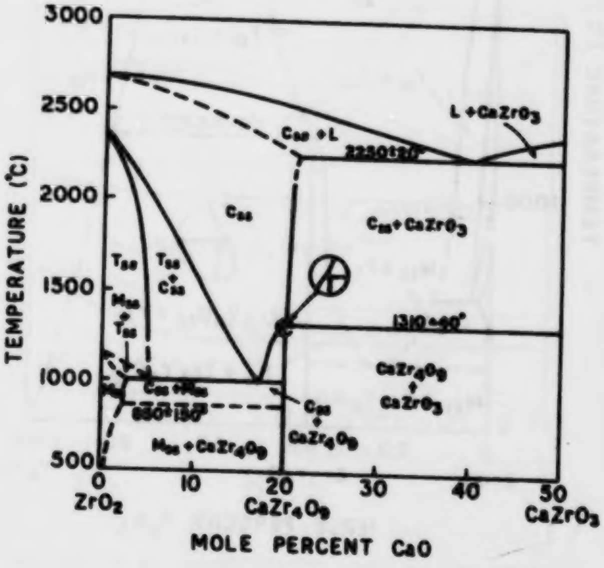

Fig. 1 Phase diagram for the system ZrO_2-CaO (ref. 14).

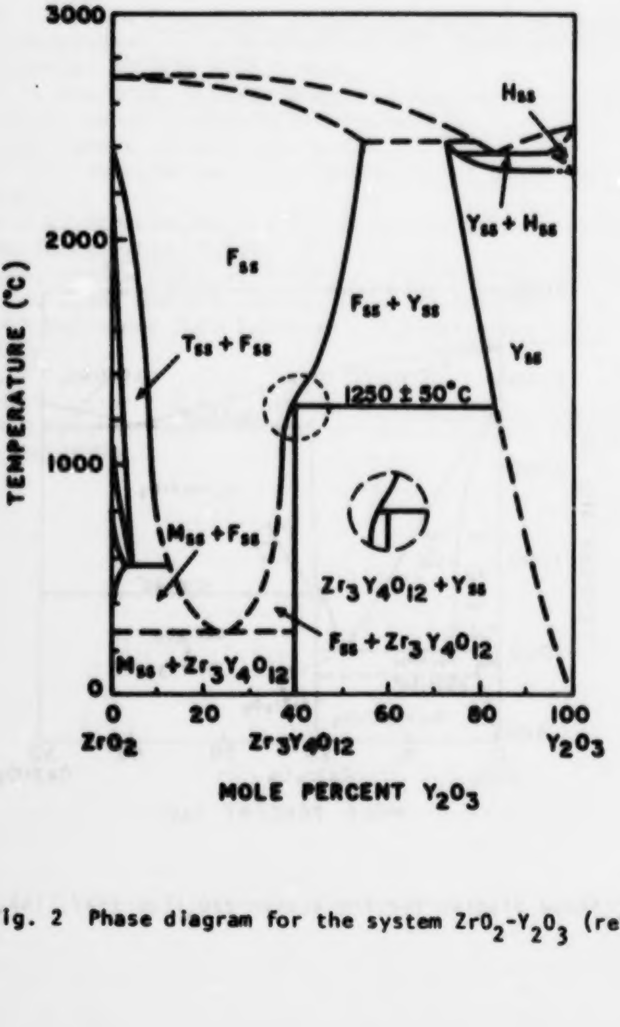

Fig. 2 Phase diagram for the system ZrO_2-Y_2O_3 (ref. 11).

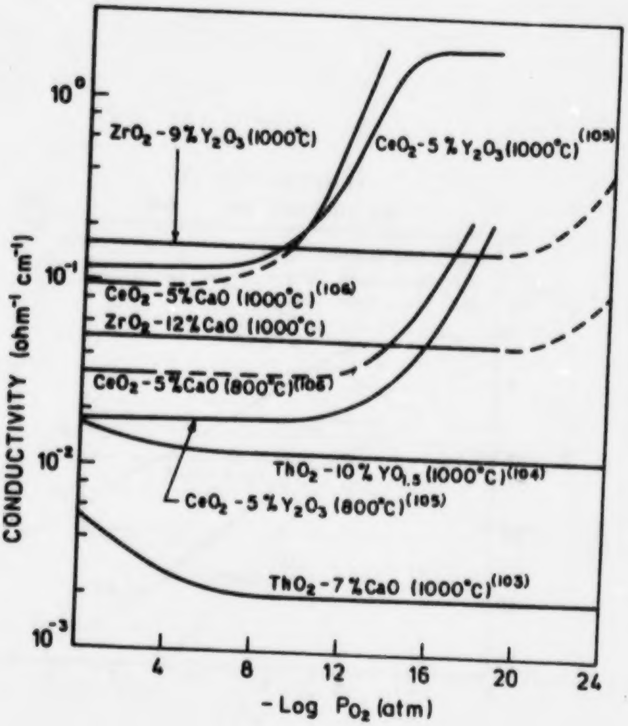

Fig. 3 Variation of conductivity with oxygen partial pressure for important electrolytes.

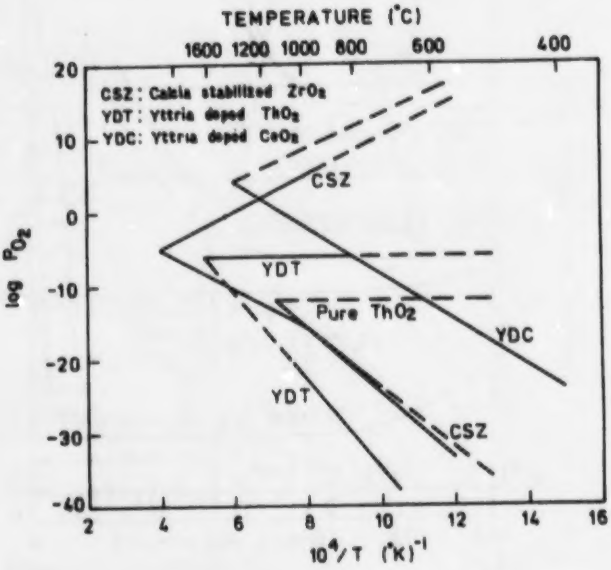

Fig. 4 Ionic domain of important oxide electrolytes (compiled from refs. 30 and 105).

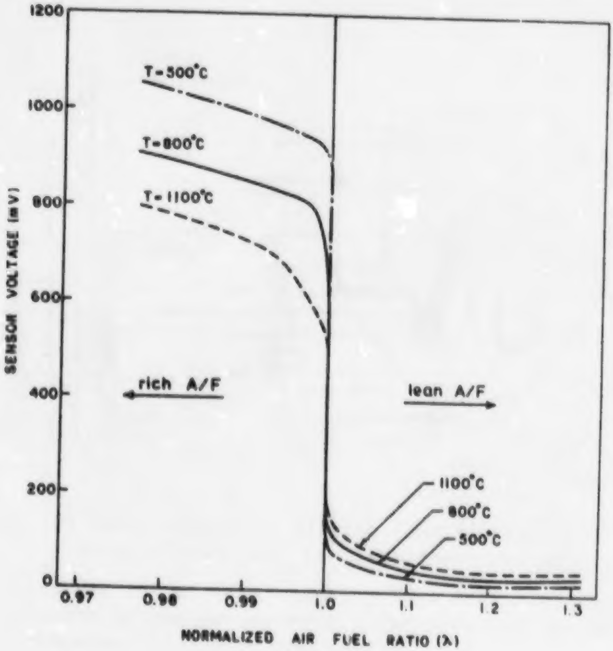

Fig. 5 Typical variation of sensor voltage with A/F ratio (ref. 44).

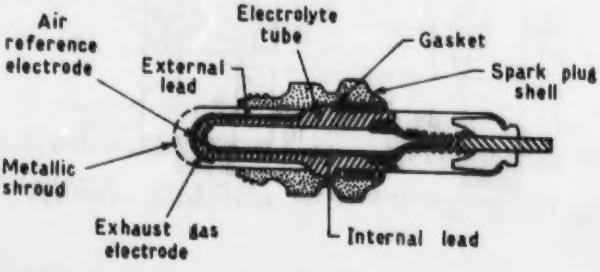
Air reference electrode
Electrolyte tube
Gasket
External lead
Spark plug shell
Metallic shroud
Exhaust gas electrode
Internal lead

Fig. 6 Cross-section of a car exhaust sensor.

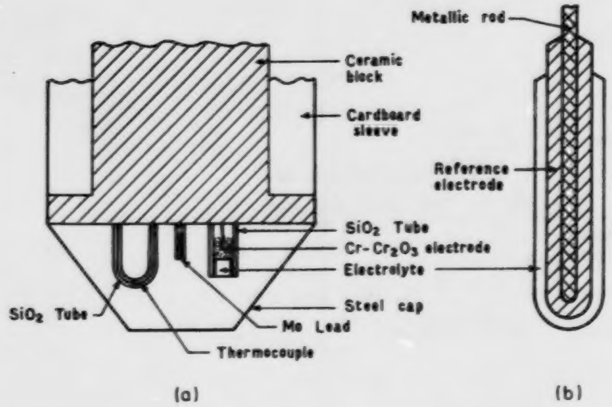
Metallic rod
Ceramic block
Cardboard sleeve
Reference electrode
SiO2 Tube
Cr-Cr2O3 electrode
Electrolyte
Steel cap
Mo Lead
SiO2 Tube
Thermocouple
(a)
(b)

Fig. 7 Constructional details of oxygen probe for steel melt
(a) Conventional (b) needle probe.

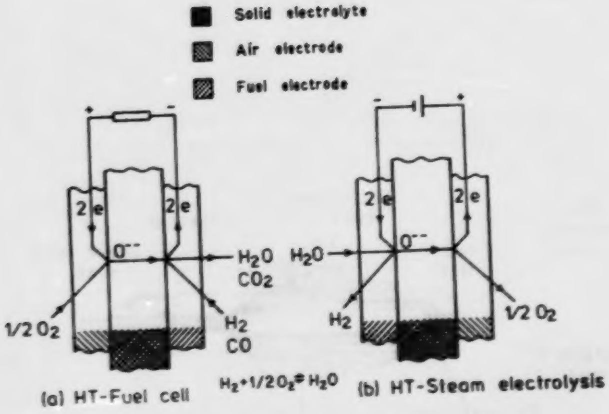
Solid electrolyte
Air electrode
Fuel electrode
+
-
-
+
2e
2e
2e
2e
O--
O--
H2O
CO2
H2O
1/2 O2
H2
CO
H2
1/2 O2
H2+1/2O2⇌H2O
(a) HT-Fuel cell
(b) HT-Steam electrolysis

Fig. 8 Electrochemical principle in HTFC and HTSE
(ref. 76).

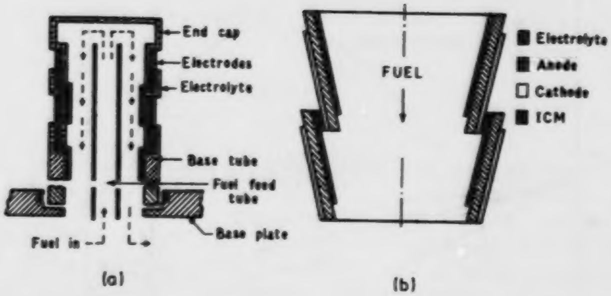
End cap
Electrodes
Electrolyte
Base tube
Fuel feed tube
Base plate
Fuel in
FUEL
■ Electrolyte
▨ Anode
□ Cathode
■ ICM
(a)
(b)

Fig. 9 Cross-section of free standing fuel cell battery (a) bell and spigot arrangement (b) cone and socket arrangement (refs. 76 and 83).

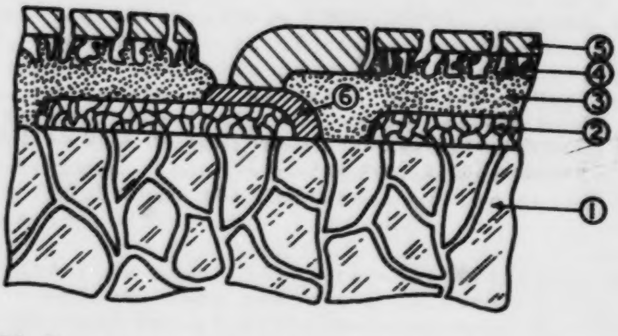

(1) Porous support; (2) Fuel electrode;
(3) Electrolyte; (4) Air electrode;
(5) Current collector; (6) Interconnection

Fig. 10 Cross-section of a thin film supported electrolyte fuel cell (ref. 85).

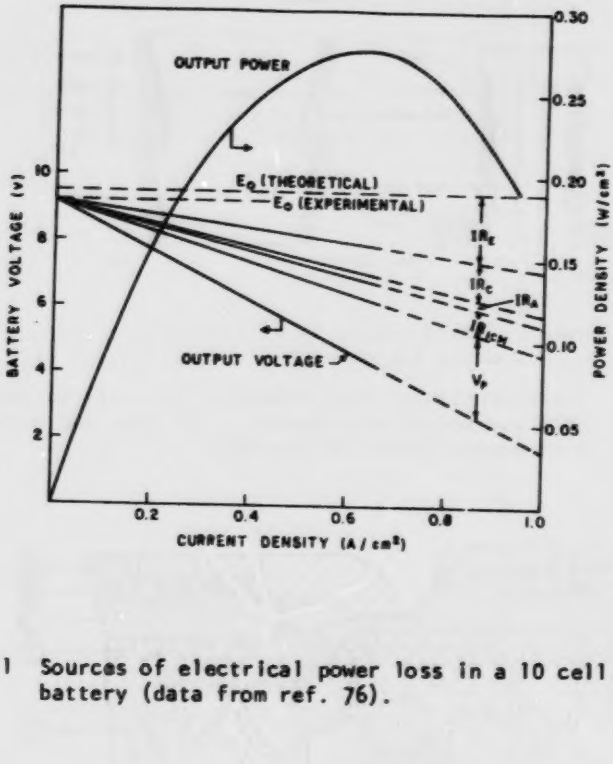

Fig. 11 Sources of electrical power loss in a 10 cell HTFC battery (data from ref. 76).

ELECTRICAL PROPERTIES OF CERAMIC SOLID SOLUTIONS BASED ON CERIA

K. El Adham and A. Hammou

Laboratoire d'Energétique Electrochimique (LA 265 CNRS)
ENSEE - INP Grenoble Domaine Universitaire
BP 44 38401 Saint Martin d'Hères (France)

ABSTRACT

The present work deals with the electrical properties of oxide solid solutions having a fluorite structure. Ceria was chosen as the basic oxide and doped with di- (CaO) or trivalent ($YO_{1.5}$) metallic oxides. The electrical conductivity was studied as a function of dopant content, temperature, and oxygen partial pressure. The experimental results are presented in complex impedance diagrams which allow separation of the bulk, grain boundary and electrode polarization effects from the overall impedance of the electrochemical cell. Maximum ionic conductivity is obtained for compositions of 11 mole % CaO and 15 mole % $YO_{1.5}$. The CaO solubility limit in CeO_2, determined by X-ray and conductivity analyses, is ~23 mole % at the sintering temperature. In the two systems investigated, Arrhenius plots of conductivity show a transition temperature which depends on dopant concentration. Nakamura and Wagner's model has been used to interpret quantitatively the variation of ionic conductivity versus dopant concentration in $(CeO_2)_{1-x}(CaO)_x$ solid solutions. Good agreement is observed in the range $0.04 \leq x \leq 0.2$ when the influence of the third nearest neighbour is considered.

In order to study intergranular transport properties in oxides, some measurements were conducted on single, bi- and polycrystalline samples. A simple model based on the existence of vacancy and dopant concentration gradients is proposed to account for grain boundary resistance in polycrystalline samples.

Finally, the addition of SiO_2 leads to a variation of both bulk conductivity and grain boundary resistance which may be explained using the Lewis acid-base theory.

KEYWORDS: Electrical conductivity, doped ceria, grain boundary.

RÉSUMÉ

Le présent travail a pour objet l'étude des propriétés électriques des solutions solides d'oxydes de structure fluoritique. CeO_2 a été choisi comme oxyde de base, dopé par des oxydes métalliques di (CaO) ou trivalents ($YO_{1,5}$). La conductivité électrique est étudiée en fonction des paramètres suivants : la teneur en dopant, la température et la pression partielle d'oxygène. Les résultats expérimentaux sont représentés en diagramme d'impédance complexe, ce qui permet de séparer les contributions volumiques,intergranulaires et de polarisation aux électrodes à l'impédance totale de la cellule électrochimique. Les résultats montrent l'existence d'un maximum de conductivité à 11 mol % et 15 mol % de CaO et $YO_{1,5}$ respectivement. La limite de solubilité de CaO dans CeO_2 est déterminée par analyse aux rayons X et par conductivité. Elle se situe au voisinage de 23 mol % CaO à la température de frittage. Dans les deux systèmes étudiés, il apparait sur les diagrammes d'Arrhénius, une température de transition qui dépend du taux de dopant. Le modèle de Nakamura et Wagner est utilisé pour interpréter quantitativement la variation de la conductivité ionique avec la teneur en dopant dans les solutions solides $(CeO_2)_{1-x}$ $(CaO)_x$. Un bon accord est observé dans le domaine $0,04 \leqslant x \leqslant 0,2$ lorsque l'on fait intervenir l'influence du troisième proche voisin.

Dans le but d'étudier en particulier les propriétés de transport intergranulaire dans les oxydes, quelques expériences ont été conduites sur des échantillons mono, bi et polycristallins, de même composition. Les résultats expérimentaux ont montré que la contribution d'un joint de grain parallèle au champ électrique est négligeable devant celle du joint perpendiculaire. Un modèle simple, basé sur l'existence de trous et d'un gradient de concentration est proposé pour rendre compte de la conductivité intergranulaire dans les échantillons polycristallins.

Enfin, l'addition de SiO_2 modifie aussi bien la résistance volumique que la résistance intergranulaire. Ce comportement peut être expliqué qualitativement par l'acido-basicité des oxydes en présence selon la théorie de Lewis.

INTRODUCTION

The oxide solid solutions of fluorite structure have a large field of application, either for thermodynamic and kinetic measurements, or for high temperature oxygen sensors, fuel cells and electrolysers. These systems consist generally of oxides of tetravalent elements doped with oxides of di-or trivalent elements. The resulting defects are anion vacancies. Solid solutions based on zirconia have been extensively studied giving rise to a considerable amount of literature and many applications. Nevertheless, the fluorite structure can only be obtained by doping zirconia with a relatively high amount of dopant, leading to "stabilized" zirconia. This feature makes zirconia unsuitable for the study of the variation of transport properties as a function of dopant concentration. Thoria has the disadvantage of toxicity and radioactivity; moreover, the thoria based solid solutions show a mixed conductivity (ionic + electronic) at high oxygen partial pressures. On the other hand, ceria crystallises in the fluorite structure in the pure state (undoped) and behaves as an ionic conductor at atmospheric oxygen partial pressure. It was selected as a basic oxide to follow the variation of electrical - mainly ionic - conductivity with composition. Calcium oxide and yttrium oxide were used in a large range of compositions. The a.c. method used in the measurements enabled us to study the bulk, grain boundary and electrode polarization phenomena.

EXPERIMENTAL PROCEDURE

We have studied the two following series :

$(CeO_2)_{1-x} - (CaO)_x$ with $0,0028 \leqslant x \leqslant 0,5$

$(CeO_2)_{1-x} - (YO_{1,5})_x$ with $0,0005 \leqslant x \leqslant 0,2$

The calcia doped ceria solid solutions were prepared by mixing the desired quantities of cerium oxide and calcium carbonate by wet milling. Yttria doped ceria solid solutions were prepared by coprecipitation of cerium and yttrium oxalates and their decomposition at 1000°C. The dry mixture is pressed and sintered for two hours at 1600°C. The density of the pellets so obtained is close to 95 % of the theoretical one. Single crystals of CeO_2 - CaO solid solutions were prepared by induction melting of oxide mixtures according to the self-crucible method (1). The preparation procedure is described elsewhere in detail (2). Table I gives the compositions and sample notations. The samples were subjected to X-ray analysis to identify the phases and to measure the lattice constants. For the CeO_2 - $YO_{1,5}$ system in the studied composition range, we observe a single phase of fluorite structure. Concerning the CeO_2 - CaO system, we obtain a single phase of fluorite structure in the $0 \lesssim x \lesssim 0,2$ range ; the lattice constant is a linear increasing function of dopant concentration. For $x > 0,3$, the lattice constant has a constant value, as shown in Figure 1.

The electrical measurements were carried out using a symmetrical cell of the type :

P_{O_2}, Me / OSE / Me, P_{O_2}

where P_{O_2} is the oxygen partial pressure
Me the metallic electrode (Pt or Ag)
OES the oxide solid electrolyte.

An alternating voltage is applied to this cell using 0,1 - 5.10^5 Hz frequency range. The elementary cell response to the applied voltage is represented by five arcs in the complex impedance diagram (see Figure 2). The first arc represents the bulk contribution to the total polarization , the second the grain boundary contribution and the other three the electrode polarization. The five arcs cannot be obtained simultaneously because of the limitation of the frequency range of the apparatus used. Examples are given in Figures 3, 4 and 5.

EXPERIMENTAL RESULTS AND DISCUSSION

Bulk ionic conductivity in the CeO_2-CaO system.

For all studied compositions, the bulk electrical conductivity in oxygen is practically ionic below 800°C, as it has been shown elsewhere (2). For clarity, Arrhenius plots of ionic conductivity of all studied compositions are shown in the two Figures 6 and 7.

For each dopant concentration, we notice a transition temperature T_t which separates two domains of temperature. This transition temperature is an increasing function of dopant concentration, as far as the single fluorite structure is concerned. Furthermore, the activation energy corresponding to the high temperature domain ($T > T_t$) is systematically smaller than that observed in the low temperature domain ($T < T_t$). The variation of activation energy with dopant concentration is plotted in Figure 8. A comparison of Figures 1 and 8 shows that for $x > 0,3$, lattice constant and activation energy are constant while they increase linearly in the $0,04 < x < 0,2$ range. The two lines corresponding to the two concentration ranges meet at the same value of concentration, situated around 23 mole % CaO ; this value determines the solubility limit of CaO in cerium oxide, probably at the sintering temperature. The constancy of activation energy in the range $x \geqslant 0{,}3$ indicates that the conducting phase has the same composition in the different samples. The excess of calcia, revealed by X-ray analysis, precipitates at grain boundaries. The decrease of electrical conductivity in this composition range is very likely due to the decrease of the amount of the conducting phase which is the saturated calcia doped ceria with fluorite structure. We have to emphasise that these experimental results were obtained using specimens with the same geometrical factor.

The variation of ionic conductivity as a function of dopant concentration at constant temperature is given in figure 9. We notice a jump in conductivity between 2 and 4 % mole CaO, corresponding to an activation energy drop (see **Figure 8**), and a maximum of ionic conductivity at about 11 mole % CaO.

Effect of SiO_2 on the electrical characteristics of $CaO - CeO_2$ solid solutions.

Silica was considered as a sintering inhibitor. We have studied the influence of its addition on the electrical properties of the $(CeO_2)_{0,89} - (CaO)_{0,11}$ solid solution which has the maximum conductivity in the binary system. Five specimens with different percentages of SiO_2 have compositions and symbols as represented in Table II. Figure 10 shows the complex impedance diagrams, obtained for different concentrations of silica. The observed arcs correspond to the grain boundary contribution. The left hand side intersection of these arcs with the real axis determines the bulk resistance. These diagrams show clearly the influence of the addition of SiO_2 in both bulk and grain boundary resistances. Arrhenius plots of ionic bulk conductivity, represented in Figure 11, are linear in the whole temperature range with slightly different slopes. Table III gives the variation of activation energy with SiO_2 content. Furthermore, at constant temperature, a maximum of conductivity is observed at 2 mole % SiO_2 ; the corresponding activation energy is the lowest. The influence of SiO_2 addition on electrical conductivity can be explained using the Lewis acido-basicity theory. In the studied ternary system, we have a basic oxide, namely CaO, and two acidic oxides CeO_2 and SiO_2. Due to the difference of cationic radius ($r_{Si^{4+}} = 0{,}41$ Å and $r_{Ce^{4+}} = 1{,}01$ Å), Si^{4+} is a more acidic oxide than Ce^{4+}. This fact leads to a concentration of CaO in the zones which are richer in SiO_2 and which precipitates preferentially at grain boundaries. The enrichment of silica zones with calcia is at the expense of the CeO_2 - CaO solid solution zones, leading to a decreasing calcia concentration in the grain bulk. The existence of a maximum conductivity at 2 mole % CaO indicates that the maximum conductivity in the binary CeO_2 - CaO system appears at a concentration lower than 11 mole % CaO, previously determined. According to our experimental results, this concentration lies between 10 and 11 mole % CaO.

SEM observations confirmed the existence of three zones illustrated in Figure 12. The first one, adjacent to grain boundaries, is rich in calcium and silicon ; the corresponding structure has not been determined. The second zone concerns the bulk of grain where the binary solid solution CeO_2 - CaO predominates, showing a very low silica content. Finally, the third zone separates the two first described ; it is formed by a mixture of the silica-rich and the ceria-rich phases. The higher the silica content in the sample, the higher is the transfer of calcium oxide. The decrease of bulk ionic conductivity, when the SiO_2 content is higher than 2 mole %, may be explained qualitatively by the two following effects :

- the high decrease of CaO in the bulk grain, leading to a decrease of the oxygen vacancy concentration, which are the charge carriers.

- the decrease of the amount of the conducting phase which is the binary CeO_2 - CaO solid solution. This is revealed by the variation of density with the silica content.

Electrical bulk conductivity of CeO_2 - $YO_{1,5}$ solid solutions.

The sample compositions and symbols are detailed in Table I. Electrical conductivity was measured throughout the 100-700°C range, generally under oxygen at one atmosphere. In order to determine the conduction mode at high temperature, some measurements were obtained with varying oxygen partial pressure, using A-O_2 and CO-CO_2 mixtures. Figure 13 gives an example of the variation of the total bulk conductivity as a function of oxygen partial pressure. One observes a conductivity plateau at high oxygen chemical potential. The higher the dopant concentration, the larger is the conductivity plateau. The corresponding value of conductivity can be regarded as equivalent to the ionic conductivity value. On the other hand, one observes an increase of electrical conductivity at low oxygen partial pressure. This is due to the n type electronic conductivity. From these results, we deduced the variation of transference number versus oxygen partial pressure, assuming that the intrinsic oxygen vacancy concentration is negligible in comparison with the extrinsic one (see Figure 14). In order to study the variation of ionic conductivity with temperature, two series of measurements were undertaken. The results corresponding to the first one are plotted in Figure 15, showing a transition temperature T_t which depends on dopant concentration as well. The second series concerns a large composition range and measurements were carried out at $T > T_t$. The Arrhenius plots are shown in Figure 16, from which one can deduce the activation energy and its variation with dopant concentration (see Figure 17). Table IV allows to compare activation energy values obtained by other authors in the same range of temperature and composition (3-5). The variation of ionic conductivity with dopant content, in logarithmic scale, is shown in Figure 18. A maximum of conductivity appears at 15 mole % $YO_{1,5}$. This concentration does not vary with temperature. The same behaviour was observed in yttria doped thoria (6).

Finally, the results obtained at high temperature and low oxygen partial pressure allow the study of the n-type electronic conductivity in $(CeO_2)_{1-x}(YO_{1,5})_x$ solid solutions. Its variation with oxygen partial pressure and dopant concentration are plotted in logarithmic scale in Figures 19 and 20, respectively. Such behaviour can be explained by the existence of the following chemical equilibrium :

$$\frac{1}{2} O_2 + 2 e' + V_o^{\cdot\cdot} \rightleftarrows O_o^x \qquad (^*)$$

and the assumption that electron mobility is independent of oxygen vacancy concentration and oxygen partial pressure.

Attempt at quantitative interpretation of ionic conductivity results.

Several quantitative theoretical models were developped to account for the variation of ionic conductivity with dopant concentration. An extended Lidiard's model (7), based on the existence of dopant-vacancy complexes and Debye-Huckel type interactions, was used to explain the conductivity results concerning the CeO_2 - CaO system. This model does not appear to be applicable to the heavely doped electrolytic oxides. A simple model proposed by Subbarao and Ramakrishnan (8), based on statistical distribution of dopant cations and oxygen vacancies to promote the jump of vacancies, was used to account for the behaviour of calcia and yttria doped ceria. The calculated curves deduced from this model exhibit a conductivity maximum located at a dopant concentration close to the experimental value ; nevertheless, this model does not give values of ionic conductivity and does not consider temperature effects. Honke (9) has proposed a model, based on thermodynamic considerations, characterized by the

---

(*) Kroger's notation is used.

existence of a characteristic temperature T_o, where the Arrhenius plots related to the high composition range intersect. This model was used by Honke (9) to explain the experimental results of doped zirconia with a good agreement. Its application to calcia doped ceria seems satisfactory for $x > 0,11$ but the determination of the characteristic temperature is quite inaccurate. On the other hand, the significance of the characteristic temperature and the variation of ionic conductivity at higher temperature remains to be clarified. The theoretical model which was used successfully to account for our experimental data is the model proposed by Nakamura and Wagner (10). It was applied by these authors to calcia stabilized zirconia results of ionic conductivity. This model extends the conventional concept of dopant-defect complexes and demonstrates that ionic conduction in such systems proceeds by a multimode mechanism through and between different degrees of dopant-defect associations. Three types of configuration are introduced depending upon the distribution of dopant cation and anion sites. An effective coordination number is suggested to determine the number of anion sites effectively coordinated to a dopant cation, considering (due to distance effect) that the influence of dopant cation on an anion site in second nearest neighbour equals $\frac{1}{3}$ its influence in the first nearest neighbour site. Nakamura and Wagner (10) have considered the first and second nearest neighbour anion sites and assumed that the maximum ionic conductivity occurs when all the anion sites are onefold coordinated. This configuration, I, is achieved by one of the following distributions :

- anion site has one first-neighbour dopant cation
- anion site has three second-nearest-neighbour dopant cations.

This configuration corresponds to $(ZrO_2)_{0,875}(CaO)_{0,125}$ and the corresponding distribution is shown in Figure 21. The second configuration, II, appears when the anion sites are twofold coordinated to dopant cation. It is achieved when the anion site has one first-nearest neighbour and three second-nearest-neighbour dopant cations. The corresponding composition is $(ZrO_2)_{0,75}(CaO)_{0,25}$ and the distribution of the different sites is illustrated in Figure 22. Finally the third configuration, III, corresponds to the case in which the anion site has no dopant cation in first and second nearest neighbour sites. Each configuration gives rise to a characteristic mobility of oxygen vacancies. The vacancy transfer between different configurations takes place with another characteristic mobility. A mathematical model, using a quasi-chemical equilibrium between different species at different configurations, was developed. The measured conductivities at 12,5 and 25 mol %

CaO were used to calculate the corresponding mobilities while the conductivity of the lowest dopant concentration was used to calculate the mobility at configuration III. The other mobilities and the equilibrium constant were derived from curve fitting. Applying this model to our experimental data concerning $(CeO_2)_{1-x}$ $(CaO)_x$ has given good agreement in the $0,125 \leqslant x \leqslant 0,2$ range. When $x < 0,125$, a great divergence is observed. In the Nakamura and Wagner's model (10), only first-and second-nearest neighbour sites were considered, giving a maximum conductivity at 12,5 mole % CaO. Trying to improve the model, we introduced the influence of the third-nearest neighbour sites assuming that the effect depends inversely on the square of the distance between the dopant cation and the anion site. We obtain maximum conductivity at 10,9 mole % CaO which is very close to that found experimentally. Applying to the model the approximation that the transport takes place with a single mobility equal to that corresponding to $x = 0,11$, we obtain good agreement with experimental results in the range $0,04 \leqslant x \leqslant 0,2$. Details of the model and its application are given elsewhere (2).

Grain boundary effects in the CeO_2 - CaO system.

The influence of grain boundaries on the total conductivity of the oxide solid electrolytes is very small at high temperature. Their use in technical devices needs intermediate or low temperatures, leading to a considerable influence of grain boundaries in transport properties. This influence is due to several parameters, e.g., porosity, dopant and impurity concentrations, grain size, thermal history, cooling procedure... The majority of the studies undertaken in this field concern stabilized zirconia (11-16). The object of this paper is to study the grain boundary effects on the electrical conductivity of oxide solid solutions in a large scale of dopant concentrations. The first part of our study dealt with single and bicrystalline samples. It concerns the following solid solutions :

$$(CeO_2)_{0,995} - (CaO)_{0,005} \text{ and } (CeO_2)_{0,89} - (CaO_2)_{0,11}$$

We have chosen these two compositions to study the intergranular behaviour in a diluted and concentrated medium. Three elementary cells C_R, $C_{\perp}$ and $C_{\parallel}$ were set up in the same furnace : the first one C_R used a reference single crystal specimen, the two others $C_{\perp}$ and $C_{\parallel}$ used bicrystalline samples. The electric field was perpendicular to the grain boundary in $C_{\perp}$ and parallel to the grain boundary in $C_{\parallel}$. The complex impedance diagrams obtained are shown in Figure 23. We notice that the influence of the grain boundary effect is negligible in the $C_{\parallel}$ sample. Arrhenius plots of the inverse of the grain boundary resistance R_{jg} are shown in Figure 24. The deduced activation energies are very close to those corresponding to polycrystalline samples with the same or very close dopant concentration. The results are summarised in Table V.

SEM observations of the grain boundary region in the C_1 cell show that the calcium concentration in the intergranular zone is higher than in the bulk. This segregation is observed for the two investigated samples. However, no difference in silicon concentration was detected. These observations suggest that grain boundary effects are essentially due to dopant segregation and porosity. The second part of our study dealt with polycrystalline samples in a large range of dopant concentrations. All the investigated CeO_2-CaO solid solutions were prepared under the same conditions. The variation of the inverse of grain boundary resistance with temperature is plotted in Figure 25. It indicates that the grain boundary resistance depends on dopant concentration: the lower CaO content gives the higher intergranular resistance. Activation energy of the intergranular transport process is constant, and equal to 1,2 eV. SEM observations taken on the C13 sample have shown that :

- the silicon content is negligible in the intergranular area and in the bulk.

- when the dopant concentration is low ($x < 1$ mole % CaO) the calcium content is practically the same all over the sample ; this means the oxygen vacancy concentration is the same in the bulk and in grain boundaries ; this feature must be expressed by the same value of activation energy. That is what we observe experimentally : $E_a = 1,13$ eV for bulk conduction and $E_a = 1,20$ eV for grain boundary conduction.

- when the dopant concentration is high ($x \simeq 11$ mole % CaO), grain boundaries are characterised by an increase of calcium content and a decrease of cerium content in comparison with the bulk. This difference in composition must be expressed by a difference in activation energy ; furthermore, the intergranular process must have a higher activation energy. That is what we observe experimentally in both bi- and polycrystalline samples : $E_a = 0,85$ eV for bulk conduction and $E_a = 0,98$ eV for grain boundary conduction. These observations contrast with the results obtained by Wang and Nowick (17) who suggest that the effective dopant concentration near the grain boundaries may be substantially lower than the bulk value. A simple model is proposed to explain the results obtained on polycrystalline samples ; it is based on the three following assumptions :

- the sample is formed by elementary cubes whose edges are equal to the average value of the grain size.

- the cubes are joined by faces.
- an elementary cube is formed by two zones :
  - the first one has the bulk properties of the samples.
  - the second forms the grain boundary part. Its thickness is deduced from SEM observations.

Taking into account the result obtained in single and bicrystalline samples we neglect the influence of the grain boundaries parallel to electric field. The cell is then reduced to an electric circuit with two "samples" A and B in series. Sample A consists of a solid solution with a bulk conductivity σ_A ; this latter is easily deduced from the results obtained on the C_R cell. Sample B consists of an "intergranular" phase. Its conductivity σ_B and its thickness ℓ_B are deduced mainly from the results obtained on the $C_\perp$ cell.

The calculated resistances from this model are 475 Ω and 2920 Ω for bulk and grain boundaries respectively. The corresponding experimental values are 480 Ω and 211 Ω showing a good agreement with the calculated values for bulk resistance. The sharp disagreement for grain boundary resistance is very likely due to the reducing of the contact area across which the transport can occur.

CONCLUSION

Complex impedance diagrams, X Ray analysis and SEM observations allowed to analyse the electrical properties of ceramic oxides based on ceria. The concentration of the maximum conductivity is determined with more accuracy in the two investigated systems. Intergranular transport properties were studied, using single, bi and polycrystalline samples. The main result concerns the small influence of the grain boundaries parallel to the electric field in comparison to the perpendicular ones. Finally the addition of SiO_2, considered as the major impurity in ceramics, led to the variation of both bulk conductivity and grain boundary resistance.

REFERENCES

(1) Y. Roulin, G. Vitter and C. Deportes, "Nouveau dispositif de fusion en autocreuset" Rev Int Hautes Temp Réfract 6: 153-158; 1969.

(2) K. El Adham, "Contribution à l'étude des phénomènes de conduction électrique dans les solutions solides à base de dioxide de cérium" Thesis, University of Grenoble, 1981.

(3) M. Forestier, "Structure et conductivité électrique à haute température dans le système ZrO_2-CeO_2-Y_2O_3" Thesis, University of Grenoble, 1969.

(4) A.S. Nowick, D.Y. Wang, D.S. Park and J. Griffith, "Oxygen-ion conductivity and defect structure of CeO_2 doped with CaO and Y_2O_3", Proc Fast Ion Transport in Solids, May 21-25 ; Lake Geneva ; 673-677, 1979.

(5) H.L. Tuller and A.S. Nowick, "Doped ceria as a solid oxide electrolyte" J Electrochem Soc 122: 255 - 259; 1975.

(6) A. Hammou, "Etude de la conductivité électrique dans le système ThO_2-$YO_{1,5}$, "J Chim Phys 431 - 438; 1975.

(7) A.B. Lidiard, "Ionic conductivity", Encyclopedia of Physics, Springer Verlag, 246 - 348 1957.

(8) E.C. Subbarao and T.V. Ramakrishnan, "Ionic conductivity of highly defective oxides, Proc Fast Ion Transport in Solids, May 21-25, 1979 ; Lake Geneva ; 653-656, 1979.

(9) D.K. Honke, "Ionic conduction in doped zirconia", Proc Fast Ion Transport in Solids, May 21-25, 1979 ; Lake Geneva ; 669-672, 1979.

(10) A. Nakamura and J.B. Wagner, Jr "Defect structure ionic conductivity and diffusion in calcia - stabilized zirconia" J Electrochem Soc 127: 2325-2333; 1980.

(11) J.E. Bauerle, "Study of solid electrolyte polarization by a complex admittance method" J Phys Chem Solids 30: 2657-2670; 1969.

(12) H. Bernard, "Microstructure and conductivity of sintered stabilized zirconia" Thesis, University of Grenoble, 1980.

(13) S.H. Chu and M.A. Seitz, "The ac electrical behaviour of polycrystalline ZrO_2-CaO" J Solid State Chem 23: 297-314; 1978.

(14) E. Schouler, G. Giroud and M. Kleitz, "Applications according to Bauerle of the plot of complex admittance diagrams in the electrochemistry of solids. II Conductivity of yttrium stabilized zirconia". J Chim Phys 70: 1309-1316; 1973.

(15) N.M. Beekman and L. Heyne, "Correlation between impedance, microstructure and composition of calcia stabilized zirconia" Electrochim Acta 21: 303; 1976.

(16) M.J. Verkerk, B.J. Middelhuis and Burggraaf, "Effect of grain boundaries on the conductivity of high purity ZrO_2-Y_2O_3 ceramics " Solid State Ionics 159-170; 1982.

(17) D.Y. Wang and A.S. Nowick "The grain boundary conductivity effect in doped ceria" Grain boundary phenomena in electronic ceramics, Advances in Ceramics, Vol. 1, 130-137; 1981.

TABLE I: Dopant concentrations and symbols of samples.

$(CeO_2)_{1-x} - (CaO)_x$		$(CeO_2)_{1-x} - (YO_{1,5})_x$	
x	Symbol	x	Symbol
1×10^{-3}	C1	5×10^{-4}	Y1
2.79×10^{-3}	C2	10^{-3}	Y2
3.56×10^{-3}	C3	2×10^{-3}	Y3
6×10^{-3}	C4	10^{-2}	Y4
1×10^{-2}	C5	2×10^{-2}	Y5
1.9×10^{-2}	C6	5×10^{-2}	Y6
4.76×10^{-2}	C7	10^{-1}	Y7
6×10^{-2}	C8	15×10^{-2}	Y8
7×10^{-2}	C9	17×10^{-2}	Y9
8×10^{-2}	C10	20×10^{-2}	Y10
9×10^{-2}	C11		
10×10^{-2}	C12		
11×10^{-2}	C13		
13×10^{-2}	C14		
15×10^{-2}	C15		
17×10^{-2}	C16		
20×10^{-2}	C17		
30×10^{-2}	C18		
35×10^{-2}	C19		
40×10^{-2}	C20		
45×10^{-2}	C21		
50×10^{-2}	C22		
5×10^{-3}	C1m*		
11×10^{-2}	C2m*		

* single crystal.

TABLE II: Compositions and symbols of samples in the system $[(CeO_2)_{0,89} - (CaO)_{0,11}]_{1-x}\ [SiO_2]_x$

$\left[(CeO_2)_{0,89} - (CaO)_{0,11}\right]_{1-x} - \left[SiO_2\right]_x$	
x	Symbol
5×10^{-3}	S1
1×10^{-2}	S2
2×10^{-2}	S3
4×10^{-2}	S4
8×10^{-2}	S5

TABLE III: Variation of activation energy with SiO_2 content.

Sample	E_a (eV)
C13	0,85
S1	0,84
S2	0,82
S3	0,81
S4	0,84
S5	0,85

TABLE IV: Comparison of activation energies.

mol % $YO_{1,5}$	E_a (eV)	Reference
10	0,76	(5)
10	0,72	(2)
10	0,71	This work
8	0,77	(4)

TABLE V: Activation energies of grain boundary conduction obtained from poly and bicrystals.

Sample	Activation energy (eV)
$(CeO_2)_{0,994}(CaO)_{0,006}$ Poly.	1,2
$(CeO_2)_{0,995}(CaO)_{0,005}$ Bi.	1,1
$(CeO_2)_{0,89}(CaO)_{0,11}$ Poly.	0,96
$(CeO_2)_{0,89}(CaO)_{0,11}$ Bi.	0,98

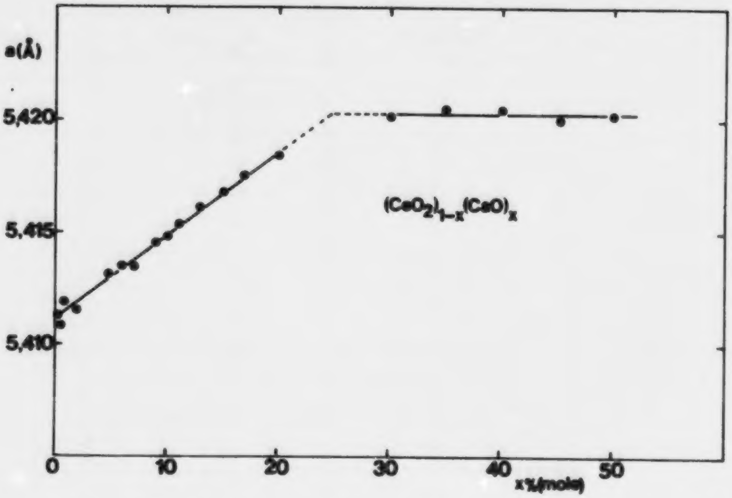

Figure 1: Variation of the lattice constant in the CeO_2-CaO system.

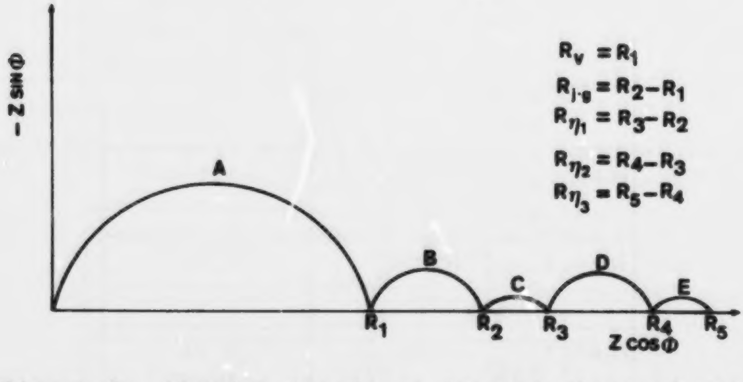
$- Z \sin\Phi$
A
B
C
D
E
R_1
R_2
R_3
R_4
R_5
$Z \cos\Phi$
$R_v = R_1$
$R_{j \cdot g} = R_2 - R_1$
$R_{\eta_1} = R_3 - R_2$
$R_{\eta_2} = R_4 - R_3$
$R_{\eta_3} = R_5 - R_4$

Figure 2: Complex impedance diagram obtained with solid electrolyte based on ceria.
R_v: bulk resistance
R_{jg}: grain boundary resistance
$R_{\eta 1}$, $R_{\eta 2}$, $R_{\eta 3}$: electrode polarizations.

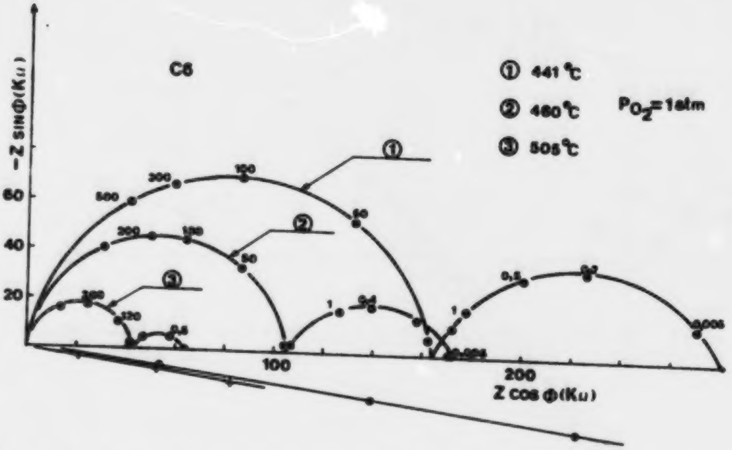

Figure 3: Evolution of complex impedance diagrams with temperature for the sample C6. (Frequency kHz).

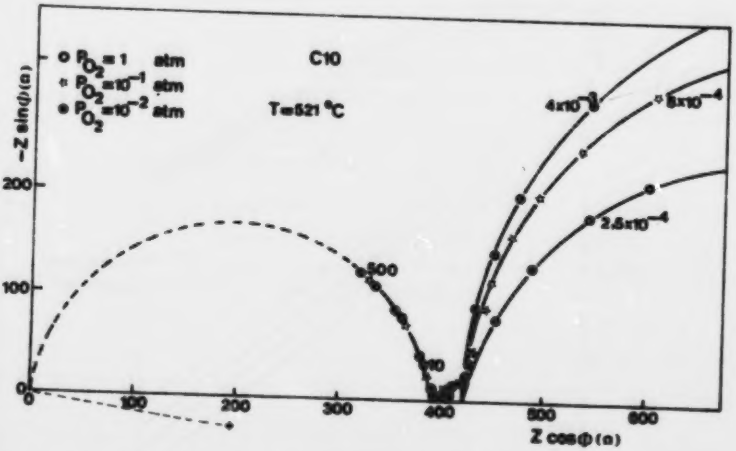

Figure 4: Evolution of complex impedance diagrams with oxygen partial pressure P_{O_2} (Frequency in kHz).

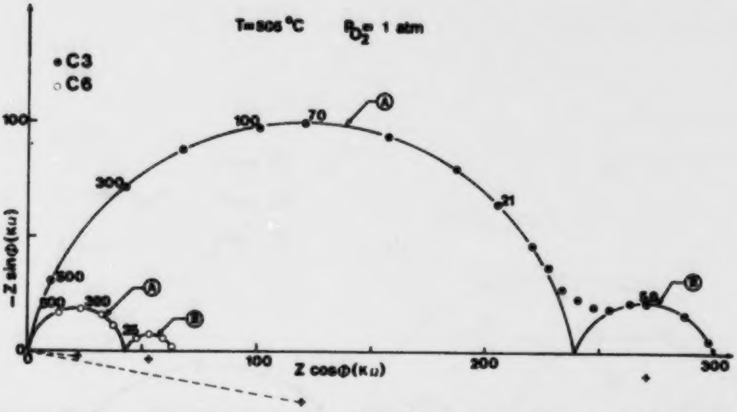

Figure 5: Evolution of complex impedance diagram with CaO content (Frequency in kHz).

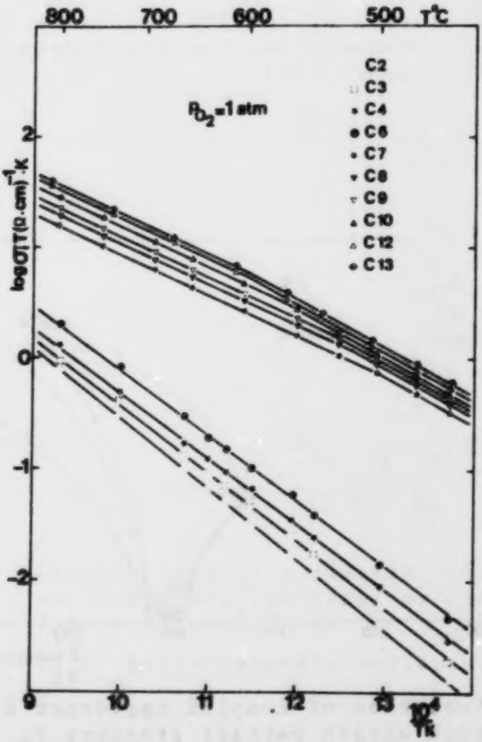

Figure 6: Plot of log $\sigma_i T$ versus 1/T for the CeO_2 - CaO system (x ≤ 0,11).

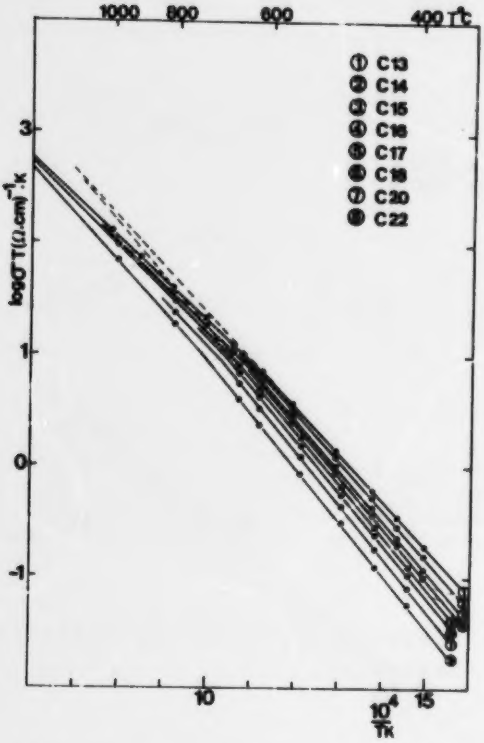

Figure 7: Plot of log $\sigma_1 T$ versus 1/T for the CeO_2 - CaO system ($x \geq 0,11$).

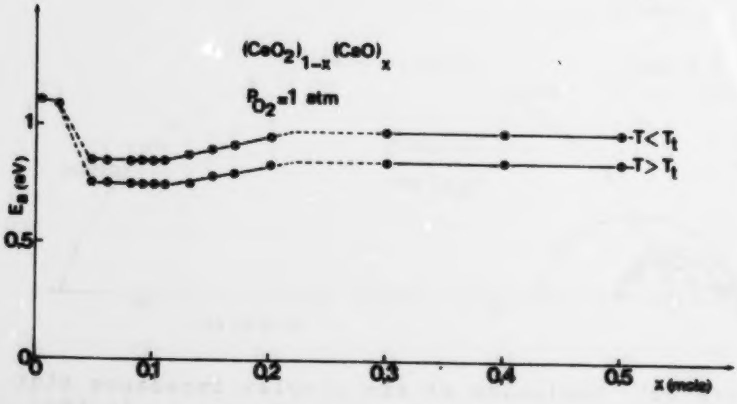

Figure 8: Variation of activation energy with CaO content.

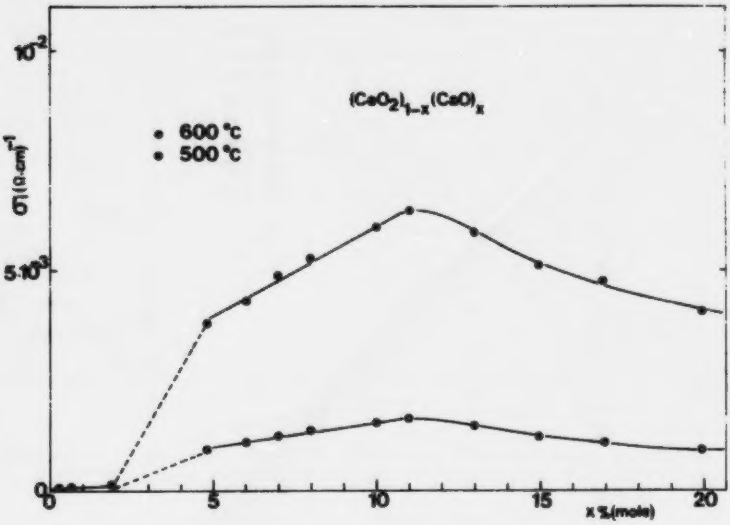

Figure 9: Variation of ionic conductivity with CaO content.

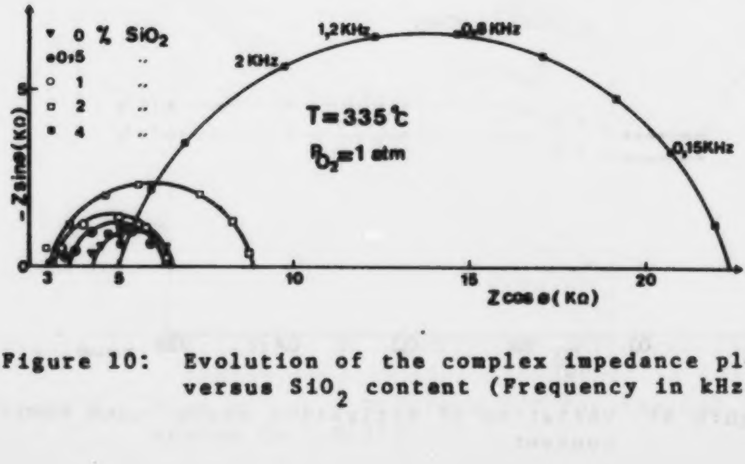

Figure 10: Evolution of the complex impedance plot versus SiO_2 content (Frequency in kHz).

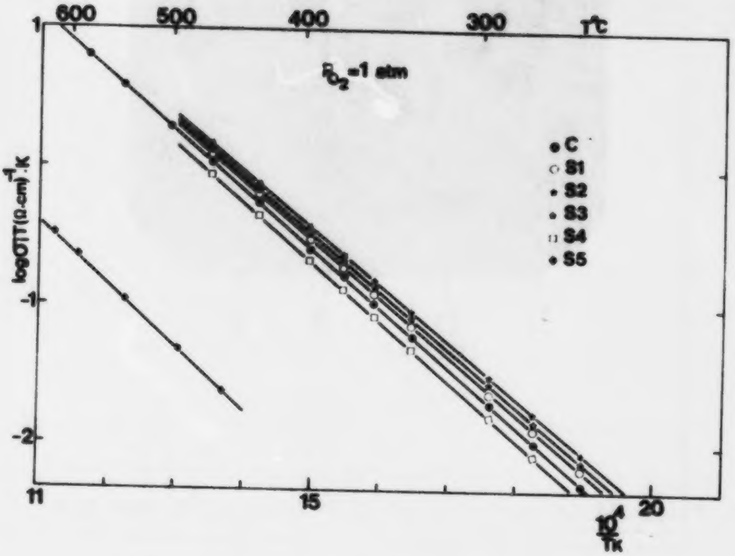

Figure 11. Plots of log $\sigma_i T$ versus 1/T for the $[(CeO_2)_{0,89} - (CaO)_{0,11}]_{1-x}\ [SiO_2]_x$ system.

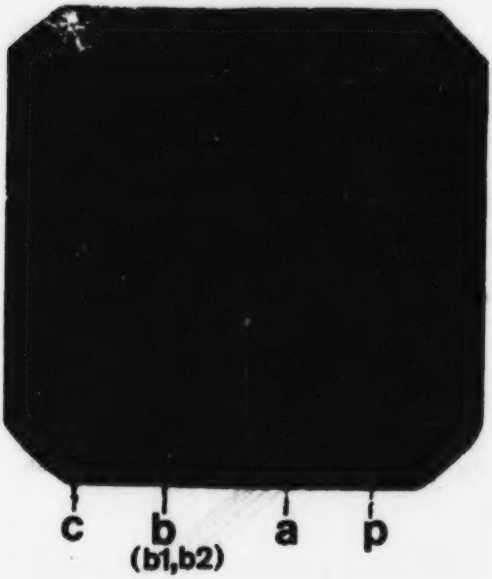

Figure 12 (a): Micrograph of intergranular zone in S3 sample

p: pore
a: phase rich in silicon and calcium
c: phase rich in solid solution
b: intermediate zone (b_1 is black and b_2 is white).

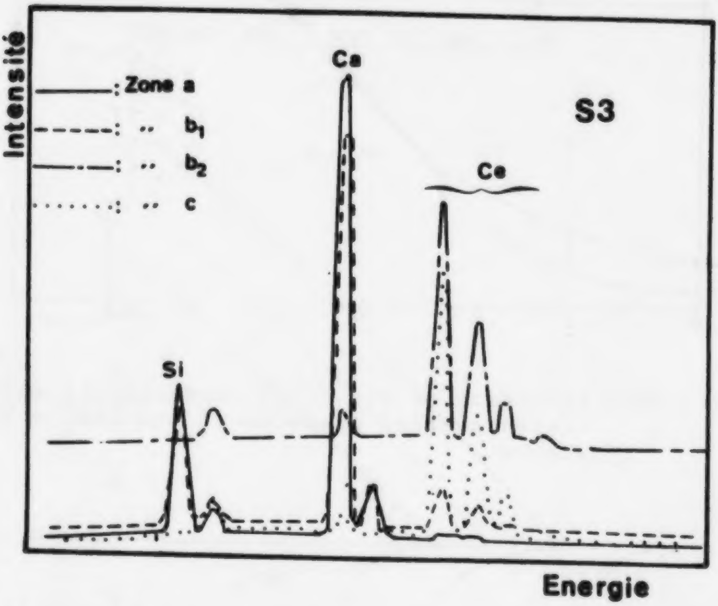

Figure 12 (b): Ce, Ca and Si analysis in the various zones.

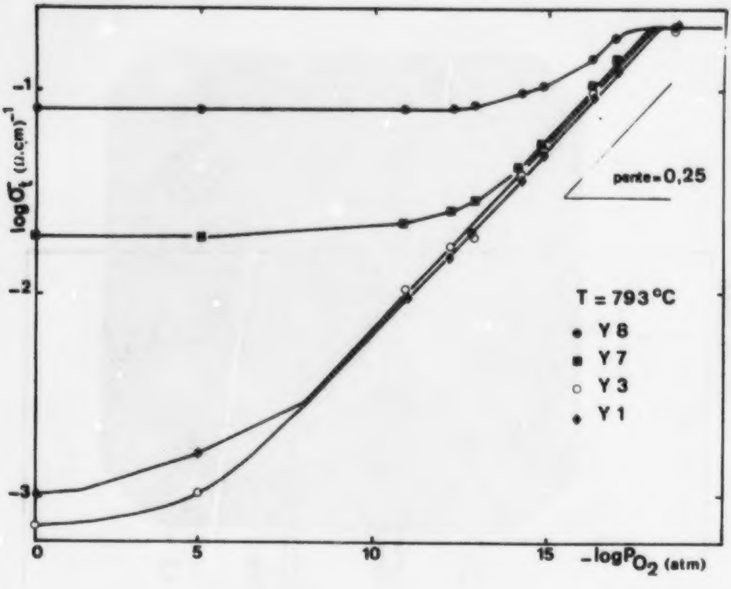

Figure 13: Variation of the total conductivity with oxygen partial pressure in the CeO_2 - $YO_{1,5}$ system.

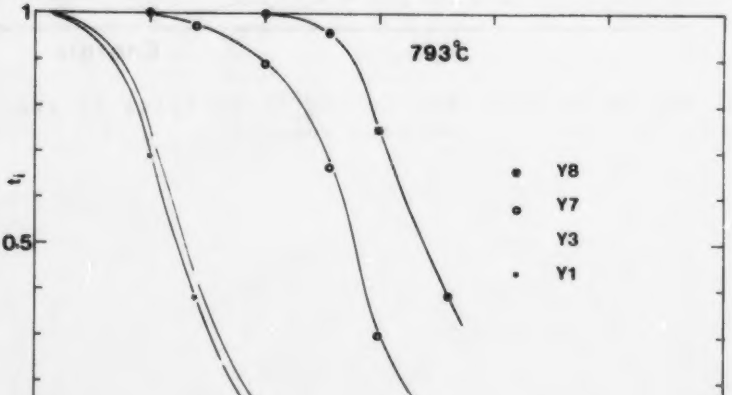

Figure 14: Variation of the ionic transference number with oxygen partial pressure in the CeO_2 - $YO_{1,5}$ system.

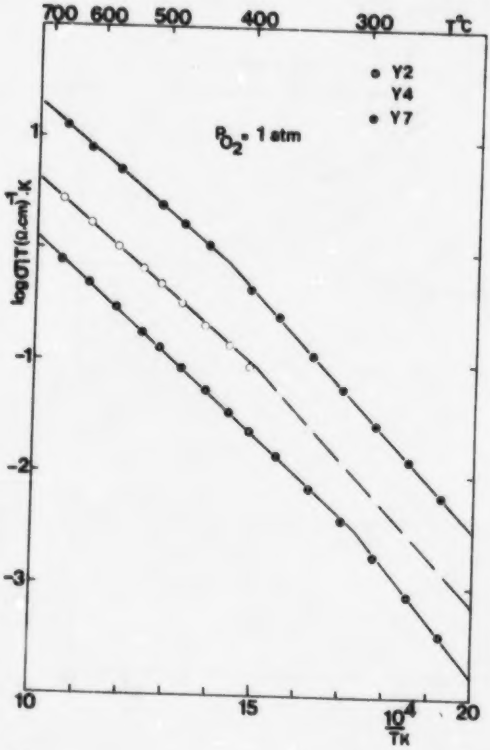

Figure 15: Plots of log $\sigma_i T$ versus 1/T for the CeO_2 - $YO_{1,5}$ system.

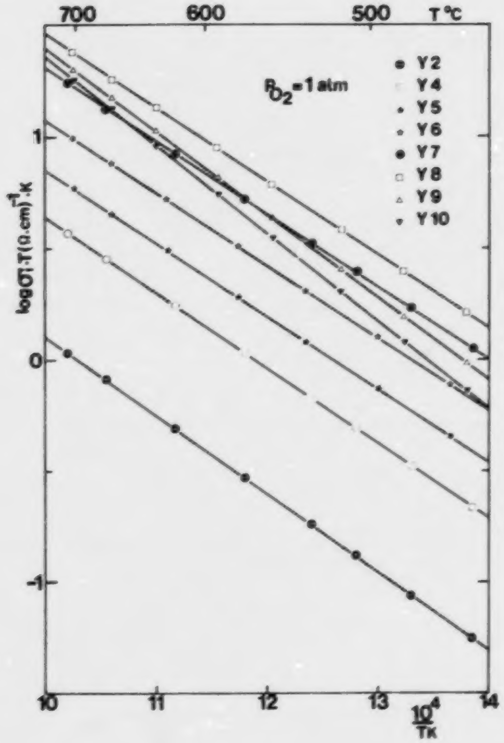

Figure 16: Plots of log $\sigma_i T$ versus 1/T for the CeO_2 - $YO_{1,5}$ system.

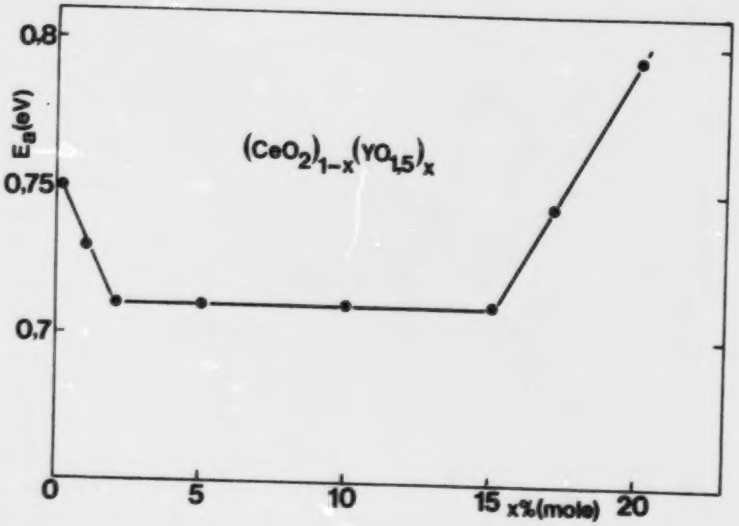

Figure 17: Variation of activation energy with $YO_{1,5}$ content.

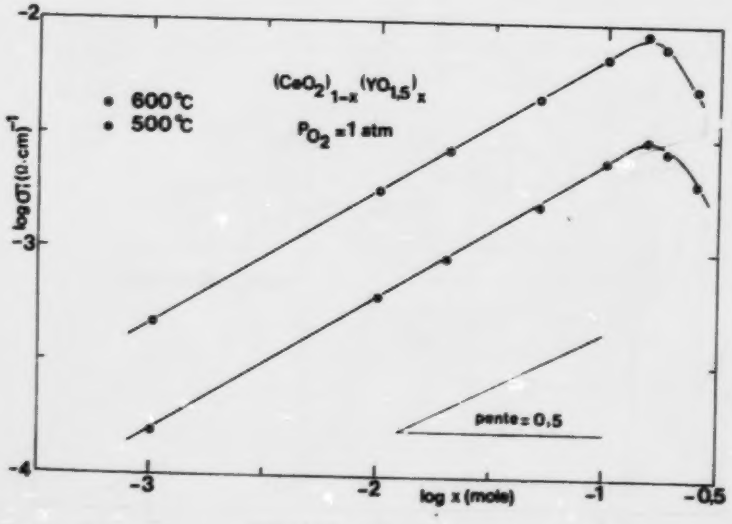

Figure 18: Variation of ionic conductivity with $YO_{1,5}$ content.

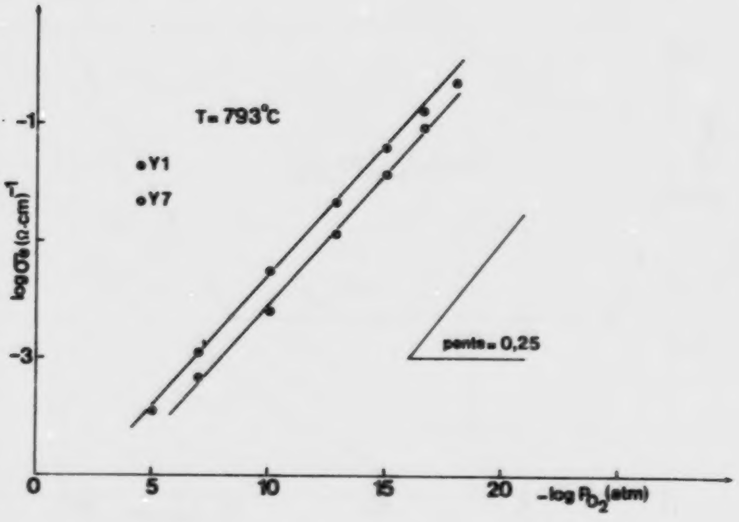

Figure 19: Variation of electronic conductivity with oxygen partial pressure in Y1 and Y7 solid solutions.

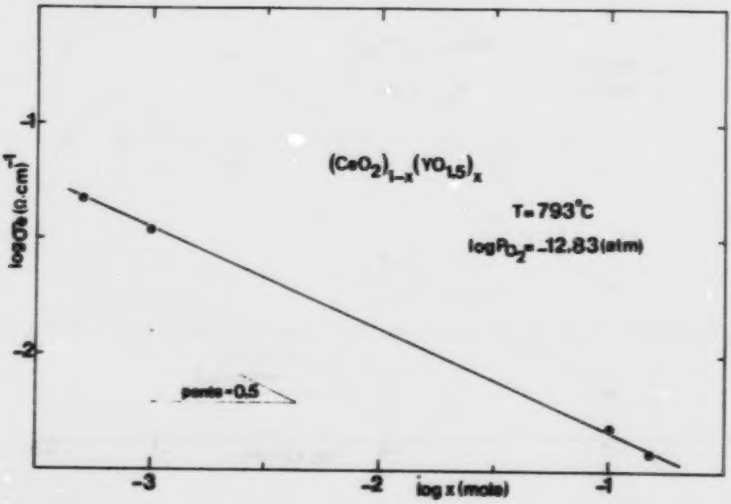

Figure 20: Variation of electronic conductivity with $YO_{1,5}$ content.

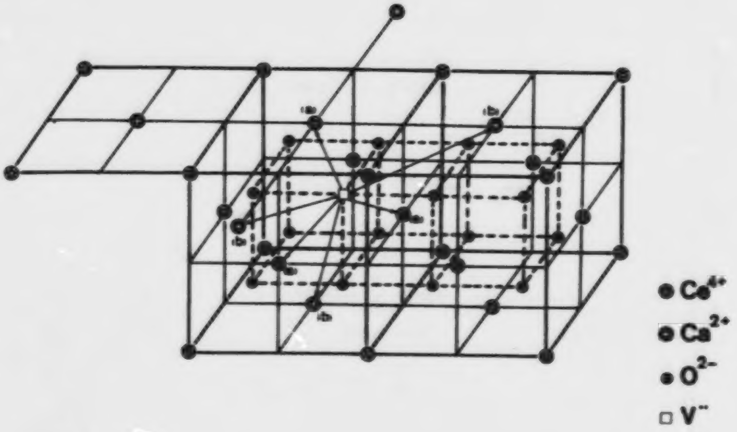
(a)
(b)
(b)
(a)
(b)
Ce^{4+}
Ca^{2+}
O^{2-}
$V^{\cdot\cdot}$

Figure 21: Cell corresponding to configuration I:
a) First nearest neighbour
b) Second nearest neighbour.

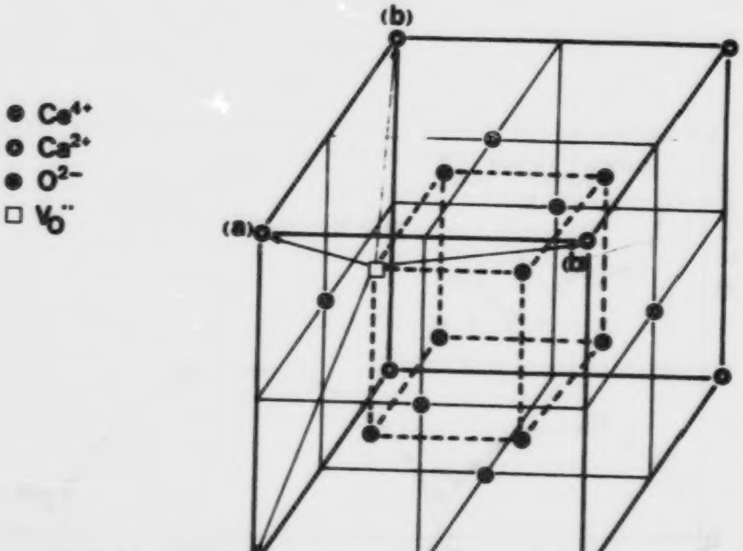
(b)
Ce^{4+}
Ca^{2+}
O^{2-}
$V_O^{\cdot\cdot}$
(a)
(b)
(b)

Figure 22: Cell corresponding to configuration II:
a) First nearest neighbour
b) Second nearest neighbour.

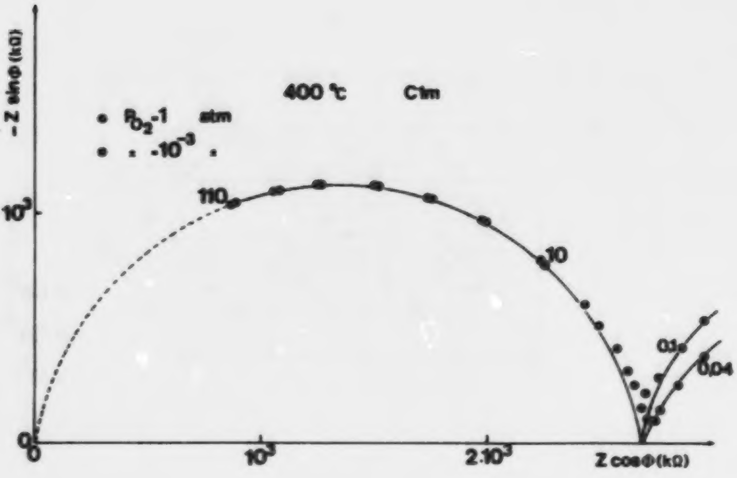

Figure 23 (a): Complex impedance diagram obtained with C_R (Frequency in kHz).

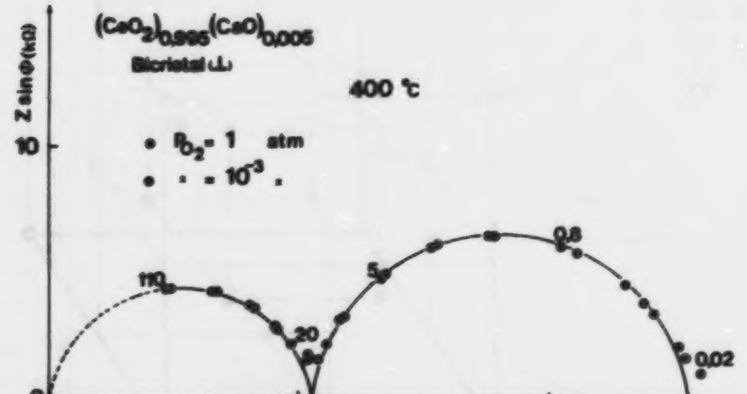

Figure 23 (b): Complex impedance diagram obtained with C_1 (Frequency in kHz).

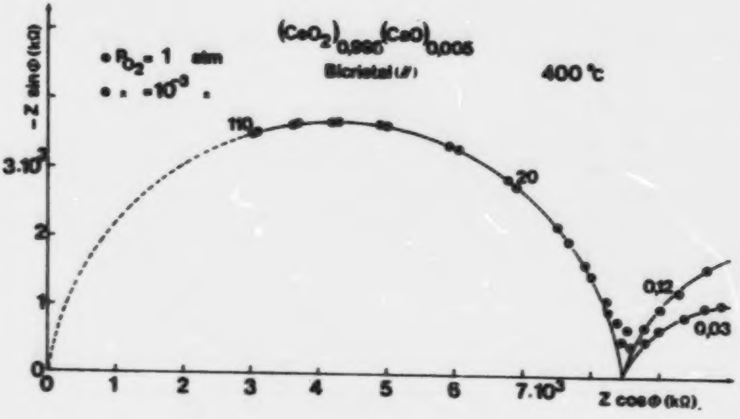

Figure 23 (c): Complex impedance diagram obtained with C// (Frequency in kHz).

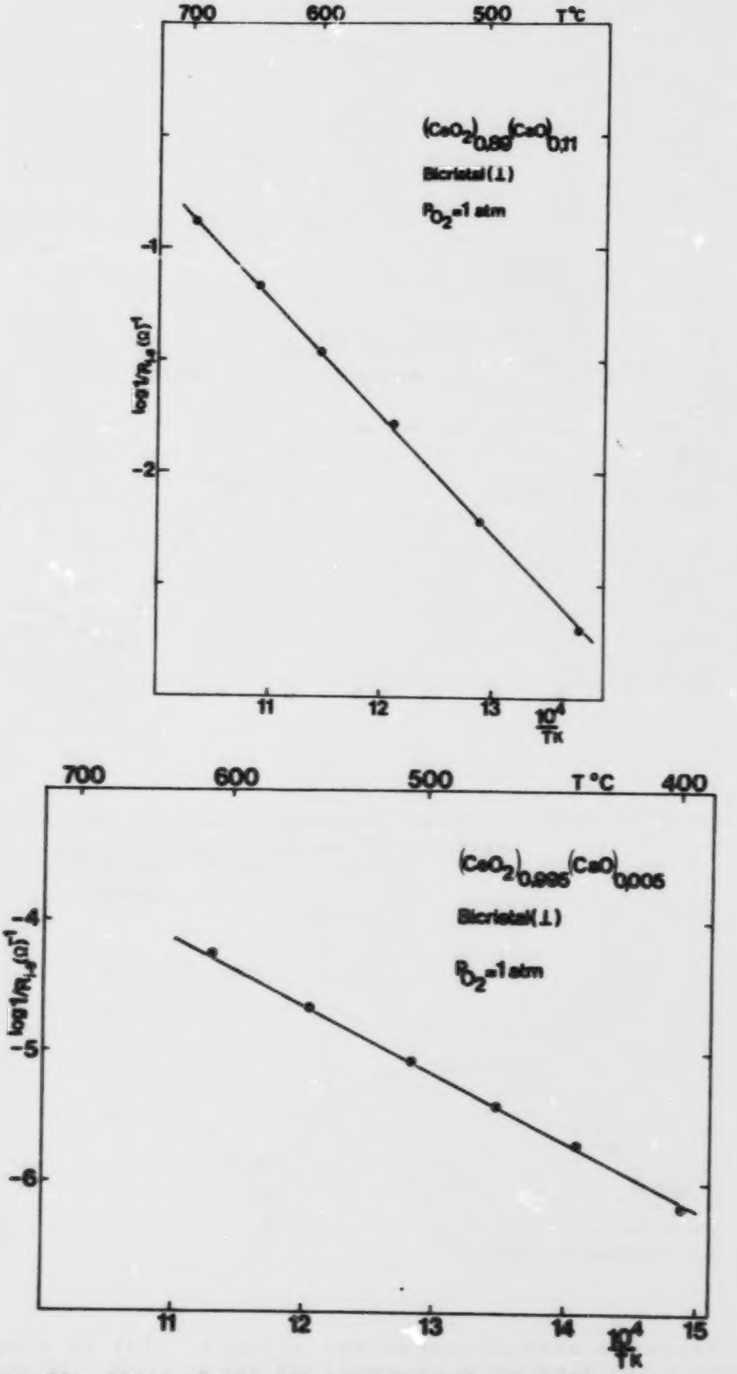

Figure 24: Plots of log $1/R_{jg}$ versus $1/T$ obtained with C_1 type cell.

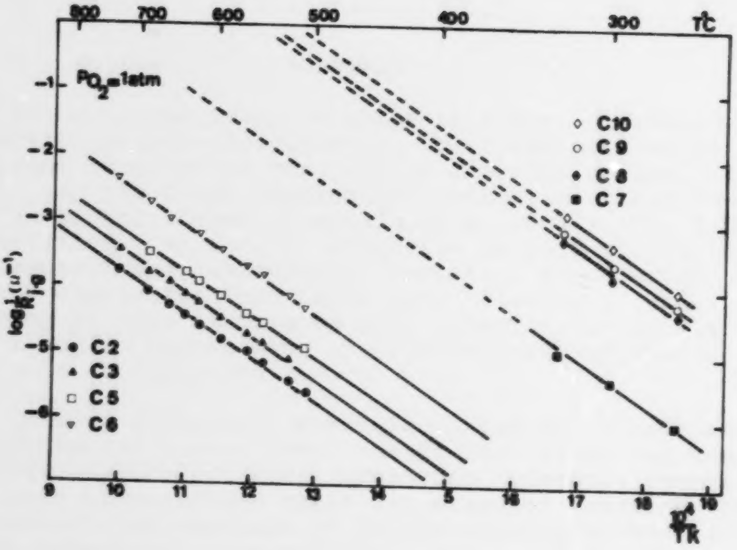

Figure 25: Plots of log $1/R_{jg}$ versus $1/T$ obtained with polycrystalline samples.

ANION CONDUCTIVITY IN OXIDES WITH THE FLUORITE AND RELATED STRUCTURES.

J.A. Kilner and J.D. Faktor

Wolfson Unit for Solid State Ionics
Imperial College of Science and Technology
London, SW7 2BP.

ABSTRACT

Anion conductivity in these oxides is discussed as a function of non-stoichiometry where the stoichiometric point is taken as the perfect fluorite composition (MO_2). In the first section the conductivity mechanisms in lightly doped materials (e.g. $CeO_2 + 5^m/_o\ Y_2O_3$) are detailed. Particular attention is paid to the role of dopant-vacancy associates. Recently, advances in lattice simulation techniques have afforded an understanding of this associated pair interaction and its importance in determining the conductivity of these materials is explained.

In more defective materials, where the simple pair representation breaks down, the factors affecting the conductivity are not well understood. Several theories have been proposed and these are examined together with microstructural evidence of defect clustering and micro domain formation. Conductivity studies of the fluorite and related pyrochlore compounds, near to the stoichiometry $MO_{1.75}$ are discussed.

Finally, heavily defective materials, based on δ-Bi_2O_3 ($MO_{1.5}$), are reviewed. Very little is understood as to the nature of the high conductivity in these structures but attempts are made to correlate structural data and observed transport mechanisms.

Keywords: Ionic Conductivity, Fluorite Oxides,
Pyrochlores, δ-Bismuth Oxide.

RÉSUMÉ

On discute de la conductivité anionique des oxydes en question en fonction du défaut de stocehiométrie, en prenant le point stoechiométrique comme étant la composition de la fluorine parfaite (MO_2). Dans la première partie, on détaille le mécanisme de conductivité dans des matières légèrement dopées (c.-à-d. CeO_2 + 5m/$_o$ Y_2O_3). On prête surtout attention au rôle des associations poison-trou. Récemment, des progrès des techniques de simulation des réseaux ont permis de permis de comprendre cette interaction de paires associées et l'on explique son importance pour la détermination de la conductivité de ces matières.

Dans les matières plus imparfaites, où la simple représentation de paires ne tient plus, on ne comprend pas bien les facteurs influençant la conductivité. On a proposé de nombreuses théories qui sont examinées en même temps que des signes de formation de microdomaines et de groupements de défauts. On discute des études sur la conductivité de la fluorine et des pyrochlores analogues au voisinage de la stoechiométrie ($MO_{1,75}$).

Enfin, on revoit les matières très imparfaites à base de δ-Bi_2O_3 ($MO_{1,5}$). On comprend très peu la nature de la forte conductivité de ces structures, mais on tente de fiare une corrélation entre les données structurales et les mécanismes observés de transport.

INTRODUCTION

The study of mass transport phenomena in the group of oxides adopting the fluorite and related structures is a particularly interesting field of research. The high anion mobilities possessed by these oxides mean that they can be used as solid electrolytes and consequently put to practical use in the fields of energy conversion and conservation. For example, present applications include devices such as; oxygen sensors for determining the dissolved oxygen in liquid metals: the lambda sensor for the control of exhaust emission in automobiles: gas sensors for the control of combustion in oil-fired boilers. In addition, there are several potential applications to which these materials may be put. These include electrolytes for the high-temperature fuel cell, high-temperature water electrolysers and oxygen separation membranes. Clearly, there is much technological interest in the continued development of these materials.

The fluorite oxides exhibit a wide range of stoichiometry. This can be achieved in two ways, by variation of the host cation valency as in CeO_{2-x} and UO_{2+x} or by doping with aliovalent cations as in $Zr(Y)O_{2-x}$ and $Ce(Gd)O_{2-x}$. Because of this wide variation in stoichiometry it is possible to observe a very wide range of defect processes within one host lattice type, from the very 'dilute' concentrations of defects where classical point defect analysis is valid to the highly defective oxides where extremely complex defect interactions can take place.

Our aim in this review is to give an account of the current theories of anion conductivity in the fluorite oxides as a function of the non-stoichiometry, starting with the point defect regime and moving towards the highly defective oxides. It is also our aim to stress the important role that computer calculations of defect energies are now playing in the interpretation of the mass transport data available.

We shall limit the analysis in this article to the investigation of lattice properties i.e. we do not include any data or discussion of grain boundary and electrode phenomena. The reader is refered to other reviews for an account of these topics (1,2).

Structure and Properties

The ideal fluorite lattice has the stoichiometry MO_2 and adopts the structure shown in Figure (1). The anion sublattice has a simple cubic stacking with the cations occupying every other cube centre, thus forming a three dimensional chequer pattern. When the oxides are doped with lower valent cations Mf^{3+} or Mf^{2+} the dopant cations substitute for the host cations and anion vacancies form as charge compensating defects. These anion vacancies are highly mobile and give rise to high ionic conductivities.

The oxides ZrO_2 and HfO_2 do not naturally crystallise in the fluorite structure except at high temperatures; the Zr^{4+} and Hf^{4+} cations are just too small to stabilise the structure. However, when the materials are doped with a few percent of aliovalent cations the fluorite structure can be stabilised to room temperature. CeO_2 and ThO_2, on the other hand, are stable in this structure and consequently are of importance for the study of the effects of low dopant concentrations in the fluorite lattice.

The ionic conductivity of these doped fluorite oxides shows some very complex behaviour, however, one point is common to all systems. A plot of the isothermal conductivity against composition always shows a maximum. Figure (2) shows the isothermal conductivity of several ZrO_2-based oxides in which the maximum is quite clear. In the following sections of this article we will first, analyse data from material which falls into the region below the concentration maximum and then second, look at compositions where the conductivity falls off rapidly with concentration. Finally data for materials with the fluorite-related pyrochlore and δ-Bi_2O_3 structures will be discussed.

Point Defect and Defect Associates

The equation governing the anion conductivity in these oxides, at low dopant concentrations, can be expanded in the following manner (2).

$$\sigma T = B\,[V\dot{o}^{\cdot}]\,\exp(-\Delta H_m/kT) \qquad \ldots\ldots(1)$$

where σ is the ionic conductivity at temperature T,
ΔH_m is the enthalpy of migration of an oxide ion,
$[V\dot{o}^{\cdot}]$ is the concentration of oxygen vacancies,
k is the Boltzmann constant

and B is a temperature independent parameter which can be expanded to give;

$$B = \frac{No(Ze)^2 a_o^2}{k}\,\nu_o\,\gamma\,\exp\left(\frac{\Delta Sm}{k}\right) \qquad \ldots\ldots(2)$$

where No is the number of anion sites/unit volume,
a_o is the jump distance,

ν_o the jump attempt frequency,

γ a geometrical factor,

Z the charge of the carriers and
e is the electronic charge.

Clearly most of the parameters within this equation are well defined and can be qualitatively estimated (except perhaps ΔSm). The remaining unknowns in equation (1) are thus $[V\dot{o}^{\cdot}]$ and ΔH_m. If we assume that ΔH_m will not change within an oxide type and with defect concentration, then clearly any differences must be due to changes in $[Vo^{\cdot}]$. Initially it was thought that all the vacancies must be free to take part in the conduction process. It is now accepted, however, that defect pairs form in which the oxygen vacancies are bound to the dopant cations (2,3). Here a distinction must be made between the two most common types of cations used as dopants in the fluorite oxides, i.e. divalent and trivalent cations.

For the case of divalent dopant cations the simplest defect associate that can form is the fully compensated pair. Taking CaO-doped CeO_2, as an example, we can write the following defect equation governing the association of oxygen vacancies e.g.:-

$$V\dot{o}^{\cdot} + Ca_{Ce}'' \rightarrow \{Ca_{Ce}'' \, V\dot{o}^{\cdot}\}^{x} \qquad \ldots\ldots(3)$$

If we ascribe an enthalpy of association to such a reaction, ΔH_{A2}, then it is quite easy to show that the free vacancy concentration has the following temperature dependence

$$[V\dot{o}^{\cdot}] = C_{M2}^{\frac{1}{2}} \text{ const } \exp\left(\frac{-\Delta H_{A2}}{2kT}\right) \qquad \ldots\ldots(4)$$

where C_{M2} is the total concentration of divalent cation.

The case for trivalent dopants is somewhat more complex. If we take, as an example, CeO_2 doped with Y_2O_3 then the simplest associate that can form is the uncompensated pair e.g.:-

$$V\dot{o}^{\cdot} + Y_{Ce}' \rightarrow \{V\dot{o}^{\cdot} \, Y_{Ce}'\}^{\cdot} \qquad \ldots\ldots(5)$$

The existence of these pairs is inferred from ESR data (4). Formation of these associates means that an equal number of Y_{Ce}' must be left to charge compensate, and the ESR data for fluorite doped with trivalent dopants does show a significant population of trivalent dopants with cubic point symmetry i.e. no vacancy in the near neighbour position. Again it is quite easy to show that given equation (5) the free vacancy population has the following temperature dependence.

$$[V_{\ddot{O}}^{\cdot}] = \text{const} \exp\left(- \frac{\Delta H_{A1}}{kT} \right) \qquad \ldots\ldots(6)$$

Note that no term in equation (6) shows any dependence on the composition of dopant and thus the concentration dependence in this case is quite different from that found for the divalent dopants.

By introducing both equations (4) and (6) into equation (2) we can examine the expected form of the conductivity equation and its variation with dopant concentration or temperature. Table 1 shows the results of such an analysis, for di- and trivalently doped fluorites.

Comparison with Experiment

The confirmation of this defect associate behaviour is primarily due to the work of Nowick and coworkers, (3,5-7) working with low dopant concentrations in CeO_2-based materials. The divalently doped material behaves exactly as predicted by the simple defect analysis. Figure (3) shows a plot of data taken by Wang and Nowick for Ca-doped CeO_2. The activation energy for the doped materials is constant throughout the concentration range and is quite high having an average value of 0.93 eV. Because the activation energy remains constant the isothermal conductivity reflects the composition dependence of the pre-exponential factor and follows the expected $C_{M2}^{\frac{1}{2}}$ power law. This good correspondence is particularly interesting because it applies up to ∿ 15 mole % calcia, which is a very concentrated solid solution.

The trivalent dopants show a somewhat more complex behaviour. The pre-exponential factor does remain constant as predicted by the point defect theory, however, the activation energy shows some compositional variation. A particularly good example of this type of behaviour has been reported by Hammou (8) for the two systems CeO_2-Y_2O_3 and ZrO_2-CeO_2-Y_2O_3. In both systems the pre-exponential factor remains independent of composition over an appreciable range of concentration, again into regions which must be considered as rather concentrated solid solutions. The behaviour of the pre-exponential and activation energy is shown in Figure (4). Instead of showing a flat compositional independence the activation energy initially decreases with concentration and then increases causing a distinct minimum. This minimum in activation energy coupled with the flatness of the pre-exponential causes a maximum to occur in a plot of the isothermal conductivity. This effect is shown in Figure (5), where the correspondence between the minimum in activation energy and maximum in conductivity is well-illustrated for CeO_2 doped with Y_2O_3.

This minimum in activation energy has been shown to occur in other systems e.g. ThO_2-Y_2O_3 (9) and ZrO_2-Y_2O_3 (10), and is clearly a distinct feature of the trivalently doped fluorites. An explanation of why the activation energy initially falls with increasing concentration has been provided by Wang et al (7). They have suggested that coulombic interactions occur between the associated pairs and the equal numbers of free dopant ions. The model is developed by supposing that the charged defects form a regular array of charges of alternating sign within the host lattice. The effect of this is to lower the association enthalpy, ΔH_{A1}, and thus lower the total activation energy measured by experiment. Clearly, the model is idealised, however, it shows good agreement with the data, obtained by these workers, for the system CeO_2-Y_2O_3.

The theories which have been proposed to explain the increase which occurs in the observed activation energy at more concentrated solutions will be examined in a later section.

Calculated energies and relaxation effects

So far we have only considered the qualitative aspect of the effect of point defects and association. Although there is good qualitative agreement between the defect theories and experiment there are also some quantitative aspects which have now to be discussed.

Before we explore the results of these analyses we shall give some explanation of the methods used in the calculation of defect energies. For a full account the reader is referred to some excellent reviews by Catlow et al (11,12). All the calculations we shall describe are based on the code HADES. This uses a modified Mott-Lyttleton approach to calculate defect energies in ionic solids. The crystal is split up into two regions, an inner region surrounding the defect in which all atomic relaxations are treated explicitly and a matched outer region which is treated as a continium dielectric. The polarisability of the ions themselves is represented using the shell model. The code then finds the minimum energy, for the defect structure, that is consistent with the interatomic potential and shell model data used. Let us take, as an example of this quantification, the fluorite oxides doped with trivalent dopants. There is a wide range of reported conductivity data covering these oxides, however, it is generally accepted that materials in the CeO_2-Gd_2O_3 (13) system show the highest conductivities (lowest activation energies) and conversely materials in the ThO_2-Y_2O_3 system show some of the lowest conductivities (highest activation energies).

These differences are hard to quantify because activation energies can depend upon many factors e.g. dopant concentration, temperature of measurement, method of measurement. Recently one set of measurements, by Gerhart-Anderson and Nowick (14), has provided directly comparable activation energies for CeO_2-M_2O_3 systems at a low concentration. These show some surprising results. Gerhart-Anderson and Nowick have assumed that the migration enthalpy in these oxides remains unchanged and have used a value of $\Delta H_m = 0.6$ eV, determined from earlier studies. The association enthalpy, ΔH_{A1}, then turns out to be dependent upon the dopant ion type. The results from these experiments are shown in Figure 6 , where the association enthalpy is plotted against dopant ion radius. We should point out here that 'classically' the association enthalpy was only thought to depend upon the charge of the two defects and thus, no differences should be observed.

Some indication of what may cause these effects has been described by Kilner and Brook (15). These authors tried to find a reason for the differences between the known fluorite oxygen-ion conductors. They used a combination of calculation and experiment, using the perovskites, $ReAlO_3$, as a model, in order to obtain information about the relative importance of the terms ΔH_m and ΔH_{A1}. Their main conclusions can be stated as follows. In an isostructural series, ΔH_m is likely to have similar values for different host lattices. This implies that ΔH_m for ZrO_2, CeO_2 and ThO_2 should be about equal, with a value ~ 0.6 eV. Experimentally, there is some justification for this result. Furthermore, they propose that the most significant parameter, in the conductivity equation is ΔH_{A1} and this term is dependent upon the size of the dopant cation. By drawing an analogy with earlier calculations, on doped MgO (16), Kilner and Brook suggested that the binding energy of this defect pair (ΔH_{A1}) should increase with the size mis-match between host and dopant. The reason for the increase in binding energy is due to a change in strain energy. The wrong size dopant will be surrounded by a strain field and it seems that when a near-neighbour vacancy associates with this dopant, relaxations can occur which lower the total strain energy. In other words, the two defects have a binding energy.

The binding of defects by strain energy has been thought to occur in insulators and has been found to occur in metals and semiconductors (17). These findings are suprising for two reasons. Firstly the effect is much larger when the dopant is smaller than the host and secondly, in such a case, the binding due to strain energy alone can be as high as 1 eV.

Butler has performed a series of calculations on the fluorite oxides including ZrO_2 and CeO_2 (18). Of particular interest here are the calculations of the same binding energies, in M_2O_3-doped CeO_2, that were measured by Gerhart-Anderson. The results of these calculations are shown together with the experimental results in Figure 6 . Clearly there is good quantitative agreement between experiment and calculation and good qualitative agreement with the ideas proposed by Kilner and Brook (15).

Kilner (19,20) has suggested that, because the binding energy is dependent upon the relative radii of host and dopant, plots of lattice parameter vs. concentration should yield relevant qualitative information about the expected strain component. He chose, as an example, the trivalently doped CeO_2 oxides. Figure 7a shows data, first presented by Bevan and Summerville (21), which details the changes in lattice parameter for various solid solutions. Two points are informative.

A. Lattice Parameter Maps

The change in lattice parameter for the system CeO_2-Gd_2O_3 is the smallest for all the systems studied. In fact, it is quite surprising how little the introduction of Gd^{3+} ions into the host lattice alters the lattice parameter. This corresponds well to the idea that the ionic radii of Ce^{4+} and Gd^{3+} are well matched in the fluorite structure; a pre-requisite for a corresponding minimum in the strain-energy term. This simple idea can be extended to cover all the fluorite oxides doped with trivalent rare earth elements. Figure 7b shows a plot taken from ref. (20)of a schematic version of Figure 7a on which the other typical fluorite hosts have been included. Some interesting conclusions can easily be drawn from this plot,

(1) Th^{4+} (ThO_2) is, in general, too large a host cation; most dopants are smaller and thus high strain components can be expected in the pair binding energies.

(2) Zr^{4+} is, in general, too small a host cation; most

dopants are larger in size and thus some strain component can be expected although this may not be as large as in case (1).

B. Deviations from Vegard's Law

If the variation of lattice parameter is examined in more detail two regions of curvature are found. Figure 8 shows the data for CeO_2-Y_2O_3 systems taken from ref (21). This curvature is clearly a deviation from Vegard's Law and the original authors suggest that this is due to attractive defect interactions. Kilner (20) has suggested that these interactions are the same ones that give rise to the vacancy binding. It is interesting to note that the break in slope occurs at ∿ 10% dopant concentration, very near to the observed conductivity maximum.

The second region of curvature is very similar in nature to the first. This suggests that the type of defect interaction is the same, but that the type of defect is more complex. Bevan and Summerville (21) point out that in this region it is possible to observe weak diffuse reflections of C-type rare earth structure which may be due to the growth of microdomains, coherent with the host matrix. It is tempting to suggest that this break in slope indicates the region where the simple pair representation breaks down and more complex behaviour (e.g. microdomains) begins. If the size of the deviation from Vegard's Law is examined for the second region then it is found to be dependent upon the dopant cation type (within the rare earth series) and follows the same ion-size dependence as has been found for the dilute region (20). This would suggest that even in concentrated solutions, elastic effects could be important.

HIGHLY DEFECTIVE OXIDES

In the introduction we showed that, experimentally, a maximum is always found in the concentration vs. isothermal conductivity plots for the doped fluorite oxides. There have been many attempts to explain why such a maximum should occur and the situation still remains unclear. The models used to explain this phenomenon can broadly be classified into two groups, those which use statistical arguments and those which use structural arguments. We do not intend to present a complete survey of this phenomenon, merely to highlight the two different approaches and examine new evidence provided by lattice simulations.

A. Statistical Considerations

We showed earlier in the section on point defects that, even given the formation of associates, the conductivity of a defect fluorite should increase with concentration. No mechanism given earlier can account for the sudden drop in conductivity that occurs with concentration. Barker and Knop (22) have shown that if simple constraints are put on the movement of vacancies then a maximum will occur. They calculated the conductivity of a simple cubic anion array containing vacancies for three cases, (1) The classical theory where no constraints apply; (2) no vacancy can jump to sites with anion vacancies as near neighbours and (3) no vacancy can jump to sites with anion vacancies as first or second near neighbours. They showed that for case (3) a maximum occurs at ∿ 6% vacancies (for purely random vacancies this would occur at 50%) although after this the conductivity does not drop rapidly as observed experimentally. O'Keefe (23) has given a similar treatment which precludes any configuration with near neighbour vacancy pairs. This supposes that the vacancy-vacancy interaction is strongly repulsive and leads to anion order.

Subbarao and Ramakrishnan (24) have further extended the model to include the effect of vacancy trapping at dopant cation sites. The Barker and O'Keefe treatment does not take into account the cation sublattice. Clearly, because large interactions can take place between dopant cations and anion vacancies, vacancies with near-neighbour dopant cations can be strongly trapped. This produces a somewhat better fit to experimental data but still does not achieve the rapid fall off seen experimentally.

Nakamura and Wagner (25) take a slightly different approach in an analysis of calcia-stabilized zirconia. They assume that movement of oxygen vacancies through the lattice is a multimode process. They define three possible pathways through the crystal, consisting of connected anion sites having different dopant coordination numbers. A conceptual difficulty arises at this point because this coordination number is an effective coordination number made up of the number of near neighbour dopants plus one third of the number of second neighbour dopants. No satisfactory explanation is given why this should be. The effective coordination numbers of the pathways are then found to be 0, 1 and 2. At the maximum ($[V_O^{\cdot\cdot}] = 0.125$) all the pathways are found to be 1 coordinated, at a higher concentration ($[V_O^{\cdot\cdot}] = 0.25$) the pathways are all 2 coordinated.

By using experimental conductivity data, mobilities within the 1 and 2 coordinated channels can be obtained; these are then used to re-calculate the conductivity data. The fit to experimental data is good, however, it is unsatisfactory to have conductivity calculations in which unknown mobilities have to be obtained from experimental data; these should be derivable from first principles.

Catlow (26) has provided an alternative theory in an analysis of CeO_2-Y_2O_3. He abandons the discrete cluster model i.e. associates separated by regions of perfect crystal and like Nakamura and Wagner (25) examines the dopant cation coordination of each anion site, limiting the argument to the first neighbour shell. The distribution of cations throughout the lattice is assumed to be random, and the populations of 0, 1 etc. defect-coordinated anion sites are calculated using a simple binomial expression. The binding energies of oxygen vacancies to each of these sites is then calculated using the HADES method and the distribution of vacancies between these sites calculated using Fermi-Dirac (27) statistics. Vacancy migration then takes place by jumps between the differently coordinated sites and activation energies are calculated for each jump, again using HADES. In the first attempt at calculation a satisfactory fit was obtained to the maximum but the fall off was not sharp, in fact the conductivity levelled off at a reasonably high value. The interatomic potential used in these first calculations neglected ion size effects and simply reflected the coulombic interactions. When ion size effects were included the conductivity in the post maximum region dropped by three orders of magnitude, in good accord with experimental data, although the fit close to the maximum was less satisfactory. Catlow also shows that the cause of the maximum at ∿ 8 mole % dopant is the increasing number of deep traps, implying that up to this concentration a discrete representation may be adequate; this, however breaks down at higher concentrations. Evidence which may support this theory has come from two recent papers describing work on yttria stabilised zirconia (28,29); these both imply that a gaussian distribution of activation energies is seen by the migrating oxygen atoms. The yttria concentrations studied, i.e. 9 and 12 mole % yttria, are both slightly above the concentration of the maximum and thus into the region where the discrete cluster approach breaks down.

B. Structural Considerations

All the above descriptions of the conductivity of these oxides have one major drawback in that they assume a random or pseudo-random arrangement of the dopant cations. The highly mobile anion lattice is then assumed to adjust to this cation distribution. This is Summerville's description of "operational equilibrium", quoted in reference (21), and is distinct from the true equilibrium state of the lattice. In many of the systems under study intermediate, fluorite related, phases can occur and these may be represented by the general formula M_nO_{2n-2} (e.g. $CaZr_4O_9$, $Nd_2Zr_2O_7$ etc). The study of these phases is a complete and complex subject in itself. For example, there are phases where both sub-lattices are ordered and those where only the anions are ordered (30). When such heavily doped materials are annealed for prolonged periods at elevated temperatures ordering can occur, either short range or long range, depending upon the system and concentration. It must be remembered that cation diffusion in the lattice is extremely slow when compared to the anion mobility and consequently any ordering can be an extremely slow process; the true equilibrium state of the lattice may be practically unattainable due to kinetic barriers.

In general, the tendency to cation order depends upon the size difference between the dopant and host cation. For example, at the stoichiometry $Ln_2Zr_2O_7$, when the rare-earth atom becomes larger than Gd^{3+} (1.06 Å in VIII co-ordination) the ordered pyrochlore structure forms, but when the rare-earth ion is smaller the disordered fluorite phase forms. These ordered phases can, however, disorder at high temperatures; $Gd_2Zr_2O_7$ disorders at ∿ 1550°C. This disorder temperature increases as the size difference between the two cations becomes larger reflecting the increasing stability of the ordered lattice.

Anion order is slightly more difficult to define. Where the cation sizes are sufficiently different to provide a stable ordered cation lattice, the anion lattice will follow and order. This indicates that there is a strong interaction between the two lattices analagous to the bonding described earlier for the dopant cation-oxygen vacancy pair. This link between cation and anion order has been demonstrated by Rossell (30) for $Zr_3Er_4O_{12}$ and by Faktor et al (32) for the system $Nd_2Zr_2O_7$ - $Nd_2Ce_2O_7$.

When the cation size difference is small, as in $Zr_3Sc_4O_{12}$, no cation ordering takes place. At low temperatures, however, the highly mobile anion lattice can order leading to an example of 'anion only order' of the type described by O'Keefe (23). This implies that the coupling between the two lattices is very small, otherwise the anion lattice might be expected to adjust to the random distribution of dopant cations. Further, the vacancy-vacancy interaction must be strong enough to overcome any interactions between the lattices and drive the anion lattice into order.

What the previous arguments tell us is that ordering can significantly alter the distribution of ions from a random distribution over the available fluorite lattice sites. This must be taken into account when attempting to explain the observed transport behaviour, and in particular, when comparing different systems, the differing tendency to order must also be recognised.

Most work on order and its effect upon the conductivity has been directed at explaining data for one of the oldest known anion conductors: calcia-stabilized zirconia. Most of these structural arguments have centred on attempts to explain the diffuse scattering first seen in the neutron scattering experiments of Carter and Roth (31). They also observed a slow ageing process taking place at ∿ 1100°C which they assumed to be due to the growth of small zones of an ordered phase. Since those experiments a variety of techniques have been used, including x-ray, neutron and electron scattering, in attempts to elucidate the nature of the diffuse scattering and the ordering process (33-36).

The results of these studies have been a division of opinion into two schools of thought, particularly as to the origin of the diffuse scatter in the high temperature form. Those concerned with "macro-diffraction", i.e. x-ray and neutron scattering, favour a model which involves a random distribution of dopant cations with oxygen vacancies as nearest neighbours. Significant relaxations of the oxygens surrounding a vacancy, along the <100> directions, are also found for this model.

Those experiments concerned with "micro diffraction" (i.e. electron diffraction) favour another explanation in which the diffuse scatter is caused by coherent microdomains of an ordered phase (30), oriented at random within the parent fluorite matrix. Allpress, Rossell and Scott (36) propose that the domain structure is that of the zirconium analogue of Ca Hf_4O_9 and Rossell (30) points out that in this structure the larger Ca^{++} ion is eight co-ordinated by oxygen and the smaller Zr^{4+} is six or seven co-ordinated, as might be expected from simple size considerations. The Ca^{++} is now a second neighbour to an oxygen vacancy, not a first neighbour, as in a defect pair.

In an attempt to resolve this apparent conflict of opinion as to the local environment of the oxygen vacancy, Butler et al (37) have used lattice simulation techniques to calculate the energy of both structures. Unfortunately they could not estimate the magnitude of the interfacial energy, between the microdomain and the host matrix, which may not be negligible. The results of the calculation show that microdomains of $CaZr_4O_9$ are favoured over isolated pairs by an energy of only 0.09 eV. Clearly, even given a component from the interfacial energy, the difference in energy is likely to remain small with perhaps point defect clusters favoured at low dopant concentrations and microdomains at higher concentrations. If only a small difference in energy exists between the two competing structures then the equilibrium between defect pairs and domains e.g.

$$m\ (\ 4Zr_{Zr}^{x} + 9O_{O}^{x} + \{Ca_{Zr}^{''}\ V_{O}^{\cdot\cdot}\}^{x}) \rightleftharpoons mCaZr_4O_9$$

is unlikely to be strongly biased towards either side of the equilibrium at temperatures where the kinetic barriers are small.

What we have tried to emphasise in this section is the variety of different states that can be taken up by a highly defective fluorite lattice, and that ordering of one or both sublattices can occur. This ordering can be either long range or short range but, as pointed out by Barker et al (38), some degree of ordering seems inevitable in such highly defective systems. We have also tried to emphasise that because relative size is an important factor no two systems can be considered to be the same, e.g. ZrO_2-Y_2O_3 cannot reasonably be expected to show the same features as ThO_2-Y_2O_3. Finally we have tried to point out that, because of the large difference in mobility of the cations and anions, kinetic barriers can give rise to non-equilibrium states. Thus it would seem to be necessary to document the thermal history of any samples used for comparisons of order or disorder.

We would also like to point out that some similarities may be drawn between the preceding discussions and experiments on the alkaline earth doped alkali halides e.g. $NaCl:CdCl_2$. The evolution of precipitates of Suzuki type phases occurs by the aggregation of dopant cation vacancy pairs into dimers, trimers etc. This leads, eventually, to the precipitation of a second phase which, due to the mobility of both vacancy and dopant, occurs at low dopant concentrations compared to the fluorite oxides. In the fluorites any such process may be considered to be very slow, and so the evolution of higher order aggregates occurs at much larger concentrations, where statistical fluctuations (rather than dopant transport) give higher order clusters.

THE PYROCHLORES ($MO_{1.75}$)

The oxide pyrochlores have the general formula $A_2B_2O_7$. The structure is closely related to that of the fluorite and for the present purposes it is best visualised as a fluorite with $^1/_8$ of all oxygen sites vacant. Unlike defect fluorites of the same stoichiometry, in the perfect pyrochlore the oxygen and the cation sublattices are both ordered. Intrinsic Frenkel disorder on the oxygen sublattice places some oxygens on the normally unoccupied sites, thus creating vacancies, and it is these vacancies which are responsible for the observed ionic conductivity.

Studies of conductivity have been restricted to the $A_2^{3+}B_2^{4+}O_7$ pyrochlores and most attention has been paid to the $Ln_2Zr_2O_7$ materials (39-50). The exception is a study, by Uematsu et al (51) of $Ti_2Y_2O_7$. Early investigations (39-44) produced rather conflicting results as is evident from a comparison of some of the data. For $Gd_2Zr_2O_7$, Peters and Radeke (39) found a local maximum in the conductivity vs. composition curve, whereas Fomina and Pal'guev (43) found a local minumum. For $Sm_2Zr_2O_7$, Steele et al (40) measured an activation energy, Eact, of 1.41 eV and Gouet et al (42) of 1.38 eV, but Shinozaki et al (44) found the Eact to be less than half these values at 0.57 eV. The most probable reason for these conflicting results is the difficulty in attaining equilibrium in these pyrochlore systems. $Gd_2Zr_2O_7$ and $Sm_2Zr_2O_7$ undergo fluorite-pyrochlore phase transitions at ∿ 1550°C and 2350°C respectively (48). Thus, different preparative procedures and cooling rates could be responsible for the differing results of the various experiments.

Infra-red (52) and Raman spectroscopy (53) have shown that not all the $Ln_2Zr_2O_7$ pyrochlores are totally ordered and though both $Sm_2Zr_2O_7$ and $Gd_2Zr_2O_7$ show the X-ray super-structure lines of a pyrochlore, their spectra indicate a good deal of disorder, on both the cation and the anion sublattices. The infra-red spectra (52) show clearly that structural disorder increases as the lanthanide ion becomes closer to Zr^{4+} in size, thus the structure of $La_2Zr_2O_7$ is the most ordered and $Gd_2Zr_2O_7$ the least. Comparison of this data with the Raman spectra (53), which are sensitive only to the oxygen sublattice, shows that the oxygens in

$La_2Zr_2O_7$ are the most ordered and those in $Gd_2Zr_2O_7$ the least. This indicates that in the pyrochlore structure the behaviour of the cation sublattice is closely imitated by that of the oxygen.

Van Dijk et al (47) have made a very detailed study of the conductivity of the $Gd_2Zr_2O_7$ and $Nd_2Zr_2O_7$ pyrochlores and their solid solutions. For both stoichiometric compositions they found a minimum in the activation energy (Eact) and pre-exponential (σ_0) vs. composition curves. Those obtained for $Gd_2Zr_2O_7$ are illustrated in Figures 9 and 10 . For $Nd_2Zr_2O_7$ σ_0 is about three orders of magnitude lower than for $Gd_2Zr_2O_7$ and this causes a local minimum in the conductivity. For $Gd_2Zr_2O_7$ a local maximum is seen. Neutron diffraction studies (46), on $Nd_2Zr_2O_7$, showed that Frenkel disorder on the oxygen sublattice was always less than 5%, even at 600°C, and this accounts for the low value of σ_0 and also agrees with the Raman data (53) which showed greater oxygen disorder for $Gd_2Zr_2O_7$. Greater oxygen disorder creates more charge carriers and thus increases σ_0. In both systems Eact and σ_0 increase dramatically for the hyper- and hypostoichiometry compositions, consequently the conductivity decreases (47). No breaks in the Eact, σ_0 and conductivity curves are observed at the transition from pyrochlore to fluorite solid solution indicating the coherent intergrowth of the two phases (47). The influence of long-range order on Eact and σ_0, and so on the conductivity, was illustrated by Van Dijk et al (47). They took an annealed single crystal of $Gd_{0.52}Zr_{0.48}O_{1.74}$, which showed pyrochlore X-ray reflections, and a quenched crystal of the same composition which showed only the fluorite reflections. The quenched crystal had a higher σ_0, and also a higher Eact, than did the annealed crystal. Overall, the annealed pyrochlore sample was the better conductor. The higher value of σ_0 for the fluorite is due to the increased number of charge carriers brought about by greater disorder on the oxygen sublattice. Burggraaf et al (49) explain the lower activation energy for the pyrochlore as follows. They propose that, as a direct result of the ordered cation sublattice, there exist preferential diffusion paths in the pyrochlore structure. They maintain that the dominant term in the Eact is the strain energy involved in the passage of an oxygen ion through the sides of a cation tetrahedron. The lengths of these sides are determined by the occupation of the tetrahedron corners. In the pyrochlore it is possible for an oxygen to choose a path which takes it through many of the large tetrahedron sides that are formed by two Zr^{4+} and one Ln^{3+}. No such path way can exist in the fluorite because of the random arrangement of cations.

The studies of conductivity in the pyrochlores have shown that cation order reduces the activation energy, Eact, and that oxygen order, by reducing the concentration of charge carriers, lowers the pre-exponental σ_o, relative to a fluorite of the same stoichiometry. Order on the oxygen sublattice appears to be determined by the degree of order on the cation sublattice. Thus, a large difference in cation size will give a small Eact but also a small σ_o; a small difference in size will give a higher σ_o, but also a higher Eact. The Eact does not appear to change dramatically as the degree of cation order decreases. For $Nd_2Zr_2O_7$ it is 0.77 eV and for $Gd_2Zr_2O_7$ it is 0.87 eV (49). The difference in σ_o, on the other hand is quite large. For $Nd_2Zr_2O_7$ σ_o is $\sim 2 \times 10^4\ \Omega^{-1}m^{-1}K$ and for $Gd_2Zr_2O_7$ it is $\sim 1\times10^7\ \Omega^{-1}\ m^{-1}K$.

These two competing factors would seem to preclude the development of useful oxygen-ion conductors in these systems as, ideally, full cation order and anion disorder would be required.

Bi_2O_3 BASED MATERIALS

The high temperature, δ-phase of Bi_2O_3 is the best oxygen-ion conductor known. Unfortunately it is only thermodynamically stable between the melting point (824°C) and 729°C. Within this range it has a conductivity of the order of 1 $\Omega^{-1}cm^{-1}$ (54). On cooling, large thermal hysteresis occurs and the δ-phase transforms either, at 650°C, to the tetragonal β-phase,or, at 639°C, to the b.c.c. γ-phase (55). Figure 11 shows the conductivities of all the Bi_2O_3 polymorphs, including the low-temperature, monoclinic α-phase. Conduction in this phase is predominantly electronic, but in the other three it has been shown to be mainly ionic (54).

δ-Bi_2O_3 has a defect fluorite structure with 25% of all oxygen sites vacant. Thus, were the oxygen sublattice completely ordered, each unit cell would contain two vacancies. Neutron diffraction data, obtained by Harwig (56) give no obvious indication of long range order on the oxygen sublattice. Harwig (56) has also noted that the entropy gain due to the α → δ transition is 75% of the total entropy gained in going from the α-phase to the liquid state. This indicates a very large degree of disorder in the δ-phase and supports the neutron diffraction data. Harwig (56) has shown that the neutron diffraction results agree very well with a calculation based on a Willis type model in which there is an average occupancy of all the oxygen sites and the oxygen ions are displaced towards the faces of the bismuth tetrahedra. Any proposed model for the structure of δ-Bi_2O_3 should include an explanation of why the oxygen vacancies, which are formally uncharged, can give rise to charge transport. Details of calculated structures which overcome this difficulty are given below.

Electrostatic energy calculations using the Ewald method (57) and more sophisticated calculations using HADES computer simulations (58) agree on the following two points. Firstly, the vacancies are most likely to be paired along the face diagonal of the cube defining the oxygen sublattice (see Figure 1). Colbourn and Mackrodt (58) have shown that this gives rise to small distortions, of the ideal unit cell, along the direction perpendicular to that face, while the other directions remain unaffected. Secondly, both sets of calculations predict short-range order, on the oxygen sublattice, giving rise to small domains in which the structure is completely regular. These domains can orient in a random manner giving rise to what looks, on a macroscopic scale, to be a cubic structure with a completely disordered oxygen sublattice.

The fourier map, shown in Figure 12 was produced from neutron scattering data collected by Catlow, Drennan and Kilner (59). It shows a pronounced anisotropic distribution of the oxygen ions about their lattice sites. Elongation of the oxygen density along the <110> direction is particularly evident. This is only a preliminary result, and further work is needed to refine this structure and compare with that calculated by lattice simulations.

The calculated structure of an ordered domain is a complex arrangement of fully-occupied and half-occupied {100} planes of oxygen. The full structure will be detailed elsewhere (60), however, a simple analysis of the structure and possible jump mechanisms would suggest that:

(a) the possibility exists for jumps to be highly correlated.

and

(b) boundaries between adjacent domains may have either an excess or a deficiency of oxygen, relative to the normal occupancy, which would render them charged. Charge transport could then take place by domain wall movement as has been proposed by Van Gool (61) for β-Al_2O_3.

De Wit et al (62) measured the heat of transport, Q^*, for δ -Bi_2O_3 and showed that it is not equal to the activation energy, Eact, for conduction (0.13 eV vs 0.30 eV). Gillan (63) has noted, for vacancy migration in ionic crystals the two values are generally equal. They will only be so, however, if Eact is simply the migration enthalpy, ΔH_m. Obviously this should be the case here since δ-Bi_2O_3 is a stoichiometric material; consequently there are no dopant vacancy association terms to be considered. Thus the difference between Eact and Q^* is due to some other mechanism, possibly a "cooperative migration" term, brought about by the movement of domain boundaries (61).

Though the structure and electrical behaviour of δ-Bi_2O_3 are not yet fully understood, the picture is becoming clearer. The proposed mechanism is as follows. Oxygen ions move through the lattice due to the need to neutralise localised areas of charge at the domain boundaries. It seems probable that the high conductivity is the result of cooperative movement of these domain walls rather than isolated vacancy transport.

In attempts to stabilise δ-Bi_2O_3 down to ambient temperatures, thus maintaining its high conductivity, many different dopants have been added and some related stoichiometric materials studied. Discussions of these will be divided into the following sections.

(i) The addition of divalent dopants, e.g. Ba^{2+}

(ii) The addition of trivalent dopants, e.g. Er^{3+}

(iii) The addition of dopants with valencies greater than three.

(iv) The study of related stoichiometric compounds.

The conductivities of the best materials, from these groups, are shown in Figure 13.

(i) The addition of divalent dopants

The addition of Ca^{2+}, Sr^{2+} and Ba^{2+} has been studied by Takahashi and co-workers (64,65) and by Boivin and co-workers (66-72). The conductivity for the best material of this group, $(Bi_2O_3)_{.8}(BaO)_{.2}$ (64) is shown in Figure 13 as line 4. It exhibits a noticeable conductivity jump at ∿ 550°C. This feature is common to all those divalently doped Bi_2O_3 materials having a rhombohedral structure. Above a certain concentration (for BaO it is about 25 mole %), the structure becomes f.c.c.. This change is accompanied by a change in conductivity from ionic to electronic.

Boivin and Thomas (72) have made an extensive study of the structural changes that accompany the conductivity jump. The materials are made up of blocks, the size of which depends on the dopant cations. Some of the oxygens are found in the interblock spaces and it is these that are the mobile, charge carrying, ions. Boivin and Thomas (72) showed this by measurements, parallel and perpendicular to the blocks, on a single crystal of Bi_2O_3-SrO. There is a difference of about two orders of magnitude in the conductivities. Measurements on poly-crystalline materials show conductivities about midway between the two orientations. Above the jump temperature, the structure remains rhombohedral, but Conflant et al (67) have shown that, for Bi_2O_3-CaO systems, the size of the lattice increases. This corresponds to a rearrangement of the oxygen sublattice and indicates a thermally-activated increase in the concentration of oxygen ions in the interblock space, i.e. an increase in the number of charge carriers. Finally, this second rhombohedral phase transforms into an f.c.c., δ-Bi_2O_3 related structure, the conductivity of which has not been measured.

(ii) The addition of trivalent dopants

Addition of the rare earths to Bi_2O_3 has been studied extensively (49,73-77). Cahan et al (73) have shown that for 25 mole % dopant, only the smaller ions, Tb^{3+} to Lu^{3+}, will stabilize the f.c.c. phase down to room temperature. Larger quantities of Gd^{3+} (> 35 mole %) will also stabilize this phase (74). Verkerk and Burggraaf (76) have demonstrated the difficulty of achieving an equilibrium structure in these systems. $(Bi_2O_3)_{.8}$ $(Dy_2O_3)_{.2}$, quenched from high temperature, has an f.c.c. structure. If it is cooled at ½°C per minute, it becomes diphasic with a rhombohedral component present in comparable amounts to the f.c.c. phase. Annealing for 350 hours, at 700°C, increases the amount of rhombohedral phase, thereby decreasing the amount of f.c.c. phase. Consequently, for many Bi_2O_3-Ln_2O_3 materials, changes in conductivity, with time, are expected as a result of ordering.

Line 6 in Figure 13 shows the conductivity of $(Bi_2O_3)_{.8}$ $(Er_2O_3)_{.2}$ (77), which has the best low-temperature conductivity of all the Bi_2O_3-based materials studied. Verkerk et al (77) have made a detailed study of it and of other compositions in the Bi_2O_3-Er_2O_3 system, and have thoroughly investigated the changes in structure that cause the changes in conductivity. Between 15 and 17.5 mole% Er_2O_3 the conductivity vs. $^1/_T$ plots show a jump in conductivity together with a hysteresis loop. Thermal expansion and high-temperature Guinier measurements suggest that, at ∿ 460°C, the f.c.c. phase undergoes a tetragonal distortion. This distortion increases with temperature until, at ∿ 610°C the structure transforms into another f.c.c. phase with a larger lattice constant than the low-temperature phase. The tetragonal distortion may be related to the metastable β-phase of pure Bi_2O_3, which has a tetragonally distorted f.c.c. structure (55). For concentrations of 20 mole% Er_2O_3, or more, there is no conductivity jump, but for 20 and 25 mole% there is a "knee" in the conductivity vs. $^1/_T$ plot at ∿ 600°C. This is caused by a large decrease in the activation energy, Eact. The same phenomenon has been observed in Bi_2O_3-Dy_2O_3 (76), Bi_2O_3-Y_2O_3 (75) and Bi_2O_3-Gd_2O_3 (74). High-temperature Guinier measurements show that it corresponds to a change from the small lattice constant f.c.c. phase to the one with a larger lattice constant. For $(Bi_2O_3)_{.8}\,(Er_2O_3)_{.2}$ this increase in size is 1.5%, but in other compositions it is smaller than this and cannot be measured quantitatively. Burggraaf et al (49) have shown, by neutron diffraction measurements, that microdomains, in which both the cations and the oxygen ions are ordered, exist at low temperatures, (below the knee or jump temperature). In these microdomains the oxygens are displaced towards the small Er^{3+} ions, thus causing strain fields through which vacancies can only pass with difficulty. At higher temperatures (above the knee or jump temperature) the lattice relaxes and expands. As with Bi_2O_3-SrO (72), this expansion is probably accompanied by a thermally-activated disordering of the oxygen sublattice and dissipation of the strain fields. It seems feasible that this high-temperature disordered structure is the true δ-Bi_2O_3 related structure.

For concentrations greater than 30 mole% Er_2O_3, a single straight line is observed in the conductivity vs. $^1/_T$ plots and these compositions are worse conductors than $(Bi_2O_3)_{.75}(Er_2O_3)_{.25}$. Above 40 mole% the conductivity becomes electronic. These last two phenomena are also observed in other systems, but the limiting concentrations of dopant differ.

(iii) The addition of dopants with valency greater than three.

Esaka et al (78) have studied the ionic conductivity of Bi_2O_3-$Pr_2O_{11/3}$, over a wide range of composition. $Pr_2O_{11/3}$ is a mixed valence compound with the valency of Pr alternating between 3+ and 4+. Below ∿ 40 mole%

$Pr_2O_{11/3}$ this instability appears to have little effect on the electrical conductivity of the materials. The concentration of oxygen remains true to the stoichiometry dictated by $Pr_2O_{11/3}$ and the conductivity is predominantly ionic. Line 5 in Figure 13 shows the conductivity of $(Bi_2O_3)_{.9}\ (Pr_2O_{11/3})_{.1}$. At ∿ 600°C there is a jump in conductivity. On cooling hysteresis is observed. Materials in the range 10 to 35 mole % have the rhombohedral structure of Bi_2O_3 - SrO (72). X-ray diffraction and differential thermal analysis indicate that the conductivity jump is due to a phase change from the rhombohedral structure to an f.c.c. structure. The second, high temperature, larger latticed rhombohedral structure of Bi_2O_3-SrO (72) was not observed. Above ∿ 40 mole% $Pr_2O_{11/3}$, the conductivity becomes partially, and then fully electronic, due to the change in valency of the Pr^{4+} to Pr^{3+}.

Addition of pentavalent dopants to Bi_2O_3 reduces the concentration of oxygen vacancies in the f.c.c. phase. Materials of this type have been studied by Takahashi et al (79), who doped Bi_2O_3 with V^{5+}, Nb^{5+} and Ta^{5+}. In the Bi_2O_3-V_2O_5 system no single-phase f.c.c. region could be found, but in Bi_2O_3-Nb_2O_5 and Bi_2O_3-Ta_2O_5 single-phase f.c.c. regions extended from 15 to 25 mole% and from 18 to 25 mole%, respectively. Line 7 in Figure 13 shows the conductivity of $(Bi_2O_3)_{.95}\ (Nb_2O_5)_{.15}$. For both systems, conductivity in the f.c.c. region is ionic. As is common for many oxygen-ion conductors, the conductivity was found to decrease with increasing dopant concentrations. This may be due to the formation of increased numbers of ordered microdomains, as in the Bi_2O_3-Er_2O_3 system, in which the oxygens are displaced towards the small pentavalent ions, causing extensive strain fields through which the vacancies find it difficult to pass.

Another system, in which addition of the dopant decreases the concentration of oxygen vacancies, is Bi_2O_3-WO_3 (80). Line 8, in Figure 13, represents the conductivity of $(Bi_2O_3)_{.78}(WO_3)_{.22}$ which lies at the lower end of the single phase f.c.c. region. There is a "knee" in the plot where the activation energy, Eact, increases at high temperature. The reason for this increase is not clear. Conductivity in the f.c.c. region (22 to 28 mole% WO_3) is ionic, as it is in the diphasic region between 14.3 and 22 mole% WO_3. In this latter region a conductivity jump is observed corresponding to a phase transition to a single phase f.c.c. lattice.

(iv) The study of related compounds

Kilner et al (81) have studied two compounds, $Bi_{12}SiO_{20}$ and $Bi_{12}PbO_{19}$. Both have the sillenite structure which is related to the b.c.c. γ-phase of pure Bi_2O_3, with the second cation (Si^{4+} or Pb^{2+}) being in tetrahedral coordination. $Bi_{12}SiO_{20}$ exhibits electronic conductivity which is attributed to the fact that there should be no ionic charge carriers due to the completely occupied oxygen sublattice. This sublattice does not disorder, even at high temperatures, and this is probably due to the strong preference of Si^{4+} for tetrahedral coordination. $Bi_{12}PbO_{19}$ and δ-Bi_2O_3, on the other hand, are oxygen deficient and show oxygen-ion conductivity at low temperatures. At higher temperatures Bi^{3+} and Pb^{2+} are too large to remain in tetrahedral coordination. Thus, at $\sim$ 730°C, $Bi_{12}PbO_{19}$ undergoes a phase transition from the b.c.c. structure to an f.c.c., δ-Bi_2O_3 related, structure. A jump corresponding to this transition is observed in the conductivity vs. $^1/_T$ plot. On cooling, from the f.c.c. phase, hysteresis is observed. In total, the electrical behaviour of $Bi_{12}PbO_{19}$ closely resembles the transition from the γ - to the δ-phase, found in pure Bi_2O_3.

Demonchy et al (82) have examined the electrical behaviour of $Bi_{1-x}Pb_xO_{1.5-x/2}$ with $x = 0.384$. This material exists as three polymorphs; the low temperature, tetragonal, β_2-phase, the cubic $Bi_8Pb_5O_{17}$ phase, and the high temperature, f.c.c. β-phase. The transition from the β_2 to the $Bi_8Pb_5O_{17}$ phase involves rearrangement of the cation sublattice and is accompanied by a decrease in conductivity. The transition from $Bi_8Pb_5O_{17}$ to the β-phase, however, is accompanied by a rise in conductivity of about three orders of magnitude. Hysteresis is observed on cooling. The conductivity of the β-phase is shown as line 2 in Figure 13 .It is the best known conductor between 560°C and 640°C, but like pure δ-Bi_2O_3 it is unstable and the conductivities of the polymorphs to which it transforms, are too low for device applications.

Summary

The simple conduction mechanisms, postulated for the lightly doped fluorites are not valid for δ-Bi_2O_3 because of the high concentration of vacancies. It is thought that the fast ionic conductivity of δ-Bi_2O_3 may be due to a domain-type structure giving rise to the "cooperative migration" of domain boundaries. Addition of dopants, such as the rare earths, leads to the formation of a low-temperature f.c.c. structure. It has a higher ionic conductivity than the low-temperature polymorphs of Bi_2O_3, but a much lower conductivity than δ-Bi_2O_3 and this is probably due to the strain fields which seem to be introduced into the lattice by the incorporation of small dopant ions.

At high temperatures the lattice expands and the conductivity increases. This expansion is probably accompanied by a large reduction in strain effects and possibly signals the formation of the true δ-Bi_2O_3 related structure. Addition of other dopants, notably the alkaline earth metals, leads to the formation of a, highly conductive, layer-type rhombohedral structure, in which the oxygen ions diffuse through the interlayer spaces.

Further study of these, and other, layer-type structures may lead to the discovery of new oxygen-ion conductors.

CONCLUSIONS

The analysis of the electrical conductivity in the fluorite and fluorite-related oxides has revealed a wide range of defect behaviour. Simple defect pairs are applicable to the dilute solid solutions prior to the maximum in conductivity, however, at more concentrated solutions this treatment is no longer valid and higher order clusters must be invoked. Lattice simulations have played an important role in the development of these ideas. For example, the elucidation of ion-size effects would have been much more difficult without this technique.

There are still many questions to be answered. It is by no means clear what mechanisms are dominant in the highly concentrated regime. Microdomains are certainly seen by experimenters using electron diffraction. Experimenters using different techniques propose other models of disorder. More work is required on many more systems before these problems can be solved, particularly as to the importance of relative charge and size in this regime.

Finally the nature of the disorder in the high temperature form of Bi_2O_3 is now becoming clearer, again due to the role of lattice simulations. It would seem that a domain explanation of the ionic transport in this material could overcome the problem that the vacancies are formally uncharged. The conductivity of this material is very high, close to the limit set by O'Keefe (83), for processes taking place by a hopping mechanism and may represent the upper limit of anion conductivity in these fluorite-structure oxides.

REFERENCES

1. M. Kleitz, H. Bernard, E. Fernandez and E. Schouler *Advances in Ceramics*, 3, 310, 1981.

2. J. Kilner and B.C.H. Steele in "*Nonstoichiometric Oxides*" (ed. O.T. Sorensen) Academic Press, New York, 1981.

3. A.S. Nowick, *Comments on Solid State Physics,* 9, 85, 1979.

4. M.M. Abraham, R.A. Weeks, G.W. Clark and C.B. Finch *Phys Rev* 148, 350, 1966.

5. A.S. Nowick and D.S. Park in "*Superionic Conductors*" (G. Mahan and W. Roth,eds) Plenum, New York, 1976.

6. A.S. Nowick, D.Y. Wang, D.S. Park and J. Griffith, in "*Fast Ion Transport in Solids*" (P. Vashishta, J.N. Mundy and G.K. Shenoy, eds). Elsevier/North Holland, Amsterdam, 1979.

7. D.Y. Wang, D.S. Park, J. Griffiths and A.S. Nowick, *Solid State Ionics* 2, 95, 1981.

8. A. Hammou, *J Chim Phys* 72, 439, 1975.

9. E. Schouler, A. Hammou and M. Kleitz, *Mat Res Bull* 11, 1137, 1976.

10. A.I Ioffe, D.S. Rutman, and S.V. Karpachov, *Electrochimica Acta* 23, 141, 1978.

11. C.R.A. Catlow and W.C. Mackrodt, in "*Computer Simulation of Defects and Defective Solids*" (eds. C.R.A. Catlow and W.C. Mackrodt), Springer Verlag, 1982.

12. C.R.A. Catlow, R. James, W.C. Mackrodt and R.F. Stewart, *Phys Rev B* 25, 1006, 1982.

13. T. Kudo and H. Obayashi, *J Electrochem Soc* 122, 142, 1975.

14. R. Gerhart-Anderson and A.S. Nowick, *Solid State Ionics* 5, 547, 1981.

15. J.A. Kilner and R.J. Brook, *Solid State Ionics* 6, 237, 1982.

16. W.C. Mackrodt and R.F. Stewart, J Phys C 12, 5015, 1979.

17. R.A. Swalin, "Thermodynamics of Solids" Wiley and Sons, New York 1962, Ch. 4.

18. V. Butler, C.R.A. Catlow, B.E.F. Fender and J.H. Harding, Solid State Ionics, in press.

19. J.A. Kilner, J Solid State Chemistry, in press.

20. J.A. Kilner, Solid State Ionics, in press.

21. D.J.M. Bevan and E. Summerville in 'Handbook on the Physics and Chemistry of Rare Earths (K.A. Gschneider and L. Eyring, eds), Vol. 4, Elsevier/North Holland, Amsterdam, 1979,p.401.

22. W.W. Barker and O. Knop, Proc Brit Ceram Soc 19, 15, 1971.

23. M. O'Keefe in "The Chemistry of Extended Defects in Non-Metallic Solids" (L. Eyring and M. O'Keefe eds). North Holland, Amsterdam, 1970, p.609.

24. E.C. Subbarao and T.V. Ramakrishnan, in "Fast Ion Transport in Solids" (P. Vashishta, J.N. Mundy and G.K. Shenoy, eds) Elsevier/North Holland, Amsterdam 1979, p.653.

25. A. Nakamura and J.B. Wagner, J Electrochem Soc 127, 2325, 1980.

26. C.R.A. Catlow in "Computer Simulation in the Physics and Chemistry of Solids" (C.R.A. Catlow, W.C. Mackrodt and V.R. Saunders, eds). Daresbury Laboratory report no. DL/SCI/R15, 1980,p.36.

27. C.R.A. Catlow, Phys Stat Sol (a) 38, 191, 1978.

28. P. Abelard and J.F. Baumard, Phys Rev B26, 1005, 1982.

29. A. Baudry, P. Boyer and A.L. de Oliveira, Physics Letters 79A, 345, 1980.

30. H.J. Rossell, Adv in Ceramics 3, 47, 1981.

31. R.E. Carter and W.L. Roth, in "Electromotive Force Measurements in High Temperature Systems" (C.B. Alcock ed.), The Inst. of Mining & Metallurgy New York, p.125, 1968.

32. J.D. Faktor, J.A. Kilner and B.C.H. Steele, to be published in J Solid State Chem.

33. J.B. Cohen, J. Faber and M. Moringa, Adv in Ceramics 3, 37, 1981.

34. D. Steele and B.E.F. Fender, J Phys C7,1, 1974.

35. J. Faber, M.H. Mueller and B.R. Cooper, Phys Rev B17 4884, 1978.

36. J.G. Allpress, H.J. Rossell and H.G. Scott, J Solid State Chem 14, 264, 1975.

37. V. Butler, B.E.F.Fender and C.R.A. Catlow, to be published in Radiation Effects.

38. W.W. Barker, J.C. Graham, T.C. Parks and T.P. Speed, J Solid State Chem 22, 321, 1977.

39. H. Peters and K.H. Radeke, Monatsber Deut Akad Wiss Berlin 10, 53, 1968.

40. B.C.H. Steele, B.E. Powell and P.M.R. Moody, Proc Brit Ceram Soc 10, 87, 1968.

41. Z.S. Volchenkova, Inorg Mat 5, 930, 1969.

42. M. Gouet, B. Chappey and M. Guillou, C R Acad Sc Paris Ser C 280, 1117, 1975.

43. L.N. Fomina and S.F. Pal'guev, Russ J Inorg Chem 22, 177, 1977.

44. K. Shinozaki, M. Miyauchi, K. Kuroda, O. Sakurai, N. Mizutani and M. Kato, J Am Cer Soc 62, 538, 1979.

45. A.M. Gavrish, L.S. Alekseenko, L.A. Tarasova and G.P. Orekhova, Inorg Mat 18, 214, 1982.

46. T. van Dijk, R.B. Helmholdt and A.J. Burggraaf, Phys Stat Sol (b) 101, 765, 1980.

47. T. van Dijk, K.J. de Vries and A.J. Burggraaf, Phys Stat Sol (a) 58, 115, 1980.

48. T. van Dijk, Ph.D. Thesis, Twente Univ. of Tech. Holland, 1981.

49. A.J. Burggraaf, T. van Dijk and M.J. Verkerk, Solid State Ionics 5, 519, 1981.

50. K.J. de Vries, M.P. van Dijk, G.M.H. van de Velde and A.J. Burggraaf, To be published in J Solid State Chem.

51. K. Uematsu, K. Shinozaki, O. Sakurai, N. Mizutani and M. Kato, J Am Cer Soc 62, 219, 1979.

52. W.E. Klee and G. Weitz, J Inorg Nucl Chem 31, 2367, 1969.

53. B.E. Scheetz and W.B. White, J Am Cer Soc 62, 468, 1979.

54. H.A. Harwig and A.G. Gerards, J Solid State Chem 26, 265, 1978.

55. H.A. Harwig, and A.G. Gerards, Thermochimica Acta 28, 121, 1979.

56. H.A. Harwig, Z Anorg Allg Chem 444, 151, 1978.

57. H.A. Harwig and J.W. Weenk, Z Anorg Allg Chem 444, 167, 1978.

58. E.A. Colbourn and W.C. Mackrodt, To be published.

59. C.R.A. Catlow, J. Drennan and J.A. Kilner, to be published.

60. J.A. Kilner and J.D. Faktor, to be published.

61. W. van Gool, J Solid State Chem 7, 55, 1973.

62. J.H.W. De Wit, T. Honders and G.H.J. Broers, in "Fast Ion Transport in Solids" (P. Vashishta, J.N. Mundy and G.K. Shenoy, eds) Elsevier/North Holland, Amsterdam, 1979.

63. M.J. Gillan in "Computer Simulation in the Physics and Chemistry of Solids" (C.R.A. Catlow, W.C. Mackrodt and V.R. Saunders, eds). Daresbury Laboratory report no. DL/SCI/R15, 1980, p.65.

64. T. Takahashi, T. Esaka and H. Iwahara, J Solid State Chem 16, 317, 1976.

65. T. Takahashi and H Iwahara, Mat Res Bull 13, 1447, 1978.

66. P. Conflant, J.C. Boivin and G. Tridot, C R Acad Sc Paris, Ser. C 279, 457, 1974.

67. P. Conflant, J.C. Boivin and D. Thomas, *J Solid State Chem* 18, 133, 1976.

68. P. Conflant and J.C. Boivin, *C R Acad Sc Paris, Ser. C* 288, 161, 1979.

69. P. Demonchy, P. Conflant, J.C. Boivin and D. Thomas *C R Acad Sc Paris, Ser. C* 289, 317, 1979

70. P. Conflant, J.C. Boivin and D. Thomas, *J Solid State Chem* 35, 192, 1980.

71. J.C. Boivin and D.J. Thomas, *Solid State Ionics* 3/4, 457, 1981.

72. J.C. Boivin and D.J. Thomas, *Solid State Ionics* 5, 523, 1981.

73. M.T. Cahan, T.G.M. Van Den Belt, J.H.W De Wit and G.H.J. Broers, *Solid State Ionics* 1, 411, 1980.

74. T. Takahashi, T. Esaka and H. Iwahara, *J Appl Electrochem* 5, 197, 1975.

75. T. Takahashi, H. Iwahara and T. Arao, *J Appl Electrochem* 5, 187, 1975.

76. M.J. Verkerk and A.J. Burggraaf, *J Electrochem Soc* 128, 75, 1981.

77. M.J. Verkerk, K. Keizer and A.J. Burggraaf, *J Appl Electrochem* 10, 81, 1980.

78. T. Esaka, H. Iwahara and H. Kunieda, *J Appl Electrochem* 12, 235, 1982.

79. T. Takahashi, H. Iwahara, and T. Esaka, *J Electrochem Soc* 124, 1563, 1977.

80. T. Takahashi and H. Iwahara, *J Appl Electrochem* 3, 65, 1973.

81. J.A. Kilner, J. Drennan, P. Dennis and B.C.H. Steele, *Solid State Ionics* 5, 527, 1981.

82. P. Demonchy, J.C. Boivin and D. Thomas, *C R Acad Sc Paris, Ser. C* 290, 279, 1980.

83. M.O'Keefe in "*Fast Ion Transport in Solids: Solid State Batteries and Devices*" (W. Van Gool, ed) Elsevier/North Holland, 1973, p.232.

TABLE 1

	Pre-exponential Factor	Activation energy
Divalent Dopants	proportional to $C_{M2}^{\frac{1}{2}}$	$\Delta H_m + \frac{\Delta H_{A2}}{2}$
Trivalent dopants	Independent of dopant concentration.	$\Delta H_m + \Delta H_{A1}$

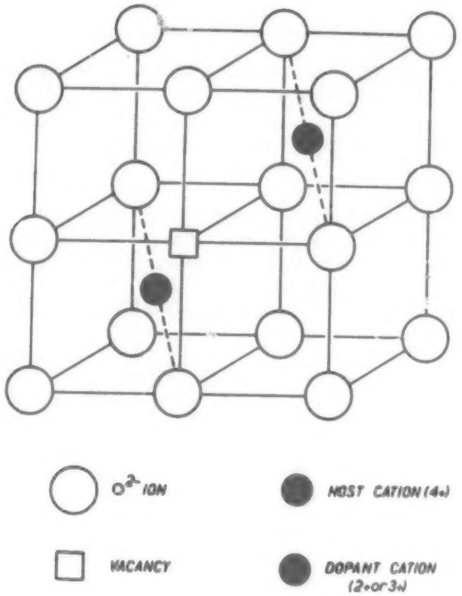
O^{2-} ION
HOST CATION (4+)
VACANCY
DOPANT CATION (2+ or 3+)

Fig. 1 - The ideal fluorite lattice showing half a unit cell including a dopant cation and a charge-compensating oxygen vacancy.

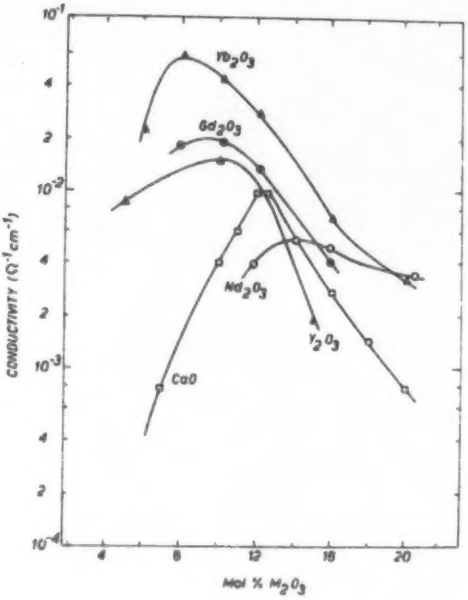

Fig. 2 - A plot of the isothermal conductivity vs. concentration for various zirconia-based ion conductors, showing the maximum in the conductivity.

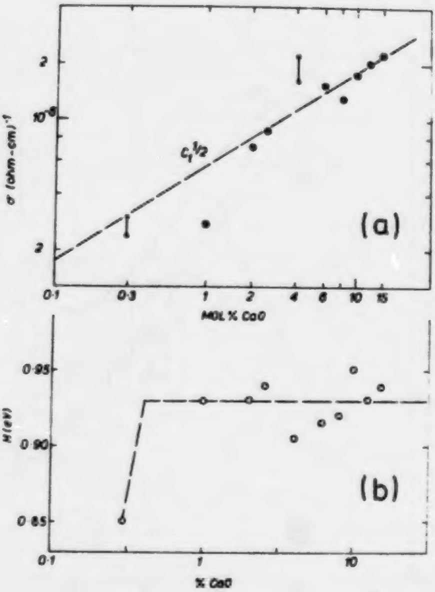

Fig. 3 - The concentration dependence of (a) the isothermal conductivity and (T = 500K) and (b) the activation energy for CaO doped CeO_2 solid solutions. From Reference (6).

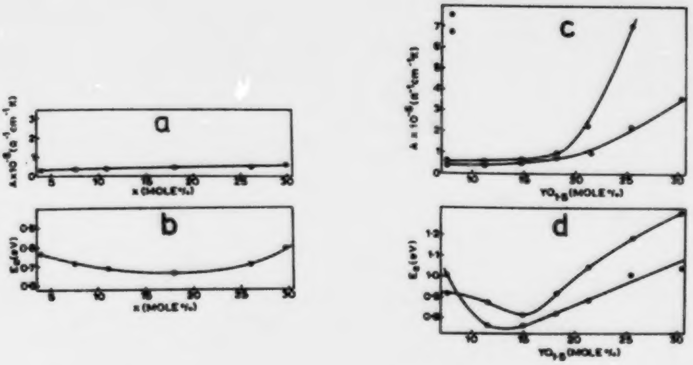

Fig. 4 - Compositional dependence of the pre-exponential and activation energy for $(CeO_2)_{1-x}$ $(YO_{1.5})_x$ ((a) and (b)) and $(ZrO_2)_{1-p}$ $(CeO_2)_{p-x}$ $(Y_2O_3)_x$ ((c) and (d)). Open circles P = 0.3; solid circles P = 0.75 (from Ref (8)).

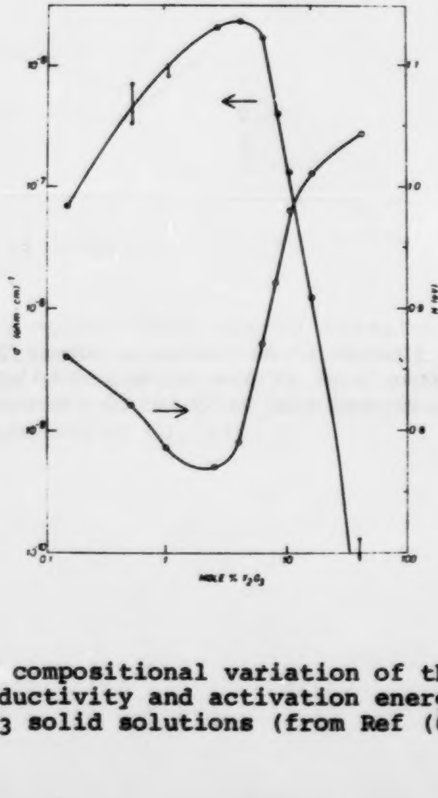

Fig. 5 - The compositional variation of the isothermal conductivity and activation energy for CeO_2-Y_2O_3 solid solutions (from Ref (6)).

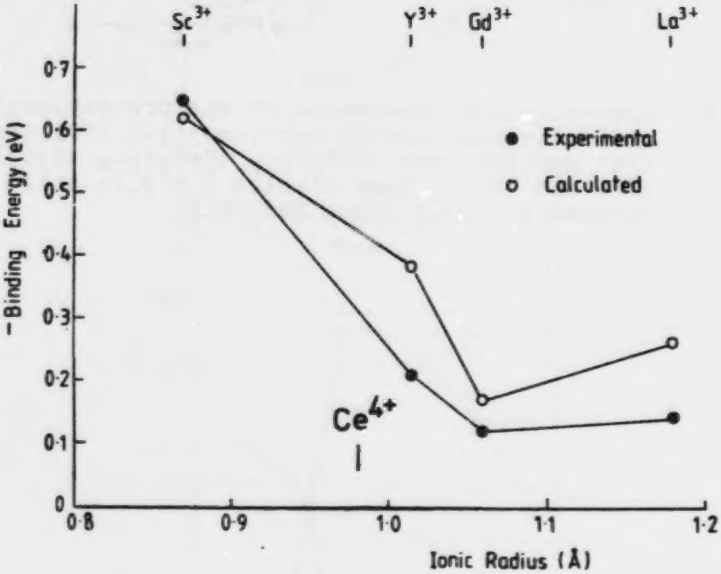

Fig. 6 - **The variation of the association enthalpy with ionic radius in trivalenty doped CeO_2. What is shown here is the experimental results from Ref (14) and the calculated results from Ref (18).**

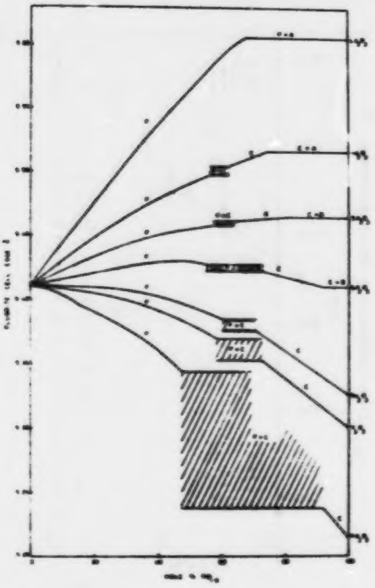

Fig. 7a - Lattice parameter vs. composition plots for the systems CeO_2-M_2O_3 from reference (21). Reproduced by kind permission of North Holland Publishing Co. Ltd.

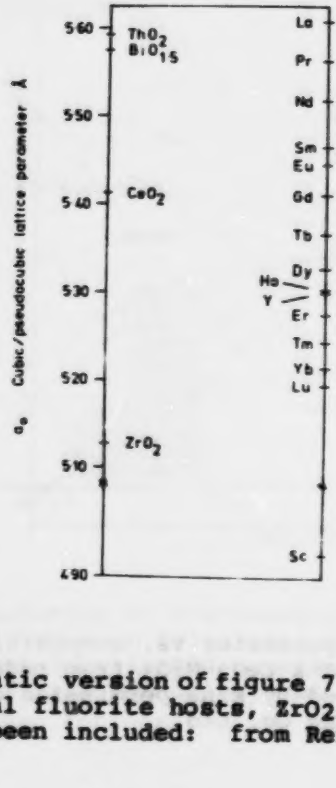

Fig. 7b - Schematic version of figure 7(a). The other typical fluorite hosts, ZrO_2, ThO_2 and $BiO_{1.5}$, have been included: from Ref (20).

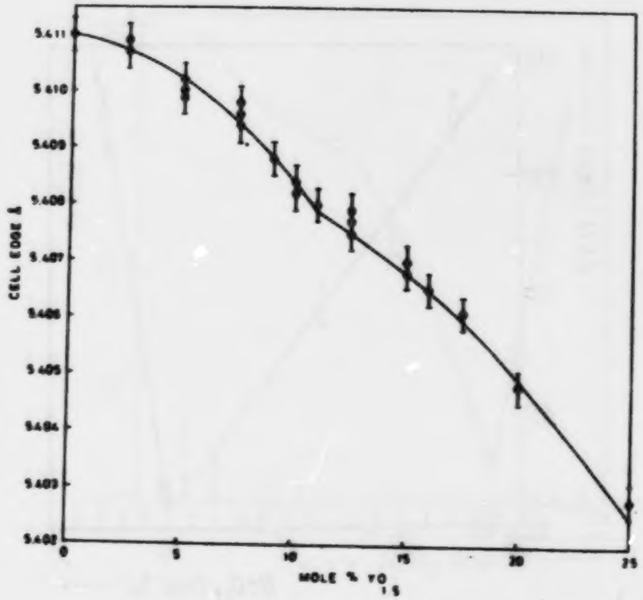

Fig. 8 - Lattice parameter vs. composition plot for the system CeO_2-Y_2O_3 from reference (21). Reproduced by kind permission of North Holland Pub Publishing Co. Ltd.

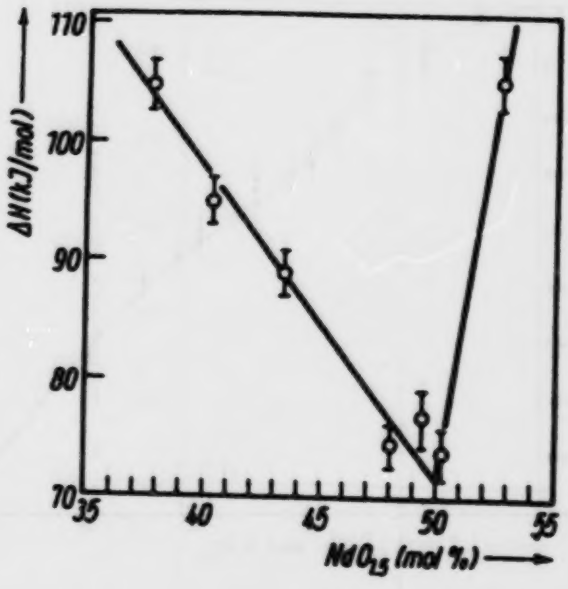

Fig. 9 - The activation energy for ionic conductivity as a function of composition in the ZrO_2-$GdO_{1.5}$ system. From reference (47). Reproduced by kind permission of Academic Press.

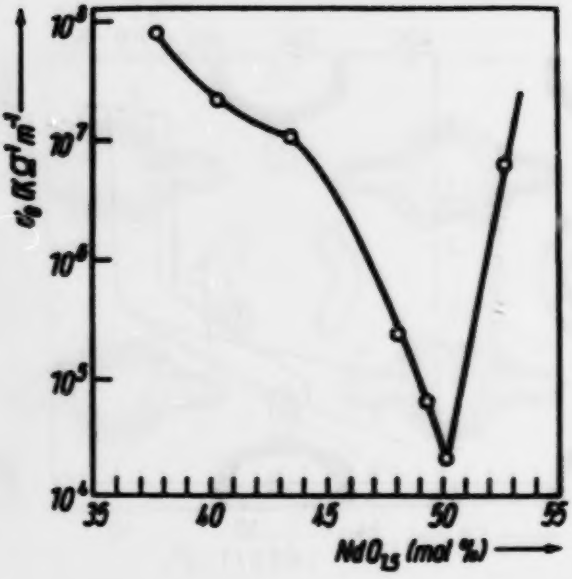

Fig. 10 - The pre-exponential factor for ionic conductivity as a function of composition in the ZrO_2-$GdO_{1.5}$ system. From reference (47). Reproduced by kind permission of Academic Press.

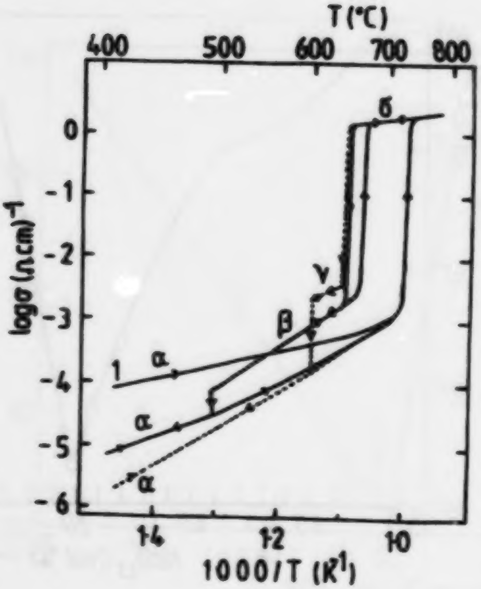

Fig. 11 - Plot of the conductivities of the four Bi_2O_3 polymorphs. The position marked "1" indicates the starting point of the measurements.

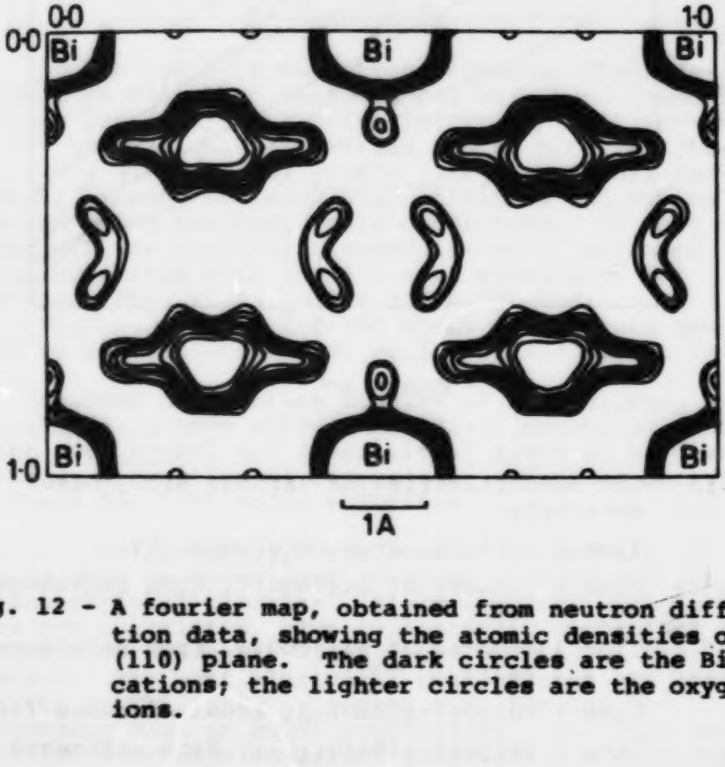
0·0
1·0
0·0
1·0
Bi
Bi
Bi
Bi
Bi
Bi
1A

Fig. 12 - A fourier map, obtained from neutron diffraction data, showing the atomic densities on a (110) plane. The dark circles are the Bi3- cations; the lighter circles are the oxygen ions.

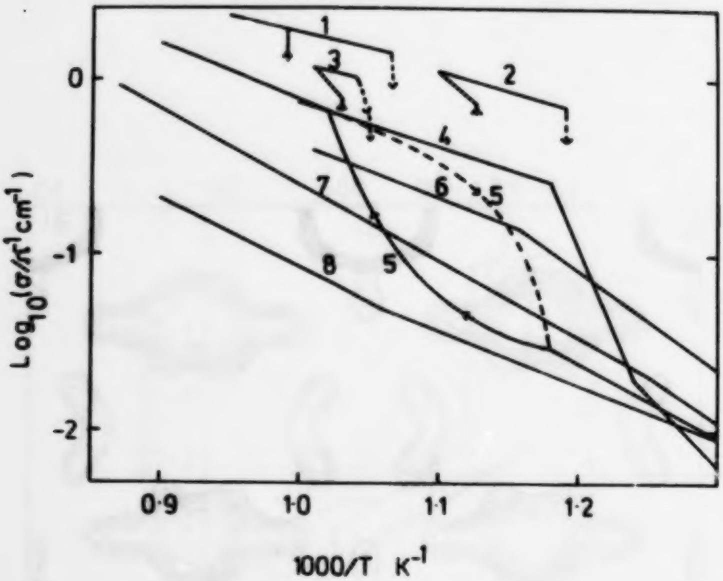

Fig. 13 - The conductivities of various Bi_2O_3 based materials.

line 1 δ-Bi_2O_3. From reference (54).

line 2 β-phase of $Bi_8Pb_5O_{17}$. From reference (82).

line 3 δ-phase of $Bi_{12}PbO_{19}$. From reference (81).

line 4 $(Bi_2O_3)_{\cdot 8}(BaO)_{\cdot 2}$. From reference (64).

line 5 $(Bi_2O_3)_{\cdot 9}(Pr_6O_{11})_{\cdot 1}$. From reference (78).

line 6 $(Bi_2O_3)_{\cdot 8}(Er_2O_3)_{\cdot 2}$. From reference (77).

line 7 $(Bi_2O_3)_{\cdot 95}(Nb_2O_5)_{\cdot 15}$. From reference (79).

line 8 $(Bi_2O_3)_{\cdot 78}(WO_3)_{\cdot 22}$. From reference (80).

DETERMINATION OF F^- PATHWAY BY NEUTRON DIFFRACTION TECHNIQUE IN FLUORITE TYPE FLUORIDES :MF_{2+n}

J.M. REAU, S.F. MATAR and J.L. SOUBEYROUX

Laboratoire de Chimie du Solide du C.N.R.S.
Université de BORDEAUX I - 351 cours de la
Libération, 33405 TALENCE Cédex, France.

ABSTRACT

On the basis of selection criteria, fluoride-ion conductors with high performances have been found in systems based on β-PbF_2 with Sn(II), M'(III) (M'=Sb,Bi), M"(IV) (M" = Zr,Th,U) fluorides and AF-BiF_3 (A=K,Rb,Tl). $Pb_{0.75}M'_{0.25}F_{2.25}$, $Pb_{0.875}M"_{0.125}F_{2.25}$, $PbSnF_4$ and β-$ABiF_4$ possess enhanced conductivities and may be considered among the best ionic conductors. In fact these materials are particular compositions of extended solid solutions with the fluorite structure, for instance, $Pb_{1-x}Bi_xF_{2+x}$ ($0 \leq x \leq 0.50$) and $Pb_{1-x}Th_xF_{2+2x}$ ($0 \leq x \leq 0.25$) where defects are generated by the replacement of Pb(II) by Bi(III) or Th(IV).

Neutron diffraction studies of $Pb_{1-x}Bi_xF_{2+x}$ and $Pb_{1-x}Th_xF_{2+2x}$ have allowed the distribution of fluorine atoms over normal and interstitial sites to be determined as a function of composition. Similar behaviour is found for both solid solutions.

For $Pb_{1-x}Th_xF_{2+2x}$, the conduction pathway of mobile ions is visualized to occur through the presence of interstitial fluorine. Electrical and structural data are correlated. Two conductivity mechanisms are proposed according to whether the pathway is free or blocked. The best electrical performances are obtained for $Pb_{0.875}Th_{0.125}F_{2.25}$ composition for the two mechanisms have an equal probability. For this composition a maximum number of vacancies are developed.

A solid solution of the fluorite structure $Rb_{1-x}Bi_xF_{1+2x}$ ($0.50 \leq x \leq 0.60$) and a single phase $RbBi_3F_{10}$ have been isolated in the $RbBiF_4$-BiF_3 system. While the solid solution is crystallographically disordered, $RbBi_3F_{10}$ is characterized by a 1:3 order between Rb and Bi and repetition in the lattice of $(RbBi_3F_8)^{2+}$ and $(RbBi_3F_{12})^{2-}$ units.

The distribution of F^- over normal and interstitial sites as a function of composition has been also determined by neutron diffraction techniques for $Rb_{1-x}Bi_xF_{1+2x}$. The main result is the increase with x of the number of interstitials and the decrease of that of normal F^-. By extrapolation, we obtain for $x = 0.75$ ($RbBi_3F_{10}$), $n_{F'II} = 1.50$ and $n_{FI} = 1.0$ which is in good agreement with the structure of that phase. A substitution mechanism is proposed. The decrease of conductivity could thus be explained by the progressive clustering of F^- around Bi^{3+} to form antiprisms (BiF_8) and the trapping of vacancies in the $(RbBi_3F_{12})^{2-}$ units.

KEYWORDS: Neutron diffraction, fluorite structures, fluoride-ion conductors

RÉSUMÉ

Sur la base de critères de sélection, des conducteurs de l'ion fluor de hautes performances ont été mis en évidence dans les systèmes comportant $PbF_2\beta$ et les fluorures SnF_2, $M'F_3$ (M' = Sb, Bi), $M''F_4$ (M" = Zr, Th, U) et dans les systèmes $AF-BiF_3$ (A = K, Rb, Tl): $Pb_{0,75}M'_{0,25}F_{2,25}$, $Pb_{0,875}M''_{0,125}F_{2,25}$, $PbSnF_4$ et $ABiF_4\beta$ possèdent des conductivités élevées et se placent parmi les meilleurs conducteurs ioniques. En fait ces matériaux sont des compositions particulières de solutions solides étendues de structure type fluorine : il en est ansi de $Pb_{1-x}Bi_xF_{2+2x}$ ($0 \leqslant x \leqslant 0,50$) et de $Pb_{1-x}Th_xF_{2+2x}$ ($0 \leqslant x \leqslant 0,25$) où la formation de défauts est due au remplacement de Pb^{2+} par Bi^{3+} ou Th^{4+}.

Les études par diffraction de neutrons de $Pb_{1-x}Bi_xF_{2+x}$ et $Pb_{1-x}Th_xF_{2+2x}$ ont permis de déterminer en fonction de la composition les répartitions des fluors dans les sites normaux et interstitiels. Un comportement analogue a été mis en évidence pour les deux solutions solides.

Dans le cas de $Pb_{1-x}Th_xF_{2+2x}$, le trajet élémentaire des ions mobiles est visualisé à travers le volume de présence des fluors interstitiels. Les propriétés électriques et structurales sont corrélées. Deux processus de diffusion sont proposés selon que des fluors interstitiels sont déjà présents ou non sur le trajet des ions mobiles. Les meilleures performances électriques sont obtenues pour $Pb_{0,875}Th_{0,125}F_{2,25}$, composition pour laquelle les deux processus ont une probabilité comparable. Cette composition comporte un maximum de lacunes.

Une solution solide de structure fluorine $Rb_{1-x}Bi_xF_{1+2x}$ ($0,50 \leqslant x \leqslant 0,60$) et un composé défini $RbBi_3F_{10}$ ont été isolés dans le système $RbBiF_4-BiF_3$. Alors que la solution solide est cristallographiquement désordonnée, $RbBi_3F_{10}$ est caractérisé par un ordre 1-3 entre le rubidium et le bismuth et la répétition dans le réseau des motifs $|RbBi_3F_8|^{2+}$ et $|RbBi_3F_{12}|^{2-}$.

La répartition des fluors dans les sites normaux et interstitiels en fonction de la composition a été également déterminée par diffraction de neutrons pour $Rb_{1-x}Bi_xF_{1+2x}$. Le principal résultat est l'augmentation du nombre d'interstitiels lorsque x augmente et la diminution du nombre des fluors dans les sites normaux. Par extrapolation, nous obtenons pour x = 0,75($RbBi_3F_{10}$) $n_{F'_{II}} = 1,50$: $n_{F_I} = 1,0$ ce qui est en excellent accord avec la structure de cette phase. Un mécanisme

de substitution est proposé. La diminution de conductivité pourrait s'expliquer par l'association progressive des fluors autour des bismuths avec formation d'antiprismes (BiF_8) et le piégeage des lacunes à l'intérieur des motifs $(RbBi_3F_{12})^{2-}$.

INTRODUCTION

It is well known that electrolytic oxides with the CaF_2-type structure, whose conduction is due to O^{2-} ions, have good conductivities only at high temperatures ($t > 600°C$) (1,2). On the contrary, isostructural fluorides have significantly higher conductivities at relatively low temperatures. This property is obviously a consequence of the enhanced mobility of F^- ions, as a result of smaller electric charge and less covalent bonding.

The criteria responsible for high ionic conductivity in solid electrolytes have been determined in several exhaustive studies (3,4). These factors allowed to identify many highly conducting fluorides. Fluorite-type materials are very interesting because of the holes present in the lattice. Fig.1 shows a fluorite unit cell with anions at normal sites (they will be called F_I) and the cations occupying only half of the eight-coordinated sites. Furthermore the fluorides MF_2 (M = Ca,Sr,Ba,Pb) react with the trivalent or tetravalent fluorides to give extensive solid solutions whose structure is also related to the fluorite structure. The excess F^- ions resulting from the replacement of M^{2+} cations by M^{3+} or M^{4+} cations are located at interstitial sites (they will be called F_{II}). Fluorides with such a structure are among the best ionic conductors when the cations present in these materials have a high polarizability. As a consequence, high conductivity materials have been obtained in solid solutions based upon PbF_2 with Sn(II), Sb(III), Bi(III), Th(IV) and Zr(IV) fluorides as well as in the $AF-BiF_3$ systems (A = Na, K, Rb, Tl) (4 to 10).

This article deals with the correlations between electrical properties and crystallographic data determined by a neutron diffraction technique in fluorite-type fluorides. We shall mention here studies concerning two types of solid solutions :

I - $Pb_{1-x}Bi_xF_{2+x}$ and $Pb_{1-x}Th_xF_{2+2x}$

II - $Rb_{1-x}Bi_xF_{1+2x}$

I - PbF_2-BiF_3 and PbF_2-ThF_4 systems

Large domains of solid solutions with fluorite type structure have been isolated in the PbF_2-BiF_3 and PbF_2-ThF_4 systems (4,7). They may be respectively formulated $Pb_{1-x}Bi_xF_{2+x}$ $(0 \leqslant x \leqslant 0.50)$ and $Pb_{1-x}Th_xF_{2+2x}$ $(0 \leqslant x \leqslant 0.25)$.

The variation of log σ at various temperatures as a function of composition for the solid solutions $Pb_{1-x}Bi_xF_{2+x}$ and $Pb_{1-x}Th_xF_{2+2x}$ is given in Fig.2a. A conductivity maximum has been observed for the solid solutions of bismuth and thorium at $x = 0.25$ and $x = 0.125$ respectively. These values correspond to the same number of extra-fluorine ions introduced in the matrix of β-PbF_2. These conductivity maxima are connected to activation energy minima (Fig.2b). It was reasonable to foresee that these extremes are related to a maximum vacancy number similar to that observed in $Ca_{0.75}Y_{0.25}F_{2.25}$ (11). To verify this hypothesis, a neutron diffraction study of the non-stoichiometric phases $Pb_{1-x}Bi_xF_{2+x}$ and $Pb_{1-x}Th_xF_{2+2x}$ has been undertaken (12,13).

Neutron diffraction studies have allowed the distribution of fluorine over normal (F^{I}) and interstitial (F^{II}) sites in $Pb_{1-x}Bi_xF_{2+x}$ and $Pb_{1-x}ThF_{2+2x}$ to be determined as a function of composition, x.

The results are given in Fig.3 for $Pb_{1-x}Bi_xF_{2+x}$ and compared to those obtained for $Ca_{1-x}Y_xF_{2+x}$ by CHEETHAM, FENDER and COOPER (14). For both solid solutions there are two types of interstitials : one (F'_{II}) displaced along the <110> direction from the crystallographic position (1/2, 1/2, 1/2) and the other (F''_{II}) displaced along the <111> direction.

For $Ca_{1-x}Y_xF_{2+x}$, the substitution model which had been proposed is as follows :

$$Ca^{2+} + F^-_I = Y^{3+} + F'_{II} + F''_{II} + V_{F_I} \quad (a)$$

With this mechanism, the replacement of one calcium atom by one yttrium atom involves two fluorine ions in interstitial sites with production of one vacancy V_{F_I}.

Transposing this model to $Pb_{1-x}Bi_xF_{2+x}$ without distinguishing between F'_{II} and F''_{II} yields :

$$Pb^{2+} + F^-_I = Bi^{3+} + 2F^-_{II} + V_{F_I} \quad (a')$$

In fact this model is only satisfactory for the boundary composition ($x = 0.50$) which can be written $Pb_{0.50}Bi_{0.50}F_{I1.50}F_{II}V_{F_{I_{0.50}}}$. For other compositions of the solid solution, experimental points deviate from calculated ones.

Maximum of conductivity for $Pb_{0.75}Bi_{0.25}F_{2.25}$ can be explained by the presence of an important number of vacancies. For $x > 0.25$, an ordering between vacancies and interstitials might be at the origin of the conductivity decrease (12).

By anology with solid solution $Pb_{1-x}Bi_xF_{2+x}$, the following mechanism of passage from PbF_2 to the upper limit $Pb_{0.75}Th_{0.25}F_{2.50}$ of the solid solution $Pb_{1-x}Th_xF_{2+2x}$ might be proposed :

$$Pb^{2+} + 2F_I^- = Th^{4+} + 4F_{II}^- + 2V_{F_I} \quad \text{(b)}$$

It was therefore interesting to undertake the study of $Pb_{1-x}Th_xF_{2+2x}$ by neutron diffraction techniques in order to confirm this mechanism and correlate its structural and electrical properties.

Thanks to FOURIER difference maps the nuclear densities of interstitial fluorine atoms have been determined. Fig.4 shows such maps for various compositions of the $Pb_{1-x}Th_xF_{2+2x}$ solid solution. We can note the presence of four types of fluorine : 1 normal F_I and 3 interstitials F'_{II}, F''_{II} and F'''_{II}, all of which have the same meaning as in the formerly studied solid solutions except for F'''_{II} which can be regarded as a normal F_I slightly displaced from its original position.

Fig.5 shows the composition dependence of the number of fluorine and vacancies. The total number of interstitial fluorines is $n_{F_{II}} = n_{F'_{II}} + n_{F''_{II}} + n_{F'''_{II}}$ and that of vacancies is :

$$n_{V_{F_I}} = 2 - n_{F_I}$$

For $x < 0.10$ the simultaneous increase of $n_{F_{II}}$ and $n_{V_{F_I}}$ is strong. On the other hand, for higher values of x, $n_{F_{II}}$ increases linearly whereas $n_{V_{F_I}}$ becomes nearly constant ($\simeq 0.50$). It is interesting to note that this evolution is similar to that of the $Pb_{1-x}Bi_xF_{2+x}$ solid solution. Nevertheless, the increase of $n_{F_{II}}$ and $n_{V_{F_I}}$ for $Pb_{1-x}Th_xF_{2+2x}$ is twice as rapid. Experimental values verify the model of equation (b) for the boundary composition which can be written $Pb_{0.75}Th_{0.25}F_{I1.50}F_{II}V_{FI0.50}$.

That boundary composition has a structure close to that of Pb_3ZrF_{10} (15) which can be regarded as an ordered intergrowth of fluorite columns $(Pb_2F_4)_\infty$ and of more complex ones $(Pb_4Zr_2F_{16})_\infty$ (Fig.6). Defects are formed near Zr atoms which are surrounded by 8 fluorine atoms forming ZrF_8 antiprisms, $4F_I$ (noted F_2) and $4F_{II}$ (noted F_3 and F_4).

The replacement of Pb^{2+} by Zr^{4+} involves the introduction of two fluorines in interstitial sites ($2F_3$) and the crossing of two fluorines from normal sites to interstitial sites ($2F_4$) with liberation of two vacancies V_{F_I}. The elementary composition is $Pb_3ZrF_{I6}F_{II4}V_{FI2}$ in good agreement with the substitution mechanism proposed for $Pb_{0.75}Th_{0.25}F_{2.50}$.

By connecting of two ZrF_8 antiprisms in the lattice of Pb_3ZrF_{10}, a double chain of vacancies is created between these antiprisms, orthogonal to the XOY plane.

The formation of defects due to the replacement of one M^{2+} ion by one M'^{3+} or M''^{4+} ion in fluorite-type solid solutions would consequently be bound by the establishment of a local order which becomes progressively longer range for those compositions near to the boundary.

The study of $Pb_{1-x}Bi_xF_{2+x}$ and $Pb_{1-x}Th_xF_{2+2x}$ by neutron diffraction has shown that interstitial fluorines are settled in well-defined sites and their number varies as a function of x.

On the other hand, these fluorines can be partly delocalized when they are placed in electric fields or when the temperature is increased. This is the case for β-PbF_2 for which the migration of fluorine from normal (FI) to interstitial (FII) sites has been shown at increasing temperatures (16).

Fig.7 shows, for $Pb_{0.77}Th_{0.23}F_{2.46}$ of the $Pb_{1-x}Th_xF_{2+2x}$ solid solution, the envelope of different crystallographic sites for anions. The elementary pathway has the shape of a ring.

Two principal diffusion processes can be thought of according to whether intermediate interstitial sites are occupied or not :

Process A : $F_I \rightarrow V_{F_I}$ where a normal fluorine atom shifts to a vacant normal position. This mechanism occurs only if intermediate interstitial sites are vacant.

Process B : $F_I \rightarrow V_{F_{II}}$ involving the shifting of a normal fluorine atom to a vacant interstitial position $V(F_{II})_1$ while a neighbouring interstitial position $(F_{II})_2$ is already occupied. The $(F_{II})_1$-$(F_{II})_2$ distance is too short to allow the simultaneous presence of two interstitials in the same pathway. Consequently process B is only possible in a coupled migration :

$$F_I \rightarrow V(F_{II})_1, \quad (F_{II})_2 \rightarrow V_{F_I}$$

Taking these two diffusion processes into account, it was interesting to study their respective influence on the electrical properties of $Pb_{1-x}Th_xF_{2+2x}$. This is illustrated in Fig.8 which gives the variation of $n_{V_{F_I}}$, $n_{F_{II}}$, log $\sigma_{60°C}$ and ΔE as a function of x. Two domains can be distinguished :

1) Domain where $x < 0.125$

In this domain, there is a substantial increase in the numbers of vacancies and interstitials corresponding to an increasing disorder. This gives an enhancement of conductivity and a decrease of activation energy. As the number of interstitials being is limited in this region, we can suppose that fluorine diffusion is mainly ruled by process A.

2) Domain where $x > 0.125$

For $x > 0.125$, the number of vacancies reaches a threshold whereas interstitials increase regularly. As a consequence, conductivity drops while activation energy increases.

The conductivity decrease observed for $x > 0.25$ in $Pb_{1-x}Bi_xF_{2+x}$ has been explained by the formation of a progressive ordering of vacancies and interstitials, first locally then over a long range as the boundary composition is reached (12).

Such a phenomenon can be transposed to $Pb_{1-x}Th_xF_{2+2x}$. Moreover since the number of interstitials increases when x increases, the process B is the likeliest in this domain. Here mobile fluorine are mostly stable in their F_{II} positions and shifting to vacant sites become more difficult. Activation energy increases and conductivity drops.

3) $x = 0.125$

Both processes A and B have the same probability of occurring for $Pb_{0.875}Th_{0.125}F_{2.25}$. It is also the composition possessing the best electrical performances. This composition corresponds to the smallest value of x for which the maximum number of vacancies has been reached. This is also the case for $Pb_{0.75}Bi_{0.25}F_{2.25}$.

II - $RbBiF_4$-BiF_3 system

An other example, very representative of such investigations is the solid solution $Rb_{1-x}Bi_xF_{1+2x}$.

The high-temperature form of $RbBiF_4$ (β) is a good ionic conductor ($\sigma_{100°C} \approx 10^{-2}\ \Omega^{-1}\ cm^{-1}$). β-$RbBiF_4$ is metastable and it can be stabilized by introduction of excess BiF_3. This characteristic led to the study of the $RbBiF_4$-BiF_3 system.

The synthesis of the phases has been discussed elsewhere (17). Radiocrystallographic analysis reveals the existence of :

- a solid solution with a cubic symmetry, $Rb_{1-x}Bi_xF_{1+2x}$ ($0.50 \leqslant x \leqslant 0.60$). The structure is of the fluorite-type.
- a single phase $RbBi_3F_{10}$ at $x = 0.75$.

As x increases, the lattice constant within the solid solution decreases linearly. The substitution of Rb(I) by Bi(III) of smaller size should induce a strong decrease of a_c but there occurs, simultaneously, an insertion of two F^- into interstitial sites. This results in a weak decrease of the cell constant.

Whereas the solid solution domain is crystallographically disordered, $RbBi_3F_{10}$ has an X-ray diffraction pattern typical of a fluorite superstructure with a cell constant twice as large as that of a corresponding fluorite. Isostructural with KY_3F_{10} (18), $RbBi_3F_{10}$ is characterized by a 1:3 ordering of Rb and Bi and the repetition in the lattice of two types of units: $|RbBi_3F_8|^{2+}$ (fluorite-type) and $|RbBi_3F_{12}|^{2-}$ in which fluorine atoms form a cubooctahedral cluster. The coordination polyhedron of bismuth in this phase is an antiprism $|BiF_8|$ formed of $4F_I$ (fluorine in normal position) and $4F_{II}$ (fluorine in interstitial site) (Fig.9).

We have reported in Fig.10 the temperature dependence of the conductivity for several compositions of the $Rb_{1-x}Bi_xF_{1+2x}$ solid solution and for the ordered phase $RbBi_3F_{10}$. When x increases, at a given temperature, conductivity decreases and there is an increase of the activation energy. The lowest performances are obtained for $RbBi_3F_{10}$.

Such an evolution of the electrical properties in $Rb_{1-x}Bi_xF_{1+2x}$ cannot be readily explained. Consequently the neutron diffraction study of $Rb_{1-x}Bi_xF_{1+2x}$ has been undertaken (19).

The aim of this investigation was to refine the atomic positions of fluorine atoms within the lattice and to determine their distribution over normal (F_I) and interstitial (F'_{II}) sites as a function of composition.

Contrary to findings in the $Pb_{1-x}Th_xF_{2+2x}$ solid solution where three types of interstitials were found [$F'_{II}(1/2, u, u)$ with u = 0.40, $F''_{II}(v_1, v_1, v_1)$ with v_1 = 0.40, and $F'''_{II}(v_2, v_2, v_2)$ with v_2 = 0.30], the interstitial positions for $Rb_{1-x}Bi_xF_{1+2x}$ are only centered in F'_{II} positions with u = 0.34.

We have reported on Fig. 11 the composition dependence of the number of fluorine atoms at normal and interstitial positions as well as that of the number of vacancies in normal sites ($n_{V_{F_I}} = 2-n_{F_I}$). β-$RbBiF_4$ may be written: $Rb_{0.50}Bi_{0.50}F_{I1.50}F'_{II0.50}V_{FI0.50}$

When x increases within the solid solution, $n_{F'_{II}}$ increases while n_{F_I} decreases linearly. Extrapolation to the value x=0.75, gives $n_{F'_{II}}$=1.50 and n_{F_I}=1. The theoretical formulation of $RbBi_3F_{10}$ would then be: $Rb_{0.25}Bi_{0.75}F_IF'_{II1.50}V_{F_I}$. This is in agreement with the structure proposed for this phase.

We can then suggest a mechanism of substitution when bismuth replaces rubidium in $RbBiF_4$:

$$Rb^{+} + 2F_{I}^{-} = Bi^{3+} + 4F_{II}^{-} + 2V_{F_I}$$

With a substantial number of vacancies and interstitials, β-$RbBiF_4$ is characterized like $Pb_{0.875}Th_{0.125}F_{2.25}$ and $Pb_{0.75}Bi_{0.25}F_{2.25}$ by a maximum of disorder.

When x increases in $Rb_{1-x}Bi_xF_{1+2x}$, $n_{F'_{II}}$ and $n_{V_{F_I}}$ increase linearly and it is possible to predict the formation of isolated BiF_8 antiprisms. This results in the onset of ordering between Rb and Bi atoms on one hand and elementary cubes F_8 and cubooctahedra F_{12} on the other hand. This local order becomes a long range one with increasing x, and becomes well established for $RbBi_3F_{10}$.

The increase with x of the number of vacancies, $n_{V_{F_I}}$, should lead to enhanced conductivity, however, the latter are trapped within the cubooctahedra F_{12} and their contribution to conductivity at long range is hindered.

Both processes of diffusion which have been formerly considered in $Pb_{1-x}Th_xF_{2+2x}$ can be differentiated in $RbBi_3F_{10}$ which contains two types of units:

process A will be predominant in $|RbBi_3F_8|^{2+}$ units and process B in $|RbBi_3F_{12}|^{2-}$ units. Two relaxation times correspond to these two processes, which is confirmed by N.M.R. studies (20).

Within the solid solution which has a relatively narrow domain of homogeneity, the distribution of rubidium and bismuth is random although a short range order starts occuring with increasing x. Interstitials cannot be considered as totally localized and both processes A and B have the same probability of occurring which is confirmed by N.M.R. as only one relaxation time can be observed (20).

SUMMARY

Neutron diffraction has proved to be a very helpful technique. It has revealed that the elementary pathway of mobile ions occurs through the presence of interstitial fluorine in fluorite-type fluorides. Two conductivity mechanisms have been proposed according to whether the pathway is free or blocked. Consistent correlations between electrical properties and crystallographic data have been consequently determined.

REFERENCES

(1) J.W. Patterson, E.C. Bugrew and R.A. Rapp, J Electrochem Soc 114: 752; 1967.

(2) A. Hammou, Ch. Deportes and G. Robert, J Chem Phys 7-8: 1162; 1971.

(3) R.D. Armstrong, R.S. Bulmer and T. Dickinson, J Solid State Chem 8, 219; 1973.

(4) J.M. Réau and J. Portier, Solid Electrolytes, Fluorine ion conductors, chap. 19 (Ed.P.Hagenmuller and W. Van Gool), Academic Press ,1978 .

(5) C. Lucat, A. Rhandour, J.M. Réau, J. Portier and P. Hagenmuller, J Solid State Chem 29: 373; 1979.

(6) Ph. Darbon, J.M. Réau and P. Hagenmuller, Mat Res Bull 16: 273; 1981.

(7) J.M. Réau, A. Rhandour, C. Lucat, J. Portier and P. Hagenmuller, Mat Res Bull 13: 827; 1978.

(8) Ph. Darbon, J.M. Réau, P. Hagenmuller, Ch. Depierrefixe, J.P. Laval and B. Frit, Mat Res Bull 16: 389; 1981.

(9) J.M. Réau, J. Grannec, C. Lucat, C. Chartier, S. Matar, J. Portier and P. Hagenmuller, J Fluorine Chem 19: 363; 1982.

(10) S. Matar and J.M. Réau, C.R. 294: 649; 1982.

(11) J.M. Réau, S. Matar, C. Lucat, G. Campet, J. Portier and A. Hammou, J Solid State Chem 17: 123; 1976.

(12) C. Lucat, J. Portier, J.M. Réau, P. Hagenmuller and J.L. Soubeyroux, J Solid State Chem 32: 279; 1980.

(13) J.L. Soubeyroux, J.M. Réau, S. Matar, P.Hagenmuller and C. Lucat, Solid State Ionics 2: 215; 1981.

(14) A.K. Cheetham, B.E.F. Fender and H.J. Cooper, J Phys C Solid State Phys 4: 3107; 1971.

(15) J.P. Laval and B. Frit, Mat Res Bull 14: 1517; 1979.

(16) K. Koto, H. Schulz and R.A. Huggins, Solid State Ionics 1: 355; 1980.

(17) S. Matar, J.M. Réau, C. Lucat, J. Grannec and P. Hagenmuller, Mat Res Bull 15: 1295; 1980.

(18) J.W. Pierce and H.Y.P. Hong, Proc. 10th Rare Earth Res. Conf., carefree U.S.A. A2, 527; 1973.

(19) J.L. Soubeyroux, J.M. Réau, S. Matar, G. Villeneuve and P. Hagenmuller, Solid State Ionics, 6: 103; 1982.

(20) G. Villeneuve, S. Matar, J.M. Réau and P. Hagenmuller, Solid State Ionics, in Press.

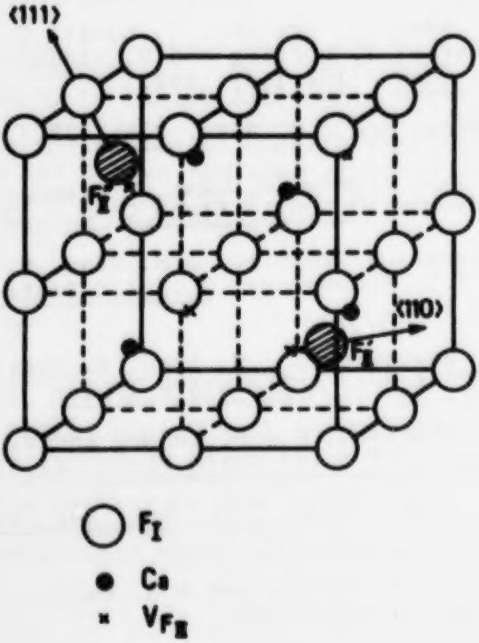
⟨111⟩
F_{II}'
⟨110⟩
F_{II}'
F_I
Ca
$V_{F_{II}}$

Fig. 1 **The fluorite structure.**

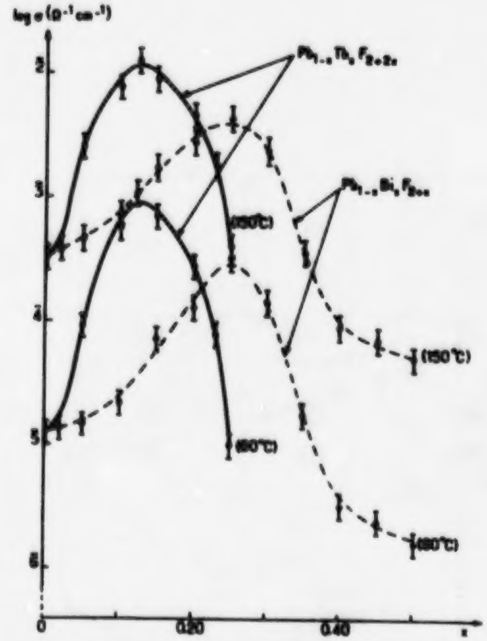

Fig. 2a Composition dependence of the conductivity for $Pb_{1-x}Bi_xF_{2+x}$ ($0 \leq x \leq 0.50$) and $Pb_{1-x}Th_xF_{2+2x}$ ($0 \leq x \leq 0.25$).

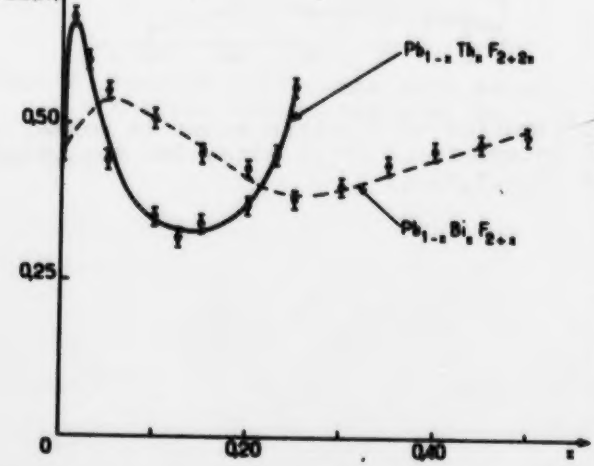

Fig. 2b Variation of the activation energy of $Pb_{1-x}Bi_xF_{2+x}$ ($0 \leq x \leq 0.50$) and $Pb_{1-x}Th_xF_{2+2x}$ ($0 \leq x \leq 0.25$) with composition.

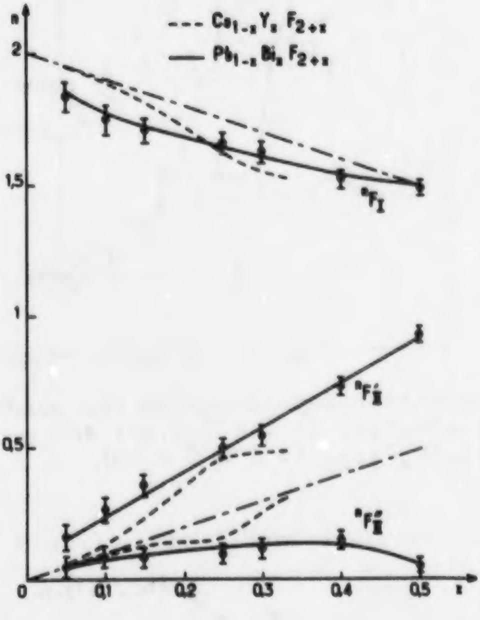

Fig. 3 Distribution of fluorine atoms in normal (F_I) and interstitial (F_{II}) sites for $Pb_{1-x}Bi_xF_{2+x}$ and $Ca_{1-x}Y_xF_{2+x}$.

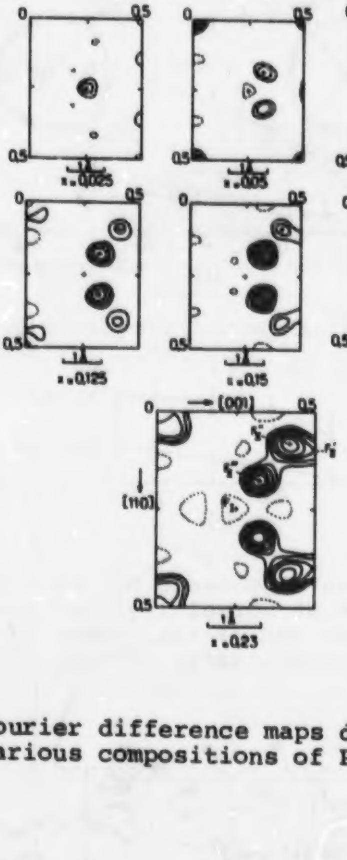

Fig. 4 Fourier difference maps determined for various compositions of $Pb_{1-x}Th_{x}F_{2+2x}$.

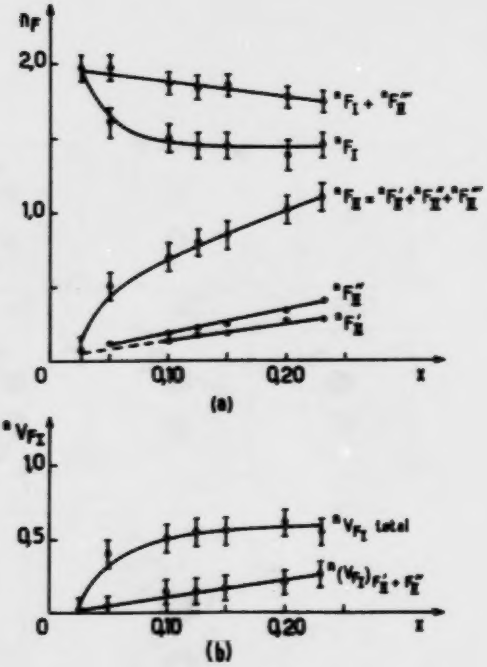

Fig. 5 Composition dependence of the number of fluorine atoms at normal (F_I) and interstitial (F_{II}) sites and of the number of vacancies (V_{F_I}) at normal sites for $Pb_{1-x}Th_xF_{2+2x}$.

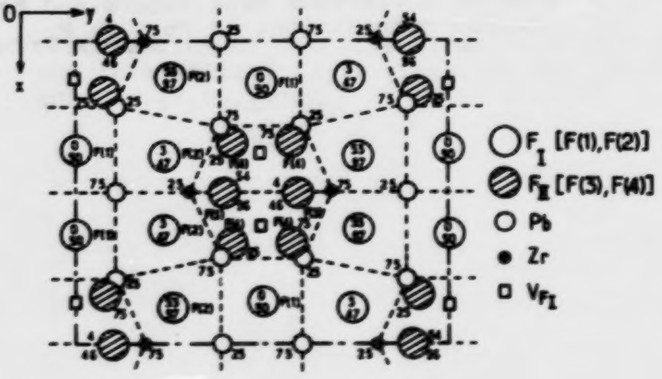
O
y
x
F_I [F(1),F(2)]
F_{II} [F(3),F(4)]
Pb
Zr
V_{F_I}

Fig. 6 Projection of the Pb_3ZrF_{10} structure on XOY plane (15).

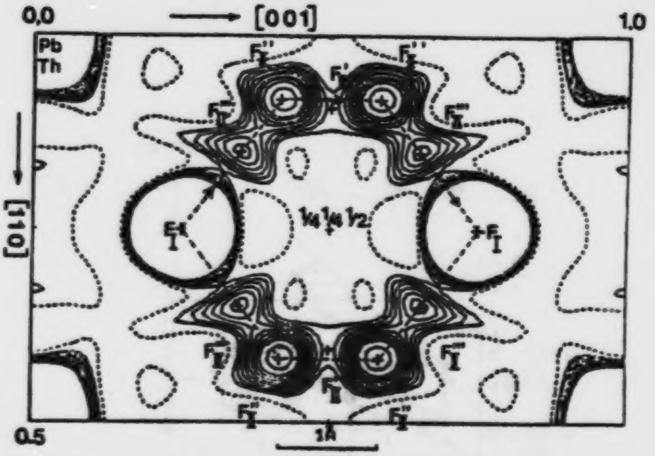
0,0
[001]
1,0
Pb
Th
[110]
0.5
1Å
¼¼½
F'
F''
F'''
F_I
F_II

Fig. 7 Envelope of crystallographic sites of fluorine atoms for $Pb_{0.77}Th_{0.23}F_{2.46}$.

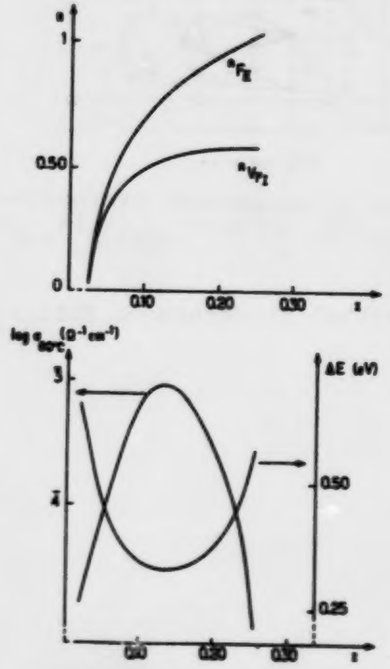

Fig. 8 Composition dependence of $n_{V_{F_I}}$, $n_{F'_{II}}$, log $\sigma_{60°C}$ and ΔE for $Pb_{1-x}Th_xF_{2+2x}$.

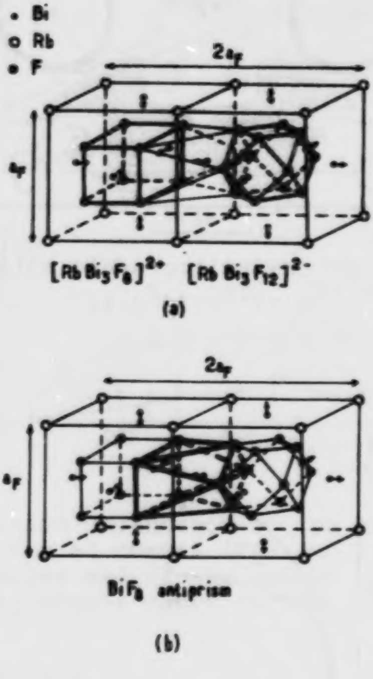
• Bi
○ Rb
• F
2a_F
a_F
[Rb Bi3 F8]2+
[Rb Bi3 F12]2-
(a)
2a_F
a_F
BiF8 antiprism
(b)

Fig. 9 Crystal structure of $RbBi_3F_{10}$.

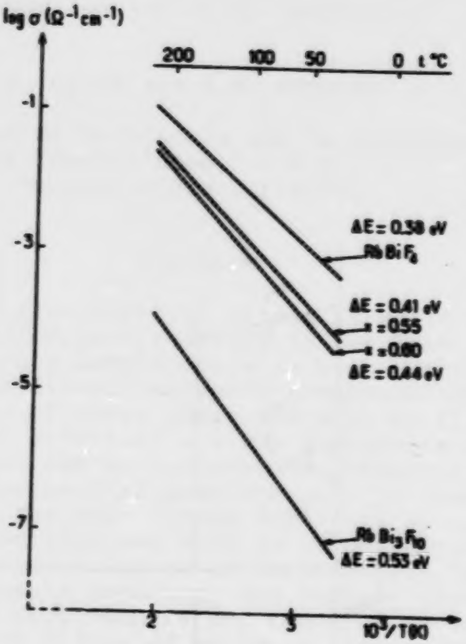

Fig. 10 Temperature dependence of conductivity for $Rb_{1-x}Bi_xF_{1+2x}$ and for $RbBi_3F_{10}$.

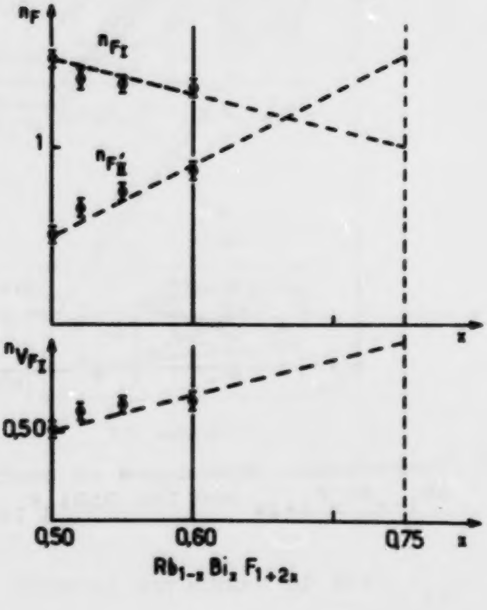

Fig. 11 Composition dependence of the number of fluorine atoms at normal (F_I) and interstitial (F_{II}) sites and of the number of vacancies (V_{F_I}) at normal sites for $Rb_{1-x}Bi_xF_{1+2x}$.

FLUORITE-TYPE SOLID ELECTROLYTES AS OXYGEN ION AND MIXED CONDUCTORS

B. CALES and A.M. ANTHONY

Centre de Recherches sur la Physique des
Hautes Températures,C.N.R.S.
45045 Orléans-cédex , France.

ABSTRACT

The use of fluorite-type oxides as solid electrolytes has motivated much research in the last few years and has led to many developments in high temperature applications.The crystallographic structure and the stability ranges of these materials will be first pointed out.Their defect structure and the dependence of their electrical properties on temperature, chemical composition and oxygen partial pressure will be then reported. On these bases, the most common applications of these compounds will be outlined such as oxygen gauges, fuel cells and electrolysers at intermediate temperature, oxygen semipermeable membranes and heating elements for furnaces in the high-temperature range. A survey of the present status of knowledge in these fields will be thus provided.

KEYWORDS: oxide-electrolyte,oxygen gauge, fuel cell, electrolyser, semipermeable membrane, heating element.

RÉSUMÉ

L'utilisation des oxydes de type fluorite comme électrolytes solides a suscité de nombreuses recherches durant ces dernieres années. Leur emploi a été largement développé dans diverses applications à haute température. Aussi, aprés un bref rappel de la structure cristallographique et du domaine de stabilité de ces matériaux, on indiquera la nature de leurs défauts ponctuels et l'influence de divers paramètres, tels la température, la composition chimique ou la pression partielle d'oxygène, sur leurs propriétés électriques. Les principales applications de ces oxydes comme électrolytes solides seront alors présentées, en particulier, pour des températures relativement peu élevées, les jauges à oxygène, les piles à combustible et les électrolyseurs, et, à haute température, les membranes semiperméables à l'oxygène et les éléments chauffants pour fours en atmosphère oxydante. On donnera ainsi un aperçu de l'état actuel des connaissances dans ces domaines.

INTRODUCTION

Solid electrolytes have been extensively studied during the last few years because of the large diversity of their applications. Indeed their use is often invoked, for instance in the domain of energy conversion and storage and also for thermodynamic measurements. These materials are generally characterized by a predominant ionic-type conductivity resulting from a large concentration and mobility of charge carriers. Among the solid electrolytes, fluorite-type oxides MO_2 are the most successfûl owing to their large interest for potential uses in high temperature investigations. Thus oxides derived from the IV-group elements, such as ZrO_2 or HfO_2 are currently the most used as oxygen ion conductors. Nevertheless, their solid electrolyte character is enhanced by forming solid solutions with oxides of lower valency cations, such as M'^{2+} or M''^{3+}. The introduction of small quantities of alkaline earth(M'^{2+}) or rare earth(M''^{3+}) oxides into the MO_2 lattice leads to the formation of lattice and electronic defects, in order to maintain the charge neutrality of the material. These defects are accountable for the specific electrical properties of the fluorite-type oxides. For instance, although the ionic-type conductivity remains predominant, the presence of electronic defects gives rise to an electronic partial conductivity which may alter the electrolyte character.

The purpose of the present chapter is to give an extended overview of the present research and development in this field. Thus after a brief survey of the physical properties of the fluorite-type oxides and mainly of their electrical characteristics, the different common applications of these compounds as solid electrolyte will be detailed.

GENERAL SURVEY

The structure of fluorite-type oxides may be described as a cubic close-packed array of metal ions, in which the tetrahedral sites are filled by oxygen ions and the octahedral sites are void. It is characterized by a face-centered cubic symmetry with a Fm3m space group. The cations are thus cubic eightfold coordinated to oxygen ions.

Many MO_2 oxides corresponding to tetravalent metals present a fluorite-type structure, this is the case for some lanthanide oxides as CeO_2,PrO_2 or TbO_2 for instance, and some actinide oxides like ThO_2,UO_2 or PuO_2. Such a structure may be thermally very stable as in ThO_2 which possesses a fluoritic structure, without any polymorphic transformation, up to its melting point, about 3300°C. In addition to these compounds, two oxides of the IVA-group elements, ZrO_2 and HfO_2, are liable to crystallize with a fluorite-type structure. However, in both cases the cubic symmetry is only observed at high temperature. Indeed, zirconia may exist under three allotropic varieties respectively (1): monoclinic, tetragonal and cubic from low to high temperature. The room-temperature symmetry is monoclinic with a sevenfold coordination of cations (1). At about 1170°C, there is a martensitic phase transformation from the monoclinic to a tetragonal symmetry which is preserved up to 2370°C (2). Beyond this temperature the cubic structure may be observed, with cubic coordinated zirconium ions, up to the melting point, about 2680°C (3,56). The monoclinic-tetragonal allotropic transformation is associated with a rapid change in the lattice parameters at the phase transition and with an abrupt variation of the linear expansion coefficient which leads to the failure of the pure zirconia ceramics (4).

Nevertheless zirconia or hafnia may be stabilized as the fluorite-type phase, over extended ranges of composition and temperature (5), by addition of various oxides characterized by a cubic symmetry and a lower cation valency than in zirconia (6), such as M'O or M''_2O_3 oxides. Among those, the most currently used are CaO and MgO for the divalent metals group and Y_2O_3 and some rare earth oxides for the trivalent one. In such fluorite-type solid solutions, doping M'^{2+} or M''^{3+} cations substitute on zirconium sublattice sites and the electroneutrality of the material is preserved by formation of oxygen vacancies in the anion sublattice. These vacancies and dopant ions induce a relaxation of the neighbouring oxygen ions (1) which can be invoked in order to explain the thermodynamical stability of the fluoritic structure down to relatively low temperature.

The chemical composition range of stability for the fluoritic form of zirconia largely depends on the nature of the dopant oxide (7). As an example, the phase diagrams of ZrO_2-CaO and ZrO_2-Y_2O_3 systems reported by Stubican et al (8,9) are shown on figures 1 and 2. The fluoritic phase, which should be unstable below the eutectoid temperature, is still observed down to room temperature. This could be attributed to the extremely low diffusional kinetics of cations (10). For the same reason, ordering of cation or anion sublattices, which can lead to precipitates or formation of intermediate phases are rather slow rate processes that need prolonged annealing below the decomposition temperature to be observed (11).

A large variety of similar fluoritic solid solutions may be obtained in binary or ternary systems by doping the various fluorite-type oxides. Extended reviews on all these compounds are reported in the litterature (7,12).

DEFECT STRUCTURE AND ELECTRICAL PROPERTIES

The presence of oxygen vacancies in the anionic sublattice of fluoritic solid solutions, as charge-compensating defects, are partly accountable for the electrical properties of these compounds, so that the nature and the concentration of such defects should be carefully investigated. As an example, the case of $Zr_{1-x}Ca_xO_{2-x}$ solid solutions will be detailed later on and the Kröger-Vink notation (13) will be used in this analysis.

Addition of calcium oxide to the zirconia matrix, with formation of charge compensated defects, may be described by the following reaction:

$$CaO \xrightarrow{ZrO_2} Ca_{Zr}^{''} + O_O^{X} + V_O^{\bullet\bullet} \qquad /1/$$

The concentration of oxygen vacancies is thus controlled by the content of calcium oxide. This is slightly modified by thermodynamical equilibria of the oxide with the surrounding atmospheres, which may induce ,under reducing conditions, additional oxygen vacancies (14) as:

$$O_O^{X} \rightleftharpoons V_O^{\bullet\bullet} + 2e' + 1/2\ O_2(g) \qquad /2/$$

or reduce their initial concentration by incorporation of oxygen in the lattice under high oxygen activities (14) :

$$1/2\ O_2(g) + V_O^{\bullet\bullet} \rightleftharpoons O_O^{X} + 2h^{\bullet} \qquad /3/$$

The concentrations of electronic defects, electrons e' or electron holes $h^{\bullet}$, are elsewhere related by means of the intrinsic ionization equilibrium, since at high temperature some electrons of the valence band can be excited to the conduction band. Finally, in order to satisfy the material electroneutrality, the different electronic or lattice defects must obey the following relationship (14) :

$$2\left[V_O^{\bullet\bullet}\right] + p = 2\left[Ca_{Zr}^{''}\right] + n \qquad /4/$$

where n and p denote the concentrations of electrons and electron holes respectively. The mass action law may be applied to the different equilibria (13) and taking two limiting cases into account (15), according to the oxygen vacancy concentration being controlled i) extrinsically by the calcia content, reaction or ii) intrinsically by the thermodynamical equilibria 2 or 3, it may be shown that, at a given temperature, the concentration of the different defects is only a function of the oxygen partial pressure of the surrounding atmosphere, as shown on the Brouwer's diagram reported on Figure 3. From such a diagram, the electrical conductivity behaviour for stabilized zirconia may be directly deduced, since for a charge carrier k the partial conductivity σ_k is related to the concentration C_k of species k, by (16) :

$$\sigma_k = Z_k \, q \, \mu_k \, C_k$$

where Z_k denotes the valency and μ_k the mobility of species k and q is the elementary charge. Assuming that μ_k remains constant for a given temperature, σ_k must follow the same oxygen pressure law as C_k.

Thus, in the extrinsic domain (Fig. 3), n is much smaller than the oxygen vacancy concentration $[V_O^{\cdot\cdot}]$ and the conductivity should be practically ionic in nature. The partial ionic conductivity σ_i is related to $[V_O^{\cdot\cdot}]$ and independent of the oxygen partial pressure. In the same part, the electronic conductivity σ_e will follow a $pO_2^{-1/4}$ dependence for electrons and a $pO_2^{+1/4}$ law for electron holes. This domain has been largely investigated and the predicted variations of partial electronic and ionic conductivities have been experimentally verified (17).

In the intrinsic domain, corresponding to low oxygen activities, both ionic and n-type electronic conductivities should obey a $pO_2^{-1/6}$ law. In the very high oxygen pressure range, not reported on Figure 3, a $pO_2^{+1/6}$ dependence would be observed for both σ_i and σ_e.

Owing to the rapid increase of the electronic defect concentration with temperature, the extrinsic domain, often called electrolytic domain, diminishes and depending on the nature of the fluorite-type oxide it may even vanish at high temperature (18). In the case of stabilized zirconias, this should be observed for temperatures of the order of 2200°C; in return, at 1000°C the electrolytic domain stretches from oxygen partial pressure of about 10^{-20} to 10^{2} atm. (18), so that in most of their applications only this domain will be invoked. For ThO_2 based solid electrolytes, the electrolytic domain is shifted to lower oxygen partial pressures, 10^{-24} to 10^{-6} atm. in the case of ThO_2-Y_2O_3 system (18). This is due to a large p-type conductivity which is yet predominant in pure thoria down to very low oxygen pressure (19). On the other hand, pure and doped CeO_2 exhibit an n-type electronic conductivity at comparatively high oxygen pressure because of the reduction of cerium ions from tetravalent to trivalent state. The difference between the two families of solid solutions clearly appears on Figure 4 where is reported the oxygen pressure dependence of the ionic transport number t_i ($t_i = \sigma_i / \sigma_i + \sigma_e$) for CeO_2-Y_2O_3 (20) and ThO_2-Y_2O_3 (19) solid solutions. On this figure, the electrolytic domain is approximately indicated by thick lines.

The temperature dependence of partial conductivities σ_j obeys a classical Arrhenius law and may be expressed as (7):

$$\sigma_j = \sigma_j^o/T \ \exp(-\Delta E_j/kT)$$

where σ_j^o is a constant, k the Boltzman constant and ΔE_j denotes the activation energy of the j-type conductivity. For ionic conductivity, the activation energy falls into the range 0.5 to 1.5 eV (7). Recently, fine investigations on the ionic conductivity of monocrystalline yttria stabilized zirconia, have shown a gradual change of the activation energy when increasing the temperature (21). The ionic conductivity appears to be frequency dependent which is the consequence of interactions between mobile oxygen vacancies and yttrium dopant ions. The partial electronic conductivities are thermally activated with higher activation energies and in the case of stabilized zirconias, values of about 3 to 4 eV for the n-type conductivity and 1.5 to 2.5 eV for the p-type one have been reported (22).

The isothermal variation of the electrical conductivity against dopant oxide content exhibits a maximum at a composition close to that corresponding to the lowest limit for the fluoritic phase stabilization and then decreases when increasing the dopant concentration (12). Thus any proportionality relationship between conductivity and dopant or vacancy concentration, which could be invoked in the dilute solution range, lower than about 8 mol % of dope oxide, is no longer appropriate, since the anionic mobility is then largely dependent on the composition. Different models have been developed, based for instance on a multimode conduction process, depending on the local environment of oxygen vacancies (24), or on electrostatic interactions (25) and/or ordering of oppositely charged defects (25), which attempt to explain the compositional dependence of the conductivity.

In the same way, the decrease of electrical conductivity of stabilized zirconias which occurs during ageing processes, due to prolonged annealing, may be attributed to defect ordering or microdomain formation (26).

APPLICATIONS AT INTERMEDIATE TEMPERATURES

Oxygen Gauges

Oxygen sensing is one of the most current uses of oxygen solid electrolytes and mainly of stabilized zirconias. Oxygen galvanic cells are composed of an oxide electrolyte wall, generally a closed-ended tube, coated on both sides with porous metal electrodes (Fig.5). Such a device, under the appliance of an oxygen potential gradient, develops an electromotive force across the electrodes which is given, under stationary conditions, by the following relationship (27):

$$E = RT/4F\int_{pO_2(I)}^{pO_2(II)} t_i \, d\mathrm{Ln}\left(pO_2\right) \qquad /5/$$

where t_i is the ionic transport number of the electrolyte, R the ideal gas constant and F the Faraday's constant. Under usual conditions of temperature and oxygen partial pressure, the ionic transport number of the required electrolyte should be close to unity and the emf E may be written as:

$$E = \left(RT/4F\right)\mathrm{Ln}\ pO_2(II)/pO_2(I) \qquad /6/$$

Thus, at a given temperature, if one of the oxygen pressures is known and taken as a reference ($pO_2(II)$= p ref.), the measurement of E allows one to deduce the value of the unknown oxygen pressure $pO_2(I)$. The fields of application of such systems mainly concern the control of the air/fuel ratio in automotive engines (28) and the oxygen monitoring in metallurgical processes, such as steelmaking (29).

Partially or fully stabilized zirconias are commonly used as solid electrolyte wall (30). Yttria-doped thoria has been also studied for oxygen sensors in the low oxygen activity range (30). Oxygen galvanic cells based on pure or doped ceria electrolyte have been likewise developed for low operating temperatures (31). Finally, double cells involving a combination of ZrO_2-CaO and ThO_2-Y_2O_3 solid electrolytes have been perfected (32) for emf measurements at elevated temperature.

The electrode material should be an electronic conductor and present a high chemical inertness with respect to the different gaseous atmospheres. Furthermore any kinetics of oxygen electrode adsorption or desorption should be fast enough to allow a rapid thermodynamical equilibrium between gaseous phases and electrodes. The oxygen transfer between the gaseous phase and the electrolyte may follow various ways (33) as schematically shown on Figure 6. The oxygen exchange may be directly obtained at the triple contact gas-electrode-electrolyte or by a two-step process including first a volume diffusion of oxygen in the metal. In fact, the oxygen-electrode reaction should be an intermediate process between these two border-line cases depending on the nature and the morphology of the electrode (33). The most common electrodes are made of a thin porous film of noble metal, especially platinum.

The oxygen partial pressure of the reference atmosphere may be fixed by means of air, inert gas-oxygen mixtures or reactive gas mixtures as $CO-CO_2$ or H_2-H_2O. Another possibility consists of using a solid metal-metal oxide equilibrium; at a given temperature, the oxygen pressure is then controlled by the chemical equilibrium constant.

Inaccuracy of oxygen sensors may result from various factors and mainly from uncertainties in defining the reference oxygen pressure (particularly when gas mixtures or metal-metal oxide equilibria are chosen to define a reference (30)) or in the knowledge of the electronic transport number t_e ($t_e = 1-t_i$). Indeed, a frequent source of error is due to the electrochemical semipermeability of the electrolyte which is induced by a partial electronic conductivity of the material (34). In such a case, t_i slightly differs from unity and equation 6 is no longer appropriate to explain the cell behaviour. The electronic conductivity provides an internal partial short circuit and gives rise to a net transfer of oxygen through the electrolyte which can strongly disturb the oxygen pressures on both sides of the cell or induce electrode overvoltages(35). As pointed out in the previous part, the value of the electronic conductivity is directly related to temperature and oxygen partial pressure. Thus, these disturbances are expected to decrease with temperature and may be generally neglected below 700°C for oxygen pressures higher than 10^{-6} atm. (35). These effects may also be largely eliminated on using a reference electrode and zirconia tip electrode (30) which prevents the semipermeability flux reaching the electrode surface in contact with the measuring electrode. However, the electrochemical semipermeability is largely dependent on the nature of electrolyte and electrodes (30) and the cells should be carefully tested before any use (30).

Uncertainties resulting from a thermal gradient between the two electrodes (30) or a departure from the thermodynamical equilibrium at the electrolyte-electrode-gas three-phase interface (35), hence from the ideal electrode reversibility, have been also reported. The effect of electrode surface impurities and morphology on the mechanism and the rate of oxygen reaction at platinum electrodes has been likewise investigated (36).

Actually, an important development of oxygen monitors consists of reducing the size of the cells and of decreasing their rise-time and operating temperature. Mini-gauges, a few millimeters in diameter, have been thus proposed (37). Such miniaturizations allow a more rapid thermal equilibrium and also lower the power consumption of the cells. Several investigations have also been led to decrease the electrolyte thickness in order to reduce the electrical resistance. A thin-layer gauge, the operating temperature of which may be lowered below 400°C, has been perfected (38) by R.F. sputtering of thin films of stabilized zirconia and nickel reference electrode. The use of diffusion barrier, provided by a porous material on the cathodic side of the cell has been studied by Dietz (39) for measurements in the high oxygen concentration range.

More recently, the International Union of Pure and Applied Chemistry (IUPAC) has promoted a large research project to study the properties of different commercially available zirconia electrolytes and to define the conditions for a standard oxygen monitor (40,57).

Fuel Cells and Steam Electrolysers

Fluorite-type solid electrolytes are also useful in fuel cells and in high-temperature steam electrolysis, the principles of operation of which are identical to that of oxygen gauges, as shown on Figure 7. In fuel cells electrical energy is generated by an electrochemical fuel combustion. A gaseous fuel, such as hydrogen or carbon monoxide, is fed to the fuel electrode which is generally provided by a porous nickel or cobalt film, while the air electrode is contacting an oxidizing atmosphere as air or pure oxygen. The difference in oxygen chemical potentials at the electrodes gives rise to an emf and, in the case of a purely ion-conducting electrolyte, the open-cell voltage is deduced from equation 6. In operating conditions, oxygen is reduced at the air electrode to O^{2-} ions which migrate through the electrolyte wall in order to use up the fuel provided at the fuel electrode. The anodic oxidation of the fuel releases electrons which flow back to the cathode through an external circuit, supplying a power generation.

Such a device can also be used as a steam electrolyser without any underlying modification, by reversing all the reaction processes, on applying an electrical potential between the electrodes. The electrons injected in the fuel cathode initiate the steam reduction into hydrogen and oxygen ions which flow in the opposite direction to the air electrode, where they release electrons and oxygen. One can notice that, in both present cases, an oxygen flow is allowed through the electrolyte whereas an oxygen transport generally induces spurious effects in oxygen monitors.

In both systems, fuel cells and electrolysers, stabilized zirconia ceramics are often used as electrolyte wall (41) because of their satisfactory ionic conductivity at operating temperature, of the order of 800° to 1300°C (42). However, their electrical resistance is still high enough to lead to noticeable ohmic losses (43). Thus, as in the case of oxygen sensors, thin-layer fuel cells have been proposed in order to reduce these effects (43). Fuel cells based on electrolytes having higher conductivity, such as doped ceria, have been also developed (44). Nevertheless, it should be noticed that this material may present a significant n-type electronic conductivity which may induce a fuel consumption even in open-cell conditions and hence reduce the cell efficiency. Some investigations have been done on this subject (45,46) and it has been shown (47) that the maximum power output of such cells is in fact only about 3% lower than in the case of purely ionic electrolytes.

Material requirement for the air electrode is also a critical problem owing to oxygen corrosion at high temperature. Contrary to the case of oxygen monitors, platinum electrodes are here rather inaccurate because of their insufficient long-term stability (41). The aim of the present research in this field is to develop metal-oxide electrodes, such as tin-doped indium oxide or electronic conducting perovskites like $LaNiO_3$ or $PrCoO_3$ (41). Several problems, as the adherence of electrodes at the electrolyte surface or their porosity, are also to be solved.

An extended review on the different designs for fuel cells and electrolysers have been reported by Rohr (41). A series of short thin-layer fuel cells deposited on porous supports, overlapping each other by means of an interconnecting material and connected in batteries, appears to be an attractive device. Deviations from ideal behaviour and overvoltage losses due to physical or electrochemical factors have been recently analyzed by Isaacs (43).

HIGH TEMPERATURE APPLICATIONS

Oxygen semipermeable membranes

As previously mentioned, for relatively high temperatures, higher than about 1400°C, solid oxide electrolytes may exhibit a partial electronic conductivity which superimposes on the partial ionic conductivity, the value of which is extrinsically fixed by the dopant oxide content. This phenomenon, which is of minor importance at lower temperature and which is the source of a temperature limitation for the use of oxygen monitors owing to the resulting oxygen flow through the electrolyte, can account for a selective oxygen pumping at high temperature. Thus stabilized zirconia walls have been used as oxygen semipermeable membranes (48). As a general rule, such membranes, which should be impervious to the gaseous components other than oxygen, are characterized by a mixed, ionic and electronic, conductivity and operate under a gradient of oxygen chemical potential. Indeed, as illustrated in Figure 8 , under the appliance of this gradient, the ionic component of the conductivity allows the oxygen to diffuse through the semipermeable membrane as O^{2-} ions; the electronic component ensures an internal partial short circuit which is necessary for the oxygen exchange at the electrolyte-gas interfaces and to avoid any use of external electrodes. The value of the oxygen flow, $J(O_2)$, through the electrolyte may be derived from the diffusion equations (16) and it may be written as (27):

$$J(O_2) = \frac{1}{16\ qFl} \int_0^l \sigma_e \, d\mu O_2 \tag*{/7/}$$

where l is the thickness of the electrolyte wall. In the case of calcia-stabilized zirconia, for low oxygen activities, any contribution of electron holes may be reasonably neglected and the electronic conductivity is given by (17):

$$\sigma_e = \sigma_e^\circ \exp(-\Delta E_e/kT).pO_2^{-1/4} \tag*{/8/}$$

where σ_e° is a constant and ΔE_e the activation energy which amounts to about 4eV (17). So that the oxygen flow may be represented by the following relationship:

$$J(O_2) = \frac{kT}{4qFl} \sigma_e^\circ \exp(-\Delta E_e/kT) \times \left[pO_2(II)^{-1/4} - pO_2(I)^{-1/4}\right] \tag*{/9/}$$

where $pO_2(II)$ and $pO_2(I)$ denote the oxygen partial pressures on each side of the zirconia membrane.

Such an oxygen semipermeable membrane has been recently investigated in the case of hydrogen production by direct thermal decomposition of water at temperatures of the order of 1400°C to 1800°C (49). In such experiments a stabilized zirconia electrolyte, the chemical composition of which was $0.9ZrO_2$-$0.1CaO$, has allowed the extraction of oxygen arising from the steam decomposition thereby avoiding any hydrogen-oxygen recombination at lower temperatures in the colder parts of the apparatus, the schematic arrangement of which is depicted on Figure 9 . The stabilized zirconia membrane, which consists of a closed-ended tube, is centered inside a high temperature furnace. Such a furnace, described in the following section, allows the zirconia wall to be heated up to about 2200°C. Water is injected, by means of steam-saturated argon, inside the zirconia tube, compartment I, in which it dissociates partially. The oxygen partial pressure in the outer part of the electrolyte tube, compartment II, is kept down to a value, $pO_2(II)$, lower than the value of the oxygen pressure, $pO_2(I)$, fixed in dynamical rate by the steam decomposition in compartment I. After migration of the oxygen arising from the thermal water decomposition, hydrogen evolves from compartment I and the hydrogen flow, $D(H_2)$, may be easily related to the oxygen flux $J(O_2)$ per unit area. Effectively, due to stoichiometric considerations and under stationary conditions, $D(H_2)$ is twice the oxygen flow $D(O_2)$ through the total effective permeation area S of the membrane:

$$D(H_2) = 2\ D(O_2) = 2\ J(O_2)\ S$$

In the temperature range between 1400°C and 1800°C, such a process has allowed production of significant amounts of hydrogen. Moreover, the variations of $D(O_2)$ versus the applied gradient of oxygen chemical potential or versus temperature (Fig.10) are in fair agreement with the variations predicted by equation 9. Indeed, one can notice than the 4eV activation energy for the thermal dependence of the semipermeability coefficient $D(O_2)/\left[pO_2(II)^{-1/4} - pO_2(I)^{-1/4}\right]$, corresponds to the activation energy for the electronic conductivity of stabilized zirconia containing 10 mol % CaO (17).

Thus, the oxygen flow appears to be directly controlled by the electronic conductivity of the electrolyte which is yet very small, at operating temperatures, when compared to the ionic component. Some materials, such as the solid solutions of the ZrO_2-CeO_2-Y_2O_3 system (50), appear to be more promising than usual stabilized zirconias, since they are characterized by ionic and electronic conductivities of the same order of magnitude. The use of such compounds as oxygen selective membranes could allow a large increase in the efficiency of the process reported above.

Heating Elements for High Temperature Furnaces

The realization of a high temperature may be a critical problem, particularly in the range higher than

1600°C. Indeed, most of the materials which can be used as heating elements in high temperature furnaces, e.g. graphite, tungsten or molybdenum, are characterized by a very poor chemical inertness with respect to oxygen. Thus, in spite of their high melting point, their use is restricted to the cases of neutral, reducing atmospheres or vacuum. Under oxidizing atmospheres, owing to their rapid corrosion, these materials are inadequate and the maximum temperature attainable with usual high-temperature furnaces, which are based on heating elements made of platinum, silicon carbide or lanthanum chromite, are markedly lower (58). However, the use of refractory oxides as heating elements increases this limit to higher temperatures, of the order of 2000°C to 2400°C. Among these oxides, partially or fully stabilized zirconias are prime candidates owing to their high melting point, about 2700°C, and chemical inertness with respect to many gaseous components. For cost considerations, calcia-stabilized or partially stabilized zirconias are more commonly used, with a calcia content of about 4 to 8 mol %. Nevertheless, it should be observed that stabilized zirconias are insulators at room temperature and their electrical conductivity is strongly thermally activated. Below about 1200°C, the value of the conductivity is still not large enough to ensure a resistive self heating. It is thus necessary to heat the ceramic resistor up to this temperature, with the aid of an external heating device, before attempting direct heating by energy dissipation through ohmic losses in zirconia. The temperature thus obtained, on supplying a.c. power to the zirconia resistor, is a function of the electrical energy, dissipated by Joule effect. The value of the current intensity in the ceramic element should be then carefully regulated in order to prevent a rapid raising of temperature up to the melting point of the resistor. Indeed, for a given applied a.c. voltage the more the temperature increases, the more the electrical resistivity of stabilized zirconia decreases and hence the more the current intensity increases.

The preheating device, which may be either a platinum or a kanthal-Al furnace, should be effectively shielded from the radiative heat of the ceramic heating element at high temperature, higher than 1200°C, by means of a series of thermal screens made of zirconia or alumina bricks or felts. The thickness of this insulating wall should be elsewhere carefully adjusted in order to preserve the preheating effects on the ceramic resistor. A major problem is the power delivery to the zirconia heating element, which is usually made via platinum or lanthanum chromite. Taking the melting point of these compounds and their mechanical or chemical properties at high temperature into account, the temperature of the electrical contacts must not exceed about 1500°C (51).

This can be achieved by cutting the zirconia heating element into an appropriate form which allows dissipation of a smaller quantity of energy at the extremities than in the middle part (52). A typical arrangement of the heating and preheating elements is depicted on Figure 11.

Finally, it should be mentioned that in comparison with usual refractory metals, refractory oxides are generally characterized by rather poor thermomechanical properties. This is particularly the case of calcia-stabilized zirconias which are very sensitive to thermal shocks or to large temperature gradients. The shape of the heating element is then adjusted in order to minimize the thermomechanical stresses and to avoid failures of the ceramic material (51). On these bases, two kinds of zirconia resistors have been developed.

The first one, which consists in a single piece material directly cut from a relatively "dense" stabilized zirconia, with a porosity of about 20%, into a typical form as shown on Figure 11, is more appropriate for small laboratory furnaces (53) or furnaces for very specific applications (52).

Another kind is obtained on using stabilized zirconias with a higher porosity, about 50%, and by stacking elementary heating modules (54) as shown on Figure 12. This technique allows one to increase the size of the furnace chamber up to one litre or more (58) and owing to their better mechanical behaviour, such heating elements can also be used in combination with a flame-furnace preheating device. Furnaces built on this principle may be useful for industrial needs as for instance optical fiber manufacturing (55).

Some characteristics of the different types of furnaces based on zirconia resistors are reported and compared on Table I.

TABLE I

	Laboratory furnace	Space applications furnace	Industrial furnace
Maximum temperature	2400°C	2000°C	1900°C
Temperature range	1600 to 2200°C	1600 to 2000°C	1500 to 1900°C
Lifetime 1800°C	10000 h	1000 h	5000 h
Energy consumption $50 cm^3$ - 2000°C	1200 W	300 W	1200 W
Insulating material	Felt	Advanced felt	Brick
Preheating device	Electric (platinum, kanthal)	Electric (platinum)	Electric (platinum), Flame
Chamber size ±20°C- 2000°C	50 to 100 cm^3	10 to 50 cm^3	1000 to 10000 cm^3

REFERENCES

(1) D. Steele and B.E.F. Fender, "The structure of cubic ZrO_2-$YO_{1.5}$ solid solutions by neutron scattering" J Phys C 7:1-11; 1974.

(2) S.T. Buljan, H.A. McKinstry and V.S. Stubican, "Optical and X-ray single crystal studies of the monoclinic-tetragonal transition in ZrO_2" J Am Ceram Soc 59:351-354; 1976.

(3) D. Viechnicki and V.S. Stubican, "Phase studies with the system ZrO_2-MgO" J Am Ceram Soc 48:292-297; 1965.

(4) E.C. Subbarao, "Zirconia - an overview" Science and Technology of Zirconia, A.H. Heuer and L.W. Hobbs Eds., The American Ceramic Society, Columbus, Ohio; 1981.

(5) M. Morinaga, J.B. Cohen and J. Faber, "X-ray diffraction study of zirconium calcium yttrium oxide" Acta Cryst A35:789-795; 1979.

(6) J. Stocker, Bull Soc Chim Fr 78; 1961.

(7) T.H. Etsell and S.N. Flengas, "The electrical properties of solid oxide electrolytes" Chem Rev 70: 339-376; 1970.

(8) V.S. Stubican and S.P. Ray, "Phase equilibria and ordering in the system ZrO_2-CaO" J Am Ceram Soc 60:534-537; 1977.

(9) V.S. Stubican, R.C. Hink and S.P. Ray, "Phase equilibria and ordering in the system ZrO_2-Y_2O_3" J Am Ceram Soc 61:17-21; 1978.

(10) W.H. Rhodes and R.E. Carter, "Cationic self-diffusion in calcia-stabilized zirconia" J Am Ceram Soc 49:244-249; 1966.

(11) H.J. Rossell, "Ordering in anion-deficient fluorite related oxides" Ref. 4.

(12) R.M. Dell and A. Hooper, "Oxygen ion conductors" Solid Electrolytes, P. Hagenmuller and W. van Gool Eds., Academic Press, New York; 1978.

(13) F.A. Kröger and H.J. Vink, "Relations between the concentrations of imperfections in crystalline solids" Solid State Physics Vol.3, F. Seitz and D. Turnbull Eds., Academic Press, New York; 1956.

(14) J.F. Baumard, "Point defects in ceramics" Encyclopedia of Materials Science and Engineering, M.B. Bever Ed., to be published in 1982 by Pergamon Press.

(15) G. Brouwer, "A general asymptotic solution of reaction equations common in solid state chemistry" Phillips Res Rep 9:366-376; 1954.

(16) P. Kofstad, "Diffusion and electrical conductivity" Nonstoichiometry, Diffusion and Electrical Conductivity in Binary Metal Oxides, Wiley Interscience, New York; 1972.

(17) L. Heyne and N.M. Beekmans, "Electronic transport in calcia-stabilized zirconia" Proc Brit Ceram Soc 19:229-263; 1971.

(18) J.W. Patterson, "Conduction domains for solid electrolytes" J Electrochem Soc 118:1033-1039; 1971.

(19) M.F. Lasker and R.A. Rapp, "Mixed conduction in ThO_2 and $ThO_2-Y_2O_3$ solutions" Z Physik Chem Neue Folge 49:198-221; 1966.

(20) H.L. Tuller and A.S. Nowick, "Doped ceria as a solid electrolyte" J Electrochem Soc 122:255-259; 1975.

(21) P. Abelard and J.F. Baumard, "Study of the dc and ac electrical properties of a stabilized zirconia single crystal" Phys Rev B 26:1005-1017; 1982.

(22) M. Kleitz, E. Fernandez, J. Fouletier and P. Fabry, "Determination of electronic conductivities and ionic domains of $ZrO_2-Y_2O_3$ by semipermeability measurements" Ref. 4 .

(23) R.N. Blumenthal, F.S. Brugner and J.E. Garnier, " The electrical conductivity of Ca-doped nonstoichiometric cerium dioxide from 700° to 1500°C" J Electrochem Soc 120:1230-1237; 1973.

(24) A. Nakamura and J.B. Wagner, "Defect structure, ionic conductivity and diffusion in calcia stabilized zirconia" J Electrochem Soc 127:2325-2335; 1980.

(25) H. Schmalzried, "On correlation effects of vacancies in ionic crystals" Z Physik Chem Neue Folge 105:47-62; 1977.

(26) E. Schouler, G. Giroud and M. Kleitz, "Study of the conductivity of yttria-stabilized zirconia" J Chim Phys 70:1309-1316; 1973.

(27) L. Heyne, "Mass transport in oxides" Special Publi-

cation 296, National Bureau of Standards, Washington; 1968.

(28) E.M. Logothetis, "ZrO_2 sensors in automotive applications" Ref.4 .

(29) W.A. Fischer and D. Janke, "Electrochemical determination of the oxygen partial pressure in iron melts containing oxygen" Arch Eisenhüttenwes 39: 89-99; 1968.

(30) J. Fouletier, "New method for the study of oxide solid electrolyte cells with the aid of oxygen gauges and pumps" Thesis, Grenoble, France; 1976.

(31) R.T. Dirstine, W.O. Gentry, R.N. Blumenthal and W. Hammetter, "Calcia-doped ceria ceramic tubes for low temperature oxygen sensors" Ceram Bull 58:778-783; 1979.

(32) J. D. Tretyakov and A. Muan, "A new cell for electrochemical studies at elevated temperatures" J Electrochem Soc 116:331-334; 1969.

(33) S. Pizzini, "General aspects of kinetics of ion-transfer across interfaces Fast Ion Transport in Solids, W. van Gool Ed., North-Holland, Amsterdam; 1973.

(34) M. Iwase and T. Mori, "Oxygen permeability of calcia stabilized zirconia at low oxygen partial pressures" Metall Trans 9B:653-656; 1978.

(35) M. Gauthier, A. Belanger, Y. Meas and M. Kleitz, " Solid state potentiometric gauges for gaseous species" Ref.12 .

(36) L.J.Olmer and H.S. Isaacs, "The effect of electrode surface impurities on the oxygen electrode reaction at zirconia electrolytes" J Electrochem Soc 129: 345-347; 1982.

(37) G. Vitter, "Electrochemical oxygen gauges for industrial controls" Thesis, Grenoble, France; 1980.

(38) M. Croset, P. Schnell and G. Velasco, "Study of calcia-stabilized zirconia thin film sensors" J Vac Sci Technol 14:777-781; 1977.

(39) H. Dietz, "Gas-diffusion-controlled solid-electrolyte oxygen sensors" Solid State Ionics 6:175-183; 1982.

(40) B.C.H. Steele, J. Drennan, R.K. Slotwinski,

N. Bonanos and E.P. Butler, "Factors influencing the performance of zirconia-based oxygen monitors" Ref.4 .

(41) F.J. Rohr, "High temperature fuel cells" Ref.12 .

(42) E. Schouler, E. Fernandez and H. Bernard, "High temperature steam electrolysis" Rev Gen Elect 3: 193-199; 1982.

(43) H.S. Isaacs, "Zirconia fuel cells and electrolysers" Ref.4 .

(44) D. Singman, "Preliminary evaluation of ceria- lanthana as a solid electrolyte for fuel cells" J Electrochem Soc 113:502-504; 1966.

(45) P.N. Ross and T.G. Benjamin, "Thermal efficiency of solid electrolyte fuel cells with mixed conduction" J Power Sources 1:311-321; 1976/77.

(46) D.S. Tannhauser, "The theoretical energy conversion efficiency of a high temperature fuel cell based on a mixed conductor" J Electrochem Soc 125:1277-1282; 1978.

(47) I. Riess,"Theoretical treatment of the transport equations for electrons and ions in a mixed conductor" J Electrochem Soc 128:2077-2081; 1981.

(48) M. Iwase, M. Tanida, A. McLean and T. Mori, "Electronically driven transport of oxygen from liquid iron to $CO-CO_2$ mixtures through stabilized zirconia" Metall Trans 12B:517-524; 1981.

(49) A. Ounalli, B. Calès, K. Dembinski and J.F. Baumard, "Hydrogen production by direct thermolysis of water on semipermeable membrane" C R Acad Sci Paris II 292:1185-1190; 1981.

(50) B. Calès and J.F. Baumard, "Electrical properties of the ternary solid solutions $[(1-x)ZrO_2-xCeO_2]0.9-[Y_2O_3]0.1$ $(0 \leq X \leq 1)$" Rev Int Htes Temp Refract 17: 137-147; 1980.

(51) A.M. Anthony, "High temperature heating elements in oxidizing atmospheres" Ref.12 .

(52) A.M. Anthony, K. Dembinski, J.L. Dunand, L. Dupont and R. Mottu, "Adaptation to space applications of a 2000°C furnace in oxidizing atmosphere" Ceram Int 3:29-33; 1977.

(53) D. Billard and K. Dembinski, "Small laboratory

furnace, 2300 K in oxidizing atmosphere" Rev Phys Appl 14:977-984; 1979.

(54) D. Pavy, "Contribution to the development of zirconia furnace elements for industrial needs" Thesis, Orléans, France; 1979.

(55) R. Viladrosa, L. Dupont, A. Dumas, S. Baudet and A.M. Anthony, "Furnace with temperature gradients for crystal growth and non crystalline fiber manufacturing" Verres Refract 31:15-19; 1977.

(56) A.M. Anthony, A. Guillot, T. Sata and J.L. Bourgeois, "Electrical conductivity of pure and doped zirconia between 1500 and 2500 K" Rev Int Htes Temp Refract 3:157-165; 1966.

(57) A.M. Anthony, J.F. Baumard and J. Corish, to be published in Pure Appl Chem.

(58) A.M. Anthony, "High temperature refractory applications of zirconia" Ref. 4.

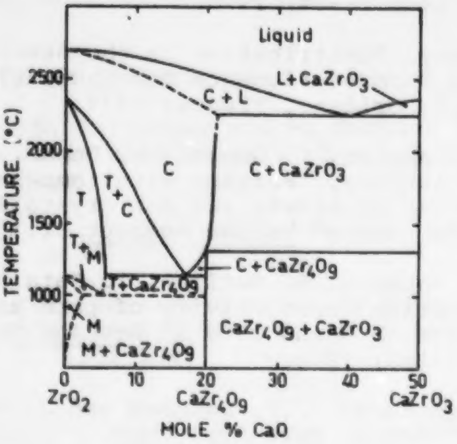

Fig. 1 - Phase diagram for the system ZrO_2-CaO (8). Reprinted by permission of the publisher; The American Ceramic Society, Inc.

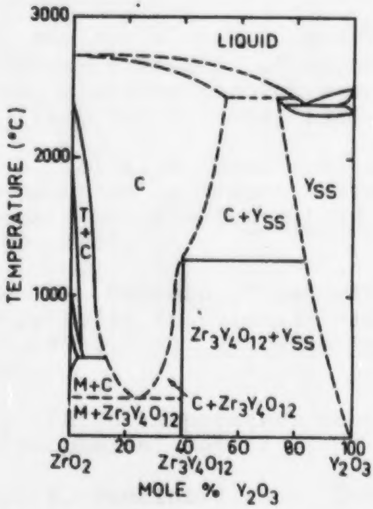

Fig. 2 - Phase diagram for the system ZrO_2-Y_2O_3 (9). Reprinted by permission of the publisher; The American Ceramic Society, Inc.

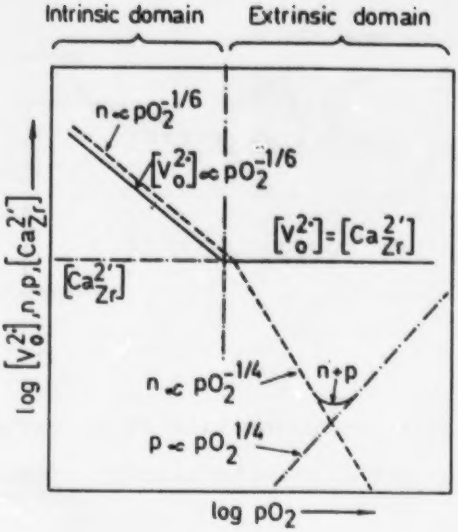
Intrinsic domain
Extrinsic domain
$n \propto pO_2^{-1/6}$
$[V_o^{2\cdot}] \propto pO_2^{-1/6}$
$[V_o^{2\cdot}] = [Ca_{Zr}^{2'}]$
$[Ca_{Zr}^{2'}]$
$n \propto pO_2^{-1/4}$
$n+p$
$p \propto pO_2^{1/4}$
$\log [V_o^{2\cdot}], n, p, [Ca_{Zr}^{2'}]$ →
$\log pO_2$ →

Fig. 3 - Brouwer's diagram for isothermal variations of electronic and atomic defects in calcia-stabilized zirconia.

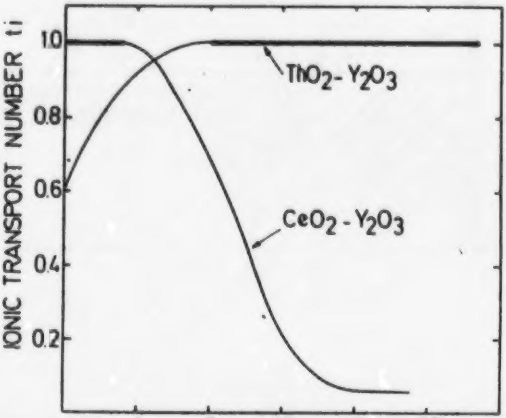

Fig. 4 - Ionic transport number t_i vs oxygen partial pressure for CeO_2-Y_2O_3 (5 mol%) and ThO_2-Y_2O_3 (6 mol%) (19,20).

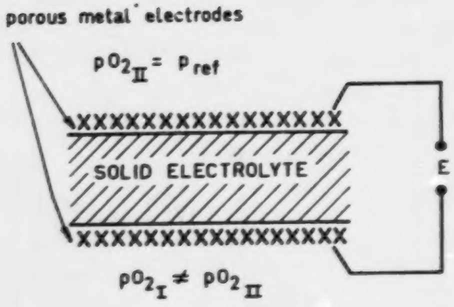
porous metal electrodes
$pO_{2_{II}} = p_{ref}$
SOLID ELECTROLYTE
E
$pO_{2_I} \neq pO_{2_{II}}$

Fig. 5 - Schematic representation of an oxygen galvanic cell.

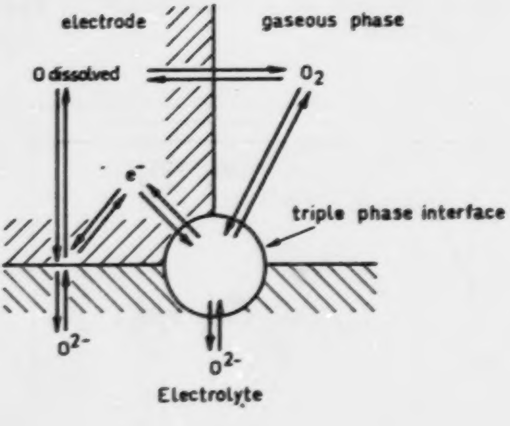
electrode
gaseous phase
O dissolved
O_2
e^-
triple phase interface
O^{2-}
O^{2-}
Electrolyte

Fig. 6 - Schematic illustration of oxygen electrode reactions; after (33).

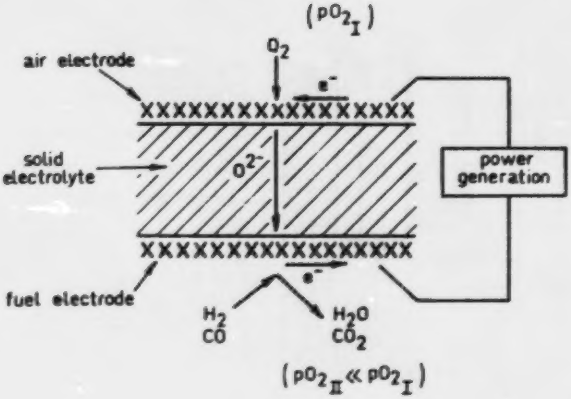
(pO_{2_I})
O_2
air electrode
e^-
solid electrolyte
O^{2-}
power generation
fuel electrode
e^-
H_2
CO
H_2O
CO_2
($pO_{2_{II}} \ll pO_{2_I}$)

Fig. 7 - Schematic representation of a high-temperature fuel cell.

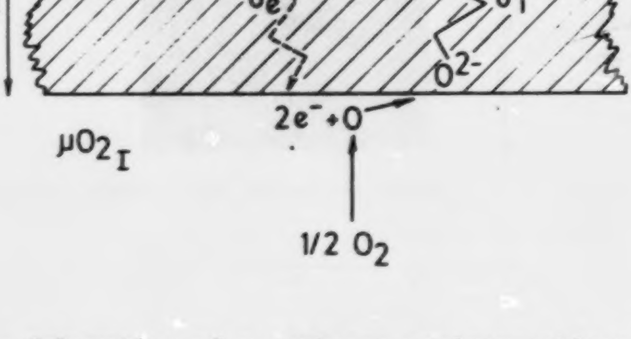
1/2 O_2
$\mu O_{2_{II}} < \mu O_{2_I}$
$2e^- + O \leftarrow O^{2-}$
semipermeable membrane
l
σ_e
σ_i
O^{2-}
$2e^- + O$
μO_{2_I}
1/2 O_2

Fig. 8 - Schematics of a membrane semipermeable to oxygen.

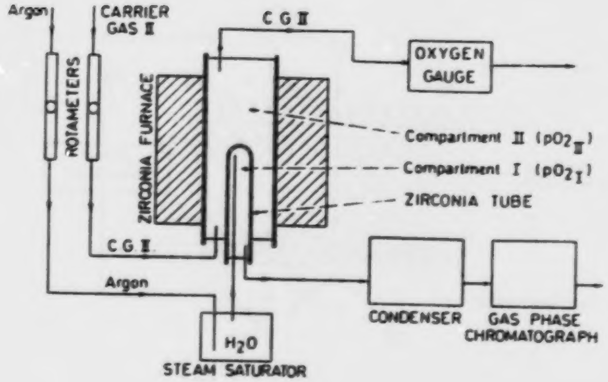
Argon
CARRIER GAS II
C G II
OXYGEN GAUGE
ROTAMETERS
ZIRCONIA FURNACE
Compartment II ($pO_{2_{II}}$)
Compartment I ($pO_{2_{I}}$)
ZIRCONIA TUBE
C G II
Argon
H_2O
STEAM SATURATOR
CONDENSER
GAS PHASE CHROMATOGRAPH

Fig. 9 - Schematic arrangement of the apparatus for steam thermolysis.

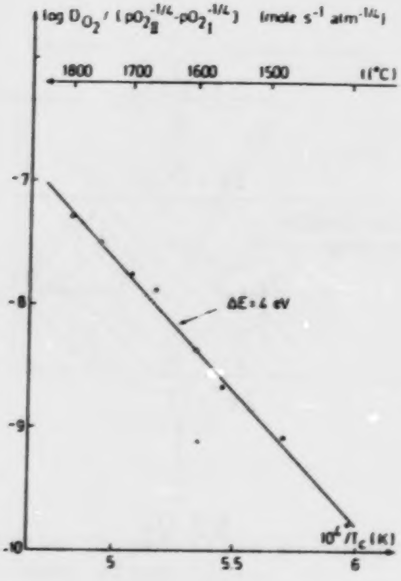

Fig. 10 - Temperature dependence of the semipermeability coefficient $DO_2/[pO_2(II)^{-1/4} - pO_2(I)^{-1/4}]$.

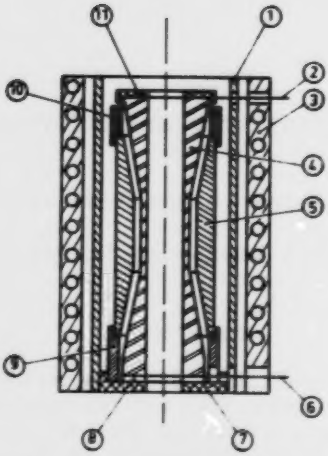

Fig. 11 - Arrangement of zirconia heating and preheating elements. ②⑥:platinum electrodes and electrical leads, ③:preheating device, ④:stabilized zirconia resistor, ①⑤⑦ - ⑪ :insulating and centering elements.

Fig. 12 - Furnace for industrial needs.

KINETIC INVESTIGATIONS WITH SOLID ELECTROLYTES

H. Rickert and G. Holzäpfel

University of Dortmund, F.R. Germany

ABSTRACT

Galvanic cells using solid electrolytes have become increasingly important in the study of the kinetics of reactions in solids and at their surface. This is because cells based on ionically conducting solid electrolytes provide information on reaction rates by measurement of the current flow through suitably built cells in addition to the thermodynamic data such as Gibbs free energies, chemical potentials, partial pressures and the activities of certain species by emf measurements. The combination of reaction rate measurements via electric current with determinations of thermodynamic quantities via the emf often permits the analysis of kinetic processes. Kinetic studies with solid state galvanic cells involve diffusion processes or diffusion controlled reactions and reactions occurring at solid/gas or solid/solid phase boundaries respectively.

The use of solid electrolytes in kinetic studies is reviewed and data are presented on the following topics:

- Diffusion processes in solid and liquid metals and compounds.
- Solid state reactions that result in new compounds.
- Reactions at solid/gas and solid/solid phase boundaries.

KEYWORDS: kinetics, galvanic cells, solid-state reactions, diffusion, phase-boundary reactions.

RÉSUMÉ

Les cellules galvaniques munies d'électrolytes solides ont pris de l'importance dans l'étude de la cinétique des réactions à l'intérieur et à la surface des solides, puisque les cellules fondées sur des électrolytes solids conducteurs d'ions fournissent des renseignements sur la vitesse des réactions en mesurant le flux du courant dans les cellules appropriées ainsi que des données thermodynamiques comme les énergies libres de Gibbs, les potentiels chimiques, les pressions partielles et les activités de certaines espèces en mesurant la force électromotrice. La combinaison de la détermination des vitesses de réaction au moyen d'un courant électrique et des quantités thermodynamiques grâce à la fem permet souvent d'analyser les procédés cinétiques. L'étude de la cinétique au moyen de cellules galvaniques à l'état solide comprend des procédés de diffusion ou des réactions contrôlées par la diffusion et des réactions qui ont lieu aux couches limites des phases solid/gaz ou solide/solide, respectivement.

Les auteurs résument l'utilisation des électrolytes solides pour l'étude de la cinétique et présentent des données sur les sujets suivants:

- procédés de diffusion dans les métaux et les composés et liquides;
- réactions à l'état solide qui ont pour résultat la formation de nouveaux composés;
- réactions aux couches limites des phases solide/gaz et solide/solide.

INTRODUCTION

The existence of solid ionic conductors has made it possible to construct galvanic cells with solid electrolytes. In the electrochemistry of solids such cells play a most important role for thermodynamic as well as for kinetic investigations.

The emf of such cells gives information about thermodynamic quantities such as e.g. Gibbs energies, chemical potentials, thermodynamic activities or partial pressures of certain species.

The kinetic information obtained from galvanic cells with solid electrolytes arises from the fact that the current flowing through the cell is a measure of the rate with which certain species are moving from one side of the cell to the other. The relation between the particle flux J, which gives the rate of transport of the ionic species (with the valency z) in moles through the solid electrolyte of the cell, and the electrical current I passing through the cell is given by

$$J = \frac{I}{zF} \tag{1}$$

In this case it is assumed that the transference number of the species considered is equal to one. F is the Faraday-constant. The transport of matter through the cell can often be attributed to a chemical reaction in a general sense at one electrode, e.g., to diffusion processes, diffusion-controlled reactions or phase-boundary reactions. These processes can then be studied by measuring the electrical current flowing through the cell. The combination of the determination of reaction rates via measuring currents and of thermodynamic quantities via simultaneously measuring emf's often enables a detailed analysis of a reaction mechanism.

Kinetic measurements can be carried out in different ways. In the case of zero current measurements the electrical potential difference between the two end phases of the cell is measured under open circuit conditions. Information about thermodynamic quantities of reaction systems, e.g. about chemical potentials, activities or partial pressures, are obtained from such measurements. An important application of this method is for example the determination and control of oxygen partial pressures using ZrO_2-sensors in combustion processes within or behind combustion chambers, e.g., in Otto-engines or furnaces. Since the method is simply an emf-measurement it will not be discussed here in more detail.

In the case of measurements under steady state conditions there is no time dependence of currents and potentials. Therefore it is experimentally unimportant whether the potentials or the currents are controlled. Here the steady-state current which represents a reaction rate may be measured as a function of the potential or vice versa.

Generally one obtains more information in investigations where the current or the potential changes with time while the other parameter is kept constant.

If a constant potential difference is applied to the cell and the resulting current is measured as a function of time, the investigations are called "potentiostatic".

If a constant current is passed through the cell and the resulting potential difference is measured as a function of time the investigations are called "galvanostatic".

If galvanostatic or potentiostatic measurements or investigations under steady-state conditions are carried out it is often preferable to use separate cells of the same type under zero current to measure potential differences, so that the reference electrode is not polarized by a current. In the following the potentiostatic and galvanostatic techniques will be described in more detail using various examples. The results obtained by applying these techniques for kinetic investigations with the aid of galvanic cells containing solid electrolytes will be reviewed. The material presented is ordered according to the following main topics:

1. Diffusion processes in solid and liquid metals and compounds.
2. Solid-state reactions leading to the formation of new compounds.
3. Phase-boundary reactions at the phase boundaries solid/gas and solid/solid.

Measurements of ionic and electronic partial conductivities will not be discussed in this paper.

Some other review articles on kinetic investigations using solid electrolytes already exist in the literature (1-8). The reader is referred to these for further studies.

DIFFUSION PROCESSES IN SOLID AND LIQUID METALS AND IN COMPOUNDS

Electrochemical measurements of oxygen diffusion in solid and liquid metals

Principle

The galvanic cell generally used for this measurement is of the type

$$a_O', \mathrm{Pt} \overset{'}{|} \mathrm{ZrO_2(+Y_2O_3)} \overset{''}{|} \mathrm{Me+O(dissolved),\ Pt} \qquad (I)$$

where Y_2O_3-doped ZrO_2 is a solid ionic conductor with virtually pure oxygen-ion conductivity (9). The left hand electrode is a reversible electrode which has to establish a constant reference oxygen activity a_O'. It may consist, e.g., of porous Pt in contact with air or of a metal/metal-oxide mixture which also fixes a reference oxygen activity. The right-hand electrode is the one to be investigated. It consists of the metal containing dissolved oxygen.

The thermodynamic property of the cell is given by its emf E which is related to the activities a_O' and a_O'' on both sides of the cell by the equation:

$$E = \frac{RT}{2F} \ln \frac{a_O''}{a_O'} \qquad (2)$$

According to this equation the activity a_O'' of oxygen can be determined if a_O' is known.

The kinetic property of the cell follows from equation (1) which may be rewritten in the form

$$j_{O^{2-}} = \frac{i}{2F} \qquad (3)$$

where $j_{O^{2-}}$ and i are the particle flux rate and the current density respectively. The current of oxygen ions gives the rate of adding or removing oxygen into or out of the right-hand electrode, i.e., it gives the diffusion current which is therefore equivalent to the measurable electrical current flowing through the cell. Evaluation of the diffusion coefficient depends on the method chosen for the investigation.

Potentiostatic method

The principle of the potentiostatic method for studying oxygen diffusion is to change the oxygen concentration in the metal at the phase boundary metal/solid electrolyte from a well defined initial value to another one by a sudden application of a fixed potential. Then the interesting kinetic parameter, in this case the diffusion coefficient of oxygen in the metal, can be evaluated from the observed current-time relationship. For example, a silver sample containing dissolved oxygen may be placed on one side of the solid electrolyte doped zirconia; on the other side of this electrolyte there may be a virtually unpolarizable Fe/FeO electrode fixing the oxygen partial pressure at this site. The following cell can thus be used (10):

$$\mathrm{Fe,FeO} \mid \mathrm{ZrO_2(+Y_2O_3)} \mid \mathrm{Ag+O(dissolved)} \qquad \text{(II)}$$

At the beginning the silver contains dissolved oxygen with the concentration $c = c_o$. By applying a potential of about 100 mV to cell (II) with the negative pole at the silver an oxygen activity at the phase boundary $Ag/ZrO_2(+Y_2O_3)$ is stipulated which is still smaller than the oxygen activity corresponding to the equilibrium of Fe/FeO. In this way the oxygen concentration at the phase boundary $Ag/ZrO_2(+Y_2O_3)$ is kept at approximately zero. An arrangement shown in Fig. 1, involving a plane silver electrode, a doped zirconia pellet and a Fe/FeO pellet, may be used. In this case linear diffusion into a semi-infinite phase occurs whereby the following solution of the diffusion equation applies for the current density i:

$$i = |2Fj_{O^{2-}}| = 2\,F\,\frac{c_o\sqrt{D}}{\sqrt{\pi t}} \qquad (4)$$

Here t denotes the time and D the diffusion coefficient of the oxygen in silver.

According to equation (4) the electrical current density i is proportional to $t^{-1/2}$, i.e., a plot of i versus $t^{-1/2}$ allows the calculation of the diffusion coefficient D if the initial concentration c_o is known.

Using a configuration allowing radial diffusion, which can be achieved with a doped zirconia electrolyte-tube containing the cylindrical silver sample and air as reference electrode as shown in Fig. 2, it is possible to calculate the diffusion coefficient of oxygen without prior knowledge of the oxygen solubility (11).

The basic principles of the measurements are the same as described in the case of linear geometry. By applying a potential of about 900 - 1000 mV with the negative pole at the silver, the oxygen concentration at the phase boundary $Ag/ZrO_2(+Y_2O_3)$ is kept at approximately zero and in this arrangement oxygen diffuses in a radial direction from the cylinder axis to the electrolyte tube. Solution of the diffusion equation for longer times t leads to the following expression for the current I as a function of the time t:

$$I(t) \ = \ A \exp(-\ t/\tau) \qquad (5)$$

Here A is a constant and τ the time constant which is given by $\tau = a^2/2{,}402^2\ D$, where a denotes the radius of the silver cylinder. From the slope of a logarithmic plot of current I versus time, the time constant τ can be obtained and from this one can calculate the diffusion coefficient of oxygen without knowledge of the solubility in this case.

Galvanostatic method

The principle of the galvanostatic method is to apply a constant current-density i_o to cell (II) due to which a constant diffusion current occurs (12). According to Fick's first law the flowing constant current stipulates a constant gradient of the concentration of oxygen at the phase boundary $Ag/ZrO_2(+Y_2O_3)$, the concentration itself diminishes with time. The time when it has reached zero is called transition time τ. It is indicated by a strong change of the measured potential.

Here the same symbol τ is used for the transition time as was used for the time constant in the potentiostatic section, but of course the meaning of both is quite different.

From the measurement of the potential-time relationship it is possible to calculate diffusion coefficients. If linear diffusion into a semi-infinite space is assumed the solution of the corresponding diffusion equations leads to the following relation for the potential E of cell (II):

$$E = E^o + RT\ \frac{\tau^{1/2} - t^{1/2}}{\tau^{1/2}} \qquad (6)$$

E^o denotes the potential at the beginning of the experiment when the oxygen concentration is c^o, and τ the transition time which is given by

$$\tau^{1/2} \ = \ \frac{z\ F\ \pi^{1/2}\ D^{1/2}\ c^o}{2\ i_o} \qquad (7)$$

z, the valency, is in this case equal to 2.

From the measurement of the transition time the product $D^{1/2}\ c^o$ can be calculated. Equations (6) and (7) are also valid in the case of radial diffusion for short times where the diffusion only takes place in a thin layer of the metal next to the zirconium dioxide/

metal phase boundary. With the help of the methods described above many diffusion coefficients of oxygen in different liquid and solid metals have been obtained. They are listed in Table 1 (10-27).

Measurements of chemical diffusion coefficients

The process of attaining a uniform composition which occurs in compounds where an existing gradient of stoichiometry is allowed to equalize can be described by the chemical diffusion coefficient $\tilde{D}$. For such equilibration processes it is necessary, on the grounds of electrical neutrality, that both ions and electrons or electron defects must migrate simultaneously whereby the fluxes of ions and electrons are related to one another. The electrochemical method for the determination of chemical diffusion coefficients $\tilde{D}$ will be shown for the mixed conductors FeO and Ag_2S. The basic element for the investigation of wüstite $Fe_{1-\delta}O$ (28,29) (δ = deviation from ideal stoichiometry) is the solid state galvanic cell

$$p'_{O_2}, \text{Pt} \mid ZrO_2(+Y_2O_3) \mid Fe_{1-\delta}O \mid \text{Pt} \qquad \text{(III)}$$

with doped ZrO_2 as solid electrolyte, an electrode consisting of porous platinum in contact with air at one side and the wüstite being investigated as electrode at the other side. The experimental set-up is shown in Fig. 3. The principle of the measurement is that, starting from a suitable initial state, the potential difference E of cell (III) or the current I, respectively are varied systematically. The other variable I or E is measured as a function of time. From the obtained results the chemical diffusion coefficient $\tilde{D}$ of wüstite can be calculated. In a potentiostatic experiment a definite value of a chemical potential of oxygen, corresponding to a certain deviation δ from the ideal stoichiometry, is set up in the wüstite before starting the measurement. Then a sudden change of the potential of the cell stipulated potentiostatically causes a current flow which is measured as a function of time. This current is primarily a measure of the addition or removal of oxygen at the phase boundary ZrO_2/wüstite. As a consequence of this iron diffuses whithin the wüstite to or from the phase boundary. Thus the current is equivalent to the diffusion current of iron. During this process the stoichiometry in the compound changes with time until a new δ-value is attained. From the solution of the diffusion equations for this problem the following relation for the time dependence of the electrical current density i is obtained:

$$i = \frac{2e\sqrt{\tilde{D}}(c'' - c')}{\sqrt{\pi t}} \quad \text{for } t \ll \frac{l^2}{\tilde{D}} \qquad (8)$$

Here c" and c' denote the concentrations of the metal at the phase boundary $ZrO_2/Fe_{1-\delta}O$, before and after starting the potentiostatic experiment, l is the length of the wüstite sample and e the elementary charge.

A plot of i versus $1/\sqrt{t}$ yields the information about the chemical diffusion coefficient.

Such a plot is shown in Fig. 4 for $\delta = 0{,}106$ and $T = 1000°C$.

For longer times $t > l^2/4\tilde{D}$ the following expression is valid:

$$\log i = \log \frac{4e\tilde{D}(c''-c')}{l} - \frac{1.071\ \tilde{D}}{l^2}\ t \qquad (9)$$

In this case the current decreases exponentially. From the slopes of the straight lines resulting from a log i versus t plot the chemical diffusion coefficient can be determined, even without knowledge of the concentration difference (c"-c'). The intercept on the ordinate axis can also be used for the determination of $\tilde{D}$ where, however, the knowledge of (c"-c') is necessary. The results obtained for the chemical diffusion coefficient of wüstite at 1000°C and a deviation $\delta = 0{,}106$ from ideal stoichiometry are $\tilde{D} = 3{,}4\cdot10^{-6}\ cm^2\ s^{-1}$ (for short times), $\tilde{D} = 3{,}2\cdot10^{-6}\ cm^2\ s^{-1}$ (for long times) and $\tilde{D} = 3{,}2\cdot10^{-6}\ cm^2\ s^{-1}$ (from the intercept on the ordinate axis).

For the determination of the chemical diffusion coefficient of $Ag_{2+\delta}S$ in equilibrium with liquid sulfur the following galvanic cell can be used:

$$\underset{\text{Pt}}{\text{Pt} \mid \text{Ag} \mid \text{AgI} \mid \text{Ag}_2\text{S} \mid \text{S(l)}} \qquad (IV)$$

To set up a stationary concentration gradient of silver within the Ag_2S-sample between the phase boundaries $Ag_{2+\delta}S/AgI$ and $Ag_{2+\delta}S/S(l)$ a constant current or a constant potential is applied to cell (IV). Then the external circuit is disconnected and the time dependence of the potential of the cell is measured. This gives the change of the chemical potential of silver and thus the change of the Ag-concentration by using information obtained from coulometric titration curves

(30,31). From the solution of the corresponding diffusion equation one obtains for the concentration c of Ag in Ag_2S as a function of time at the above mentioned interface:

$$c = c'' - 2 \frac{(c''-c')}{l} \left(\frac{\tilde{D}t}{\pi}\right)^{1/2} \quad \text{for } t \ll \frac{4l^2}{\pi^2 \tilde{D}} \qquad (10)$$

Here c' and c" denote the concentrations of silver in Ag_2S at the phase boundaries $Ag_{2+\delta}S/S(l)$ and $Ag_{2+\delta}S/AgI$ respectively starting from the time when the external circuit is disconnected. A plot of (c-c") versus $\sqrt{t}$ which is shown in Fig. 5 allows the calculation of the chemical diffusion coefficient. At 200°C a value of 0,47 cm^2/s was obtained.

By the use of an improved experimental set-up shown in Fig. 6 the chemical diffusion coefficient $\tilde{D}$ can be determined over the total range of stoichiometric composition of $Ag_{2+\delta}S$ (32). As can be seen the experimental set-up consists of 4 galvanic cells of the type

$$Pt \mid Ag \mid AgI \mid Ag_{2+\delta}S \mid Pt \qquad (V)$$

With the help of a potentiostat and the cells at the right-hand side of the Ag_2S sample, which is a cylindrical rod about 10 cm long, the chemical potential of the silver at this side of the Ag_2S is fixed. By a current flow through one cell at the left-hand side silver can be either added to or withdrawn from this side of the sample. Under steady-state conditions the removal or addition of silver from or to the right-hand side of the sample attains the same rate. Thus an activity gradient of silver is established along the Ag_2S rod in the stationary state. If the difference of the silver activities between both ends of the sample is small, i.e., there is only a small potential difference, one can assume an approximately linear variation of the silver concentration along the sample. For the measurement the current circuit at the left-hand side of the sample is disconnected and the time dependence of the potential of the cell is measured. In this case the solution of the diffusion equation is the same as above given by equation (10). The chemical diffusion coefficient $\tilde{D}$ of $Ag_{2+\delta}S$ measured at 200 and 300°C as a function of the deviation   from ideal stoichiometry are shown in Fig. 7. Further electrochemical measurements have been performed among others on the following solid compounds (partly with molten salt-electrolytes):

Ag_2Se (33), $Cu_xMo_6S_{7,59}$ ($1,5 < x < 3,6$) (34), Cu_2S (35), $Li_{1-\delta}Al$ (36), Li_3Bi (37), Li_3Sb (38), $Li_{1-\delta}Ga$ (39). Relaxation measurements on Ag_2S without calculating the chemical diffusion coefficient have also been carried out (40,41). An extension of the theory to larger applied potentials has also been developed (42).

SOLID STATE REACTIONS LEADING TO THE FORMATION OF NEW COMPOUNDS

Solid state reactions due to which new compounds are formed are for example oxidation of metals with oxygen, sulfur or halogens at higher temperatures. The solid reaction products formed grow at the surface of the metal. Since the metal and the oxidant are separated by the tarnishing layer the following reaction steps are involved: the transfer of metal across the phase boundary metal/solid metal compound, the diffusion of cations or anions and electrons or electron defects through the reaction layer and the incorporation of the oxidant at the phase boundary reaction product/ oxidant.

The interaction between these reaction steps determines the rate law for the formation of the new compound. There exist different rate laws to describe the connection between the thickness ΔX of the new compound and the time t at constant chemical potential or activity of the oxidant.

Most important are:

a) the linear rate law:

$$\Delta X = kt$$

where k denotes a constant.

This rate law is valid if one or several reactions at phase boundaries are rate determining. Examples are the reaction of iron in CO/CO_2 mixtures at 900°C (43, 44) and the initial reaction of silver with liquid sulfur where the rate-determining step is the reaction at the interface silver/silver sulfide (45,46).

b) the parabolic rate law which was first observed by Tammann(47) and Pilling and Bedworth (48) and theoretically treated by C. Wagner (49):

$$(\Delta X)^2 = 2\,kt \qquad (12)$$

k denotes the parabolic rate constant.

It follows from the assumption that the rate of growth $\frac{d\Delta X}{dt}$ of the thickness ΔX of the tarnishing layer is inversely proportional to the thickness according to:

$$\frac{d\Delta X}{dt} = \frac{k}{\Delta X} \qquad (12a)$$

The parabolic rate law holds if diffusion processes within the reaction layer are rate determining. Examples are the oxidation of copper to Cu_2O (59), the oxidation of zinc (50) and the formation of nickel sulfide on nickel (51) which will be treated below.

c) the logarithmic rate law:

$$\Delta X = a + b \cdot \log t \qquad (13)$$

where a and b are constants.

In the case of small layer thicknesses this rate law is sometimes found to be valid (52,53).

An electrochemical method which allows the investigation of diffusion-controlled tarnishing reactions and thus the determination of the parabolic rate constant k using a galvanic cell with a solid electrolyte is exemplified in the formation of nickel sulfide on nickel (51) for which the validity of the parabolic rate law is known. The following galvanic cell with AgI as silver ion conducting solid electrolyte may be used:

$$\ominus \; Pt,Ag \mid AgI \mid Ag_2S \mid NiS \mid Ni,Pt \; \oplus \qquad (VI)$$

If a potential difference is applied to this cell with the negative pole at the left-hand side, the resulting electrical current corresponds to the removal of silver from the Ag_2S, since only silver ions are migrating through AgI while electrons flow through the platinum leads connected to the external circuit. The rate of silver loss from Ag_2S is equivalent to the rate of formation of NiS because nickel displaces the silver. The experiments can be carried out by applying the galvanostatic or the potentiostatic method.

In the galvanostatic technique, a constant current is forced to flow through the cell thus leading to a definite rate of formation of NiS. The chemical potential of sulfur at the Ag_2S/NiS boundary is measured as a function of time. In the potentiostatic performance a constant potential difference is applied to the cell. As the observed current density i flowing through the nickel sulfide layer of cross-section q is equivalent to the flux of nickel ions in this case the current density is thus a measure of the growth rate of the NiS layer of molar volume V_m. With j as the flux of nickel ions in moles per unit area and unit time, it follows that

$$\frac{d\Delta X}{dt} = jV_m = \frac{iV_m}{2F} . \qquad (14)$$

The combination of equations (12), (12a) and (14) gives the following relation for the current density i as function of time t:

$$i = \frac{F}{V_m} \left(\frac{2k}{t}\right)^{1/2} \qquad (15)$$

A plot of i versus $1/\sqrt{t}$ gives a straight line, the slope of which equals $F \cdot V_m^{-1} \cdot \sqrt{2k}$. The parabolic rate constand k can thus be calculated. The second method of determining k involves the calculation of the thickness ΔX of the NiS layer using the following relation:

$$\Delta X = \frac{V_m}{2F} \int_o^t i\, dt \qquad (16)$$

Plotting $(\Delta X)^2$ versus t according to the parabolic rate law $(\Delta X)^2 = 2\,kt$ (equation (12)) it is possible to evaluate k from the slope of the resulting straight line.

A plot of the current density i versus $1/\sqrt{t}$ obtained at 400°C and a potential of E = 140 mV is shown in Fig. 8. The value of the parabolic rate constant k amounts to $5 \cdot 10^{-9}$ cm^2 s^{-1}. In a similar way, the parabolic rate constant was measured for other potential differences E. At 400°C the k values increase by a power of 10 if the emf E increases by 67 mV. This shows that the k value is proportional to the activity of the sulfur in Ag_2S and thus at the phase boundary NiS/Ag_2S. This conclusion is in agreement with the defect model of NiS.

According to this the electrons have a high intrinsic disorder with approximately equal concentrations of excess electrons and electron defects and the main ionic defects are nickel-ion vacancies.

The galvanostatic measurements (51), which will not be discussed here, give the same values of k as the potentiostatic studies.

PHASE BOUNDARY REACTIONS AT THE PHASE BOUNDARY SOLID/SOLID AND SOLID/GAS

In this section, electrochemical methods for studying reactions taking place at the phase boundaries solid/solid and solid/gas are described. The reaction rate of these interface reactions often depends on the activities of the reactants in both phases near the phase boundary. Therefore it is necessary to measure the reaction rate which is given by the current flowing through a galvanic cell as a function of the activities of the reactants. These activities are related to the potential difference E of a suitable cell. Both methods, i.e., the galvanostatic one which fixes the flow of a constant current as well as the potentiostatic one fixing a constant potential difference, may be applied.

Phase boundary reactions at the phase boundary solid/solid

As an example the electrochemical investigation of the transport of silver across the interface solid silver/solid silver sulfide (54-57) will be discussed. The following galvanic cell with AgI as solid silver ion conductor is used:

$$\mathrm{Pt} \mid \mathrm{Ag} \mid \mathrm{AgI} \mid \mathrm{Ag_2S} \mid \mathrm{Pt} \qquad \text{(VII)}$$

The experimental set-up is shown in Fig. 9. When the positive pole of an external current source is connected to the right-hand side of cell (VII), the current passing through the cell is a measure of the rate with which silver is removed from the Ag_2S. The silver ions are migrating through the AgI, the electrons through the platinum. The emf E of the cell depends on the chemical potential μ_{Ag} of the silver - or its activity - in the Ag_2S. Under zero current conditions the following equation holds:

$$\mu^{o}_{Ag} - \mu_{Ag} = E\,F \qquad (17)$$

where μ^{o}_{Ag} denotes the chemical potential of pure silver. As can be seen from Fig. 9 the emf E is measured using a second cell of the type $Ag/AgI/Ag_2S$ which is kept currentless to avoid polarization effects, which would disturb the results. Due to the constant current silver is removed with a definite rate from the Ag_2S. Under steady state conditions the loss of silver from the Ag_2S is balanced by the transport of silver from the upper silver rod pressed against the Ag_2S. The presence of the steady state is indicated by the fact that the chemical potential of silver in Ag_2S does not vary with time which can be checked using the emf of the second cell. In this way the rate of the interface reactions can be determined as a function of the chemical potential, or of the activity, of silver in Ag_2S.

An extended experimental arrangement makes it also possible to measure electrochemical potential differences of silver ions and electrons and allows silver ions and electrons to pass separately through the phase boundary.

Figure 10 shows stationary current-density potential curves, obtained at 200, 300 and 400°C. The silver rod was pressed against the Ag_2S pellet with a pressure of 7 kp/cm^2. Pressure variations between 1 and 10 kp/cm^2 showed only a slight influence on the results. At very high pressures (more than 50 kp/cm^2), the polarization effects of the dissolution of silver in Ag_2S nearly vanishes. A similar behaviour was found using in situ generated silver whiskers. The dotted line in Fig. 10 is an example of a high pressure measurement (200 kp/cm^2) at 300°C.

The results of the high-pressure measurements, where no polarization effects occur, indicate that the transfer of silver through the phase boundary Ag/Ag_2S is a very fast reaction, if efficient microcontacts are present at the phase boundary. At high pressures, silver sulfide exhibits plastic deformation so that silver and silver sulfide are in close contact at all sites, i.e. we have a situation similar to that existing in liquids. It may be assumed that this very good contact partly disappears if there is no plastic deformation, especially if half-crystal positions on the silver surface lose their contact with silver sulfide. Other mechanisms are then necessary to establish again the contact with the reacting sites. One of these may involve evaporation of S_2-molecules from silver sulfide and their diffusion to the silver over microdistances whereby reaction with the silver may take place, thus leading to new microcontacts for dissolution. This picture is consistent with the fact that for low pressures the current-potential curves have slopes corresponding to an increase of current by one order of magnitude, if the rise in voltage is about 30 mV. This shows that the stationary rates of dissolution of silver at low load pressures are proportional to the activity a_S of S_2-molecules, which indicates a participation of S_2-molecules in the process. Further arguments which support this mechanism may be found in the literature (57).

Similar measurements have been carried out at the phase boundaries Ag/Ag_2Se (57,58), Ag/Ag_2Te (57) and Cu/Cu_2S (59). The reactions taking place at the phase boundaries Ag_2S/S(liquid) (69) and Ag_2Se/Se(liquid)(58) have also been investigated.

Phase boundary reactions at the phase boundary solid/gas

The first electrochemical measurements using solid electrolytes for the determination of reaction rates which occur at the phase boundary solid/gas have been carried out at the phase boundary $Ag_2S/H_2,H_2S$ by Kobayashi and Wagner (61). This phase boundary has been investigated later on by other authors (62,63). Another investigation of a phase boundary reaction using an electrochemical method is the study of the oxidation of iron by a CO/CO_2 gas mixture (64,65). Further studies are investigations of evaporation and condensation processes (66-72). These will be described in the following as examples.

Measurement of evaporation rates

As an example, the evaporation of sulfur molecules from an Ag_2S surface into vacuum at higher temperatures (66-68) will be discussed. The solid-state galvanic cell used is cell (VII), which has been described above. The experimental arrangement is shown in Fig. 11. It contains two cells of type (VII). The current flowing through one of these cells causes the removal of silver from the Ag_2S and in the steady state an equivalent amount of sulfur is evaporated from the silver sulfide surface into the vacuum where it is condensed on a liquid-air-cooled area. The steady state is again indicated by the fact that the chemical potential of silver in Ag_2S is constant which is shown by a constant emf E of the second cell which is kept currentless to avoid polarization effects. In this way the evaporation rate of sulfur given by the electrical current density i with reference to the exposed Ag_2S area as a function of the chemical potential of silver, given by the emf E of the second cell, can be measured. The experimental results obtained (68) and the calculated maximum theoretical rates of evaporation of sulfur into vacuum are shown in Fig. 12. It can be seen that the measured rates are not more than a factor 1/2 smaller than the sum of the maximum possible rates. This indicates that the sulfur molecules in the adsorbed layer at the Ag_2S-surface are, even under the conditions of evaporation, nearly in equilibrium with the volume of the Ag_2S. In a similar way the evaporation of iodine from copper (I) iodide can be investigated (69).

If the space above the Ag_2S in the arrangement shown in Fig. 11 is enclosed by a glass vessel so that only a small orifice makes the connection to the vacuum an electrochemical cell is combined with a Knudsen cell thus leading to an electrochemical Knudsen cell (70). It is then possible to study electrochemically the effusion of sulfur from the Knudsen cell and to determine the evaporation rate via electrical current measurements. If there are many molecular species, as is the case for sulfur, it is advantageous to combine the electrochemical Knudsen cell with a mass spectrometer (71,72). In this way, it is possible to investigate the thermodynamic properties of the various molecular species present in the vapour.

Measurement of condensation rates

As an example, the electrochemical investigation of the incorporation of sulfur molecules into Ag_2S from the vapour phase (68) will be discussed. In this case three cells of type (VII) (see page 454) are used. The experimental arrangement is shown in Fig. 13. Through cell 3 a constant current is passed due to which sulfur evaporates into an evacuated vessel, which is directly connected to a high-vacuum system. The sulfur evaporation compensates the loss of sulfur from the vessel resulting from the loss into the vacuum system and from the incorporation of sulfur into Ag_2S which takes place in cell 2 if the activity of sulfur in the Ag_2S of that cell is smaller than that in the gas phase. For measuring the rate of incorporation, the chemical potential of sulfur in Ag_2S in this cell is fixed at low values by a potentiostat. The current flow is then a measure of the rate of addition of silver to the Ag_2S which, under steady-state conditions, is equivalent to the rate of incorporation of sulfur into Ag_2S. The chemical potential of sulfur in the gas phase - or its partial pressure - is measured by the emf E of cell 1. In this way the rate of incorporation of gaseous sulfur into Ag_2S can be determined as a function of the partial pressure of sulfur. The results show that from about two collisions on the Ag_2S-surface one sulfur molecule is added under conditions where S_2-molecules are the predominant species in the vapour at about 400°C.

Table 1: Determination of the diffusion coefficient of oxygen in various solid and liquid metals.

Investigator	Metal	Solid: s Liquid: l	Technique	Temperature range/°C	Diffusion coefficient $cm^2\ s^{-1}$	Ref.
Rickert, Steiner	Ag	s	Potentiostatic	800	$1.8\cdot10^{-8}$	(10)
Rickert, Steiner	Ag	s	Potentiostatic	760-900	$1.5\cdot10^{-5}$ - $2.9\cdot10^{-5}$	(11)
Masson, Whiteway	Ag	l	Galvanostatic	970-1200	$8.2\cdot10^{-5}$ - $1.7\cdot10^{-4}$	(13)
Rickert, El Miligy	Cu	l	Potentiostatic and galvanostatic	990-1220 1100-1250	$1.4\cdot10^{-4}$ - $2.2\cdot10^{-4}$ $6.2\cdot10^{-5}$ - $1.0\cdot10^{-5}$	(12) (14)
Pastorek, Rapp	Cu	s	Potentiostatic and galvanostatic	800-1030 950-1030	$9.3\cdot10^{-6}$ - $3.5\cdot10^{-5}$ $2.8\cdot10^{-5}$ - $4.1\cdot10^{-5}$	(15) (15)
Ramanarayanan, Rapp	Sn Ag Ni	l s	Potentiostatic	730-930 750-950 1393	$4.5\cdot10^{-5}$ - $7.4\cdot10^{-5}$ $1.6\cdot10^{-5}$ - $4.1\cdot10^{-5}$ $1.3\cdot10^{-6}$	(16) (16) (16)
Sano, Homma, Matsushita	Ag	l	Galvanostatic	1000-1200	$9.6\cdot10^{-5}$ - $1.5\cdot10^{-4}$	(17)
Sano, Homma, Matsushita	Pb	l	Galvanostatic	800-1100	$1.0\cdot10^{-5}$ - $1.7\cdot10^{-5}$	(18)
Szwarc, Oberg Rapp	Pb	l	Potentiostatic	740-1080	$6.6\cdot10^{-5}$ - $1.4\cdot10^{-4}$	(19)
Obert, Friedmann, Szwarc, Boorstein, Rapp	Fe	l	Potentiostatic	1620	$1.5\cdot10^{-4}$	(20)
Ramana Rao, Tare	Cu	s	Potentiostatic	800-1000	$2.3\cdot10^{-6}$ - $7.6\cdot10^{-6}$	(21)
Otsuka, Kozuka	Ag	l	Galvanostatic	1000-1150	$9.0\cdot10^{-5}$ - $1.3\cdot10^{-4}$	(22)

Investigator	Metal	Solid: s Liquid: l	Technique	Temperature range/°C	Diffusion coefficient/ $cm^2\ s^{-1}$	Ref.
Ramanarayanan, Worrell	Cu	s	Galvanostatic	800-1000	$3.9\cdot10^{-6}$ - $1.5\cdot10^{-5}$	(23)
Otsuka, Kozuka	Pb	l	Combined potentiostatic, galvanostatic	900-1000	$2.0\cdot10^{-4}$ - $2.7\cdot10^{-4}$	(24)
Otsuka, Kozuka	Cu	l	Combined potentiostatic, galvanostatic	1125-1300	$7.8\cdot10^{-5}$ - $1.3\cdot10^{-4}$	(25)
Kawahami, Goto	Fe In Ga	l	Galvanostatic	1550	$1.9\cdot10^{-4}$ $1.7\cdot10^{-6}$ - $4.5\cdot10^{-6}$ $4.3\cdot10^{-5}$ - $8.3\cdot10^{-5}$	(26)
Heshtmatpour, Stevenson	Sb Bi	l l	Potentiostatic	750-950	$1.4\cdot10^{-6}$ - $2.9\cdot10^{-6}$ $8.6\cdot10^{-6}$ - $1.4\cdot10^{-5}$	(27)

REFERENCES

(1) H. Rickert, "Electrochemistry of Solids - An Introduction", Inorganic Chemistry Concepts, Vol. 7, Springer Verlag, Berlin, Heidelberg, New York, 168 pp.(1982)

(2) V.B. Tare, A.V. Ramana Rao and T.A. Ramanarayanan in "Solid Electrolytes and Their Applications", Ed. E.C. Subbarao, Plenum Press Publ. Corporation New York, 165 pp.(1980)

(3) J. Mizusaki, K. Fueki in "Applications of Solid Electrolytes", Eds. T. Takahashi and A. Kozawa, JEC Press. Inc., Cleveland/Ohio, 12 pp. (1980)

(4) S. Geller, "Solid Electrolytes", Topics in Applied Physics, Vol. 21, Springer Verlag, Berlin, Heidelberg, New York (1977)

(5) B.C.H. Steele, Solid State Chemistry, Vol. 10, Ed. L.E.J. Roberts, Butterworth, London, p. 117 (1972)

(6) B.C.H. Steele in "Heterogeneous Kinetics at Elevated Temperatures", Eds. G.R. Belton, W.L. Worrell, Plenum Publishing Corp. New York, 135 pp. (1970)

(7) H. Rickert in "EMF Measurements in High Temperature Systems", Ed. C.B. Alcock, Inst. Mining Metallurgy London, 59 pp. (1968)

(8) D.O. Raleigh, "Progress in Solid State Chemistry", Vol. 3, Ed. H. Reiss, The Macmillan, New York, p. 83 (1966)

(9) H. Rickert, "Electrochemistry of Solids - An Introduction" Inorganic Chemistry Concepts, Vol. 7, Springer Verlag,Berlin, Heidelberg, New York, 169 pp. (1982)

(10) H. Rickert and R. Steiner, Naturwissenschaften 15, 451 (1965)

(11) H. Rickert and R. Steiner, Z phys Chem N.F 49, 9 (1966)

(12) H. Rickert and A.A. El Miligy, Z Metallk 59, 635 (1968)

(13) C.R. Masson and S.G. Whiteway, Can Met Quart 6, 199 (1967)

(14) H. Rickert and A.A. El Miligy, Reactivity of Solids, Ed. J.W. Mitchell, Vol. 17, New York, Wiley-Interscience, p. 17 (1969)

(15) R.L. Pastorek and R.A. Rapp, Trans Met Soc AIME 245, 1711 (1969)

(16) T.A. Ramanarayanan and R.A. Rapp, Met Trans 3, 3239 (1972)

(17) N. Sano, S. Honma and Y. Matsushita, Met Trans 1, 301 (1970)

(18) N. Sano, S. Honma and Y. Matsushita, Met Trans 2, 1494 (1971)

(19) R. Szwark, K.E. Oberg and R.A. Rapp, High-Temp Sci 4, 347 (1972)

(20) K.E. Oberg, et al., J Iron Steel Inst 210, 359 (1972)

(21) A.V. Ramana Rao, V.B. Tare, Z Metallk 63, 70 (1972)

(22) S. Otsuka and Z. Kozuka, J Japan Inst Met 37, 364 (1973)

(23) T.A. Ramanarayanan, W.L. Worrell, Met Trans 5, 1773 (1974)

(24) S. Otsuka and Z. Kozuka, Met Trans 6B, 389 (1975)

(25) S. Otsuka and Z. Kozuka, Met Trans 7B, 147 (1976)

(26) M. Kawakami and K.S. Goto, Trans Iron Steel Inst Jpn 16, 204 (1976)

(27) B. Heshmatpour and D.A. Stevenson, J Electroanal Chem Interf Electrochem 130, 47 (1981)

(28) W.F. Chu, H. Rickert and W. Weppner, Proceedings of the Advanced Study Institute "Fast-ion transport in solids, solid-state batteries and devices", Belgirate September 5-15 1972, p. 181, Amsterdam: North-Holland Publ. Comp. (1973)

(29) H. Rickert and W. Weppner, Z Naturforsch 29a, 1849 (1974)

(30) C. Wagner, J Chem Phys 21, 1819 (1953)

(31) H.Rickert, V. Sattler and Ch. Wedde, Z phys Chem N F 98, 339 (1975)

(32) B. Hartmann, H. Rickert and W. Schendler, Electrochim Acta 21, 319 (1976)

(33) T. Ohachi, Thesis, Doshisha (1974)

(34) G.J. Dudley, K.Y. Cheung and B.C.H. Steele, J Solid State Chem 32, 259 (1980)

(35) S. Mrowec, Defects and diffusion in Solids, Elsevier, Amsterdam (1980) tables 16, 4.4., 4.5.

(36) C.J. Wen, B.A. Boukamp, R.A. Huggins and W. Weppner, J Electrochem Soc 126, 2258 (1979)

(37) W. Weppner and R.A. Huggins, J Solid State Chem 22, 297 (1977)

(38) W. Weppner and R.A. Huggins, J Electrochem Soc 124, 1569 (1977)

(39) C.J. Wen and R.A. Huggins, J Electrochem Soc 128, 1636 (1981)

(40) S. Miyatani, J phys Soc Japan 10, 786 (1955)

(41) S. Miyatani, J phys Soc Japan 24, 328 (1968)

(42) S. Miyatani, J phys Soc Japan 50, 1595 (1981)

(43) K. Hauffe and H. Pfeiffer, Z Elektrochem 56, 390 (1952)

(44) F.S. Petit, R. Yinger and J.B. Wagner, Acta Met 8, 617 (1960)

(45) L. Czerski, S. Mrowec and T. Werber, Arch Hutnictwa 3, 49 (1958)

(46) H. Rickert, Z phys Chem N.F 23, 355 (1960)

(47) G. Tammann, Z anorg Chem 111, 78 (1920)

(48) N.B. Pilling and R.E. Bedworth, J Inst Met 29, 529 (1923)

(49) C. Wagner, Z phys Chem B21, 25 (1933)

(50) C. Wagner and K. Grünewald, Z phys Chem B40, 455 (1938)

(51) S. Mrowec and H. Rickert, Z phys Chem N F 36, 329 (1963)

(52) G. Tammann and W. Köster, Z anorg Chem 123, 196 (1922)

(53) C. Wagner, Werkst Korrosion 21, 886 (1971)

(54) H. Rickert and C.D. O'Briain, Z phys Chem N F 31, 71 (1962)

(55) H. Rickert and C. Wagner, Z phys Chem N F 31 32 (1962)

(56) C.J. Warde, J. Corish and C.D. O'Briain, J Electrochem Soc 122, 1427 (1975)

(57) L. Contreras and H. Rickert, Ber Bunsenges phys Chem 82, 292 (1978)

(58) J. Mizusaki, K. Fueki and T. Mukaibo, Bull Chem Soc Japan 47, 2851 (1974)

(59) D. Donner and H. Rickert, Z phys Chem N F 60, 11 (1968)

(60) J. Sasaki, J. Mizusaki and K. Fueki, Bull Chem Soc Japan, 51, 1927 (1978)

(61) H. Kobayashi and C. Wagner, J Chem Phys 26, 1609 (1957)

(62) P. Roy and H. Schmalzried, Ber Bunsenges Phys Chem 71, 201 (1967)

(63) E. Bechthold and U. Schwabe, Z phys Chem N F 81, 230 (1972)

(64) V.B. Tare and H. Schmalzried, Trans Met Soc AIME 236, 444 (1966)

(65) G.R. Fitterer and C.D. Cassler, in Heterogeneous Kinetics at elevated Temperatures, Eds. G.R. Belton and W.L. Worrell, Plenum Press, New York, p. 165 (1970)

(66) H. Rickert, Z Elektrochem 65, 463 (1961)

(67) N. Birks and H. Rickert, Ber Bunsenges phys Chem 67, 501 (1963)

(68) H. Rickert and K.-H.Tostmann, Werkstoffe, Korrosion 21, 965 (1970)

(69) S. Mrowec and H. Rickert, Z Elektrochem 66, 14 (1962)

(70) R.J. Ratchford and H. Rickert, Z Elektrochem 66, 497 (1962)

(71) D. Detry, J.Drowart, P. Goldfinger, H. Keller and H. Rickert, Z phys Chem N F 55, 314 (1967)

(72) H.Keller, H. Rickert, D. Detry, J.Drowart and P. Goldfinger, Z phys Chem N F 75, 273 (1971)

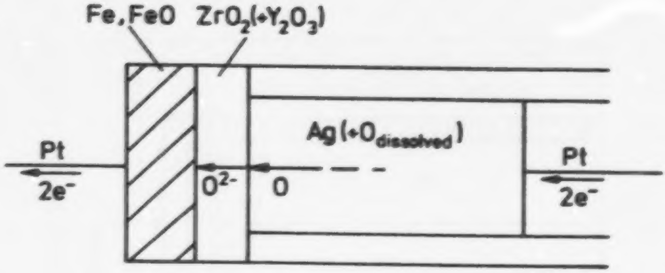
Fe,FeO
$ZrO_2(+Y_2O_3)$
$Ag(+O_{dissolved})$
Pt
$2e^-$
O^{2-}
O
Pt
$2e^-$

Fig. 1 Schematic arrangement for the determination of oxygen diffusion in silver using linear geometry.

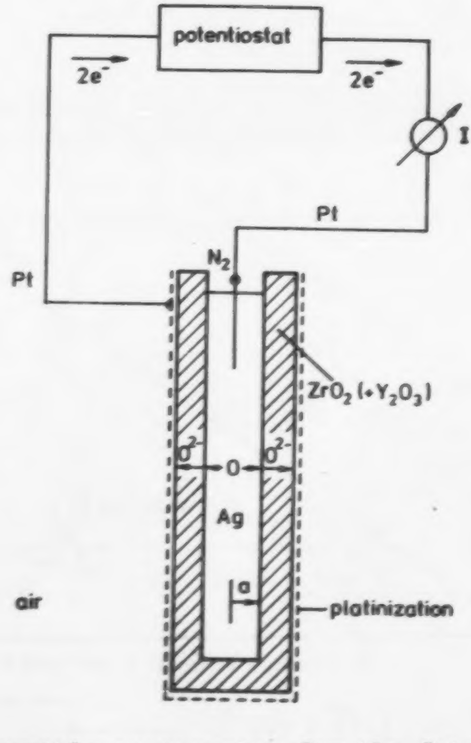
potentiostat
$2e^-$
$2e^-$
I
Pt
N_2
Pt
$ZrO_2(+Y_2O_3)$
O^{2-}
O
O^{2-}
Ag
a
air
platinization

Fig. 2 Schematic arrangement for the determination of oxygen diffusion in silver using cylindrical geometry.

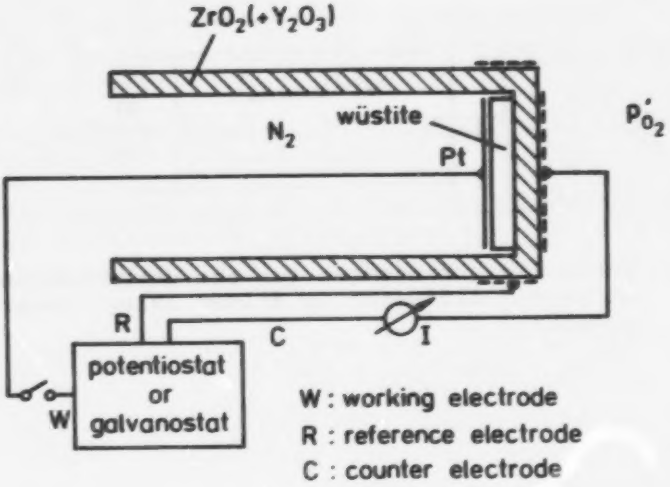
ZrO2(+Y2O3)
wüstite
N2
Pt
P'O2
R
C
I
potentiostat or galvanostat
W
W : working electrode
R : reference electrode
C : counter electrode

Fig. 3 Experimental set-up for the measurement of the chemical-diffusion coefficient of wüstite.

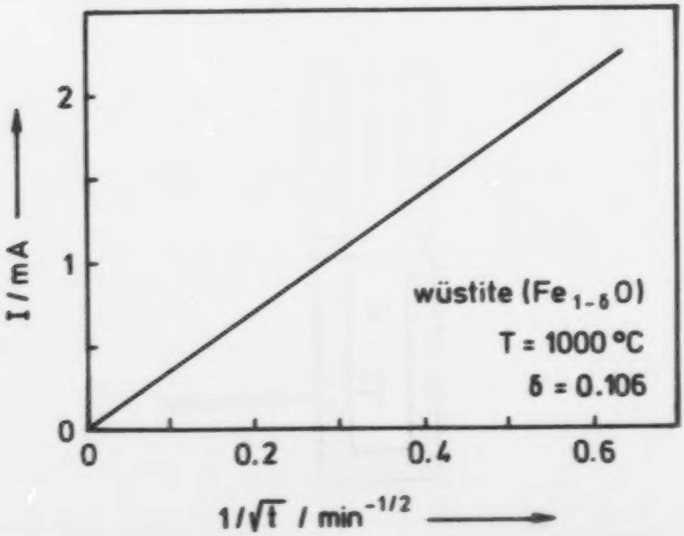

Fig. 4 Plot of the current i versus the reciprocal root of the time $1/\sqrt{t}$ for the determination of the chemical-diffusion coefficient of wüstite.

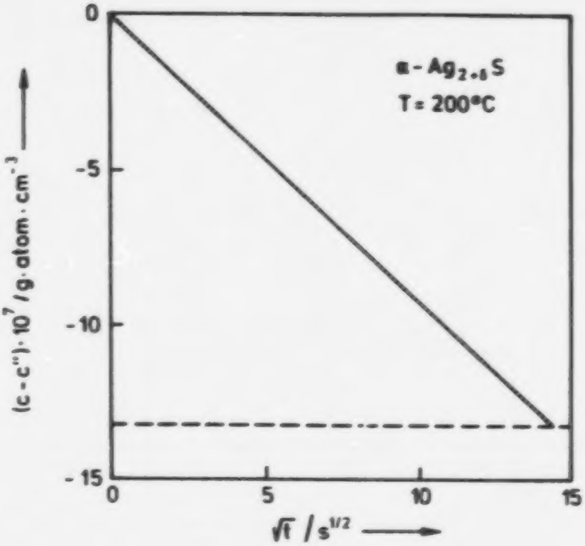

Fig. 5 Plot of the concentration (c-c") versus $\sqrt{t}$ for the determination of the chemical-diffusion coefficient of Ag_2S.

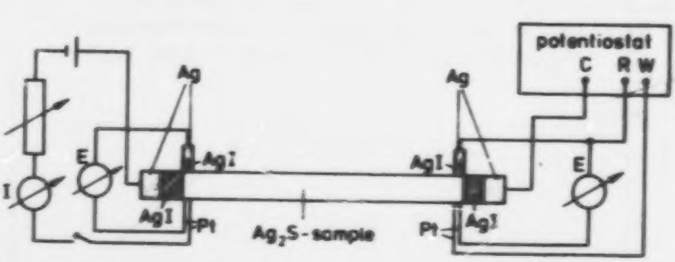
potentiostat
C
R
W
Ag
Ag
AgI
AgI
AgI
AgI
E
E
I
Pt
Pt
Ag$_2$S-sample

C: counter electrode, R: reference electrode

W: working electrode

Fig. 6 Experimental set-up for the determination of the chemical-diffusion coefficient of $Ag_{2+\sigma}S$ as a function of stoichiometry.

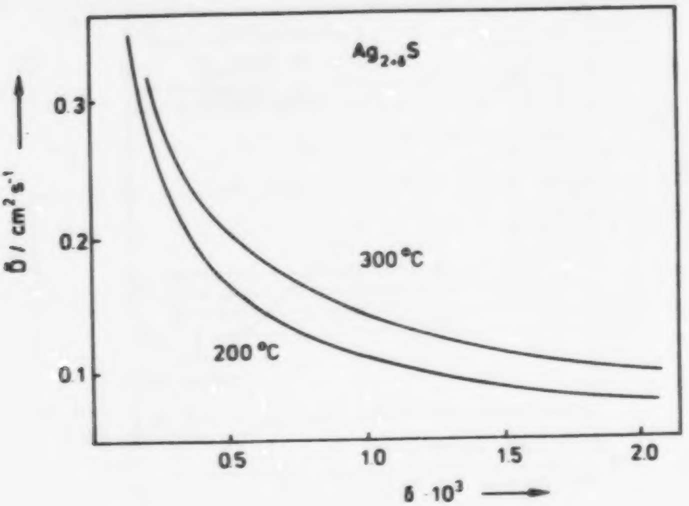

Fig. 7 Chemical-diffusion coefficients of $Ag_{2+\sigma}S$ as a function of the deviation σ from stoichiometry at 200 and 300°C.

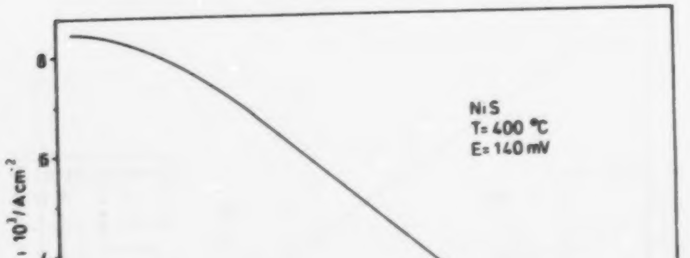

Fig. 8 Plot of the current density i versus $1/\sqrt{t}$ for the determination of the parabolic rate law constant k.

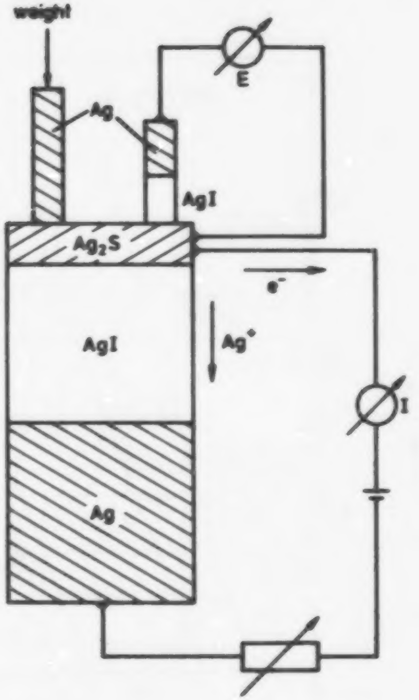
weight
Ag
E
AgI
Ag_2S
e^-
AgI
Ag^+
I
Ag

Fig. 9 Experimental set-up for the electrochemical measurement of the transfer of silver across the solid phase boundary Ag/Ag_2S.

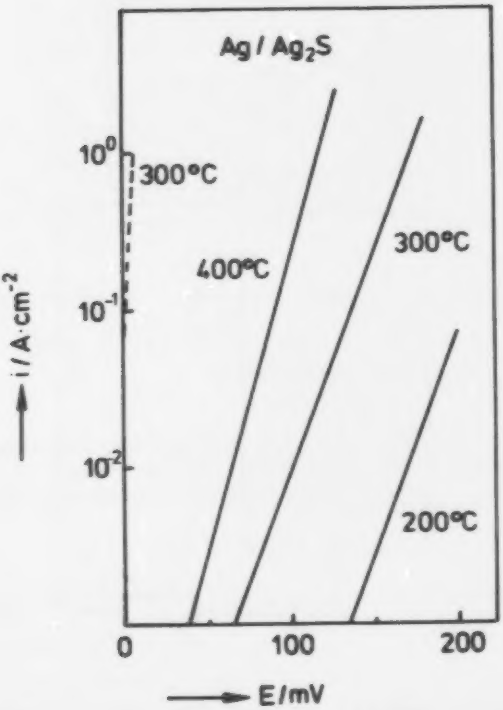

Fig. 10 Stationary current density potential curves obtained at different temperatures.

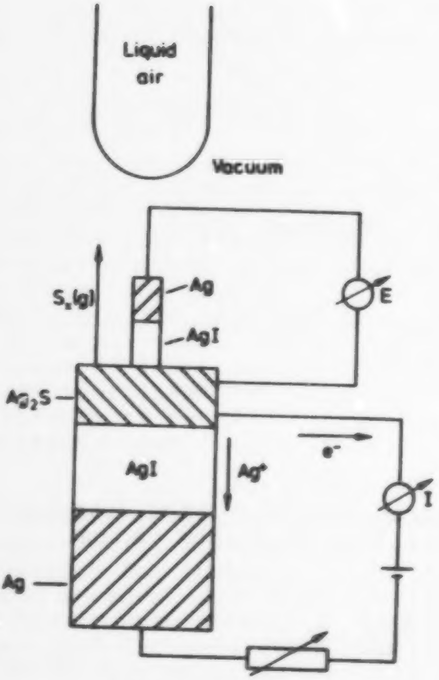
Liquid air
Vacuum
$S_x(g)$
Ag
AgI
E
Ag_2S
AgI
Ag^+
e^-
I
Ag

Fig. 11 Experimental arrangement for the evaporation of sulfur from an Ag_2S surface into vacuum.

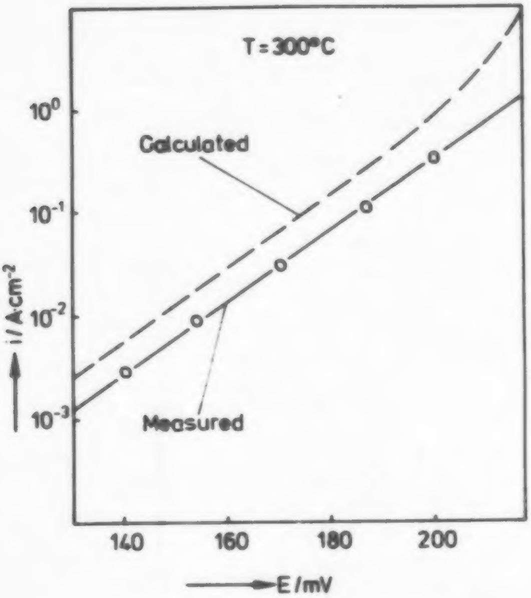

Fig. 12 Measured and calculated evaporation rates of sulfur from Ag_2S into vacuum.

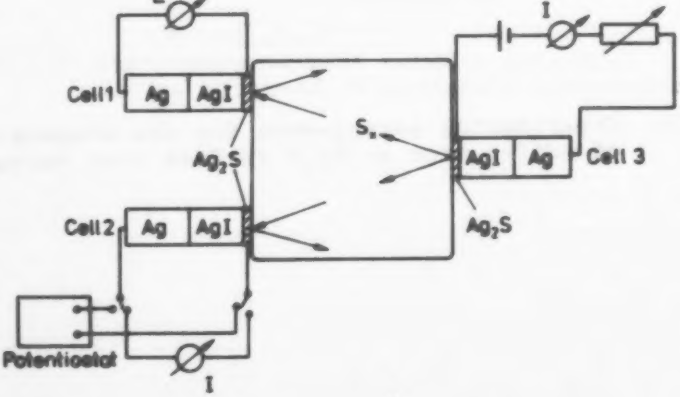
E
I
Cell1
Ag
AgI
Ag2S
Sx
AgI
Ag
Cell 3
Ag2S
Cell2
Ag
AgI
Potentiostat
I

Fig. 13 Experimental arrangement for the measurement of the incorporation of sulfur molecules into Ag_2S from the vapour phase.

ELECTROLYTES FOR ALL-SOLID-STATE LITHIUM BATTERIES AND HYDROGEN FUEL CELLS

J. Jensen

Energy Research Laboratory, Odense University,
Campusvej 55, 5230 Odense M, Denmark

ABSTRACT

In recent years a rather sudden increase in basic research in the field of advanced electrochemical storage and conversion systems has taken place at European scientific laboratories and universities. The main emphasis has been on new systems involving solid electrolytes. The appearance of a range of completely new ideas for advanced batteries, stemming mostly from solid state science on one hand and based on the other hand on improvements of already known battery systems, inspired the European Commission (EC) to set up a battery research programme in 1976. Five out of six projects have involved solid electrolyte research.

In this paper a review of the progress made in a partly EC funded Anglo-Danish project entitled "Materials Research for Advanced Batteries" and progress within a recent scientific collaboration between research groups in Denmark, England and France on solid-state protonic conductors for fuel cells and sensors will be given. New single-crystal, ceramic, composite and polymer lithium and hydrogen-ion conducting materials are described. The experimental work carried out, has permitted an identification of particularly promising materials for further work towards system design of all-solid-state laboratory cells capable of later prototype and engineering development.

KEYWORDS: electrolytes, lithium, solid-state battery, hydrogen, fuel cell.

RÉSUMÉ

Les dernières années ont été marquées en Europe par un développement rapide de recherches fondamentales orientées vers de nouveaux systèmes de stockage et conversion de l'energie. Le principal effort a porté sur le mise en oeuvre d'électrolytes solides. L'apparation de nouvelles conceptions de batteries de stockage ussies d'une part des sciences de l'état solide et d'autre part d'amelioration de systèmes existants a conduit les Communautés Européennes à lancer un programme de recherche sur les batteries en 1976. Cinq des six projets développés ont porté sur des application d'électrolytes solides.

Cet article présente les résultats obtenus dans le cadre d'un programme Anglo-Danois partiellement financé par les Communautés Européennes et d'un programme parallèle de collaboration entre plusieurs groupes anglais, danois et français et portant sur les conducteurs protoniques en vue d'applications aux piles à combustible et capteurs. De nouveaux monocristaux, matériaux céramiques, composites et polymères conducteurs par ions Li^+ et H^+ sont décrits. Les travaux expérimentaux effectués ont abouti en particulier à la mise en évidence de nouveaux matériaux très prometteurs, susceptibles de conduire à la mise au point de prototypes et à des développement technologiques.

INTRODUCTION

All-solid-state electrochemical energy conversion and storage devices provide a particularly telling example of inter-disciplinary science and technology. To gain the scientific understanding necessary to predict appropriate materials for constructing such devices and then technically to build a successful device, one must bring together such subjects as structural chemistry, solid and liquid state electrochemistry, interfacial and surface science, ceramics, corrosion science and metallurgy. Solid state physics and computer modelling of ionic motions within phases and across interfaces also have an important role to play. To assess the economic viability of particular systems, one has to take account of projected performance parameters as well as such features as cost and availability of raw materials, processing technology, construction and fabrication costs, installation costs, safety, pollution and a comparison of these aspects weighed against alternative means of doing the same job.

The development of all-solid-state cells can be regarded as the most recent attempt to design new advanced electrochemical systems for storage and conversion of energy (see Figure 1). To some extent the incentive has been based on the results obtained from the work on the sodium-sulphur battery solid electrolyte beta-alumina. Simultaneously with the work on Na/S battery development in the early seventies, many research centers and university laboratories in Europe started programmes to try to discover new fast ion conducting solid electrolyte materials. The success of these programmes together with the concept of the insertion compound or solid solution electrode first outlined by Steele at Imperial College, London and Whittingham at Exxon, USA, made the appearance of a range of new ideas for advanced batteries possible in the mid seventies. This brought about the EC and national public funds for rather fundamental research in several European countries.

In 1978 three small EC contracts on exploratory research were signed with the French universities at Bordeaux, Nantes and Rennes. At Bordeaux (Hagenmüller) synthesis and characterization of new solid lithium electrolytes was carried out. Glasses formed from the components B_2O_3-Li_2O-LiCl were investigated. The project which is part of the new EC programme (started in 1980) showed promising results. At Nantes (Rouxel) the research was focused on the development of new electrode materials based on lithium intercalation, and in Rennes, Lucas did a study on new electrolyte materials with fluoride-ion conduction. These rather small projects were closely linked to the largest basic research EC-project - the Anglo/Danish project entitled "Materials Research for Advanced Batteries". There has been a frequent information exchange between the research groups of all these four projects thus leading to an Anglo/Danish/French collaboration (cf. Jensen, 1981). The Anglo/Danish project began in January 1978 and continued until March 1980. The project involved seven participating laboratories, four in Britain (at AERE, Harwell; Leeds University; Imperial College, London and Oxford University) and three in Denmark (at Odense University; the Danish Technical University, Lyngby and Risø National Laboratory). The EC, who paid half of the cost of the research from its Energy Conservation programme, placed separate contracts with Harwell in the UK and Odense University in Denmark (cf. Tofield et al., 1981). The aim of the project which has rightly been described as "A New Experiment in Science and Technology" (cf. Tofield et al., 1978) has been to develop and characterize materials for second generation advanced, rechargeable (secondary) batteries and to identify materials and cell types most promising for further development. In 1980 the EC issued two new contracts on all-solid-state battery research (cf. Ehringer et al., 1982), one project being "Investigation of New Solid Electrolytes and their Associated Cathodes - study and realization of new batteries". This project, which is concentrating on vitreous electrolytes, is carried out by a French research group at University of Bordeaux. The other project "Advanced Battery Development" is continued Anglo/Danish collaboration between four British and three Danish research institutes. In this paper a progress overview of the two Anglo/Danish projects will be given.

European research on materials for all-solid-state fuel cells and sensors is even more recent than the research on battery materials. Attempts are being made to establish a collaborative EC research programme based on work at British, Danish and French laboratories (cf. Jensen and Kleitz, 1982). An overview of the concepts of solid-state protonic conductors for fuel cells and sensors will be given in the following.

LITHIUM ION CONDUCTING ELECTROLYTES FOR ALL-SOLID-STATE SECONDARY BATTERIES

Fast cation conduction in solids is generally restricted to the group I metals, of which only the alkali-metals can also provide high energy densities. Lithium was chosen because of its low atomic weight and also because of the greater range of positive electrode materials, capable of reversibility, accomodating this metal ion.

The study of lithium halide-based composite electrolytes reproduced earlier work (cf. Liang et al, 1978) demonstrating that the ionic conductivity may be enhanced by dispersing the halide in a very finely divided alumina. This is a specially prepared mixture of lithium iodide and alumina which has a far higher conductivity than either of the pure components. Such behaviour is often encountered in the doping of a pure solid to produce extrinsic defects. However, in this case there is no apparent solubility of alumina in lithium iodide and it is difficult to explain the enhancement of almost two orders of magnitude in the conductivity of lithium iodide by the addition of an apparently inert component. The lithium iodide/alumina system was specially difficult to study because lithium iodide is extremely hygroscopic and many forms of alumina contain structural water: bearing in mind that $LiI.H_2O$ is a better conductor than anhydrous LiI, it was important to demonstrate a genuine enhancement of the lithium-ion conductivity of LiI rather than an increased conductivity due to the formation of $LiI.H_2O$. This was important for two reasons: firstly, genuine conductivity enhancement is a fundamental phenomenon which could be applied to other systems and secondly $LiI.H_2O$ is known to react with metallic lithium and is thus an undesirable choice of electrolyte in a solid-state battery incorporating lithium metal (cf. Owen, 1982).

The LiI/Al_2O_3 composite is only one of a family of electrolytes based on lithium salts with suitable dispersed oxide additives. A comprehensive study would require a very large number of preparations given that the lithium salt, the oxide and its volume fraction are all independently variable. A fourth variable which has recently shown its importance is the method of mixing the two materials. Therefore the approach taken was to understand and optimize this last factor before widening the study to include alternative lithium salts and oxides.

In the lithium iodide/alumina system it has been shown that the enhancement effect increases with a decreasing particle size of alumina. Therefore the grade of oxide chosen was important as well as the drying procedure. Whereas the elimination of water was very important to avoid hydrating the lithium iodide, it was realized that significant changes in the oxide's crystal structure could take place during heating. X-ray and neutron diffraction studies were undertaken to investigate these changes: the as-received material, ALCOA H151 appeared amorphous, giving no diffraction peaks, whereas the characteristic peaks of alpha-alumina began to appear at 600° and at 1150°C the material was completely converted to the alpha phase. Composite electrolyte material was then made from lithium iodide dried at 400°C and alumina dried at 600°C. The best conductivity of 6×10^{-3} (ohm.cm)$^{-1}$ at 200°C was observed at 30 mole % Al_2O_3. This composition corresponded to a situation where the amount of LiI was just sufficient to fill the natural porosity of the alumina.

Much higher ionic conductivity was shown for single crystal lithium nitride due to the highly mobile lithium vacancies in this material. The most important experimental result was the development of new preparative techniques related to hydrogen-doped Li_3N. Single crystals were grown by the Czochralski method. The conductivity of the optimum doped crystal at room temperature is very high (6×10^{-3} ohm^{-1} cm^{-1}), a factor of two higher than previously achieved elsewhere. In Figure 2 the effect of hydrogen dopant level is shown. The highest conductivity was observed when doping with 0.5 atomic % hydrogen. Polycrystalline material has been made by melting and fast cooling. The samples which have good mechanical properties have a conductivity of $2\text{-}3 \times 10^{-3}$ (ohm.cm)$^{-1}$ at room temperature. The application of lithium nitride as electrolyte in rechargeable batteries will now depend on the ability to fabricate thin ceramic material successfully and the degree to which the low decomposition potential can be kinetically hindered over the lifetime of a cell.

Lithium salt doped polyethylene oxides (PEO) were studied briefly during the first phase of the Anglo/Danish project, and further investigations on these materials have been of major concern during the second phase of the project. The very attractive mechanical properties of this electrolyte material stimulated a wider investigation of ion-conducting polymers. The conductivities of 10^{-4}-10^{-3} (ohm.cm)$^{-1}$ at 100-140°C for $LiCF_3SO_3\ (PEO)_x$ show that about eight PEO per Li are required to give a high value for ionic conduction. Although the high conductivity persists for compositions richer in PEO, too much PEO yields a material too soft to be used at higher temperatures and $x=8$ or 9 is generally regarded as the optimum composition (cf. Owen, 1982). Differential scanning calorimetry experiments on sodium thiocyanate-doped PEO have revealed two melting peaks. The relative sizes of the peaks depended on the salt content, so that compositions containing more than four PEO per alkali metal were identified as mixtures of a relatively undoped amorphous PEO and the crystalline $(PEO)_4$ complex between the two melting points. Extending this result to the lithium-doped polymers, which also show both amorphous and crystalline phases in the polarizing microscope, it was concluded that the optimum composition, having eight PEO per metal, represented a quasi-solid material.

It is not clear whether the highest conductivity occurs in the crystalline phase, amorphous phase, or at the interphase. To investigate this aspect, doped PEO was oriented by drawing at 100°C. It was expected that this treatment would show an anisotropy of conduction, from which it could be deduced which phase was the better conductor. However, initial experiments have shown no significant change in conductivity on drawing.

Complex impedance measurements using lithium metal electrodes have been done to evaluate the lithium ion transport number, which had previously been assumed to be unity. A slightly disconcerting result of $t_{Li^+} \approx 0.5$ was obtained, and efforts are being made to reduce anion conductivity in order to avoid limiting current effects. One approach has been to synthesize the sodium salt of a polymeric acid, poly(methacryloyl-oxy-benzoic acid) and to blend this material as the dopant into PEO. In this case the anion is considered immobile as part of a polymer chain. The conductivity is about 3×10^{-5} $(\mathrm{ohm.cm})^{-1}$ at 93°C, rather too low to be used in cells. However, a polysalt with a side group containing a stronger acid will be prepared, where one may expect a lower degree of ion-pairing and a higher conductivity.

Alternative polymer systems to PEO have been investigated, for example nylon-6, polyvinylidene fluoride, polyethylene sulphide, and polyethylene imine. However, in cases where the salt was insoluble, the resulting materials were too brittle to be useful. A blend of polyvinylmethyl ether (PVME) with PEO was made in an effort to increase the PEO free volume. Initial conductivity results are promising, and the adhesive properties of PVME may be advantageous in preserving good interfacial contact with electrode material (cf. Owen, 1982).

A very limited number of actual cell tests involving the above mentioned solid electrolytes have been carried out. However, these tests have revealed problems regarding dendrite formation at pure metal and metal alloy negative electrodes as well as mechanical problems related to the close pack of three solids during cell operation. The cell concepts under investigation are shown in Table 1 and the concepts likely to be further developed are the ones that include double insertion electrodes or mechanically compressable (plastic) components in a suitable combination.

SOLID STATE PROTONIC CONDUCTORS FOR FUEL CELLS AND SENSORS

The attractive features of a solid electrolyte for fuel cells are: the prospects for relatively simple product removal, invariability of the electrolyte during cell life, maximization of the utilization of expensive catalyst (low temperature) by impregnation of particles on both sides of the electrolyte, thermal stability at high temperatures (no need for expensive catalysts) and the resistance to pressure differentials across the electrolyte. Two solid electrolyte concepts (zirconia and Nafion electrolyte) have been used in actual fuel cells up till now. Both concepts fail to be competitive with the phosphoric acid system such as developed by The United Technologies, USA - the zirconia cell because of considerable corrosion problems and the Nafion cell because of expensive current collector and electrode materials. A third concept being that of a medium temperature (150-250°C) cell with a solid protonic conductor as electrolyte has been studied in USA (General Electric and University of Pennsylvania) and Europe (AERE Harwell and universities in Denmark, England and France) since 1975 (cf. Jensen and Kleitz, 1982).

The main requirements for medium temperature electrolytes in hydrogen-oxygen cells are thermal stability, pure ionic conductivity and resistivity to water. For practical fuel cells, the conductivity must be 10^{-3}-10^{-1} (ohm·cm)$^{-1}$, whereas electrochemical sensors essentially passing no current through the electrolyte allow for much less (10^{-7}-10^{-5} (ohm·cm)$^{-1}$).

A major breakthrough came about early 1975 where a cooperative effort at Danish and English laboratories - on the basis of previous discoveries (cf. Lundsgaard and Brook, 1974) - resulted in the demonstration of hydrogen exchanged sodium beta-alumina material and its use in a concentration cell shown in Figure 3 (cf. Jensen and McGeehin, 1979). With the exception of beta-/beta"-aluminas which have been studied extensively (cf. e.g. Colomban and Novak, 1982), the known solid proton conductors suitable for use in fuel cells tend to be unstable above 100°C, at least losing water and hence their protonic conductivity. However, the existence of H_3O^+ β''-Al_2O_3 with good thermal stability (cf. Jensen and McGeehin, 1978; Roth et al., 1978) provides hope that other hydrated compounds may be found that support fast proton conduction and hold their water to medium temperatures. Another approach is to control the water vapour of proton conductors in order to maintain good ionic conductivity at medium temperatures. A promising material for this approach is the layered hydrogen uranyl phosphate tetrahydrate (HUO_2 PO_4, $4H_2O$). This material named HUP shows a good selective proton conductivity at ambient temperatures (cf. Howe and Shilton, 1979). Figure 4 shows the current-voltage curve for a small HUP-test cell (area 1 cm^2 and thickness 1 mm) operating at 20°C with supply gases (10 % H_2 / 90 % N_2-air) saturated with water (cf. Lundsgaard et al., 1982).

The hydrogen-oxygen (air) fuel cell with a solid state protonic conducting electrolyte is in the early stage of R&D. In general, ionic migration requires interconnected channels in which the mobile ions occupy only partially the lattice sites with very close site occupation energies. Moreover, for fast ion transport, the activation energy for an ion hopping from one site to another, must be small and the channels large enough for easy crossing. In order to understand the conduction mechanism in solid ionic conductors and to develop a new class of such conductors having sufficient conductivity, one will have to clarify the influence of the crystal structure on the conductivity as well as the role of the size and polarizability of the mobile ions and their interaction. Furthermore, the influence of water and factors governing chemical and thermal stability have to be clarified (cf. Poulsen, 1982). An attempt is made to establish a joint European research programme the aim of which is to develop solid electrolyte cells with operating temperatures low enough to avoid serious corrosion problems (<350°C) and high enough (>150-200°C) to avoid the need for large amounts of precious metal catalysts (cf. Jensen, 1982).

Acknowledgements

The author thanks Dr. J.R. Owen of Imperial College, London for valuable discussions and the Danish Government's Department of Energy for providing financial support during the preparation of the paper.

REFERENCES

Colomban, Ph. and A. Novak, 1982 : "Protonic species conductivity and vibrational spectra of β-and β''-alumina", pp. 153-201 in J. Jensen and M. Kleitz (eds.), *Solid State Protonic Conductors I for fuel cells and sensors*, Odense University Press

Ehringer, H., P. Zegers, G. Hoyaux and J.A.A. Ketelaar (eds.), 1982 : "*Proceedings of the second contractors meeting on advanced batteries and fuel cells*", Commission of the European Communities, Energy Conservation, Directorate General, Science, Research and Development, EC publication : EUR 8078 EN

Howe, A.T. and M.G. Shilton, 1979 : "Studies of layered uranium VI compounds I-High H^+ conductivity in polycrystalline HUP", *J Solid State Chem* 28:345-361

Jensen, J. and P. McGeehin, 1978 : "Thermal stability of hydrogen exchanges beta-alumina", *J Mat Sci* 13: 909-913

Jensen, J. and P. McGeehin, 1979 : "The properties of hydrogen exchanged beta-alumina and their use in gaseous concentration cells", *Silicates Industriels*, A27/78 1-8

Jensen, J., 1981 : "Solid electrolyte battery research within the EEC research programme on energy conservation", *Solid State Ionics* 5:9-14

Jensen, J. , 1982 : "Materials requirements targets and applications", pp. 3-20 in J. Jensen and M. Kleitz (eds.), *Solid State Protonic Conductors I for fuel cells and sensors*, Odense University Press

Jensen, J. and M. Kleitz (eds.), 1982 : "*Solid State Protonic Conductors I for fuel cells and sensors*", Odense University Press

Liang, C.C., A.V. Joshi and N.E. Hamilton, 1978, *J App Electrochem* 8:445

Lundsgaard, J.S. and R.J. Brook, 1974 : "The use of β-alumina electrolyte in gaseous concentration cells", *J Mat Sci* 2:2061-2062

Lundsgaard, J.S., E.K. Andersen, E. Skou and J. Malling, 1982 : "An investigation of the influence of water vapour of the proton conductivity in HUP", pp. 222-234 in J. Jensen and M. Kleitz (eds.), *Solid State Protonic Conductors I for fuel cells and sensors*, Odense University Press

Owen, J.R., 1982 : "Advanced battery development - materials evaluation", pp. 54-68 in H. Ehringer et al. (eds.) Proc. of the 2nd contractors meeting on advanced batteries and fuel cells, EC publication EUR 8078 EN

Poulsen, F.W., 1982 : "Limitations on the performance of solid state proton conductors", pp. 21-26 in J. Jensen and M. Kleitz (eds.), Solid State Protonic Conductors I for fuel cells and sensors, Odense University Press

Roth, W.L., M.W. Breiter and G.C. Farrington, 1978 : "Stability and dehydration of alumina hydrates with the beta alumina structure", J Solid State Chemistry 24: 321-330

Tofield, B.C., R.M. Dell and J. Jensen, 1978 : "Advanced batteries", Nature 276:5685:217-220

Tofield, B.C., J. Jensen and R.M. Dell, 1981 : "Materials research for advanced batteries", Anglo/Danish EEC Project, Final Summary Report, 1st Jan. 1978-31st March 1980, Report C14 H.M. Stationary Office, U.K.

Table 1. All solid-state battery concepts

Negative Electrode	Electrolyte	Positive Electrode
Metal	Polymer	Insertion
Metal alloy	Polymer	Insertion
Insertion	Polymer	Insertion
Polymer	Ceramic	Polymer
Metal	Composite	Insertion
Metal alloy	Composite	Insertion
Insertion	Composite	Insertion
Polymer	Polymer	Polymer

From J. Jensen and B. Sørensen : Fundamentals of Energy Storage (Table 7.14), to be published by John Wiley & Sons, New York, 1983

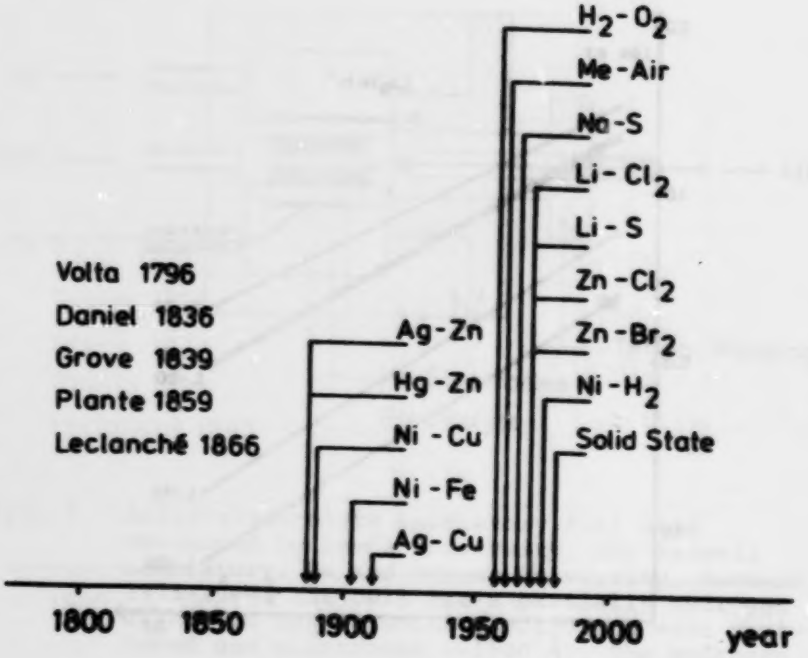

Fig. 1 - The development of electrochemical power sources.

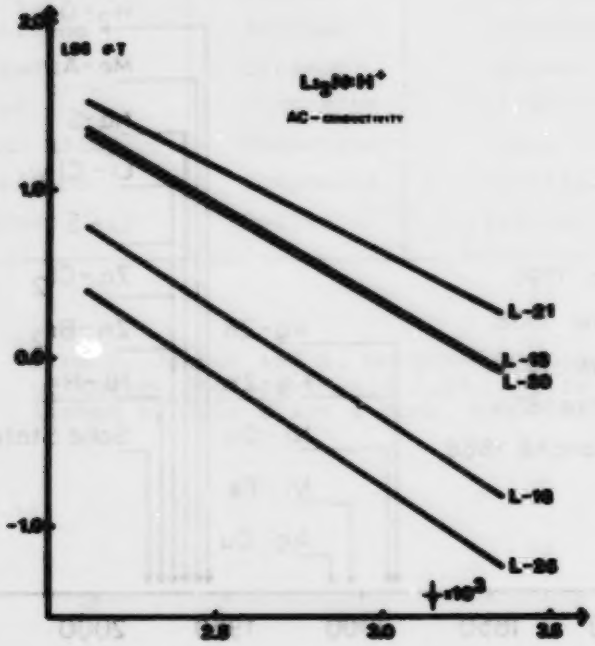

Fig. 2 - Ionic conductivity of Li_3N crystals with varying amounts of hydrogen. Hydrogen dopant level increases in the order L-25<L-18<L-19<L-20<L-21.

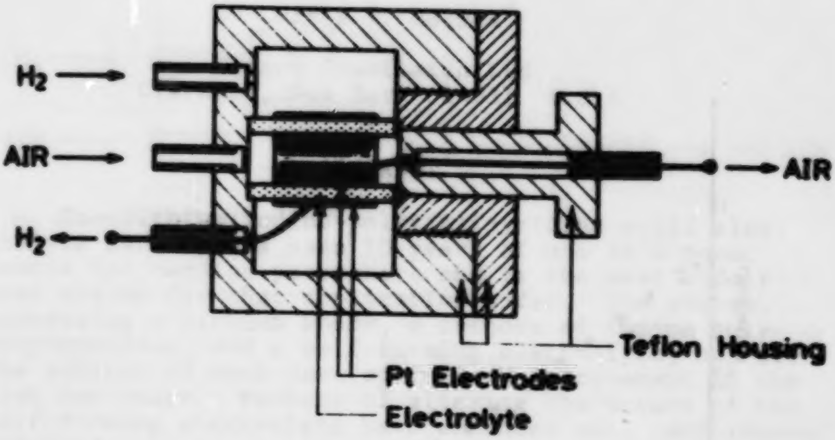
H_2
AIR
H_2
AIR
Teflon Housing
Pt Electrodes
Electrolyte

Fig. 3 - Solid-electrolyte laboratory fuel cell developed by Leeds University, UK; Harwell Laboratory, UK and Odense University, Denmark, 1975-1976. The cell has a partially hydrogen exchanged beta-alumina electrolyte with sputtered gas electrodes (~1500 Å). The hydrogen ion exchange was performed by applying an electric field across the electrolyte with wet hydrogenflowing at the hydrogen electrode.

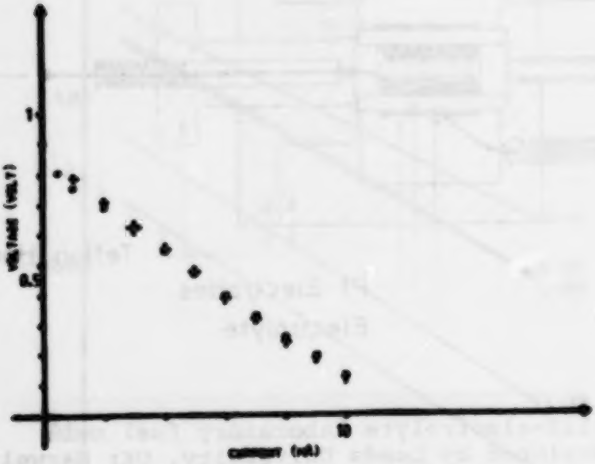

Fig. 4 - Voltage-current relationship for an H_2-HUP-O_2 fuel cell at 20°C. The dots are from an experiment with rising currents and the crosses are from an experiment with falling currents.

THE LITHIUM/IODINE SOLID ELECTROLYTE PACEMAKER BATTERY

Curtis F. Holmes

Wilson Greatbatch Ltd.
Clarence, New York 14031 U.S.A.

ABSTRACT

The lithium/iodine-polyvinylpyridine solid electrolyte battery has seen 10 years of use as a power source for cardiac pacemakers and is the most widely-used system for that application today. The system, comprising a lithium anode, a cathode of iodine-polyvinylpyridine, and a self-forming electrolyte, has been the subject of much development and improvement in the last few years. Methods of altering the nature of the self-forming electrolyte have enhanced cell performance. Energy density and current-delivery capability have been improved. Experience in the field and in life testing has shown the cell to perform in a predictable manner.

KEYWORDS: solid electrolyte, battery, pacemaker, conductivity, performance, reliability.

RÉSUMÉ

Les piles à couple lithium/iode-polyvinylpyridine avec l'électrolyte solide ont été utilisées pendant dix ans comme source d'énergie pour les stimulateurs cardiaques, et, aujourd'hui, elles sont les piles les plus usitées pour cette application. Le système, composé d'une anode de lithium, une cathode d'iode et de polyvinylpyridine, et un électrolyte qui se guérit soi-même, a été le sujet des améliorations depuis plusieurs années. On a trouvé que c'est possible de modifier l'électrolyte solide pour améliorer les performances de ces piles. La densité d'énergie a été plus élevée, et l'intensité des courants disponibles a été augmenté. Les performances de ces piles en temps réel et aussi sous essais ont démontré que le comportement des piles lithium/iode peut être bien prédit.

INTRODUCTION

One of the more important uses of solid electrolyte batteries is as power sources for cardiac pacemakers. Specifically, the lithium/lithium iodide/iodine-polyvinylpyridine battery is the most commonly-used power source for cardiac pacemakers today. Well over 600,000 such batteries have been implanted since 1972, and nearly 80% of all pacemakers produced in 1982 will be powered by this battery system.

A cardiac pacemaker presents a unique set of conditions and requirements which make a solid electrolyte battery system a particularly attractive candidate power source. The current requirements are fairly low; typically 10-30 microamperes, and only rarely higher than 60-75 microamperes. Unlike many battery applications which require the ability to operate over a wide temperature range, the pacemaker environment presents an isothermal, 37°C condition, alleviating concerns about ionic conductivity at low temperatures. Since surgical intervention is necessary to replace the life-supporting pacemaker, high energy density and high reliability leading to long life and safe operation are obvious requirements of this power source. Finally, a gradual decrease in cell voltage rather than an abrupt drop resulting in sudden cessation of operation is desirable.

It is the purpose of this article to discuss the lithium/lithium iodide/iodine-polyvinylpyridine solid electrolyte system in some detail. Cell chemistry and cell construction will be presented. The properties of the lithium iodide solid electrolyte and methods to enhance performance of this system will be discussed, and discharge characteristics of the battery will be presented.

THE $Li/LiI/I_2$-PVP SYSTEM

The lithium/iodine system is somewhat unique in that the solid electrolyte LiI is formed in situ as the cell is discharged. The anode is elemental lithium. The cathode/depolarizer is a combination of iodine and polyvinylpyridine (PVP). The iodine and PVP react to form a species which exhibits electronic conductivity. The material also contains excess free iodine at unit activity. The electronic conductivity is a function of the iodine/PVP ratio and exhibits a maximum at approximately 8 parts of iodine per one part PVP by weight. The maximum electronic conductivity is around 10^{-3} ohm^{-1} cm^{-1} at 37°C, and it decreases to 10^{-6} ohm^{-1} cm^{-1}

at an iodine/PVP weight ratio of 4:1.

When manufactured, the iodine-PVP material is placed in contact with elemental lithium. A thin layer of lithium iodide immediately forms between the lithium anode and the cathode material. As the cell is discharged, this solid electrolyte grows between anode and cathode. As a lithium atom is ionized, the electron lost by that atom travels externally through the load causing the electrical current. The resultant lithium ion migrates through the electrolyte to the cathode interface where it reacts with an iodide ion formed from electrochemical reduction of iodine. This results in the formation of another molecule of lithium iodide, as shown in Figure 1. The cell reaction proceeds in this manner until the impedance of the cell, due to both the increased resistance of the lithium iodide to lithium ion migration and the increased electronic resistivity of the cathode material, reaches a point such that the voltage of the cell is no longer usefully high.

The ionic conductivity of pure polycrystalline LiI is on the order of 10^{-7} ohm^{-1} cm^{-1} (1), suggesting that batteries using this electrolyte would show limited current-delivery capability. However, as will be discussed below, techniques for improving this conductivity have been incorporated into cell designs.

The mobility of the iodide ion in LiI, however, is extremely low and decreases as the layer of LiI increases in thickness. The electronic conductivity of LiI is also negligible. This means that self-discharge, which can be caused either by iodide ion migration to the anode interface or electronic leakage current through the electrolyte, is small even in initial stages of discharge and decreases to negligible levels as the lithium iodide layer becomes thicker. Indeed, Liang and Holmes have demonstrated using the technique of microcalorimetry that self-discharge of these batteries under pacemaker load decreases to negligible levels after 20 months of operation (2). The total self-discharge loss is estimated to be less than 7% over the projected 10 year life of the cell.

The lithium iodide layer serves two purposes in the cell. It is the medium through which lithium ions migrate from anode to cathode, and it is the separator between anode and cathode. An attractive feature of this system is the self-forming, self-healing nature of the electrolyte/separator. Separator fracture, a fairly common cause of failure in some battery systems, is of little concern in this system since, even if cracks developed in the electrolyte allowing cathode material to touch the anode, a new layer of lithium iodide would be reformed, thus alleviating a long-term short circuiting problem. This feature is a major contributor to the inherent reliability of the system.

ENHANCEMENT OF PERFORMANCE

Cells using metal anodes, iodine charge transfer complex cathodes, and self-forming solid electrolytes were reported by Gutmann and co-workers in 1967 (3). In 1972 Moser obtained a patent on the lithium/iodine cell (4). The potential usefulness of this system in the pacemaker application was recognized in 1971 (5), and the first clinical implant occurred in 1972.

Cells produced today typically have a configuration as shown in Figure 2. The lithium anode is centered in the cell. In some versions of the cell, this anode is corrugated to increase interface surface area. The iodine-PVP material is poured into the cell and surrounds the lithium anode. An alternate approach to construction is to press solid pellets of particulate iodine and PVP around the anode. The anode current is brought out of the battery through a well-insulated lead and a glass-to-metal or ceramic seal. The metal case serves as cathode current collector. The cell is welded to seal the internal components. The result is a hermetically-sealed unit suitable for use in a cardiac pacemaker. This basic cell design is amenable to changes in shape and size, providing pacemaker manufacturers with a variety of physical configurations suitable for their needs.

In the last ten years many significant improvements have been made, resulting in a threefold increase in energy density over early versions of the cell (6). Many of the improvements made in the last few years involve changes in internal configuration and removal of unneeded inert material. However, some improvements relate directly to the role of the solid electrolyte and will be discussed here.

The rather low ionic conductivity of lithium iodide imposes considerable restraint on the current-delivery capability of the cell. Accordingly, enhancing this conductivity would enhance cell performance. Techniques such as doping the solid electrolyte can be used to increase conductivity. For example, Liang and co-workers found that the ionic conductivity of LiI dispersed in alumina was three orders of magnitude higher than that of pure polycrystalline LiI, making the altered electrolyte much more useful in solid state batteries (7). Other methods of altering the structure of solid electrolytes can also enhance ionic conductivity.

In the lithium/iodine-PVP cell, it has been found that the nature of the solid electrolyte formed in situ can be substantially altered by applying a thin film of polyvinylpyridine to the lithium anode before cell fabrication (8). Cells made with this anode precoating process exhibit substantially lower internal impedance and higher current-delivery capability than do otherwise identical cells made without this precoating. In fact, cells made with anode precoating exhibit internal impedances typically an order of magnitude lower than cells with uncoated anodes.

Holmes and Brown have made a detailed study of the differences in morphology and crystal growth formed in cells with and without anode precoating (9). Cells made with and without anode precoating were discharged. The cells were then destructively analyzed and the solid electrolytes formed during discharge were studied by optical and scanning electron microscopy.

Profound differences between the two discharge products were apparent at both the macroscopic and microscopic levels. On a macroscopic level, the electrolyte formed in the uncoated-anode cell was very regular, rigid, and strong, providing a uniform barrier between the residual anode and the cathode material. The macroscopic appearance of the coated-anode cell featured a lack of regularity, with numerous fissures and a columnar growth of electrolyte. The interface between lithium and electrolyte was much tighter and well-bound in the coated-anode cell.

On a microstructural level (2000X SEM), the uncoated-anode cell gave the appearance of a bonded mass of granules between 1 and 20 microns. A matrix of apparently amorphous LiI is present, leading one to conclude that the overall structure is one of relatively high density. The electrolyte formed in the coated-anode cell gives the appearance of a granular mass of equiaxed, well-formed crystallites of apparently lower density. No matrix phase is present.

These differences in electrolyte structure lead to substantial differences in electrical performance, which is illustrated in Figure 3. This graph shows comparative discharge curves of two lithium/iodine pacemaker cells, one with the standard coating and an otherwise identical cell without the coating. Both cells were discharged under a resistive load of 10 kohms, some ten times heavier than a typical pacemaker current drain. The difference in performance between the two cells is striking. The difference in performance between coated and uncoated cells is attributed to a better interface contact area and a lower ionic resistance due to the difference in macro- and microstructure between the electrolytes formed during discharge.

In a solid electrolyte cell the integrity and area of the electrode/electrolyte interface are important factors in the performance of the cell. In addition to the beneficial effect of anode precoating on the anode/electrolyte interface, a further enhancement of the interface properties was obtained by corrugating the central lithium anode. The anode corrugation increased the effective surface area of the lithium/lithium iodide interface by over 30% without increasing the size of the battery. A substantial increase in the current-delivery capacity of the cell was noted (10). In addition to this automatic increase in surface area, anode corrugation also resulted in the elimination of macroscopic distortion of the anode and potential loss of interface integrity seen in previous cells with a flat central anode.

Cells made with coated, corrugated anodes exhibit a distinctive discharge profile when examined microscopically. Figure 4 shows a cross-sectional view of a cell discharged under a 5 kohm load. The sample was prepared by fracturing the discharged cell, grinding, and polishing the cross-section. All operations were done in an extremely dry environment because of the sensitivity of the cell components to water. The remainder of the central lithium anode is shown in the center of the cell. Surrounding the lithium is the solid electrolyte lithium iodide which was formed as the cell was discharged. The dark material at the edges and extending in columns through the lithium iodide is the residual iodine-PVP cathode material. The columns of lithium, banded by lithium iodide, are intermingled with columns of the cathode material. Because of the original corrugated anode structure and the columnar growth of lithium iodide, the thickness of the electrolyte area has been effectively reduced, producing a shorter path through which the lithium ion must travel during discharge.

The combination of anode precoating and anode corrugation has thus produced a solid electrolyte whose interface to the lithium anode is maximized for surface area, whose bonding to both anode and cathode is excellent, and whose resistance to lithium ion migration is minimized.

Schneider and co-workers have reported another method for reducing the resistivity of the lithium iodide formed in lithium/iodine-PVP batteries (11). These workers have developed batteries in which the cathode material is formed by pressing pellets of mixed particulate iodine and polyvinylpyridine. The resultant pellets are not thermally reacted as in more traditional cathode preparations. These workers report that cells made with the pelletized, unheated cathode materials exhibit higher current delivery capability than do cells made with uncoated anodes and the traditional heated cathode. This phenomenon is attributed to the fact that the electrolyte layer formed during cell discharge is composed of smaller crystallites of LiI which results in higher ionic conductivity (12).

CELL PERFORMANCE

Since its introduction in 1972 the lithium/iodine-PVP battery has amassed an outstanding record of reliability. In 1970, pacemaker failure due to premature depletion or failure of the zinc-mercuric oxide batteries then in use was responsible for at least half the clinical explants. Today, pacemaker failure due to battery problems is much less common. Indeed, the FDA lithium pacemaker implant registry in April of 1981 estimated the cumulative survival of lithium/iodine pacemakers at 92.7% after six years (13), and this figure reflects all pacer failures, battery or otherwise.

The lithium/iodine-PVP battery has also exhibited a gradual, predictable approach to the elective replacement voltage. This gradual decrease in voltage and increase in impedance is easily sensed by the pacemaker and is reflected by identifiable changes in the pacemaker rate which signals to the monitoring physician the prospect of pacemaker replacement. This approach to the elective replacement voltage is caused by the gradual buildup in the cell of the lithium iodide electrolyte and the rise in cathode resistance.

In a paper published in 1981 Holmes and Stinebring compared real time performance of a group of cells made in 1975 to accelerated test predictions made six years ago (14). They found that the average voltage of a group of 55 cells on test under simulated pacemaker conditions (i.e. 100 kohm load at 37°C) was within 5% of the predicted voltage. Furthermore, the approach of the battery to the elective replacement voltage was indeed smooth and gradual as predicted.

The earliest cells made with the corrugated, coated lithium anode have been on test for 48 months under simulated pacemaker conditions. One configuration of this cell was assigned a rated capacity of 1.3 ampere hours and, as such, was expected to perform for approximately 64 months before the voltage dropped to 1.8 volts.

Figure 5 shows both the projected discharge curve formulated in 1978 and the average voltage of a group of 20 of the earliest production cells. It was predicted that the voltage would be 2.5 volts at the four year point. The average voltage is in fact 2.66 volts, with a range of 2.57 to 2.71 volts. The batteries are demonstrating the gradual voltage drop desired in the clinical application. Of the 1,971 cells of this model kept as part of the routine in-house monitoring of cell performance, not one judged initially acceptable has failed, a total of 51,810 months of cumulative test time with no failures.

CONCLUSION

The lithium/lithium iodide/iodine-PVP solid electrolyte battery , the most commonly used power source for pacemakers today, has proven to be a reliable power source for this important medical application. Efforts to enhance performance of the cell by altering the nature of the solid electrolyte have proven successful. Performance of the battery in real time tests has shown to be predictable, and the approach of the cell voltage to the elective replacement point is smooth and gradual. The battery is a good example of the use of a solid electrolyte system in an important application.

REFERENCES

(1) J. Hladik, editor, Physics of Electrolytes, 2, Academic Press, New York (1972), p. 1112.

(2) C. C. Liang and C. F. Holmes, J Power Sources 5: 3; 1980.

(3) F. Gutmann, A. M. Herman, and A. Rembaum, J Electrochem Soc, 114: 343; 1967.

(4) J. Moser, "Solid State Lithium-Iodine Primary Battery," U. S. Patent 3,660,163, 1972.

(5) W. Greatbatch, J. Lee, W. Mathias, M. Eldridge, J. Moser, and A. A. Schneider, IEEE Trans Biomed Eng, BME 18: 317; 1971.

(6) R. T. Mead, C. F. Holmes, and W. Greatbatch, Proc Symp on Cell Design and Optimization, The Electro-

chemical Society, Princeton, N. J., Vol. 79-1, p. 327.

(7) C. C. Liang, A. V. Joshi, and N. E. Hamilton, J Appl Electrochem, 8: 445; 1978.

(8) R. T. Mead, W. Greatbatch, and F. W. Rudolph, "Lithium-Iodine Battery Having Coated Anode," U. S. Patent 3,957,533, 1976.

(9) C. F. Holmes and W. R. Brown, Proc Symp on Power Sources for Biomedical Implantable Applications, The Electrochemical Society, Vol. 80-4, 187 (1980).

(10) C. F. Holmes and J. M. Greenwood, Proc 29th Power Sources Symp, The Electrochemical Society, 62 (1980).

(11) A. A. Schneider, G. C. Bowser, and H. Foxwell, Lithium Iodine Primary Cells Having Novel pelletized Depolarizer, U. S. Patent 4,148,975, 1979.

(12) A. A. Schneider, S. E. Snyder, T. DeVan, M. J. Harney, and D. E. Harney, Proc Symp on Power Sources for Biomedical Implantable Devices, The Electrochemical Society, 144 (1980).

(13) B. B. Owens, K. R. Brennan, and J. Kim, Stimucoeur, 9: 371; 1981.

(14) C. F. Holmes and R. C. Stinebring, Proc Symp on Lithium Batteries, The Electrochemical Society, 81-4, 293 (1981).

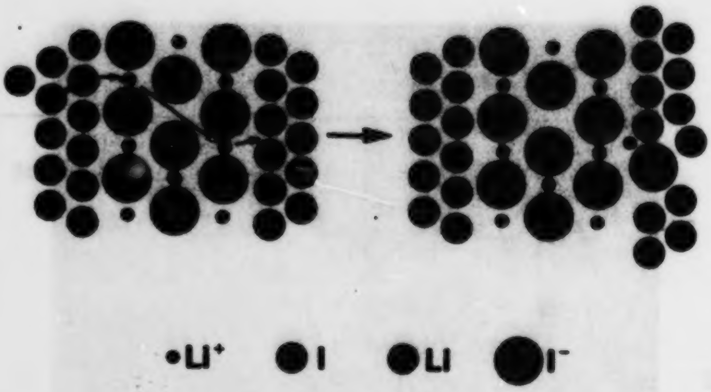

Fig. 1 - Schematic drawing of lithium/iodine battery reaction.

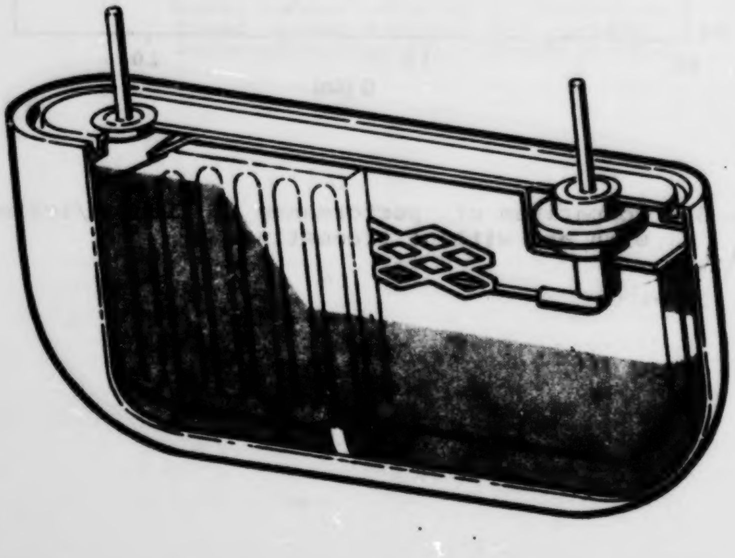

Fig. 2 - Cutaway drawing of a lithium/iodine pacemaker battery.

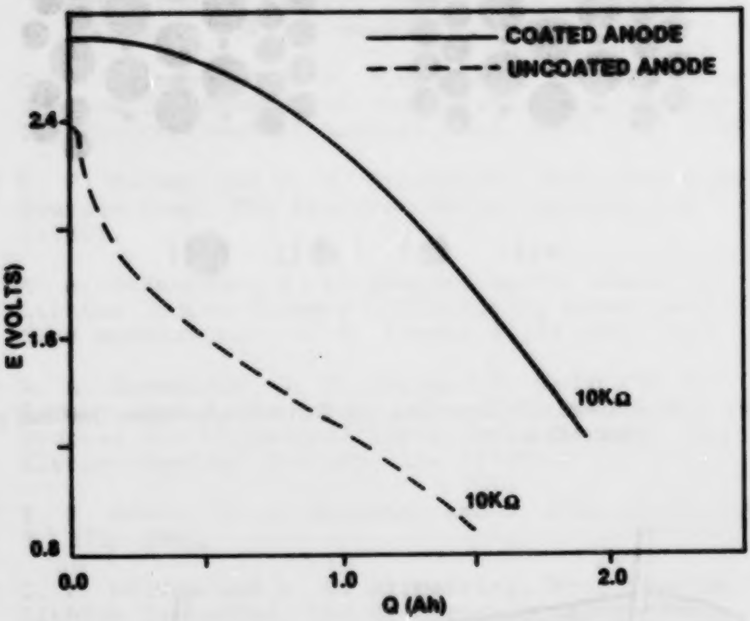

Fig. 3 - Comparison of performance of lithium/iodine with and without precoating.

Fig. 4 - Cross-sectional view of depleted lithium/iodine battery showing central lithium anode, lithium iodide solid electrolyte formed during discharge, and residual iodine-polyvinylpyridine cathode material.

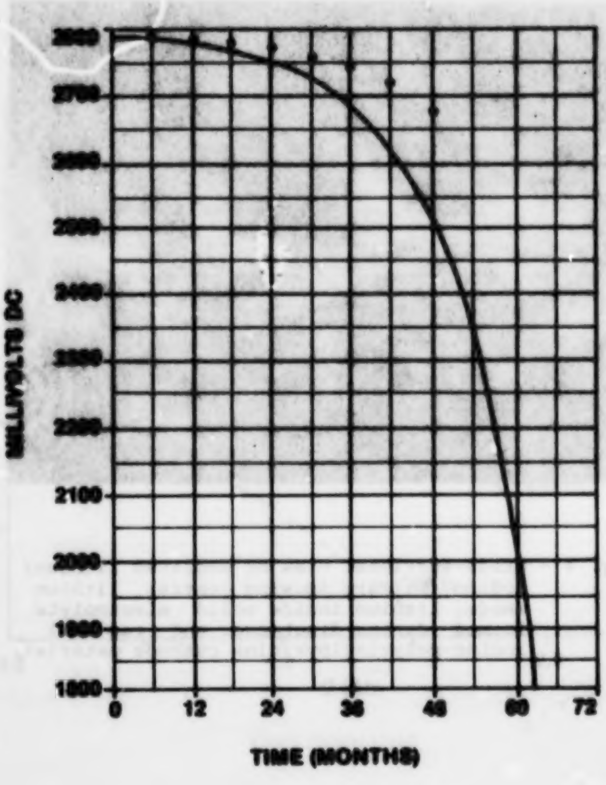

Fig. 5 - Comparison of projected discharge curve (solid line) and real time performance of a group of 20 lithium/iodine batteries on test for four years.

THE DEVELOPMENT OF BETA-ALUMINA PROBES

A.D. Pelton, A. Dubreuil and M. Malenfant

Département de Génie Métallurgique
Ecole Polytechnique
P.O. Box 6079, Station "A"
Montréal, Québec H3C 3A7

ABSTRACT

The use of beta-alumina and cation-substituted beta-alumina as electrolytes in galvanic cell measurements is reviewed. Topics discussed include the fabrication and sealing of beta-alumina tubes, the choice of reference electrodes, limits of detection, stability and reproducibility. The use of two-phase (α-Al_2O_3 + beta-alumina) tubes as Na reference electrodes or as low temperature oxygen probes is described. The application of beta-alumina probes to monitor the Na content of molten Al is discussed.

KEYWORDS: Beta-alumina fabrication, beta-alumina probes, solid electrolytes, sodium probe, sodium reference electrodes, slip-casting, oxygen probe.

RÉSUMÉ

L'utilisation comme électrolyte solide dans des cellules galvaniques de l'alumine-bêta au sodium ainsi que d'alumines-bêtas où les cations ont été substitués, a été revisée. Les sujets discutés comprennent la fabrication et le scellement de tubes d'alumine-bêta, le choix des électrodes de référence, les limites de détection de même que la stabilité et la reproductibilité. L'emploi de tubes biphasés (Al_2O_3-α + alumine-bêta) comme électrode de référence pour le sodium ou comme électrode indicatrice d'oxygène à basse température est décrit. L'utilisation de sondes employant l'alumine bêta pour suivre la concentration de sodium dans l'aluminium liquide est discutée.

INTRODUCTION

Beta-alumina exhibits very high ionic conductivity, very low electronic conductivity and is highly selective to Na^+ ion transport. Hence, the open circuit emf, E, of a galvanic cell of the type

$$\text{Na (I)} \,\Big|\, \text{beta-alumina} \,\Big|\, \text{Na (II)} \qquad [1]$$

is given by:

$$E = \frac{RT}{F} \ln \left(a_{Na}^{II}/a_{Na}^{I}\right) \qquad [2]$$

where a_{Na}^{I} and a_{Na}^{II} are the chemical activities of Na at the two electrodes. If a_{Na}^{I} is fixed by a suitable choice of reference electrode, a_{Na}^{II} may be measured. The ionic conductivity of beta-alumina is so high that measurements at temperatures as low as -60°C have been made (1), and its thermodynamic stability is such that the upper temperature limit of its use is above 1300°C and may be as high as 1600°C. It may be used in aggressive media such as molten oxides and fluorides. Furthermore, Na^+ may be replaced in the beta-alumina structure by other monovalent cations such as Li^+, K^+, Ag^+ etc., the high ionic conductivity being maintained. Hence, ion-selective sensors for these elements can also be constructed.

Although much research has been conducted on the use of beta-alumina for battery applications, relatively little work has been done on the potential uses of this material in industrial and laboratory probes and sensors. The present article reviews such work carried out in this and in other laboratories. Practical aspects such as methods of fabricating and sealing beta-alumina tubes are stressed. Various experimental problems and limitations are identified. The choice of reference electrodes is discussed, particular attention being paid to two-phase (α-Al_2O_3 + beta-alumina) tubes. These may be used as Na reference electrodes over a wide range of temperatures and as well, they may be used as oxygen probes.

Although β''-alumina is preferred over β-alumina for battery applications because of its somewhat higher ionic conductivity, this higher conductivity confers no particular advantage in galvanic cell measurements. In point of fact, for galvanic probe applications, β-alumina is preferred over β'', firstly since the fabrication of β''-alumina is more difficult because of the more complex sintering cycle (2,3) required, secondly since

β-alumina powder is commercially available while β'' is not, and thirdly since β-alumina is more selective than β'' against the entry of divalent cations into its structure (4).

FABRICATION

Starting Material

Beta-alumina powder can be produced by heating Na_2CO_3 (or $NaNO_3$ or NaOH) with Al_2O_3 or its hydrates (5, 6) or by solid state reaction between $NaAlO_2$ and γ-Al_2O_3 (7). In order to produce a dense product, the material should be melted, then crushed and milled (8, 9). Fused beta-alumina "Monofrax H" bricks are available from Harbison Carborundum Co., Falconer, N.Y. The principal impurity is ≈0.1% SiO_2. Fused beta-alumina "XB2" powder (≈200 mesh) is available from Alcoa Corp. The principal impurities are Fe_2O_3, CaO, SiO_2, K_2O and Li_2O (≈0.02% each) (10). This latter product has been used exclusively, after further milling, in this laboratory.

Pellets

Dense pellets are produced by cold-pressing and sintering (11-13). However, in order to separate the electrode compartments on either side of a pellet, the pellet must be sealed in a tube of another material such as alumina or quartz. Mechanical seals are subject to leaks, while seals employing cements are subject to attack in corrosive environments. All seals are difficult to make leak-tight. The problem is particularly acute when the electrode compartments contain gaseous or liquid phases. The most satisfactory configuration is obtained with closed-end tubes which permit complete separation of the electrode compartments.

Closed-end tubes

Tubes of beta-alumina have been prepared by extrusion (14), by electrophoretic deposition (8, 15-17) and by isostatic pressing (14, 18-20). These techniques all require special equipment. Slip-casting a technique requiring little investment in special equipment, has been used by Byckalo et al (21) who used aqueous suspensions with additions of HCl and an organic deflocculating agent to control the viscosity. Casting was performed in plaster moulds.

In this laboratory it has been found that control of an aqueous slip is difficult since the HCl continually leaches the Na_2O from the beta-alumina.

The use of additives can introduce impurities and porosity into the final product. Finally, the cast tubes have a strong tendency to adhere to plaster moulds, necessitating the use of demoulding agents, and limiting the technique to the production of relatively thick-walled tubes which can be removed from the mould without breaking.

Hence, a new slip-casting process involving no additives and employing non-adhering "powder moulds" was developed (22). The XB2 beta-alumina powder is ground for several days in a ball mill with dry methanol. As long as all water is rigorously excluded, no deflocculating agents are required. Grinding to a mean particle size < 1 µm permits sintering to be carried out later at much lower temperatures. After grinding, the slip is poured into a "powder mould" formed by compacting dry alumina powder around a mandril. In Fig. 1 the mould is formed by compressing the powder in a breaker by thumb pressure around a glass test tube which is then removed. The resulting mould holds its shape, and has approximately the same porosity as a plaster mould. When the slip is introduced, the methanol is absorbed into the mould and the beta-alumina is deposited on the mould wall. About 1 min. is required to build up a deposit of 1 mm thickness, whereupon the remaining liquid is decanted. The article may then be allowed to dry completely in the mould. Removal from the mould involves no mechanical stress since the powder is simply scooped and brushed away. Hence, tubes with very thin walls (< 0.5 mm), and thus with low electrical resistance, can be produced.

The article is then fired at 1550°C for 3 hrs to obtain approximately 96% of theoretical density. In order to prevent loss of Na_2O by volatilization, the piece should be packed in coarse beta-alumina powder during firing. As stated above, a reduction of several hundred degrees in the required sintering temperature is achieved by keeping the particle size in the slip < 1 µm. Average grain size after sintering is about 30 µm.

The tubes are impervious. Helium leak rates $< 10^{-9}$ std cc/cm^2 sec are obtained. The resistance to corrosive attack is very good. Only some discoloration of the surface was observed after several hours in molten cryolite at 1050°C. Beta-alumina tubes have been used as probes in Na_2O-SiO_2-CaO melts at 1100°C (23) as well as in Na_2O-WO_3 melts (23) and in molten Na_2CrO_4 (20).

Thermal shock resistance increases as the diameter of the tube decreases. Tubes of 5 mm O.D. are preferred by the present authors. These have been plunged into molten Al after 20 min. preheating just above the melt surface.

Slip-cast tubes of beta-alumina, as well as of other ceramics, made by the powder mould technique are available from the authors via Polyceram, Inc., P.O. Box 6079, Station "A", Montreal, Quebec H3C 3A7.

Seals and joints to beta-alumina

Although long tubes of beta-alumina can be fabricated by slip-casting, electrophoretic deposition, or extrusion, sintering of tubes greater than about 10 cm in length requires special equipment to maintain straightness. Thus, it is often preferable to join a relatively short beta-alumina tube to a longer extension tube of α-Al_2O_3. For many probe applications, long tubes are not desirable in any case since one wishes to seal off the electrode compartment within the hot zone of the furnace in order to prevent volatilization losses.

Therefore, techniques of making high-temperature impervious joints and seals to beta-alumina tubes are required.

Completely impervious pyrex to beta-alumina graded seals employing two Kovar glasses have been made in this laboratory (24). For seals at temperature up to 1100°C, several authors (25-27) including the present authors have used "Autostic" ceramic cement (Carlton-Brown Partners Ltd., Elford Mill, Elford, North Tamworth, Staffordshire, England). This cement must be applied in several thin coats, each coat being permitted to dry for several hours. It is attacked quite quickly by Na vapour and other corrosive media and is somewhat porous. "Cotronix 940" cement (Cotronix Corp., 37 W. 39th St., New York, N.Y. 10018) can be applied in one coat. Provided that it is cured at 950°C for 12 hrs, it provides a virtually impervious bond between α- and β-alumina which can be used to 1100°C. It reacts slowly with Na vapour. It cannot be used to seal a metal electrode into a tube without a glass intermediary.

Very good seals and joints have been obtained with an aluminosilicate glass of composition 58% SiO_2, 23% Al_2O_3, 7% CaO, 6% MgO, 5% B_2O_3, 1% Na_2O. The components are melted together at 1200°C, cooled, crushed and applied with a binder. Melting is carried out at 1200°C. The seal is completely impervious and can be used to 850°C or, if it is covered with Cotronix 940 cement to confer more rigidity, it can be used to 1000°C. It is resistant to thermal shock and can be sealed to a Pt electrode.

GALVANIC CELLS WITH SODIUM BETA-ALUMINA ELECTROLYTE

In this section we shall discuss various galvanic cells employing sodium beta-alumina electrolytes with a view to illustrating the applications and limitations of such cells. At the same time, the advantages and disadvantages of various sodium reference electrodes will be discussed.

Electrodes containing metallic sodium

When each electrode consists of a solution of metallic Na with another component X:

$$\text{Na-X (I)} \,\Big|\, \text{beta-alumina} \,\Big|\, \text{Na-X (II)} \qquad [3]$$

then, from eq [2] the open circuit emf, E, gives the ratio of the activities of Na in the two solutions. If, in addition, one "solution" is pure Na, then $a_{Na} = 1$ in this reference electrode, and the measurement of E gives the activity of Na in the other electrode compartment directly.

Such cells have been used to measure Na activities in Na-Hg amalgams (28-30), in liquid Na-Sn (12) and Na-Pb (25) alloys, in molten Na-S (31), and in liquid $Na\text{-}NH_3$ solutions at -60°C (1).

In order to test the limits of precision of this type of alloy concentration cell, a study was undertaken in this laboratory on molten Na-Sn alloys (24). The apparatus is shown in Fig. 2. A slip-cast tube of beta-alumina, 1 cm O.D., 5 cm long, was joined by a Kovar-glass graded seal to a pyrex tube. The tube was filled with high purity Sn, and this inner electrode compartment was flame sealed under vacuum to avoid any oxidation or loss of Na by volatilization. Purified argon was circulated over the pure liquid Na in the reference compartment.

The selectivity of beta-alumina for Na^+-ion transport as well as its low electrical resistivity (the apparatus in Fig. 2 has a resistance of 1 ohm at 350°C) permits the composition of the alloy to be conveniently, rapidly, and accurately changed by the passage of a measured current (coulometric titration). The composition of the alloy was varied in this way from 0 to 25 a/o Na and back again. Emf's measured as the composition was decreased agreed within 0.5 mV of those measured as the composition was increased. Emf's were stable to 0.5 mV during one week at 400°C, and the agreement among 3 separate cells was ±0.5 mV. Such precision permits partial molar entropies of Na to be calculated to ±0.5 J K^{-1} mol^{-1} from the temperature dependence of the measured emf.

Curves of E versus log X_{Na} (where X_{Na} = mole fraction of Na) at low X_{Na} were linear (Nernst behaviour) down to $X_{Na}=10^{-3}$.

Saboungi and Corbin (32) have recently made similar measurements in Na-Pb, Na-Sn and Na-Bi alloys using slip-cast tubes from Polyceram, Inc., and employing coulometric titration techniques. They obtained similar reproducibility, precision and stability. Nernst behaviour was observed at Na concentrations down to $X_{Na} = 10^{-4}$.

Measurements in molten Na-Al alloys have been carried out with reversible emf's and Nernst behaviour at Na concentration $<$ 1 ppm as will be discussed in a later section.

From the preceding results it can be seen that pure molten Na is an excellent reference electrode for use with beta-alumina at lower temperatures. Small re-usable reference electrode assemblies have been made in this laboratory by sealing pure Na in 5 cm long, 5 mm O.D. beta-alumina tubes with a tungsten electrode through a Cotronix 940 cement seal. The tungsten was sealed to the cement via a glass intermediary. In order to prevent oxidation and volatilization of the Na during sintering of the seal, the Na was introduced into the tube by coulometric titration only after the seal was sintered. To this end, some tungsten powder was placed inside the tube to act as electrical contact to initiate the titration..

Clearly, the use of pure Na as a reference electrode is limited to lower temperatures because of its high vapour pressure (boiling point = 889°C). As well, at high temperatures, cement or glass seals are rapidly corroded. Also, a further problem known as "blackening" occurs when beta-alumina is in contact with metallic Na at high temperatures. A dark colouration of the beta-alumina is observed to gradually progress across the tube from the Na/beta-alumina interface over a period of hours or days depending upon the temperature. Significant blackening can occur at temperatures below 300°C, but only after several days or weeks. For most probe applications where only short service lives are required, blackening does not become important until the temperature exceeds about 550°C. Although it is well known that blackening can lead to eventual failure of the tube by cracking, again this is not a serious problem for probe applications. The most important question is whether blackening affects the electrolytic properties of beta-alumina. It has been proposed that blackening is due to reduction of the beta-alumina by sodium, introducing oxygen vacancies compensated by electrons (33), while other authors (34) propose the formation of unpaired electron centers or of very fine colloidal particles of Na. Weber (35) found that chemical colouration at high temperatures appears to lead to a measurable increase in electronic conductivity, while other authors (36) state that no clear evidence of any significant electronic conductivity has been found even in very heavily blackened tubes. Experience in this laboratory indicates that blackened tubes can be used as probes above 550°C in contact with pure Na, but that reproducibility and stability may decline.

It has recently been shown (37) that beta-alumina may be used with gaseous Na electrodes to measure sodium partial pressures in the range 10^{-5} to 10^{-8} atm from 200° to 350°C. This probe can be used to monitor Na concentration in the cover gas of fast breeder atomic reactors.

Multiphase Electrodes

Liang and Elliott (20) used the following cell to measure the Gibbs energy of formation of liquid Na_2CrO_4 in the range 1100°-1220°K:

$W(s)$, $WS_2(s)$, $Na_2S(s)$	β-alumina	$Na_2CrO_4(\ell)$, $Cr_2O_3(s)$, O_2 (0.21 atm), Pt
I (reference)		II.

[4]

The three-phase reference electrode fixes a sodium activity via the equilibrium:

$$W + 2\,Na_2S = 4\,Na + WS_2 \qquad \Delta G^{o} = -RT \ln a^{4}_{Na(I)} \qquad [5]$$

while, in the working electrode the Na activity is fixed by the equilibrium:

$2\,Na_2CrO_4 = Cr_2O_3 + 2.5\,O_2 + 4\,Na$

$$\Delta G^o = -RT\,\ell n\,a^4_{Na(II)}\,(0.21)^{2.5} \qquad [6]$$

The open circuit emf is then given, as always, by eq [2]. The Gibbs energies of formation of Na_2S, WS_2 and Cr_2O_3 being known, the Gibbs energy of formation of Na_2CrO_4 can be determined. The (W, WS_2, Na_2S) reference electrode has subsequently been used by Elrefaie and Smeltzer (26) and by the present authors (38). In the range 600° to 1000°C, the reference electrode potential E^o is reproducible to ±15 mV. However, the absolute value of E^o (i.e. relative to the potential of a pure Na reference) is only known to 100 mV because of uncertainties in the literature values of the Gibbs energies of formation of Na_2S and WS_2. The use of this reference electrode is limited to temperatures above 550°C. At lower temperatures, thermodynamic equilibrium is not obtained, and response is extremely sluggish.

Other 3-phase solid sodium reference electrodes which have been used are (Ni, NiF_2, NaF) (11, 26), and (Co, CoF_2, NaF) (11). These suffer from the same limitations as the (W, WS_2, Na_2S) electrode.

In this laboratory, the following cell has been used (27) to measure the activity of NaCl in molten NaCl-$NiCl_2$ solutions in the range 800°-1000°C:

$$\begin{array}{c|c|c} Ni(s),\ NaCl\text{-}NiCl_2\ (\ell) & \beta\text{-alumina} & NaCl\text{-}NiCl_2\ (\ell),\ Ni(s) \\ I\ (reference) & & II \end{array} \qquad [7]$$

Each electrode was sealed in a beta-alumina tube, and both tubes were immersed in a molten NaCl bath. At either electrode the Na activity is fixed by the equilibrium:

$Ni + 2\,NaCl = NiCl_2 + 2\,Na$

$$\Delta G^o = -RT\,\ln a^2_{Na}\,(a_{NiCl_2}/a^2_{NaCl}) \qquad [8]$$

The open-circuit emf, E, is again given by eq [2] which may be combined with eq [8] at each electrode to yield:

$$E = \frac{RT}{2F} \ln (a_{NiCl_2}/a^2_{NaCl})_I (a^2_{NaCl}/a_{NiCl_2})_{II} \quad [9]$$

If E is measured at several compositions of the solution in the working electrode down to $X_{NaCl(II)} = 0$, the composition in the reference electrode being held constant, then integration of the Gibbs-Duhem equation allows $a_{NaCl(II)}$ to be determined. Emf's were stable to ±0.2 mV over several days. Precision of the results was such as to permit partial molar entropies to be calculated from the temperature dependence of E.

The concentration of NaCl in the working electrode compartment was varied by coulometric titration of Na^+ from the external bath of pure NaCl. Titration in the other direction (i.e. from the NaCl-$NiCl_2$ solution to the NaCl bath) could not be carried out since, when a current was passed, Ni^{2+} ions also crossed the beta-alumina tube, turning it green throughout. Interestingly, no nickel entered the beta-alumina at open-circuit. An apparently similar phenomenon has been observed for beta-alumina in contact with $ZnCl_2$-NaCl melts (39). The explanation is not clear.

Flinn and Stern (39) have employed cells similar to cell [7] with (Zn (ℓ), $ZnCl_2$-NaCl (ℓ)) electrodes.

The 2-phase (Ni, $NiCl_2$-NaCl) or (Zn, $ZnCl_2$-NaCl) electrodes can be used as references. Neudorf and Elliott (23) used a similar 2-phase electrode, (Na_2O-WO_3 (ℓ), O_2 (0.21 atm), Pt), as reference. The problem with all these is that the composition of the liquid solution must be accurately known and must not change during the course of the measurements. Furthermore, all are limited to use at relatively high temperatures.

The (α-Al_2O_3, beta-alumina, oxygen) electrode

When α-Al_2O_3 and beta-alumina are in thermodynamic equilibrium, the concentration of Na_2O, and hence its activity, in the beta-alumina is fixed. If the oxygen partial pressure is also fixed, then the activity of Na is fixed.

A reference electrode assembly employing this principle is shown in Fig. 3. The solid electrolyte is a 5 cm long, 5 mm O.D., 2-phase (α-Al_2O_3 + beta-alumina) tube fabricated by grinding together an approximately 80% beta-alumina, 20% α-Al_2O_3 mixture and then slip-casting. The grain size of the sintered tube being ≈30 μm, intimate contact between the phases is obtained, thus ensuring that thermodynamic equilibrium is achieved. Pt is deposited on the inner surface of the tube by decomposition of chloroplatinic acid and electrical contact is made via a Pt lead. The inner compartment is left open to the air so that $p_{O_2} = 0.21$ atm, although other gas mixtures or solid metal/metal oxide mixtures can also be used to fix p_{O_2} inside the tube.

This reference electrode gives fast response at temperatures as low as 325°C with a reproducibility of ±25 mV or better.

This electrode has been calibrated directly versus pure liquid Na over the range 325°-550°C and versus the (W, WS_2, Na_2S) electrode over the range 600-900°C (38). Results are presented in Fig. 4 as a plot of measured log a_{Na_2O} where a_{Na_2O} is the activity of Na_2O in beta-alumina in equilibrium with α-Al_2O_3. Error bars shown on the points obtained versus the (W, WS_2, Na_2S) reference are calculated from the uncertainties in the literature values of the Gibbs energies of formation of WS_2 and Na_2S.

The least-squares line passing through these two sets of points is shown on Fig. 4. Its equation is:

$$\log_{10} a_{Na_2O} = -11.49 \times 10^3\ T^{-1} - 0.03 \qquad [10]$$

(where T = °K). Equivalently, the results can be presented as the electrode potential, E^o, of the (α-Al_2O_3, beta-alumina, oxygen) electrode relative to pure liquid Na:

$$E^o(\text{volts}) = 3.2421 - 6.68 \times 10^{-4}\ T + 49.6 \times 10^{-6}\ T \log_{10} p_{O_2}(\text{atm}) \qquad [11]$$

Over the range 90°-150°C, results shown in Fig. 4 were obtained by a chronopotentiometric technique.

While these results are less precise than the galvanic cell measurements, they do lie on the straight line given by extrapolating the high-temperature results (i.e. eq [10]), thus helping to confirm the slope of this line.

Also shown on Fig. 4 is a point obtained by Fray (13) who used a beta-alumina pellet with a compacted (α + β) powder mixture in one electrode compartment and pure Na as counter-electrode. The curve obtained by Elrefaie and Smeltzer (26) who used (α + β) tubes cast from aqueous slips is also shown on Fig. 4. These authors used (Ni, NiO), (Cu, Cu_2O) or (Fe, FeO) powder mixtures to fix p_{O_2} and either (W, WS_2, Na_2S) or (Ni, NiF_2, NaF) as counter-electrode. The points of Choudhury (11) on Fig. 4 were obtained with beta-alumina discs, with (Cu, Cu_2O) mixtures to fix p_{O_2}, and with (Ni, NiF_2, NaF) as counter-electrode. The curve of Weber, reported by (5), was obtained with a beta-alumina electrolyte separating a mixture of α-Al_2O_3 and beta-alumina in equilibrium with air on one side and a mixture of beta alumina and $NaAlO_2$ in equilibrium with air on the other side.

(α-Al_2O_3, beta-alumina, air) reference electrodes of the type shown in Fig. 3 were used to measure the activity of Na in liquid Al in equilibrium with solid NaF and solid cryolite by means of the cell:

$$Al(\ell),\ NaF(s),\ Na_3AlF_6(s)\ \left|\ \begin{matrix}\alpha\text{-}Al_2O_3\\ +\\ \beta\text{-}Al_2O_3\end{matrix}\ \right|\ O_2\ (0.21\ atm),\ Pt \qquad [12]$$

With eq [11] for E^o, results gave $a_{Na(\ell)} = 0.1168$ at 788°C and $a_{Na(\ell)} = 0.1643$ at 878°C. Values obtained by Dewing (40) by means of vapour-pressure measurements by a gas-transference method gave values of 0.1077 and 0.1630. This means that the measurements with cell [12] gave emf's differing by only 7 mV at 788°C and by 1 mV at 878°C from those values that would reproduce Dewing's activities exactly.

A problem with the (α, β, air) reference electrode in Fig. 3 is its sensitivity to humidity. When humid air, saturated with water vapour at 25°C, is passed slowly into the electrode at 700°C by means of a quartz tube extending to the bottom of the (α + β) tube, the emf slowly deviates over a period of several hours. After 3 days the deviation stabilizes at 100-150 mV. If dry air is then passed into the electrode, the emf gradually returns over a period of 2-3 days to its former value. Thus it appears that the surface of the beta-alumina is slowly conditioned by exposure to water vapour and that this conditioning is reversible. Dunn (41) observed that the room temperature resistivity of beta-alumina increases considerably in humid atmospheres due to the formation of a hydrated surface region and that heating the tubes in dry air at 600°C restores the original resistivities. All such (α, β, air) reference electrodes should thus be baked in dry air at 700°C for several hours before use and should be stored in dessicators. They should not be used in humid atmospheres for long periods, although brief exposures appear to have no effect.

The problem of sensitivity to humidity can be reduced appreciably by coating the inner surface of the (α + β) tube with a very thin layer of calcia-stabilized ZrO_2. This can be done as a second step in slip-casting. Micrographic examination reveals that, after sintering, contact between the two ceramics is excellent and that the ZrO_2 layer is dense and nearly pore-free. The ZrO_2 layer permits the passage of O^{2-} ions, so that the (α + β) surface is in equilibrium with the air, but blocks contact between the (α + β) tube and humidity in the air. When humid air is passed into a ZrO_2-coated tube, no change in emf is observed. The characteristics of these composite ceramic electrode assemblies are currently being studied.

The problem of sensitivity to humidity can also be alleviated by using metal/metal oxide mixtures to fix the oxygen potential inside the (α + β) tube which can be sealed in the hot zone. One disadvantage of this arrangement is that the electrode cannot be used below about 600°C because thermodynamic equilibrium is not attained at lower temperatures. Most success has been obtained with such electrodes by the present authors when compacted mixtures of finely powdered Cu, Cu_2O, α-Al_2O_3 and β-alumina are used. The inclusion of α-Al_2O_3 and beta alumina in the powder mixture yields faster response and minimizes polarizability.

Although (α-Al_2O_3 + beta-alumina) tubes have been discussed here as sodium reference electrodes, they can clearly also be used as oxygen probes. That is, the emf of the cell:

$$\mathrm{Pt},\ O_2\ (p_{O_{2(I)}})\ \left|\ \begin{matrix}\alpha\text{-}Al_2O_3\\ +\\ \beta\text{-alumina}\end{matrix}\ \right|\ O_2\ (p_{O_{2(II)}}),\ \mathrm{Pt} \qquad [13]$$

is given by:

$$E = \frac{RT}{4F} \ln p_{O_2(II)}/p_{O_2(I)} \qquad [14]$$

This will be discussed in a later section.

Finally, it has been proposed that 2-phase ($\alpha + \beta$) electrolytes can be used in aluminium concentration cells. If an activity of Al is fixed in an electrode compartment, then the Na activity is also fixed via the equilibrium:

$$2\ Al + 3\ Na_2O\ (\text{in } \beta\text{-alumina}) = 6\ Na + Al_2O_3\ (\alpha) \qquad [15]$$

Hence, if the activities of Al in the two electrode compartments are $a_{Al(I)}$ and $a_{Al(II)}$, then the emf of the cell is given from eqs [2] and [15] as:

$$E = \frac{RT}{3F} \ln a_{Al(II)}/a_{Al(I)} \qquad [16]$$

This principle has been used with some success with aluminium foil electrodes (11), with (AlF_3, NiF_2, Ni) electrodes (11) and with (Al_4C_3, C) electrodes (42), all of which define an activity of Al.

A BETA-ALUMINA PROBE FOR SODIUM IN MOLTEN ALUMINIUM

During the refining of Al, the Na content must be reduced to 1 or 2 ppm, particularly if thin sheets are to be rolled. A continuous monitoring of the sodium content of molten Al during refining would be useful.

An (α, β, air) probe of the design shown in Fig. 3 was tested for this purpose. The ($\alpha + \beta$) tube was 5 mm O.D. by 5 cm long. The α-Al_2O_3 extension tube was joined with Cotronix 940 cement. This joint would be placed in the molten Al. The inner electrode compartment was left open to the air. The probe was immersed in 150 g of pure molten Al containing several ppm Na at 747°C. Emf's were measured periodically as the Na content decreased by evaporation, and samples were simultaneously drawn off for chemical analysis by absorption spectroscopy. The accuracy of these analyses is ±0.5 ppm. Results are shown on Fig. 5.

The line shown on Fig. 5 was calculated from eq. [11] for E^o of the reference electrode and from the activity coefficient, $\gamma^o_{Na} = 391$, of Na at infinite dilution in Al at 747°C as measured by Dewing (40). Agreement is well within the limits of uncertainty of E^o and γ^o_{Na}, and the Nernst slope, dE/dlog(ppm) = 2.303 RT/F is observed.

The results in Fig. 5 are from two experiments. Other experiments are now being undertaken in an industrial environment. Results to date indicate that the probes can remain immersed in molten Al for at least 10 hrs; that emf's are stable and reproducible over this period; that thermal shock upon plunging the probe into the bath can be avoided by pre-heating the probe by holding it above the bath for 20 min; that sodium contents to <1 ppm can be measured; and that there is no interference from K or Ca in the bath, although the presence of Li causes some interference. Blackening is not a problem since the Na content is very low.

Two-phase (α-Al_2O_3 + β-alumina) oxygen probes

As discussed previously, two-phase (α-Al_2O_3 + beta-alumina) electrolytes can be used as oxygen sensors in cells of type [13], the measured emf giving the oxygen partial pressure ratio directly via eq [14]. An advantage of such probes over other solid electrolyte oxygen probes such as calcia-stabilized zirconia probes is that they may be used at lower temperatures due to the very high ionic conductivity of beta-alumina. Reversible emf's within 10 mV of theoretical have been measured at temperatures down to 325°C in gaseous atmospheres. In these experiments, probes of the design shown in Fig. 3 were used with a platinized Pt contact also on the outer surface of the tube at the bottom.

The emf was insensitive to humidity in the gas over short periods of a few minutes but, as discussed previously, if humidity is present for longer periods of time, the emf starts to drift. When p_{O_2} was fixed with Cu/Cu_2O mixtures, emf's within 10 mV of theoretical were obtained at temperatures down to 550°C, provided that α-Al_2O_3 and beta-alumina powders were included in the powder mixture as discussed in a previous section.

The measured emf is also dependent upon the flow rate of the gas at the electrode on the outer surface of the tube. Theoretical emf's are obtained only when the flow rate approaches zero. A possible explanation is that gaseous Na is formed at the electrolyte surface and is carried away by the flowing gas so that the chemical potential of Na at the surface never reaches its equilibrium value. Since the (α + β)

probe is basically a Na probe whose emf is related to the Na activity ratio by eq [2] and which acts as an oxygen sensor only by virtue of the equilibrium of O_2 with α-saturated beta-alumina, it is essential that the chemical potential of Na at the surface be the thermodynamic equilibrium value. The effect of gas flow rate in the inner electrode compartment on the emf is much less pronounced.

Two-phase (α + β) probes should also conduct ionically over a wide range of p_{O_2}. Hence, they should be useful for measuring very low oxygen pressures.

CATION-SUBSTITUTED BETA-ALUMINAS

As first discussed by Yao and Kummer (43, 5) it is possible to substitute other monovalent cations such as Ag^+, Li^+, K^+, Rb^+, Cu^+, Tl^+, Ga^+, In^+, NH_4^+, and H_3O^+ for Na^+ ions in beta-alumina and still retain the high ionic conductivity. Such cation-substituted beta-aluminas have applications as ion-selective membranes for the cation in question.

In some cases, such as K-beta-alumina, the powder can be made (for example by reaction of the carbonate with Al_2O_3) and then formed and sintered as in the case of Na-beta-alumina. However, given the commercial availability of Na-beta-alumina powder, it is often as easy or easier to produce tubes or pellets of cation-substituted beta-alumina by ion-exchange of already formed and sintered tubes or pellets of Na-beta-alumina. In other cases, such as Ag- or hydronium-beta-alumina, it is essential to pass via the ion-exchange route, since the compounds dissociate when heated to sintering temperatures.

Certain cations such as Ag^+ can be exchanged to >99% by simply immersing a tube of Na-beta-alumina in the appropriate molten nitrate. In the case of Li^+, exchange in molten $LiNO_3$ gives only about 50% substitution. 99% substitution can be obtained by first exchanging for Ag^+ in $AgNO_3$ and then exchanging Ag^+ for Li^+ in $LiNO_3$ (5). Alternatively, one step substitution of Li^+ for Na^+ can be effected in a large bath of high purity LiCl (44). Experience in this laboratory shows that for >99% substitution, two passes are required. That is, the LiCl from the first pass, which has become contaminated with Na^+, is removed and the tube is then placed in a fresh LiCl bath.

In the case of K, exchange of Na-beta-alumina powder in molten KNO_3 gives nearly complete substitution. However, polycrystalline tubes of Na-beta-alumina fracture upon immersion in KNO_3 presumably because of stresses induced in accommodating the larger cations. Crosbie and Tennenhouse (45) have shown that this problem can be circumvented by carrying out the exchange in KCl vapour at high temperatures where creep mechanisms can alleviate the stresses. Although only about 50% exchange occurs, the exchange can then be completed in molten KNO_3 without fracture. These results have been repeated by the present authors, who have also used the same process to produce tubes of Rb-beta-alumina.

Cu^+ (5) and Ga^+ (46) beta-aluminas have been produced by passage of electrical current from molten salt baths.

Exchange of divalent cations in β-alumina appears to be slow and incomplete (4). However in β"-alumina, substitution of divalent cations appears to be relatively easy (4).

Hydronium-beta-alumina may be produced by reaction with concentrated sulphuric acid at 290°C (47). It has been reported that hydrogen may be exchanged for Ag in Ag-beta-alumina (48). The use of hydrogen-exchanged beta-aluminas in gaseous concentration cells for measuring p_{H_2} has been discussed (49). However, the nature of the conducting species, the ion-exchange characteristics, the chemical stability, and the electrochemical characteristics of hydrogen-or hydronium-substituted beta-aluminas are still not well documented.

To date, very few studies of the applications of cation-substituted beta-aluminas as galvanic sensors have been carried out. K-beta-alumina has been used to measure the Gibbs energy of formation of $K_{1-x}Fe_{11}O_{17}$ (50) and of molten potassium polysulphides (51). Ag-beta-alumina has been used with a Ag_2S electrode as a sulphur pressure monitor (52), while Cu-beta-alumina has reportedly been used to measure copper activities in Cu-Sn alloys (53). The selective transfer of Ga through a Ga-beta-alumina membrane from a Ga-Sn alloy has been reported (46) and proposed as a technique for purifying Ga. Partially exchanged Fe , Cu^{II}, and Zn-beta-aluminas have reportedly been used in galvanic cell measurements (54).

Because of the fact that only monovalent cations are easily exchanged in beta-alumina, beta-alumina probes may be used as ion-specific membranes for monovalent elements in the presence of divalent or higher-valent species. All the galvanic cell measurements discussed in the preceding sections bear this out although, as shown in regard to the results on cell [7], care must be taken when a current is passed as in the case of coulometric titration, since divalent ions may then be forced into the beta-alumina.

In the presence of other monovalent species, however, ion-selectivity may be lost since many monovalent cations enter easily into beta-alumina and are highly mobile. Mixed potentials may then arise. Yao and Kummer (43) have measured the distribution of pairs of monovalent cations between beta-alumina and some molten salt baths. The question of under what conditions A^+ substituted beta-alumina may or may not be used to measure the activity of A in the presence of another monovalent species B merits further study.

CONCLUSIONS

Beta-alumina solid electrolytes have great potential for use in industrial probes and sensors. They can be used over the temperature range from -100°C to 1300°C or higher and are very resistant to corrosive attack in a wide variety of media. Very reproducible and stable emf's are obtained.

A method of slip-casting high purity high density tubes of beta-alumina which requires little investment in equipment has been described. Cements and glasses for forming high temperature joints and seals have been discussed.

Pure liquid Na can be used as reference electrode up to 550°C. Small contained electrode assemblies can be made by coulometric titration of Na into sealed tubes. Above 550°C, (W, WS_2, Na_2S) reference electrodes are useful.

Two-phase (α-Al_2O_3 + beta-alumina) tubes, in contact with air, act as reversible sodium reference electrodes at temperatures down to 325°C. These tubes can also be used as oxygen sensors over the same temperature range.

The development of a sodium probe for use during the refining of molten Al has been discussed. The detection limit is less than 1 ppm.

ACKNOWLEDGEMENTS

The authors wish to thank Mr. D. Cook for his assistance. Funding from the Natural Sciences and Engineering Research Council of Canada is gratefully acknowledged. Chemical analyses were performed by Reynolds Metals Co., Richmond, VA.

REFERENCES

1. K. Ichikawa and J.C. Thompson, J Chem Phys; 59:1680-91; 1973.
2. M.L. Miller, B.J. McEntire, G.R. Miller and R.S. Gordon, Ceram Bull; 58:522-526; 1979.
3. R.S. Gordon, B.J. McEntire, M.L. Miller and A.V. Virkar, "Processing of Crystalline Ceramics", H. Palmour, R.F. Davis and T.M. Hare eds., Plenum, N.Y., pp. 405-420; 1978.
4. R.E. Seevers, G.C. Farrington and B.S. Dunn, Extended abstract No. 716 of Physical Electrochemistry Group, Electrochem. Soc. Meeting, Montreal; 1982.
5. J.T. Kummer, Prog Solid State Chem; 7:141-75; 1972.
6. I. Wynn Jones and L.J. Miles, Proc Brit Ceram Soc; 19:161-78; 1971.
7. T. Takahashi and K. Kuwabara, J Sol St Chem Soc; 30:321-28; 1979.
8. J. Fally, C. Lasne, Y. Lazennec, Y. Le Cars and P. Margotin, J Electrochem Soc; 120:1296-98; 1973.
9. R. Collongues, Mat Res Bull; 13:1281-85; 1978.
10. T.L. Francis, F.E. Phelps and G. MacZura, Ceram Bull; 50:615-19; 1971.
11. N.S. Choudhury, J Electrochem Soc; 120:1663-67; 1973.
12. B.V. Joglekar, P.S. Nicholson and W.W. Smeltzer, Canad Met Quart; 12:155-58; 1973.
13. D.J. Fray, Met Trans; 8B:153-56; 1977.
14. S.A. Weiner and R.P. Tischer, "Research on Electrodes and Electrolyte for the Ford Sodium-Sulfur Battery"; Ford Motor Co. Annual Report, Dearborn, Mich.; 1976; 232 p.
15. J.H. Kennedy and A. Foissy, J Electrochem Soc; 122:482-86; 1975.
16. J.H. Kennedy and A. Foissy, J Am Ceram Soc; 60:33; 1977.
17. R.W. Powers, J Electrochem Soc; 122:490-500; 1975.
18. I. Wynn Jones and I.J. Miles, Power Sources; 3:245-64; 1970.

19. P. Popper, "Isostatic Pressing", Hayden, London; 1976.

20. W.W. Liang and J.F. Elliott, J Electrochem Soc; 123:617-20; 1976.

21. W. Byckalo, G. Rosenblatt, J. Lam and P.S. Nicholson, Ceram Bull; 55:286-88; 1976.

22. M. Rivier and A.D. Pelton, Ceramic Bull; 57:183-85; 1978; - U.S. Patent no. 4,338,272 (1982); Canad. Patent no. 1,128,736 (1982).

23. D.A. Neudorf and J.F. Elliott, Met Trans; 11B:607-14; 1980.

24. M. Rivier and A.D. Pelton, J Electrochem Soc; 125:1377-82; 1978.

25. D.J. Fray and B. Savory, J Chem Thermo; 7:485-91; 1975.

26. F.A. Elrefaie and W.W. Smeltzer, J Electrochem Soc; 128:1443-47; 1981.

27. R. Roumieu and A.D. Pelton, J Electrochem Soc; 128:50-55; 1981.

28. L. Hsueh and D.N. Bennion, J Electrochem Soc; 118:1128-30; 1971.

29. R. Galli, P. Longhi, T. Mussini and F.A. Tropeano, Electrochim Acta; 18:1013-16; 1973.

30. J. Balej, F.P. Dousek and J. Jansta, Coll Czech Chem Commun; 43:3123-29; 1978.

31. N.K. Gupta and R.P. Tischer, J Electrochem Soc; 119:1033-37; 1972.

32. M.L. Saboungi and T. Corbin, J Phys F Metal Physics; In Press.

33. L.C. De Jonghe and A. Buechele, J Mat Sci; 17:885-92; 1982.

34. D. Gourier and A. Wicker, Extended abstract No. 722 of Physical Electrochemistry Group, Electrochem. Soc. Meeting, Montreal; 1982.

35. N. Weber, Energy Conversion; 14:1 (1974).

36. D.S. Park, M.W. Breiter and R.W. Powers, Extended abstract no. 721 of Physical Electrochemistry Group, Electrochem. Soc. Meeting, Montreal; 1982.

37. O. Takikawa, A. Imai and M. Harata, Solid State Ionics; 7:101-7; 1982.

38. A. Dubreuil, M. Malenfant and A.D. Pelton, J Electrochem Soc; 128:2006-8; 1981.

39. D.R. Flinn and K.H. Stern, J Electrochem Soc; 123:978-81; 1976.

40. E.W. Dewing, Met Trans; 1:1691-4; 1970.

41. B. Dunn, J Am Ceram Soc; 64:125-28; 1981.

42. N. Obata, H. Sakai, M. Tachiki, M. Yamada and T. Kirihara, Solid State Ionics; 3/4:551-54; 1981.

43. Y.F. Yu Yao and J.T. Kummer, J Inorg Nucl Chem; 29:2453-75; 1967.

44. J.L. Briant and G.C. Farrington, J Electrochem Soc; 128:1830-34; 1981.

45. G.M. Crosbie and G.J. Tennenhouse, J Am Ceram Soc 65:187-91; 1982; G.J. Tennenhouse, U.S. Patent no. 3,446,677 (1969).

46. R. Gee and D.J. Fray, Electrochim Acta; 24:765-7; 1979.

47. G.C. Farrington and J.L. Briant, Mat Res Bull; 13:763-73; 1978.

48. W.A. England, A.J. Jacobson and B.C. Tofield, J C S Chem Comm; 895-96; 1976.

49. J. Jensen and P. McGeehin, Silicates Industriels; 44:191-97; 1979.

50. G.J. Dudley, B.C. Steele and A.T. Howe, J Solid State Chem; 18:141; 1976.

51. G.M. Crosbie, J Electrochem Soc; 129:2707-11; 1982.

52. M. Sato,"Research Techniques for High Pressure and High Temperature"; G.C. Ulmer ed., p. 43, Springer-Verlag, Berlin; 1971.

53. J.A. Little and D.J. Fray, "Fast Ion Transport in Solids"; P. Vashishta, J.N. Mundy and G.K. Shenoy eds., North-Holland, N.Y., pp. 323-27; 1979.

54. G. Rog, S. Kozinski and A. Kozlowska-Rog, Electrochim Acta; 26:1819-21; 1981.

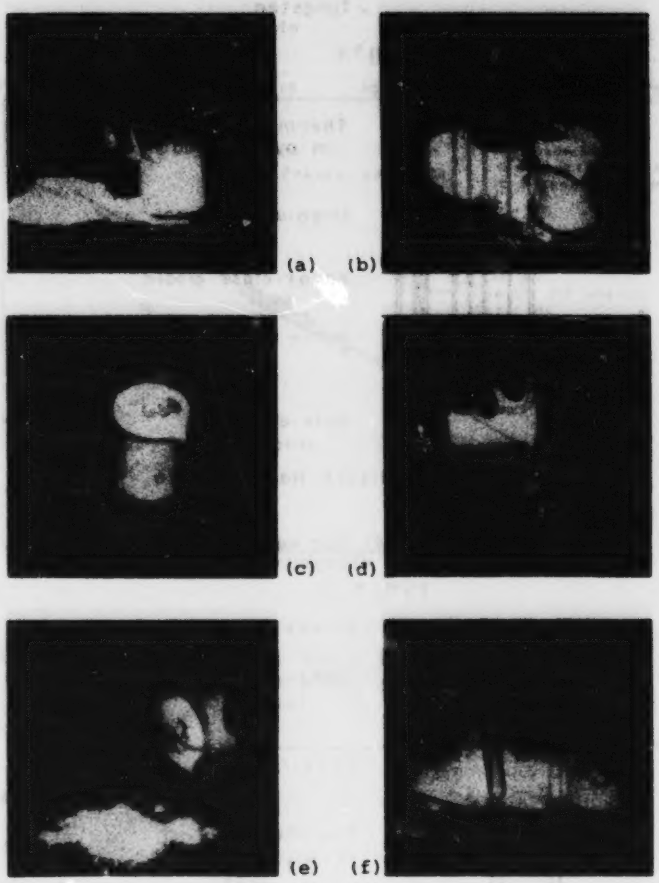

Fig. 1. Slip-casting in a powder mould: (a) powder compacted in beaker around glass tube which is then removed; (b) suspension poured in; (c) liquid absorbed into mould with deposited wall thickness increasing; (d) excess suspension decanted; (e) mould powder removed; (f) moulded tube removed ready for firing.

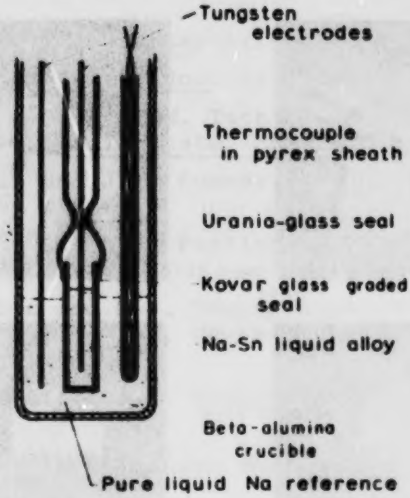
Tungsten electrodes
Thermocouple in pyrex sheath
Urania-glass seal
Kovar glass graded seal
Na-Sn liquid alloy
Beta-alumina crucible
Pure liquid Na reference

Fig. 2. Apparatus (24) for measuring activities in liquid Na-Sn alloys.

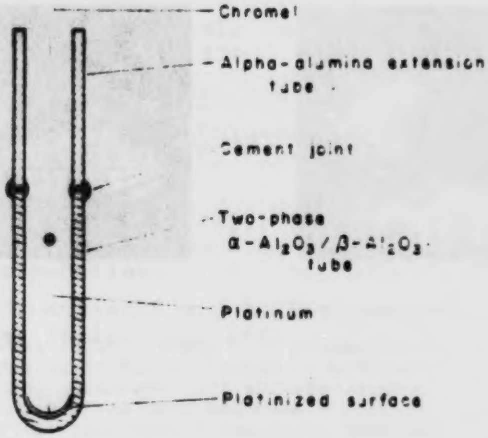
Chromel
Alpha-alumina extension tube
Cement joint
Two-phase α-Al$_2$O$_3$/β-Al$_2$O$_3$ tube
Platinum
Platinized surface

Fig. 3. α-Al$_2$O$_3$ + beta-alumina electrode assembly.

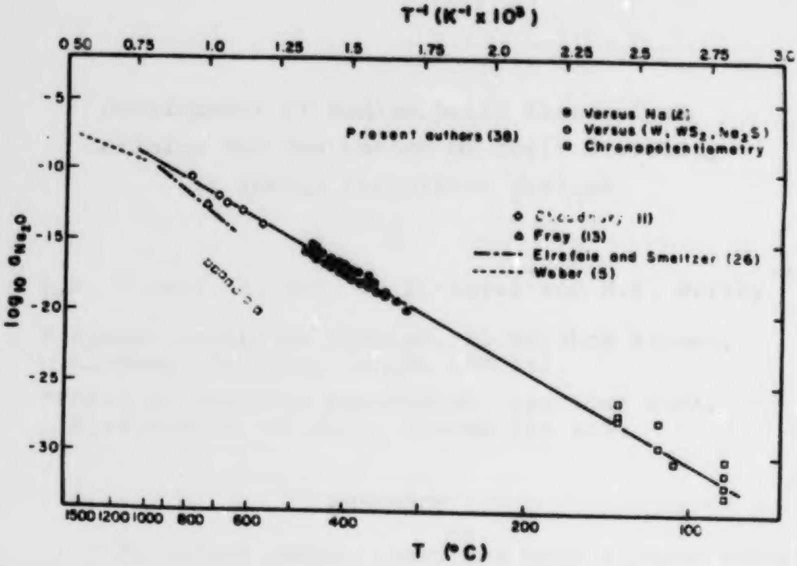

Fig. 4. Activity of Na_2O in beta-alumina in equilibrium with α-Al_2O_3.

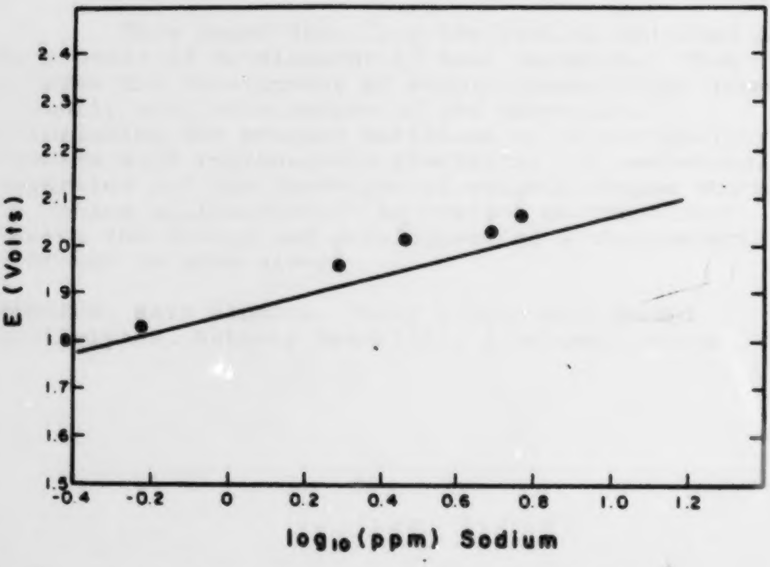

Fig. 5. Emf of the cell: Na (in liquid Al) | α-Al_2O_3 + beta-alumina | O_2(0.21 atm), Pt at 747°C.

Development Of Sodium Solid Electrolyte Ceramics And Evaluation Of Their Stability In Energy Conversion Devices

S.E. Prasad[*], R. Roy[**], K. El-Assal[*] and M.K. Murthy[**]

[*] Almax Industries Limited, 61 Needham Street,
Lindsay, Ontario, Canada K9V 4Z7.

[**] Ontario Research Foundation, Sheridan Park,
Mississauga, Ontario, Canada L5K 1B3.

ABSTRACT

In recent years, there has been a large effort devoted to the development of solid-state ionic conductors for use in high-efficiency electrical energy storage and conversion systems. Sodium-ion conductors such as beta-alumina have played a leading role in this application.

This paper describes the results obtained in the process of development of such ceramics. This includes the development of stable compositions from a readily available source of raw materials, establishing the process variables to obtain quality ceramics with reproducible electrical and mechanical properties and the formation of ceramic shapes suitable for device applications. An outline of the effort towards the design and development of a thermoelectric generator is also given.

KEYWORDS: Beta Alumina, Ionic Conductors, Solid Electrolytes, Battery Materials, Aluminosilicates.

RÉSUMÉ

On tente depuis quelques années de mettre au point des conducteurs ioniques à l'état solide qui seraient utilisés dans les systémes de stockage et de conversion de l'énergie électrique à haut rendement énergétique. Les conducteurs d'ions sodium comme la béta-alumine ont joué un rôle clé dans cette application.

Le rapport décrit les résultats obtenus lors de la mise au point de ces céramiques, y compris la fabrication de composés solides à partir de matières brutes facilement disponibles, l'établissement des variables du procédé afin d'obtenir des céramiques de qualité dont les propriétés électriques et mécaniques sont susceptibles d'être reproduites et la création de formes céramiques qui seront utilisées dans les appareils. Il résume également les travaux de conception et de mise au point d'une génératrice thermoélectrique.

INTRODUCTION

A growing awareness of the energy requirements of a technologically advanced society coupled to a deepening understanding of the environmental implications of that technology has brought about a renewed interest in electrochemical storage devices. This interest has manifested itself in a growing effort directed towards the development of high-energy battery systems for energy storage. The major applications foreseen for these devices are as batteries for electric vehicles and as load levelling storage systems for electric utilities. The unique properties of the solid electrolyte Beta-Alumina and cells based on this material, viz., Sodium-Sulphur batteries and Sodium thermoelectric generators have been the centre of much of the development and attention (1-5).

Sodium-Sulphur cell operation can be described as the reduction of sulphur by sodium with sodium ions being transported through the solid electrolyte while the electrons flow in the external circuit. The reverse process also has a high Coulombic efficiency.

The thermoelectric generator is essentially a concentration cell. Such a cell based on sodium as working fluid is also known as the sodium heat engine. In such a cell, the working fluid is physically divided into two regions by the solid electrolyte which bears a porous metal electrode. The concentration cell is formed by a temperature difference across two regions by a heat source - heat sink configuration. Such generators have projected efficiencies of up to 40%. Other attractive features are high specific-power output, simplicity in design etc (6,7).

The sodium solid electrolyte and related cells development program at Almax Industries is engineering oriented and for this reason emphasis has been placed on overall development of a process on a laboratory scale. The work included the optimization of process variables, fabrication into required shapes and characterization of sintered ceramics as well as testing these ceramics in a thermoelectric generator. These investigations are described in the following pages.

THE ELECTROLYTE

Beta-Alumina is a general term used to refer to a family of sodium aluminates with closely related structures and chemical properties. Although the material has been known for over sixty years, it was only recently that Yao and Kummer (8) reported that beta-alumina exhibits sodium-ion diffusion and high ionic conductivity. These materials can be described by the general formula $Na_2O.\ 11Al_2O_3$. The β'' phase of such materials has been identified as useful and highly conducting to sodium ions.

Early studies indicated that β'' phase in alumina can be stabilized by the addition of MgO and/or Li_2O to the host material (9). In the present investigations, effects of both materials have been investigated on the final properties of the solid electrolyte.

PRECURSOR POWDER DEVELOPMENT

Research work over the last ten years has shown that-ion conducting ceramics may be produced using several techniques. These include coprecipitation of materials (10), decomposition of nitrate or sulphate solutions (11) and the Zeta process. In the later process, lithium zeta aluminate is first prepared and then blended with a non-stoichiometric aluminate before firing.

In the present work more conventional sequences of ball milling and calcining were adopted. This required special attention being devoted to selection of reactive and pure raw materials for the preparation of ionically conductive ceramics. Two techniques have been adopted in the preparation of ceramics. These are designated as 'calcined' and 'non-calcined' processes and the salient features of each are presented in Figure 1.

In the calcining process, extensive use was made of dry milling for the purpose of achieving uniform mixing prior to calcining. Another major consideration was the choice of a suitable raw material particularly for the minor constituents such as Li_2O of which less than 1% by weight is required. This can be accomplished by two methods; either the use of a compound with large associated groups which may be driven off during calcination or the use of a prereacted material containing only desirable components but with the minor constituent in a larger concentration. For example, in the case of lithium this involved the use of oxalates and aluminates in the second case.

A third consideration in calcining was that compounds used decompose cleanly without melting at a sufficiently low temperature. It is for this reason that sodium carbonate has generally not been used in this work. Finally cost/purity trade off was considered. Generally the literature reports that both calcium and silica impurities must be minimized because of their association with the degradation and failure of the ceramic electrolyte in sodium-sulphur cell applications. It has been observed in the present studies that the substitution of low-priced A16 alumina for higher purity and higher cost Reynolds HBS-DBM alumina can produce comparable conductivity at 300°C.

In the case of the simpler non-calcined processing route, the same criteria apply with the additional one that no solid to solid-and-gas decomposition reaction can take place as these may disrupt the shapes during firing. Because there is no secondary milling operation beyond mixing, it is important that the particle sizes of the raw materials be suitable for the pressing and sintering operations. Table 1 lists the raw materials used in the present work based on the above criteria.

During the bulk of the development work, particularly the formulation evaluation phase, dry milling using borundum media in a polyurethene lined jar mill was utilized both for blending of the raw materials and for milling of the calcined batch to a suitable size for pressing. It was found that this technique consistently produced more reactive powders when compared to milling in an alcohol slurry. Typically the powders had a surface area in excess of $6m^2/g$ and failure to achieve this resulted in reduced sintered density. The calcination was carried out at temperatures ranging from 1250 to 1350°C and up to 24 hours to achieve complete reaction. Sodium loss was monitored using neutron activation techniques and was kept to a minimum. During the present study it was realized that the technique of producing flowable powders which develop good β" ceramics upon firing by the non calcined route is the most advantageous one.

FABRICATION OF CERAMICS

β"-alumina ceramics can be formed into the required shapes using several techniques commonly used for oxide ceramics. The powder may be shaped by electrophoretic deposition (12) or slip casting (13) from suspensions. The ceramic ware can also be produced by isostatic pressing (14) and extrusion (15). These green shapes are then sintered to produce ceramics of high density. Sodium oxide has a high vapour pressure at elevated temperatures and techniques such as saturated atmosphere and rapid sintering are used to suppress the loss of soda.

Two methods have been investigated for shaping of greenware in the present study. Tubes of β"-alumina were prepared from slip casting and isostatic pressing. In the slip casting method an alcohol based slurry was used. To reduce the calcium contamination from the molds, packed powder casting molds (16) were used. Although β -alumina tubes could be produced with this technique, β"-alumina processing was rather difficult. In general the method produced rapid changes in viscosity of the slurry. This was compounded by the problem of separating mold from the casting. The latter problem also resulted in non-uniform geometries.

Tubes were successfully pressed using an isostatic press. Polyurethane mold bags in conjunction with stainless steel or teflon coated aluminum mandrel were used for pressing. The pressures ranged from 100 MPa to 200 MPa. The powders were spray dried after a binder was added. In addition to the binder, a plasticizer (1.5 - 2.5%) consisting of carbowax methoxy polyethylene glycol was also added.

The pressed tubes were fired under varying conditons to study the sintering conditions. Best firing conditions were achieved at temperatures ranging from 1580 to 1620°C with soak times of up to one hour. The study included low temperature annealing, slower heating rates as well as complex firing schedules. The results are summarized in Table 2.

Studies were also carried out with regard to zone firing of tubes. A radio frequency tube furnace was constructed to generate a five Cm hot zone reaching to 1700°C. A mechanical pusher system was set up to move the sample through the hot zone.

The ceramics obtained from the above firing schedules were tested for various properties and are discussed in detail in the following section.

OPTIMIZATION OF CERAMIC PROPERTIES

The optimum composition of the ceramic electrolyte was identified by a systematic evaluation of the Na-Li-Mg-Al-0 phase system, where Mg and Li perform the role of stabilizers. The optimum composition identified in terms of weight percent was:

Al_2O_3 88.5% ; Na_2O 9.5% ; Li_2O 0.5% ; MgO 1.5%

In the present studies optimum composition was identified utilizing mechanical, electrical and other properties.

The β" phase content of the ceramics was monitored using X-ray diffraction patterns. Four point bending provided a convenient method of measuring the strength of the ceramics. The optimum composition had strengths in excess of 140 MPa. Ionic conductivity was measured using molten salt electrodes. Figure 2 shows the impedance diagram for an optimized composition of the ceramic. The figure also suggests the absence of any grain boundary conductivity in the ceramic.

Chemical analysis for compositional variations in Li and Na content during firing were carried out by conventional techniques for Li and by neutron activation analysis for Na. The neutron activation studies showed that MgO improves the sodium retention during firing. These studies in general, indicated that elaborate sagger systems are not essential in the processing of β"-alumina. Further confirmation of these results have been obtained from proton microprobe analysis (17).

The concentration profiles of Na, Al and Li were monitored across a fractured surface of the ceramic using proton microprobe. The results showed that while there was no appreciable sodium gradient, the Li concentration showed a relative depletion within 150μm of the surface for Li stabilized materials. Such depletion layers did not exist in Mg-Li stabilized materials. Representative results are shown in Figure 3.

THE THERMOELECTRIC GENERATOR

The ceramics prepared in the current investigations were tested under sodium environment by utilizing them in a sodium thermoelectric generator. In the present work, a demountable test cell has been developed to facilitate routine monitoring of electrolyte ceramics and as such has served as a quality control tool for the materials.

The thermoelectric generator was conceived by Kummer and Weber (6) of Ford Motor Company during the early stages of sodium-sulphur battery development. Several versions of the generator have been described in the literature (7,18,19,20). These generators have efficiencies of up to 20% and power outputs exceeding 0.5 watts/sq.cm of the electrolyte surface area.

The thermoelectric generator is schematically shown in Figure 4. The cell is comprised of an outer and inner tube of metal made of corrosion resistant steel. At the lower end of the cell these tubes form an annular region and are used as a sodium reservoir. A beta"-alumina tube is positioned over the inner tube and within the outer tube so that the open end of the ceramic dips into a liquid sodium pool. A heater element will provide heat to the inner annulus and thus increase the sodium vapour pressure there. The sodium from the hotter and high pressure region passes through the electrolyte to condense on the cooler outer annulus. In order to pass through the electrolyte, sodium will ionize and thus generate an electric potential between the two surfaces of the tube. The outer surface of the electrolyte tube is provided with an electrode porous to sodium. This electrode provides a means for current collection. Figure 5 shows the assembled cell.

The potential difference E at zero current of such a cell obeys the Nernst equation. The voltage E is given by (7):

$$E = \frac{RT}{F} \ln \frac{P_2}{P_1}$$

where F is the Faraday Constant and R is the gas constant. T is related to the local vapour pressure at the outer surface of the electrode. When current is drawn from the generator, losses occur due to electrode polarization and due to the finite resistance of the electrolyte itself. The voltage-current relationship under load can be described by(21):

$$E = A - BT \ln I - IR_o$$

where R_o is the resistance of the electrolyte. The efficiency of the generator including the losses is given by:

$$\text{Efficiency} = \frac{W_1}{W_1+L+\Delta H+ K(T_2-T_1) + \frac{\sigma}{2} (T_2^{\,4} - T_1^{\,4})}$$

where W_1 is the work output, L is the latent heat of vapourization of sodium, ΔH is the enthalphy change on heating sodium from T_1 to T_2, K is the conductivity of the output leads and σ is the Stefan-Boltzman constant.

Figure 6 shows the variation of voltage with current for the thermoelectric generator described above. The results are typical of the behaviour of the optimum electrolyte composition and the electrode materials used in the studies. The electrical behaviour is in accordance with the theory and the estimated efficiency for this generator at 500°C is 5%.

CONCLUSIONS

From the present studies it can be concluded that the potential for realizing highly conducting and quality ceramics through the conventional processing route is good. The studies also suggest that Mg-Li stabilization increases the potential for sodium retention during sintering. Preliminary studies on the design and development of the thermoelectric generator indicate the usefulness of these ceramics in device applications.

ACKNOWLEDGEMENTS

This work has been supported by the Department of Energy Mines and Resources, Government of Canada. The authors wish to note the accurate contributions made by the technical staff of Almax Industries Limited and Ontario Research Foundation. In particular we acknowledge the work of J. Bobak, J.D. Dunn, G. Mathews and D. Tansley.

REFERENCES

(1) W.J. Welsh, "Advanced batteries for electric vehicles- A look at the future" Physics Today p34, June 1980.

(2) TRW Inc, "Development program for solid electrolyte batteries" Electrical Power Research Institute Report #127-1, October 1974.

(3) J.B. Bush, " Sodium-Sulphur battery development for bulk power storage" General Electric Company, Schenectady NY, EPRI Report #128-2, September 1975.

(4) Brown Boveri & Cie AG, Heidelberg, "Research and development of a Sodium-Sulphur battery" Federal Ministry of Research & Technology (BMFT) Research Report # T:76-40.

(5) Ford Motor Company, "Research on electrodes and electrolyte for the Ford Sodium-Sulphur battery" NSF/RA-761787, July 1976.

(6) J.T. Kummer and N.Weber, U.S. Patent 3,458,356 1968.

(7) N. Weber, " A thermoelectric device based on beta-alumina solid electrolyte" Energy Conversion 14:1;1974.

(8) Y.F.Y. Yao and J.T. Kummer, Journal of Inorganic Nuclear Chemistry 29: 2453; 1967.

(9) J.T. Kummer, Progress in Solid State Chemistry 7: 4; 1972.

(10) Ford Motor Company, " Research on electrodes and electrolyte for Sodium-Sulphur battery" NSF-RA-N-75-056, July 1975.

(11) S.P. Mitoff, Fast Ion Transport In Solids Ed. W. van Gool, p415, North Holland/Elsevier NY 1973.

(12) R.W. Powers, "Electrophoretic forming of beta-alumina ceramic" Journal of Electrochemical Society 122: 490; 1975.

(13) W. Byckalo, " Slip casting of beta-alumina for alkali probes in molten salts" American Ceramic Society Bulletin 55: 286; 1976.

(14) I.W. Jones and L.J. Miles, "Production of beta-alumina electrolyte" Proceedings of the British Ceramic Society 19: 161; 1971.

(15) Ford Motor Company, "Research on electrodes and electrolyte for Sodium-Sulphur battery" NSF-C805, December 1974.

(16) A. Pelton, Private Communication.

(17) D. Amm, J.D. MacArthur, K. Barfoot and M. Sayer, "The application of a proton microprobe to analysis of ceramics" Journal of The Canadian Ceramic Society 50: 1; 1981.

(18) R.B. Saillant and N. Weber, U.S. Patent 4,049,877; September 1972.

(19) I.W. Jones, U.S. Patent 4,042,757; April 1977.

(20) N. Weber, T. Cole and T.K. Hunt, Proceedings of the Intersociety Energy Conversion Conference: 2011; 1978.

(21) N. Weber, T. Cole and T.K. Hunt, Proceedings of the Conference on Fast Ion Transport in Solids, Gatlinberg,USA, May 1981. Eds. J.B. Bates and G.C. Farrington, North Holland Publishing Co. p263.

TABLE 1

SELECTION OF RAW MATERIALS

Material	Calcined Route	Non-Calcined Route
Alumina	Reynolds HPS-DBM Alcoa A-16	Reynolds HPS-DBM Alcoa A-16
Soda	Sodium Oxalate	Anhydrous Sodium Aluminate
Magnesia	Magnesium Carbonate	Magnesium Aluminate
Lithia	Lithium Oxalate Lithium Aluminate Lithium Zeta Aluminate	Lithium Aluminate
Milling Solvent	- - -	Ethyl Alcohol

TABLE 2

Effect of sintering condition on the properties of optimized composition of the solid electrolyte.

Soak Temp °C.	Soak Duration Min.	Density gm/cc	β"-content %	Resistivity ohm.cm*
1570	15	3.22	82	8.2
1580	5	3.23	82	7.0
1580	15	3.22	82	9.3
1580	45	3.23	84	7.3
1590	15	3.24	80	8.7
1600	5	3.23	84	8.4
1600	15	3.24	82	5.9
1600	45	3.24	87	7.1
1600	90	3.21	94	5.5
1610	15	3.24	84	8.1
1620	15	3.19	84	12.0

* Resistivity was measured at 300°C.

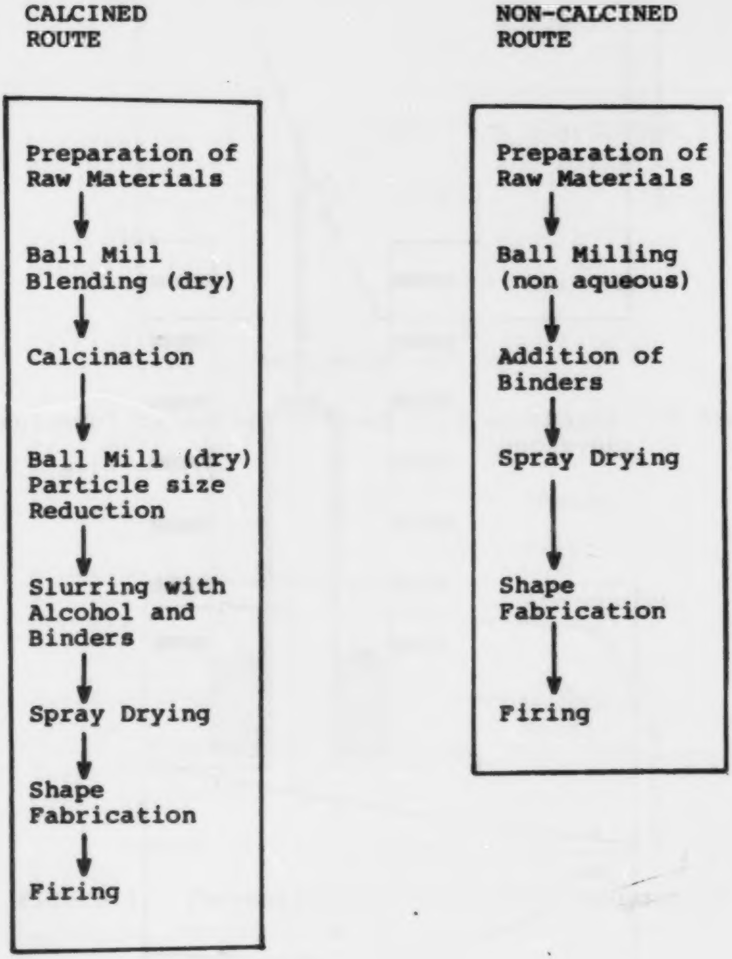
CALCINED ROUTE
Preparation of Raw Materials
Ball Mill Blending (dry)
Calcination
Ball Mill (dry) Particle size Reduction
Slurring with Alcohol and Binders
Spray Drying
Shape Fabrication
Firing
NON-CALCINED ROUTE
Preparation of Raw Materials
Ball Milling (non aqueous)
Addition of Binders
Spray Drying
Shape Fabrication
Firing

Figure 1.

Processing steps in the calcined and non-calcined processes as carried out in the present study.

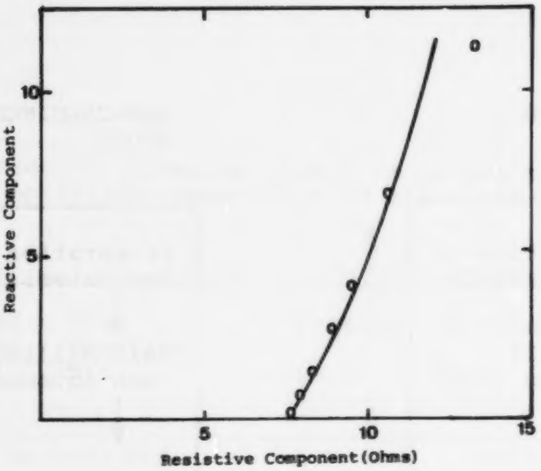

Figure 2: Impedance plot for the optimized formulation developed.

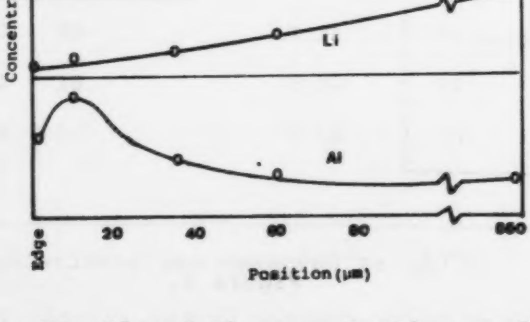

Figure 3: Na, Li and Al concentration profiles at the surface of Li stabilized sample.

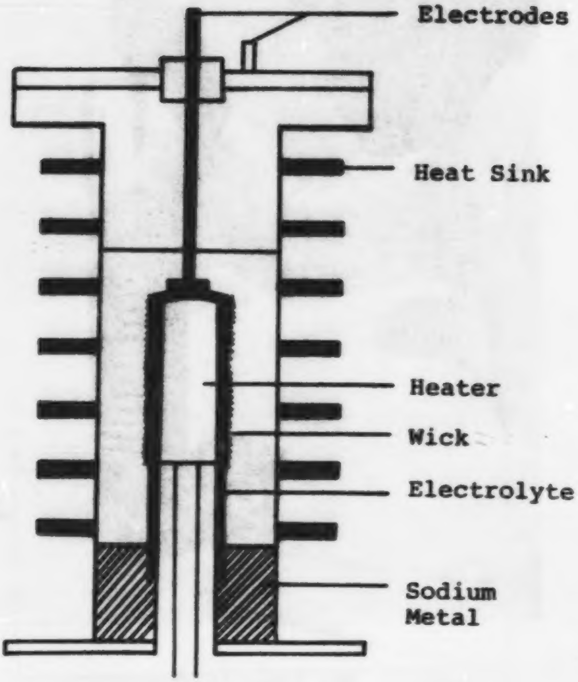
Electrodes
Heat Sink
Heater
Wick
Electrolyte
Sodium
Metal

Figure 4: Thermoelectric Generator (Schematic).

Figure 5: The Almax thermoelectric generator.

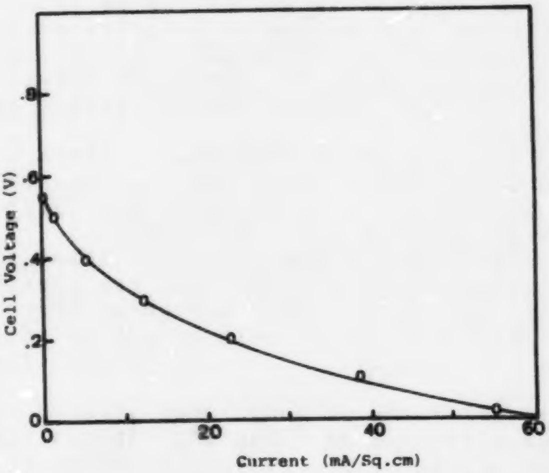

Figure 6: Variation of voltage with current for thermoelectric generator at 500°C.

STATIC AND DYNAMIC PROPERTIES OF ZrO_2 OXYGEN SENSOR

C. T. Young

Bendix Materials Technology Center
Southfield, Michigan 48037
U.S.A.

ABSTRACT

The theoretical cell potential of the O_2(exh.), $Pt/ZrO_2-Y_2O_3/Pt$, O_2(air) solid-electrolyte cell, made in the form of an automotive exhaust-gas oxygen sensor, was discussed using an oxygen vacancy model and an equivalent circuit. The static and dynamic behavior of the sensor were characterized using a program-controlled propane burner tester.

Under static conditions, where the air-fuel mixture was kept constant or varied at a near equilibrium rate, sensor voltage was measured as a function of temperature and air-fuel mixture under different external resistance loads. Equilibrium oxygen partial pressure of the exhaust gas over the platinum catalyst electrode was determined using the Nernst equation. Deviation of sensor behavior due to electrolyte polarization was also investigated.

Under dynamic conditions in which the air-fuel mixture was rapidly changed from one ratio to the other passing the point of stoichiometry, sensor voltages were recorded and analyzed. Sensor voltage switching characteristics were found separable into two stages. The first was a physical desorption stage in which desorption reactions proceeded following the Langmuir-Hinshelwood mechanism in rich-to-lean switching, and the Eley-Rideal mechanism in lean-to-rich switching. In the second stage the sensor voltage varied with the rates of catalytic and electrochemical reactions.

KEYWORDS: ZrO_2, oxygen sensor, properties, vacancy model, equivalent circuit.

RÉSUMÉ

Le potentiel électrochimique théorique de la pile à électrolyte solide de O_2 (gaz d'échappement), $Pt/ZrO_2-Y_2O_3/Pt$, O_2 (air), sous la forme d'un détecteur d'oxygène des gaz d'échappement des automobiles, est étudié au moyen d'un modèle de vide d'oxygène et d'un circuit équivalent. Les caractéristiques du comportement statique et dynamique du détecteur sont établies à l'aide d'un tester d'un brûleur de propane commandé par un programme.

Dans des conditions statiques, où le mélange air-carburant était constant ou variait à un taux voisin de l'équilibre, la tension du détecteur a été mesurée en fonction de la température et du mélange air-carburant sous différentes charges de résistance externes. La pression partielle d'équilibre des gaz d'échappement sur l'électrode catalytique en platine a été déterminée au moyen de l'équation de Nernst. Les écarts de comportement du détecteur attribuables à la polarisation de l'électrolyte ont également été étudiés.

Dans des conditions dynamiques, où les proportions du mélange air-carburant variaient rapidement passé le point de stoechiométrie, la tension du détecteur a été enregistrée et analysée. On a constaté que la variation de tension pouvait être séparée en deux phases. Dans un premier temps, des réactions de désorption se produisent suivant le mécanisme de Langmuir-Hinshelwood lorsque le mélange passe de riche à pauvre, et suivant le mécanisme d'Eley-Rideal dans le cas contraire. Dans un second temps, la tension du détecteur varie en fonction des vitesses des réactions catalytiques et électrochimiques.

INTRODUCTION

The first demonstration of solid ZrO_2 electrolyte as an ionic conductor was in 1900. It was the Nernst glower (1), an early electric lamp, consisted of a bar of ZrO_2 - 15% Y_2O_3 through which electric current was passed. Since then, through advances in materials science and processing technologies, various types of stabilized ZrO_2 electrolytes have been employed in applications such as high temperature fuel cell (2-4), water vapor dissociation cell for hydrogen generation (5,6), oxygen pump (7,8), oxygen concentration monitor for furnace combustion control (9,10), carbon sensor (11,12), high temperature electrode for magneto hydrodynamic power generator (13), and high temperature pH sensor (14).

Recently, the Y_2O_3-stabilized ZrO_2 electrolyte has been widely used as an exhaust-gas oxygen sensor in the automotive industry for closed-loop control of intake air-fuel (A/F) mixture for internal combustion engines. The primary purpose of the closed-loop system is to maintain the intake A/F mixture near the point of stoichiometry where the three-way catalytic converter will function at its highest efficiency to reduce exhaust emissions. A schematic diagram showing an oxygen sensor mounted in the exhaust pipe is given in Figure 1. The electrolyte is made into the shape of a closed-end thimble, with both inner and outer surfaces coated with a layer of catalytic platinum electrode. An oxide layer (not shown in the figure) is coated over the outer platinum electrode to protect the platinum from fast erosion in the high-speed, high-temperature exhaust gas environment. When heated in the exhaust gas with the outer electrode exposed to the exhaust gas and the inner electrode to the ambient air, the sensor cell develops a galvanic potential between the two electrodes. This potential varies with the oxygen content in the exhaust gas, and exhibits a large step change at the point of A/F stoichiometry. The sensor therefore provides an electrical signal indicating whether the exhaust gas is richer or leaner than stoichiometry. The signal is fed to an electronic unit that modulates the A/F metering system to control continuously the inlet A/F mixture to stay within a narrow window at the stoichiometric point.

The physical principles and characteristics of ZrO_2 sensor (15-22) and the electrode processes and electrolyte polarization (23-29) have been extensively studied. Most of these studies focussed on the static properties of the ZrO_2 cell. Recently, Young (30) investigated the dynamic sensor properties in terms of transient switching behavior responding to rapid changes in A/F mixture using a computer-controlled propane burner tester. The purpose of this paper is to summarize the static and dynamic properties of the sensor based on the results obtained from the burner tests and from the literature search.

EXPERIMENTAL PROCEDURES

ZrO_2 oxygen sensors made by three different manufacturers were studied. Although sensor construction was different for each of the sensors, the basic principle and sensor construction were all similar to that shown in Figure 1. The ZrO_2 electrolyte had various compositions containing Y_2O_3 from 8% to 14%, and Al_2O_3 from 3% to 10% as a sintering aid (all percentages in weight).

A program-controlled propane burner tester was used to investigate sensor behavior. Details of this tester have been described in a previous paper (30). In brief, the tester consisted of a long exhaust pipe within which an oxygen sensor can be tested at temperatures from 175° to 870°C. An HP-9825A computer was used to control test parameters and test procedures. The A/F mixture with normalized ratio, λ , varying from 0.91 to 1.10, the external shunting resistance load ranging from 10^1 to 10^{12} Ω, and the sequence of static and dynamic test procedures were all controlled automatically by the computer. The normalized A/F ratio, λ, is defined to be the ratio of actual A/F to stoichiometric A/F. The data acquisition system used for voltage measurement has an input impedance of 10^{12} Ω. Sensor voltages measured with such a system, without other shunting loads, were taken as open-circuit voltages, since the 10^{12} Ω load produced only a maximum of 0.01% error at 195°C.

SENSOR POTENTIAL

Under gas-solid equilibrium, the surface chemical potentials, μ_c and μ_a, of oxygen at the cathodic (inner) and anodic (outer) electrolyte surfaces are related to the partial pressures of oxygen in the gas phases, PO_2 (air) and PO_2 (exh.), by the expressions:

$$\mu_c = \mu_c^o + \frac{RT}{2} \ln [PO_2 \text{ (air)}] \tag{1}$$

$$\mu_a = \mu_a^o + \frac{RT}{2} \ln [PO_2 \text{ (exh.)}] \tag{2}$$

where R is the universal gas constant, T the absolute temperature, and μ_c^o and μ_a^o the standard surface chemical potentials at $PO_2 = 1$ atm. Under open-circuit conditions, there is no net flow of ionic species in the electrolyte because the chemical potential difference between the two surfaces is opposed by an electrical potential difference established between the two electrodes (= -ZFE). The electrical voltage, E_o, between the electrodes under the condition of unity transference number is therefore given by:

$$E_o = \frac{-1}{ZF} (\mu_c^o - \mu_a^o) - \frac{RT}{2ZF} \ln \left[\frac{PO_2\ (air)}{PO_2\ (exh.)}\right] \qquad (3)$$

where Z is the oxygen-ion charge number (= -2) and F the Faraday constant. If no polarization occurs at the interfaces, μ_c^o equals μ_a^o, and Eq. (3) becomes:

$$E_o = \frac{RT}{4F} \ln \left[\frac{PO_2\ (air)}{PO_2\ (exh.)}\right] \qquad (4)$$

This is the well-known form of the Nernst equation.

The electrochemical reaction which governs the surface chemical potentials at the two electrolyte surfaces is:

$$O_{ad}(ERS) + V_o^{++}(ERS) + 2\,\bar{e} \rightleftharpoons O_o^{x}(ERS) \qquad (5)$$

where O_{ad} is an adsorbed atom, V_o^{++} an oxygen vacancy with two positive effective charges, and O_o^{x} an oxygen ion in its normal crystalline site. This reaction can occur only at or near an electrochemical reaction site (ERS), or a triple-point site, where gas, electrolyte and electrode co-exist. Other equilibrium reactions associated with Eq. (5) are:

$$\frac{1}{2} O_2(g) \rightleftharpoons \frac{1}{2} O_{2,ad}(Pt) \qquad (6)$$

$$\frac{1}{2} O_{2,ad}(Pt) \rightleftharpoons O_{ad}(Pt) \qquad (7)$$

$$O_{ad}(Pt) \rightleftharpoons O_{ad}(ERS) \qquad (8)$$

$$V_o^{++}(ERS) \rightleftharpoons V_o^{++}(N\text{-}ERS) \qquad (9)$$

$$O_o^{x}(ERS) \rightleftharpoons O_o^{x}(N\text{-}ERS) \qquad (10)$$

Eq.'s (9) and (10) are diffusion of V_o^{++} and O_o^{x} between an ERS and a non-ERS (N-ERS).

The oxygen chemical potential at the electrolyte surface is inversely proportional to the number of V_o^{++} generated under gas-solid equilibrium. The ZrO_2 cell potential can therefore be studied using the oxygen vacancy model shown in Figure 2. Static and dynamic sensor behavior can be more easily interpreted with this vacancy model. At the anodic electrolyte surface which is in contact with the exhaust gas, a large number of oxygen vacancies are created in the electrolyte surface layer according to Eq. (5). Each of the vacancies so created produces two positive charges at the vicinity of the vacant site in order to maintain electrical neutrality in the electrolyte. This makes the electrolyte surface layer assume a positive charge. The outer platinum electrode takes the electrons produced in Eq. (5) and becomes negatively charged. This constitutes an electrochemical capacitor with its capacitance governed by the number of ERS (N_{ERS}). On the other side of the electrolyte, the cathodic surface remains in equilibrium with the ambient air, and floats at or near the neutral potential.

When an external electrical circuit with resistance R_ℓ is connected to the sensor (see Figure 3), the open-circuit equilibrium is altered. The chemical and electrical potentials cause ionic flow in the electrolyte and electronic flow in the external circuit. Across the electrode-electrolyte (E-E) interfaces the reactions are complicated.

At the anodic interface oxygen ions arrive randomly. Three possible situations develop, which are respectively represented by Eq.'s (11), (12) and (13):

$$O_o^{=}(ZrO_2) + V_o^{x}(ERS) \rightarrow O_o^{=}(ERS) \quad (11a)$$

$$O_o^{=}(ERS) \rightarrow O_{ad}(ERS) + V_o^{x}(ERS) + 2\bar{e} \quad (11b)$$

$$O_o^{=}(ZrO_2) + V_o^{++}(ERS) \rightarrow O_o^{x}(ERS) \quad (12a)$$

$$O_o^{x}(ERS) \rightarrow O_{ad}(ERS) + V_o^{++}(ERS) + 2\bar{e} \quad (12b)$$

$$O_o^{=}(ZrO_2) + V_o^{x}(N\text{-}ERS) \rightarrow O_o^{=}(N\text{-}ERS) \quad (13a)$$

$$O_o^{=}(ZrO_2) + V_o^{++}(N\text{-}ERS) \rightarrow O_o^{x}(N\text{-}ERS) \quad (13b)$$

$$O_o^{=}(N\text{-}ERS) \rightarrow O_o^{=}(ERS) \quad (13c)$$

$$O_o^{x}(N\text{-}ERS) \rightarrow O_o^{x}(ERS) \quad (13d)$$

$$O_o^{=}(ERS) \rightarrow O_{ad}(ERS) + V_o^{x}(ERS) + 2\bar{e} \quad (13e)$$

$$O_o^{x}(ERS) \rightarrow O_{ad}(ERS) + V_o^{++}(ERS) + 2\bar{e} \quad (13f)$$

Some $O_o^{=}$ arrive at ERS's, (11a), and complete (11b).

Some annihilate the V_o^{++} at ERS's, (12a), which is followed by vacancy regeneration, (12b), to restore gas-solid equilibrium. Others arrive at the interface away from ERS's, 13(a) and 13(b), and require surface diffusion in the electrolyte surface layer to the nearby ERS's, (13c) and (13d), before completing (13e) and (13f). This last group of reactions causes a pile-up of $O_o^=$'s , which co-exist with V_o^{++}'s at the E-E interface. The extent of this pile-up depends on the rates of arrival and dissipation of $O_o^=$, and the rate of annihilation between V_o^{++} and $O_o^=$. For an unaged sensor with active outer Pt electrode and large N_{ERS}, the amount of $O_o^=$ pile-up is negligible since the rates of dissipation and annihilation are both high. For an aged sensor in which the N_{ERS} is generally reduced, the amount of $O_o^=$ pile-up may become significant. This $O_o^=$ pile-up causes an anodic interface polarization, and in effect constitutes an $O_o^=$ capacitor across the interface. At the same time, those V_o^{++}'s scattering away from ERS's also forms a V_o^{++} capacitor. These two capacitors, together with the electrochemical capacitor governed by Eq. (5), all combined affect the sensor nonsteady-state properties.

On the cathodic side, molecular dissociation of oxygen on Pt and diffusion of adatoms through Pt first take place.

$$\frac{1}{2}O_2(g) \rightarrow O_{ad}(Pt) \qquad (14a)$$

$$O_{ad}(Pt) \rightarrow O_{ad}(ERS) \qquad (14b)$$

Three possible conditions represented by Eq.'s (15), (16) and (17) subsequently develop:

$$O_{ad}(ERS) + V_o^x(ERS) + 2\bar{e} \rightarrow O_o^=(ERS) \qquad (15)$$

$$O_{ad}(ERS) + V_o^{++}(ERS) + 2\bar{e} \rightarrow O_o^x(ERS) \qquad (16a)$$

$$O_{ad}(ERS) + V_o^{++}(ERS) + 4\bar{e} \rightarrow O_o^=(ERS) \qquad (16b)$$

$$V_o^x(ZrO_2) + O_o^x(ZrO_2) \rightarrow V_o^{++}(ZrO_2) + O_o^=(ZrO_2\text{- to anode}) \qquad (17a)$$

$$V_o^{++}(N\text{-}ERS) + O_o^x(ERS) \rightarrow V_o^{++}(ERS) + O_o^x(N\text{-}ERS) \qquad (17b)$$

$$O_{ad}(ERS) + V_o^{++}(ERS) + 2\bar{e} \rightarrow O_o^x(ERS) \qquad (17c)$$

$$O_{ad}(ERS) + V_o^{++}(ERS) + 4\bar{e} \rightarrow O_o^=(ERS) \qquad (17d)$$

$$V_o^{++}(ZrO_2) + O_o^=(ZrO_2) \rightarrow V_o^x(ZrO_2) + O_o^x(ZrO_2) \qquad (17e)$$

The oxygen adatoms enter the electrolyte through the interface reactions, Eq.'s (15) and (16). The capacitive generation of V_o^{++}, Eq. (17a), occurs when the inner electrode is charged with electrons, which may come from the sensor current itself or from an external current source. It can proceed at ERS or N-ERS. The $O_o^{=}$'s migrate toward the anode, leaving behind V_o^{++}'s piling up at the interface. The extent of this pile-up again depends on the balance between the rates of ionic generation, Eq. (17a), dissipation, Eq.'s (17b), (17c) and (17d), and annihilation, Eq. (17e). This V_o^{++} pile-up causes a cathodic interface polarization. It constitutes a V_o^{++} capacitor across the interface, and has an effect on sensor nonsteady-state properties.

A simplified equivalent circuit for the closed-circuit ZrO_2 oxygen cell is given in Figure 4. The anodic interface is represented by: (1) an electrochemical capacitor (C_{ae}) charged by a variable potential source (E_o) with a variable charging-discharging resistor (R_1); (2) an $O_o^{=}$ capacitor (C_{ao}); (3) a V_o^{++} capacitor (C_{av}) with diffusional charging-discharging resistors R_2 and R_3; and (4) an interface resistor (R_a) corresponding to the average resistance to the interface reactions of Eq.'s (11b) and (12b). The cathodic interface is represented by: (1) a V_o^{++} capacitor (C_{cv}) with a diffusional charging-discharging resistor (R_4); and an interface resistor (R_c) corresponding to the average resistance to the interface reactions of Eq.'s (15), (16a) and (16b). The sensor internal resistance, R_i, becomes:

$$R_i = R_a + R_b + R_c + R_1 \tag{18}$$

where R_b is the bulk electrolyte resistance. The closed-circuit sensor voltage, E, is given by:

$$E = E_o - (E_a + E_b + E_c) \tag{19}$$

where E_o is the open-circuit voltage, and E_a, E_b and E_c are the voltages across the anodic interface, the bulk electrolyte and the cathodic interface. With C_{av}, C_{ao} and C_{cv} across the interfaces, E_a and E_c are variants with time, temperature and sensor current under nonsteady-state conditions. Under steady-state conditions,

$$E = R_\ell \; E_o/(R_\ell + R_i) \tag{20}$$

where R_ℓ is the external resistor load.

It can be seen that the microstructure of the Pt electrodes plays an important role in determining the sensor properties. It controls the N_{ERS}, which affects the charging, discharging and annihilation rates of the pile-up species, and the capacitances of the various capacitors. It also controls the total surface area of the Pt electrode, and the number of diffusion paths (micro-channels in Pt) of oxygen adatoms to ERS's. The former affects the reaction rate of Eq. (14a) and the latter of Eq. (14b), and both combined dictate the catalytic activity of the Pt electrodes.

RESULTS AND DISCUSSION

The afore-mentioned oxygen vacancy model and sensor equivalent circuit developed to describe sensor cell potentials and polarization behavior were based on the results of an extensive testing of sensors using a program-controlled burner tester. Sensor properties were characterized under static as well as dynamic conditions in terms of A/F mixture. Under the static conditions where A/F ratio was kept constant or varied at a near equilibrium rate, sensor voltage was measured as a function of A/F ratio at different temperatures and external resistor loads. Under dynamic conditions where A/F was changed rapidly from one ratio to the other passing the point of stoichiometry, sensor voltage was measured as a function of time for different temperatures and A/F excursions. Test data were recorded on magnetic tapes, and were analyzed. Some of the results representing the static and dynamic properties of aged and unaged sensors are presented in the following sections.

Theoretical Voltage and Equilibrium PO_2

Figure 5 shows two plots of sensor voltage as a function of normalized A/F ratio, λ, measured at 195° and 870°C with an external resistance load of 10^{12} Ω (i.e., the input impedance of the data acquisition system). The measured voltage is taken as the open-circuit voltage, with a maximum error of 0.01% at 195°C. The sensor voltage was measured while the λ value was programmed to have 100 step-changes from 0.91 to 1.10 in the rich-to-lean (R-L) sweep, and another 100 steps from 1.10 back to 0.91 in the lean-to-rich (L-R) sweep. The delay times between two neighboring steps were 13 and 8.5 seconds for 195° and 870°C, respectively, corresponding to a λ-scan rate of 0.0088 λ/min and 0.0134 λ/min for the two temperatures. These slow scan rates were selected in order to allow the sensor sufficient time to establish steady-state voltage under the 10^{12} Ω load condition.

In the two R-L scans in Figure 5, the voltage is seen to decrease with increasing λ, i.e. increasing PO_2. A large step change occurs in each plot at or near the point of stoichiometry. This step change is the direct consequence of a large variation in PO_2 in the exhaust gas over the catalytically active platinum electrode at the stoichiometric point. It is this step-change behavior that provides the useful signal to the A/F metering system for modulating the engine intake A/F mixture.

The λ-response step, i.e., the λ values at which the voltage step took place, was determined at different temperatures. Here, the λ value at which the voltage curve intersected the 450-millivolt level was taken as the λ-response point. The λ values so determined were accurate to within ± 0.001. The results of the measurements are listed in Table I. For both R-L and L-R scans the λ-response step occurs at $\lambda = 1 \pm 0.001$ for temperatures $\geq$ 250°C. Below 250°C the step shifts slightly toward the lean side.

In the above V-λ measurements, the sensor voltage was found to vary with the PO_2 according to the Nernst equation, Eq. (4). The transference number of the ZrO_2 electrolyte was observed to assume a unity value for the present test conditions with 10^{12} Ω load (see the section - Sensor Voltage and Internal Resistance). The equilibrium PO_2 of the exhaust gas can thus be calculated as a function of λ for different temperatures using the Nernst equation. The results of the calculation for a sensor with an active catalytic outer Pt electrode are illustrated in Figure 6. At $\lambda = 0.91$, the equilibrium PO_2 varies from 10^{-46} to 10^{-15} atm when temperature increases from 195° to 870°C. At $\lambda > 1.0$, the PO_2 curves superimpose on top of each other for $T >$ 415°C, and drop to a lower position as the temperature decreases below 415°C. The calculated results for $T >$ 415°C are in good agreement with those of Eddy's (15), who took the data of the equilibrium concentrations of internal engine exhaust gas species computed by Barnes et. al. (31) and converted them into a V-λ plot. The lean PO_2 obtained for $T <$ 400°C was often found to be dependent on the catalytic nature of the outer Pt electrode. The lean PO_2 curves for $T <$ 415°C in Figure 6 may not represent the true equilibrium PO_2.

Voltage Deviation by Interface Polarization

When a sensor is loaded with an external resistor and a significant magnitude of sensor current flows in the circuit, the sensor exhibits a behavior which deviates from that predicted by the Nernst equation. Figure 7 shows six V-λ curves of an unaged sensor obtained at different temperatures and with different loads. The λ was programmed to scan back and forth between 0.945 and 1.062 at a scan rate of 0.0176λ/min.

It should be noted that the unaged sensor had an inner Pt electrode covering only about one-third of the active inner electrolyte surface. The outer Pt electrode had a catalytic activity slightly less than that of the sensor used to obtain those V-λ plots shown in Figure 5.

Figures 7(a), 7(b) and 7(c) were obtained at the same temperature (255°C), but with different resistor loads. With 10^{12} Ω loads, Figure 7(a), a reversible V-λ behavior is observed, in which the R-L and L-R curves retrace each other. A small segment of the L-R curve deviates from the reversible path when λ approaches the stoichiometric point. This type of deviation is typical of a sensor with its outer electrode possessing inadequate catalytic activity compared to an ideal sensor at this temperature. With a 10^6 Ω load, Figure 7(b), a non-reversible behavior of the V-λ curves is detected. The R-L and L-R curves take different paths to complete the λ-scan cycle. At the starting point of the R-L scan, the sensor delivers a voltage of 628 mv and a current of 0.628 μa. The voltage decreases gradually, as does the sensor current, as the λ sweeps toward the lean region. When passing the stoichiometric point, the current drops from 0.6 μa to 0 μa and further to a minimum of -0.08 μa before it shows an increase with increasing λ. This increase in voltage with increasing λ deviates from the V-λ relationship predicted by the Nernst equation. This deviation is obviously caused by the large drop in sensor current after passing the point of stoichiometry where depolarization through discharge of interface pile-up species takes place. The reverse effect occurs in the L-R sweep, in which polarization takes place with increased sensor current after the point of stoichiometry. The same non-reversible behavior, only to a slightly larger extent, was also observed with a 2 x 10^4 Ω load, Figure 7(c).

Figures 7(b), 7(d) and 7(e) are three plots obtained at different temperatures, but with the same resistor load, 10^6 Ω. The sensor currents at λ = 0.945 are roughly the same for the three temperatures (0.628, 0.896 and 0.898 μa for 255°, 350° and 525°C, respectively). The non-reversible nature of the V-λ curves decreases as the temperature increases, and become undistinguishable at temperatures above 400°C.

Figures 7(e) and 7(f) are two plots obtained at the same temperature (525°C) with different loads. With a 10^6 Ω load, the sensor current (0.898 μa) is too small to cause significant polarization at this high temperature. With a 330 Ω load, the current is about 1.3 ma in the rich region. This current is high enough to cause behavior deviation. Although the V-λ curves become reversible, the sensor voltage in the rich region, however, is seen to increase with increasing λ, in contrast to the Nernst relationship. The reason for this deviation is unclear.

The deviate sensor behavior illustrated in Figure 7 is consistent with that of sensors with partially covered inner electrodes, and for sensors with poorly bonded inner electrodes. The extent of deviation increases as the inner Pt electrode coverage decreases, or the electrode bonding is degraded. This suggests that the deviate behavior results primarily from cathodic polarization, i.e., from polarization at the inner E-E interface.

To determine the effect of anodic polarization on loaded sensor behavior, two sensors each with a full inner electrode strongly bonded to the ZrO_2 electrolyte were characterized. These two sensors had gone through a 1000-hour engine dynamometer test. One of the sensors had less degradation of the outer Pt electrode than the other in terms of ERS number and catalytic activity. This was indicated by the results of changes in dynamic A/F transient switching response and increases in sensor internal resistance. The former had a three-fold increase and the latter had an eight-fold increase in internal resistance. Figure 8 shows the V-λ curves of the two sensors both taken at 350°C, 10^6 Ω load and 0.0176 λ/min scan rate. Figure 8(a) is from the sensor with less degradation, in which a reversible V-λ response is detected. This observation, when compared with Figure 7(d), provides an evidence that the non-reversible V-λ characteristics of the unaged sensor illustrated in Figure 7 are primarily the results of cathodic polarization. Figure 8(b) depicts the V-λ curves of the worse sensor. The non-reversible behavior shows up in the picture, and this is due mainly to the reduction of N_{ERS} at the outer E-E interface. Loss of steepness of the voltage step is also detected, which is attributed to the decline of Pt catalytic activity.

It is apparent that the non-reversible V-λ behavior observed at low temperatures is a transient sensor property. It is caused primarily by the time-dependent V_o^{++} polarization and depolarization at the cathodic interface. At 0.0176 λ/min scan rate, it does not allow time for the sensor to establish steady-state conditions for charging or discharging of the V_o^{++} capacitor at the interface after the large step change occurs at the point of stoichiometry.

Sensor Voltage and Internal Resistance

Figure 9 shows the rich ($\lambda = 0.94$) and lean ($\lambda = 1.06$) sensor voltage taken from V-λ scans obtained at different temperatures with three different resistor loads. With a 10^{12} Ω load, the rich voltage varies linearly with temperature according to the Nernst equation at temperatures above 350°C. Below 350°C, the voltage deviates from linearity toward the low side, and amounts to a 2% drop at 195°C. This voltage drop is believed to be associated either with the onset of electronic conductivity or with a decrease in catalytic activity. In any case, the linearity of the rich voltage indicates that the transference number of the ZrO_2 electrolyte for oxygen sensor application has a unity value (0.98 - 1.0) under the test conditions presently employed. The lean output also varies linearly with temperature for $T > 400°C$. Below 400°C the voltage shows an up-swing with decreasing temperature. This deviation results from a declining catalytic activity of the outer Pt as the temperature decreases.

With a 10^7 Ω and a 10^6 Ω load, the sensor voltage decreases rapidly with decreasing temperature below 300° and 400°C, respectively. The output voltages are given by Eq. (20).

The sensor internal resistance, R_i, under steady-state conditions can be determined by measuring the steady-state sensor voltages, V_1 and V_2, under two different resistor loads, R_1 and R_2. The internal resistance is calculated from:

$$R_i = (V_1 - V_2) / (V_2/R_2 - V_1/R_1) \qquad (21)$$

The results obtained from several unaged and aged sensors are given in Figure 10. The two unaged sensors, despite the difference in Y_2O_3 contents, have the same resistance values at all temperatures. The slopes of the straight line yield a single activation energy of 21.0 kcal/mole, which agrees with those of other resistivity or admittance measurements (16,21,32,33).

The sensor internal resistance increases upon aging in application. The hatched band in Figure 10 defines the typical R_i values of sensors after a long time (500-1000 hours) engine dynamometer test or a high mileage (50,000-80,000 KM) vehicle test. The slopes of the straight lines remain about the same as those of the unaged ones. Many of the aged sensors were reworked by stripping-off and recoating the outer Pt electrodes. All the reworked sensors were found to have low internal resistance, the same as the unaged ones.

Apparently, the increase in sensor internal resistance by aging is mainly the result of outer Pt electrode degradation. During the aging period, the Pt electrode underwent sintering, grain-growth and debonding from the ZrO_2 substrate, all leading to a reduction in N_{ERS}. The reduction of N_{ERS} raises the anodic interface resistance R_a, and hence the sensor internal resistance R_i.

Some sensors were prepared using a fritted Pt paste for inner electrode. These sensors exhibited low voltage output and high internal resistance. These undesirable properties were the direct consequence of very limited N_{ERS} at the cathodic interface. Most of the ERS's were blocked by molten frit. The sensors could be activated by rinsing the inner electrode with an acid solution to remove the blocking frit (34). The activated sensor showed high voltage output and low internal resistance.

Dynamic Voltage Switching Behavior

When A/F ratio is changed rapidly from one ratio to the other, passing the $\lambda=1$ point, the sensor voltage switches in responding to the A/F change. A schematic diagram showing typical R-L and L-R switching curves is shown in Figure 11. Details of a study of the voltage transient switching behavior have been described elsewhere (30). The results are briefly discussed here.

When the A/F mixture is suddenly changed from a rich to a lean ratio at time t_0, a gas chemistry transition zone forms and travels along with the gas stream in the exhaust pipe of the burner tester. The gas transition zone reaches and leaves the sensor test site at t_1 and t_2. After the transition zone passes the sensor site, the excess free oxygen in the lean exhaust is first consumed to react with the rich molecular species, which have physically adsorbed on the oxide overcoat, Pt electrode and ZrO_2 electrolyte. The desorption processes of the rich molecules are thermally activated, and proceed following the Langmuir-Hinshelwood mechanism (35) with an activation energy of 2.4 ~ 2.9 kcal/mole (30,35,36). The desorption time, defined to be $t_e-(t_1+t_2)/2$, is given by (30):

$$t_{d\ (R-L)} = C_1 \exp(\Delta H_1/RT)\,[(1-\lambda_R)/(\lambda_L-1)]^{0.3} \qquad (22)$$

where C_1 is a constant, ΔH_1 = 2.4 ~ 2.9 kcal/mole,

λ_R and λ_L the A/F excursion end points, and t_e the end of desorption period.

During the desorption period the outer Pt electrode behaves non-catalytically. The voltage switching rate is controlled by the rate of molecular dissociation of oxygen:

$$\frac{1}{2}\ O_2(g) \rightarrow O_{ad}(Pt), \qquad (23)$$

which has an activation energy of 53 ~ 70 kcal/mole (37,38). The voltage switches slowly during the desorption period.

At the end of the desorption period, t_e, the outer Pt electrode starts to act catalytically and quickly establishes equilibrium PO_2 at ERS's. The voltage switches more rapidly from this point on, depending on the rates of the reactions:

$$O_{ad}(Pt) \rightarrow O_{ad}(ERS) \qquad (24a)$$

$$O_{ad}(ERS) + V_o^{++}(ERS) + 2\,\bar{e} \rightarrow O_o^{x}(ERS) \qquad (24b)$$

$$V_o^{++}(N\text{-}ERS) + O_o^{x}(ERS) \rightarrow V_o^{++}(ERS) + O_o^{x}(N\text{-}ERS) \qquad (24c)$$

For sensors with highly activated outer Pt electrode and large N_{ERS}, Eq. (24b) is rate limiting, and the R-L voltage switching rate is expressed by (30):

$$-\left(\frac{dV}{dt}\right)_{R\text{-}L} = C_2 \exp(-\Delta H_2/RT)\ (V-V_L)^2\ (\lambda_L-1)^{0.3} \qquad (25)$$

where ΔH_2 = 4 ~ 6 kcal/mole, and V_L the voltage at λ_L. An example of this R-L switching behavior is illustrated in Figure 12(a). For other sensors with active outer Pt electrode but having limited N_{ERS}, the values of C_{av}, R_2 and R_a may all be large enough that both Eq.'s (24b) and (24c) become the rate limiting steps in the R-L switching at low temperatures. An example of this type is shown in Figure 12(b). The R-L voltage curve exhibits a break from a fast to a slow rate. The fast switching period is limited by Eq. (24b). The slow period is controlled by Eq. (24c) to move V_o^{++}'s from N-ERS to ERS after the initial V_o^{++}'s at ERS all reacted in Eq. (24b). This slow switching step disappears at high temperatures where diffusional discharge of C_{av} is fast. It also disappears after a short time aging in engine, during which the outer Pt electrode becomes more porous and the capacitance of C_{av} decreases.

In the L-R switch a desorption period is also detected. The L-R desorption processes depend on the

A/F excursion, and are independent of temperature. They proceed following the Eley-Rideal mechanism (35,39). The desorption time is (30):

$$t_{d\ (L\text{-}R)} = C_3\ [(\lambda_L - 1)/(1 - \lambda_R)]^{0.3} \qquad (26)$$

where C_3 is a constant, and λ_L and λ_R as previously defined. During this desorption period the voltage changes slowly with time.

After the desorption period the voltage switches more rapidly according to the rates of:

$$CO(g) + O_o^{\,x}(ERS) \rightarrow CO_2(g) + V_o^{\,++}(ERS) + 2\,\bar{e} \qquad (27a)$$

$$H_2(g) + O_o^{\,x}(ERS) \rightarrow H_2O(g) + V_o^{\,++}(ERS) + 2\,\bar{e} \qquad (27b)$$

$$V_o^{\,++}(ERS) + O_o^{\,x}(N\text{-}ERS) \rightarrow V_o^{\,++}(N\text{-}ERS) + O_o^{\,x}(ERS) \qquad (27c)$$

The voltage switching rate has the expression (30):

$$\left(\frac{dV}{dt}\right)_{L\text{-}R} = C_4\ \exp(-\Delta H_4/RT)\ (V_R - V)^2\ (1-\lambda_R)^{0.3} \qquad (28)$$

where ΔH_4 = 3 ~ 4 kcal/mole, and V_R the voltage at λ_R.

Many aged sensors display an abnormal L-R switching behavior at low temperatures. An example is illustrated in Figure 13. In Figure 13(a) an abrupt change in the L-R switching rate is observed. The voltage curve after this change becomes linear with time. The rate change of this linear period is independent of temperature at T < 300°C, and increases rapidly with temperature at T > 300°C. This linear rate behavior is attributed to the reduction in N_{ERS} due to aging, which leads to a decrease in C_{ae} and increases in C_{av}, C_{ao}, R_2 and R_a. This linear L-R behavior is also found in lead-poisoned sensors tested at temperatures above 650°C (21), where a number of ERS's become plugged by lead-containing fuel residue of low melting point.

With proper selection of the capacitor and resistor components, it was able to simulate the dynamic voltage switching curves shown in Figures 12 and 13 using the equivalent circuit given in Figure 4. It was also able to simulate the V-λ curves illustrated in Figure 7.

SUMMARY

In this paper the operating mechanisms of the ZrO_2 oxygen sensor for automotive application were described. Theoretical sensor potential and voltage polarization behavior, based on mechanistic studies, were discussed in detail. An oxygen vacancy model and a sensor equivalent circuit were proposed. Some test results characterizing the static and dynamic properties of unaged and aged sensors were presented. The results are summarized as follows:

A. Static Properties

1) With a 10^{12} Ω load, a catalytic active sensor behaves normally according to the Nernst equation for $T > 400°C$. Below 400°C the sensor deviates from its normal behavior due to a decline in catalytic activity.

2) Equilibrium PO_2 of the exhaust gas can be determined from sensor voltage measurement for $T > 400°C$. Below 400°C errors set in, particularly for lean PO_2. The measured PO_2 ranges from 10^{-46} atm at 195°C to 10^{-15} atm at 870°C for rich exhaust, and 10^{-2} atm for lean exhaust with $T > 400°C$.

3) The λ-response step of an active sensor occurs at $\lambda = 1.0 \pm 0.001$ for $T > 250°C$. Below 250°C a shift to the lean side is accompanied by decreasing catalytic activity.

4) With an external load resistor which draws significant sensor current, a nonreversible V-λ behavior was detected for $T < 400°C$ at 0.0176 λ/min scan rate. This non-reversible behavior is a transient sensor property caused primarily by a time-dependent V_o^{++} polarization and depolarization at the cathodic interface.

5) The sensor internal resistance increases upon aging due to degradation of the outer Pt electrode. A decrease in the N_{ERS} is the primary mechanism causing the increase in internal resistance.

B. Dynamic Properties

1) In responding to R-L and L-R A/F excursions, the voltage switching processes can be separated into two stages: a physical desorption stage and an electrochemical reaction stage.

2) The R-L desorption process proceeds following the Langmuir-Hinshelwood mechanism. The

desorption time depends on A/F excursion and temperature. The L-R desorption process proceeds following the Eley-Rideal mechanism. The desorption time depends on A/F excursion, but is independent of temperature.

3) The R-L and L-R voltage switching rates after the desorption period are limited by the electrochemical reactions for unaged sensors having catalytically active outer Pt electrodes with large N_{ERS}. For aged sensors with reduced N_{ERS}, the switching rates are controlled by both the electrochemical reactions and the diffusional charging and discharging of V_o^{++} and $O_o^{=}$ piling up at the anodic interface. For aged sensors with declined catalytic activity, the switching rates are limited by molecular dissociation of oxygen on Pt.

ACKNOWLEDGEMENT

The author owed deep appreciations to Dr. J. D. Bode for his technical guidance, and to Messrs. H. P. Wertheimer and J. C. Miller of Autolite Corporation for providing numerous test sensors.

REFERENCES

1. W. Nernst and E. Bose, "Zur Theorie des Auerlichtes," Phys. Zeits. 1 (26), 289-291, 1900.

2. J. Weissbart and R. Ruka, "A Solid Electrolyte Fuel Cell, "J. Electrochem. Soc., 109 (8), 723-726, 1962.

3. B. C. H. Steele, "High Temperature Fuel Cells and Electrolysers," Electrode Processes in Solid State Ionics, D. Reidel Publ. Comp., 367-386, 1976.

4. F. J. Rohr, "High-Temperature Fuel Cells," Solid Electrolytes, Academic Press, 431-451, 1978.

5. H. S. Spacil and C. S. Tedmon, Jr., "Electrochemical Dissociation of Water Vapor in Solid Oxide Electrolyte Cells - I. Thermodynamics and Cell Characteristics," J. Electrochem. Soc., 116 (12), 1618-1627, 1969.

6. H. S. Spacil and C. S. Tedmon, Jr., "Electrochemical Dissociation of Water Vapor in Solid Oxide Electrolyte Cells - II. Materials, Fabrication and Properties," J. Electrochem. Soc., 116 (12), 1628-1633, 1969.

7. D. Yuan and F. A. Kröger, "Stabilized Zirconia as an Oxygen Pump," J. Electrochem. Soc., 116 (5), 594-600, 1969.

8. C. B. Alcock and S. Zador, "Electrolytic Removal of Oxygen from Gases by means of Solid Electrolyte," J. Appl. Electrochem., 2, 289-299, 1972.

9. J. Weissbart and R. Ruka, "Oxygen Gauge," Rev. Sci. Instru., 32 (5), 593-595, 1961.

10. J. A. Brothers and F. Hirschfeld, "Some New Applications for Zirconia Sensors," Mech. Eng'g, 35-37, November, 1980.

11. T. M. Meyers, "Experience With the Carbon Sensor in Furnace Atmosphere Control," Metal Progress, 36-39, 1978.

12. R. N. Blumenthal and A. T. Melville, "Control of Carbon Potential in Heat Treating Atmospheres Using a Carbon Sensor," Industrial Heating, 26-34, May, 1976.

13. R. E. W. Casselton and M. D. S. Watson, "High-Temperature Electrodes Using Stabilized Zirconia," Sci. of Ceramics, IV, 349-365, 1968.

14. L. W. Niedrach, "pH Electrode Works Under Severe Conditions," C & EN, 24, November, 1979.

15. D. S. Eddy, "Physical Principles of the Zirconia Exhaust Gas Sensor," IEEE Trans., VT-23 (4), 125-128, 1974.

16. H. Dueker, K. H. Friese and W. D. Haecker, "Ceramic Aspects of the Bosch Lambda-Sensor," Soc. Automotive Eng'r., 750223, 1975.

17. W. J. Fleming, "Physical Principles Governing Nonideal Behavior of the Zirconia Oxygen Sensor," J. Electrochem. Soc., 124 (1), 21-28, 1977.

18. G. T. Engh and S. Wallman, "Development of the Volvo Lambda-Sond System," Soc. Automotive Eng'r., 770295, 1977.

19. E. Hamann, H. Manger and L. Steinke, "Lambda-Sensor with Y_2O_3-Stabilized ZrO_2-Ceramic for Application in Automotive Emission Control Systems," *Soc. Automotive Eng'r.*, 770401, 1977.

20. D. S. Howarth and R. V. Wilhelm, Jr., "A Zirconia-Based Lean Air-Fuel Ratio Sensor," *Soc. Automotive Eng'r.*, 780212, 1978.

21. C. T. Young and J. D. Bode, "Characteristics of ZrO_2-Type Oxygen Sensors for Automotive Applications," *Soc. Automotive Eng'r.*, 790143, 1979.

22. H. U. Gruber and H. M. Wiedenmann, "Three Years Field Experience with the Lambda-Sensor in Automotive Control Systems," *Soc. Automotive Eng'r.*, 800017, 1980.

23. H. Yanagida, R. J. Brook and F. A. Kroger, "Direct Current-Voltage Characteristics of Calcia-Stabilized Zirconia with Porous Platinum Electrodes," *J. Electrochem. Soc.*, 117 (5), 593-602, 1970.

24. R. J. Brook, W. L. Pelzmann and F. A. Kroger, "Platinum Electrodes and Calcia-Stabilized Zirconia," *J. Electrochem. Soc.*, 118 (2), 185-192, 1971.

25. T. H. Etsell and S. N. Flengas, "Overpotential Behavior of Stabilized Zirconia Solid Electrolyte Fuel Cells," *J. Electrochem. Soc.*, 118 (12), 1890-1900, 1971.

26. S. Pizzini, M. Bianchi, A. Corradi and C. Mari, "Influence of Cell Geometry on the Shape of Polarization Curves of Porous Pt Electrodes on a YSZ Electrolyte," *J. Appl. Electrochem.*, 4, 7-16, 1974.

27. J. Fouletier, P. Fabry and M. Kleitz, "Electrochemical Semi-permeability and the Electrode Microsystem in Solid Oxide Electrolyte Cells," *J. Electrochem. Soc.*, 123 (2), 204-213, 1976.

28. T. G. Gur, I. D. Raistrick and R. A. Huggins, "Steady-State D-C Polarization Characteristics of the O_2,Pt/Stabilized Zirconia Interface," *J. Electrochem. Soc.*, 127 (12), 2620-2628, 1980.

29. R. M. Dell and A. Hooper, "Oxygen Ion Conductors," *Solid Electrolytes*, Academic Press, 291-312, 1978.

30. C. T. Young, "Experimental Analysis of ZrO_2 Oxygen Sensor Transient Switching Behavior," Soc. Automotive Eng'r., 810380, 1981.

31. G. J. Barnes, R. L. Klimisch and B. B. Krieger, "Equilibrium Considerations in Catalytic Emission Control," Soc. Automotive Eng'r., 730200, 1973.

32. J. E. Bauerle, "Study of Solid Electrolyte Polarization by A Complex Admittance Method," J. Phys. Chem. Solids, Pergamon Press, 30, 2657-2670, 1969.

33. T. M. Gur, I. D. Raistrick and R. A. Huggins, "AC Admittance Measurements on Stabilized Zirconia with Porous Platinum Electrodes," Solid State Ionics, 1, 251-271, 1980.

34. C. T. Young, D. J. Romine, P. R. Woodruff, D. C. Davis, J. D. Bode and T. Y. Tien, "Process for Producing an Activated Oxygen Gas Sensor Element," U.S. Patent 4,169,777, 1979.

35. H. P. Bonzel and R. Ku, "Mechanisms of The Catalytic Carbon Monoxide Oxidation on Pt (110)," Surface Science, 33, 91-106, 1972.

36. R. Lewis and R. Gomer, "Adsorption of Oxygen on Platinum," Surface Science, North-Holland Publ. Comp., 12, 157-176, 1968.

37. O. D. Gonzalez and G. Parravano, J. Am. Ceram. Soc., 78, 4533, 1956.

38. G. A. Somorjai, Principle of Surface Chemistry, Prentice-Hall, N.J., 1972.

39. H. P. Bonzel and R. Ku, "Carbon Monoxide Oxidation on a Pt (110) Single Crystal Surface," J. Vac. Sci. Tech., 9 (2), 663-667, 1971.

Table I. λ-RESPONSE STEPS AT DIFFERENT TEMPERATURES

TEMP (°C)	λ-RESPONSE STEP	
	R-L	L-R
195	1.003	1.004
220	1.001	1.002
250	1.001	1.001
285	1.001	0.999
335	0.999	1.001
415	1.000	1.001
515	1.001	0.999
625	0.999	0.999
735	1.001	1.001
870	1.001	1.000

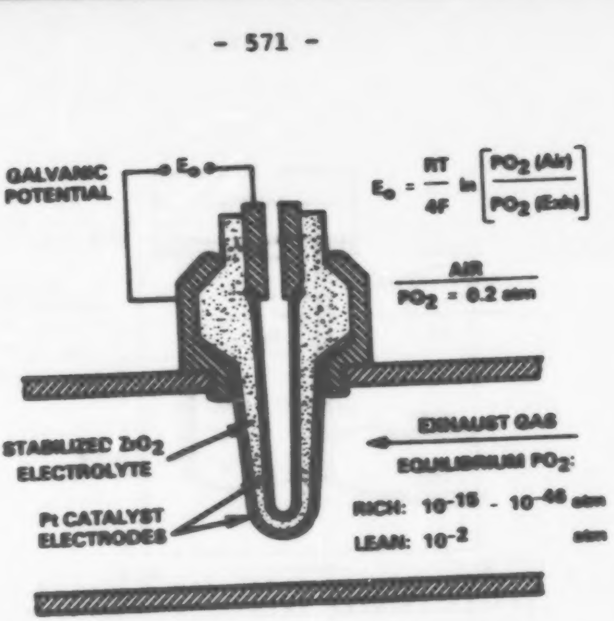
GALVANIC POTENTIAL
E_o
$E_o = \frac{RT}{4F} \ln \left[\frac{PO_2\,(Air)}{PO_2\,(Exh)}\right]$
AIR
PO_2 = 0.2 atm
EXHAUST GAS
EQUILIBRIUM PO_2:
RICH: 10^{-15} - 10^{-48} atm
LEAN: 10^{-2} atm
STABILIZED ZrO_2 ELECTROLYTE
Pt CATALYST ELECTRODES

Fig. 1 Schematic of a ZrO_2 oxygen sensor mounted in an exhaust pipe.

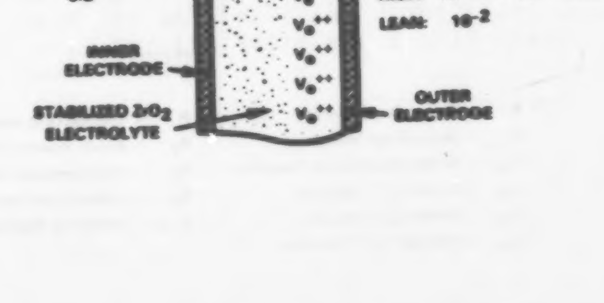
E_o
$E_o = \frac{RT}{4F} \ln \left[\frac{PO_2\,(Air)}{PO_2\,(Exh)}\right]$
REFERENCE AIR
PO_2 (atm)
0.2
EXHAUST GAS
EQUILIBRIUM PO_2:(atm)
RICH: 10^{-15} ~ 10^{-48} atm
LEAN: 10^{-2}
V_o^{++}
INNER ELECTRODE
STABILIZED ZrO_2 ELECTROLYTE
OUTER ELECTRODE

Fig. 2 Oxygen vacancy model for an open-circuit sensor showing generation of cell potential.

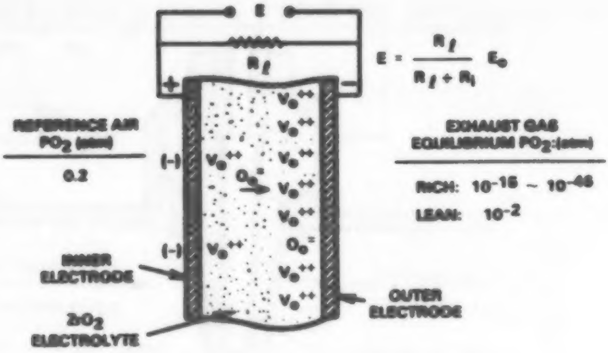
E
R_ℓ
+
−
$E = \frac{R_\ell}{R_\ell + R_i} E_o$
REFERENCE AIR
PO_2 (atm)
0.2
EXHAUST GAS
EQUILIBRIUM PO_2:(atm)
RICH: $10^{-16} \sim 10^{-46}$
LEAN: 10^{-2}
(−)
(−)
V_o^{++}
$O_o^{=}$
INNER
ELECTRODE
OUTER
ELECTRODE
ZrO_2
ELECTROLYTE

Fig. 3 Oxygen vacancy model for a closed-circuit sensor showing interface polarization with pile-up of $O_O^{=}$ at the anodic interface and V_O^{++} at the cathodic interface.

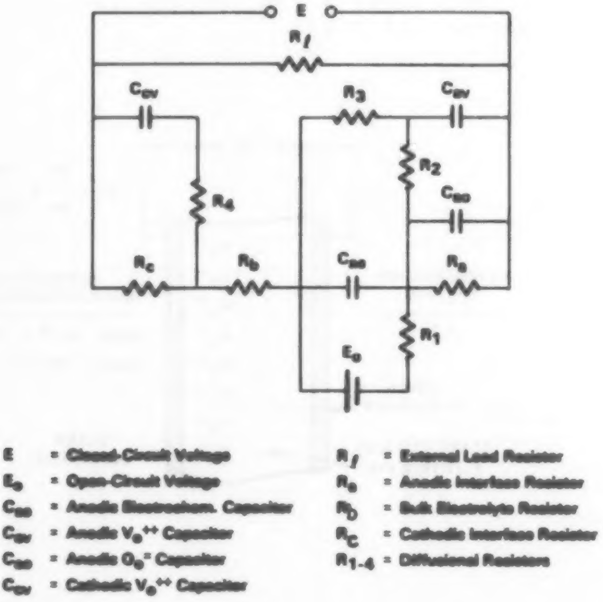
E
R_ℓ
C_{cv}
R_4
R_c
R_b
R_3
C_{av}
R_2
C_{ao}
C_{ae}
R_a
R_1
E_o
E = Closed-Circuit Voltage
E_o = Open-Circuit Voltage
C_{ae} = Anodic Electrochem. Capacitor
C_{av} = Anodic V_o^{++} Capacitor
C_{ao} = Anodic $O_o^{=}$ Capacitor
C_{cv} = Cathodic V_o^{++} Capacitor
R_ℓ = External Lead Resistor
R_a = Anodic Interface Resistor
R_b = Bulk Electrolyte Resistor
R_c = Cathodic Interface Resistor
R_{1-4} = Diffusional Resistors

Fig. 4 Sensor equivalent circuit.

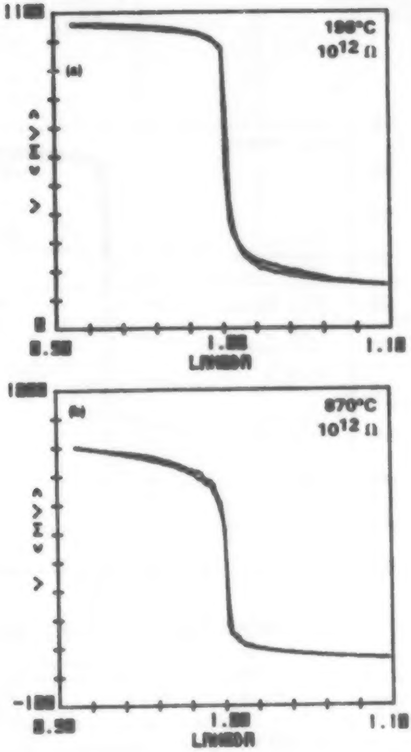

Fig. 5 Voltage vs. λ plots obtained with a 10^{12} Ω load for (a) 195°C and 0.008 λ/min scan rate, and (b) 870°C and 0.0133 λ/min scan rate.

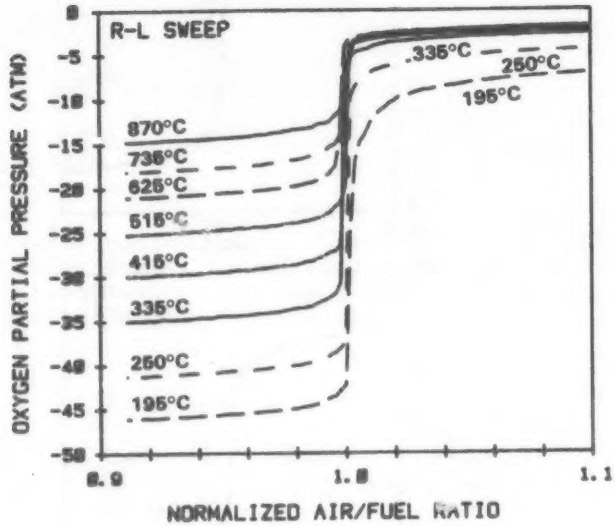

Fig. 6 Oxyen partial pressure calculated from sensor voltage measurement using Nernst equation. Results for T > 400°C are true equilibrium PO_2.

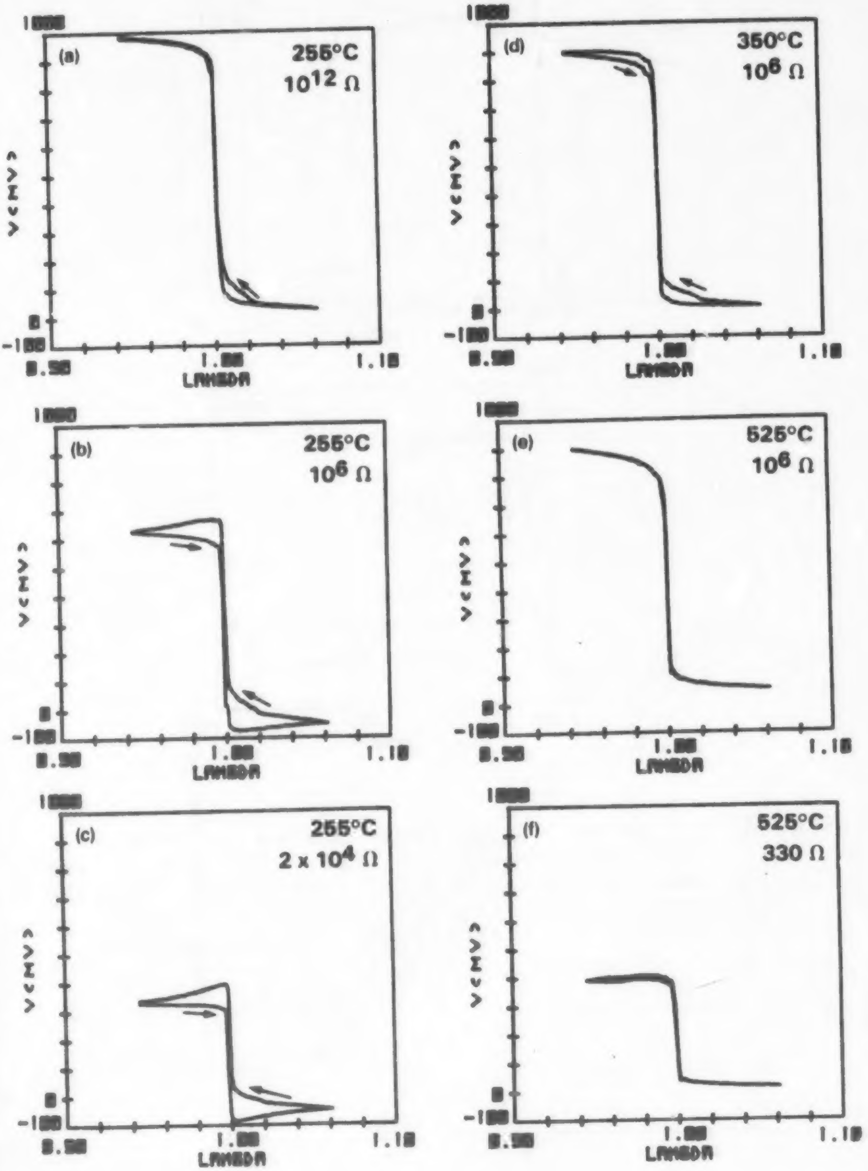

Fig. 7 V-λ curves obtained with a 0.0176 λ/min scan rate for various temperatures and resistor loads.

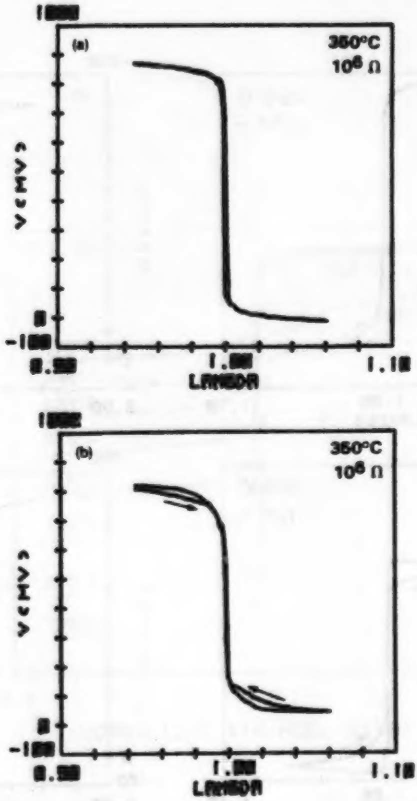

Fig. 8 V-λ curves of two sensors after 1000 hours of engine dynamometer test. (a) from a less degraded sensor and (b) from a more degraded sensor. Note the non-reversible behavior and loss of steepness of the voltage step in (b).

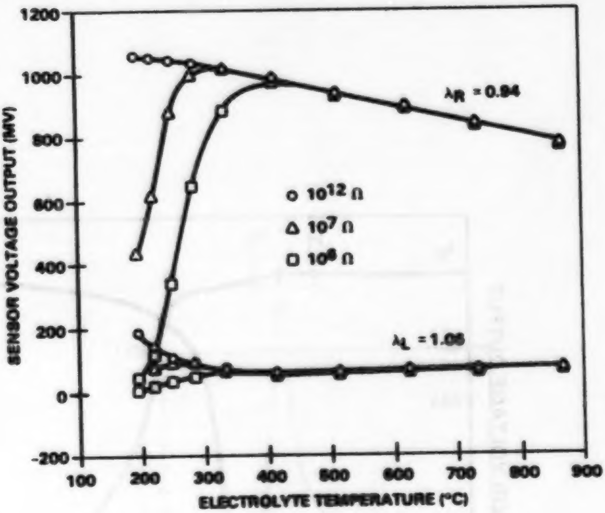

Fig. 9 Sensor voltage as a function of temperature with three different external loads.

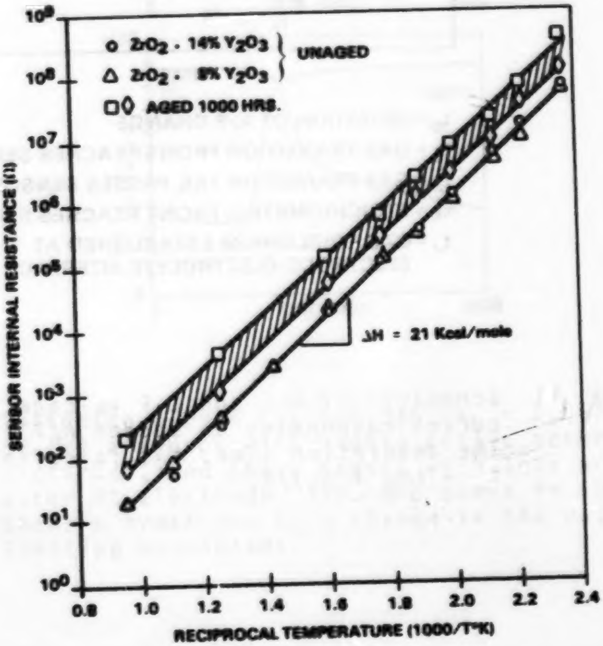

Fig. 10 Sensor internal resistance vs. reciprocal temperature. The hatched band shows the typical resistance value of sensors after long time or high mileage aging.

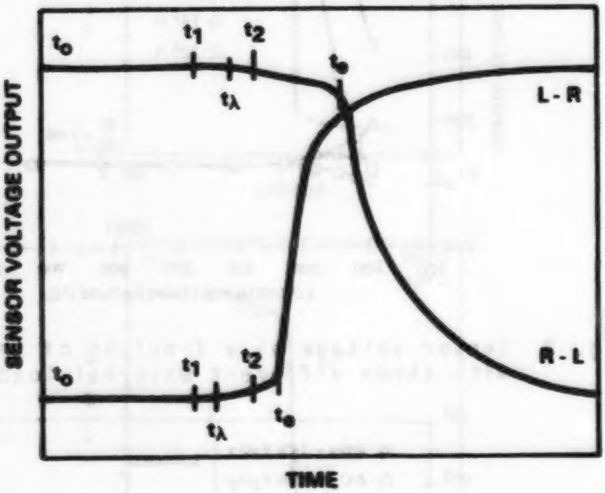
SENSOR VOLTAGE OUTPUT
t_o
t_1
t_2
t_λ
t_e
L - R
t_o
t_1
t_2
t_λ
t_e
R - L
TIME

t_o = INITIATION OF A/F CHANGE
t_1 = GAS TRANSITION FRONT REACHES SENSOR
t_2 = GAS TRANSITION TAIL PASSES SENSOR
t_λ = STOICHIOMETRIC FRONT REACHES SENSOR
t_e = GAS EQUILIBRIUM ESTABLISHED AT ELECTRODE-ELECTROLYTE INTERFACE

Fig. 11 Schematic of R-L and L-R voltage switching curves responding to sudden A/F changes. The desorption time, t_d, is defined to be $t_e - (t_1 + t_2)/2$.

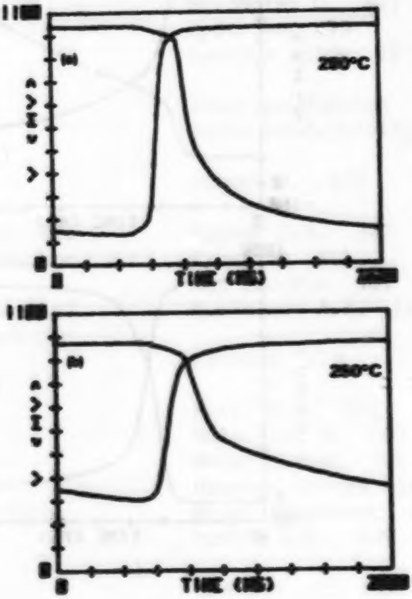

Fig. 12 Switching curves ($\lambda_R = 0.946$, $\lambda_L = 1.051$) of (a) a sensor with highly active outer Pt electrode, and (b) a sensor with less active outer Pt electrode. The R-L curve in (b) shows a break due to a change in the rate limiting mechanisms.

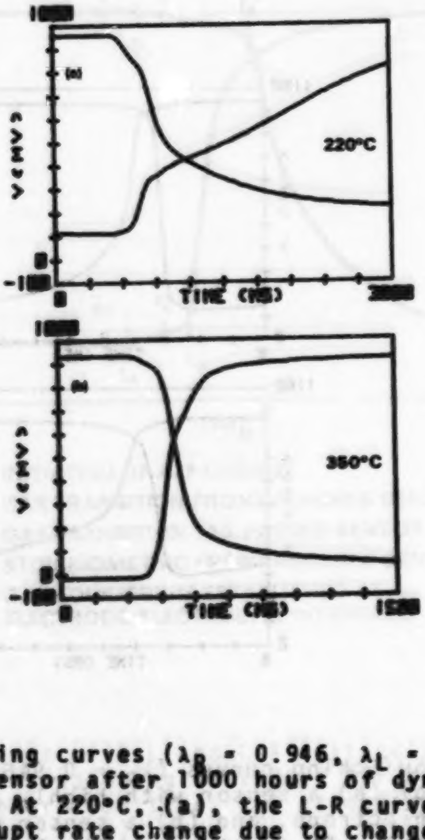

Fig. 13 Switching curves ($\lambda_R = 0.946$, $\lambda_L = 1.061$) of a sensor after 1000 hours of dynamometer test. At 220°C, (a), the L-R curve shows an abrupt rate change due to changes in rate limiting mechanisms. The abnormal behavior disappears at higher temperatures, (b).

INDEX

Ahmad A. 141
Aluminosilicates 529
Anharmonic thermal
  vibrations 27
Anthony A.M. 413

Battery 123, 473, 489
  materials 529
Beta alumina 529
  fabrication 503
  probes 503
Boilot J.P. 91
Brinkman D. 1

Cales B. 413
Capacitor 221, 257
Collin G. 91
Colomban Ph. 91
Conductivity 1, 313, 489
Copper (I) ion conductor 221

Delta bismuth oxide 347
Deterioration beta/beta"
  alumina 169
Diffusion 53, 441
  path 27
Doped ceria 313
Dubreuil A. 503

Effective one particle
  potential 27
El-Adham K. 313
El-Assal K. 529
Electrical conductivity 313
Electrical properties 91
Electrolyser 281, 413
Electron probe analysis 123
Equivalent circuit 549

Faktor J.D. 347
Fluoride ion conductors 391
Fluorite 281
  oxides 347
  structures 391
Framework structures 53
Fuel cell 197, 281, 413, 473

Galvanic Cells 441
Glass 141, 257
Goodenough J.B. 53
Grain boundary 313

Hamou A. 313
Heat of Transport 221
Heating element 413
Holmes C.F. 489
Holzapfel G. 441
Hydrogen 473
Hydrous oxide 197

Ionic conduction 1
Ionic conductivity 347

Jensen J. 473

Kilner J.A. 347
Kinetics 441
Kuo Chu-Kun 441
Kuriakose A.K. 141

Lithium 473

Maiti H.S. 281
Malenfant M. 503
Matar S.F.M. 391
Microstructure 141
Mixed conductor 221
Murthy M.K. 529

Nasicon 91, 141
Neutron diffraction 391
Nicholson P.S. 169
Non metals 1
Non stoichiometry 91
Nuclear magnetic resonance 1

Oxide electrolyte 281, 413
Oxygen gauge 413
Oxygen probe 503
Oxygen sensor 281, 549

Pacemaker 489
Particle hydrate 197

Pelton A.D. 503
Performance 489
Phase boundary reactions 441
Phase transition 53, 91
Potential memory element 221
Prasad S.E. 529
Preparation 91
Probability density 27
Processing 141
Properties 549
Proton conduction 197
Pyrochlores 347

Reactivity 141
Reau J.M. 391
Relaxation 1
Reliability 489
Rickert H. 441
Roy R. 529

Schulz H. 27
Scrosati B. 257
Self diffusion 1
Semi permeable membrane 413
Silver
  ion conductor 221, 257
  solid electrolytes 257
  solid state devices 257
Slip casting 503
Sodium cells 169
Sodium deposition 123
Sodium electrolyte 53
Sodium ion conductor 123, 169
Sodium probe 503
Sodium reference electrodes 503
Sodium sensor 123
Sodium sulphur battery 123
Solid state battery 473
Solid state reactions 441
Soubeyroux J.L. 391
Structural aspects 91
Structural investigation 27, 53, 391
Subbarao E.C. 281
Supersaturation degradation 169

Takahashi T. 221

Vacancy model 549
Vitreous electrolytes 257

Wheat T.A. 141
Wiseman P.J. 197

Young C.T. 549

Zirconia 549